Coupling schemes and unfitted mesh methods for fluid-structure interaction

Mikel Landajuela Larma

Coupling schemes and unfitted mesh methods for fluid-structure interaction

THÈSE DE DOCTORAT

Présentée par

Mikel Landajuela

pour obtenir le grade de

DOCTEUR DE
L' UNIVERSITÉ PIERRE ET MARIE CURIE - Paris VI

Spécialité : Mathématiques Appliquées

Soutenue publiquement le 29 Mars 2016 devant le jury composé de :

Thierry Coupez	Examinateur
Miguel A. Fernández	Directeur de thèse
Lucia Gastaldi	Examinatrice
Céline Grandmont	Examinatrice
Peter Hansbo	Rapporteur
Emmanuel Maitre	Rapporteur
Olivier Pironneau	Examinateur
Erik Burman	Invité

Après avis favorables des rapporteurs: Peter Hansbo et Emmanuel Maitre

Thèse préparée au sein de l'équipe-projet REO
Laboratoire Jacques-Louis Lions
Université Pierre et Marie Curie - Paris 6
et **Centre de Recherche Inria Paris-Rocquencourt**
Domaine de Voluceau, BP 105
78153 Le Chesnay CEDEX

A Luis y a Agurtzane,

Remerciements

Tout d'abord, je tiens à exprimer ma profonde gratitude à mon directeur de thèse Miguel Ángel Fernández. Je le remercie de m'avoir encouragé à travailler tant sur des sujets fortement appliqués que sur des aspects plus theoriques, ce qui m'a permis de développer une idée précise et approfondie de ce qui constitue la recherche en mathématiques appliquées. En plus d'une énorme quantité de nouvelles connaissances, il a aussi su me transmettre sa passion et son dévouement pour la recherche. Je tiens à le remercier pour sa disponibilité et son investissement tout au long de la thèse, ainsi que pour son soutien humain, bien au-dessus de ses obligations strictement académiques.

Je remercie très sincèrement toute l'équipe de professionnels qui constituent le projet REO à Inria. Comme représentant de l'équipe, je tiens à exprimer ma gratitiude à Jean-Frédéric Gerbeau pour le chaleureux accueil dans l'institut et son soutien pendant ces années. Je tiens à remercier en particulier à Marina Vidrascu pour avoir partager son expertise sur le couplage avec des modèles solides non linéaires, cela a grandement contribue a cette thèse. Merci également à Dominique Chappelle (Inria Saclay), avec qui j'ai eu l'occasion de collaborer dans le contexte du *FSI challenge*. Je remercie aussi Maryse pour sa grande assistance avec les laborieuses tâches bureaucratiques. Finalement, je voudrais aussi mettre en valeur le travail de tous ceux qui rendent l'environnement idéal de travail que nous avons à Inria, non seulement pour l'aspect scientifique mais aussi pour le côté humaine.

Je voudrais remercier les rapporteurs Peter Hansbo et Emmanuel Maitre pour avoir accepté de lire ce manuscrit et pour leurs remarques constructives. Je remercie également Thierry Coupez, Lucia Gastaldi, Céline Grandmont et Olivier Pironneau pour avoir accepté de faire partie de mon jury de thèse.

Ensuite, je souhaite remercier tout le bâtiment 16. D'abord, tous ceux qui y étaient déjà et qui m'ont accueilli quand je suis arrivé (je pense à Elisa, Saverio, Grégory et Damiano). Je voudrais saluer aussi tous ceux qui nous ont rejoint aprés. En particulier, merci à Sanjay pour son humour noir, à Chloé pour sa patience avec mon français, à Matteo pour avoir survécu à la Death Valley avec moi (*It was kinda cool!*), á Noémie *por no dejar que se me oxidase el castellano*, et finalement a Fabien et Elliot, la "vraie France", pour toujours avoir la porte de leurs bureaux ouverte. Je ne peux pas ne pas remercier Benoit, avec qui j'ai eu le plaisir de collaborer et sans lequel une partie de cette thèse n'aurait pas été possible. Je n'oubli pas non plus Nora, Nicolas, Yi, Faisal, Paul,... bonne continuation!

Et maintenant les derniers remerciements dans ma langue maternelle. *Un saludo a la pequeña comunidad hispanohablante de Paris, formada por María, Thomas,*

Félix, Mikel e Iñar. Gracias por las tardes de juegos, las cenas y las conversaciones. Agradezco a mis padres, Agurtzane y Luis, a mi hermana, Ane, y a mis tías, Maite y Rosa, el apoyo inquebrantable y el cariño con el que me han acompañado todos estos años. Gracias por participar en esas escapadas de fin de semana en Bilbao que tanto me han ayudado a reponer fuerzas durante este período. Quiero dar las gracias, para terminar, a mi compañera Alba por su comprensión, su cariño y su apoyo todos estos años. Le agradezco especialmente su sonrisa y su alegría contagiosas, y su fuerza, capaz de tirar del carro por los dos en los momentos difíciles. Esta tesis no habría sido posible sin ella.

Paris, France *Mikel Landajuela*
Mars 2016

Coupling schemes and unfitted mesh methods
for fluid-structure interaction

Abstract: This thesis is devoted to the development and analysis of efficient numerical algorithms for the simulation of mechanical systems involving the interaction of a deformable thin-walled structure with an internal or surrounding incompressible fluid flow.

In the first part, we introduce two new classes of explicit coupling schemes using fitted fluid and solid meshes. The methods proposed combine a certain (parameter free) Robin-consistency in the system with (i) a projection-based time-marching in the fluid or (ii) second-order time-stepping in both the fluid and the solid. The stability properties of the methods are analyzed within representative linear settings. This part includes also a comprehensive numerical study in which state-of-the-art coupling schemes (including some of the methods proposed herein) are compared and validated against the results of an experimental benchmark.

In the second part, we consider unfitted mesh formulations. These approaches are more versatile at simulating problems with large interface deflections and/or topological changes. The spatial discretization in this case is based on variants of Nitsche's method with cut elements. Robustness with respect to arbitrary interface intersections is guaranteed through suitable stabilization. For a fictitious domain setting using overlapping meshes, we present two new classes of splitting schemes which exploit the aforementioned interface Robin-consistency in the unfitted framework. The semi-implicit or explicit nature of the splitting in time is dictated by the order in which the spatial and time discretizations are performed. In the case of the coupling with immersed structures, weak and strong discontinuities across the interface are allowed for the velocity and pressure, respectively. Stability and error estimates are provided, using energy arguments within a linear setting. A series of numerical tests, involving static and moving interfaces, illustrates the performance of the different methods proposed.

Keywords: Fluid-structure interaction, Coupling schemes, Partitioned algorithms, Time-accurate schemes, Unfitted mesh methods, Nitsche's method, XFEM, Thin-walled solids.

Schémas de couplage et méthodes de maillage non compatibles pour l'interaction fluide-structure

Resumé: Cette thèse est dédiée au développement et à l'analyse des algorithmes numériques efficaces pour la simulation des systèmes mécaniques impliquant l'interaction entre une structure mince déformable et un fluide incompressible interne ou qui l'entoure.

Dans la première partie, nous introduisons deux nouvelles classes de schémas de couplage explicites en utilisant des maillages compatibles pour le fluide et le solide. Les méthodes proposées combinent une certaine consistance Robin dans le système avec (i) un schéma à pas fractionnaire pour le fluide ou (ii) une discrétisation temporelle d'ordre deux pour le fluide et le solide. Les propriétés de stabilité des méthodes sont analysées dans un cadre linéaire représentatif. Cette partie inclut aussi une étude numérique exhaustive dans laquelle plusieurs schémas de couplage (dont certains proposés ici) sont comparés et validés avec des résultats expérimentaux.

Dans la seconde partie, nous considérons des maillages non compatibles. Ces approches sont plus versatiles quand il s'agit de simuler des problèmes avec des grands déplacements et/ou des changements topologiques. La discrétisation spatiale est basée, dans ce cas là, sur des variantes de la méthode de Nitsche avec éléments coupés. La méthode est robuste par rapport à des intersections arbitraires entre les maillages fluide et solide grâce à des termes de stabilisation appropriés. Dans un contexte de domaine fictif avec des maillages superposés, nous présentons deux nouveaux types de schémas de découplage qui exploitent la susmentionée condition de Robin en utilisant des maillages incompatibles. Le caractère semi-implicite ou explicite du couplage en temps dépend de l'ordre dans lequel les discrétisations spatiales et temporelles sont effectuées. Dans le cas d'un couplage avec des structures immergées, la vitesse et la pression discrètes permettent des discontinuités faibles et fortes à travers l'interface, respectivement. Des estimations de stabilité et d'erreur sont fournies en utilisant des arguments d'énergie dans un cadre linéaire. Une série de tests numériques, avec des interfaces statiques et mobiles, illustre la performance des différentes méthodes proposées.

Mots-clés: Interactions fluide-structure, Schémas de couplage, Algorithmes partitionnés, Méthodes de maillages non compatibles, Méthode de Nitsche, XFEM, Structures minces.

Contents

Introduction

Thesis general context

Mechanical systems involving the interaction of a deformable thin-walled structure with an internal or surrounding incompressible fluid flow appear in a wide variety of scientific and engineering fields: from the aeroelasticity of sailing boats and parachutes, to sloshing dynamics in tanks, heat exchangers design, microencapsulation technology and the biomechanics of animal cells and physiological flows (see, e.g., [LPQR12, TT12, ESM09, PPdL11, Poz10, YM10, HH11, MXA+12]).

An application of particular interest in this thesis is the numerical simulation of blood flows. This includes, for instance, the interaction between blood and the vessel wall in large arteries (see, e.g., [HH11, MXA+12]) or the opening and closing dynamics of heart valves when blood is propelled into the arteries (see, e.g., [AGPT09]). The underlying motivation is that, computer based simulations in patient-specific geometries, can be used by the physicians to enhance diagnosis and therapy planing (see, e.g., [TDK+99, FQV09]). Moreover, such simulations can also be a major ingredient in the design and optimization of medical devices (see, e.g., [LJGO+03, SS04]). These applications, together with the growing interest in addressing inverse problems for model personalization (see [PVV11, BMG12]), call for efficient and accurate numerical methods.

Position of the thesis

The basic principle of this work is that, for efficiency, the numerical methods must introduce a significant degree of splitting between the fluid and solid time-steppings. In other words, they must avoid strong coupling (i.e., the fully implicit treatment of the kinematic-dynamic coupling). This is a challenging problem since, in incompressible fluid-structure interaction, the interface coupling can be extremely stiff (see Section 1.4.3.3).

With regard to the spatial discretization, the numerical approximations of these coupled systems are generally tailored to the amount of solid displacement within the fluid. Hence, problems with low or moderate interface displacements are treated by using a moving fitted mesh technique, based on an ALE (arbitrary Lagrangian-Eulerian) description of the fluid. This enables a simple and accurate prescription of the interface conditions. Since the beginning of this century, the development of efficient splitting methods within this framework has been a very active field of research and the subject of numerous achievements (see Section 1.3.2). In particular, unconditional stability and optimal first-order accuracy can be obtained via a specific explicit Robin-Neumann treatment of the interface coupling (see Section 1.4.3.5). This enables the full splitting of the fluid and solid time-marchings. In the first part of this thesis, different (first- and second-order) time discretizations are investigated

within this coupling paradigm, including some comparisons with experimental data.

For problems involving large structural deflections, with solids that might come into contact or that might break up, the situation is much more delicate. In this case, the ALE formalism becomes cumbersome. A favoured alternative is to combine an Eulerian formalism in the fluid with an unfitted mesh discretization, in which the fluid-structure interface deforms independently of a background fluid mesh (see Sections 1.3.1.2-1.3.1.3). In general, these methods are known to be inaccurate in space, e.g., because the space discretization does not allow for weak and strong discontinuities across the immersed interface (sub-optimal convergence and spurious oscillations). Moreover, the design and analysis of splitting schemes which avoid strong coupling in this unfitted mesh framework have been rarely addressed in the literature so far. These difficulties are addressed in the second part of the thesis.

Thesis outline and main contributions

We highlight below the contributions of this work chapter by chapter. For the sake of completeness, they are recalled and motivated at the beginning of each chapter.

Chapter 1. This is an introductory chapter. We present some standard material regarding the mathematical modeling of fluid-structure interaction problems. A review of the state-of-the-art on numerical techniques for fluid-structure interaction is presented. For a representative linear model, the full discretization, using fitted and unfitted meshes and different coupling schemes, is discussed. In particular, two cornerstones of this thesis are described in detail: the Robin-Neumann explicit coupling paradigm of [Fer13] and the unfitted Nitsche discretization using overlapping meshes of [BF14b].

Part I. Fitted mesh methods

Chapter 2. This chapter shows how the Robin-Neumann coupling paradigm of can be formulated with a projection-based time-marching in the fluid. The resulting schemes enable (for the first time) a fully decoupled computation of the entire fluid-solid state (velocity, pressure, displacement). For a linear coupled problem, we present a priori energy estimates which guarantee unconditional stability for some of the variants. The proposed fully decoupled schemes are also formulated within a non-linear framework. A thorough numerical study, including the simulation of blood flow within a patient-specific geometry under physiological conditions, shows that the proposed methods preserve the stability and accuracy of the original Robin-Neumann schemes.

Chapter 3. We investigate the extension of the explicit Robin-Neumann coupling to deliver second-order time-accuracy through suitable time-stepping in the fluid and solid subsystems. We present theoretical results which give some insight

on the stability properties of the methods. Two second-order time-accurate methods are presented and investigated numerically.

Chapter 4. We present a thorough numerical study in which a representative sample of state-of-the-art coupling schemes for fluid-structure interaction (including the schemes introduced in Chapter 2) are, for the first time, compared and validated against the experimental results of a benchmark.

Part II. Unfitted mesh methods

Chapter 5. We address the formulation and the analysis of the Robin-Neumann splitting in the unfitted mesh framework. Two new classes of semi-implicit or explicit splitting schemes are derived, depending on the order in which the space and time discretization are performed. For the first class of schemes, a complete energy-based stability and a priori error analysis is presented. For the second class, stability and a priori error estimates are presented for one of the variants. A numerical study in a benchmark confirms that the stability and accuracy of the original splitting is preserved in the unfitted framework.

Chapter 6. In this chapter we introduce an accurate and robust Nitsche-XFEM method for the coupling of an incompressible fluid with immersed thin-walled structures. The second contribution has to do with the time-discretization. Several coupling schemes with different degrees of fluid-solid splitting are presented, some of them based on the ideas reported in Chapter 5. A thorough numerical study, involving static and moving interfaces, illustrates the performance of the methods introduced. In particular, the proposed semi-implicit schemes (i) deliver superior stability and accuracy with respect to alternative methods of explicit nature; (ii) avoid the strong coupling of alternative coupling schemes without compromising stability and accuracy.

Author's bibliography

- Papers in peer reviewed journals:

  1. M. A. Fernández, M. Landajuela, **A fully decoupled scheme for the interaction of a thin-walled structure with an incompressible fluid**. *Comptes Rendus Mathématique, 351(3):161-164, 2013.*
  2. M. A. Fernández, M. Landajuela, **Splitting schemes for incompressible fluid/thin-walled structure interaction with unfitted meshes**. *Comptes Rendus Mathématique, 353(7):647-652, 2015.*
  3. M. A. Fernández, M. Landajuela, M. Vidrascu, **Fully decoupled time-marching schemes for incompressible fluid/thin-walled structure interaction**. *Journal of Computational Physics, 297:156-181, 2015.*

4. F. Alauzet, B. Fabrèges, M. A. Fernández, M. Landajuela, **Nitsche-XFEM for the coupling of an incompressible fluid with immersed thin-walled structures**. *Computer Methods in Applied Mechanics and Engineering,* To appear*, 2015,* *https://hal.inria.fr/hal-01149225*.

- Papers in conference proceedings:

5. M. A. Fernández, M. Landajuela, J. Mullaert, M. Vidrascu, **Robin-Neumann schemes for incompressible fluid-structure interaction**. *In Domain Decomposition Methods in Science and Engineering XXII, Lecture Notes in Computer Science (LNCS)*. Dickopf, Th., Gander, M.J., Halpern, L., Krause, R., Pavarino, L.F. (Eds.), Lugano, Switzerland, 2015, DOI: 10.1007/978-3-319-18827-0, https://hal.inria.fr/hal-01113088.

- Submitted papers:

6. M. Landajuela, M. Vidrascu, D. Chapelle, M. A. Fernández, **Coupling schemes for the FSI forward prediction challenge: comparative study and validation**. Submitted to *International Journal for Numerical Methods in Biomedical Engineering*. https://hal.inria.fr/hal-01239931.
7. M. A. Fernández, M. Landajuela, **Unfitted formulations and splitting schemes for incompressible fluid/thin-walled structure interaction**. Submitted to *ESAIM: Mathematical Modelling and Numerical Analysis*.

Funding

This work was supported by Inria and the French National Research Agency (ANR) through the EXIFSI project (ANR-12-JS01-0004) (see https://project.inria.fr/exifsi/).

Chapter 1

Numerical methods for incompressible fluid-structure interaction

In this chapter we present some standard material regarding the mathematical modeling of fluid-structure interaction problems. Some of the available numerical techniques for this type of problems are reviewed according to two classification criteria: the modeling framework adopted and the degree of fluid-solid splitting. We present the detailed fully discrete (space and time) treatment of a linear problem, using fitted and unfitted meshes and a range of different coupling schemes.

Contents

1.1 Introduction

In the following, it is assumed that the reader is familiar with the fundamentals of continuum mechanics (*kinematics of continuum media*, *conservation laws* and *constitutive relations*). We refer to [Mal69, Gur81] for introductory texts to continuum mechanics. For general introductions to fluid-structure interaction, we refer to [FFGQ09, Ast10] and the references therein. We refer also to [Nob01] for an extensive discussion of the *Arbitrary Lagrangian-Eulerian* (ALE) formulation, which is only briefly presented in this chapter. The reader interested in a more in-depth discussion in the mathematical aspect of solid mechanics is referred to [Cia88]. The material reported in this chapter regarding the modeling of thin-walled solids

is basically based on [CB11] and [FFGQ09]. Regarding the numerical treatment of the coupled problem, introductory material can be found in [FG09]. See also [HWL12, Fer11a] for recent reviews.

This chapter is organized as follows. Section 1.2 is devoted to the mathematical modeling of fluid-structure interaction problems. A review of some of the state-of-the-art numerical techniques for their approximation is presented in Section 1.3. The full discretization of a model linear coupled problem is discussed, using both fitted and unfitted meshes and different coupling schemes, in Section 1.4.

1.2 Fluid-structure interaction

We consider a mechanical system involving a deformable structure and a fluid medium occupying, respectively, the domain $\Omega^{\mathrm{s}}(t)$ and $\Omega^{\mathrm{f}}(t)$ in their current configuration. Here, $\Omega^{\mathrm{s}}(t), \Omega^{\mathrm{f}}(t) \subset \mathbb{R}^d$, $d = 2, 3$, for all $t \in \mathbb{R}^+$. The domain $\Omega^{\mathrm{f}}(t)$ evolves in time according to the deformation of $\Omega^{\mathrm{s}}(t)$, but $\Omega \stackrel{\mathrm{def}}{=} \Omega^{\mathrm{f}}(t) \cup \Omega^{\mathrm{s}}(t)$ is assumed to be fixed for all $t \in \mathbb{R}^+$ (see Figure 1.1). The current configuration of the fluid-structure interface is given by $\Sigma(t) \stackrel{\mathrm{def}}{=} \partial\Omega^{\mathrm{f}}(t) \cap \partial\Omega^{\mathrm{s}}(t)$. We denote by $\Omega^{\mathrm{f}} \cup \Omega^{\mathrm{s}}$ a reference configuration of the system, which can be taken, for instance, as the initial configuration. The reference fluid-structure interface is given by $\Sigma \stackrel{\mathrm{def}}{=} \partial\Omega^{\mathrm{f}} \cap \partial\Omega^{\mathrm{s}}$. Furthermore, the following partitions of the fluid and solid boundaries are considered,

$$\partial\Omega^{\mathrm{f}} = \Gamma_{\mathrm{in}} \cup \Gamma_{\mathrm{out}} \cup \Gamma_{\mathrm{wall}} \cup \Sigma, \quad \partial\Omega^{\mathrm{s}} = \Gamma_{\mathrm{d}}^{\mathrm{s}} \cup \Sigma,$$

with Γ_{in}, Γ_{out}, Γ_{wall} and $\Gamma_{\mathrm{d}}^{\mathrm{s}}$ remaining fixed during the evolution of the system (see Figure 1.1). Finally, we denote by $\boldsymbol{n}$ and $\boldsymbol{n}^{\mathrm{s}}$ the outward normal vector of the fluid and solid boundaries respectively, the same notation being used for the current and reference configuration.

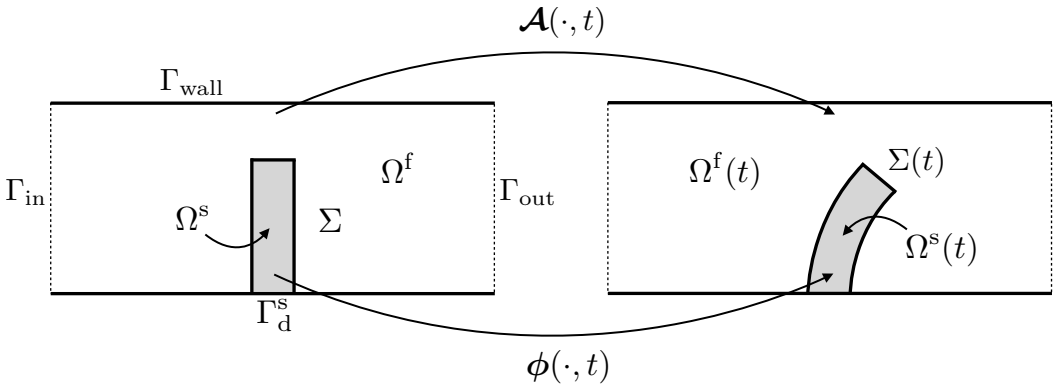

Figure 1.1: Geometrical configuration.

1.2.1 Fluid equations

The fluid, which is assumed to be *homogeneous*, *incompressible* and *Newtonian*, is governed by the *Navier-Stokes equations*. This is a common modeling assumption when describing blood in large (or medium size) arteries (see, e.g., [Thi08, FPQ09]). In the sequel, we introduce these equations in the Eulerian and in the ALE framework.

1.2.1.1 Eulerian formulation of the Navier-Stokes equations

The Navier-Stokes equations in the Eulerian frame reads: find the fluid velocity $\boldsymbol{u} : \Omega^{\mathrm{f}}(t) \times \mathbb{R}^+ \to \mathbb{R}^d$ and the pressure $p : \Omega^{\mathrm{f}}(t) \times \mathbb{R}^+ \to \mathbb{R}$, such that

$$\begin{cases} \rho^{\mathrm{f}}\big(\partial_t \boldsymbol{u} + \boldsymbol{u} \cdot \boldsymbol{\nabla} \boldsymbol{u}\big) - \mathbf{div}\boldsymbol{\sigma}(\boldsymbol{u}, p) = \mathbf{0} & \text{in} \quad \Omega^{\mathrm{f}}(t), \\ \qquad\qquad\qquad\qquad \mathrm{div}\boldsymbol{u} = 0 & \text{in} \quad \Omega^{\mathrm{f}}(t), \end{cases} \tag{1.1}$$

where ρ^{f} stands for the *fluid density* and $\boldsymbol{\sigma}(\boldsymbol{u}, p) \overset{\text{def}}{=} -p\boldsymbol{I} + 2\mu\boldsymbol{\varepsilon}(\boldsymbol{u})$ for the *fluid Cauchy stress tensor*, with μ the *fluid dynamic viscosity* and $\boldsymbol{\varepsilon}(\boldsymbol{u}) \overset{\text{def}}{=} \frac{1}{2}\big(\boldsymbol{\nabla}\boldsymbol{u} + \boldsymbol{\nabla}\boldsymbol{u}^{\mathrm{T}}\big)$ the *strain rate tensor*.

System (1.1) has to be complemented with an initial condition for the velocity, $\boldsymbol{u}(0) = \boldsymbol{u}_0$ in $\Omega^{\mathrm{f}}(0)$, and with suitable boundary conditions. For instance, Dirichlet and Neumann boundary conditions can be prescribed on Γ_{in}, Γ_{wall} and Γ_{out} as follows

$$\begin{cases} \boldsymbol{u} = \boldsymbol{u}_{\mathrm{in}} & \text{on} \quad \Gamma_{\mathrm{in}}, \\ \boldsymbol{u} = \mathbf{0} & \text{on} \quad \Gamma_{\mathrm{wall}}, \\ \boldsymbol{\sigma}(\boldsymbol{u}, p)\boldsymbol{n} = -p_{\mathrm{out}}\boldsymbol{n} & \text{on} \quad \Gamma_{\mathrm{out}}, \end{cases} \tag{1.2}$$

where $\boldsymbol{u}_{\mathrm{in}}$ and p_{out} denote, respectively, an inlet velocity and an outlet pressure profile. The discussion regarding boundary conditions over $\Sigma(t)$ is postponed until Section 1.2.3.

1.2.1.2 ALE formulation of the Navier-Stokes equations

In the ALE framework, the moving fluid domain $\Omega^{\mathrm{f}}(t)$ is supposed to be parametrized by a smooth injective map

$$\boldsymbol{\mathcal{A}} : \Omega^{\mathrm{f}} \times \mathbb{R}^+ \to \mathbb{R}^d, \quad (\widehat{\boldsymbol{x}}, t) \longrightarrow \boldsymbol{x} = \boldsymbol{\mathcal{A}}(\widehat{\boldsymbol{x}}, t),$$

such that $\Omega^{\mathrm{f}}(t) = \boldsymbol{\mathcal{A}}(\Omega^{\mathrm{f}}, t)$ for all $t \in \mathbb{R}^+$ (see Figure 1.1), and which is given by the relation $\boldsymbol{\mathcal{A}} = \boldsymbol{I}_{\Omega^{\mathrm{f}}} + \boldsymbol{d}^{\mathrm{f}}$, where $\boldsymbol{d}^{\mathrm{f}} : \Omega^{\mathrm{f}} \times \mathbb{R}^+ \to \mathbb{R}^d$ is the fluid domain displacement. The fluid domain velocity is denoted by $\widehat{\dot{\boldsymbol{d}}}^{\mathrm{f}} \overset{\text{def}}{=} \partial_t \boldsymbol{\mathcal{A}}$. The deformation gradient and Jacobian associated to the deformation $\boldsymbol{\mathcal{A}}_t \overset{\text{def}}{=} \boldsymbol{\mathcal{A}}(\cdot, t)$ are given, respectively, by $\boldsymbol{F} \overset{\text{def}}{=} \boldsymbol{\nabla}\boldsymbol{\mathcal{A}}_t$ and $J \overset{\text{def}}{=} \det \boldsymbol{F}$.

Any physical field q involved in the description of the fluid can be alternatively evaluated on the reference configuration, adopting $(\widehat{\boldsymbol{x}}, t)$ as independent variables,

or on the current configuration, adopting instead $(\boldsymbol{x}, t)$. Using the superscript $\widehat{\ }$ to indicate the former alternative, the relation between both formulations is given by

$$\begin{aligned} \widehat{q}(\widehat{\boldsymbol{x}}, t) &\stackrel{\text{def}}{=} q(\boldsymbol{\mathcal{A}}_t(\widehat{\boldsymbol{x}}), t) \qquad && \forall \widehat{\boldsymbol{x}} \in \Omega^{\text{f}}, \\ q(\boldsymbol{x}, t) &\stackrel{\text{def}}{=} \widehat{q}(\boldsymbol{\mathcal{A}}_t^{-1}(\boldsymbol{x}), t) \qquad && \forall \boldsymbol{x} \in \Omega^{\text{f}}(t). \end{aligned} \tag{1.3}$$

Along this chapter, if the same field appears evaluated on the reference and current configuration, we adopt the superscript $\widehat{\ }$ to distinguish between formulations. If a field is defined always in the same configuration, there is no place for confusion, and the superscript is not used.

The Navier-Stokes equations in the ALE frame reads: find the fluid velocity $\widehat{\boldsymbol{u}} : \Omega^{\text{f}} \times \mathbb{R}^+ \to \mathbb{R}^d$ and the pressure $\widehat{p} : \Omega^{\text{f}} \times \mathbb{R}^+ \to \mathbb{R}$, such that

$$\begin{cases} \rho^{\text{f}} \partial_t \boldsymbol{u}|_{\boldsymbol{\mathcal{A}}} + \rho^{\text{f}} (\boldsymbol{u} - \dot{\boldsymbol{d}}^{\text{f}}) \cdot \boldsymbol{\nabla} \boldsymbol{u} - \mathbf{div} \boldsymbol{\sigma}(\boldsymbol{u}, p) = \boldsymbol{0} \quad \text{in} \quad \Omega^{\text{f}}(t), \\ \qquad\qquad\qquad\qquad\qquad \text{div} \boldsymbol{u} = 0 \quad \text{in} \quad \Omega^{\text{f}}(t), \end{cases} \tag{1.4}$$

where $\partial_t \boldsymbol{u}|_{\boldsymbol{\mathcal{A}}}$ stands for the ALE time derivative. We recall that $\widehat{\partial_t \boldsymbol{u}|_{\boldsymbol{\mathcal{A}}}} \stackrel{\text{def}}{=} \partial_t \widehat{\boldsymbol{u}}$. As in the previous section, the system is complemented with the initial condition $\boldsymbol{u}(0) = \boldsymbol{u}_0$, with the boundary conditions (1.2) and with suitable coupling conditions over $\Sigma(t)$.

Remark 1.1 *The benefits of formulation* (1.4) *with respect to* (1.1)*, when working with an evolving computational domain, comes from the presence of the ALE time-derivative. This time-derivative can be naturally approximated when using moving meshes, since incremental quotients in that case involve nodal values associated to different spatial locations.*

1.2.2 Structure equations

We suppose that an elastic material governed by the general d-dimensional *non-linear elastodynamics equations* fills the domain $\Omega^{\text{s}}(t)$. We use this model to write the non-linear coupled fluid-structure problem in Section 1.2.3. Nevertheless, in view of the prominent role played by thin-walled solid models in this work, we also present different alternatives to describe the solid behavior in terms of equations written in domains of co-dimension one (shell, plate or string models). This allows to effectively reduce the full d-dimensional solid problem to a $(d-1)$-dimensional problem.

1.2.2.1 The elastodynamics equations

The solid domain $\Omega^{\text{s}}(t)$ is supposed to be parametrized in terms of a smooth, injective and orientation preserving mapping

$$\boldsymbol{\phi} : \Omega^{\text{s}} \times \mathbb{R}^+ \longrightarrow \mathbb{R}^d, \quad (\widehat{\boldsymbol{x}}, t) \longrightarrow \boldsymbol{x} = \boldsymbol{\phi}(\widehat{\boldsymbol{x}}, t)$$

such that $\Omega^{\rm s}(t) = \boldsymbol{\phi}(\Omega^{\rm s}, t)$ for all $t \in \mathbb{R}^+$ (see Figure 1.1). In the following, we denote by $\boldsymbol{d}(\widehat{\boldsymbol{x}}, t) \stackrel{\rm def}{=} \boldsymbol{\phi}(\widehat{\boldsymbol{x}}) - \widehat{\boldsymbol{x}}$, $\widehat{\boldsymbol{x}} \in \Omega^{\rm s}$, the solid displacement. Associated to $\boldsymbol{\phi}_t \stackrel{\rm def}{=} \boldsymbol{\phi}(\cdot, t)$, we have the solid deformation gradient $\boldsymbol{F}^{\rm s} \stackrel{\rm def}{=} \boldsymbol{\nabla}\boldsymbol{\phi}_t$ and the Jacobian $J^{\rm s} \stackrel{\rm def}{=} \det \boldsymbol{F}^{\rm s}$. The non-linear elastodynamics equations in the Lagrangian frame reads: find the solid displacement $\boldsymbol{d} : \Omega^{\rm s} \times \mathbb{R}^+ \to \mathbb{R}^d$ and the velocity $\dot{\boldsymbol{d}} : \Omega^{\rm s} \times \mathbb{R}^+ \to \mathbb{R}^d$, such that

$$\begin{cases} \rho^{\rm s}\partial_t \dot{\boldsymbol{d}} - \mathbf{div}\boldsymbol{\Pi}(\boldsymbol{d}, \dot{\boldsymbol{d}}) = \boldsymbol{0} & \text{in} \quad \Omega^{\rm s}, \\ \dot{\boldsymbol{d}} = \partial_t \boldsymbol{d} & \text{in} \quad \Omega^{\rm s}, \end{cases} \tag{1.5}$$

where $\rho^{\rm s}$ represents the *solid density* and $\boldsymbol{\Pi}$ the *first Piola-Kirchhoff stress tensor* of the structure. We recall that $\boldsymbol{\Pi} \stackrel{\rm def}{=} J^{\rm s}\boldsymbol{\sigma}^{\rm s}(\boldsymbol{F}^{\rm s})^{-T}$, with $\boldsymbol{\sigma}^{\rm s}$ the *solid Cauchy stress tensor*. Here, we assume that

$$\boldsymbol{\Pi}(\boldsymbol{d}, \dot{\boldsymbol{d}}) \stackrel{\rm def}{=} \boldsymbol{F}^{\rm s}\boldsymbol{\Sigma}(\boldsymbol{d}) + \beta\boldsymbol{\partial}_{\boldsymbol{d}}\boldsymbol{\Sigma}(\boldsymbol{0})\dot{\boldsymbol{d}}, \tag{1.6}$$

where the symmetric tensor $\boldsymbol{\Sigma}(\boldsymbol{d})$ stands for the elastic *second Piola-Kirchhoff stress tensor* of the solid. In (1.6), the the tensors $\boldsymbol{F}^{\rm s}\boldsymbol{\Sigma}(\boldsymbol{d})$ and $\beta\boldsymbol{\partial}_{\boldsymbol{d}}\boldsymbol{\Sigma}(\boldsymbol{0})\dot{\boldsymbol{d}}$ describe, respectively, the elastic and viscous behavior of the solid. Here, $\boldsymbol{\partial}_{\boldsymbol{d}}\boldsymbol{\Sigma}(\boldsymbol{0})$ denotes the *Fréchet derivative* of $\boldsymbol{\Sigma}$ at $\boldsymbol{0}$ and $\beta > 0$ is the damping coefficient.

System (1.5) has to be complemented with initial conditions for the displacement and the velocity, $\boldsymbol{d}(0) = \boldsymbol{d}_0$ and $\dot{\boldsymbol{d}}(0) = \dot{\boldsymbol{d}}_0$, and with suitable boundary conditions. For instance, the following homogeneous Dirichlet condition may be prescribed,

$$\boldsymbol{d} = \boldsymbol{0} \quad \text{on} \quad \Gamma^{\rm s}_{\rm d}.$$

The discussion regarding boundary conditions over $\Sigma(t)$ is postponed until Section 1.2.3.

The relation between $\boldsymbol{\Sigma}(\boldsymbol{d})$ and $\boldsymbol{d}$ is stablished through an appropriate constitutive law (see, e.g., [Gur81, Cia88, LT94b]). For an *hyper-elastic material*, for instance, we have

$$\boldsymbol{\Sigma}(\boldsymbol{E}) = \frac{\partial W}{\partial \boldsymbol{E}}(\boldsymbol{E}),$$

where

$$\boldsymbol{E} \stackrel{\rm def}{=} \frac{1}{2}\big((\boldsymbol{F}^{\rm s})^{\rm T}\boldsymbol{F}^{\rm s} - \boldsymbol{I}\big) \tag{1.7}$$

stands for the G*reen-Lagrange strain tensor* and $W : \mathbb{R}^{d\times d} \to \mathbb{R}^+$ is a given *density of elastic energy*. For a *homogenous isotropic material* whose reference configuration is the natural state, a simple example entering this framework is given by the *Saint Venant-Kirchhoff model*, which corresponds to

$$W\big(\boldsymbol{E}\big) = \frac{L_1}{2}\big(\text{tr } \boldsymbol{E}\big)^2 + L_2 \text{ tr } \boldsymbol{E}^2,$$

and, consequently, to

$$\boldsymbol{\Sigma}\big(\boldsymbol{E}\big) = L_1\big(\text{tr } \boldsymbol{E}\big)\boldsymbol{I} + 2L_2\boldsymbol{E}. \tag{1.8}$$

Here, L_1 and L_2 denote the *Lamé coefficients* of the material. Relation (1.8) is also known as *generalized Hooke's law*. Usually the elastic properties of a material are given in terms of its *Young modulus* E and *Poisson ratio* ν. Loosely speaking, E measures the force (per unit area) that is needed to stretch (or compress) a material sample whereas ν measures lateral contraction. These quantities are related to the Lamé coefficients through the relations,

$$L_1 = \frac{E\nu}{(1-2\nu)(1+\nu)}, \quad L_2 = \frac{E}{2(1+\nu)}.$$

Let us recall that, under the hypothesis of infinitesimal strains (*linear elasticity theory*), the Green-Lagrange strain tensor $\boldsymbol{E}$ can be approximated by the *linearized strain tensor*

$$\boldsymbol{\varepsilon}(\boldsymbol{d}) \stackrel{\text{def}}{=} \frac{1}{2}\big(\boldsymbol{\nabla d} + \boldsymbol{\nabla d}^{\mathrm{T}}\big). \tag{1.9}$$

The linearized stress-strain relation then reads

$$\boldsymbol{\sigma}^{\mathrm{s}}(\boldsymbol{d}, \dot{\boldsymbol{d}}) \stackrel{\text{def}}{=} \boldsymbol{\sigma}^{\mathrm{e}}(\boldsymbol{d}) + \beta\boldsymbol{\sigma}^{\mathrm{e}}(\dot{\boldsymbol{d}}), \quad \boldsymbol{\sigma}^{\mathrm{e}}(\boldsymbol{d}) \stackrel{\text{def}}{=} L_1\big(\mathrm{tr}\ \boldsymbol{\varepsilon}(\boldsymbol{d})\big)\boldsymbol{I} + 2L_2\boldsymbol{\varepsilon}(\boldsymbol{d}). \tag{1.10}$$

1.2.2.2 Thin-walled solid models

Along this work, different reduced structural models, defined on domains of co-dimension one, will be intensively used. In that case, we consider that the solid reference configuration Ω^{s} is defined by its *mid-surface* Σ and its *thickness* $\epsilon > 0$, which we take as a constant for simplicity. Note that we refer to the solid mid-surface as Σ, which is also used to denote the fluid-structure interface. The reason for this abuse of notation will be justified in Section 1.2.3.

In general, thin-walled models may be used in cardiovascular simulations whenever the ratio thickness/size of the solid structure is small, as it is the case in cardiac valve simulation (see, e.g., [DSGB08, AGPT09, KHS+15]).

We start this presentation of thin-walled solid models by considering a rather general *shell model*. Afterwards, the consideration of simplifying modeling assumptions leads to the derivation of decreasingly complex thin-walled solid models. A detailed presentation of the theory of shells is out of the scope of this introductory chapter. We refer to [CB11, BBWR04] for general introductions. Furthermore, we restrict the discussion herein to the linear theory of shells (infinitesimal deformations), although non-linear shell models will be used in Chapters 2 and 4. We refer to [CB11, Chapter 9] (see also [LS05]) for texts discussing to the non-linear theory.

In the following we assume that $d = 3$. We consider a chart

$$\boldsymbol{\psi} : \omega \subset \mathbb{R}^2 \longrightarrow \mathbb{R}^3, \quad (\xi_1, \xi_2) \longrightarrow \boldsymbol{\psi} = \boldsymbol{\psi}(\xi_1, \xi_2),$$

parametrizing the solid reference mid-surface, i.e., $\Sigma = \boldsymbol{\psi}(\omega)$. The local *covariant basis* are given by $(\boldsymbol{a}_1, \boldsymbol{a}_2)$, with $\boldsymbol{a}_\alpha = \partial_\alpha \boldsymbol{\psi} = \frac{\partial \boldsymbol{\psi}}{\partial \xi_\alpha}$, $\alpha = 1, 2$. The corresponding

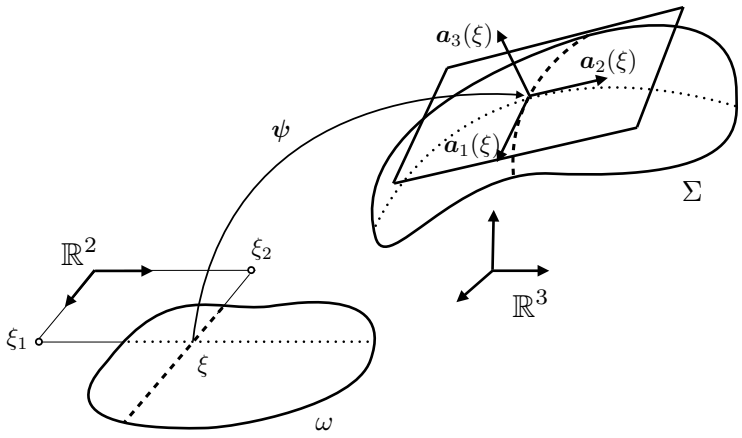

Figure 1.2: The chart $\boldsymbol{\psi}$ and the triad $\{\boldsymbol{a}_1, \boldsymbol{a}_2, \boldsymbol{a}_3\}$.

contravariant basis are denoted by $(\boldsymbol{a}^1, \boldsymbol{a}^2)$. The normal unit vector is defined as

$$\boldsymbol{a}_3 = \frac{\boldsymbol{a}_1 \times \boldsymbol{a}_2}{|\boldsymbol{a}_1 \times \boldsymbol{a}_2|}.$$

In the sequel, Greek indexes take values in $\{1, 2\}$ and Latin indexes in $\{1, 2, 3\}$. The Einstein summation convention for repeating indices is adopted. The *surface metric tensor*, or *first fundamental form*, is given by $a_{\alpha\beta} = \boldsymbol{a}_\alpha \cdot \boldsymbol{a}_\beta$, with inverse $a^{\alpha\beta} = \boldsymbol{a}^\alpha \cdot \boldsymbol{a}^\beta$. The *second* and *third fundamental forms* are given, respectively, by $b_{\alpha\beta} = \boldsymbol{a}_3 \cdot \partial_\alpha \boldsymbol{a}_\beta$ and $c_{\alpha\beta} = b_{\alpha\gamma} b^\gamma_\beta$, with $b^\gamma_\beta = a^{\gamma\lambda} b_{\lambda\beta}$. Given a vector field $\boldsymbol{q} = \boldsymbol{q}(\xi_1, \xi_2)$ on the mid-surface, we denote by $q_{\alpha|\beta}$ the *surface covariant derivative* of its covariant component q_α, defined as $q_{\alpha|\beta} = \partial_\beta q_\alpha - \Gamma^\lambda_{\alpha\beta} q_\lambda$, where $\Gamma^\lambda_{\alpha\beta} = \boldsymbol{a}_\alpha \cdot \partial_\beta \boldsymbol{a}_\beta$ denote the *Christoffel's symbols*. Finally, we consider the mapping

$$\boldsymbol{\Psi} : \Theta \subset \mathbb{R}^3 \longrightarrow \mathbb{R}^3, \quad (\xi_1, \xi_2, \xi_3) \longrightarrow \boldsymbol{\Psi}(\xi_1, \xi_2, \xi_3) = \boldsymbol{\psi}(\xi_1, \xi_2) + \xi_3 \boldsymbol{a}_3(\xi_1, \xi_2),$$

with $\Theta \stackrel{\text{def}}{=} \left\{ (\xi_1, \xi_2, \xi_3) \in \mathbb{R}^3 \,/\, (\xi_1, \xi_2) \in \omega, \quad \xi_2 \in \left[-\frac{\epsilon}{2}, \frac{\epsilon}{2}\right] \right\}$. The reference configuration Ω^{s} is assumed to be parametrized by $\boldsymbol{\Psi}$, i.e, $\Omega^{\text{s}} = \boldsymbol{\Psi}(\Theta)$.

Under the *Reissner-Mindlin kinematic assumption* [Rei45, Min51], a material line orthogonal to the reference mid-surface is assumed to remain straight and unstretched during the deformation. The assumed displacement during loading is given by

$$\boldsymbol{\eta}(\xi_1, \xi_2, \xi_3) \stackrel{\text{def}}{=} \boldsymbol{d}(\xi_1, \xi_2) + \xi_3 \theta_\lambda(\xi_1, \xi_2) \boldsymbol{a}^\lambda(\xi_1, \xi_2), \tag{1.11}$$

with $\boldsymbol{d}(\xi_1, \xi_2)$ the global infinitesimal displacement of the mid-surface and $\boldsymbol{\theta}(\xi_1, \xi_2) \stackrel{\text{def}}{=} \theta_\lambda(\xi_1, \xi_2) \boldsymbol{a}^\lambda(\xi_1, \xi_2)$ the rotation vector around the normal to the mid-surface (see, e.g., [CB11, Section 4.1]). Assuming (1.11), a general viscoelastic thin-walled solid is described by: find the solid displacement $\boldsymbol{d} : \Sigma \times \mathbb{R}^+ \to \mathbb{R}^3$ and

the rotation vector $\boldsymbol{\theta} : \Sigma \times \mathbb{R}^+ \to \mathbb{R}^3$, such that

$$\begin{cases} \rho^{\mathrm{s}}\epsilon\partial_t\dot{\boldsymbol{d}} + \boldsymbol{L}^{\mathrm{e}}_{\boldsymbol{d}}(\boldsymbol{d},\boldsymbol{\theta}) + \boldsymbol{L}^{\mathrm{v}}_{\boldsymbol{d}}(\dot{\boldsymbol{d}},\dot{\boldsymbol{\theta}}) = \boldsymbol{f}_\Sigma & \text{on} \quad \Sigma, \\ \boldsymbol{L}^{\mathrm{e}}_{\boldsymbol{\theta}}(\boldsymbol{d},\boldsymbol{\theta}) + \boldsymbol{L}^{\mathrm{v}}_{\boldsymbol{\theta}}(\dot{\boldsymbol{d}},\dot{\boldsymbol{\theta}}) = \boldsymbol{0} & \text{on} \quad \Sigma, \\ \dot{\boldsymbol{d}} = \partial_t\boldsymbol{d}, \quad \dot{\boldsymbol{\theta}} = \partial_t\boldsymbol{\theta} & \text{on} \quad \Sigma, \\ \boldsymbol{d} = \boldsymbol{\theta} = \boldsymbol{0} & \text{on} \quad \Gamma^\Sigma_{\mathrm{d}}, \end{cases} \tag{1.12}$$

with $\Gamma^\Sigma_{\mathrm{d}} \subset \partial\Sigma$ and satisfying the initial conditions $\boldsymbol{d}(0) = \boldsymbol{d}_0$, $\boldsymbol{\theta}(0) = \boldsymbol{\theta}_0$, $\dot{\boldsymbol{d}}(0) = \dot{\boldsymbol{d}}_0$ and $\dot{\boldsymbol{\theta}}(0) = \dot{\boldsymbol{\theta}}_0$. The relation $(1.12)_2$ represents the additional equation for the rotations and $\boldsymbol{f}_\Sigma$ denotes a given force per unit area. The surface operators $\big(\boldsymbol{L}^{\mathrm{e}}_{\boldsymbol{d}}, \boldsymbol{L}^{\mathrm{e}}_{\boldsymbol{\theta}}\big)$ and $\big(\boldsymbol{L}^{\mathrm{v}}_{\boldsymbol{d}}, \boldsymbol{L}^{\mathrm{v}}_{\boldsymbol{\theta}}\big)$ represent the strong formulation of the thin-solid elastic and viscous contributions, respectively. Since they are supposed to be linear, they admit the following decomposition:

$$\begin{aligned} \boldsymbol{L}^{\mathrm{e}}_{\boldsymbol{d}}(\boldsymbol{d},\boldsymbol{\theta}) &\stackrel{\mathrm{def}}{=} \boldsymbol{A}^{\mathrm{e}}_{\boldsymbol{d}}\boldsymbol{d} + \boldsymbol{B}^{\mathrm{e}}_{\boldsymbol{d}}\boldsymbol{\theta}, \quad \boldsymbol{L}^{\mathrm{v}}_{\boldsymbol{d}}(\boldsymbol{d},\boldsymbol{\theta}) \stackrel{\mathrm{def}}{=} \boldsymbol{A}^{\mathrm{v}}_{\boldsymbol{d}}\boldsymbol{d} + \boldsymbol{B}^{\mathrm{v}}_{\boldsymbol{d}}\boldsymbol{\theta}, \\ \boldsymbol{L}^{\mathrm{e}}_{\boldsymbol{\theta}}(\boldsymbol{d},\boldsymbol{\theta}) &\stackrel{\mathrm{def}}{=} \boldsymbol{B}^{\mathrm{e}}_{\boldsymbol{\theta}}\boldsymbol{d} + \boldsymbol{A}^{\mathrm{e}}_{\boldsymbol{\theta}}\boldsymbol{\theta}, \quad \boldsymbol{L}^{\mathrm{v}}_{\boldsymbol{\theta}}(\boldsymbol{d},\boldsymbol{\theta}) \stackrel{\mathrm{def}}{=} \boldsymbol{B}^{\mathrm{v}}_{\boldsymbol{\theta}}\boldsymbol{d} + \boldsymbol{A}^{\mathrm{v}}_{\boldsymbol{\theta}}\boldsymbol{\theta}. \end{aligned} \tag{1.13}$$

Remark 1.2 *As usual in shell dynamic analysis, the rotational inertial term is neglected in* $(1.12)_1$. *The modeling of the viscous effects may be simplified by considering* $\boldsymbol{L}^{\mathrm{v}}_{\boldsymbol{d}}(\dot{\boldsymbol{d}},\dot{\boldsymbol{\theta}}) = \boldsymbol{L}^{\mathrm{v}}(\dot{\boldsymbol{d}})$ *with* $\boldsymbol{L}^{\mathrm{v}}_{\boldsymbol{\theta}} = \boldsymbol{0}$ *(see Chapters 2 and 4).*

In order to provide examples of the abstract operators involved in (1.13), we must resort to constitutive laws giving the relationship between stresses and strains. The actual setting being linear, the strain measures are given by the linearized strain tensor (1.9). The components of the strain tensor (1.9) corresponding to the displacement (1.11) are given, in curvilinear coordinates, by

$$\begin{aligned} \varepsilon_{\alpha\beta} &= \gamma_{\alpha\beta}(\boldsymbol{d}) + \xi_3\chi_{\alpha\beta}(\boldsymbol{d},\boldsymbol{\theta}) - \xi_3^2\kappa_{\alpha\beta}(\boldsymbol{\theta}), \\ \varepsilon_{\alpha 3} &= \zeta_\alpha(\boldsymbol{d},\boldsymbol{\theta}), \\ \varepsilon_{33} &= 0, \end{aligned}$$

where

$$\begin{aligned} \gamma_{\alpha\beta}(\boldsymbol{d}) &= \frac{1}{2}\big(d_{\alpha|\beta} + d_{\beta|\alpha}\big) - b_{\alpha\beta}d_3, \\ \chi_{\alpha\beta}(\boldsymbol{d},\boldsymbol{\theta}) &= \frac{1}{2}\big(\theta_{\alpha|\beta} + \theta_{\beta|\alpha} - b^\lambda_\beta d_{\lambda|\alpha} - b^\lambda_\alpha d_{\lambda|\beta}\big) + b_{\alpha\beta}d_3, \\ \kappa_{\alpha\beta}(\boldsymbol{\theta}) &= \frac{1}{2}\big(b^\lambda_\beta\theta_{\lambda|\alpha} + b^\lambda_\alpha\theta_{\lambda|\beta}\big), \\ \zeta_\alpha(\boldsymbol{d},\boldsymbol{\theta}) &= \frac{1}{2}\big(\theta_\alpha + \partial_\alpha d_3 + b^\lambda_\alpha d_\lambda\big). \end{aligned}$$

The quantities $\gamma_{\alpha\beta}(\boldsymbol{d})$, $\chi_{\alpha\beta}(\boldsymbol{d},\boldsymbol{\theta})$ and $\zeta_\alpha(\boldsymbol{d},\boldsymbol{\theta})$ represent the covariant components of the *membrane*, *bending* and *shear strain tensors* of the shell, respectively (see, e.g., [CB11, Section 4.2.2] for further details).

As usual in shell modeling, we make the assumption of *plane stresses* (zero stresses along the normal direction). The stress-strain relationship is given by

Hooke's law. In the following, the scalar product in $L^2(\omega)$ is denoted by $(\cdot,\cdot)_\omega$ and its norm by $\|\cdot\|_{0,\omega}$, with ω being a given domain or surface in $\mathbb{R}^3$. Considering the standard variational formulation of a linear elastic problem (see Section 1.4.2.1 below) written in curvilinear coordinates over the 3D domain Ω^{s}, truncating the higher order terms in ξ_3 and integrating with respect to ξ_3 (see [CB11, Section 4.2.1-4.2.2] for the details), we obtain the following *shear-membrane-bending model*:

$$\rho^{\mathrm{s}}\epsilon\big(\partial_t\dot{\boldsymbol{d}},\boldsymbol{w}\big)_\Sigma+\epsilon\big(C^{\alpha\beta\lambda\xi}\gamma_{\alpha\beta}(\boldsymbol{d}),\gamma_{\lambda\xi}(\boldsymbol{w})\big)_\Sigma+\frac{\epsilon^3}{12}\big(C^{\alpha\beta\lambda\xi}\chi_{\alpha\beta}(\boldsymbol{d},\boldsymbol{\theta}),\chi_{\lambda\xi}(\boldsymbol{w},\boldsymbol{\vartheta})\big)_\Sigma \\ +\epsilon\big(D^{\alpha\lambda}\zeta_\alpha(\boldsymbol{d},\boldsymbol{\theta}),\zeta_\lambda(\boldsymbol{w},\boldsymbol{\vartheta})\big)_\Sigma=\big(\boldsymbol{f}_\Sigma,\boldsymbol{w}\big)_\Sigma, \quad (1.14)$$

with arbitrary test functions $(\boldsymbol{w},\boldsymbol{\vartheta})$ vanishing on $\Gamma_{\mathrm{d}}^\Sigma$ and

$$\boldsymbol{C}^{\alpha\beta\lambda\xi}\overset{\text{def}}{=}\frac{E}{2(1+\nu)}\left(a^{\alpha\lambda}a^{\beta\xi}+a^{\alpha\xi}a^{\beta\lambda}+\frac{2\nu}{1-\nu}a^{\alpha\beta}a^{\lambda\xi}\right),\quad D^{\alpha\lambda}\overset{\text{def}}{=}\frac{2E}{1+\nu}a^{\alpha\lambda},$$

In this framework, the abstract operators introduced in (1.13) are given by:

$$\begin{aligned}
\big(\boldsymbol{A}_{\boldsymbol{d}}^{\mathrm{e}}\boldsymbol{d},\boldsymbol{w}\big)_\Sigma&=\epsilon\big(C^{\alpha\beta\lambda\xi}\gamma_{\alpha\beta}(\boldsymbol{d}),\gamma_{\lambda\xi}(\boldsymbol{w})\big)_\Sigma+\frac{\epsilon^3}{12}\big(C^{\alpha\beta\lambda\xi}\chi_{\alpha\beta}(\boldsymbol{d},\boldsymbol{0}),\chi_{\lambda\xi}(\boldsymbol{w},\boldsymbol{0})\big)_\Sigma\\
&\quad+\epsilon\big(D^{\alpha\lambda}\zeta_\alpha(\boldsymbol{d},\boldsymbol{0}),\zeta_\lambda(\boldsymbol{w},\boldsymbol{0})\big)_\Sigma,\\
\big(\boldsymbol{B}_{\boldsymbol{d}}^{\mathrm{e}}\boldsymbol{\theta},\boldsymbol{w}\big)_\Sigma&=\frac{\epsilon^3}{12}\big(C^{\alpha\beta\lambda\xi}\chi_{\alpha\beta}(\boldsymbol{0},\boldsymbol{\theta}),\chi_{\lambda\xi}(\boldsymbol{w},\boldsymbol{0})\big)_\Sigma+\epsilon\big(D^{\alpha\lambda}\zeta_\alpha(\boldsymbol{0},\boldsymbol{\theta}),\zeta_\lambda(\boldsymbol{w},\boldsymbol{0})\big)_\Sigma,\\
\big(\boldsymbol{B}_{\boldsymbol{\theta}}^{\mathrm{e}}\boldsymbol{d},\boldsymbol{\vartheta}\big)_\Sigma&=\frac{\epsilon^3}{12}\big(C^{\alpha\beta\lambda\xi}\chi_{\alpha\beta}(\boldsymbol{d},\boldsymbol{0}),\chi_{\lambda\xi}(\boldsymbol{0},\boldsymbol{\vartheta})\big)_\Sigma+\epsilon\big(D^{\alpha\lambda}\zeta_\alpha(\boldsymbol{d},\boldsymbol{0}),\zeta_\lambda(\boldsymbol{0},\boldsymbol{\vartheta})\big)_\Sigma,\\
\big(\boldsymbol{A}_{\boldsymbol{\theta}}^{\mathrm{e}}\boldsymbol{\theta},\boldsymbol{\vartheta}\big)_\Sigma&=\frac{\epsilon^3}{12}\big(C^{\alpha\beta\lambda\xi}\chi_{\alpha\beta}(\boldsymbol{0},\boldsymbol{\theta}),\chi_{\lambda\xi}(\boldsymbol{0},\boldsymbol{\vartheta})\big)_\Sigma+\epsilon\big(D^{\alpha\lambda}\zeta_\alpha(\boldsymbol{0},\boldsymbol{\theta}),\zeta_\lambda(\boldsymbol{0},\boldsymbol{\vartheta})\big)_\Sigma.
\end{aligned}\quad (1.15)$$

Note that $\boldsymbol{A}_{\boldsymbol{d}}^{\mathrm{e}},\boldsymbol{A}_{\boldsymbol{\theta}}^{\mathrm{e}}$ are symmetric and that $\boldsymbol{B}_{\boldsymbol{d}}^{\mathrm{e}}$ is the adjoint of $\boldsymbol{B}_{\boldsymbol{\theta}}^{\mathrm{e}}$ (and vice versa).

The viscous operators $\boldsymbol{A}_{\boldsymbol{d}}^{\mathrm{v}},\boldsymbol{A}_{\boldsymbol{\theta}}^{\mathrm{v}},\boldsymbol{B}_{\boldsymbol{d}}^{\mathrm{v}},\boldsymbol{B}_{\boldsymbol{\theta}}^{\mathrm{v}}$ introduced in (1.13) depend on the modeling assumptions made on the shell physical dissipation. For instance, we may consider the so-called *Rayleigh damping*, namely,

$$\begin{aligned}
\boldsymbol{L}_{\boldsymbol{d}}^{\mathrm{v}}(\dot{\boldsymbol{d}},\dot{\boldsymbol{\theta}})&=\alpha\rho^{\mathrm{s}}\epsilon\dot{\boldsymbol{d}}+\beta\boldsymbol{L}_{\boldsymbol{d}}^{\mathrm{e}}(\dot{\boldsymbol{d}},\dot{\boldsymbol{\theta}}),\\
\boldsymbol{L}_{\boldsymbol{\theta}}^{\mathrm{v}}(\dot{\boldsymbol{d}},\dot{\boldsymbol{\theta}})&=\beta\boldsymbol{L}_{\boldsymbol{\theta}}^{\mathrm{e}}(\dot{\boldsymbol{d}},\dot{\boldsymbol{\theta}}),
\end{aligned}\quad (1.16)$$

where $\alpha,\beta>0$ are given parameters (see, e.g., [Hug87]). The expression of the operators $\boldsymbol{A}_{\boldsymbol{d}}^{\mathrm{v}},\boldsymbol{A}_{\boldsymbol{\theta}}^{\mathrm{v}},\boldsymbol{B}_{\boldsymbol{d}}^{\mathrm{v}},\boldsymbol{B}_{\boldsymbol{\theta}}^{\mathrm{v}}$ follows straightforwardly from the relations (1.13), (1.15) and (1.16). The terms multiplied by β in (1.16) corresponds to the *Kelvin-Voigt model*, which is often used in arterial wall modeling (see, e.g., [KS08, ČTG+06, VJBH+09]). The first term in $(1.16)_1$ takes into account the dissipative effects of external tissue on blood vessels (see [MXA+12]).

As a first step towards a simpler thin-walled solid model, we may consider plate and shell models derived under the *Kirchhoff-Love kinematic assumption* (see, e.g., [Kir76, Lov27, CB11]). Under this assumption, a material line orthogonal to the

reference mid-surface is assumed to remain straight, unstretched and orthogonal to the mid-surface during the deformation. In terms of the displacement (1.11), this assumption implies that

$$\theta_\alpha = -\partial_\alpha d_3 - b_\alpha^\lambda d_\lambda. \tag{1.17}$$

Owing to relation (1.17), we can effectively remove the rotation vector as unknown in the solid problem. As a matter of fact, a general viscoelastic Kirchhoff-Love model reads as: find the solid displacement $\boldsymbol{d} : \Sigma \times \mathbb{R}^+ \to \mathbb{R}^d$, such that

$$\begin{cases} \rho^{\mathrm{s}}\epsilon\partial_t\dot{\boldsymbol{d}} + \boldsymbol{L}^{\mathrm{e}}\boldsymbol{d} + \boldsymbol{L}^{\mathrm{v}}\dot{\boldsymbol{d}} = \boldsymbol{f}_\Sigma & \text{on} \quad \Sigma, \\ \dot{\boldsymbol{d}} = \partial_t\boldsymbol{d} & \text{on} \quad \Sigma, \\ \boldsymbol{d} = \boldsymbol{0} & \text{on} \quad \Gamma_{\mathrm{d}}^\Sigma, \end{cases} \tag{1.18}$$

satisfying the initial conditions $\boldsymbol{d}(0) = \boldsymbol{d}_0$ and $\dot{\boldsymbol{d}}(0) = \dot{\boldsymbol{d}}_0$ and with the surface operators $\boldsymbol{L}^{\mathrm{e}}$ and $\boldsymbol{L}^{\mathrm{v}}$ representing the strong formulation of the thin-solid elastic and viscous contributions, respectively. As an example of shell model entering this framework, we consider the so-called *membrane-bending model* (see, e.g., [CB11, Section 4.2.2]). For its derivation, note that under assumption (1.17), we have

$$\zeta_\alpha(\boldsymbol{d}, \boldsymbol{\theta}) = 0 \quad \text{and} \quad \chi_{\alpha\beta}(\boldsymbol{d}, \boldsymbol{\theta}) = -\rho_{\alpha\beta}(\boldsymbol{d}) \tag{1.19}$$

with

$$\rho_{\alpha\beta}(\boldsymbol{d}) = d_{3|\alpha\beta} + b^\mu_{\alpha|\beta} d_\mu + b^\mu_\alpha d_{\mu|\beta} + b^\mu_\beta d_{\mu|\alpha} - c_{\alpha\beta} d_3.$$

Substitution of (1.19) into (1.14) yields

$$\rho^{\mathrm{s}}\epsilon\big(\partial_t\dot{\boldsymbol{d}}, \boldsymbol{w}\big)_\Sigma + \epsilon\big(C^{\alpha\beta\lambda\xi}\gamma_{\alpha\beta}(\boldsymbol{d}), \gamma_{\lambda\xi}(\boldsymbol{w})\big)_\Sigma + \frac{\epsilon^3}{12}\big(C^{\alpha\beta\lambda\xi}\rho_{\alpha\beta}(\boldsymbol{d}), \rho_{\lambda\xi}(\boldsymbol{w})\big)_\Sigma = \big(\boldsymbol{f}_\Sigma, \boldsymbol{w}\big)_\Sigma. \tag{1.20}$$

In this framework, the elastic surface operator $\boldsymbol{L}^{\mathrm{e}}$ is given by

$$\big(\boldsymbol{L}^{\mathrm{e}}\boldsymbol{d}, \boldsymbol{w}\big)_\Sigma = \epsilon\big(C^{\alpha\beta\lambda\xi}\gamma_{\alpha\beta}(\boldsymbol{d}), \gamma_{\lambda\xi}(\boldsymbol{w})\big)_\Sigma + \frac{\epsilon^3}{12}\big(C^{\alpha\beta\lambda\xi}\rho_{\alpha\beta}(\boldsymbol{d}), \rho_{\lambda\xi}(\boldsymbol{w})\big)_\Sigma \tag{1.21}$$

and the Rayleigh modeling of the damping gives

$$\boldsymbol{L}^{\mathrm{v}}\dot{\boldsymbol{d}} \overset{\mathrm{def}}{=} \alpha\rho^{\mathrm{s}}\epsilon\dot{\boldsymbol{d}} + \beta\boldsymbol{L}^{\mathrm{e}}\dot{\boldsymbol{d}}, \tag{1.22}$$

with $\alpha, \beta > 0$.

Further simplifications may be obtained by considering a cylindrical reference domain. For instance, if we consider a cylindrical domain and make the additional assumption of axi-symmetric displacements, the model (1.20) readily leads to the well known *cylindrical Koiter-type model* (see, e.g., [FFGQ09, Section 3.4.3]). One dimensional models may be obtained by considering a straight cylindrical configuration, assuming radial displacements and neglecting bending responses. In this

work, we will often used the *generalized string model*, which is obtained by considering longitudinal sections ($\theta = \text{const.}$) of a 2D cylindrical surface of radius R and length L (rigorous derivations of this model can be found in [Cia04, FFGQ09]). In 2D, with the longitudinal and perpendicular direction lying on the x-axis and y-axis respectively, the model is retrieved by considering

$$\boldsymbol{d} = \begin{pmatrix} 0 \\ \eta \end{pmatrix}, \quad \boldsymbol{L}^{\mathrm{e}}\boldsymbol{d} = \begin{pmatrix} 0 \\ -\lambda_1 \partial_{xx}\eta + \lambda_0 \eta \end{pmatrix}, \quad \boldsymbol{L}^{\mathrm{v}}\dot{\boldsymbol{d}} = \begin{pmatrix} 0 \\ \alpha\rho^{\mathrm{s}}\epsilon\dot{\eta} - \beta\lambda_1\partial_{xx}\dot{\eta} \end{pmatrix}, \tag{1.23}$$

with

$$\lambda_1 \overset{\text{def}}{=} \frac{E\epsilon}{2(1+\nu)}, \quad \lambda_0 \overset{\text{def}}{=} \frac{E\epsilon}{R^2(1-\nu^2)}, \quad \alpha, \beta > 0$$

in (1.18).

1.2.3 Fluid-structure coupled problem

The dynamics of the solid and the fluid mediums are coupled through the so-called *kinematic* and *dynamic coupling conditions*,

$$\begin{cases} \widehat{\boldsymbol{u}} = \partial_t \boldsymbol{d} & \text{on} \quad \Sigma, \\ \boldsymbol{\Pi}(\boldsymbol{d}, \dot{\boldsymbol{d}})\boldsymbol{n}^{\mathrm{s}} = -J\widehat{\boldsymbol{\sigma}}(\boldsymbol{u}, p)\boldsymbol{F}^{-\mathrm{T}}\boldsymbol{n} & \text{on} \quad \Sigma, \end{cases} \tag{1.24}$$

for all $t \in \mathbb{R}^+$, written here in the reference configuration and for the solid problem (1.5). The first condition represents the fact that, due to its viscosity, the fluid sticks perfectly to the fluid-structure interface (no-slip condition), while the second accounts for the balance of stresses (Newton's third law).

In the case of coupling with a thin-walled solid model, a widely used modeling simplification (see, e.g., [CF03]) is to consider that the interface conditions (1.24) are enforced on the shell mid-surface, instead of on the real fluid-solid interface. In other words, the shell thickness is neglected in the interface coupling. For the model (1.12) and (1.18), this approach leads to the coupling conditions

$$\begin{cases} \widehat{\boldsymbol{u}} = \partial_t \boldsymbol{d} & \text{on} \quad \Sigma, \\ \boldsymbol{f}_\Sigma = -J\widehat{\boldsymbol{\sigma}}(\boldsymbol{u}, p)\boldsymbol{F}^{-\mathrm{T}}\boldsymbol{n} & \text{on} \quad \Sigma. \end{cases} \tag{1.25}$$

On the other hand, there is a *geometrical compatibility condition* between the domains $\Omega^{\mathrm{s}}(t)$ and $\Omega^{\mathrm{f}}(t)$ that must be satisfied for all $t \in \mathbb{R}^+$. In terms of the ALE formulation, this can be expressed as

$$\boldsymbol{d}^{\mathrm{f}} = \boldsymbol{d} \quad \text{on} \quad \Sigma. \tag{1.26}$$

Apart from the constrains (1.26) and $\boldsymbol{d}^{\mathrm{f}} = \boldsymbol{0}$ on $\Gamma_{\mathrm{in}} \cup \Gamma_{\mathrm{out}}$ (recall that we are assuming Γ_{in} and Γ_{out} fixed), the definition of the ALE map $\boldsymbol{\mathcal{A}}$ inside the domain Ω^{f} can be taken, at least from the theoretical point of view, rather arbitrarily. In the sequel, we use $\mathrm{Ext}\,(\boldsymbol{d}|_\Sigma)$ to denote the operation of extending $\boldsymbol{d}|_\Sigma$ over Ω^{f} subjected

to the aforementioned conditions on $\Gamma_{\text{in}} \cup \Gamma_{\text{out}}$. We then set

$$\boldsymbol{d}^{\text{f}} = \text{Ext}\,(\boldsymbol{d}|_{\Sigma}) \quad \text{on} \quad \Omega^{\text{f}}. \tag{1.27}$$

Finally, note that condition (1.26) together with $(1.24)_1$ yields $\boldsymbol{u} = \dot{\boldsymbol{d}}^{\text{f}}$ on $\Sigma(t)$.

Remark 1.3 *It is noteworthy that, at the computational level, the choice of the extension operator* $\text{Ext}\,(\cdot)$ *may have an important impact in the solution procedure, even risking the feasibility of the simulations. Problems with large interface deflections may require advanced moving mesh techniques (See Section 4.3.3 in Chapter 4).*

In this work, two different formulations of the fluid-structure interaction problem will be considered: the *ALE-Lagrangian* and the *Eulerian-Lagrangian* formulations.

1.2.3.1 ALE-Lagrangian formulation of the coupled problem

Considering the ALE form of the Navier-Stokes equations (1.4), the non-linear elastodynamics equations (1.5) and the interface coupling conditions (1.24) and (1.27), we obtain the following problem: find the fluid domain displacement $\boldsymbol{d}^{\text{f}} : \Omega^{\text{f}} \times \mathbb{R}^+ \to \mathbb{R}^d$, the fluid velocity $\widehat{\boldsymbol{u}} : \Omega^{\text{f}} \times \mathbb{R}^+ \to \mathbb{R}^d$, the fluid pressure $\widehat{p} : \Omega^{\text{f}} \times \mathbb{R}^+ \to \mathbb{R}$, the structure displacement $\boldsymbol{d} : \Omega^{\text{s}} \times \mathbb{R}^+ \to \mathbb{R}^d$ and the structure velocity $\dot{\boldsymbol{d}} : \Omega^{\text{s}} \times \mathbb{R}^+ \to \mathbb{R}^d$, such that

$$\begin{cases} \rho^{\text{f}} \partial_t \boldsymbol{u}|_{\boldsymbol{\mathcal{A}}} + \rho^{\text{f}} (\boldsymbol{u} - \dot{\boldsymbol{d}}^{\text{f}}) \cdot \boldsymbol{\nabla} \boldsymbol{u} - \mathbf{div} \boldsymbol{\sigma}(\boldsymbol{u}, p) = \boldsymbol{0} & \text{in} \quad \Omega^{\text{f}}(t), \\ \qquad\qquad \text{div} \boldsymbol{u} = 0 & \text{in} \quad \Omega^{\text{f}}(t), \\ \qquad\qquad \boldsymbol{u} = \boldsymbol{u}_{\text{in}} & \text{on} \quad \Gamma_{\text{in}}, \\ \qquad\qquad \boldsymbol{u} = \boldsymbol{0} & \text{on} \quad \Gamma_{\text{wall}}, \\ \qquad\qquad \boldsymbol{\sigma}(\boldsymbol{u}, p)\boldsymbol{n} = -p_{\text{out}} \boldsymbol{n} & \text{on} \quad \Gamma_{\text{out}}, \end{cases} \tag{1.28}$$

$$\begin{cases} \rho^{\text{s}} \partial_t \dot{\boldsymbol{d}} - \mathbf{div} \boldsymbol{\Pi}(\boldsymbol{d}, \dot{\boldsymbol{d}}) = \boldsymbol{0} & \text{in} \quad \Omega^{\text{s}}, \\ \qquad\qquad \dot{\boldsymbol{d}} = \partial_t \boldsymbol{d} & \text{in} \quad \Omega^{\text{s}}, \\ \qquad\qquad \boldsymbol{d} = \boldsymbol{0} & \text{on} \quad \Gamma_{\text{d}}^{\text{s}}, \end{cases} \tag{1.29}$$

$$\begin{cases} \boldsymbol{d}^{\text{f}} = \text{Ext}\,(\boldsymbol{d}|_{\Sigma}), \quad \widehat{\dot{\boldsymbol{d}}}^{\text{f}} = \partial_t \boldsymbol{d}^{\text{f}}, \quad \boldsymbol{\mathcal{A}} = \boldsymbol{I}_{\Omega^{\text{f}}} + \boldsymbol{d}^{\text{f}}, \quad \Omega^{\text{f}}(t) = \boldsymbol{\mathcal{A}}(\Omega^{\text{f}}, t), \\ \qquad\qquad\qquad\qquad\qquad\qquad\qquad\qquad\qquad\qquad \widehat{\boldsymbol{u}} = \partial_t \boldsymbol{d} \quad \text{on} \quad \Sigma, \\ \qquad\qquad\qquad\qquad\qquad\qquad\qquad\qquad\qquad\qquad \boldsymbol{\Pi}(\boldsymbol{d}, \dot{\boldsymbol{d}}) \boldsymbol{n}^{\text{s}} = -J \widehat{\boldsymbol{\sigma}}(\boldsymbol{u}, p) \boldsymbol{F}^{-\text{T}} \boldsymbol{n} \quad \text{on} \quad \Sigma, \end{cases} \tag{1.30}$$

with the initial conditions $\boldsymbol{u}(0) = \boldsymbol{u}_0$, $\boldsymbol{d}(0) = \boldsymbol{d}_0$ and $\dot{\boldsymbol{d}}(0) = \dot{\boldsymbol{d}}_0$.

The coupling of the ALE Navier-Stokes equations with a thin-walled solid model, through conditions (1.25) and (1.27), is considered in Chapter 2 (Section 2.3) and Chapter 4 (Section 4.2.2.2).

1.2.3.2 Eulerian-Lagrangian formulation of the coupled problem

The Eulerian-Lagrangian formulation of the coupled problem is better written directly using the variational form of problem (1.5), taking $\boldsymbol{W}$ as the space of admissible displacements (see Section 1.4.2.1 below). Hence, formally multiplying (1.5) by $\boldsymbol{w} \in \boldsymbol{W}$, integrating by parts, using (1.24), and considering the Eulerian form of the Navier-Stokes equations (1.1), we obtain the following problem: find the fluid velocity $\boldsymbol{u} : \Omega^{\mathrm{f}}(t) \times \mathbb{R}^+ \to \mathbb{R}^d$, the fluid pressure $p : \Omega^{\mathrm{f}}(t) \times \mathbb{R}^+ \to \mathbb{R}$, the structure displacement $\boldsymbol{d} : \Omega^{\mathrm{s}} \times \mathbb{R}^+ \to \mathbb{R}^d$ and the structure velocity $\dot{\boldsymbol{d}} : \Omega^{\mathrm{s}} \times \mathbb{R}^+ \to \mathbb{R}^d$, such that

$$\begin{cases} \rho^{\mathrm{f}}\big(\partial_t \boldsymbol{u} + \boldsymbol{u} \cdot \boldsymbol{\nabla} \boldsymbol{u}\big) - \mathbf{div} \boldsymbol{\sigma}(\boldsymbol{u}, p) = \boldsymbol{0} & \text{in} \quad \Omega^{\mathrm{f}}(t), \\ \mathrm{div} \boldsymbol{u} = 0 & \text{in} \quad \Omega^{\mathrm{f}}(t), \\ \boldsymbol{u} = \boldsymbol{u}_{\mathrm{in}} & \text{on} \quad \Gamma_{\mathrm{in}}, \\ \boldsymbol{u} = \boldsymbol{0} & \text{on} \quad \Gamma_{\mathrm{wall}}, \\ \boldsymbol{\sigma}(\boldsymbol{u}, p)\boldsymbol{n} = -p_{\mathrm{out}} \boldsymbol{n} & \text{on} \quad \Gamma_{\mathrm{out}}, \end{cases} \tag{1.31}$$

$$\begin{cases} \boldsymbol{d}(t) \in \boldsymbol{W}, \quad \dot{\boldsymbol{d}} = \partial_t \boldsymbol{d}, \\ \rho^{\mathrm{s}}\big(\partial_t \dot{\boldsymbol{d}}, \boldsymbol{w}\big)_{\Omega^{\mathrm{s}}} + \big(\boldsymbol{\Pi}(\boldsymbol{d}, \dot{\boldsymbol{d}}), \boldsymbol{\nabla} \boldsymbol{w}\big)_{\Omega^{\mathrm{s}}} = -\displaystyle\int_{\Sigma(t)} \boldsymbol{\sigma}(\boldsymbol{u}, p)\boldsymbol{n} \cdot \big(\boldsymbol{w} \circ \boldsymbol{\phi}_t^{-1}\big) \quad \forall \boldsymbol{w} \in \boldsymbol{W}, \end{cases} \tag{1.32}$$

$$\begin{cases} \Omega^{\mathrm{s}}(t) = \boldsymbol{\phi}_t(\Omega^{\mathrm{s}}), \quad \Omega^{\mathrm{f}}(t) = \Omega \backslash \Omega^{\mathrm{s}}(t), \\ \boldsymbol{u} = \dot{\boldsymbol{d}} \circ \boldsymbol{\phi}_t^{-1} \quad \text{on} \quad \Sigma(t), \end{cases} \tag{1.33}$$

with the initial conditions $\boldsymbol{u}(0) = \boldsymbol{u}^0$, $\boldsymbol{d}(0) = \boldsymbol{d}^0$ and $\dot{\boldsymbol{d}}(0) = \dot{\boldsymbol{d}}_0$.

In this work, an Eulerian-Lagrangian formulation of the coupled problem will be considered in the case of coupling with immersed thin-walled structures (see Chapter 6). For instance, let us consider a thin-walled solid model in the configuration of Figure 1.1. We consider the partition $\Omega \stackrel{\text{def}}{=} \Omega_1(t) \cup \Omega_2(t) \cup \Sigma(t)$ induced by the fluid-structure interface, with $\boldsymbol{n}_1$ and $\boldsymbol{n}_2$ denoting, respectively, the outward normals on $\Sigma(t)$ to $\Omega_1(t)$ and $\Omega_2(t)$. The situation is represented in Figure 1.3. In this

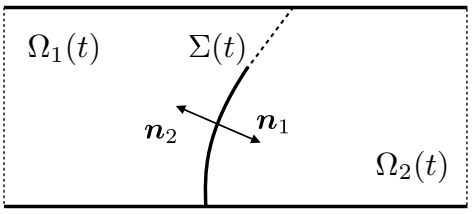

Figure 1.3: Geometrical configuration in the case of coupling with an immersed thin-walled structure.

case, the load on the structure - right hand side of (1.32) - is given by

$$-\int_{\Sigma(t)} [\![\boldsymbol{\sigma}(\boldsymbol{u},p)\boldsymbol{n}]\!]\cdot\left(\boldsymbol{w}\circ\boldsymbol{\phi}_t^{-1}\right),$$

with $[\![\boldsymbol{\sigma}(\boldsymbol{u},p)\boldsymbol{n}]\!] \overset{\text{def}}{=} \boldsymbol{\sigma}(\boldsymbol{u}_1,p_1)\boldsymbol{n}_1+\boldsymbol{\sigma}(\boldsymbol{u}_2,p_2)\boldsymbol{n}_2$ denoting the jump of the hydrodynamic stress through the immersed solid. This results in pressure and velocity solutions that are, respectively, *strongly and weakly (gradient) discontinuous* along the moving fluid-structure interface (see Figure 1.4).

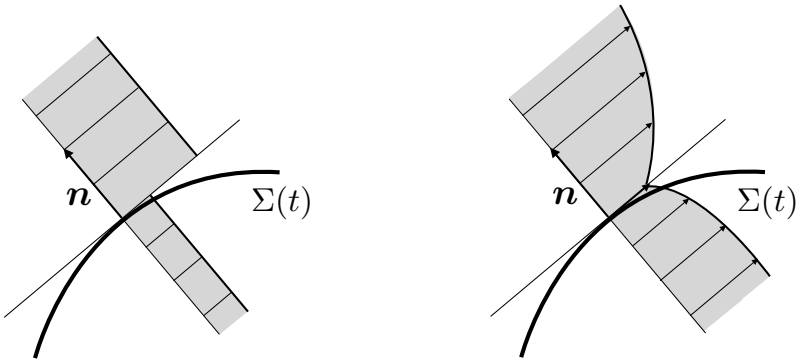

(a) (b)

Figure 1.4: Strong discontinuity in the pressure field (a) and weak discontinuity in the velocity field (b) through the interface.

1.2.3.3 Global energy balance

The interface coupling conditions guarantee a correct balance of the system mechanical energy $E(t)$, defined as

$$E(t) \overset{\text{def}}{=} \underbrace{\int_{\Omega^{\mathrm{f}}(t)} \frac{\rho^{\mathrm{f}}}{2}|\boldsymbol{u}|^2+\int_{\Omega^{\mathrm{s}}}\frac{\rho^{\mathrm{s}}}{2}|\dot{\boldsymbol{d}}|^2}_{\substack{Kinetic\\ energy}} + \underbrace{\int_{\Omega^{\mathrm{s}}} W\left(\boldsymbol{E}^{\mathrm{s}}(\boldsymbol{d})\right)}_{\substack{Elastic\\ potential\ energy}},$$

for all $t\in\mathbb{R}^+$. As a matter of fact, we have the following lemma, whose demonstration in the ALE-Lagrangian case can be found, for instance, in [FG09].

Lemma 1.1 *Consider the coupled systems* (1.28)-(1.30) *and* (1.31)-(1.33)*. Assume that the structure is hyper-elastic (with energy density function W) and that the system is isolated, i.e., $\boldsymbol{u}=\boldsymbol{0}$ on $\Gamma_{\mathrm{in}}\cup\Gamma_{\mathrm{out}}$. Then, the following energy inequality holds:*

$$E(t)\leq E(0).$$

1.3 Numerical methods: State-of-the-art

In this section, we present a review of the state-of-the-art in numerical methods for fluid-structure interaction according to two classification criteria: the modeling framework adopted and the degree of fluid-solid splitting attained.

1.3.1 Modeling frameworks

In the approximation of fluid-structure interaction problems, the formulation adopted (Lagrangian, Eulerian or Arbitrary-Lagrangian Eulerian) in each of the fluid and solid subproblems, together with the way that the two formulations are coupled at the interface, leads to different numerical solution procedures. In particular, the modeling framework adopted may favor the use of fitted or unfitted meshes.

1.3.1.1 ALE-Lagrangian techniques

Solution procedures belonging to this category build on the ALE-Lagrangian formulation of the coupled problem (see Section 1.2.3.1). The fluid subproblem is effectively solved in a time evolving computational domain, following the motion of the interface, while the solid subproblem is solved in a fixed reference domain. Note that the Lagrangian framework is the one usually adopted in solid mechanics, being the standard setting for legacy solid solvers. Among others, the ALE-Lagrangian approach is adopted in the following studies [HLZ81, DGH82, BNV08, MXA+12].

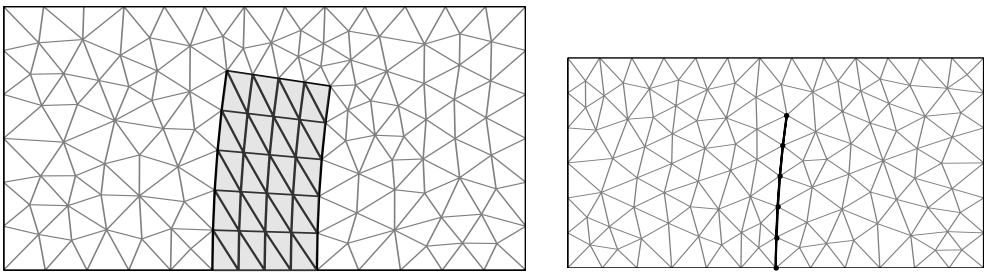

(a) (b)

Figure 1.5: Fitted fluid and solid meshes.

At the computational level, this approach generally involves fitted fluid and solid meshes (see Figure 1.5), with the fluid mesh being conveniently updated to track the motion of the fluid-structure interface. Due to the fitted nature of the meshes, an accurate computation of the transmission conditions (e.g., fluid loads on the structure) is generally guaranteed. In the case of coupling with an immersed thin-walled structure (see Figure 1.5 (b)), the discontinuous features of the fluid pressure solution can be straightforwardly incorporated within this framework by duplicating the pressure degrees of freedom matching at the interface, creating an internal discontinuous boundary, or crack, around the interface (see, e.g., Section 4.3.2 of Chapter 4).

The ALE-Lagrangian approach is the natural setting for situations with moderate structural deformations. For instance, in the context of computational hemodynamics, this approach is commonly used for blood-vessel interaction (see, e.g., [FFGQ09]). In situations with large interface deflections, however, maintaining fitted meshes can only be guaranteed by using *advanced mesh update techniques* (see, e.g., [STB04, YSH08, Wic11, Ala14, TTBA14]). Furthermore, this approach becomes cumbersome in situations with topological changes (e.g., due to contacting solids).

1.3.1.2 Eulerian-Lagrangian techniques

Numerical techniques entering this category are based on the Eulerian-Lagrangian description of the coupled problem (see Section 1.2.3.2). The approximation of the fluid subproblem is normally carried out by embedding the evolving physical domain into a larger fixed computational domain, or fictitious domain, whilst the solid subproblem is solved in its Lagrangian reference configuration. Among these approaches we can mention the *immersed boundary methods* (IB) (see, e.g., [Pes02, ZGWL04, Yu05, BCG11, BCG15]) and the *fictitious domain methods* (FD) (see, e.g., [GPHJ99a, Baa01, DSGB08, AGPT09, KHS+15, RF15]).

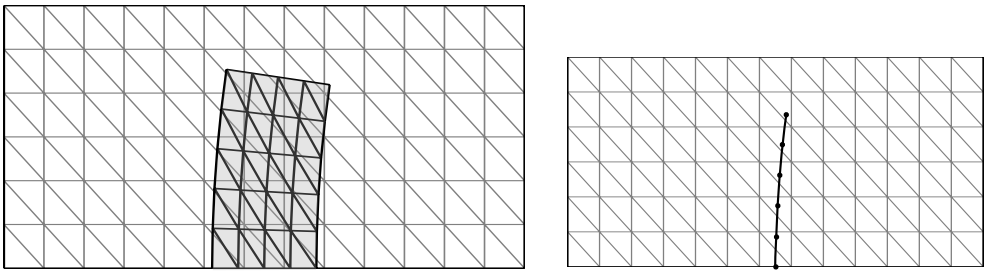

(a) (b)

Figure 1.6: Unfitted fluid and solid meshes.

At the computational level, these procedures are generally implemented using unfitted fluid and solid meshes (see Figure 1.6), with the fluid-structure interface moving independently of the background, often fixed, fluid mesh. The position of the interface is effectively tracked by displacing the solid mesh (see, e.g., [BCG15]) or by capturing it through a *level set method* (see, e.g., [LCB06]). This unfitted framework can involve, if not carefully designed, an inaccurate computation of the transmission conditions, leading to leaking across the interface or inaccuracies in the computation of the fluid loads. Furthermore, in the case of coupling with an immersed thin-walled structure (see Figure 1.6 (b)), the original IB and FD methods are known to be inaccurate in space due to the continuous nature of the fluid approximations across the interface. Mesh adaptation can alleviate these issues (e.g., [HFCC13]), but it does not cure the problem. The current trend to overcome these consistency issues is to combine a local *XFEM* enrichment with a *cut-FEM* methodology and a *Lagrange multiplier* treatment of the interface coupling (see, e.g., [LCB06, ZL08,

GW08, ST11]). The price to pay, with respect to the original IB and FD methods, is the need of a specific tracking of the interface intersections (see, e.g., [MGW09, WGMF12, MLL13]) and a loss of robustness with respect to how the interface intersects the background fluid mesh (see, e.g., [FB10, BCH+15]).

On the other hand, due to the unfitted nature of the meshes, these approaches are more versatile at simulating problems with large interface deflections with potential topological changes. In computational hemodynamics, these techniques have been widely applied to blood - cardiac valve interaction simulation (see, e.g., [DSGB08, AGPT09, KHS+15]).

1.3.1.3 Eulerian-Eulerian techniques

Techniques entering in this category have only recently been proposed in the literature and they are based on the Eulerian formulation of both the fluid and solid subproblems. The fully Eulerian framework seems to have been first considered in [Dun06], and then it has been further investigated in several studies (see, e.g., [DR06, Dun07, CMM08, RW10, Wic13, Ric13]).

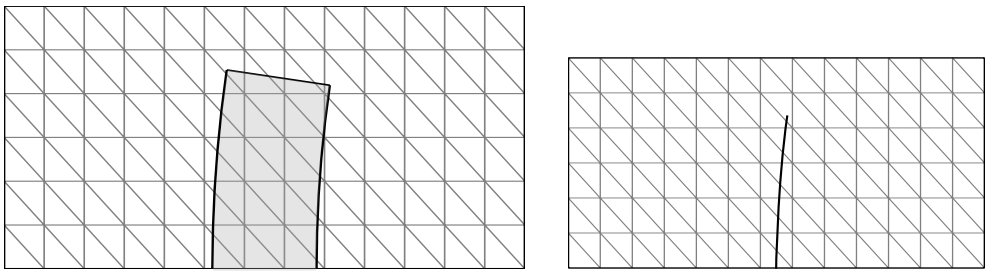

(a) (b)

Figure 1.7: A single mesh, comprising both the fluid and solid subdomains, with the solid domain being captured by a level set method.

This approach leads to a *single field system* that, computationally, is solved in a single mesh, comprising both the fluid and solid subdomains (see Figure 1.7). The fluid-structure interface must be conveniently captured, using a level set method, in order to localize the solid and fluid regions, in which the density, viscosity and the entire constitutive tensor change. Situations with large interface deflections and topological changes can, potentially, be addressed using this type of techniques. Besides the numerical issues mentioned in Section 1.3.1.2, a major drawback of these methods is that they could lead, if not carefully designed, to mass conservation issues. Moreover, they require non-standard Eulerian solid solvers, which prevents the reuse of well-stablished and developed legacy Lagrangian solvers for the solid.

1.3.2 Coupling schemes

At the fully discrete level, all the aforementioned techniques must conveniently account for the coupling mechanism, which includes the kinematic and dynamic

coupling conditions (1.24) and the geometrical compatibility (1.26) between the fluid and solid subdomains. The way in which the kinematic-dynamic coupling (1.24) is enforced between the fluid and solid time-marchings determines the so-called coupling scheme: *strongly coupled* (also referred in this work as *implicit*, see Remark 1.4), *semi-implicit* or *explicit* (see, e.g., [Fer11a, HWL12, Deg13] for recent reviews).

Remark 1.4 *In this work, we will always adopt an* explicit treatment of the geometric compatibility *condition* (1.26). *Although the terminology "implicit" often refers in the literature to approaches that treat both* (1.24) *and* (1.26) *in an implicit manner, we will use it here (see, e.g., Section 1.3.2.1) for schemes combining the aforementioned explicit treatment of* (1.26) *with an implicit treatment of* (1.24).

1.3.2.1 Implicit or strong coupling

In a *strongly coupled* scheme no time lag exits between the fluid and solid time-marchings. This can deliver unconditional stability and optimal accuracy, but at the price of solving a computationally demanding coupled problem at each time-step. The corresponding solution procedures are traditionally referred to in the literature as: *monolithic* and *partitioned*.

Monolithic methods solve the coupled problem at each time-step as a single system of equations (see, e.g., [BQQ08a, RW10, GKW11, CDFQ11, MMH12]). The work flow of this approach is represented in Figure 1.8: we simultaneously solve, in a single block, the fluid $\mathcal{F}(t_{n-1})$ and the solid $\mathcal{S}(t_{n-1})$ subproblems at time-step t_{n-1} and then, we proceed to the next time-step t_n.

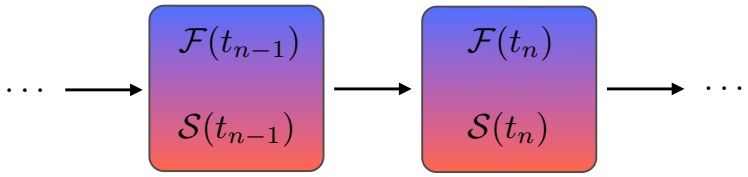

Figure 1.8: Monolithic solution of the coupled system.

Partitioned methods, on the contrary, exploit the heterogenous nature of the system via (recurrent) separate solutions of the fluid and solid equations, with appropriate interface conditions (see, e.g., [FM05, BNV08, DHV08, vB11, BK12, NPV14]). The work flow is represented in Figure 1.9, where the dotted circle represents inner iterations. Partitioned solution procedures are very appealing because of their intrinsic modularity, which enables the reuse of independent efficient solvers. Such an advantage comes however at a price, computational efficiency over a monolithic approach is not necessarily guaranteed (see, e.g., [BQQ08a, GKW11]).

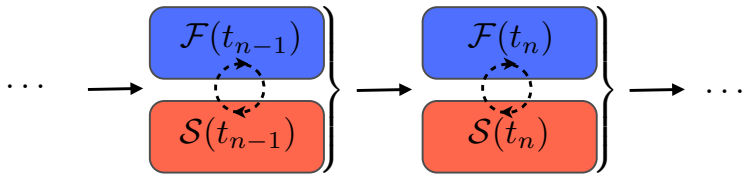

Figure 1.9: Partitioned solution of the coupled system

1.3.2.2 Semi-implicit coupling

Stable and less computationally onerous alternatives to strong coupling are the so-called semi-implicit coupling schemes, which enforce a specific explicit/implicit treatment of the kinematic-dynamic coupling conditions. They often involve a fractional-step time-marching in the fluid (see, e.g., [FGG07, QQ07, BQQ08b, ACF09, AG10]) or in the solid (see, e.g., [GGCC09, Fer11b, BCG+13, LMRHZ13]). The implicit part of the coupling (which, as above, can be solved in a monolithic or a partitioned fashion) guarantees stability, while the explicit one reduces computational complexity.

As an example, we report in Figure 1.10 the work flow corresponding to the *projection semi-implicit scheme* introduced in [FGG07]. This scheme is based on the use of a a fractional-step time-marching in the fluid, which splits its solution into an advection-diffusion $\mathcal{F}^{\mathrm{AD}}$ and a projection $\mathcal{F}^{\mathrm{P}}$ step. Afterwards, the advection-diffusion step is coupled explicitly with the solid, whereas the projection step is coupled implicitly with the solid (in a partitioned fashion in Figure 1.10).

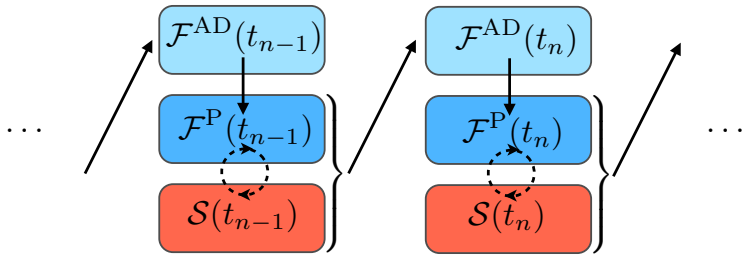

Figure 1.10: Semi-implicit projection solution of the coupled system (work flow corresponding to [FGG07]).

1.3.2.3 Explicit coupling

Explicit coupling schemes (also termed *loosely coupled*) uncouple the fluid and solid time-marchings via appropriate explicit discretizations of the interface conditions. The resulting solution procedures are thus naturally partitioned (see Figure 1.11). The design and the analysis of stable and accurate explicit coupling schemes for incompressible fluid-structure interaction problem is a challenging problem. This is due to the fact that the interface coupling can be extremely stiff. For instance, it is well-known that the standard explicit *Dirichlet-Neumann scheme* be-

comes unconditionally unstable whenever the *added-mass effect* in the system is large (see Section 1.4.3.3 below). Stability in explicit coupling has been an open problem for years (see [BF09]). The *stabilized explicit scheme* reported in [BF09, BF14a] guarantees stability but at the expense of a degradation of accuracy, which requires suitable correction iterations. In the case of the coupling with a purely elastic thin-walled solid, unconditional stability is achieved with the explicit *kinematically coupled scheme* introduced in [GGCC09], which is known to yield very poor accuracy (see [Fer11b, Fer13]). Numerical evidence suggests that enhanced accuracy can be obtained with the variants recently reported in [BCG+13, LMRHZ13]. Unfortunately, if physical damping is present in the structure equations, these coupling schemes are no longer explicit. These issues are overcome by the explicit *Robin-Neumann schemes* proposed in [Fer13, FMV13], which simultaneously deliver unconditional stability and optimal (first-order) time accuracy.

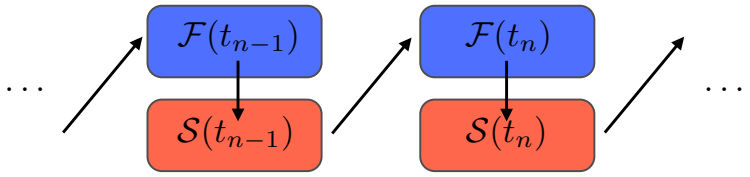

Figure 1.11: Explicit solution of the coupled system (work flow corresponding to [Fer13]).

Remark 1.5 *Some of the schemes referred to in this section are applied to a linear problem in Section 1.4.3 below. There, we provide the reader with some numerical results regarding their stability and accuracy properties. Later on, in Section 4.3.1 of Chapter 4, some of these schemes are also considered in a non-linear framework, where they are compared and validated against experimental data.*

1.4 Discretization of a model coupled problem

In the following, we address the discretization of a linear coupled model problem, involving either a thick or a thin-walled solid. Though simplified, this problem retains all the added-mass effect numerical issues that appear in complex non-linear incompressible fluid-structure interaction problems (see, e.g., [CGN05]). Remaining within this linear framework, we are able to present the ideas in a unified framework and provide the reader with some numerical stability and accuracy results. We consider both fitted and unfitted mesh discretizations and some of the coupling schemes referred to in Section 1.3.2. In particular, two fundamental concepts in the forthcoming chapters are presented in detail: the Robin-Neumann explicit coupling paradigm of [Fer11b, Fer13, FMV13] (Section 1.4.3.5 below) and the unfitted Nitsche discretization using overlapping meshes of [BF14b] (Section 1.4.2.3 below).

The treatment of the non-linear problem (1.28)-(1.30), using conformal moving meshes, is addressed in detail Chapter 4 (see also Section 2.3 in Chapter 2). The

extension of the unfitted Nitsche discretization to the non-linear problem (1.31)-(1.33), for the case of coupling with immersed thin-walled structures, is an important contribution of this work and its presentation is postponed to Chapter 6.

1.4.1 A linear model problem

In this section we consider a linearized version of problem (1.28)-(1.30) or, for what matters, of (1.31)-(1.33) (up to boundary conditions). Basically, we assume that the solid undergoes infinitesimal strains and displacements. Thus, the fluid-structure domain $\Omega^{\mathrm{f}}(t) \cap \Omega^{\mathrm{s}}(t) \equiv \Omega^{\mathrm{f}} \cap \Omega^{\mathrm{s}}$ can be assumed to be fixed in time. Furthermore, to ease the presentation, we consider the geometrical configuration displayed in Figure 1.12(a), with the solid domain disposed in one of the external boundaries of the fluid domain. The fluid and solid boundaries are partitioned as $\partial\Omega^{\mathrm{f}} = \Gamma^{\mathrm{f}} \cup \Sigma$ and $\partial\Omega^{\mathrm{s}} = \Gamma^{\mathrm{s}}_{\mathrm{d}} \cup \Sigma$, with $\Sigma = \Omega^{\mathrm{f}} \cup \Omega^{\mathrm{s}}$ the fluid-structure interface. The solid constitutive law is given by (1.10) with $\beta = 0$. Finally, we consider a *low Reynolds regime* in the fluid problem, which is described by the *Stokes equations*. The linear coupled problem reads as: find the fluid velocity $\boldsymbol{u} : \Omega^{\mathrm{f}} \times \mathbb{R}^+ \to \mathbb{R}^d$, the fluid pressure $p : \Omega^{\mathrm{f}} \times \mathbb{R}^+ \to \mathbb{R}$, the structure displacement $\boldsymbol{d} : \Omega^{\mathrm{s}} \times \mathbb{R}^+ \to \mathbb{R}^d$ and the structure velocity $\dot{\boldsymbol{d}} : \Omega^{\mathrm{s}} \times \mathbb{R}^+ \to \mathbb{R}^d$, such that

$$\begin{cases} \rho^{\mathrm{f}} \partial_t \boldsymbol{u} - \mathbf{div}\boldsymbol{\sigma}(\boldsymbol{u}, p) = \mathbf{0} & \text{in} \quad \Omega^{\mathrm{f}}, \\ \mathrm{div}\boldsymbol{u} = 0 & \text{in} \quad \Omega^{\mathrm{f}}, \\ \boldsymbol{u} = \mathbf{0} & \text{on} \quad \Gamma^{\mathrm{f}}, \end{cases} \tag{1.34}$$

$$\begin{cases} \rho^{\mathrm{s}} \partial_t \dot{\boldsymbol{d}} - \mathbf{div}\boldsymbol{\sigma}^{\mathrm{e}}(\boldsymbol{d}) = \mathbf{0} & \text{in} \quad \Omega^{\mathrm{s}}, \\ \dot{\boldsymbol{d}} = \partial_t \boldsymbol{d} & \text{in} \quad \Omega^{\mathrm{s}}, \\ \boldsymbol{d} = \mathbf{0} & \text{on} \quad \Gamma^{\mathrm{s}}_{\mathrm{d}}, \end{cases} \tag{1.35}$$

$$\begin{cases} \boldsymbol{u} = \dot{\boldsymbol{d}} & \text{on} \quad \Sigma, \\ \boldsymbol{\sigma}^{\mathrm{e}}(\boldsymbol{d})\boldsymbol{n}^{\mathrm{s}} = -\boldsymbol{\sigma}(\boldsymbol{u}, p)\boldsymbol{n} & \text{on} \quad \Sigma, \end{cases} \tag{1.36}$$

with the initial conditions $\boldsymbol{u}(0) = \boldsymbol{u}_0$, $\boldsymbol{d}(0) = \boldsymbol{d}_0$ and $\dot{\boldsymbol{d}}(0) = \dot{\boldsymbol{d}}_0$.

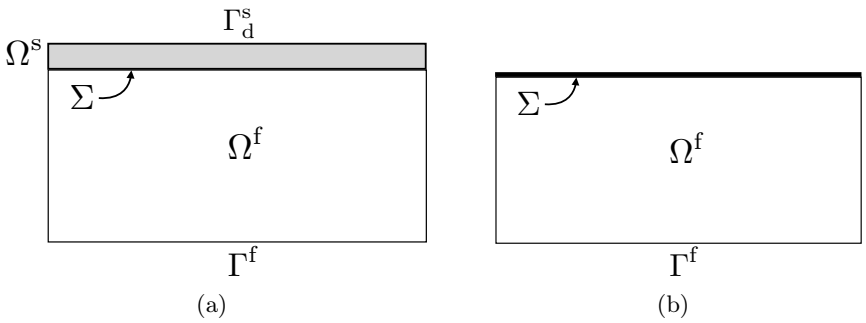

Figure 1.12: Geometrical configuration with thick (a) and thin-walled (b) solid model.

We also consider the case of the coupling with a linear elastic Kirchhoff-Love thin-walled structure (see Section 1.2.2.2). In that case, $\Sigma \equiv \Omega^{\mathrm{s}}$ (see Figure 1.12 (b)) and the relations (1.35)-(1.36) are replaced by

$$\begin{cases} \boldsymbol{u} = \dot{\boldsymbol{d}} & \text{on} \quad \Sigma, \\ \rho^{\mathrm{s}} \epsilon \partial_t \dot{\boldsymbol{d}} + \boldsymbol{L}^{\mathrm{e}} \boldsymbol{d} = -\boldsymbol{\sigma}(\boldsymbol{u}, p)\boldsymbol{n} & \text{on} \quad \Sigma, \\ \dot{\boldsymbol{d}} = \partial_t \boldsymbol{d} & \text{on} \quad \Sigma, \\ \boldsymbol{d} = \boldsymbol{0} & \text{on} \quad \partial\Sigma, \end{cases} \tag{1.37}$$

with $\boldsymbol{L}^{\mathrm{e}}$ the surface elastic operator (see Section 1.2.2.2).

Remark 1.6 *For simplicity and without loss of generality, we assume homogenous Dirichlet boundary conditions on the external boundaries of the coupled problem. However, this has no significant impact on the theoretical results presented below.*

1.4.2 Space semi-discretization

This section is devoted to the space semi-discretization of the coupled fluid-structure problems (1.34)-(1.36) and (1.34),(1.37). The fluid and solid equations are discretized by the finite element method. The solid domain Ω^{s} is supposed to be discretized using a conforming mesh, fitted to the boundary $\partial\Omega^{\mathrm{s}}$. For the sake of simplicity, we assume that Ω^{f} and Ω^{s} are *polyhedral*.

Firstly, we consider a discretization of the fluid domain Ω^{f}, such that the solid and fluid meshes are fitted at the interface (see Figure 1.14). This setting leads to a standard conformal discretization of the coupled problem. In that case, the kinematic coupling is strongly enforced and the dynamic coupling is treated weakly. This guarantees stability and accuracy.

Afterwards, we remove the condition on the conformity of the meshes at the interface, by letting the fluid mesh overlap the solid one (see Figure 1.15). The fluid problem is then solved in a fictitious extended domain. In this unfitted setting, the strong imposition of $(1.36)_1$ (or $(1.37)_1$) is no longer possible and other alternatives have to be considered to enforce the transmission conditions. A classical alternative is the use of Lagrange multipliers. The *Lagrange multiplier/Fictitious Domain method*, originally proposed in [GPP94], has been extensively used for fluid-structure interaction problems, involving moving immersed rigid particles (see, e.g., [GPHJ99b, GPH+01]) or more general immersed flexible structures (see, e.g., [Baa01, SDHBVdV04, DSGB08, AGPT09]). A well-known alternative to the discrete treatment of the interface conditions via Lagrange multipliers is *Nitsche's method* (see, e.g., [Nit71, Ste95, Han05]). Because of its flexibility and mathematical soundness, the Nitsche's mortaring has been applied to the design of numerical methods for a number of interface problems, including robust and accurate FD methods for elliptic and mixed problems [BH12, MLLR14, BH14]. Nitsche's method was first applied to fluid-structure interaction problems with fitted meshes in [HHS04] and used to design stable explicit coupling (or loosely coupled) schemes

in [BF09, BF14a]. In this section, we consider an extension of Nitsche's method, recently introduced in [BF14b], to fluid-structure interaction problems with unfitted meshes.

1.4.2.1 Weak form of the linear problem

In the sequel, we consider the usual *Sobolev spaces* $H^m(\omega)$ $(m \geq 0)$, with norm $\|\cdot\|_{m,\omega}$ and semi-norm $|\cdot|_{m,\omega}$. For a given part $\Gamma \subset \partial\omega$ of the boundary $\partial\omega$, the closed subspace consisting of functions in $H^1(\omega)$ with zero trace on $\Gamma \subset \partial\omega$ is denoted by $H^1_\Gamma(\omega)$. We recall that the L^2-scalar product on ω is denoted by $(\cdot,\cdot)_\omega$ and its norm by $\|\cdot\|_{0,\omega}$.

For the *weak formulation* of the solid problem (1.35), we consider $\boldsymbol{W} \overset{\text{def}}{=} [H^1_{\Gamma^{\text{s}}_{\text{d}}}(\Omega^{\text{s}})]^d$, as the space of admissible displacements, and the elastic bilinear form $a^{\text{s}} : \boldsymbol{W} \times \boldsymbol{W} \to \mathbb{R}$ defined as

$$a^{\text{s}}(\boldsymbol{d},\boldsymbol{w}) \overset{\text{def}}{=} L_1\big(\text{div}\boldsymbol{d},\text{div}\boldsymbol{w}\big)_{\Omega^{\text{s}}} + 2L_2\big(\boldsymbol{\varepsilon}(\boldsymbol{d}),\boldsymbol{\varepsilon}(\boldsymbol{w})\big)_{\Omega^{\text{s}}},$$

for all $\boldsymbol{d},\boldsymbol{w} \in \boldsymbol{W}$. In the case of coupling with a thin-walled structure, the elastic bilinear form is instead given by the weak form of the (unbounded linear) surface differential operator $\boldsymbol{L}^{\text{e}} : \boldsymbol{D}(\boldsymbol{L}^{\text{e}}) \subset [L^2(\Sigma)]^d \to [L^2(\Sigma)]^d$, namely,

$$a^{\text{s}}(\boldsymbol{d},\boldsymbol{w}) = (\boldsymbol{L}^{\text{e}}\boldsymbol{d},\boldsymbol{w})_\Sigma \tag{1.38}$$

for all $\boldsymbol{d} \in \boldsymbol{D}(\boldsymbol{L}^{\text{e}})$ and $\boldsymbol{w} \in \boldsymbol{W} \subset [H^1_{\partial\Sigma}(\Sigma)]^d$, which is assumed to be symmetric, coercive and continuous on $\boldsymbol{W}$. We define the elastic energy norm by $\|\cdot\|_{\text{s}} \overset{\text{def}}{=} a^{\text{s}}(\cdot,\cdot)^{\frac{1}{2}}$. In the case of coupling with a thin-walled structure, the following continuity estimate is also assumed

$$\|\boldsymbol{w}\|^2_{\text{s}} \leq \beta^{\text{s}}\|\boldsymbol{w}\|^2_{1,\Sigma}, \quad \forall \boldsymbol{w} \in \boldsymbol{W}, \tag{1.39}$$

with $\beta^{\text{s}} > 0$. In what follows, the symbol $(\cdot,\cdot)_*$ designates either $\rho^{\text{s}}(\cdot,\cdot)_{\Omega^{\text{s}}}$, or $\rho^{\text{s}}\epsilon(\cdot,\cdot)_\Sigma$, depending on wether the coupling is with a thick or a thin-walled solid, respectively. Similarly, $\|\cdot\|_*$ designates either $\rho^{\text{s}}\|\cdot\|_{\Omega^{\text{s}}}$ or $\rho^{\text{s}}\epsilon\|\cdot\|_\Sigma$.

For the weak formulation of the fluid problem (1.34), we consider $\boldsymbol{V} \overset{\text{def}}{=} [H^1_{\Gamma^{\text{f}}}(\Omega^{\text{f}})]^d$ and $Q \overset{\text{def}}{=} L^2(\Omega^{\text{f}})$, as velocity and pressure functional spaces, and the standard *Stokes bilinear forms* $a : \boldsymbol{V} \times \boldsymbol{V} \to \mathbb{R}$ and $b : Q \times \boldsymbol{V} \to \mathbb{R}$, given by

$$a(\boldsymbol{u},\boldsymbol{v}) \overset{\text{def}}{=} 2\mu\big(\boldsymbol{\varepsilon}(\boldsymbol{u}),\boldsymbol{\varepsilon}(\boldsymbol{v})\big)_{\Omega^{\text{f}}}, \quad b(q,\boldsymbol{v}) \overset{\text{def}}{=} -(q,\text{div}\boldsymbol{v})_{\Omega^{\text{f}}}. \tag{1.40}$$

For the shake of conciseness, we use the notation

$$a^{\text{f}}\big((\boldsymbol{u},p),(\boldsymbol{v},q)\big) \overset{\text{def}}{=} a(\boldsymbol{u},\boldsymbol{v}) + b(p,\boldsymbol{v}) - b(q,\boldsymbol{u}).$$

Formally, we obtain the weak formulation of the linear problems (1.34)-(1.36) and (1.34),(1.37), by multiplying (1.34) by $(\boldsymbol{v},q) \in \boldsymbol{V} \times Q$ and (1.35) (or (1.37)) by $\boldsymbol{w} \in \boldsymbol{W}$, integrating by parts and adding the resulting equations. This leads to the

following problem: find

$$(\boldsymbol{u}(t), p(t), \boldsymbol{d}(t), \dot{\boldsymbol{d}}(t)) \in \boldsymbol{V} \times Q \times \boldsymbol{W} \times \boldsymbol{W}$$

such that

$$\begin{cases} \boldsymbol{u}|_\Sigma = \dot{\boldsymbol{d}}|_\Sigma, \quad \dot{\boldsymbol{d}} = \partial_t \boldsymbol{d} \\ \rho^{\mathrm{f}} \left(\partial_t \boldsymbol{u}, \boldsymbol{v}\right)_{\Omega^{\mathrm{f}}} + a^{\mathrm{f}}\left((\boldsymbol{u}, p), (\boldsymbol{v}, q)\right) + \left(\partial_t \dot{\boldsymbol{d}}, \boldsymbol{w}\right)_* + a^{\mathrm{s}}(\boldsymbol{d}, \boldsymbol{w}) = 0 \end{cases} \tag{1.41}$$

for all $(\boldsymbol{v}, q, \boldsymbol{w}) \in \boldsymbol{V} \times Q \times \boldsymbol{W}$ with $\boldsymbol{v}|_\Sigma = \boldsymbol{w}|_\Sigma$. For the well-posedness of this type of linear fluid-structure coupled problems we refer to [LTM00, DGHL03].

Conforming mesh discretization of the solid domain Let $\{\mathcal{T}_h\}_{0<h\leq 1}$ denote a generic (fluid or solid) family of triangulations. The subscript $h \in (0, 1]$ refers to the level of refinement, which is defined as $h \stackrel{\text{def}}{=} \max_{K\in\mathcal{T}_h} h_K$, with h_K the diameter of a simplex $K \in \mathcal{T}_h$. In the sequel, all the families of triangulations considered are *non-degenerate* and, in order to simplify the presentation, *quasi-uniform*. This implies

$$\frac{h_K}{\rho_K} < C, \quad h_K \geq C_q h, \quad \forall K \in \mathcal{T}_h, \quad h \in (0, 1],$$

where ρ_K is the diameter of the largest ball inscribed in K and $C, C_q > 0$ are fixed constants independent of h.

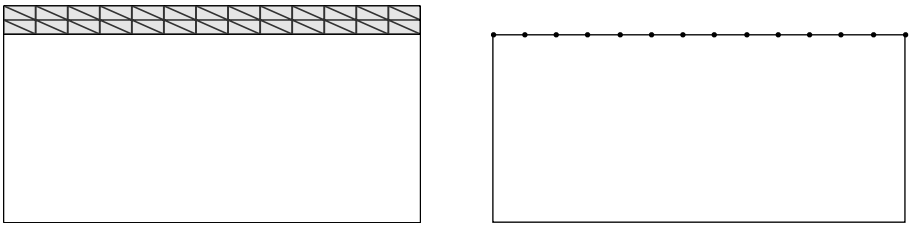

(a) (b)

Figure 1.13: Conforming discretization of the thick (a) and thin-walled (b) solid domain.

Consider a family of conforming triangulations $\{\mathcal{T}_h^{\mathrm{s}}\}_{0<h\leq 1}$ of Ω^{s}, i.e.,

$$\Omega^{\mathrm{s}} = \bigcup_{K\in\mathcal{T}_h^{\mathrm{s}}} \tag{1.42}$$

(see Figure 1.13), and let X_h^{s} denote the standard space of continuous piecewise affine functions associated to $\mathcal{T}_h^{\mathrm{s}}$,

$$X_h^{\mathrm{s}} \stackrel{\text{def}}{=} \left\{ v_h \in C^0(\overline{\Omega^{\mathrm{s}}}) \,/\, v_{h|K} \in \mathbb{P}_1(K) \quad \forall K \in \mathcal{T}_h^{\mathrm{s}} \right\}.$$

The solid approximation space is chosen as

$$\boldsymbol{W}_h \stackrel{\text{def}}{=} [X_h^{\text{s}}]^d \cap \boldsymbol{W}. \tag{1.43}$$

1.4.2.2 Fitted mesh spatial semi-discretization

Let $\{\widetilde{\mathcal{T}}_h^{\text{f}}\}_{0<h\leq 1}$ denote a family of conforming triangulations of Ω^{f}, i.e., $\Omega^{\text{f}} = \bigcup_{K\in\widetilde{\mathcal{T}}_h^{\text{f}}}$, such that $\widetilde{\mathcal{T}}_h^{\text{f}}$ matches at the interface with $\mathcal{T}_h^{\text{s}}$ for all $h \in (0,1]$ (see Figure 1.14). We denote by $\widetilde{X}_h^{\text{f}}$ the standard space of continuous piecewise affine

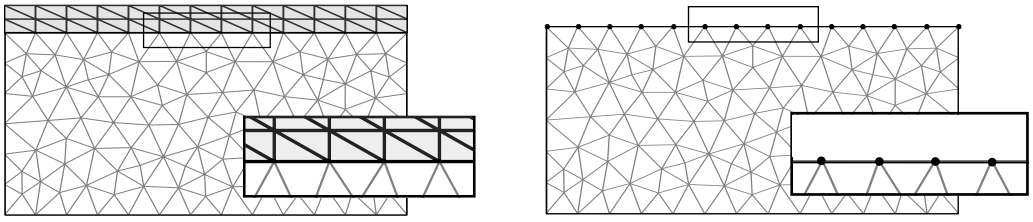

(a) (b)

Figure 1.14: Matching fluid and solid meshes.

functions associated to $\mathcal{T}_h^{\text{f}}$,

$$\widetilde{X}_h^{\text{f}} \stackrel{\text{def}}{=} \left\{ v_h \in C^0(\overline{\Omega^{\text{f}}}) \,/\, v_{h|K} \in \mathbb{P}_1(K) \quad \forall K \in \widetilde{\mathcal{T}}_h^{\text{f}} \right\}.$$

For the approximation of the fluid velocity and pressure, we consider the spaces $\widetilde{\boldsymbol{V}}_h \stackrel{\text{def}}{=} [\widetilde{X}_h^{\text{f}}]^d \cap \boldsymbol{V}$ and $\widetilde{Q}_h \stackrel{\text{def}}{=} \widetilde{X}_h^{\text{f}} \subset Q$, respectively. Note that the fluid and solid trace spaces on the interface coincide, i.e.,

$$\left\{ \boldsymbol{v}_h|_\Sigma \,/\, \boldsymbol{v}_h \in \widetilde{\boldsymbol{V}}_h \right\} \equiv \left\{ \boldsymbol{w}_h|_\Sigma \,/\, \boldsymbol{w}_h \in \boldsymbol{W}_h \right\}. \tag{1.44}$$

REMARK 1.7 *We use the superscript $\widetilde{\ }$ to refer to the fluid conforming meshes and discretization spaces (i.e., $\widetilde{\mathcal{T}}_h^{\text{f}}$, $\widetilde{X}_h^{\text{f}}$, $\widetilde{\boldsymbol{V}}_h$ and $\widetilde{Q}_h$). The superscript will be dropped in the non-conforming case of Section 1.4.2.3.*

Since the standard inf-sup condition (see, e.g., [GR86]) is not satisfied by the velocity/pressure pair $\widetilde{\boldsymbol{V}}_h/\widetilde{Q}_h$, we will resort to a stabilization technique. We consider a *symmetric pressure stabilization method* (see [BF09, Fer13]), given in terms of a positive and symmetric bilinear form $\widetilde{s}_h : \widetilde{Q}_h \times \widetilde{Q}_h \to \mathbb{R}$, such that

$$c_1 \mu^{-1} h^2 |q_h|^2_{1,\Omega^{\text{f}}} \leq \widetilde{s}_h(q_h, q_h) \leq c_2 \mu^{-1} h^2 |q_h|^2_{1,\Omega^{\text{f}}}, \tag{1.45}$$

for all $q_h \in \widetilde{Q}_h$ and with $c_1, c_2 > 0$. For instance, the classical *Brezzi-Pitkäranta bilinear form* [BP84] may be used,

$$\widetilde{s}_h(p_h, q_h) \stackrel{\text{def}}{=} \frac{\gamma_{\text{p}} h^2}{\mu} (\boldsymbol{\nabla} p_h, \boldsymbol{\nabla} q_h)_{\Omega^{\text{f}}} \tag{1.46}$$

with $\gamma_{\mathrm{p}} > 0$.

Property (1.44) of the discretization setting enables a conforming semi-discrete approximation of (1.41): for $t > 0$, find

$$\big(\boldsymbol{u}_h(t), p_h(t), \dot{\boldsymbol{d}}_h(t), \boldsymbol{d}_h(t)\big) \in \widetilde{\boldsymbol{V}}_h \times \widetilde{Q}_h \times \boldsymbol{W}_h \times \boldsymbol{W}_h,$$

such that

$$\begin{cases} \boldsymbol{u}_h|_\Sigma = \dot{\boldsymbol{d}}_h|_\Sigma, \quad \dot{\boldsymbol{d}}_h = \partial_t \boldsymbol{d}_h, \\ \rho^{\mathrm{f}}\big(\partial_t \boldsymbol{u}_h, \boldsymbol{v}_h\big)_{\Omega^{\mathrm{f}}} + a^{\mathrm{f}}\big((\boldsymbol{u}_h, p_h), (\boldsymbol{v}_h, q_h)\big) + \widetilde{s}_h(p_h, q_h) \\ \quad + \big(\partial_t \dot{\boldsymbol{d}}_h, \boldsymbol{w}_h\big)_* + a^{\mathrm{s}}(\boldsymbol{d}_h, \boldsymbol{w}_h) = 0 \end{cases} \tag{1.47}$$

for all $(\boldsymbol{v}_h, q_h, \boldsymbol{w}_h) \in \widetilde{\boldsymbol{V}}_h \times \widetilde{Q}_h \times \boldsymbol{W}_h$ with $\boldsymbol{v}_h|_\Sigma = \boldsymbol{w}_h|_\Sigma$.

As starting point for partitioned approaches, it is convenient to reformulate the monolithic formulation (1.47) in a partitioned Dirichlet-Neumann fashion. For that purpose, we consider the space $\boldsymbol{V}_\Sigma \overset{\text{def}}{=} [H^1_\Sigma(\Omega^{\mathrm{f}})]^d$ and set $\boldsymbol{V}_{\Sigma,h} \overset{\text{def}}{=} \widetilde{\boldsymbol{V}}_h \cap \boldsymbol{V}_\Sigma$. Using the standard *fluid-sided discrete lifting operator* $\boldsymbol{\mathcal{L}}_h : \boldsymbol{W}_h \to \widetilde{\boldsymbol{V}}_h$, such that, the nodal values of $\boldsymbol{\mathcal{L}}_h \boldsymbol{w}_h$ vanish out of Σ and $(\boldsymbol{\mathcal{L}}_h \boldsymbol{w}_h)|_\Sigma = \boldsymbol{w}_h|_\Sigma$ for all $\boldsymbol{w}_h \in \boldsymbol{W}_h$, we can decompose the test space as follows

$$\begin{aligned} \big\{(\boldsymbol{v}_h, \boldsymbol{w}_h) \in \widetilde{\boldsymbol{V}}_h \times \boldsymbol{W}_h \,/\, \boldsymbol{v}_h|_\Sigma = \boldsymbol{w}_h|_\Sigma\big\} = \big\{(\boldsymbol{v}_h, \boldsymbol{0}) \,/\, \boldsymbol{v}_h \in \boldsymbol{V}_{\Sigma,h}\big\} \\ \oplus \big\{(\boldsymbol{\mathcal{L}}_h \boldsymbol{w}_h, \boldsymbol{w}_h) \,/\, \boldsymbol{w}_h \in \boldsymbol{W}_h\big\}. \end{aligned}$$

Thus, problem (1.47) equivalently reads as: for $t > 0$,

- Fluid subproblem: find $\big(\boldsymbol{u}_h(t), p_h(t)\big) \in \widetilde{\boldsymbol{V}}_h \times \widetilde{Q}_h$, such that

$$\begin{cases} \boldsymbol{u}_h|_\Sigma = \dot{\boldsymbol{d}}_h|_\Sigma, \\ \rho^{\mathrm{f}}\big(\partial_t \boldsymbol{u}_h, \boldsymbol{v}_h\big)_{\Omega^{\mathrm{f}}} + a^{\mathrm{f}}\big((\boldsymbol{u}_h, p_h), (\boldsymbol{v}_h, q_h)\big) + \widetilde{s}_h(p_h, q_h) = 0 \end{cases} \tag{1.48}$$

  for all $(\boldsymbol{v}_h, q_h) \in \boldsymbol{V}_{\Sigma,h} \times \widetilde{Q}_h$.

- Solid subproblem: find $\big(\dot{\boldsymbol{d}}_h(t), \boldsymbol{d}_h(t)\big) \in \boldsymbol{W}_h \times \boldsymbol{W}_h$, such that

$$\begin{cases} \dot{\boldsymbol{d}}_h = \partial_t \boldsymbol{d}_h, \\ \big(\partial_t \dot{\boldsymbol{d}}_h, \boldsymbol{w}_h\big)_* + a^{\mathrm{s}}(\boldsymbol{d}_h, \boldsymbol{w}_h) \\ \quad = -\rho^{\mathrm{f}}\big(\partial_t \boldsymbol{u}_h, \boldsymbol{\mathcal{L}}_h \boldsymbol{w}_h\big)_{\Omega^{\mathrm{f}}} - a(\boldsymbol{u}_h, \boldsymbol{\mathcal{L}}_h \boldsymbol{w}_h) - b(p_h, \boldsymbol{\mathcal{L}}_h \boldsymbol{w}_h) \end{cases} \tag{1.49}$$

  for all $\boldsymbol{w}_h \in \boldsymbol{W}_h$.

Note that the fluid stress in (1.49) is given in terms of a *variational residual* using the discrete lifting operator $\boldsymbol{\mathcal{L}}_h$.

The following result states the optimal accuracy of (1.47) in the energy norm. In the sequel, the symbol $\lesssim$ denotes inequality up to a multiplicative constant independent of h.

THEOREM 1.1 *Let $(\boldsymbol{u}, p, \dot{\boldsymbol{d}}, \boldsymbol{d})$ be the solution of (1.34)-(1.36) (or (1.34),(1.37)). and $(\boldsymbol{u}_h, p_h, \dot{\boldsymbol{d}}_h, \boldsymbol{d}_h)$ be given by (1.47). Assume that the interface Σ is flat. Then, for regular enough solutions and $t > 0$, there holds:*

$$\frac{\rho^{\mathrm{f}}}{2}\|(\boldsymbol{u}_h - \boldsymbol{u})(t)\|^2_{0,\Omega^{\mathrm{f}}} + \frac{1}{2}\|(\dot{\boldsymbol{d}}_h - \dot{\boldsymbol{d}})(t)\|^2_* + \frac{1}{2}\|(\boldsymbol{d}_h - \boldsymbol{d})(t)\|^2_{\mathrm{s}} \lesssim h^2.$$

Proof. The proof follows from the arguments of [DGHL03] (see also [Fer13]). ∎

1.4.2.3 Unfitted mesh spatial semi-discretization

In this section, we let the fluid triangulations $\{\mathcal{T}_h^{\mathrm{f}}\}_{0<h\leq 1}$ be unfitted to the fluid domain Ω^{f}, overlapping the solid meshes $\{\mathcal{T}_h^{\mathrm{s}}\}_{0<h\leq 1}$ at the interface zone. More precisely, we assume that:

(A1) $\overline{\Omega^{\mathrm{f}}} \subsetneq \bigcup_{K\in\mathcal{T}_h^{\mathrm{f}}}$, but for every simplex $K \in \mathcal{T}_h^{\mathrm{f}}$, it holds $K \cap \Omega^{\mathrm{f}} \neq \varnothing$.

(A2) $\mathcal{T}_h^{\mathrm{f}}$ is fitted to Γ^{f} but, in general, not to Σ.

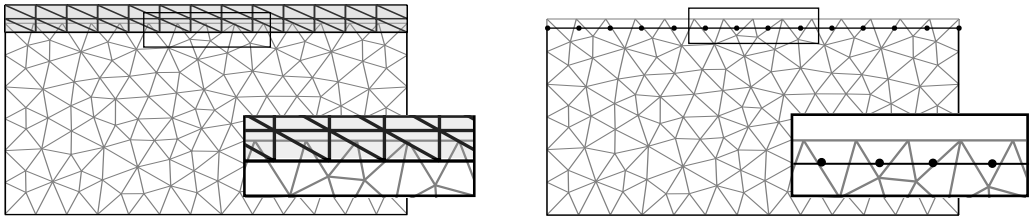

(a) (b)

Figure 1.15: Overlapping fluid and solid meshes.

A prototypical configuration is displayed in Figure 1.15. We denote by Ω_h the domain covered by $\mathcal{T}_h^{\mathrm{f}}$ (*computational domain*), by $\mathcal{G}_h$ the set of elements in $\mathcal{T}_h^{\mathrm{f}}$ that are intersected by Σ and by $\mathcal{F}_{\mathcal{G}}$ the set of edges or faces of elements in $\mathcal{G}_h$ that do not belong to $\partial\Omega_h$, that is,

$$\begin{aligned} \Omega_h &\stackrel{\text{def}}{=} \operatorname{int}\left(\cup_{K\in\mathcal{T}_h^{\mathrm{f}}} K\right), \\ \mathcal{G}_h &\stackrel{\text{def}}{=} \left\{K \in \mathcal{T}_h^{\mathrm{f}} \,/\, K \cap \Sigma \neq \varnothing\right\}, \\ \mathcal{F}_{\mathcal{G}} &\stackrel{\text{def}}{=} \left\{F \in \partial K \,/\, K \in \mathcal{G}_h, F \cap \partial\Omega_h \neq F\right\}. \end{aligned} \tag{1.50}$$

For a simplex $K \in \mathcal{G}_h$, we denote by Σ_K the part of the interface intersecting K, i.e, $\Sigma_K \stackrel{\text{def}}{=} \Sigma \cap K$. The standard space of continuous piecewise affine functions associated to $\mathcal{T}_h^{\mathrm{f}}$ reads as

$$X_h^{\mathrm{f}} \stackrel{\text{def}}{=} \left\{v_h \in C^0(\overline{\Omega_h}) \,/\, v_{h|K} \in \mathbb{P}_1(K) \quad \forall K \in \mathcal{T}_h^{\mathrm{f}}\right\}.$$

For the approximation of the fluid velocity and pressure spaces, we consider, respectively,

$$\boldsymbol{V}_h \stackrel{\text{def}}{=} \left\{ \boldsymbol{v}_h \in [X_h^{\text{f}}]^d / \, \boldsymbol{v}_h|_{\Gamma^{\text{f}}} = \boldsymbol{0} \right\}, \quad Q_h \stackrel{\text{def}}{=} X_h^{\text{f}}. \tag{1.51}$$

A pressure stabilization bilinear form $s_h : Q_h \times Q_h \to \mathbb{R}$, is used to treat the instabilities associated to the inf-sup incompatible choice of fluid spaces. The stability condition (1.45) is required to hold over the whole computation domain Ω_h, i.e,

$$c_1 \mu^{-1} h^2 |q_h|^2_{1,\Omega_h} \leq s_p(q_h, q_h) \leq c_2 \mu^{-1} h^2 |q_h|^2_{1,\Omega_h}, \tag{1.52}$$

or all $q_h \in Q_h$ and with $c_1, c_2 > 0$. This is crucial to gain control over the interfacial pressure-velocity coupling. An extended version of (1.46) may be used in the following form

$$s_h(p_h, q_h) \stackrel{\text{def}}{=} \frac{\gamma_{\text{p}} h^2}{\mu} (\boldsymbol{\nabla} p_h, \boldsymbol{\nabla} q_h)_{\Omega_h}, \tag{1.53}$$

with $\gamma_{\text{p}} > 0$.

To guarantee the robustness of the method irrespectively of the way the interface intersects the fluid mesh, we make use of a *ghost-penalty stabilization method* [Bur10, BH14], given in terms of a bilinear form $g_h : \boldsymbol{V}_h \times \boldsymbol{V}_h \to \mathbb{R}$. This operator brings additional control over the velocity ghost values so that the following strengthened stability holds

$$\tilde{c}_{\text{g}} \left(\mu \|\boldsymbol{\varepsilon}(\boldsymbol{v}_h)\|^2_{0,\Omega_h} + g_h(\boldsymbol{v}_h, \boldsymbol{v}_h) \right) \leq \mu \|\boldsymbol{\varepsilon}(\boldsymbol{v}_h)\|^2_{0,\Omega^{\text{f}}} + g_h(\boldsymbol{v}_h, \boldsymbol{v}_h), \tag{1.54}$$

for all $\boldsymbol{v}_h \in \boldsymbol{V}_h$ and with $\tilde{c}_{\text{g}} > 0$. The ghost-penalty operator must satisfy certain weak consistency properties that are properly described in Section 5.2.2.2 of Chapter 5. For the purpose of the presentation, and without loss of generality, we consider the following operator

$$g_h(\boldsymbol{u}_h, \boldsymbol{v}_h) = \gamma_{\text{g}} \mu h \sum_{F \in \mathcal{F}_{\mathcal{G}}} \left([\![\boldsymbol{\nabla} \boldsymbol{u}_h]\!]_F, [\![\boldsymbol{\nabla} \boldsymbol{v}_h]\!]_F \right)_F, \tag{1.55}$$

where the symbol $[\![\cdot]\!]_F$ denotes the jump of a given quantity across the edge or face F (see [BH14] for a proof of (1.54) in that case). We denote the total fluid stabilization by

$$S_h\big((\boldsymbol{u}_h, p_h), (\boldsymbol{v}_h, q_h)\big) \stackrel{\text{def}}{=} s_h(p_h, q_h) + g_h(\boldsymbol{u}_h, \boldsymbol{v}_h), \tag{1.56}$$

with associated semi-norm $|(u_h, p_h)|_S \stackrel{\text{def}}{=} S_h\big((\boldsymbol{u}_h, p_h), (\boldsymbol{v}_h, q_h)\big)^{\frac{1}{2}}$.

Remark 1.8 *Following [BH14], we could have split the pressure stabilization into a part defined over to $\Omega_h / \mathcal{G}_h$, to ensure the inf-sup condition, and a ghost-penalty part over the interface zone $\mathcal{G}_h$, to extend the stability up to the mesh boundary. Here, we choose however to treat all the pressure stabilization in an unified way over the whole computational domain Ω_h (see also [BF14b]).*

The unfitted discretization proposed in [BF14b] of the linear problem (1.34)-(1.36) (or (1.34),(1.37)) reads as follows: for $t > 0$, find

$$\big(\boldsymbol{u}_h(t), p_h(t), \dot{\boldsymbol{d}}_h(t), \boldsymbol{d}_h(t)\big) \in \boldsymbol{V}_h \times Q_h \times \boldsymbol{W}_h \times \boldsymbol{W}_h,$$

such that $\dot{\boldsymbol{d}}_h = \partial_t \boldsymbol{d}_h$ and

$$\begin{cases} \rho^{\mathrm{f}}\big(\partial_t \boldsymbol{u}_h, \boldsymbol{v}_h\big)_{\Omega^{\mathrm{f}}} + a^{\mathrm{f}}\big((\boldsymbol{u}_h, p_h), (\boldsymbol{v}_h, q_h)\big) + S_h\big((\boldsymbol{u}_h, p_h), (\boldsymbol{v}_h, q_h)\big) \\ \quad + \big(\partial_t \dot{\boldsymbol{d}}_h, \boldsymbol{w}_h\big)_* + a^{\mathrm{s}}(\boldsymbol{d}_h, \boldsymbol{w}_h) \underbrace{- \big(\boldsymbol{\sigma}(\boldsymbol{u}_h, p_h)\boldsymbol{n}, \boldsymbol{v}_h - \boldsymbol{w}_h\big)_\Sigma}_{T_1} \\ \underbrace{- \big(\boldsymbol{u}_h - \dot{\boldsymbol{d}}_h, \boldsymbol{\sigma}(\boldsymbol{v}_h, -q_h)\boldsymbol{n}\big)_\Sigma}_{T_2} \underbrace{+ \frac{\gamma\mu}{h}\big(\boldsymbol{u}_h - \dot{\boldsymbol{d}}_h, \boldsymbol{v}_h - \boldsymbol{w}_h\big)_\Sigma}_{T_2} = 0 \end{cases} \tag{1.57}$$

for all $(\boldsymbol{v}_h, q_h, \boldsymbol{w}_h) \in \boldsymbol{V}_h \times Q_h \times \boldsymbol{W}_h$. Here, the term T_1 guarantees the consistency of the formulation, the term T_2 is used to symmetrize the problem and the term T_3 is a stabilization term added to guarantee the coercivity of the formulation, with $\gamma > 0$ denoting the Nitsche's penalty parameter.

REMARK 1.9 *Note that the fluid's bulk terms are integrated over the physical domain Ω^{f}. From the implementation point of view, this requires non-standard quadrature techniques for the approximation of integrals over cut elements (see [MLL13, BCH+15]). This problem is addressed in this manuscript in Chapter 6 (Section 6.2.2.3).*

REMARK 1.10 *The Nitsche's coupling enforced in (1.57) was first introduced in the fitted mesh context described in Section 1.4.2.2 (see [BF09, BF14a]). Formally, the formulation in that case is equivalent to (1.57) with $\gamma_{\mathrm{g}} = 0$.*

As in the previous section, it is convenient to reformulate (1.57) in terms of two coupled subproblems by successively taking $\boldsymbol{w}_h = \boldsymbol{0}$ and $(\boldsymbol{v}_h, q_h) = (\boldsymbol{0}, 0)$ in (1.57). This yields: for $t > 0$,

- Fluid subproblem: find $\big(\boldsymbol{u}_h(t), p_h(t)\big) \in \boldsymbol{V}_h \times Q_h$, such that

$$\begin{cases} \rho^{\mathrm{f}}\big(\partial_t \boldsymbol{u}_h, \boldsymbol{v}_h\big)_{\Omega^{\mathrm{f}}} + a^{\mathrm{f}}\big((\boldsymbol{u}_h, p_h), (\boldsymbol{v}_h, q_h)\big) + S_h\big((\boldsymbol{u}_h, p_h), (\boldsymbol{v}_h, q_h)\big) \\ \quad - \big(\boldsymbol{\sigma}(\boldsymbol{u}_h, p_h)\boldsymbol{n}, \boldsymbol{v}_h\big)_\Sigma - \big(\boldsymbol{u}_h - \dot{\boldsymbol{d}}_h, \boldsymbol{\sigma}(\boldsymbol{v}_h, -q_h)\boldsymbol{n}\big)_\Sigma + \frac{\gamma\mu}{h}\big(\boldsymbol{u}_h - \dot{\boldsymbol{d}}_h, \boldsymbol{v}_h\big)_\Sigma = 0 \end{cases} \tag{1.58}$$

  for all $(\boldsymbol{v}_h, q_h) \in \boldsymbol{V}_h \times Q_h$.

- Solid subproblem: find $\big(\dot{\boldsymbol{d}}_h(t), \boldsymbol{d}_h(t)\big) \in \boldsymbol{W}_h \times \boldsymbol{W}_h$, such that $\dot{\boldsymbol{d}}_h = \partial_t \boldsymbol{d}_h$ and

$$\big(\partial_t \dot{\boldsymbol{d}}_h, \boldsymbol{w}_h\big)_* + a^{\mathrm{s}}(\boldsymbol{d}_h, \boldsymbol{w}_h) + \big(\boldsymbol{\sigma}(\boldsymbol{u}_h, p_h)\boldsymbol{n}, \boldsymbol{w}_h\big)_\Sigma + \frac{\gamma\mu}{h}\big(\dot{\boldsymbol{d}}_h - \boldsymbol{u}_h, \boldsymbol{w}_h\big)_\Sigma = 0 \tag{1.59}$$

  for all $\boldsymbol{w}_h \in \boldsymbol{W}_h$.

Note that in (1.59), the variationally-consistent expression of the fluid load comprises all the forcing terms coming from Nitsche's method, including penalties.

For the purpose of the analysis, we will assume that

(A3) Σ is well resolved by $\mathcal{T}_h^{\mathrm{f}}$ (see, e.g., [BH14]),

so that the following *trace inequality* holds for functions in $H^1(K)$, for all $K \in \mathcal{T}_h^{\mathrm{f}}$: there exists a constant $C_{\mathrm{T}} > 0$, depending only on Σ, such that

$$\|v\|_{0,\Sigma\cap K} \leq C_{\mathrm{T}}\big(h_K^{-\frac{1}{2}}\|v\|_{0,K} + h_K^{\frac{1}{2}}\|\boldsymbol{\nabla} v\|_{0,K}\big) \tag{1.60}$$

for all $v \in H^1(K)$. The proof for this result follows from [HH02, Lemma 3]. In particular, using (1.60) with a discrete inverse inequality, it follows

$$h\|\boldsymbol{\varepsilon}(\boldsymbol{v}_h)\boldsymbol{n}\|_{0,\Sigma}^2 \leq C_{\mathrm{TI}}\|\boldsymbol{\varepsilon}(\boldsymbol{v}_h)\|_{0,\Omega_h}^2, \tag{1.61}$$

for all $\boldsymbol{v}_h \in \boldsymbol{V}_h$. Note that the above trace inequality holds irrespectively of the interface position because the norm on the right-hand side is taken over the whole computational domain Ω_h. However, this control on the interfacial viscous flux can not be bounded by the natural viscous dissipation of the fluid, which is only available in the physical domain $\Omega^{\mathrm{f}} \subset \Omega_h$. The strengthened stability (1.54) provided by the ghost penalty operator, allows to extend to Ω_h the coercivity of the spatial discrete Stokes-Nitsche operator. This is stated in the following lemma from [BF14b], whose proof is presented here for completeness.

Lemma 1.2 *For $\gamma > 0$ sufficiently large, there exists a constant $c_{\mathrm{g}} > 0$ such that*

$$\begin{aligned} c_{\mathrm{g}}\Big(\mu\|\boldsymbol{\nabla}\boldsymbol{v}_h\|_{0,\Omega_h}^2 + \frac{\gamma\mu}{h}\|\boldsymbol{v}_h - \boldsymbol{w}_h\|_{0,\Sigma}^2 + |(\boldsymbol{v}_h, q_h)|_S^2\Big) \leq \\ a^{\mathrm{f}}\big((\boldsymbol{v}_h, q_h), (\boldsymbol{v}_h, q_h)\big) + S_h\big((\boldsymbol{v}_h, q_h), (\boldsymbol{v}_h, q_h)\big) - \big(\boldsymbol{\sigma}(\boldsymbol{v}_h, q_h)\boldsymbol{n}, \boldsymbol{v}_h - \boldsymbol{w}_h\big)_\Sigma \\ - \big(\boldsymbol{v}_h - \boldsymbol{w}_h, \boldsymbol{\sigma}(\boldsymbol{v}_h, -q_h)\boldsymbol{n}\big)_\Sigma + \frac{\gamma\mu}{h}\big(\boldsymbol{v}_h - \boldsymbol{w}_h, \boldsymbol{v}_h - \boldsymbol{w}_h\big)_\Sigma \end{aligned}$$

for all $(\boldsymbol{v}_h, q_h) \in \boldsymbol{V}_h \times Q_h$ and $\boldsymbol{w}_h \in \boldsymbol{W}_h$.

Proof. First, we have

$$\begin{aligned} a_h^{\mathrm{f}}\big((\boldsymbol{v}_h, q_h), (\boldsymbol{v}_h, q_h)\big) - \big(\boldsymbol{\sigma}(\boldsymbol{v}_h, q_h)\boldsymbol{n}, \boldsymbol{v}_h - \boldsymbol{w}_h\big)_\Sigma \\ - \big(\boldsymbol{v}_h - \boldsymbol{w}_h, \boldsymbol{\sigma}(\boldsymbol{v}_h, -q_h)\boldsymbol{n}\big)_\Sigma + \frac{\gamma\mu}{h}\|\boldsymbol{v}_h - \boldsymbol{w}_h\|_{0,\Sigma}^2 + |(\boldsymbol{v}_h, q_h)|_S^2 \\ = 2\mu\|\boldsymbol{\varepsilon}(\boldsymbol{v}_h)\|_{0,\Omega^{\mathrm{f}}}^2 - 2\big(\boldsymbol{\sigma}(\boldsymbol{v}_h, 0)\boldsymbol{n}, \boldsymbol{v}_h - \boldsymbol{w}_h\big)_\Sigma + \frac{\gamma\mu}{h}\|\boldsymbol{v}_h - \boldsymbol{w}_h\|_{0,\Sigma}^2 + |(\boldsymbol{v}_h, q_h)|_S^2. \end{aligned}$$

Combining the Cauchy-Schwarz inequality with (1.61), we have

$$\begin{aligned} \big(2\boldsymbol{\sigma}(\boldsymbol{v}_h, 0)\boldsymbol{n}, \boldsymbol{v}_h - \boldsymbol{w}_h\big)_\Sigma &\leq 2\big(\frac{h\mu}{\gamma}\big)^{\frac{1}{2}}\|\boldsymbol{\varepsilon}(\boldsymbol{v}_h)\boldsymbol{n}\|_{0,\Sigma}\big(\frac{\gamma\mu}{h}\big)^{\frac{1}{2}}\|\boldsymbol{v}_h - \boldsymbol{w}_h\|_{0,\Sigma} \\ &\leq \frac{8C_{\mathrm{TI}}}{\gamma}\mu\|\boldsymbol{\varepsilon}(\boldsymbol{v}_h)\|_{0,\Omega_h}^2 + \frac{1}{2}\frac{\gamma\mu}{h}\|\boldsymbol{v}_h - \boldsymbol{w}_h\|_{0,\Sigma}^2. \end{aligned}$$

We conclude by using (1.54), taking

$$\gamma > \frac{8C_{\mathrm{TI}}}{\tilde{c}_{\mathrm{g}}} \tag{1.62}$$

and using Korn's inequality. ∎

REMARK 1.11 *The proof of Lemma 1.2 provides a lower bound for the parameter $\gamma > 0$ through the relation (1.62). The constants therein could be estimated automatically from the solution of generalized eigenvalue problems associated with the inequalities (1.54) and (1.61). We refer to [HH92, Section 3] for an overview of this approach, and to [RSÖ14, EDH10] for applications in the context of Nitsche's method.*

For the convergence analysis of (1.57), a mild technical assumption has to be considered (whose use will be made clear in Section 5.2.2.2). We assume that the elements of $\mathcal{T}_h^{\mathrm{s}}$ with faces on Σ can be grouped in disjoint $(d-1)$-dimensional macropatches P_i, with $\mathrm{meas}(P_i) = \mathcal{O}(h^d)$ for the thick-walled solid $(1.35)_1$ and $\mathrm{meas}(P_i) = \mathcal{O}(h^{d-1})$ in the case of the thin-walled solid $(1.37)_2$. The restriction of the patch P_i to Σ will be denoted by $F_i \overset{\mathrm{def}}{=} P_i \cap \Sigma$. In the case of a thin-walled solid, we have $F_i \equiv P_i$. Each macropatch is assumed to contain at least one interior node and the union of F_i is assumed to cover Σ, that is, $\cup_i F_i = \Sigma$. Under the above assumptions, the following result states that the formulation (1.57) preserves the optimal convergence behavior of the conforming discretization (1.47) (see Theorem 1.1).

THEOREM 1.2 *Let $(\boldsymbol{u}, p, \dot{\boldsymbol{d}}, \boldsymbol{d})$ be the solution of (1.34)-(1.36) (or (1.34),(1.37)) and $(\boldsymbol{u}_h, p_h, \dot{\boldsymbol{d}}_h, \boldsymbol{d}_h)$ be given by (1.57). Assume that the interface Σ is flat and $\gamma > 0$ is given by Lemma 1.2. Then, for regular enough solutions and $t > 0$, there holds:*

$$\frac{\rho^{\mathrm{f}}}{2}\|(\boldsymbol{u}_h - \boldsymbol{u})(t)\|^2_{0,\Omega^{\mathrm{f}}} + \frac{1}{2}\|(\dot{\boldsymbol{d}}_h - \dot{\boldsymbol{d}})(t)\|^2_{*} + \frac{1}{2}\|(\boldsymbol{d}_h - \boldsymbol{d})(t)\|^2_{\mathrm{s}} + c_{\mathrm{g}}\int_0^t \left[\mu\|\boldsymbol{\nabla}(\boldsymbol{u}_h - \boldsymbol{u})\|^2_{0,\Omega^{\mathrm{f}}} + \frac{\gamma\mu}{h}\|\boldsymbol{u}_h - \dot{\boldsymbol{d}}_h\|^2_{0,\Sigma}\right] \lesssim h^2.$$

Proof. We refer to [BF14b, Theorem 3.1] for a proof. The main ingredients for the proof can also be found within this manuscript in Corollary 5.2 (there presented in the fully discrete case). ∎

1.4.3 Time discretization

We address now the fully discrete approximation of the linear problems (1.34)-(1.36) and (1.34),(1.37). The time discretization is carried out with different implicit, semi-implicit and explicit coupling strategies (see Section 1.3.2).

In the following, the symbol $\tau > 0$ denotes the time-step size, $t_n \overset{\text{def}}{=} n\tau$, for $n \in \mathbb{N}$, and $\partial_\tau x^n \overset{\text{def}}{=} \big(x^n - x^{n-1}\big)/\tau$ the *first-order backward difference* in time. In addition, we will also make extensive use of the superscripts $^\bullet$ and * to respectively indicate explicit extrapolations of order $s \in \{0, 1\}$ and $r \in \{0, 1, 2\}$, namely,

$$x^{n,\bullet} \overset{\text{def}}{=} \begin{cases} 0 & \text{if} \quad s = 0, \\ x^{n-1} & \text{if} \quad s = 1, \end{cases}, \qquad x^{n,\star} \overset{\text{def}}{=} \begin{cases} 0 & \text{if} \quad r = 0, \\ x^{n-1} & \text{if} \quad r = 1, \\ 2x^{n-1} - x^{n-2} & \text{if} \quad r = 2. \end{cases}$$

1.4.3.1 Implicit scheme

A fully implicit time-discretization of (1.47), via an overall *backward Euler discretization*, leads to Algorithm 1.1. Note that, at the time semi-discrete level, Algorithm 1.1 enforces an implicit treatment of the interface coupling conditions. For instance, for the case of coupling with a thick solid, Algorithm 1.1 involves the following time discretization of (1.36):

$$\begin{cases} \boldsymbol{u}^n = \dot{\boldsymbol{d}}^n & \text{on} \quad \Sigma, \\ \boldsymbol{\sigma}^{\mathrm{e}}(\boldsymbol{d}^n)\boldsymbol{n}^{\mathrm{s}} = -\boldsymbol{\sigma}(\boldsymbol{u}^n, p^n)\boldsymbol{n} & \text{on} \quad \Sigma. \end{cases}$$

Algorithm 1.1 Implicit coupling scheme.

For $n \geq 1$, find $\big(\boldsymbol{u}_h^n, p_h^n, \dot{\boldsymbol{d}}_h^n, \boldsymbol{d}_h^n\big) \in \widetilde{\boldsymbol{V}}_h \times \widetilde{Q}_h \times \boldsymbol{W}_h \times \boldsymbol{W}_h$, such that

$$\begin{cases} \boldsymbol{u}_h^n|_\Sigma = \dot{\boldsymbol{d}}_h^n|_\Sigma, \\ \dot{\boldsymbol{d}}_h^n = \partial_\tau \boldsymbol{d}_h^n, \\ \rho^{\mathrm{f}}\big(\partial_\tau \boldsymbol{u}_h^n, \boldsymbol{v}_h\big)_{\Omega^{\mathrm{f}}} + a^{\mathrm{f}}\big((\boldsymbol{u}_h^n, p_h^n), (\boldsymbol{v}_h, q_h)\big) + \widetilde{s}_h(p_h^n, q_h) \\ \qquad + \big(\partial_\tau \dot{\boldsymbol{d}}_h^n, \boldsymbol{w}_h\big)_* + a^{\mathrm{s}}(\boldsymbol{d}_h^n, \boldsymbol{w}_h) = 0 \end{cases} \tag{1.63}$$

for all $(\boldsymbol{v}_h, q_h, \boldsymbol{w}_h) \in \widetilde{\boldsymbol{V}}_h \times \widetilde{Q}_h \times \boldsymbol{W}_h$ with $\boldsymbol{v}_h|_\Sigma = \boldsymbol{w}_h$.

Algorithm 1.1 is unconditionally stable and delivers optimal accuracy in the energy norm. In particular, by denoting

$$E^n \overset{\text{def}}{=} \frac{\rho^{\mathrm{f}}}{2}\|\boldsymbol{u}_h^n\|_{0,\Omega^{\mathrm{f}}}^2 + \frac{1}{2}\|\dot{\boldsymbol{d}}_h^n\|_*^2 + \frac{1}{2}\|\boldsymbol{d}_h^n\|_{\mathrm{s}}^2,$$

the total energy of the discrete system at time t_n, and by

$$\mathcal{E}^n \overset{\text{def}}{=} \left(\frac{\rho^{\mathrm{f}}}{2}\|\boldsymbol{u}_h^n - \boldsymbol{u}(t_n)\|_{0,\Omega^{\mathrm{f}}}^2 + \frac{1}{2}\|\dot{\boldsymbol{d}}_h^n - \dot{\boldsymbol{d}}(t_n)\|_*^2 + \frac{1}{2}\|\boldsymbol{d}_h^n - \boldsymbol{d}(t_n)\|_{\mathrm{s}}^2\right)^{\frac{1}{2}},$$

the energy norm of the approximation error, the following theorem holds.

THEOREM 1.3 *Let $\{(\boldsymbol{u}_h^n, p_h^n, \dot{\boldsymbol{d}}_h^n, \boldsymbol{d}_h^n)\}_{n\geq 1}$ be the sequence given by Algorithm 1.1. Then, for $n \geq 1$, there holds*

$$E^n \leq E^0.$$

Moreover, for smooth enough solutions, the following a priori error estimate holds

$$\mathcal{E}^n \lesssim h + \tau.$$

Proof. See [Fer13] for a proof. ∎

REMARK 1.12 *An overall backward Euler discretization of (1.57) leads to the implicit scheme reported in [BF14b, Algorithm 1]. In the case of coupling with a thin-walled solid, the resulting scheme is also reported in Algorithm 5.1 (Chapter 5). The approach delivers unconditionally stability and optimal accuracy (see Remark 5.3 and Corollary 5.2 for a proof in the case of Algorithm 5.1).*

These stability and accuracy properties are obtained at the price of solving problem (1.63) at each time-step, which can be computationally demanding, whether it is solved in a monolithic or partitioned way. Reducing the complexity in fluid-structure coupling has received a lot of research effort in the mathematical community over the last decades. In the rest of this section, we consider schemes that provide different degrees of fluid-solid splitting, thus effectively reducing the computational cost of implicit coupling.

1.4.3.2 Projection-based semi-implicit schemes

Algorithm 1.1 involves a *monolithic time-stepping* in the fluid. A well known alternative to the use of a monolithic time-discretization, is the use of a projection-based time-marching. As a matter of fact, since the pioneering work by Chorin and Temam (see [Cho68, Tem68]), *projection methods* have become one of the most widespread techniques for the numerical solution of the Navier-Stokes equations in primitive variables (see, e.g., [Pro97, BCM01, GMS06, BK11] and the references therein). These methods segregate the computation of the velocity and of the pressure in terms of two decoupled *elliptic problems* which make them very appealing for large scale computations.

For the Stokes system (1.34), a projection method effectively uncouples viscous diffusion and incompressibility effects. Assume that we enforce $\boldsymbol{u} = \boldsymbol{0}$ on $\partial\Omega^{\mathrm{f}}$ in (1.34). In the first step of the projection method, an intermediate velocity $\tilde{\boldsymbol{u}}^n$ is computed using an approximation of the momentum equation in which the pressure is treated explicitly:

$$\begin{cases} \rho^{\mathrm{f}} \dfrac{\tilde{\boldsymbol{u}}^n - \boldsymbol{u}^{n-1}}{\tau} - \mathbf{div}\boldsymbol{\sigma}(\tilde{\boldsymbol{u}}^n, p^{n,\bullet}) = \boldsymbol{0} \quad \text{in} \quad \Omega^{\mathrm{f}} \\ \qquad\qquad\qquad\qquad\qquad\qquad \tilde{\boldsymbol{u}}^n = \boldsymbol{0} \quad \text{on} \quad \partial\Omega^{\mathrm{f}} \end{cases} \tag{1.64}$$

Afterwards, the end-of-step velocity $\boldsymbol{u}^n$ is obtained as the result of projecting $\tilde{\boldsymbol{u}}^n$ into the space of divergence-free velocities:

$$\begin{cases} \rho^{\mathrm{f}} \dfrac{\boldsymbol{u}^n - \tilde{\boldsymbol{u}}^n}{\tau} + \boldsymbol{\nabla}\phi^n = \boldsymbol{0} & \text{in} \quad \Omega^{\mathrm{f}}, \\ \mathrm{div}\boldsymbol{u}^n = 0 & \text{in} \quad \Omega^{\mathrm{f}}, \\ \boldsymbol{u}^n \cdot \boldsymbol{n} = 0 & \text{on} \quad \partial\Omega^{\mathrm{f}} \end{cases} \tag{1.65}$$

with $\phi^n \overset{\text{def}}{=} p^n - p^{n,\bullet}$. The choices $s = 0, 1$ in (1.64) and (1.65) correspond, respectively, to the so-called *non-incremental* and *incremental pressure-correction schemes* (see, e.g, [GMS06, Section 3]). Applying the divergence-free constraint $(1.65)_2$ on $(1.65)_1$, we may rewrite the *Darcy-step* (1.65) in the following *pressure-Poisson formulation*:

$$\begin{cases} -\dfrac{\tau}{\rho^{\mathrm{f}}}\Delta\phi^n = -\mathrm{div}\tilde{\boldsymbol{u}}^n & \text{in} \quad \Omega^{\mathrm{f}}, \\ \dfrac{\tau}{\rho^{\mathrm{f}}}\dfrac{\partial\phi^n}{\partial\boldsymbol{n}} = 0 & \text{on} \quad \partial\Omega^{\mathrm{f}}. \end{cases} \tag{1.66}$$

Moreover, the unknown $\boldsymbol{u}^{n-1}$ can be eliminated in (1.64) via the relation:

$$\frac{\rho^{\mathrm{f}}}{\tau}\boldsymbol{u}^{n-1} = \frac{\rho^{\mathrm{f}}}{\tau}\tilde{\boldsymbol{u}}^{n-1} - \boldsymbol{\nabla}\phi^{n-1} \quad \text{in} \quad \Omega^{\mathrm{f}}.$$

The projection semi-implicit scheme introduced in [FGG07] builds on the above fractional-step time-marching of the fluid subproblem to reduce the strong fluid-solid coupling of (1.63) without compromising stability. The resulting procedure is reported in Algorithm 1.2.

In [FGG07, Theorem 1], the authors proved that Algorithm 1.2 with $s = 0$ is stable under the condition

$$\left(\rho^{\mathrm{f}}\frac{h^{\mathrm{f}}}{(h^{\mathrm{s}})^{\alpha}} + 2\frac{\mu\tau}{h^{\mathrm{f}}(h^{\mathrm{s}})^{\alpha}}\right) \lesssim \rho^{\mathrm{s}}, \quad \text{with} \quad \alpha \overset{\text{def}}{=} \begin{cases} 0, & \text{if} \quad \overline{\Omega^{\mathrm{s}}} = \Sigma, \\ 1, & \text{if} \quad \overline{\Omega^{\mathrm{s}}} \neq \Sigma, \end{cases} \tag{1.70}$$

where h^{f} and h^{s} are respectively the fluid and structure space discretization steps. For $s = 0$, we refer to [AG10] for an a priori error analysis of Algorithm 1.2 which ensures an overall $O(\tau^{\frac{1}{2}} + h^{\mathrm{f}} + h^{\mathrm{s}} + (h^{\mathrm{f}})^l)$ convergence rate in the energy norm. Here, l depends on the choice of *interface matching operator*.

Remark 1.13 *In view of* (1.66)*, the fluid projection problem* (1.68) *can be replaced by the following problem: find* $p_h^n \in \widetilde{Q}_h$ *such that*

$$\frac{\tau}{\rho^{\mathrm{f}}}\left(\boldsymbol{\nabla}\phi_h^n, \boldsymbol{\nabla}q_h\right) + \widetilde{s}_h(p_h^{n,\bullet}, q_h) + \left((\dot{\boldsymbol{d}}_h^{n-1}|_\Sigma - \tilde{\boldsymbol{u}}_h^n)\cdot\boldsymbol{n}, q_h\right)_\Sigma = b(q_h, \tilde{\boldsymbol{u}}_h^n)$$

for all $q_h \in \widetilde{Q}_h$*. Thereafter set* $p_h^n = \phi_h^n + p_h^{n,\bullet}$ *and* $\boldsymbol{u}_h^n = \tilde{\boldsymbol{u}}_h^n - \frac{\tau}{\rho^{\mathrm{f}}}\boldsymbol{\nabla}\phi_h^n$.

ALGORITHM 1.2 Projection semi-implicit schemes (from [FGG07]).

1. Fluid viscous substep: Find $\tilde{\boldsymbol{u}}_h^n \in \widetilde{\boldsymbol{V}}_h$ such that

$$\begin{cases} \tilde{\boldsymbol{u}}_h^n|_\Sigma = \dot{\boldsymbol{d}}_h^{n-1}|_\Sigma, \\ \dfrac{\rho^{\mathrm{f}}}{\tau}\big(\tilde{\boldsymbol{u}}_h^n - \boldsymbol{u}_h^{n-1}, \tilde{\boldsymbol{v}}_h\big) + a(\tilde{\boldsymbol{u}}_h^n, \tilde{\boldsymbol{v}}_h) + \big(\boldsymbol{\nabla} p_h^{n,\bullet}, \tilde{\boldsymbol{v}}_h\big) = 0 \end{cases} \tag{1.67}$$

   for all $\tilde{\boldsymbol{v}}_h \in \widetilde{\boldsymbol{V}}_{\Sigma,h}$.

2. Fluid projection with solid substep: Find $(\boldsymbol{u}_h^n, \phi_h^n, \dot{\boldsymbol{d}}_h^n, \boldsymbol{d}_h^n) \in \widetilde{\boldsymbol{V}}_h \times \widetilde{Q}_h \times \boldsymbol{W}_h \times \boldsymbol{W}_h$ such that

$$\begin{cases} \boldsymbol{u}_h^n|_\Sigma = \dot{\boldsymbol{d}}_h^n|_\Sigma, \\ \dfrac{\rho^{\mathrm{f}}}{\tau}\big(\boldsymbol{u}_h^n - \tilde{\boldsymbol{u}}_h^n, \boldsymbol{v}_h\big) + b(\phi_h^n, \boldsymbol{v}_h^n) - b(q_h, \boldsymbol{u}_h^n) + \widetilde{s}_h(p_h^{n,\bullet}, q_h) = 0 \end{cases} \tag{1.68}$$

$$\begin{cases} \dot{\boldsymbol{d}}_h^n = \partial_\tau \boldsymbol{d}_h^n, \\ \big(\partial_\tau \dot{\boldsymbol{d}}_h^n, \boldsymbol{w}_h\big)_* + a^{\mathrm{s}}(\boldsymbol{d}_h^n, \boldsymbol{w}_h) = -\dfrac{\rho^{\mathrm{f}}}{\tau}\big(\tilde{\boldsymbol{u}}_h^n - \boldsymbol{u}_h^{n-1}, \boldsymbol{\mathcal{L}}_h \boldsymbol{w}_h\big) - a(\tilde{\boldsymbol{u}}_h^n, \boldsymbol{\mathcal{L}}_h \boldsymbol{w}_h) \\ \qquad - \dfrac{\rho^{\mathrm{f}}}{\tau}\big(\boldsymbol{u}_h^n - \tilde{\boldsymbol{u}}_h^n, \boldsymbol{\mathcal{L}}_h \boldsymbol{w}_h\big) - b(\phi_h^n, \boldsymbol{\mathcal{L}}_h \boldsymbol{w}_h) \end{cases} \tag{1.69}$$

   for all $(\boldsymbol{v}_h, q_h, \boldsymbol{w}_h) \in \widetilde{\boldsymbol{V}}_{\Sigma,h} \times \widetilde{Q}_h \times \boldsymbol{W}_h$. Thereafter set $p_h^n = \phi_h^n + p_h^{n,\bullet}$.

1.4.3.3 Dirichlet-Neumann explicit scheme

Although less computationally onerous than problem (1.63), Algorithm 1.2 still involves the solution of the implicit coupled problem (1.68)-(1.69). The focus of the rest of this section is on explicit coupling schemes, i.e., schemes that provide a complete decoupling in the time-marching of the fluid and the solid subproblems.

The most elementary explicit coupling scheme is based on a Dirichlet-Neumann explicit/implicit treatment of the kinematic and dynamic coupling conditions, which, for (1.36), reads as

$$\begin{cases} \boldsymbol{u}^n = \dot{\boldsymbol{d}}^{n-1} & \text{on} \quad \Sigma, \\ \boldsymbol{\sigma}^{\mathrm{e}}(\boldsymbol{d}^n)\boldsymbol{n}^{\mathrm{s}} = -\boldsymbol{\sigma}(\boldsymbol{u}^n, p^n)\boldsymbol{n} & \text{on} \quad \Sigma. \end{cases}$$

This time-marching of the coupling conditions can be easily enforced, at the fully discrete level and for a conforming discretization, using the partitioned formulation given by (1.48)-(1.49). The resulting scheme, known as the *Dirichlet-Neumann explicit scheme*, is reported in Algorithm 1.3.

Algorithm 1.3 is widely used in the aeroelasticity community (see, e.g., [PB01]). However, as already mentioned, it becomes unconditionally unstable for problems with a large added mass effect. Theoretical insight on this issue is given in [CGN05],

Algorithm 1.3 Dirichlet-Neumann explicit coupling scheme.

For $n \geq 1$:

1. Fluid substep: find $\left(\boldsymbol{u}_h^n, p_h^n\right) \in \widetilde{\boldsymbol{V}}_h \times \widetilde{Q}_h$, such that

$$\begin{cases} \boldsymbol{u}_h^n|_\Sigma = \dot{\boldsymbol{d}}_h^{n-1}|_\Sigma, \\ \rho^{\mathrm{f}}\left(\partial_\tau \boldsymbol{u}_h^n, \boldsymbol{v}_h\right)_{\Omega^{\mathrm{f}}} + a^{\mathrm{f}}\left((\boldsymbol{u}_h^n, p_h^n), (\boldsymbol{v}_h, q_h)\right) + \widetilde{s}_h(p_h^n, q_h) = 0 \end{cases} \tag{1.71}$$

   for all $(\boldsymbol{v}_h, q_h) \in \boldsymbol{V}_{\Sigma,h} \times \widetilde{Q}_h$.

2. Solid substep: find $\left(\dot{\boldsymbol{d}}_h^n, \boldsymbol{d}_h^n\right) \in \boldsymbol{W}_h \times \boldsymbol{W}_h$, such that

$$\begin{cases} \dot{\boldsymbol{d}}_h^n = \partial_\tau \boldsymbol{d}_h^n, \\ \left(\partial_\tau \dot{\boldsymbol{d}}_h^n, \boldsymbol{w}_h\right)_* + a^{\mathrm{s}}(\boldsymbol{d}_h^n, \boldsymbol{w}_h) \\ \quad = -\rho^{\mathrm{f}}\left(\partial_\tau \boldsymbol{u}_h^n, \boldsymbol{\mathcal{L}}_h \boldsymbol{w}_h\right)_{\Omega^{\mathrm{f}}} - a(\boldsymbol{u}_h^n, \boldsymbol{\mathcal{L}}_h \boldsymbol{w}_h) - b(p_h^n, \boldsymbol{\mathcal{L}}_h \boldsymbol{w}_h) \end{cases} \tag{1.72}$$

   for all $\boldsymbol{w}_h \in \boldsymbol{W}_h$.

in which the following instability condition is established for Algorithm 1.3 in a simplified framework:

$$\frac{\rho^{\mathrm{s}} \epsilon}{\rho^{\mathrm{f}} \mu_{\max}} < 1, \tag{1.73}$$

where $\mu_{\max}$ is the largest eigenvalue of so-called *added-mass operator* (See Section 3.3.1 of Chapter 3). The value of $\mu_{\max}$ only depends on geometrical quantities and increases with the length of the domain. We can clearly see that (1.73) fails to be satisfied whenever the fluid and solid densities are comparable or the domain has a slender shape. In particular, since (1.73) is independent of the time-step size, reducing it does not cure the instabilities.

1.4.3.4 Stabilized explicit coupling scheme

For problems with a large added mass effect, stability in explicit coupling demands a different treatment of the interface coupling conditions. An explicit coupling alternative is given by the Nitsche based stabilized explicit method introduced in [BF09, BF14b], which corresponds to the explicit discretization of the partitioned Nitsche formulation (1.59)-(1.58) reported in Algorithm 1.4.

Note that the following weakly consistent stabilization term

$$\frac{\gamma_0 h}{\gamma \mu}\left(p_h^n - p_h^{n-1}, q_h\right)_\Sigma, \tag{1.76}$$

with $\gamma_0 > 0$, has been added in the fluid step (1.75). This controls the temporal interface pressure fluctuations induced by the fluid-solid splitting, curing the added-mass stability issues. As a matter of fact, we have the stability result reported in

ALGORITHM 1.4 Stabilized explicit coupling scheme (from [BF09, BF14b]).

For $n \geq 1$:

1. Solid substep: find $\left(\dot{\boldsymbol{d}}_h^n, \boldsymbol{d}_h^n\right) \in \boldsymbol{W}_h \times \boldsymbol{W}_h$ with $\dot{\boldsymbol{d}}_h^n = \partial_\tau \boldsymbol{d}_h^n$ and such that

$$\begin{cases} \left(\partial_\tau \dot{\boldsymbol{d}}_h^n, \boldsymbol{w}_h\right)_* + a^{\mathrm{s}}(\boldsymbol{d}_h^n, \boldsymbol{w}_h) + \dfrac{\gamma\mu}{h}\left(\dot{\boldsymbol{d}}_h^n, \boldsymbol{w}_h\right)_\Sigma \\ \quad = \dfrac{\gamma\mu}{h}\left(\boldsymbol{u}_h^{n-1}, \boldsymbol{w}_h\right)_\Sigma - \left(\boldsymbol{\sigma}(\boldsymbol{u}_h^{n-1}, p_h^{n-1})\boldsymbol{n}, \boldsymbol{w}_h\right)_\Sigma \end{cases} \tag{1.74}$$

   for all $\boldsymbol{w}_h \in \boldsymbol{W}_h$.

2. Fluid substep: find $(\boldsymbol{u}_h^n, p_h^n) \in \boldsymbol{V}_h \times Q_h$ such that

$$\begin{cases} \rho^{\mathrm{f}}\left(\partial_\tau \boldsymbol{u}_h^n, \boldsymbol{v}_h\right)_{\Omega^{\mathrm{f}}} + a^{\mathrm{f}}\left((\boldsymbol{u}_h^n, p_h^n), (\boldsymbol{v}_h, q_h)\right) + S_h\left((\boldsymbol{u}_h, p_h), (\boldsymbol{v}_h, q_h)\right) \\ - \left(\boldsymbol{u}_h^n - \dot{\boldsymbol{d}}_h^n, \boldsymbol{\sigma}(\boldsymbol{v}_h, -q_h)\boldsymbol{n}\right)_\Sigma + \dfrac{\gamma\mu}{h}\left(\boldsymbol{u}_h^n, \boldsymbol{v}_h\right)_\Sigma + \dfrac{\gamma_0 h}{\gamma\mu}\left(p_h^n - p_h^{n-1}, q_h\right)_\Sigma \\ = \dfrac{\gamma\mu}{h}\left(\dot{\boldsymbol{d}}_h^n, \boldsymbol{v}_h\right)_\Sigma + \left(\boldsymbol{\sigma}(\boldsymbol{u}_h^{n-1}, p_h^{n-1})\boldsymbol{n}, \boldsymbol{v}_h\right)_\Sigma \end{cases} \tag{1.75}$$

   for all $(\boldsymbol{v}_h, q_h) \in \boldsymbol{V}_h \times Q_h$.

Theorem 1.4.

THEOREM 1.4 *Let $\{(\boldsymbol{u}_h^n, p_h^n, \dot{\boldsymbol{d}}_h^n, \boldsymbol{d}_h^n)\}_{n\geq 1}$ be the sequence given by Algorithm 1.4. Then, under conditions $\gamma \gtrsim C_{\mathrm{TI}}/\tilde{c}_{\mathrm{g}}$, $\gamma\tau \lesssim h$ and $\gamma_0 \gtrsim 1$, there holds*

$$E^n \lesssim E^0 + \left(\mu\|\boldsymbol{u}_h^0\|_{0,\Sigma}^2 + \mu\|\boldsymbol{\varepsilon}(\boldsymbol{u}_h^0)\|_{0,\Omega_h}^2 + \frac{\gamma_0 h}{\gamma\mu}\tau\|p_h^0\|_{0,\Sigma}^2\right)$$

for $n \geq 1$.

Proof. The result follows by combining Lemma 1.2 with the arguments reported in [BF09, Section 5.1] (see also [BF14b, Lemma 4.2]). ∎

A major drawback of Algorithm 1.4 is that the explicit treatment of the Nitsche's penalty term

$$\frac{\gamma\mu}{h}\left(\dot{\boldsymbol{d}}_h^n - \boldsymbol{u}_h^{n-1}, \boldsymbol{w}_h\right)_\Sigma,$$

in the solid substep (1.74), induces a deterioration of the accuracy. Specifically, the truncation error induced by the splitting scales as

$$\underbrace{\mathcal{O}\left(\frac{\tau}{h}\right)}_{\text{Nitsche coupling}} + \underbrace{\mathcal{O}\left((h\tau)^{\frac{1}{2}}\right)}_{\text{pressure stabilization}}, \tag{1.77}$$

in the energy norm. Hence, to guarantee overall first-order accuracy one is forced to take $\tau = \mathcal{O}\left(h^2\right)$. Alternatively, to avoid this restrictive CFL con-

straint, correction iterations with suitable extrapolations can be performed (see [BF09, BF14a, BF14b]).

Remark 1.14 *Since the fluid stresses are treated explicitly in (1.75), one could be tempted to remove the symmetrizing term,*

$$-\big(\boldsymbol{u}_h^n - \dot{\boldsymbol{d}}_h^n, \boldsymbol{\sigma}(\boldsymbol{v}_h, 0)\boldsymbol{n}\big)_\Sigma,$$

in the fluid step. This simpler variant, which preserves the stability and accuracy properties of Algorithm 1.4, enforces the following explicit Robin-Robin splitting of the interface coupling (see [BF14a]):

$$\begin{cases} \boldsymbol{\sigma}^{\mathrm{e}}(\boldsymbol{d}^n)\boldsymbol{n}^{\mathrm{s}} + \dfrac{\gamma\mu}{h}\dot{\boldsymbol{d}}^n = \dfrac{\gamma\mu}{h}\boldsymbol{u}^{n-1} - \boldsymbol{\sigma}(\boldsymbol{u}^{n-1}, p^{n-1})\boldsymbol{n} & \text{on} \quad \Sigma, \\ \boldsymbol{\sigma}(\boldsymbol{u}^n, p^n)\boldsymbol{n} + \dfrac{\gamma\mu}{h}\boldsymbol{u}^n = \dfrac{\gamma\mu}{h}\dot{\boldsymbol{d}}^n + \boldsymbol{\sigma}(\boldsymbol{u}^{n-1}, p^{n-1})\boldsymbol{n} & \text{on} \quad \Sigma. \end{cases}$$

1.4.3.5 Robin-Neumann explicit schemes

According to the discussion in the previous section, a fundamental difficulty in explicit coupling is to guarantee stability without compromising optimal accuracy. For the coupling with thin-walled solids, the Robin-Neumann methods proposed in [Fer11b, Fer13, FMV13] achieve this purpose. In the sequel, we restrict the discussion to the coupling with a linear viscoelastic Kirchhoff-Love shell (see Section 1.2.2.2). That is, we couple (1.34) with

$$\begin{cases} \boldsymbol{u} = \dot{\boldsymbol{d}} & \text{on} \quad \Sigma, \\ \rho^{\mathrm{s}}\epsilon\partial_t\dot{\boldsymbol{d}} + \boldsymbol{L}^{\mathrm{e}}\boldsymbol{d} + \boldsymbol{L}^{\mathrm{v}}\dot{\boldsymbol{d}} = -\boldsymbol{\sigma}(\boldsymbol{u}, p)\boldsymbol{n} & \text{on} \quad \Sigma, \\ \dot{\boldsymbol{d}} = \partial_t\boldsymbol{d} & \text{on} \quad \Sigma, \\ \boldsymbol{d} = \boldsymbol{0} & \text{on} \quad \partial\Sigma, \end{cases} \tag{1.78}$$

where $\boldsymbol{L}^{\mathrm{v}}$ is given by (1.22). We consider the viscous bilinear form given by the weak form of the (unbounded linear) surface differential operator $\boldsymbol{L}^{\mathrm{v}} : \boldsymbol{D}(\boldsymbol{L}^{\mathrm{v}}) \subset [L^2(\Sigma)]^d \to [L^2(\Sigma)]^d$, namely,

$$a^{\mathrm{v}}\big(\dot{\boldsymbol{d}}, \boldsymbol{w}\big) = \big(\boldsymbol{L}^{\mathrm{v}}\dot{\boldsymbol{d}}, \boldsymbol{w}\big)_\Sigma$$

for all $\dot{\boldsymbol{d}} \in \boldsymbol{D}(\boldsymbol{L}^{\mathrm{v}})$ and $\boldsymbol{w} \in \boldsymbol{W}$, which is assumed to be symmetric, coercive and continuous on $\boldsymbol{W}$.

A well-known salient feature of fluid-structure coupled problems involving a thin-walled solid, is that they enforce an intrinsic *interface Robin consistency* (see, e.g., [NV08, GGCC09, Fer13, FMV13]). Indeed, from $(1.78)_{1,2}$ it follows that

$$\boldsymbol{\sigma}(\boldsymbol{u}, p)\boldsymbol{n} + \rho^{\mathrm{s}}\epsilon\partial_t\boldsymbol{u} = -\boldsymbol{L}^{\mathrm{e}}\boldsymbol{d} - \boldsymbol{L}^{\mathrm{v}}\dot{\boldsymbol{d}} \quad \text{on} \quad \Sigma, \tag{1.79}$$

which can be viewed as a Robin-like boundary condition for the fluid. The Robin-Neumann methods exploit this relation and, instead of performing the fluid-solid

time splitting in terms of a Dirichlet-Neumann coupling, as in Algorithm 1.3, they enforce the following Robin-Neumann time-marching on the interface,

$$\begin{cases} \boldsymbol{\sigma}(\boldsymbol{u}^n, p^n)\boldsymbol{n} + \dfrac{\rho^{\mathrm{s}}\epsilon}{\tau}\boldsymbol{u}^n = \dfrac{\rho^{\mathrm{s}}\epsilon}{\tau}\dot{\boldsymbol{d}}^{n-1} - \boldsymbol{L}^{\mathrm{e}}\boldsymbol{d}^{n,\star} - \boldsymbol{L}^{\mathrm{v}}\dot{\boldsymbol{d}}^{n,\star} & \text{on} \quad \Sigma, \\ \rho^{\mathrm{s}}\epsilon\partial_\tau\dot{\boldsymbol{d}}^n + \boldsymbol{L}^{\mathrm{e}}\boldsymbol{d}^n + \boldsymbol{L}^{\mathrm{v}}\dot{\boldsymbol{d}}^n = -\boldsymbol{\sigma}(\boldsymbol{u}^n, p^n)\boldsymbol{n} & \text{on} \quad \Sigma. \end{cases} \tag{1.80}$$

Note that only the solid inertial effects are implicitly coupled with the fluid sub-problem through the Robin boundary condition $(1.80)_1$. This is enough to guarantee added-mass free stability (see Theorem 1.5 below).

It is also worth noting that, considering the r-extrapolation of step $(1.80)_2$, and adding the resulting expression to $(1.80)_1$, the coupling (1.80) can be reformulated as

$$\begin{cases} \boldsymbol{\sigma}(\boldsymbol{u}^n, p^n)\boldsymbol{n} + \dfrac{\rho^{\mathrm{s}}\epsilon}{\tau}\boldsymbol{u}^n = \dfrac{\rho^{\mathrm{s}}\epsilon}{\tau}\left(\dot{\boldsymbol{d}}^{n-1} + \tau\partial_\tau\dot{\boldsymbol{d}}^{n,\star}\right) + \boldsymbol{\sigma}(\boldsymbol{u}^{n,\star}, p^{n,\star})\boldsymbol{n} & \text{on} \quad \Sigma, \\ \rho^{\mathrm{s}}\epsilon\partial_\tau\dot{\boldsymbol{d}}^n + \boldsymbol{L}^{\mathrm{e}}\boldsymbol{d}^n + \boldsymbol{L}^{\mathrm{v}}\dot{\boldsymbol{d}}^n = -\boldsymbol{\sigma}(\boldsymbol{u}^n, p^n)\boldsymbol{n} & \text{on} \quad \Sigma. \end{cases} \tag{1.81}$$

The advantage of this new expression is its intrinsic character, in the sense that it avoids extrapolations of the solid viscoelastic terms within the fluid solver. In the fitted mesh framework introduced in Section 1.4.2.2, this alternative leads to the discretization of problem (1.34)-(1.78) given in Algorithm 1.5.

ALGORITHM 1.5 Robin-Neumann explicit schemes (from [Fer13, FMV13]).

For $n > r$:

1. Fluid step: Find $(\boldsymbol{u}_h^n, p_h^n) \in \widetilde{\boldsymbol{V}}_h \times \widetilde{Q}_h$ such that

$$\begin{cases} \rho^{\mathrm{f}}\left(\partial_\tau\boldsymbol{u}_h^n, \boldsymbol{v}_h\right)_{\Omega^{\mathrm{f}}} + a^{\mathrm{f}}\left((\boldsymbol{u}_h^n, p_h^n), (\boldsymbol{v}_h, q_h)\right) + \widetilde{s}_h(p_h^n, q_h) \\ \quad + \dfrac{\rho^{\mathrm{s}}\epsilon}{\tau}\left(\boldsymbol{u}_h^n, \boldsymbol{v}_h\right)_\Sigma = \dfrac{\rho^{\mathrm{s}}\epsilon}{\tau}\left(\dot{\boldsymbol{d}}_h^{n-1} + \tau\partial_\tau\dot{\boldsymbol{d}}_h^{n,\star}, \boldsymbol{v}_h\right)_\Sigma \\ \quad + \rho^{\mathrm{f}}\left(\partial_\tau\boldsymbol{u}_h^{n,\star}, \boldsymbol{\mathcal{L}}_h\boldsymbol{v}_h\right)_{\Omega^{\mathrm{f}}} + a(\boldsymbol{u}_h^{n,\star}, \boldsymbol{\mathcal{L}}_h\boldsymbol{v}_h) + b(p_h^{n,\star}, \boldsymbol{\mathcal{L}}_h\boldsymbol{v}_h) \end{cases} \tag{1.82}$$

   for all $(\boldsymbol{v}_h, q_h) \in \widetilde{\boldsymbol{V}}_h \times \widetilde{Q}_h$ with $\boldsymbol{v}_h|_\Sigma \in \boldsymbol{W}_h$.

2. Solid step: Find $\left(\dot{\boldsymbol{d}}_h^n, \boldsymbol{d}_h^n\right) \in \boldsymbol{W}_h \times \boldsymbol{W}_h$, such that

$$\begin{cases} \dot{\boldsymbol{d}}_h^n = \partial_\tau\boldsymbol{d}_h^n, \\ \rho^{\mathrm{s}}\epsilon\left(\partial_\tau\dot{\boldsymbol{d}}_h^n, \boldsymbol{w}_h\right)_\Sigma + a^{\mathrm{s}}(\boldsymbol{d}_h^n, \boldsymbol{w}_h) + a^{\mathrm{v}}(\dot{\boldsymbol{d}}_h^n, \boldsymbol{w}_h) \\ \quad = -\rho^{\mathrm{f}}\left(\partial_\tau\boldsymbol{u}_h^n, \boldsymbol{\mathcal{L}}_h\boldsymbol{w}_h\right)_{\Omega^{\mathrm{f}}} - a(\boldsymbol{u}_h^n, \boldsymbol{\mathcal{L}}_h\boldsymbol{w}_h) - b(p_h^n, \boldsymbol{\mathcal{L}}_h\boldsymbol{w}_h) \end{cases} \tag{1.83}$$

   for all $\boldsymbol{w}_h \in \boldsymbol{W}_h$.

REMARK 1.15 *For $r = 1, 2$, Algorithm 1.5 is a multi-step method which requires initial data. This additional data is obtained by performing one step of the scheme with $r = 0$ and then one step of scheme with $r = 1$.*

Remark 1.16 *In the particular case of an undamped thin-walled solid (i.e., $\boldsymbol{L}^{\mathrm{v}} = \boldsymbol{0}$), Algorithm 1.5 with $r = 0$ yields the splitting scheme reported in [GGCC09], which is known to deliver very poor accuracy (see [Fer13, FMV13]).*

Remark 1.17 *The Robin-Neumann time-marching* (1.80) *induces the following* incremental displacement-correction *discretization (see [Fer13]) of the solid momentum equation* $(1.78)_2$,

$$\begin{cases} \dfrac{\rho^{\mathrm{s}}\epsilon}{\tau}\big(\dot{\boldsymbol{d}}^{n-\frac{1}{2}} - \dot{\boldsymbol{d}}^{n-1}\big) + \boldsymbol{L}^{\mathrm{e}}\boldsymbol{d}^{n,\star} + \boldsymbol{L}^{\mathrm{v}}\dot{\boldsymbol{d}}^{n,\star} = -\boldsymbol{\sigma}(\boldsymbol{u}^n, p^n)\boldsymbol{n} \quad \text{on} \quad \Sigma, \\ \dfrac{\rho^{\mathrm{s}}\epsilon}{\tau}(\dot{\boldsymbol{d}}^n - \dot{\boldsymbol{d}}^{n-\frac{1}{2}}) + \boldsymbol{L}^{\mathrm{e}}(\boldsymbol{d}^n - \boldsymbol{d}^{n,\star}) + \boldsymbol{L}^{\mathrm{v}}(\dot{\boldsymbol{d}}^n - \dot{\boldsymbol{d}}^{n,\star}) = \boldsymbol{0} \quad \text{on} \quad \Sigma, \end{cases} \tag{1.84}$$

with the intermediate solid velocity $\dot{\boldsymbol{d}}^{n-\frac{1}{2}} \in \boldsymbol{W}$ being given by

$$\dot{\boldsymbol{d}}^{n-\frac{1}{2}} = \boldsymbol{u}^n|_\Sigma. \tag{1.85}$$

In the fitted mesh framework described in Section 1.4.2.2, the relation (1.85) *is straightforwardly enforced thanks to* (1.44)*, which allows to set*

$$\dot{\boldsymbol{d}}_h^{n-\frac{1}{2}} = \boldsymbol{u}_h^n|_\Sigma, \tag{1.86}$$

and embed $(1.84)_1$ *as a Robin boundary condition in the fluid step* (1.82)*. However, in the unfitted mesh framework of Section 1.4.2.3, the identification* (1.86) *is no longer possible and new strategies have to be designed in order to couple the fractional-step time discretization* (1.84) *of the solid subproblem with the discretization of the fluid subproblem (see Chapter 5).*

Theoretical results on the stability and accuracy of Algorithm 1.5 have been reported in [Fer13, FMV13]. A fundamental ingredient in the analysis of Algorithm 1.5 is the fact that it can be viewed as a kinematic perturbation of an underlying implicit coupling scheme. More precisely, from [FMV13], we have that Algorithm 1.5 is equivalent to: for $n > r$, find

$$\big(\boldsymbol{u}_h^n, p_h^n, \dot{\boldsymbol{d}}_h^n, \boldsymbol{d}_h^n\big) \in \widetilde{\boldsymbol{V}}_h \times \widetilde{Q}_h \times \boldsymbol{W}_h \times \boldsymbol{W}_h,$$

such that

$$\begin{cases} \boldsymbol{u}_h^n|_\Sigma = \dot{\boldsymbol{d}}_h^n + \dfrac{\tau}{\rho^{\mathrm{s}}\epsilon}\Big(\boldsymbol{L}_h^{\mathrm{e}}(\boldsymbol{d}_h^n - \boldsymbol{d}_h^{n,\star}) + \boldsymbol{L}_h^{\mathrm{v}}(\dot{\boldsymbol{d}}_h^n - \dot{\boldsymbol{d}}_h^{n,\star})\Big), \\ \dot{\boldsymbol{d}}_h^n = \partial_\tau \boldsymbol{d}_h^n, \\ \rho^{\mathrm{f}}\big(\partial_\tau \boldsymbol{u}_h^n, \boldsymbol{v}_h\big)_{\Omega^{\mathrm{f}}} + a^{\mathrm{f}}\big((\boldsymbol{u}_h^n, p_h^n), (\boldsymbol{v}_h, q_h)\big) + \widetilde{s}_h(p_h^n, q_h) \\ \quad + \rho^{\mathrm{s}}\epsilon\big(\partial_\tau \dot{\boldsymbol{d}}_h^n, \boldsymbol{w}_h\big)_\Sigma + a^{\mathrm{s}}(\boldsymbol{d}_h^n, \boldsymbol{w}_h) + a^{\mathrm{v}}\big(\dot{\boldsymbol{d}}_h^n, \boldsymbol{w}_h\big) = 0 \end{cases} \tag{1.87}$$

for all $(\boldsymbol{v}_h, q_h, \boldsymbol{w}_h) \in \widetilde{\boldsymbol{V}}_h \times \widetilde{Q}_h \times \boldsymbol{W}_h$ with $\boldsymbol{v}_h|_\Sigma = \boldsymbol{w}_h$ and where we have made use of the *discrete reconstructions*, $\boldsymbol{L}_h^{\mathrm{e}} : \boldsymbol{W} \to \boldsymbol{W}_h$ and $\boldsymbol{L}_h^{\mathrm{v}} : \boldsymbol{W} \to \boldsymbol{W}_h$, of the elastic

and viscous solid operators, defined by the relations

$$(\boldsymbol{L}_h^{\mathrm{e}}\boldsymbol{w},\boldsymbol{w}_h)_\Sigma = a^{\mathrm{s}}(\boldsymbol{w},\boldsymbol{w}_h), \quad (\boldsymbol{L}_h^{\mathrm{v}}\boldsymbol{w},\boldsymbol{w}_h)_\Sigma = a^{\mathrm{v}}(\boldsymbol{w},\boldsymbol{w}_h) \tag{1.88}$$

for all $(\boldsymbol{w},\boldsymbol{w}_h) \in \boldsymbol{W}\times\boldsymbol{W}_h$.

As a matter of fact, reformulation (1.87) of Algorithm 1.5 gives an implicit discretization of problem (1.34)-(1.78), in which the kinematic coupling condition $(1.78)_1$ is perturbed by the last term in $(1.87)_1$. The stability and accuracy properties of Algorithm 1.5 are driven by the impact that this perturbation has in the underlying implicit scheme. Indeed, we have that Algorithm 1.5 is unconditionally energy stable for $r=0$ and $r=1$. The scheme for $r=2$ is energy stable under a CFL-like condition. These results is stated in Theorem 1.5.

THEOREM 1.5 *Let $\{(\boldsymbol{u}_h^n, p_h^n, \boldsymbol{d}_h^n, \dot{\boldsymbol{d}}_h^n)\}_{n\geq r+1}$ be the sequence given by Algorithm 1.5. Assume that the schemes with extrapolation ($r\geq 1$) are initialized following the procedure of Remark 1.15. We have the following a priori energy estimates:*

- *For $r=0,1$ and $n>r$, there holds*

$$E^n \lesssim E^0,$$

  unconditionally of the discretization parameters.

- *For $r=2$ and $n>2$, there holds*

$$E^n \lesssim \exp\left(\frac{t_n\gamma}{1-\tau\gamma}\right)E^0 \tag{1.89}$$

  provided that (1.22) and the following conditions hold

$$\begin{cases} \alpha^2\tau^2 + \beta^2\tau^2\dfrac{(\omega^{\mathrm{s}})^4}{h^4} \leq \dfrac{\delta}{4}, \\ \dfrac{\tau^5(\omega^{\mathrm{s}})^6}{h^6} + 2\alpha\dfrac{\tau^2(\omega^{\mathrm{s}})^2}{h^2} + 2\beta\tau^2\dfrac{(\omega^{\mathrm{s}})^4}{h^4} \leq \dfrac{\gamma}{2}, \\ \tau\gamma < 1, \end{cases} \tag{1.90}$$

  where $\omega^{\mathrm{s}} \overset{\text{def}}{=} C_{\mathrm{inv}}\sqrt{\beta^{\mathrm{s}}/(\rho^{\mathrm{s}}\epsilon)}$, C_{inv} denotes the constant of an inverse estimate, $0\leq\delta\leq 1$ and $\gamma>0$.

Proof. See [FMV13] for a proof. ∎

REMARK 1.18 *As pointed out in [FMV13], the nature of the CFL-like condition induced by (1.90) is dictated by the Rayleigh coefficient β of (1.22). If $\beta=0$, a 6/5-CFL condition $\tau=\mathcal{O}(h^{\frac{6}{5}})$ is required to fulfill the relations (1.90). If $\beta>0$, the relations (1.90) are satisfied under a parabolic-CFL condition $\tau=\mathcal{O}(h^2)$.*

Regarding the accuracy, the error analysis shows that the splitting error induced by the kinematic perturbation $(1.87)_1$ scales as $\mathcal{O}(\tau^{2^{r-1}})$. Thus, Algorithm 1.5 with $r = 1$ or $r = 2$ yields an overall optimal first-order time-accuracy $\mathcal{O}(\tau)$ in the energy-norm, while a sub-optimal time convergence rate $\mathcal{O}(\tau^{\frac{1}{2}})$ is expected for the scheme with $r = 0$. This is stated in the following theorem.

Theorem 1.6 *Let $(\boldsymbol{u}, p, \boldsymbol{d}, \dot{\boldsymbol{d}})$ be the solution of the coupled problem (1.34)-(1.78) and $\{(\boldsymbol{u}_h^n, p_h^n, \boldsymbol{d}_h^n, \dot{\boldsymbol{d}}_h^n)\}_{n>r}$ be the discrete solution given by Algorithm 1.5 with properly chosen initial data (see [FMV13]). The initialization procedure of Remark 1.15 is considered for the schemes with with extrapolation ($r \geq 1$). For the scheme with $r = 2$ we assume, in addition, that (1.22) and the stability condition (1.90) hold. Then, for regular enough exact solutions, we have the following error estimates, for $n > r$ such as $n\tau < T$:*

$$\mathcal{E}^n \lesssim h + \tau + \tau^{2^{r-1}}$$

Proof. See [FMV13] for a proof. ∎

Part I

Fitted mesh methods

Chapter 2

Fully decoupled time-marching schemes for incompressible fluid/thin-walled structure interaction

In this chapter we show how the explicit Robin-Neumann coupling paradigm of Section 1.4.3.5 can be effectively combined with a projection based time-marching in the fluid. The resulting schemes enable a fully decoupled sequential computation of the fluid-solid state (velocity-pressure-displacement splitting). A priori energy estimates guaranteeing unconditional stability are established for some of the schemes. The accuracy and performance of the methods proposed are illustrated by a thorough numerical study.

The results presented in this chapter have been reported in:

- M. A. Fernández, M. Landajuela, **A fully decoupled scheme for the interaction of a thin-walled structure with an incompressible fluid**. *Comptes Rendus Mathématique, 351(3):161-164, 2013*
- M. A. Fernández, M. Landajuela, M. Vidrascu, **Fully decoupled time-marching schemes for incompressible fluid/thin-walled structure interaction**. *Journal of Computational Physics, 297:156-181, 2015.*

Contents

2.1 Introduction

The fundamental ingredient in the derivation of the explicit Robin-Neumann schemes reported in Section 1.4.3.5, is the combination of the Robin condition $(1.80)_1$ with a monolithic time-stepping in the fluid. The contribution of this chapter is to effectively combine the aforementioned explicit Robin-Neumann coupling paradigm for incompressible fluid/thin-walled structure interaction problems with a projection based time-marching in the fluid. An approach in this direction, intended to deliver second-order accuracy, has been recently reported in [BHS14]. It is however not clear how to implement the interface splitting therein within a finite element framework.

The key idea of the schemes proposed in this chapter lies in the derivation of an intrinsic fractional-step time-stepping of the interface Robin consistency featured by the coupled problem (see Section 1.4.3.5). This preserves the stability and accuracy of the original Robin-Neumann splitting without compromising the velocity/pressure uncoupling in the fluid time-marching. In particular, the resulting solution procedures enable a fully decoupled computation of the whole fluid-solid state. The velocity/pressure splitting in the fluid introduces additional perturbations of the kinematic coupling which make the analysis much more intricate than in Section 1.4.3.5. For a linear coupled problem involving the Stokes equations and a general (Reissner-Mindlin type) viscoelastic shell model, a priori energy estimates guaranteeing unconditional stability are derived for some of the variants. The proposed fully decoupled schemes are also formulated within a non-linear framework, involving the incompressible Navier-Stokes equations (in moving domains) and a non-linear viscoelastic shell model. A thorough numerical study, based on different linear and non-linear fluid-structure interaction examples, illustrates the accuracy and performance of the methods proposed.

This chapter is organized as follows. Section 2.2 is devoted to the derivation and the analysis of the methods within a linear representative setting. In Section 2.3, the proposed fully decoupled schemes are formulated within a non-linear setting. The numerical results are presented and discussed in Section 2.4. Finally, a summary of the conclusions is given in Section 2.5.

2.2 Derivation and analysis in the linear case

We consider the coupling of the Stokes system (1.34) with the linear Reissner-Mindlin shell model (1.12). The boundary of the fluid domain $\Omega^{\mathrm{f}} \subset \mathbb{R}^3$ is partitioned as $\partial\Omega^{\mathrm{f}} = \Gamma^{\mathrm{f}} \cup \Sigma$ (see Figure 2.1). For a given vector field $\boldsymbol{v}$ defined on the surface Σ, the symbols $\boldsymbol{v}_\perp \overset{\text{def}}{=} (\boldsymbol{v}\cdot\boldsymbol{n})\boldsymbol{n}$ and $\boldsymbol{v}_\parallel \overset{\text{def}}{=} \boldsymbol{v} - \boldsymbol{v}_\perp$ will denote, respectively, the normal and tangential components of $\boldsymbol{v}$ (see Figure 2.1). The resulting coupled problem reads as follows: find the fluid velocity $\boldsymbol{u} : \Omega^{\mathrm{f}} \times \mathbb{R}^+ \to \mathbb{R}^3$, the pressure $p : \Omega^{\mathrm{f}} \times \mathbb{R}^+ \to \mathbb{R}$, the solid displacement $\boldsymbol{d} : \Sigma \times \mathbb{R}^+ \to \mathbb{R}^3$ and the rotation vector

$\boldsymbol{\theta} : \Sigma \times \mathbb{R}^+ \to \mathbb{R}^3$, such that

$$\begin{cases} \rho^{\mathrm{f}} \partial_t \boldsymbol{u} - \mathbf{div}\boldsymbol{\sigma}(\boldsymbol{u}, p) = \mathbf{0} & \text{in} \quad \Omega^{\mathrm{f}}, \\ \mathrm{div}\boldsymbol{u} = 0 & \text{in} \quad \Omega^{\mathrm{f}}, \\ \boldsymbol{\sigma}(\boldsymbol{u}, p)\boldsymbol{n} = -p_\Gamma \boldsymbol{n} & \text{on} \quad \Gamma^{\mathrm{f}}, \end{cases} \tag{2.1}$$

$$\begin{cases} \boldsymbol{u} = \dot{\boldsymbol{d}} & \text{on} \quad \Sigma, \\ \rho^{\mathrm{s}} \epsilon \partial_t \dot{\boldsymbol{d}} + \boldsymbol{L}^{\mathrm{e}}_{\boldsymbol{d}}(\boldsymbol{d}, \boldsymbol{\theta}) + \boldsymbol{L}^{\mathrm{v}}_{\boldsymbol{d}}(\dot{\boldsymbol{d}}, \dot{\boldsymbol{\theta}}) = -\boldsymbol{\sigma}(\boldsymbol{u}, p)\boldsymbol{n} & \text{on} \quad \Sigma, \\ \boldsymbol{L}^{\mathrm{e}}_{\boldsymbol{\theta}}(\boldsymbol{d}, \boldsymbol{\theta}) + \boldsymbol{L}^{\mathrm{v}}_{\boldsymbol{\theta}}(\dot{\boldsymbol{d}}, \dot{\boldsymbol{\theta}}) = \mathbf{0} & \text{on} \quad \Sigma, \\ \dot{\boldsymbol{d}} = \partial_t \boldsymbol{d}, \quad \dot{\boldsymbol{\theta}} = \partial_t \boldsymbol{\theta} & \text{on} \quad \Sigma, \\ \boldsymbol{d} = \boldsymbol{\theta} = \mathbf{0} & \text{on} \quad \partial\Sigma, \end{cases} \tag{2.2}$$

satisfying the initial conditions $\boldsymbol{u}(0) = \boldsymbol{u}_0$, $\boldsymbol{d}(0) = \boldsymbol{d}_0$, $\boldsymbol{\theta}(0) = \boldsymbol{\theta}_0$, $\dot{\boldsymbol{d}}(0) = \dot{\boldsymbol{d}}_0$ and $\dot{\boldsymbol{\theta}}(0) = \dot{\boldsymbol{\theta}}_0$. A given pressure data p_Γ is prescribed on the fluid external boundary Γ^{f}. In this section, the elastic and viscous solid operators, $\left(\boldsymbol{L}^{\mathrm{e}}_{\boldsymbol{d}}, \boldsymbol{L}^{\mathrm{e}}_{\boldsymbol{\theta}}\right)$ and $\left(\boldsymbol{L}^{\mathrm{v}}_{\boldsymbol{d}}, \boldsymbol{L}^{\mathrm{v}}_{\boldsymbol{\theta}}\right)$, are supposed to be linear (see (1.13) together with (1.15) and (1.16) for an example of suitable operators).

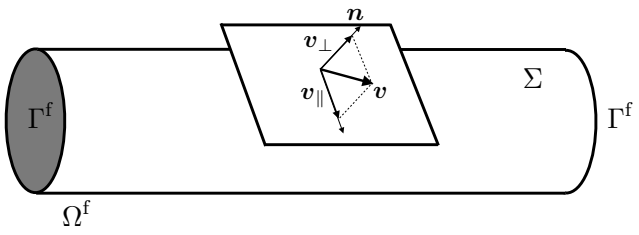

Figure 2.1: Geometrical configuration.

Remark 2.1 *The external boundary conditions of the coupled problem have no impact on the coupling schemes and theoretical results presented below.*

2.2.1 Time semi-discretization: fully decoupled schemes

Recall that the symbol τ denotes the time-step length, $t_n \overset{\text{def}}{=} n\tau$, for $n \in \mathbb{N}$, and $\partial_\tau x^n \overset{\text{def}}{=} \left(x^n - x^{n-1}\right)/\tau$ stands for the first order backward difference in time. In the following, we will make extensive use of the superscripts $^\bullet$ and * to respectively indicate explicit extrapolations of order $s \in \{0, 1\}$ and $r \in \{0, 1, 2\}$, namely,

$$x^{n,\bullet} \overset{\text{def}}{=} \begin{cases} 0 & \text{if} \quad s = 0, \\ x^{n-1} & \text{if} \quad s = 1, \end{cases}, \qquad x^{n,\star} \overset{\text{def}}{=} \begin{cases} 0 & \text{if} \quad r = 0, \\ x^{n-1} & \text{if} \quad r = 1, \\ 2x^{n-1} - x^{n-2} & \text{if} \quad r = 2. \end{cases}$$

The use of these two different notations will be made clear below (see Remark 2.2).

This section is devoted to the time discretization of the coupled problem (2.1)-(2.2). A fundamental feature of this coupled problem is that it enforces an intrinsic

Robin consistency on the interface (see Section 1.4.3.5). More specifically, from $(2.2)_{1,2}$ it follows that

$$\boldsymbol{\sigma}(\boldsymbol{u},p)\boldsymbol{n}+\rho^{\mathrm{s}}\epsilon\partial_t\boldsymbol{u}=-\boldsymbol{L}^{\mathrm{e}}_{\boldsymbol{d}}(\boldsymbol{d},\boldsymbol{\theta})-\boldsymbol{L}^{\mathrm{v}}_{\boldsymbol{d}}(\dot{\boldsymbol{d}},\dot{\boldsymbol{\theta}}). \tag{2.3}$$

In Section 1.4.3.5, this notion of interface Robin consistency has been used to avoid the infamous unconditional instability issues of standard Dirichlet-Neumann loosely coupled schemes, without compromising optimal accuracy. Applied to this problem, the methods proposed there split the time-marching of $(\boldsymbol{u},p)$ and $(\boldsymbol{d},\boldsymbol{\theta})$ by combining a monolithic time-stepping of (2.1) with a specific time discretization of (2.3). The purpose of this chapter is to show how this explicit coupling paradigm can be effectively used with a projection method in the fluid. The resulting methods enable a fully decoupled sequential computation of the whole fluid-solid state: $\boldsymbol{u}$, p and $(\boldsymbol{d},\boldsymbol{\theta})$.

The solution procedures proposed in this chapter build on the following three fundamental ingredients:

1. Projection-based time-marching of the fluid:

   (a) Viscous-step:

   $$\begin{cases}\rho^{\mathrm{f}}\,\dfrac{\tilde{\boldsymbol{u}}^n-\boldsymbol{u}^{n-1}}{\tau}-\mathbf{div}\boldsymbol{\sigma}(\tilde{\boldsymbol{u}}^n,p^{n,\bullet})=\boldsymbol{0} & \text{in}\quad\Omega^{\mathrm{f}},\\ \boldsymbol{\sigma}(\tilde{\boldsymbol{u}}^n,p^{n,\bullet})\boldsymbol{n}=-p^{n,\bullet}_{\Gamma}\boldsymbol{n} & \text{on}\quad\Gamma^{\mathrm{f}}.\end{cases} \tag{2.4}$$

   (b) Projection-step:

   $$\begin{cases}\rho^{\mathrm{f}}\,\dfrac{\boldsymbol{u}^n-\tilde{\boldsymbol{u}}^n}{\tau}+\boldsymbol{\nabla}\phi^n=\boldsymbol{0} & \text{in}\quad\Omega^{\mathrm{f}},\\ \mathrm{div}\boldsymbol{u}^n=0 & \text{in}\quad\Omega^{\mathrm{f}},\\ \phi^n=p^n_{\Gamma}-p^{n,\bullet}_{\Gamma} & \text{on}\quad\Gamma^{\mathrm{f}},\end{cases} \tag{2.5}$$

   with $\phi^n\overset{\text{def}}{=}p^n-p^{n,\bullet}$.

   We recall that the choices $s=0,1$ correspond, respectively, to the so-called non-incremental and incremental pressure-correction schemes (see Section 1.4.3.2). The arguments below can be extended with ease to a *velocity-correction time-stepping* (see, e.g, [GMS06, Section 4]) in the fluid.

2. Explicit interface conditions for (2.4) and (2.5), based on a specific fractional-step time-marching of (2.3), which preserve the velocity/pressure splitting and treat implicitly only the solid inertia contribution.

3. Fluid stresses are transmitted to the solid by solving the standard shell prob-

lem:

$$\begin{cases} \rho^{\mathrm{s}}\epsilon\partial_\tau\dot{\boldsymbol{d}}^n + \boldsymbol{L}^{\mathrm{e}}_{\boldsymbol{d}}(\boldsymbol{d}^n,\boldsymbol{\theta}^n) + \boldsymbol{L}^{\mathrm{v}}_{\boldsymbol{d}}(\dot{\boldsymbol{d}}^n,\dot{\boldsymbol{\theta}}^n) = -\boldsymbol{\sigma}(\tilde{\boldsymbol{u}}^n,p^n)\boldsymbol{n} & \text{on} \quad \Sigma, \\ \boldsymbol{L}^{\mathrm{e}}_{\boldsymbol{\theta}}(\boldsymbol{d}^n,\boldsymbol{\theta}^n) + \boldsymbol{L}^{\mathrm{v}}_{\boldsymbol{\theta}}(\dot{\boldsymbol{d}}^n,\dot{\boldsymbol{\theta}}^n) = \boldsymbol{0} & \text{on} \quad \Sigma, \\ \dot{\boldsymbol{d}} = \partial_\tau\boldsymbol{d}^n, \quad \dot{\boldsymbol{\theta}}^n = \partial_\tau\boldsymbol{\theta}^n & \text{on} \quad \Sigma, \\ \boldsymbol{d}^n = \boldsymbol{\theta}^n = \boldsymbol{0} & \text{on} \quad \partial\Sigma. \end{cases} \tag{2.6}$$

We now further elaborate on the second point. To this purpose, we first note that the projection-step (2.5) only contributes to the normal component of the fluid-stress, that is, $\boldsymbol{n}\cdot\boldsymbol{\sigma}(\boldsymbol{u},p)\boldsymbol{n}$. This is consistent with the fact that, in (2.5), only the normal component of the velocity has a well-defined trace on Σ. In terms of interface coupling, this indicates that the projection-step only contributes to the normal component of (2.3). Therefore, its tangential component has to be taken into account in the viscous-step (2.4). This motivates the following two-stage time discretization of (2.3):

$$\begin{cases} \boldsymbol{\sigma}(\tilde{\boldsymbol{u}}^n,p^{n,\bullet})\boldsymbol{n} + \dfrac{\rho^{\mathrm{s}}\epsilon}{\tau}\tilde{\boldsymbol{u}}^n = \dfrac{\rho^{\mathrm{s}}\epsilon}{\tau}\dot{\boldsymbol{d}}^{n-1} - \boldsymbol{L}^{\mathrm{e}}_{\boldsymbol{d}}(\boldsymbol{d}^{n,\star},\boldsymbol{\theta}^{n,\star})_{\|} - \boldsymbol{L}^{\mathrm{v}}_{\boldsymbol{d}}(\dot{\boldsymbol{d}}^{n,\star},\dot{\boldsymbol{\theta}}^{n,\star})_{\|}, \\ -\phi^n + \dfrac{\rho^{\mathrm{s}}\epsilon}{\tau}\boldsymbol{u}^n\cdot\boldsymbol{n} = \dfrac{\rho^{\mathrm{s}}\epsilon}{\tau}\tilde{\boldsymbol{u}}^n\cdot\boldsymbol{n} - \boldsymbol{L}^{\mathrm{e}}_{\boldsymbol{d}}(\boldsymbol{d}^{n,\star},\boldsymbol{\theta}^{n,\star})\cdot\boldsymbol{n} - \boldsymbol{L}^{\mathrm{v}}_{\boldsymbol{d}}(\dot{\boldsymbol{d}}^{n,\star},\dot{\boldsymbol{\theta}}^{n,\star})\cdot\boldsymbol{n}, \end{cases} \tag{2.7}$$

on Σ.

These interface relations preserve the original splitting of (2.4) and (2.5) and enable the interface fluid-solid splitting through the explicit treatment of the solid viscoelastic terms in (2.7). Besides, the viscoelastic extrapolations are performed to control the perturbation of the kinematic coupling, which dramatically affects accuracy in practice (see Remark 2.7 and the numerical evidence of Section 2.4).

REMARK 2.2 *From (2.4), (2.5) and (2.7) we can observe that the extrapolations represented by the superscripts $^\bullet$ and * are respectively associated to the velocity-pressure and fluid-solid splittings.*

In summary, a three-stage splitting of the coupled problem (2.1)-(2.2) could be performed by solving (2.4) with $(2.7)_1$, then (2.5) with $(2.7)_2$ and finally (2.6). However, in the spirit of Section 1.4.3.5, in order to avoid the extrapolations of the solid viscoelastic terms (which can be cumbersome in practice), we consider instead of (2.7) the following equivalent interface relations

$$\begin{cases} \boldsymbol{\sigma}(\tilde{\boldsymbol{u}}^n,p^{n,\bullet})\boldsymbol{n} + \dfrac{\rho^{\mathrm{s}}\epsilon}{\tau}\tilde{\boldsymbol{u}}^n = \dfrac{\rho^{\mathrm{s}}\epsilon}{\tau}\left(\dot{\boldsymbol{d}}^{n-1} + \tau\partial_\tau\dot{\boldsymbol{d}}^{n,\star}_{\|}\right) + \left(2\mu\boldsymbol{\varepsilon}(\tilde{\boldsymbol{u}}^{n,\star})\boldsymbol{n}\right)_{\|} & \text{on} \quad \Sigma, \\ -\phi^n + \dfrac{\rho^{\mathrm{s}}\epsilon}{\tau}\boldsymbol{u}^n\cdot\boldsymbol{n} = \dfrac{\rho^{\mathrm{s}}\epsilon}{\tau}\tilde{\boldsymbol{u}}^n\cdot\boldsymbol{n} - \phi^{n,\star} + \dfrac{\rho^{\mathrm{s}}\epsilon}{\tau}\left(\dot{\boldsymbol{d}}^{n,\star} - \tilde{\boldsymbol{u}}^{n,\star}\right)\cdot\boldsymbol{n} & \text{on} \quad \Sigma \end{cases} \tag{2.8}$$

for $n > s+r$, whose derivation is detailed in the following. To this purpose, we first note that, from $(2.6)_1$, we have

$$-\boldsymbol{L}^{\mathrm{e}}_{\boldsymbol{d}}(\boldsymbol{d}^{n,\star},\boldsymbol{\theta}^{n,\star}) - \boldsymbol{L}^{\mathrm{v}}_{\boldsymbol{d}}(\dot{\boldsymbol{d}}^{n,\star},\dot{\boldsymbol{\theta}}^{n,\star}) = \rho^{\mathrm{s}}\epsilon\partial_\tau\dot{\boldsymbol{d}}^{n,\star} + \boldsymbol{\sigma}(\tilde{\boldsymbol{u}}^{n,\star},p^{n,\star})\boldsymbol{n} \quad \text{on} \quad \Sigma \tag{2.9}$$

for $n > r$. The tangential component of this expression writes

$$-\boldsymbol{L}_{\boldsymbol{d}}^{\mathrm{e}}(\boldsymbol{d}^{n,\star},\boldsymbol{\theta}^{n,\star})_{\|} - \boldsymbol{L}_{\boldsymbol{d}}^{\mathrm{v}}(\dot{\boldsymbol{d}}^{n,\star},\dot{\boldsymbol{\theta}}^{n,\star})_{\|} = \rho^{\mathrm{s}}\epsilon\partial_\tau \dot{\boldsymbol{d}}_{\|}^{n,\star} + \big(2\mu\boldsymbol{\varepsilon}(\tilde{\boldsymbol{u}}^{n,\star})\boldsymbol{n}\big)_{\|} \quad \text{on} \quad \Sigma,$$

for $n > r$. Hence, by inserting this expression into $(2.7)_1$, we get $(2.8)_1$. We now proceed by taking the scalar product of (2.9) with $\boldsymbol{n}$, which yields

$$\begin{aligned} &-\boldsymbol{L}_{\boldsymbol{d}}^{\mathrm{e}}(\boldsymbol{d}^{n,\star},\boldsymbol{\theta}^{n,\star})\cdot\boldsymbol{n} - \boldsymbol{L}_{\boldsymbol{d}}^{\mathrm{v}}(\dot{\boldsymbol{d}}^{n,\star},\dot{\boldsymbol{\theta}}^{n,\star})\cdot\boldsymbol{n} \\ &\qquad = \rho^{\mathrm{s}}\epsilon\partial_\tau\dot{\boldsymbol{d}}^{n,\star}\cdot\boldsymbol{n} + 2\mu\boldsymbol{n}\cdot\boldsymbol{\varepsilon}(\tilde{\boldsymbol{u}}^{n,\star})\boldsymbol{n} - p^{n,\star}. \end{aligned} \tag{2.10}$$

In addition, by taking the scalar product of $(2.8)_1$ with $\boldsymbol{n}$, we get

$$2\mu\boldsymbol{n}\cdot\boldsymbol{\varepsilon}(\tilde{\boldsymbol{u}}^{n,\star})\boldsymbol{n} = (p^{n,\bullet})^\star - \frac{\rho^{\mathrm{s}}\epsilon}{\tau}\left(\tilde{\boldsymbol{u}}^{n,\star} - \dot{\boldsymbol{d}}^{n-1,\star}\right)\cdot\boldsymbol{n} \quad \text{on} \quad \Sigma$$

for $n > s + r$. Hence, by inserting this expression into (2.10), it follows that

$$\begin{aligned} &-\boldsymbol{L}_{\boldsymbol{d}}^{\mathrm{e}}(\boldsymbol{d}^{n,\star},\boldsymbol{\theta}^{n,\star})\cdot\boldsymbol{n} - \boldsymbol{L}_{\boldsymbol{d}}^{\mathrm{v}}(\dot{\boldsymbol{d}}^{n,\star},\dot{\boldsymbol{\theta}}^{n,\star})\cdot\boldsymbol{n} \\ &\qquad = \rho^{\mathrm{s}}\epsilon\partial_\tau\dot{\boldsymbol{d}}^{n,\star}\cdot\boldsymbol{n} - p^{n,\star} + (p^{n,\bullet})^\star - \frac{\rho^{\mathrm{s}}\epsilon}{\tau}\left(\tilde{\boldsymbol{u}}^{n,\star} - \dot{\boldsymbol{d}}^{n-1,\star}\right)\cdot\boldsymbol{n} \\ &\qquad = (p^{n,\bullet})^\star - p^{n,\star} + \frac{\rho^{\mathrm{s}}\epsilon}{\tau}\left(\dot{\boldsymbol{d}}^{n,\star} - \tilde{\boldsymbol{u}}^{n,\star}\right)\cdot\boldsymbol{n} \end{aligned}$$

for $n > s + r$. We retrieve $(2.8)_2$ by inserting this last identity into $(2.7)_2$.

Finally, instead of the Darcy-step (2.5), we consider the equivalent pressure-Poisson formulation complemented with the following interface Robin condition, derived from $(2.8)_2$:

$$\frac{\tau}{\rho^{\mathrm{f}}}\frac{\partial\phi^n}{\partial\boldsymbol{n}} = -(\boldsymbol{u}^n - \tilde{\boldsymbol{u}}^n)\cdot\boldsymbol{n} = \frac{\tau}{\rho^{\mathrm{s}}\epsilon}(\phi^{n,\star} - \phi^n) + \left(\tilde{\boldsymbol{u}}^{n,\star} - \dot{\boldsymbol{d}}^{n,\star}\right)\cdot\boldsymbol{n} \quad \text{on} \quad \Sigma.$$

The proposed fully decoupled schemes for problem (2.1)-(2.2) are reported in Algorithm 2.1. A salient feature of these methods is their intrinsic partitioned (or modular) character, in the sense that the overall fluid problem (2.11)-(2.12) does not depend on the specific structure of the solid model, and viceversa. In particular, the solid substep (2.13) is simply an implicit first-order time-discretization of the shell equations $(2.2)_{2-5}$ with a known forcing term. Note also that the interface Robin conditions $(2.11)_3$ and $(2.12)_3$ are nothing but consistent relaxations of the kinematic compatibility $(2.2)_1$. In this sense, it is worth recalling that for pressure-correction projection methods, Dirichlet conditions on the velocity yield homogeneous Neumann conditions for the pressure (see, e.g., [Gue96, GMS06]).

Remark 2.3 *In the vein of Section 1.3.2, the work flow diagram of Algorithm 2.1 is given in Figure 2.2. Recall that $\mathcal{F}^{\mathrm{AD}}$, $\mathcal{F}^{\mathrm{P}}$ and $\mathcal{S}$ stand for the fluid advection-diffusion, fluid projection and solid solutions, respectively. Comparing Figure 2.2 with the work flow diagram of Algorithm 1.2 (reported in Figure 1.10), we can readily see that Algorithm 2.1 goes further in the time-splitting of the coupled system with*

ALGORITHM 2.1 Fully decoupled schemes for (2.1)-(2.2).

For $n > s + r$:

1. Fluid viscous substep: find $\tilde{\boldsymbol{u}}^n : \Omega^{\mathrm{f}} \to \mathbb{R}^d$ such that

$$\begin{cases} \rho^{\mathrm{f}} \dfrac{\tilde{\boldsymbol{u}}^n - \boldsymbol{u}^{n-1}}{\tau} - \mathbf{div}\boldsymbol{\sigma}(\tilde{\boldsymbol{u}}^n, p^{n,\bullet}) = \mathbf{0} & \text{in} \quad \Omega^{\mathrm{f}}, \\ \boldsymbol{\sigma}(\tilde{\boldsymbol{u}}^n, p^{n,\bullet})\boldsymbol{n} = -p_\Gamma^{n,\bullet}\boldsymbol{n} & \text{on} \quad \Gamma^{\mathrm{f}}, \\ \boldsymbol{\sigma}(\tilde{\boldsymbol{u}}^n, p^{n,\bullet})\boldsymbol{n} + \dfrac{\rho^{\mathrm{s}}\epsilon}{\tau}\tilde{\boldsymbol{u}}^n = \dfrac{\rho^{\mathrm{s}}\epsilon}{\tau}\big(\dot{\boldsymbol{d}}^{n-1} + \tau\partial_\tau \dot{\boldsymbol{d}}_\parallel^{n,\star}\big) + \big(2\mu\boldsymbol{\varepsilon}(\tilde{\boldsymbol{u}}^{n,\star})\boldsymbol{n}\big)_\parallel & \text{on} \quad \Sigma. \end{cases} \tag{2.11}$$

2. Fluid projection substep: find $\phi^n : \Omega^{\mathrm{f}} \to \mathbb{R}$ such that

$$\begin{cases} -\dfrac{\tau}{\rho^{\mathrm{f}}}\Delta\phi^n = -\mathrm{div}\tilde{\boldsymbol{u}}^n & \text{in} \quad \Omega^{\mathrm{f}}, \\ \phi^n = p_\Gamma^n - p_\Gamma^{n,\bullet} & \text{on} \quad \Gamma^{\mathrm{f}}, \\ \dfrac{\tau}{\rho^{\mathrm{f}}}\dfrac{\partial\phi^n}{\partial\boldsymbol{n}} + \dfrac{\tau}{\rho^{\mathrm{s}}\epsilon}\phi^n = \dfrac{\tau}{\rho^{\mathrm{s}}\epsilon}\phi^{n,\star} + \big(\tilde{\boldsymbol{u}}^{n,\star} - \dot{\boldsymbol{d}}^{n,\star}\big)\cdot\boldsymbol{n} & \text{on} \quad \Sigma. \end{cases} \tag{2.12}$$

   Thereafter set $p^n = \phi^n + p^{n,\bullet}$, $\boldsymbol{u}^n = \tilde{\boldsymbol{u}}^n - \frac{\tau}{\rho^{\mathrm{f}}}\boldsymbol{\nabla}\phi^n$.

3. Solid substep: find $\boldsymbol{d}^n : \Sigma \to \mathbb{R}^3$ and $\boldsymbol{\theta}^n : \Sigma \to \mathbb{R}^3$ with $\boldsymbol{\theta}_\perp^n = \mathbf{0}$ and such that

$$\begin{cases} \rho^{\mathrm{s}}\epsilon\partial_\tau\dot{\boldsymbol{d}}^n + \boldsymbol{L}_{\boldsymbol{d}}^{\mathrm{e}}(\boldsymbol{d}^n, \boldsymbol{\theta}^n) + \boldsymbol{L}_{\boldsymbol{d}}^{\mathrm{v}}(\dot{\boldsymbol{d}}^n, \dot{\boldsymbol{\theta}}^n) = -\boldsymbol{\sigma}(\tilde{\boldsymbol{u}}^n, p^n)\boldsymbol{n} & \text{in} \quad \Sigma, \\ \boldsymbol{L}_{\boldsymbol{\theta}}^{\mathrm{e}}(\boldsymbol{d}^n, \boldsymbol{\theta}^n) + \boldsymbol{L}_{\boldsymbol{\theta}}^{\mathrm{v}}(\dot{\boldsymbol{d}}^n, \dot{\boldsymbol{\theta}}^n) = \mathbf{0} & \text{on} \quad \Sigma, \\ \dot{\boldsymbol{d}}^n = \partial_\tau\boldsymbol{d}^n, \quad \dot{\boldsymbol{\theta}}^n = \partial_\tau\boldsymbol{\theta}^n & \text{on} \quad \Sigma, \\ \boldsymbol{d}^n = \boldsymbol{\theta}^n = \mathbf{0} & \text{on} \quad \partial\Sigma. \end{cases} \tag{2.13}$$

respect to this other (also projection-based) scheme, by "breaking" the iterative inner loop between the fluid projection and the solid subproblems.

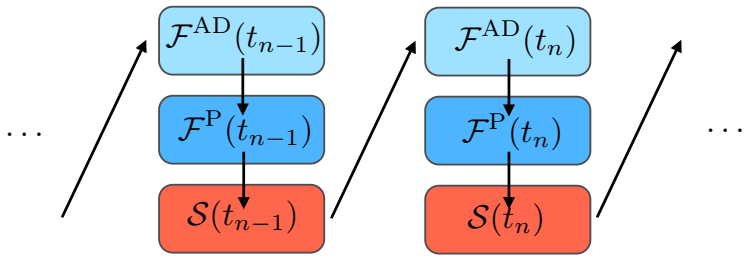

Figure 2.2: Work flow diagram of Algorithm 2.1.

REMARK 2.4 *It should be noted that, in contrast to the approach recently proposed in [BHS14], the Robin splitting provided by* $(2.11)_3$ *and* $(2.12)_3$ *admits a*

mathematically sound variational setting and, hence, can be straightforwardly combined with a finite element approximation in space (see Section 2.4).

Remark 2.5 *For $s > 1$ or $r > 1$, Algorithm 2.1 is a multi-step method which requires initial data at the time instants $t_1, \ldots, t_{r+s}$. This additional data is obtained by performing $r + s$ steps of Algorithm 2.1 with lower values of r or s, starting from $s = r = 0$. For instance, if we consider Algorithm 2.1 with $s = 1$ and $r = 2$, we proceed as follows:*

- *one step of Algorithm 2.1 with $s = r = 0$ to generate data at t_1;*
- *one step of Algorithm 2.1 with $s = 1$ and $r = 0$ (or $s = 0$ and $r = 1$) to generate data at t_2;*
- *one step of Algorithm 2.1 with $s = r = 1$ to generate data at t_3.*

2.2.2 Stability analysis

In this section, energy estimates are derived for some of the schemes reported in Algorithm 2.1.

2.2.2.1 Preliminaries

Let ω be a given domain or surface in $\mathbb{R}^3$. Recall that the scalar product in $L^2(\omega)$ is denoted by $(\cdot,\cdot)_\omega$ and its norm by $\|\cdot\|_\omega$. For the sake of simplicity, the subscript $_{\Omega^{\mathrm{f}}}$ is omitted in the rest of this chapter for the case $\omega = \Omega^{\mathrm{f}}$. Since the elastic and viscous solid surface operators, $\left(\boldsymbol{L}^{\mathrm{e}}_{\boldsymbol{d}}, \boldsymbol{L}^{\mathrm{e}}_{\boldsymbol{\theta}}\right)$ and $\left(\boldsymbol{L}^{\mathrm{v}}_{\boldsymbol{d}}, \boldsymbol{L}^{\mathrm{v}}_{\boldsymbol{\theta}}\right)$, are supposed to be linear, they admit the decomposition (1.13), that we repeat here for convenience:

$$\begin{aligned}
\boldsymbol{L}^{\mathrm{e}}_{\boldsymbol{d}}(\boldsymbol{d},\boldsymbol{\theta}) &\stackrel{\mathrm{def}}{=} \boldsymbol{A}^{\mathrm{e}}_{\boldsymbol{d}}\boldsymbol{d} + \boldsymbol{B}^{\mathrm{e}}_{\boldsymbol{d}}\boldsymbol{\theta}, \quad \boldsymbol{L}^{\mathrm{v}}_{\boldsymbol{d}}(\boldsymbol{d},\boldsymbol{\theta}) \stackrel{\mathrm{def}}{=} \boldsymbol{A}^{\mathrm{v}}_{\boldsymbol{d}}\boldsymbol{d} + \boldsymbol{B}^{\mathrm{v}}_{\boldsymbol{d}}\boldsymbol{\theta},\\
\boldsymbol{L}^{\mathrm{e}}_{\boldsymbol{\theta}}(\boldsymbol{d},\boldsymbol{\theta}) &\stackrel{\mathrm{def}}{=} \boldsymbol{B}^{\mathrm{e}}_{\boldsymbol{\theta}}\boldsymbol{d} + \boldsymbol{A}^{\mathrm{e}}_{\boldsymbol{\theta}}\boldsymbol{\theta}, \quad \boldsymbol{L}^{\mathrm{v}}_{\boldsymbol{\theta}}(\boldsymbol{d},\boldsymbol{\theta}) \stackrel{\mathrm{def}}{=} \boldsymbol{B}^{\mathrm{v}}_{\boldsymbol{\theta}}\boldsymbol{d} + \boldsymbol{A}^{\mathrm{v}}_{\boldsymbol{\theta}}\boldsymbol{\theta}.
\end{aligned}$$

Furthermore, we assume that the corresponding matrix operators

$$\boldsymbol{Q}^{\mathrm{e}} \stackrel{\mathrm{def}}{=} \begin{bmatrix} \boldsymbol{A}^{\mathrm{e}}_{\boldsymbol{d}} & \boldsymbol{B}^{\mathrm{e}}_{\boldsymbol{d}} \\ \boldsymbol{B}^{\mathrm{e}}_{\boldsymbol{\theta}} & \boldsymbol{A}^{\mathrm{e}}_{\boldsymbol{\theta}} \end{bmatrix}, \quad \boldsymbol{Q}^{\mathrm{v}} \stackrel{\mathrm{def}}{=} \begin{bmatrix} \boldsymbol{A}^{\mathrm{v}}_{\boldsymbol{d}} & \boldsymbol{B}^{\mathrm{v}}_{\boldsymbol{d}} \\ \boldsymbol{B}^{\mathrm{v}}_{\boldsymbol{\theta}} & \boldsymbol{A}^{\mathrm{v}}_{\boldsymbol{\theta}} \end{bmatrix},$$

are self-adjoint positive definite operators in $[L^2(\Sigma)]^3 \times [L^2(\Sigma)]^3$. An example of Reissner-Mindlin type shell model entering this abstract framework is given by the shear-membrane-bending model introduced in Section 1.2.2.2, which corresponds to the operators (1.15) and (1.16).

For the sake of conciseness, the following notation will also be used

$$\boldsymbol{y} \stackrel{\mathrm{def}}{=} \begin{bmatrix} \boldsymbol{d} \\ \boldsymbol{\theta} \end{bmatrix}, \quad \dot{\boldsymbol{y}} \stackrel{\mathrm{def}}{=} \begin{bmatrix} \dot{\boldsymbol{d}} \\ \dot{\boldsymbol{\theta}} \end{bmatrix},$$

as well as their corresponding elastic-energy and viscous-dissipation norms

$$\|\boldsymbol{y}\|_{\mathrm{e}} \stackrel{\mathrm{def}}{=} \left(\boldsymbol{Q}^{\mathrm{e}}\boldsymbol{y},\boldsymbol{y}\right)_{\Sigma}^{\frac{1}{2}}, \quad \|\dot{\boldsymbol{y}}\|_{\mathrm{v}} \stackrel{\mathrm{def}}{=} \left(\boldsymbol{Q}^{\mathrm{v}}\dot{\boldsymbol{y}},\dot{\boldsymbol{y}}\right)_{\Sigma}^{\frac{1}{2}}.$$

In order to ease the presentation, we will commit a slight abuse of notation by settting $\boldsymbol{L}^{\mathrm{e}}_{\boldsymbol{d}}\boldsymbol{y} \stackrel{\mathrm{def}}{=} \boldsymbol{L}^{\mathrm{e}}_{\boldsymbol{d}}(\boldsymbol{d},\boldsymbol{\theta})$ and $\boldsymbol{L}^{\mathrm{v}}_{\boldsymbol{d}}\dot{\boldsymbol{y}} \stackrel{\mathrm{def}}{=} \boldsymbol{L}^{\mathrm{v}}_{\boldsymbol{d}}(\dot{\boldsymbol{d}},\dot{\boldsymbol{\theta}})$. The same applies to operators $\boldsymbol{L}^{\mathrm{e}}_{\boldsymbol{\theta}}$ and $\boldsymbol{L}^{\mathrm{v}}_{\boldsymbol{\theta}}$.

2.2.2.2 A priori energy estimates

We define the time semi-discrete energy E^n and dissipation D^n, at time t_n, as follows:

$$E^n \stackrel{\mathrm{def}}{=} \frac{\rho^{\mathrm{f}}}{2}\|\boldsymbol{u}^n\|^2 + \frac{\rho^{\mathrm{s}}\epsilon}{2}\|\dot{\boldsymbol{d}}^n\|^2_{\Sigma} + \frac{1}{2}\|\boldsymbol{y}^n\|^2_{\mathrm{e}} + s\frac{\tau^2}{2\rho^{\mathrm{f}}}\|\boldsymbol{\nabla}p^n\|^2,$$
$$D^n \stackrel{\mathrm{def}}{=} 2\mu\|\boldsymbol{\varepsilon}(\tilde{\boldsymbol{u}}^n)\|^2 + \|\dot{\boldsymbol{y}}^n\|^2_{\mathrm{v}} + (1-s)\frac{\tau}{2\rho^{\mathrm{f}}}\|\boldsymbol{\nabla}p^n\|^2.$$

The main result of this section is stated in the next theorem.

Theorem 2.1 *Assume that the system is isolated, i.e., $p_\Gamma = 0$ (free system) and let the sequence $\left\{(\tilde{\boldsymbol{u}}^n,\boldsymbol{u}^n,p^n,\boldsymbol{d}^n,\dot{\boldsymbol{d}}^n,\boldsymbol{\theta}^n,\dot{\boldsymbol{\theta}}^n)\right\}_{n>r}$ be given by Algorithm 2.1 either with $s=0$ and $r\in\{0,1\}$, or with $s=1$ and $r=0$. Then, the following a priori energy estimate holds for $n>s+r$:*

$$E^n + \tau\sum_{m>s+r}^{n} D^m \leq E^0. \tag{2.14}$$

Proof. We first reformulate the second step of Algorithm 2.1 as the following equivalent Darcy-problem:

$$\begin{cases} \rho^{\mathrm{f}}\,\dfrac{\boldsymbol{u}^n-\tilde{\boldsymbol{u}}^n}{\tau} + \boldsymbol{\nabla}\phi^n = \boldsymbol{0} \quad \text{in} \quad \Omega^{\mathrm{f}}, \\ \mathrm{div}\boldsymbol{u}^n = 0 \quad \text{in} \quad \Omega^{\mathrm{f}}, \\ \phi^n = 0 \quad \text{on} \quad \Gamma^{\mathrm{f}}, \\ -\phi^n + \dfrac{\rho^{\mathrm{s}}\epsilon}{\tau}\boldsymbol{u}^n\cdot\boldsymbol{n} = \dfrac{\rho^{\mathrm{s}}\epsilon}{\tau}\tilde{\boldsymbol{u}}^n\cdot\boldsymbol{n} - \phi^{n,\star} + \dfrac{\rho^{\mathrm{s}}\epsilon}{\tau}\left(\dot{\boldsymbol{d}}^{n,\star}-\tilde{\boldsymbol{u}}^{n,\star}\right)\cdot\boldsymbol{n} \quad \text{on} \quad \Sigma. \end{cases} \tag{2.15}$$

Note that we have used the assumption that $p_\Gamma = 0$. From $(2.11)_3$, $(2.13)_1$ and $(2.15)_4$, it follows that (2.7) holds for $n > s+r$. Thus, by adding $(2.7)_1$ to $(2.7)_2$ multiplied by $\boldsymbol{n}$, we get

$$\frac{\rho^{\mathrm{s}}\epsilon}{\tau}\left((\tilde{\boldsymbol{u}}^n_{\parallel}+\boldsymbol{u}^n_{\perp}) - \dot{\boldsymbol{d}}^{n-1}\right) + \boldsymbol{L}^{\mathrm{e}}_{\boldsymbol{d}}\boldsymbol{y}^{n,\star} + \boldsymbol{L}^{\mathrm{v}}_{\boldsymbol{d}}\dot{\boldsymbol{y}}^{n,\star} = -\boldsymbol{\sigma}(\tilde{\boldsymbol{u}}^n,p^n)\boldsymbol{n} \quad \text{on} \quad \Sigma,$$

which, after subtraction from $(2.13)_1$, yields the following fundamental displacement-velocity correction reformulation of the solid step:

$$\frac{\rho^{\mathrm{s}}\epsilon}{\tau}\left(\dot{\boldsymbol{d}}^n - (\tilde{\boldsymbol{u}}^n_{\parallel}+\boldsymbol{u}^n_{\perp})\right) + \boldsymbol{L}^{\mathrm{e}}_{\boldsymbol{d}}(\boldsymbol{y}^n-\boldsymbol{y}^{n,\star}) + \boldsymbol{L}^{\mathrm{v}}_{\boldsymbol{d}}(\dot{\boldsymbol{y}}^n-\dot{\boldsymbol{y}}^{n,\star}) = \boldsymbol{0} \quad \text{on} \quad \Sigma \tag{2.16}$$

for $n > s + r$. As a result, from $(2.7)_2$ and (2.16), we obtain the following discrete kinematic relations on the interface Σ:

$$\left\{\begin{array}{l} \boldsymbol{u}^n \cdot \boldsymbol{n} = \tilde{\boldsymbol{u}}^n \cdot \boldsymbol{n} + \dfrac{\tau}{\rho^{\mathrm{s}}\epsilon}\big(\phi^n - \boldsymbol{L}_{\boldsymbol{d}}^{\mathrm{e}}\boldsymbol{y}^{n,\star}\cdot\boldsymbol{n} - \boldsymbol{L}_{\boldsymbol{d}}^{\mathrm{v}}\dot{\boldsymbol{y}}^{n,\star}\cdot\boldsymbol{n}\big), \\ \quad \tilde{\boldsymbol{u}}^n = \dot{\boldsymbol{d}}^n + \dfrac{\tau}{\rho^{\mathrm{s}}\epsilon}\big[\boldsymbol{L}_{\boldsymbol{d}}^{\mathrm{e}}(\boldsymbol{y}^n - \boldsymbol{y}^{n,\star}) + \boldsymbol{L}_{\boldsymbol{d}}^{\mathrm{v}}(\dot{\boldsymbol{y}}^n - \dot{\boldsymbol{y}}^{n,\star})\big] \\ \qquad\qquad - \dfrac{\tau}{\rho^{\mathrm{s}}\epsilon}\left[\phi^n\boldsymbol{n} - \big(\boldsymbol{L}_{\boldsymbol{d}}^{\mathrm{e}}\boldsymbol{y}^{n,\star}\big)_\perp - \big(\boldsymbol{L}_{\boldsymbol{d}}^{\mathrm{v}}\dot{\boldsymbol{y}}^{n,\star}\big)_\perp\right] \end{array}\right. \tag{2.17}$$

for $n > s + r$. We now proceed by taking the scalar product of $(2.11)_1$ and $(2.15)_1$ with $\tilde{\boldsymbol{u}}^n$ and $\boldsymbol{u}^n$, respectively. Hence, after integration by parts over Ω^{f}, application of the boundary conditions $(2.11)_2$ and $(2.15)_3$, and summation of the resulting expressions, we get

$$\begin{aligned} \frac{\rho^{\mathrm{f}}}{2\tau}\left(\|\boldsymbol{u}^n\|^2 - \|\boldsymbol{u}^{n-1}\|^2 + \|\boldsymbol{u}^n - \tilde{\boldsymbol{u}}^n\|^2\right) + 2\mu\|\boldsymbol{\varepsilon}(\tilde{\boldsymbol{u}}^n)\|^2 \\ - (\boldsymbol{\sigma}(\tilde{\boldsymbol{u}}^n, p^{n,\bullet})\boldsymbol{n}, \tilde{\boldsymbol{u}}^n)_\Sigma - (p^{n,\bullet}, \mathrm{div}\tilde{\boldsymbol{u}}^n) + (\phi^n, \boldsymbol{u}^n\cdot\boldsymbol{n})_\Sigma \leq 0. \end{aligned}$$

Equivalently, by using $(2.15)_1$ and rearranging the interface terms, we obtain

$$\begin{aligned} &\frac{\rho^{\mathrm{f}}}{2\tau}\left(\|\boldsymbol{u}^n\|^2 - \|\boldsymbol{u}^{n-1}\|^2\right) + 2\mu\|\boldsymbol{\varepsilon}(\tilde{\boldsymbol{u}}^n)\|^2 - (\boldsymbol{\sigma}(\tilde{\boldsymbol{u}}^n, p^n)\boldsymbol{n}, \tilde{\boldsymbol{u}}^n)_\Sigma \\ &+ (p^n, (\boldsymbol{u}^n - \tilde{\boldsymbol{u}}^n)\cdot\boldsymbol{n})_\Sigma + \underbrace{\frac{\tau}{2\rho^{\mathrm{f}}}\|\boldsymbol{\nabla}\phi^n\|^2 - (p^{n,\bullet}, \mathrm{div}\tilde{\boldsymbol{u}}^n) - (p^{n,\bullet}, (\boldsymbol{u}^n - \tilde{\boldsymbol{u}}^n)\cdot\boldsymbol{n})_\Sigma}_{T_1} \leq 0. \end{aligned} \tag{2.18}$$

The term T_1 can be controlled from $(2.15)_{1-3}$, using integration by parts, which yields

$$\begin{aligned} T_1 &= \frac{\tau}{2\rho^{\mathrm{f}}}\|\boldsymbol{\nabla}\phi^n\|^2 - \frac{\tau}{\rho^{\mathrm{f}}}(\Delta\phi^n, p^{n,\bullet}) - (p^{n,\bullet}, (\boldsymbol{u}^n - \tilde{\boldsymbol{u}}^n)\cdot\boldsymbol{n})_\Sigma \\ &= \frac{\tau}{2\rho^{\mathrm{f}}}\|\boldsymbol{\nabla}\phi^n\|^2 + \frac{\tau}{\rho^{\mathrm{f}}}\big(\boldsymbol{\nabla}\phi^n, \boldsymbol{\nabla}p^{n,\bullet}\big) - \frac{\tau}{\rho^{\mathrm{f}}}\left(\frac{\partial\phi^n}{\partial\boldsymbol{n}}, p^{n,\bullet}\right)_\Sigma - (p^{n,\bullet}, (\boldsymbol{u}^n - \tilde{\boldsymbol{u}}^n)\cdot\boldsymbol{n})_\Sigma \\ &= \frac{\tau}{2\rho^{\mathrm{f}}}\left(\|\boldsymbol{\nabla}p^n\|^2 - \|\boldsymbol{\nabla}p^{n,\bullet}\|^2\right). \end{aligned}$$

Thus, by inserting this expression into (2.18), we get

$$\begin{aligned} \frac{\rho^{\mathrm{f}}}{2\tau}\left(\|\boldsymbol{u}^n\|^2 - \|\boldsymbol{u}^{n-1}\|^2\right) + 2\mu\|\boldsymbol{\varepsilon}(\tilde{\boldsymbol{u}}^n)\|^2 + \frac{\tau}{2\rho^{\mathrm{f}}}\left(\|\boldsymbol{\nabla}p^n\|^2 - \|\boldsymbol{\nabla}p^{n,\bullet}\|^2\right) \\ - (\boldsymbol{\sigma}(\tilde{\boldsymbol{u}}^n, p^n)\boldsymbol{n}, \tilde{\boldsymbol{u}}^n)_\Sigma + (p^n, (\boldsymbol{u}^n - \tilde{\boldsymbol{u}}^n)\cdot\boldsymbol{n})_\Sigma \leq 0, \end{aligned}$$

which, owing to the relation $(2.17)_1$, yields

$$\frac{\rho^{\mathrm{f}}}{2\tau}\left(\|\boldsymbol{u}^n\|^2-\|\boldsymbol{u}^{n-1}\|^2\right)+2\mu\|\boldsymbol{\varepsilon}(\tilde{\boldsymbol{u}}^n)\|^2+\frac{\tau}{2\rho^{\mathrm{f}}}\left(\|\boldsymbol{\nabla}p^n\|^2-\|\boldsymbol{\nabla}p^{n,\bullet}\|^2\right)$$
$$\underbrace{-\left(\boldsymbol{\sigma}(\tilde{\boldsymbol{u}}^n,p^n)\boldsymbol{n},\tilde{\boldsymbol{u}}^n\right)_\Sigma}_{T_2}+\frac{\tau}{\rho^{\mathrm{s}}\epsilon}\left(p^n\boldsymbol{n},\phi^n\boldsymbol{n}-(\boldsymbol{L}_{\boldsymbol{d}}^{\mathrm{e}}\boldsymbol{y}^{n,\star})_\perp-(\boldsymbol{L}_{\boldsymbol{d}}^{\mathrm{v}}\dot{\boldsymbol{y}}^{n,\star})_\perp\right)_\Sigma\le 0. \tag{2.19}$$

On the other hand, from $(2.13)_1$ and $(2.17)_2$, it follows that

$$\begin{aligned}
T_2=&\frac{\rho^{\mathrm{s}}\epsilon}{2\tau}\left(\|\dot{\boldsymbol{d}}^n\|_\Sigma^2-\|\dot{\boldsymbol{d}}^{n-1}\|_\Sigma^2+\|\dot{\boldsymbol{d}}^n-\dot{\boldsymbol{d}}^{n-1}\|_\Sigma^2\right)+\underbrace{\left(\boldsymbol{L}_{\boldsymbol{d}}^{\mathrm{e}}\boldsymbol{y}^n+\boldsymbol{L}_{\boldsymbol{d}}^{\mathrm{v}}\dot{\boldsymbol{y}}^n,\dot{\boldsymbol{d}}^n\right)_\Sigma}_{T_{2,1}}\\
&\left.\begin{aligned}
&+\frac{\tau}{2\rho^{\mathrm{s}}\epsilon}\left(\|\boldsymbol{L}_{\boldsymbol{d}}^{\mathrm{e}}\boldsymbol{y}^n+\boldsymbol{L}_{\boldsymbol{d}}^{\mathrm{v}}\dot{\boldsymbol{y}}^n\|_\Sigma^2-\|\boldsymbol{L}_{\boldsymbol{d}}^{\mathrm{e}}\boldsymbol{y}^{n,\star}+\boldsymbol{L}_{\boldsymbol{d}}^{\mathrm{v}}\dot{\boldsymbol{y}}^{n,\star}\|_\Sigma^2\right)\\
&+\frac{\tau}{2\rho^{\mathrm{s}}\epsilon}\|\boldsymbol{L}_{\boldsymbol{d}}^{\mathrm{e}}(\boldsymbol{y}^n-\boldsymbol{y}^{n,\star})+\boldsymbol{L}_{\boldsymbol{d}}^{\mathrm{v}}(\dot{\boldsymbol{y}}^n-\dot{\boldsymbol{y}}^{n,\star})\|_\Sigma^2
\end{aligned}\right\}T_{2,2}\\
&\underbrace{+\left(\dot{\boldsymbol{d}}^n-\dot{\boldsymbol{d}}^{n-1},\boldsymbol{L}_{\boldsymbol{d}}^{\mathrm{e}}(\boldsymbol{y}^n-\boldsymbol{y}^{n,\star})+\boldsymbol{L}_{\boldsymbol{d}}^{\mathrm{v}}(\dot{\boldsymbol{y}}^n-\dot{\boldsymbol{y}}^{n,\star})\right)_\Sigma}_{T_{2,3}}\\
&\underbrace{-\left(\dot{\boldsymbol{d}}^n-\dot{\boldsymbol{d}}^{n-1},\phi^n\boldsymbol{n}-\left(\boldsymbol{L}_{\boldsymbol{d}}^{\mathrm{e}}\boldsymbol{y}^{n,\star}\right)_\perp-\left(\boldsymbol{L}_{\boldsymbol{d}}^{\mathrm{v}}\dot{\boldsymbol{y}}^{n,\star}\right)_\perp\right)_\Sigma}_{T_{2,4}}\\
&-\frac{\tau}{\rho^{\mathrm{s}}\epsilon}\left(\boldsymbol{L}_{\boldsymbol{d}}^{\mathrm{e}}\boldsymbol{y}^n+\boldsymbol{L}_{\boldsymbol{d}}^{\mathrm{v}}\dot{\boldsymbol{y}}^n,\phi^n\boldsymbol{n}-(\boldsymbol{L}_{\boldsymbol{d}}^{\mathrm{e}}\boldsymbol{y}^{n,\star})_\perp-(\boldsymbol{L}_{\boldsymbol{d}}^{\mathrm{v}}\dot{\boldsymbol{y}}^{n,\star})_\perp\right)_\Sigma.
\end{aligned} \tag{2.20}$$

In addition, thanks to $(2.13)_2$, for the term $T_{2,1}$ we have

$$\begin{aligned}
T_{2,1}&=\left(\boldsymbol{L}_{\boldsymbol{d}}^{\mathrm{e}}\boldsymbol{y}^n+\boldsymbol{L}_{\boldsymbol{d}}^{\mathrm{v}}\dot{\boldsymbol{y}}^n,\dot{\boldsymbol{d}}^n\right)_\Sigma+\left(\boldsymbol{L}_{\boldsymbol{\theta}}^{\mathrm{e}}\boldsymbol{y}^n+\boldsymbol{L}_{\boldsymbol{\theta}}^{\mathrm{v}}\dot{\boldsymbol{y}}^n,\dot{\boldsymbol{\theta}}^n\right)_\Sigma\\
&=\left(\boldsymbol{Q}^{\mathrm{e}}\dot{\boldsymbol{y}}^n,\boldsymbol{y}^n\right)_\Sigma+\left(\boldsymbol{Q}^{\mathrm{v}}\dot{\boldsymbol{y}}^n,\dot{\boldsymbol{y}}^n\right)_\Sigma\\
&=\frac{1}{2\tau}\left(\|\boldsymbol{y}^n\|_{\mathrm{e}}^2-\left\|\boldsymbol{y}^{n-1}\right\|_{\mathrm{e}}^2+\left\|\boldsymbol{y}^n-\boldsymbol{y}^{n-1}\right\|_{\mathrm{e}}^2\right)+\|\dot{\boldsymbol{y}}^n\|_{\mathrm{v}}^2.
\end{aligned} \tag{2.21}$$

Thus, by inserting this identity into (2.20) and the resulting expression into (2.19), we get the following energy inequality

$$\begin{aligned}
&\frac{\rho^{\mathrm{f}}}{2\tau}\left(\|\boldsymbol{u}^n\|^2-\|\boldsymbol{u}^{n-1}\|^2\right)+\frac{\rho^{\mathrm{s}}\epsilon}{2\tau}\left(\|\dot{\boldsymbol{d}}^n\|_\Sigma^2-\|\dot{\boldsymbol{d}}^{n-1}\|_\Sigma^2+\|\dot{\boldsymbol{d}}^n-\dot{\boldsymbol{d}}^{n-1}\|_\Sigma^2\right)\\
&\quad+\frac{1}{2\tau}\left(\|\boldsymbol{y}^n\|_{\mathrm{e}}^2-\left\|\boldsymbol{y}^{n-1}\right\|_{\mathrm{e}}^2+\left\|\boldsymbol{y}^n-\boldsymbol{y}^{n-1}\right\|_{\mathrm{e}}^2\right)+\|\dot{\boldsymbol{y}}^n\|_{\mathrm{v}}^2+2\mu\|\boldsymbol{\varepsilon}(\tilde{\boldsymbol{u}}^n)\|^2\\
&\qquad+\frac{\tau}{2\rho^{\mathrm{f}}}\left(\|\boldsymbol{\nabla}p^n\|^2-\|\boldsymbol{\nabla}p^{n,\bullet}\|^2\right)+T_{2,2}+T_{2,3}+T_{2,4}\\
&\quad\underbrace{+\frac{\tau}{\rho^{\mathrm{s}}\epsilon}\left(p^n\boldsymbol{n}-\boldsymbol{L}_{\boldsymbol{d}}^{\mathrm{e}}\boldsymbol{y}^n-\boldsymbol{L}_{\boldsymbol{d}}^{\mathrm{v}}\dot{\boldsymbol{y}}^n,\phi^n\boldsymbol{n}-\left(\boldsymbol{L}_{\boldsymbol{d}}^{\mathrm{e}}\boldsymbol{y}^{n,\star}\right)_\perp-\left(\boldsymbol{L}_{\boldsymbol{d}}^{\mathrm{v}}\dot{\boldsymbol{y}}^{n,\star}\right)_\perp\right)_\Sigma}_{T_3}\le 0
\end{aligned} \tag{2.22}$$

for $n > s + r$.

We now proceed by treating each case of extrapolation separately.

Algorithm 2.1 with $s \in \{0, 1\}$ and $r = 0$. We have

$$\begin{aligned} T_{2,3} + T_{2,4} \geq & -\frac{\rho^{\mathrm{s}}\epsilon}{2\tau}\|\dot{\boldsymbol{d}}^n - \dot{\boldsymbol{d}}^{n-1}\|_\Sigma^2 - \frac{\tau}{2\rho^{\mathrm{s}}\epsilon}\|\boldsymbol{L}_{\boldsymbol{d}}^{\mathrm{e}}\boldsymbol{y}^n + \boldsymbol{L}_{\boldsymbol{d}}^{\mathrm{v}}\dot{\boldsymbol{y}}^n - \phi^n\boldsymbol{n}\|_\Sigma, \\ T_{2,2} + T_3 = & \frac{\tau}{2\rho^{\mathrm{s}}\epsilon}\big(\|p^n\|_\Sigma^2 - \|p^{n,\bullet}\|_\Sigma^2\big) + \frac{\tau}{2\rho^{\mathrm{s}}\epsilon}\|\boldsymbol{L}_{\boldsymbol{d}}^{\mathrm{e}}\boldsymbol{y}^n + \boldsymbol{L}_{\boldsymbol{d}}^{\mathrm{v}}\dot{\boldsymbol{y}}^n - \phi^n\boldsymbol{n}\|_\Sigma^2 \\ & + \frac{\tau}{2\rho^{\mathrm{s}}\epsilon}\|\boldsymbol{L}_{\boldsymbol{d}}^{\mathrm{e}}\boldsymbol{y}^n + \boldsymbol{L}_{\boldsymbol{d}}^{\mathrm{v}}\dot{\boldsymbol{y}}^n\|_\Sigma^2. \end{aligned}$$

Therefore,

$$\begin{aligned} T_{2,2} + T_{2,3} + T_{2,4} + T_3 \geq & -\frac{\rho^{\mathrm{s}}\epsilon}{2\tau}\|\dot{\boldsymbol{d}}^n - \dot{\boldsymbol{d}}^{n-1}\|_\Sigma^2 + \frac{\tau}{2\rho^{\mathrm{s}}\epsilon}\big(\|p^n\|_\Sigma^2 - \|p^{n,\bullet}\|_\Sigma^2\big) \\ & + \frac{\tau}{2\rho^{\mathrm{s}}\epsilon}\|\boldsymbol{L}_{\boldsymbol{d}}^{\mathrm{e}}\boldsymbol{y}^n + \boldsymbol{L}_{\boldsymbol{d}}^{\mathrm{v}}\dot{\boldsymbol{y}}^n\|_\Sigma^2. \quad (2.23) \end{aligned}$$

For $s = 0$, the estimate (2.14) follows by inserting this expression into (2.22), multiplication by τ and summation over $m = 1, ..., n$. For $s = 1$, we can only sum over $m = 2, ..., n$, which yields

$$E^n + \tau\sum_{m=2}^{n} D^m \leq E^1 + \frac{\tau^2}{2\rho^{\mathrm{s}}\epsilon}\|p^1\|_\Sigma^2. \quad (2.24)$$

Since p^1 is generated with one step of the scheme with $s = r = 0$ (see Remark 2.5), the last term of (2.24) can be controlled by the extra dissipation provided by (2.23) with $s = 0$ and $n = 1$. As a result, estimate (2.14) also holds for $s = 1$ and $r = 0$.

Algorithm 2.1 with $s = 0$ and $r = 1$. From $(2.13)_2$, we have

$$\begin{aligned} T_{2,3} &= \tau^2\big(\partial_\tau\dot{\boldsymbol{d}}^n, \boldsymbol{L}_{\boldsymbol{d}}^{\mathrm{e}}\dot{\boldsymbol{y}}^n + \boldsymbol{L}_{\boldsymbol{d}}^{\mathrm{v}}(\partial_\tau\dot{\boldsymbol{y}}^n)\big)_\Sigma + \tau^2\big(\partial_\tau\dot{\boldsymbol{\theta}}^n, \boldsymbol{L}_{\boldsymbol{\theta}}^{\mathrm{e}}\dot{\boldsymbol{y}}^n + \boldsymbol{L}_{\boldsymbol{\theta}}^{\mathrm{v}}(\partial_\tau\dot{\boldsymbol{y}}^n)\big)_\Sigma \\ &= \tau^2\left(\boldsymbol{Q}^{\mathrm{e}}\dot{\boldsymbol{y}}^n, \partial_\tau\dot{\boldsymbol{y}}^n\right)_\Sigma + \tau^2\left(\boldsymbol{Q}^{\mathrm{v}}\partial_\tau\dot{\boldsymbol{y}}^n, \partial_\tau\dot{\boldsymbol{y}}^n\right)_\Sigma \\ &= \frac{\tau}{2}\left(\|\dot{\boldsymbol{y}}^n\|_{\mathrm{e}}^2 - \left\|\dot{\boldsymbol{y}}^{n-1}\right\|_{\mathrm{e}}^2 + \left\|\dot{\boldsymbol{y}}^n - \dot{\boldsymbol{y}}^{n-1}\right\|_{\mathrm{e}}^2\right) + \tau^2\left\|\partial_\tau\dot{\boldsymbol{y}}^n\right\|_{\mathrm{v}}^2 \end{aligned}$$

for $n \geq 2$. For the third term, we get

$$T_{2,4} \geq -\frac{\rho^{\mathrm{s}}\epsilon}{2\tau}\|\dot{\boldsymbol{d}}^n - \dot{\boldsymbol{d}}^{n-1}\|_\Sigma^2 - \frac{\tau}{2\rho^{\mathrm{s}}\epsilon}\|\big(\boldsymbol{L}_{\boldsymbol{d}}^{\mathrm{e}}\boldsymbol{y}^{n-1}\big)_\perp + \big(\boldsymbol{L}_{\boldsymbol{d}}^{\mathrm{v}}\dot{\boldsymbol{y}}^{n-1}\big)_\perp - p^n\boldsymbol{n}\|_\Sigma^2.$$

At last, the fourth term is estimated as follows

$$
\begin{aligned}
T_3 &= \frac{\tau}{\rho^{\mathrm{s}}\epsilon}\left(p^n\boldsymbol{n} - \boldsymbol{L}_{\boldsymbol{d}}^{\mathrm{e}}\boldsymbol{y}^n - \boldsymbol{L}_{\boldsymbol{d}}^{\mathrm{v}}\dot{\boldsymbol{y}}^n, p^n\boldsymbol{n} - \left(\boldsymbol{L}_{\boldsymbol{d}}^{\mathrm{e}}\boldsymbol{y}^{n-1}\right)_\perp - \left(\boldsymbol{L}_{\boldsymbol{d}}^{\mathrm{v}}\dot{\boldsymbol{y}}^{n-1}\right)_\perp\right)_\Sigma \\
&= \frac{\tau}{\rho^{\mathrm{s}}\epsilon}\left(p^n\boldsymbol{n} - \left(\boldsymbol{L}_{\boldsymbol{d}}^{\mathrm{e}}\boldsymbol{y}^n\right)_\perp - \left(\boldsymbol{L}_{\boldsymbol{d}}^{\mathrm{v}}\dot{\boldsymbol{y}}^n\right)_\perp, p^n\boldsymbol{n} - \left(\boldsymbol{L}_{\boldsymbol{d}}^{\mathrm{e}}\boldsymbol{y}^{n-1}\right)_\perp - \left(\boldsymbol{L}_{\boldsymbol{d}}^{\mathrm{v}}\dot{\boldsymbol{y}}^{n-1}\right)_\perp\right)_\Sigma \\
&= \frac{\tau}{\rho^{\mathrm{s}}\epsilon}\|p^n\boldsymbol{n} - \left(\boldsymbol{L}_{\boldsymbol{d}}^{\mathrm{e}}\boldsymbol{y}^{n-1}\right)_\perp - \left(\boldsymbol{L}_{\boldsymbol{d}}^{\mathrm{v}}\dot{\boldsymbol{y}}^{n-1}\right)_\perp\|_\Sigma^2 \\
&\quad - \frac{\tau}{\rho^{\mathrm{s}}\epsilon}\left(\left(\boldsymbol{L}_{\boldsymbol{d}}^{\mathrm{e}}(\boldsymbol{y}^n - \boldsymbol{y}^{n-1})\right)_\perp + \left(\boldsymbol{L}_{\boldsymbol{d}}^{\mathrm{v}}(\dot{\boldsymbol{y}}^n - \dot{\boldsymbol{y}}^{n-1})\right)_\perp, p^n\boldsymbol{n} - \left(\boldsymbol{L}_{\boldsymbol{d}}^{\mathrm{e}}\boldsymbol{y}^{n-1}\right)_\perp - \left(\boldsymbol{L}_{\boldsymbol{d}}^{\mathrm{v}}\dot{\boldsymbol{y}}^{n-1}\right)_\perp\right)_\Sigma \\
&\geq \frac{\tau}{2\rho^{\mathrm{s}}\epsilon}\|p^n\boldsymbol{n} - \left(\boldsymbol{L}_{\boldsymbol{d}}^{\mathrm{e}}\boldsymbol{y}^{n-1}\right)_\perp - \left(\boldsymbol{L}_{\boldsymbol{d}}^{\mathrm{v}}\dot{\boldsymbol{y}}^{n-1}\right)_\perp\|_\Sigma^2 \\
&\quad - \frac{\tau}{2\rho^{\mathrm{s}}\epsilon}\|\left(\boldsymbol{L}_{\boldsymbol{d}}^{\mathrm{e}}(\boldsymbol{y}^n - \boldsymbol{y}^{n-1})\right)_\perp + \left(\boldsymbol{L}_{\boldsymbol{d}}^{\mathrm{v}}(\dot{\boldsymbol{y}}^n - \dot{\boldsymbol{y}}^{n-1})\right)_\perp\|_\Sigma^2.
\end{aligned}
$$

Therefore, by collecting the above estimations, we get

$$
\begin{aligned}
T_{2,2} + T_{2,3} + T_{2,4} + T_3 \geq & -\frac{\rho^{\mathrm{s}}\epsilon}{2\tau}\|\dot{\boldsymbol{d}}^n - \dot{\boldsymbol{d}}^{n-1}\|_\Sigma^2 \\
& + \frac{\tau}{2}\left(\|\dot{\boldsymbol{y}}^n\|_{\mathrm{e}}^2 - \left\|\dot{\boldsymbol{y}}^{n-1}\right\|_{\mathrm{e}}^2 + \left\|\dot{\boldsymbol{y}}^n - \dot{\boldsymbol{y}}^{n-1}\right\|_{\mathrm{e}}^2\right) + \tau^2\left\|\partial_\tau\dot{\boldsymbol{y}}^n\right\|_{\mathrm{v}}^2 \\
& + \frac{\tau}{2\rho^{\mathrm{s}}\epsilon}\left(\|\boldsymbol{L}_{\boldsymbol{d}}^{\mathrm{e}}\boldsymbol{y}^n + \boldsymbol{L}_{\boldsymbol{d}}^{\mathrm{v}}\dot{\boldsymbol{y}}^n\|_\Sigma^2 - \|\boldsymbol{L}_{\boldsymbol{d}}^{\mathrm{e}}\boldsymbol{y}^{n-1} + \boldsymbol{L}_{\boldsymbol{d}}^{\mathrm{v}}\dot{\boldsymbol{y}}^{n-1}\|_\Sigma^2\right) \\
& + \frac{\tau}{2\rho^{\mathrm{s}}\epsilon}\left\|\left(\boldsymbol{L}_{\boldsymbol{d}}^{\mathrm{e}}(\boldsymbol{y}^n - \boldsymbol{y}^{n-1})\right)_\parallel + \left(\boldsymbol{L}_{\boldsymbol{d}}^{\mathrm{v}}(\dot{\boldsymbol{y}}^n - \dot{\boldsymbol{y}}^{n-1})\right)_\parallel\right\|_\Sigma^2.
\end{aligned}
$$

Inserting this expression into (2.22), then multiplying by τ and summing over $m = 2, ..., n$, yields the estimate

$$
E^n + \tau\sum_{m=2}^{n} D^m \leq E^1 + \frac{\tau}{2}\left\|\boldsymbol{y}^1 - \boldsymbol{y}^0\right\|_{\mathrm{e}}^2 + \frac{\tau^2}{2\rho^{\mathrm{s}}\epsilon}\|\boldsymbol{L}_{\boldsymbol{d}}^{\mathrm{e}}\boldsymbol{y}^1 + \boldsymbol{L}_{\boldsymbol{d}}^{\mathrm{v}}\dot{\boldsymbol{y}}^1\|_\Sigma^2. \tag{2.25}
$$

Owing to the initialization procedure (see Remark 2.5), $\boldsymbol{y}^1$ and $\dot{\boldsymbol{y}}^1$ are obtained from the scheme with $s = r = 0$. Hence, the right-hand side of (2.25) can be bounded from (2.14), with $s = r = 0$, and the numerical dissipation provided by (2.21) and (2.23) for $n = 1$. This completes the proof. ∎

Theorem 2.1 guarantees the unconditionally energy stability of Algorithm 2.1 with:

- $s = 0$ (non-incremental pressure-correction) and $r = 0, 1$;
- $s = 1$ (incremental pressure-correction) and $r = 0$.

Similar energy estimates are obtained in Theorem 1.5 for the original Robin-Neumann schemes with a monolithic time-stepping in the fluid and a simpler solid model. This indicates that, at least for the above variants, the extensions proposed in this chapter preserve their stability properties.

Remark 2.6 *The stability of Algorithm 2.1 with $s = 0$ and $r = 2$, or $s = 1$ and $r \in \{1, 2\}$, is not covered by the previous analysis. In fact, it appears that the arguments used in the proof above can not be straightforwardly adapted to cope with these variants. Numerical evidence, reported in Section 2.4, indicates however that these schemes deliver stable and accurate numerical approximations.*

Remark 2.7 *From (2.16) it follows that*

$$\tilde{\boldsymbol{u}}_{\parallel}^{n} + \boldsymbol{u}_{\perp}^{n} = \dot{\boldsymbol{d}}^{n} + \frac{\tau}{\rho^{\mathrm{s}}\epsilon}\big[\boldsymbol{L}_{\boldsymbol{d}}^{\mathrm{e}}(\boldsymbol{y}^{n} - \boldsymbol{y}^{n,\star}) + \boldsymbol{L}_{\dot{\boldsymbol{d}}}^{\mathrm{v}}(\dot{\boldsymbol{y}}^{n} - \dot{\boldsymbol{y}}^{n,\star})\big] \quad \text{on} \quad \Sigma. \tag{2.26}$$

Hence, the kinematic constraint $(2.2)_1$ in Algorithm 2.1 is enforced in terms of the tangent, $\tilde{\boldsymbol{u}}_{\parallel}^{n}$, and normal components, $\boldsymbol{u}_{\perp}^{n}$, of the intermediate and end-of-step fluid velocities, respectively. Note that the consistency of (2.26) is given by the order $r \in \{0, 1, 2\}$ of the explicit extrapolations on the interface, irrespectively of the non-incremental ($s = 0$) or incremental ($s = 1$) nature of the projection method in the fluid. This indicates that the accuracy of the fluid-solid splitting induced by Algorithm 2.1 is dictated by $r \in \{0, 1, 2\}$, while $s \in \{0, 1\}$ drives the accuracy of the time-marching in the fluid.

Remark 2.8 *Besides the technical difficulties introduced by the projection method in the analysis of Algorithm 2.1, the result of Theorem 2.1 makes a step forward with respect to the stability analyses reported in Section 1.4.3.5, where the solid model is assumed to be simply a membrane or a Koiter type shell (see also [GGCC09, BCG+13, LMRHZ13, BHS14]). It is also worth recalling that, in contrast to Theorem 2.1, the stability result recently reported in [BHS14] relies on modal analysis (in further simplified models and geometrical configurations) and does not cover velocity/pressure splitting in the fluid.*

2.3 The non-linear case

In this section, the splitting schemes reported in Algorithm 2.1 are formulated in a non-linear framework. We consider the coupling of the ALE Navier-Stokes equations (1.4) with a non-linear Reissner-Mindlin shell model (see, e.g., [CB11, BBWR04]. The geometrical configuration is depicted in Figure 2.3.

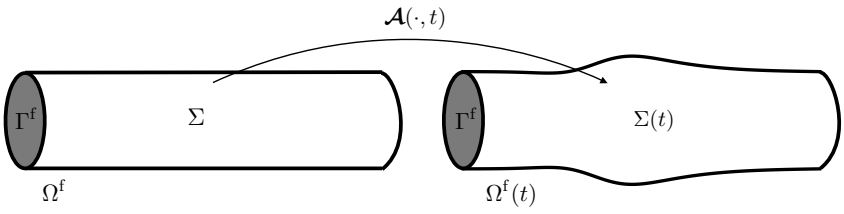

Figure 2.3: Geometrical configuration.

Remark 2.9 *In order to ease the presentation, the change of variables (1.3) will not be specified in the following equations.*

The shell kinematics are entirely characterized by the displacement field of the mid-surface $\boldsymbol{d}$ and the field of director vectors in the deformed configuration $\boldsymbol{a}$, i.e., the unit vectors that underlie the material lines originally orthogonal to the midsurface in the undeformed configuration. We recall that Reissner-Mindlin kinematics assume that such material lines, originally aligned with $\boldsymbol{n}$, remain straight and preserve their length in the deformation (see, e.g., [DB84, CB11]).

The considered non-linear fluid-structure problem reads as follows: find the fluid domain displacement $\boldsymbol{d}^{\mathrm{f}} : \Omega^{\mathrm{f}} \times \mathbb{R}^+ \to \mathbb{R}^d$, the fluid velocity $\boldsymbol{u} : \Omega^{\mathrm{f}} \times \mathbb{R}^+ \to \mathbb{R}^d$, the fluid pressure $p : \Omega^{\mathrm{f}} \times \mathbb{R}^+ \to \mathbb{R}$, the solid mid-surface displacement $\boldsymbol{d} : \Sigma \times \mathbb{R}^+ \to \mathbb{R}^3$ and the director vector $\boldsymbol{a} : \Sigma \times \mathbb{R}^+ \to \mathbb{R}^3$ of unit length $|\boldsymbol{a}| = 1$, such that

$$\begin{cases} \boldsymbol{d}^{\mathrm{f}} = \mathrm{Ext}\,(\boldsymbol{d}|_\Sigma)\,, \quad \dot{\boldsymbol{d}}^{\mathrm{f}} = \partial_t \boldsymbol{d}^{\mathrm{f}}, \quad \boldsymbol{\mathcal{A}} = \boldsymbol{I}_{\Omega^{\mathrm{f}}} + \boldsymbol{d}^{\mathrm{f}}, \quad \Omega^{\mathrm{f}}(t) = \boldsymbol{\mathcal{A}}(\Omega^{\mathrm{f}}, t), \\ \rho^{\mathrm{f}} \partial_t|_{\boldsymbol{\mathcal{A}}} \boldsymbol{u} + \rho^{\mathrm{f}}(\boldsymbol{u} - \dot{\boldsymbol{d}}^{\mathrm{f}}) \cdot \boldsymbol{\nabla} \boldsymbol{u} - \mathbf{div} \boldsymbol{\sigma}(\boldsymbol{u}, p) = \boldsymbol{0} \quad \text{in} \quad \Omega^{\mathrm{f}}(t), \\ \mathrm{div} \boldsymbol{u} = 0 \quad \text{in} \quad \Omega^{\mathrm{f}}(t), \\ \boldsymbol{\sigma}(\boldsymbol{u}, p)\boldsymbol{n} = -p_\Gamma \boldsymbol{n} \quad \text{on} \quad \Gamma^{\mathrm{f}}, \end{cases} \tag{2.27}$$

$$\begin{cases} \boldsymbol{u} = \dot{\boldsymbol{d}} \quad \text{on} \quad \Sigma, \\ \rho^{\mathrm{s}} \epsilon \partial_t \dot{\boldsymbol{d}} + \boldsymbol{L}^{\mathrm{e}}_{\boldsymbol{d}}(\boldsymbol{d}, \boldsymbol{a}) + \boldsymbol{L}^{\mathrm{v}} \dot{\boldsymbol{d}} = -J \boldsymbol{\sigma}(\boldsymbol{u}, p)(\boldsymbol{F})^{-\mathrm{T}} \boldsymbol{n} \quad \text{on} \quad \Sigma, \\ \boldsymbol{L}^{\mathrm{e}}_{\boldsymbol{a}}(\boldsymbol{d}, \boldsymbol{a}) = \boldsymbol{0} \quad \text{on} \quad \Sigma, \\ \dot{\boldsymbol{d}} = \partial_t \boldsymbol{d}, \quad \text{on} \quad \Sigma, \\ \boldsymbol{d} = \boldsymbol{0}, \quad \boldsymbol{a} = \boldsymbol{n} \quad \text{on} \quad \partial\Sigma, \end{cases} \tag{2.28}$$

hold for all $t > 0$. The surface differential operators $\boldsymbol{L}^{\mathrm{e}}_{\boldsymbol{d}}$ and $\boldsymbol{L}^{\mathrm{e}}_{\boldsymbol{a}}$ describe the (possibly non-linear) elastic behavior of the shell, with $\boldsymbol{L}^{\mathrm{e}}_{\boldsymbol{a}} = \boldsymbol{0}$ representing, in particular, the equilibrium of bending moments and shear stresses. The viscous behavior is described by the term $\boldsymbol{L}^{\mathrm{v}} \dot{\boldsymbol{d}}$.

REMARK 2.10 *A simple expression for the viscous operator $\boldsymbol{L}^{\mathrm{v}}$ is given by the generalized Rayleigh relation:*

$$\boldsymbol{L}^{\mathrm{v}} \dot{\boldsymbol{d}} = \alpha \rho^{\mathrm{s}} \epsilon \dot{\boldsymbol{d}} + \beta \partial_{\boldsymbol{d}} \boldsymbol{L}^{\mathrm{e}}_{\boldsymbol{d}}(\boldsymbol{0}, \boldsymbol{0}) \dot{\boldsymbol{d}}. \tag{2.31}$$

Here, $\alpha, \beta > 0$ are given parameters and $\partial_{\boldsymbol{d}} \boldsymbol{L}^{\mathrm{e}}(\boldsymbol{0}, \boldsymbol{0})$ denotes the Fréchet derivative *of $\boldsymbol{L}^{\mathrm{e}}_{\boldsymbol{d}}$ at $(\boldsymbol{0}, \boldsymbol{0})$. The above expressions are considered in the numerical experiments of Section 2.4. It should be noted, however, that the numerical methods proposed in this paper do not depend on a specific structure of the thin-walled solid operator and, hence, more realistic viscoelastic models can be considered (see, e.g., [Hol00]).*

Owing to the discussion of Section 2.2.1, the proposed time semi-discrete approximations of (2.27)-(2.28) are reported in Algorithm 2.2. The fluid domain geometry update is treated explicitly in the first step while the three subsequent steps perform a fully decoupled sequential computation of $\boldsymbol{u}^n$, p^n and $(\boldsymbol{d}^n, \boldsymbol{a}^n)$.

REMARK 2.11 *The adoption of an explicit treatment of the geometric compatibility condition $(2.27)_1$ (substep 1 of Algorithm (2.2)) significantly reduces*

Algorithm 2.2 Fully decoupled schemes for (2.27)-(2.28).

For $n > s + r$:

1. Fluid domain update:

$$\boldsymbol{d}^{\mathrm{f},n} = \mathrm{Ext}(\boldsymbol{d}^{n-1}|_{\Sigma}), \quad \dot{\boldsymbol{d}}^{\mathrm{f},n} = \partial_\tau \boldsymbol{d}^{\mathrm{f},n}, \quad \boldsymbol{\mathcal{A}}^n = \boldsymbol{I}_{\Omega^{\mathrm{f}}} + \boldsymbol{d}^{\mathrm{f},n}, \quad \Omega^{\mathrm{f},n} = \boldsymbol{\mathcal{A}}^n\big(\Omega^{\mathrm{f}}\big)$$

and then set $\boldsymbol{F}^n = \boldsymbol{\nabla}\boldsymbol{\mathcal{A}}^n$, $J^n = \det \boldsymbol{F}^n$.

2. Fluid viscous substep: find $\tilde{\boldsymbol{u}}^n : \Omega^{\mathrm{f}} \to \mathbb{R}^3$ such that

$$\begin{cases} \rho^{\mathrm{f}} \dfrac{\tilde{\boldsymbol{u}}^n - \boldsymbol{u}^{n-1}}{\tau}\Big|_{\boldsymbol{\mathcal{A}}} + \rho^{\mathrm{f}}\big(\tilde{\boldsymbol{u}}^{n-1} - \dot{\boldsymbol{d}}^{\mathrm{f},n}\big) \cdot \boldsymbol{\nabla}\tilde{\boldsymbol{u}}^n - \mathbf{div}\boldsymbol{\sigma}(\tilde{\boldsymbol{u}}^n, p^{n,\bullet}) = \boldsymbol{0} & \text{in} \quad \Omega^{\mathrm{f},n}, \\ \boldsymbol{\sigma}(\tilde{\boldsymbol{u}}^n, p^{n,\bullet})\boldsymbol{n} = \boldsymbol{0} & \text{on} \quad \Gamma^{\mathrm{f}}, \\ J^n\boldsymbol{\sigma}(\tilde{\boldsymbol{u}}^n, p^{n,\bullet})(\boldsymbol{F}^n)^{-\mathrm{T}}\boldsymbol{n} + \dfrac{\rho^{\mathrm{s}}\epsilon}{\tau}\tilde{\boldsymbol{u}}^n = \dfrac{\rho^{\mathrm{s}}\epsilon}{\tau}\big(\dot{\boldsymbol{d}}^{n-1} + \tau\partial_\tau \dot{\boldsymbol{d}}^{n,\star}_{\|}\big) & \\ \qquad + 2\mu\big(J\boldsymbol{\varepsilon}(\tilde{\boldsymbol{u}})\boldsymbol{F}^{-\mathrm{T}}\boldsymbol{n}\big)^{n,\star}_{\|} & \text{on} \quad \Sigma. \end{cases} \tag{2.29}$$

3. Fluid projection substep: find $\phi^n : \Omega^{\mathrm{f}} \to \mathbb{R}$ such that

$$\begin{cases} -\dfrac{\tau}{\rho^{\mathrm{f}}}\Delta\phi^n = -\mathrm{div}\tilde{\boldsymbol{u}}^n & \text{in} \quad \Omega^{\mathrm{f},n}, \\ \phi^n = p_\Gamma(t_n) - p^{n,\bullet} & \text{on} \quad \Gamma^{\mathrm{f}}, \\ \dfrac{\tau}{\rho^{\mathrm{f}}}\dfrac{\partial\phi^n}{\partial\boldsymbol{n}} + \dfrac{\tau}{\rho^{\mathrm{s}}\epsilon}\phi^n = \dfrac{\tau}{\rho^{\mathrm{s}}\epsilon}\phi^{n,\star} + \big(\tilde{\boldsymbol{u}}^{n,\star} - \dot{\boldsymbol{d}}^{n,\star}\big)\cdot\boldsymbol{n} & \text{on} \quad \Sigma. \end{cases} \tag{2.30}$$

Thereafter set $p^n = \phi^n + p^{n,\bullet}$, $\boldsymbol{u}^n = \tilde{\boldsymbol{u}}^n - \frac{\tau}{\rho^{\mathrm{f}}}\boldsymbol{\nabla}\phi^n$ in Ω^{f}.

4. Solid substep: find $\boldsymbol{d}^n : \Sigma \to \mathbb{R}^3$, $\dot{\boldsymbol{d}}^n : \Sigma \to \mathbb{R}^3$ and $\boldsymbol{a}^n : \Sigma \to \mathbb{R}^3$ with $|\boldsymbol{a}^n| = 1$, such that

$$\begin{cases} \rho^{\mathrm{s}}\epsilon\partial_\tau\dot{\boldsymbol{d}}^n + \boldsymbol{L}^{\mathrm{e}}_{\boldsymbol{d}}(\boldsymbol{d}^n, \boldsymbol{a}^n) + \boldsymbol{L}^{\mathrm{v}}\dot{\boldsymbol{d}}^n = -J^n\boldsymbol{\sigma}(\tilde{\boldsymbol{u}}^n, p^n)(\boldsymbol{F}^n)^{-\mathrm{T}}\boldsymbol{n} & \text{on} \quad \Sigma, \\ \boldsymbol{L}^{\mathrm{e}}_{\boldsymbol{a}}(\boldsymbol{d}^n, \boldsymbol{a}^n) = \boldsymbol{0} & \text{on} \quad \Sigma, \\ \dot{\boldsymbol{d}}^n = \partial_\tau \boldsymbol{d}^n & \text{on} \quad \Sigma, \\ \boldsymbol{d}^n = \boldsymbol{0}, \quad \boldsymbol{a}^n = \boldsymbol{n} & \text{on} \quad \partial\Sigma. \end{cases}$$

computational complexity without compromising stability and accuracy (see, e.g., [SS06, FGG07, BNV08, SM08, NPV13]).

2.4 Numerical experiments

In this section we investigate the performance of the proposed fully decoupled schemes in several numerical examples. Section 2.4.1 focuses on the linear model

problem (2.1)-(2.2) with a simple two-dimensional geometry. The nonlinear problem (2.27)-(2.28) and more complex geometries are considered in Sections 2.4.2-2.4.5.

The numerical tests of Section 2.4.1 are carried out using a computer implementation of Algorithm 2.1 based on FreeFem++ (see [Hec12]). The results of Sections 2.4.2-2.4.5 are obtained with a parallel implementation of Algorithm 2.2. A *master/slave paradigm* is used in which the master controls the data exchanges across the interface and the slaves are the fluid and structure parallel solvers. Different parallel approaches are used for the solid and the fluid. The parallel structural solver uses the *Newton method* at each time-step. The resulting linear systems are solved with a *balancing domain decomposition method* (see, e.g., [Man93, LTV96, LT94a]). The key point in this algorithm is the construction of the coarse space which, for robustness, is based on the stiffness matrix. The fluid solver FELiScE (see [Fel]), based on PETSc (see [BAA+14a, BAA+14b, BGMS97]), uses an *additive Schwarz method* (see, e.g., [SBG96]) with *local ILU prenconditionners*. We will use the acronym "fds" (fully decoupled scheme) to refer to Algorithms 2.1 and 2.2 in the labels of the figures.

REMARK 2.12 *It should be noted that the worst-case scenario is considered for the numerical solution of steps 2 and 3 in Algorithm 2.2, in the sense that no dedicated preconditioners are used for each of them. The computational cost reductions reported in Sections 2.4.2-2.4.5 below can hence be improved by considering more efficient solvers for the projection schemes in the fluid.*

2.4.1 Convergence study in a two-dimensional test-case

The first example simulates the propagation of a pressure-wave within an elastic straight tube in two-dimensions. The test was originally proposed in [FGNQ02] and it has now become a standard benchmark for testing fluid-structure interaction techniques for blood flow simulation (see, e.g., [GGCC09, Fer13]). Basically, we couple the Stokes system (2.1) with the generalized string model introduced in Section 1.2.2.2, i.e., in (2.2) we take

$$\boldsymbol{d} = \begin{pmatrix} 0 \\ \eta \end{pmatrix}, \quad \boldsymbol{\theta} = \boldsymbol{0}, \quad \boldsymbol{L}^{\mathrm{e}}_{\boldsymbol{\theta}}(\boldsymbol{d}, \boldsymbol{\theta}) = \boldsymbol{0}, \quad \boldsymbol{L}^{\mathrm{v}}_{\boldsymbol{\theta}}(\dot{\boldsymbol{d}}, \dot{\boldsymbol{\theta}}) = \boldsymbol{0},$$

$$\boldsymbol{L}^{\mathrm{e}}_{\boldsymbol{d}}(\boldsymbol{d}, \boldsymbol{\theta}) = \begin{pmatrix} 0 \\ -\lambda_1 \partial_{xx}\eta + \lambda_0 \eta \end{pmatrix}, \quad \boldsymbol{L}^{\mathrm{v}}_{\boldsymbol{d}}(\dot{\boldsymbol{d}}, \dot{\boldsymbol{\theta}}) = \begin{pmatrix} 0 \\ \alpha\rho^{\mathrm{s}}\epsilon\dot{\eta} - \beta\lambda_1\partial_{xx}\dot{\eta} \end{pmatrix}.$$

Recall that $\lambda_1 \overset{\text{def}}{=} \frac{E\epsilon}{2(1+\nu)}$ and $\lambda_0 \overset{\text{def}}{=} \frac{E\epsilon}{R^2(1-\nu^2)}$, where R is the radius of the tube an E, ν denote, respectively, the Young modulus and the Poisson ratio of the solid. Note that, in this simplified setting, the tangential contributions involved in $(2.11)_3$ (or $(2.7)_1$) vanish (see also [FL13]).

For the fluid we take $\rho^{\mathrm{f}} = 1.0$ and $\mu = 0.035$, and for the solid $\rho^{\mathrm{s}} = 1.1$, $\epsilon = 0.1$, $E = 0.75 \cdot 10^6$, $\nu = 0.5$, $\alpha = 1$ and $\beta = 10^{-3}$. All units are expressed in the CGS system. The fluid domain is given by $\Omega^{\mathrm{f}} = [0, L] \times [0, R]$ and the fluid-solid interface

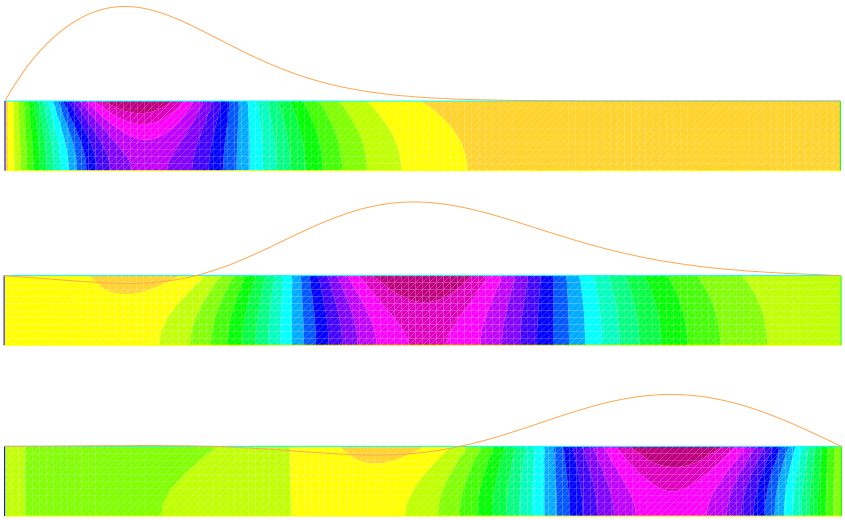

Figure 2.4: Snapshots of the fluid pressure and (exaggerated) solid displacement at time instants $t = 0.005$, 0.01, 0.015 (from top to bottom). Algorithm 2.1 with $s = 0$, $r = 1$, $\tau = 10^{-4}$ and $h = 0.05$.

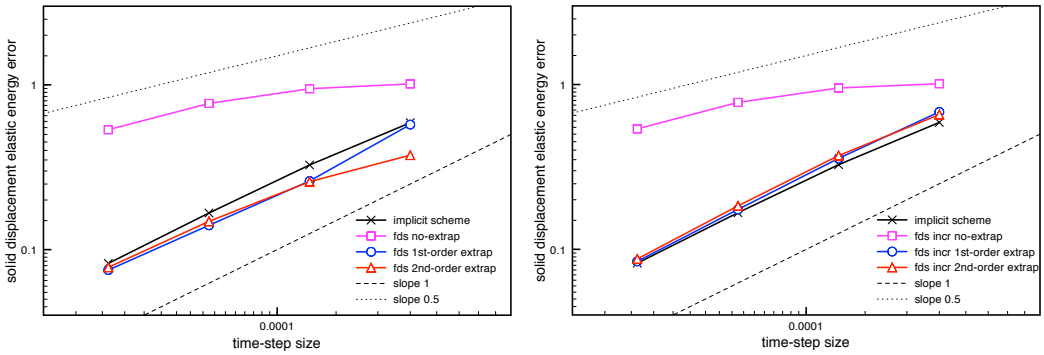

(a) $s = 0$. (b) $s = 1$.

Figure 2.5: Time-convergence history of the displacement at $t = 0.015$, with $h = \mathcal{O}(\tau)$, using the the non-incremental (a) and incremental (b) pressure-correction variants in Algorithm 2.1, and the implicit-scheme.

by $\Sigma = [0, L] \times \{R\}$, with $L = 6$ and $R = 0.5$. At $t = 0$, the whole system is at rest. A sinusoidal pressure-wave (with maximum $2 \cdot 10^4$) is prescribed on the inlet boundary $x = 0$ during $5 \cdot 10^{-3}$ time instants. Zero pressure is imposed at $x = L$ and a slip condition is enforced on the lower boundary $y = 0$. For the solid we set $\eta = 0$ at $x = 0, L$. The spatial discretization of the fluid and of the structure is based on piece-wise affine continuous finite elements. In the case $s = 1$, the Brezzi-Pitkäranta pressure stabilization (1.46) is added to step (2.12) of Algorithm 2.1.

Figure 2.4 presents the snapshots of the pressure field and the solid displacement (amplified by a factor 5) at the time instants $t = 0.005$, 0.01 and 0.015, obtained

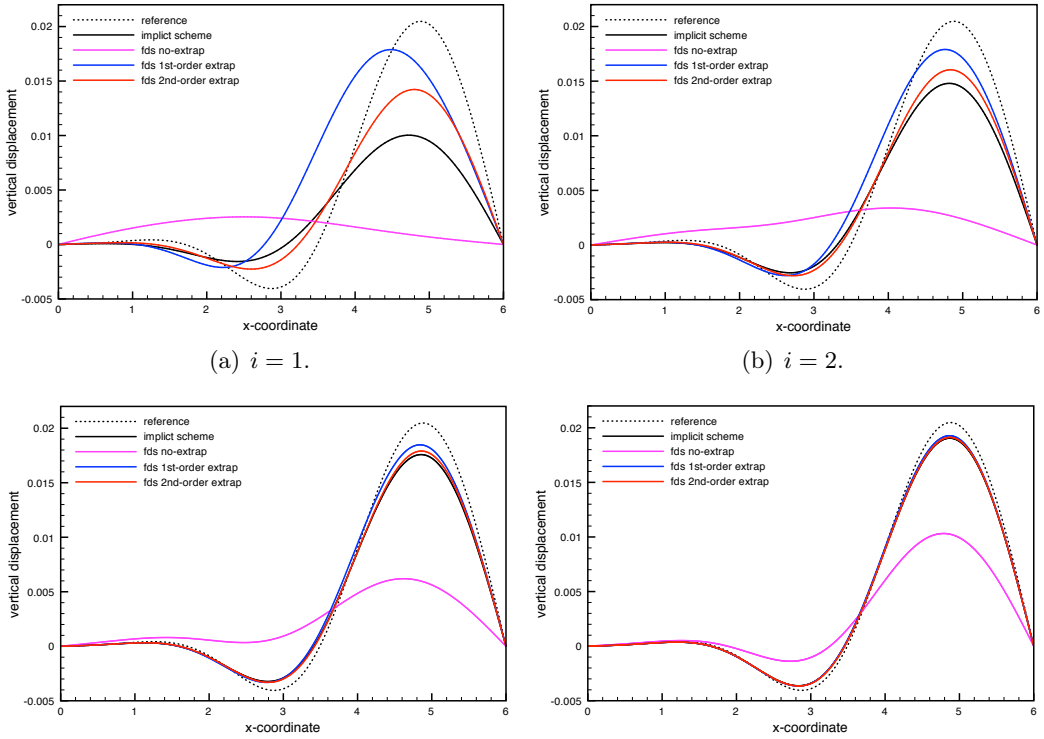

(a) $i = 1$. (b) $i = 2$.

(c) $i = 3$. (d) $i = 4$.

Figure 2.6: Comparison of the solid displacements at $t = 0.015$ for different levels of (τ, h)-refinement, given by (2.32), using Algorithm 2.1 with $s = 0$ and the implicit-scheme.

from Algorithm 2.1 with $s = 0$, $r = 1$, $\tau = 10^{-4}$ and $h = 0.05$. The scheme is able to reproduce a stable pressure-wave propagation. Similar results, not reported here, are obtained with $s = 1$.

In order to assess the overall convergence rate of Algorithm 2.1, we have uniformly refined in time and in space under a hyperbolic-CFL condition ($\tau = \mathcal{O}(h)$):

$$(\tau, h) = \{5 \cdot 10^{-4}/2^i, 10^{-1}/2^i\}_{i=1}^{4}. \tag{2.32}$$

Figure 2.5 shows the relative elastic energy-norm error of the solid displacement, at time $t = 0.015$, obtained with all the different variants of Algorithm 2.1. For comparison purposes, the errors obtained with a fully implicit first-order scheme involving a monolithic time-stepping in the fluid (Algorithm 1.1 with damping effects in the solid) are also displayed. The reference solution has been computed with the implicit scheme and high space-time resolution: $h = 3.125 \cdot 10^{-3}$ and $\tau = 10^{-6}$. The results of Figure 2.5 indicate that the proposed fully decoupled schemes with $r = 1$ or $r = 2$ are able to retrieve the optimal first-order convergence rate $\mathcal{O}(\tau)$ of the implicit scheme, irrespectively of the choice $s = 0$ or $s = 1$ in the fluid time-stepping. Conversely, a sub-optimal overall rate $\mathcal{O}(\tau^{\frac{1}{2}})$ is observed for $r = 0$. We

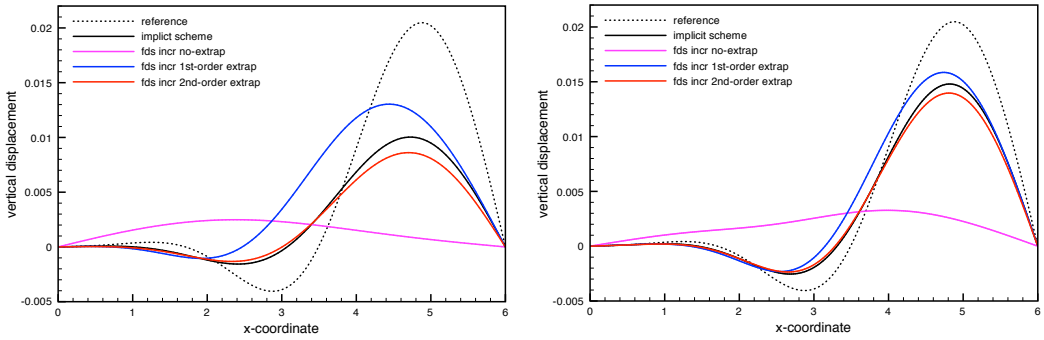

(a) $i = 1$. (b) $i = 2$.

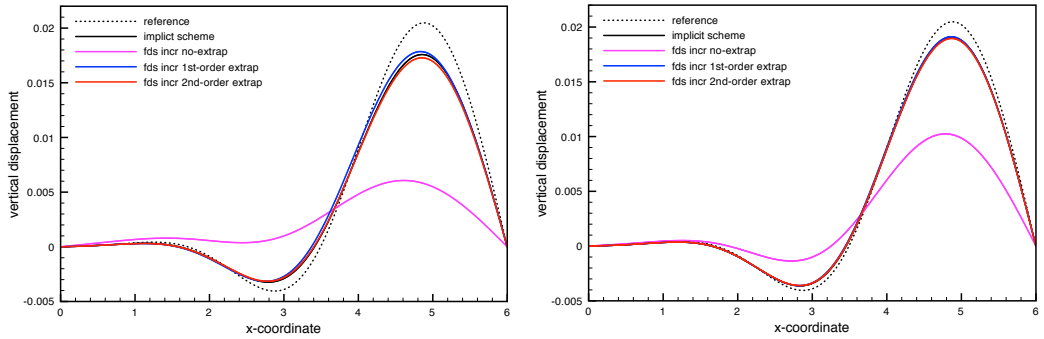

(c) $i = 3$. (d) $i = 4$.

Figure 2.7: Comparison of the solid displacements at $t = 0.015$ for different levels of (τ, h)-refinement, given by (2.32), using Algorithm 2.1 with $s = 1$ and the implicit-scheme.

can also notice that the type of projection scheme in the fluid (i.e., $s = 0, 1$) has a limited impact on the overall accuracy of Algorithm 2.1, which is mainly driven by the choices of r (see Remark 2.7). Further numerical evidence on these observations is given in Figures 2.6 and 2.7, which show the displacements at $t = 0.015$ obtained with the implicit scheme and all the variants of Algorithm 2.1, for different levels of space-time refinement.

A similar behavior in terms of r was observed in [FMV13] with the original explicit Robin-Neumann schemes, hence indicating that the fully decoupled schemes proposed in the present work preserve their accuracy properties.

Remark 2.13 *For the sake of conciseness, and owing to the above discussion, only the results obtained from Algorithm 2.2 with $s = 0$ will be reported in the next sections. This will not be the case in Chapter 4, where we will consider the fully decoupled coupling paradigm with $s = 1$.*

2.4.2 Pressure wave propagation in a straight tube

The second numerical test is basically a three-dimensional non-linear version of the previous example (see also, e.g., [FQV09]). The physical system is described

by the non-linear coupled problem (2.27)-(2.28). Note that the shell model (2.28) intrinsically involves, for its derivation, a Saint Venant-Kirchhoff constitutive relation.

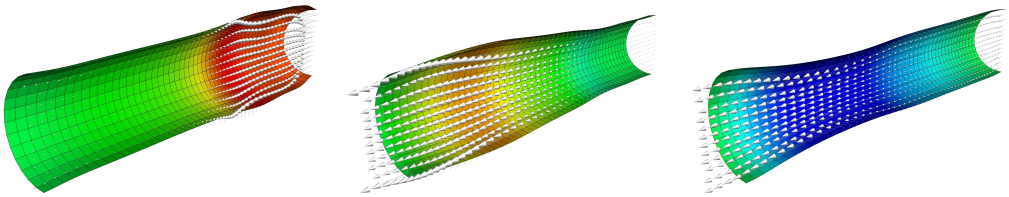

Figure 2.8: Snapshots of the velocity field and fluid interface pressure at $t = 0.005, 0.01, 0.015$ (from left to right). Algorithm 2.2 with $s = 0$, $r = 1$, $\tau = 10^{-4}$ and $h \approx 0.1$.

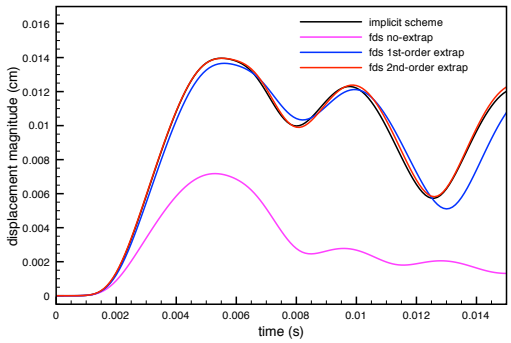

(a) $\tau = 10^{-4}$, $h \approx 0.1$.

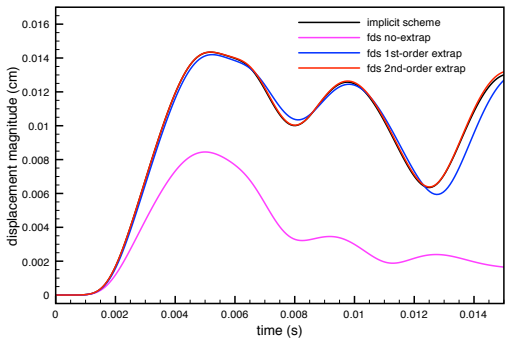

(b) $\tau = 7.5 \cdot 10^{-5}$, $h \approx 0.07$.

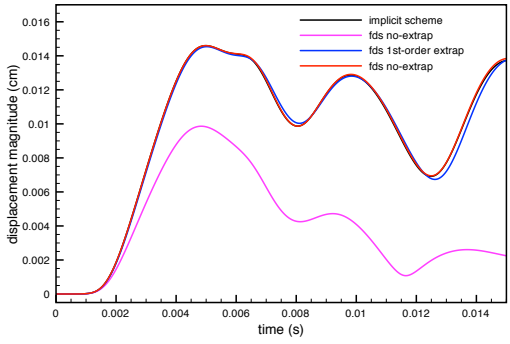

(c) $\tau = 5 \cdot 10^{-5}$, $h \approx 0.05$.

Figure 2.9: Comparison of the solid displacements at $t = 0.015$ for different levels of space-time refinement. Algorithm 2.2 with $s = 0$ and the implicit coupling scheme.

The fluid domain is a cylinder of radius $R = 0.5$ and length $L = 5$. All the units are expressed in the CGS system. The physical parameters of the fluid are $\rho^{\mathrm{f}} = 1.0$ and $\mu = 0.035$. For the structure we take $\rho^{\mathrm{s}} = 1.2$, $\epsilon = 0.1$, $E = 3 \cdot 10^6$ and $\nu = 0.5$. Damping effects in the solid are neglected in this case. A constant pressure of $1.3332 \cdot 10^4$ is imposed on the inlet boundary during $5 \cdot 10^{-3}$ time instants,

thereafter this values is set to zero. An homogeneous natural boundary condition is prescribed on the outlet boundary. The whole fluid-solid system is initially at rest. Both the velocity and the pressure are discretized in space using $\mathbb{Q}_1$ finite elements. A *streamline-upwind/Petrov-Galerkin* (SUPG) stabilization is applied to the viscous substep (2.29) of Algorithm 2.2. The shell equation is discretized in space by *quadrilateral MITC4 elements* (see [CB11, Section 8.2.1]).

We first consider Algorithm 2.2 with $s = 0$, $r = 1$, $\tau = 10^{-4}$ and $h \approx 0.1$. Figure 2.8 shows the fluid velocity field and the solid deformation (amplified by a factor 10) retrieved at the time instants $t = 0.005$, 0.01 and 0.015. A stable propagating pressure-wave is obtained.

We now turn the discussion back to the accuracy of the methods. For this purpose, we have reported in Figure 2.9 the time history of the midpoint displacements obtained from Algorithm 2.2 with $s = 0$ and a fully implicit first-order scheme for different levels of space-time refinement, namely: $\tau = 10^{-4}$, $h \approx 0.1$; $\tau = 7.5 \cdot 10^{-5}$, $h \approx 0.07$; and $\tau = 5 \cdot 10^{-5}$, $h \approx 0.05$. The convergent behavior of the two extrapolated explicit variants (i.e., $r = 1$ and $r = 2$) towards the implicit coupling solution is clearly noticeable. On the contrary, the scheme with $r = 0$ delivers a much slower convergent behavior. This confirms the convergence rates observed in Section 2.4.1.

	Algorithm 2.2	Implicit scheme
$\tau = 10^{-4}$, $h \approx 0.1$	1	10.5
$\tau = 7.5 \cdot 10^{-5}$, $h \approx 0.07$	3.8	31.1
$\tau = 5 \cdot 10^{-5}$, $h \approx 0.05$	12.4	80.6

Table 2.1: Elapsed CPU-time (dimensionless) for different space-time refinements.

In Table 2.1 we have reported the elapsed CPU-times (dimensionless) obtained with Algorithm 2.2 ($s = 0$, $r = 1$) and the implicit scheme. For the latter, the resulting coupled non-linear system at each time-step is solved in a partitioned fashion using a *Robin-Neumann iterative procedure* (see [BNV08, FMV13]). We can observe that, for a similar level of accuracy, Algorithm 2.2 ($s = 0$, $r = 1$) is about 8 times faster than the implicit solver in this case.

2.4.3 Damped structural instability with a fully enclosed fluid

We consider the example proposed in [KFW06] where an incompressible fluid is confined within two curved thin-walled structures of different stiffness. The physical system is described by the non-linear coupled problem (2.27)-(2.28). A Saint Venant-Kirchhoff constitutive relation for the (undamped) shell is assumed. We take $\rho^{\mathrm{f}} = 1.0$ and $\mu = 9$ in the fluid problem and $\rho^{\mathrm{s}} = 500$, $\epsilon = 0.1$, $E_{\mathrm{top}} = 9 \cdot 10^5$, $E_{\mathrm{bottom}} = 9 \cdot 10^8$ and $\nu = 0.3$. in the solid (the subscript notation indicates the bottom and top structures). The units are expressed in the SI system. On the left and right inflow boundaries, constant parabolic velocity profiles with maximal magnitudes 10 and 10.1 are, respectively, imposed. Homogeneous Dirichlet conditions are enforced on the remaining fluid boundaries. A vertical force of unitary magnitude loads

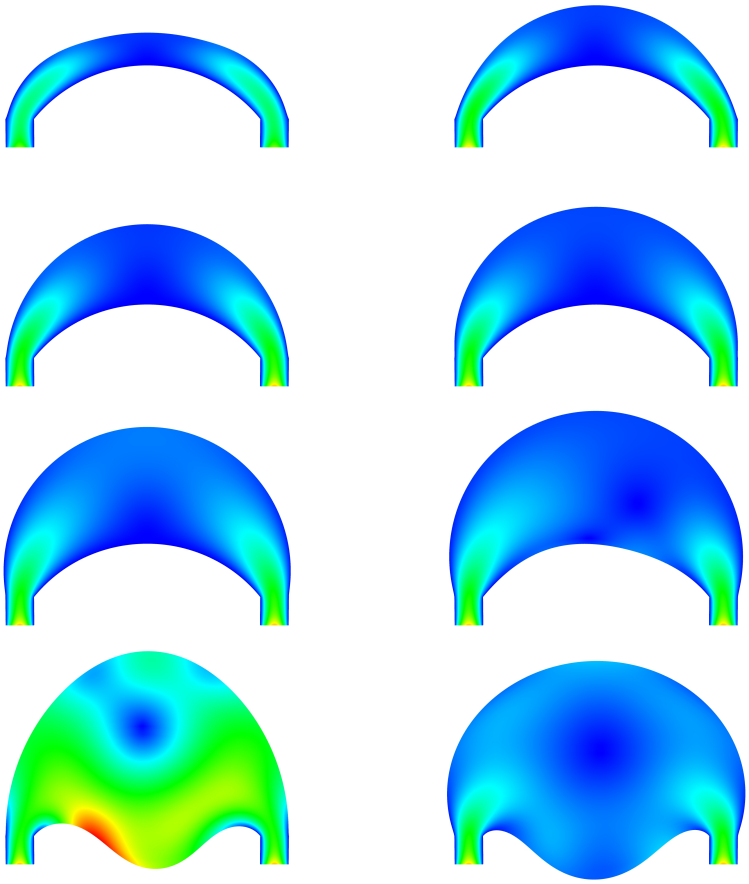

Figure 2.10: Snapshots of the fluid velocity at the time instants $t = 0.5, 1, 1.5, 2, 2.5, 3, 3.5, 4$ (from left to right and top to bottom). Algorithm 2.2 with $s = 0$, $r = 1$, $\tau = 0.005$ and $h \approx 0.07$.

downwards the fluid. We consider Algorithm 2.2 with the same spatial discretization as in the previous example. The simulations are carried out in three-dimensions by prescribing symmetry conditions on the extruded boundaries.

Figure 2.10 reports the fluid velocity magnitude at the time instants $t = 0.5$, 1, 1.5, 2, 2.5, 3, 3.5 and 4, using Algorithm 2.2 with $s = 0$, $r = 1$, $\tau = 0.005$ and $h \approx 0.07$. We can clearly observe that the excess of fluid mass causes first the deflection of the upper (less stiff) structure. The fluid cavity continues to swell along the upper boundary until the fluid pressure reaches a critical level at which the (stiffer) lower structure is no longer able to resist and collapses. A similar behavior was observed in [KFW06], using an implicit coupling solution method based on partitioned Dirichlet-Neumann iterations and an augmented procedure, which prescribes a volume constraint on the structural system. In Algorithm 2.2, the Robin condition $(2.30)_3$ removes the indetermination of the fully enclosed fluid

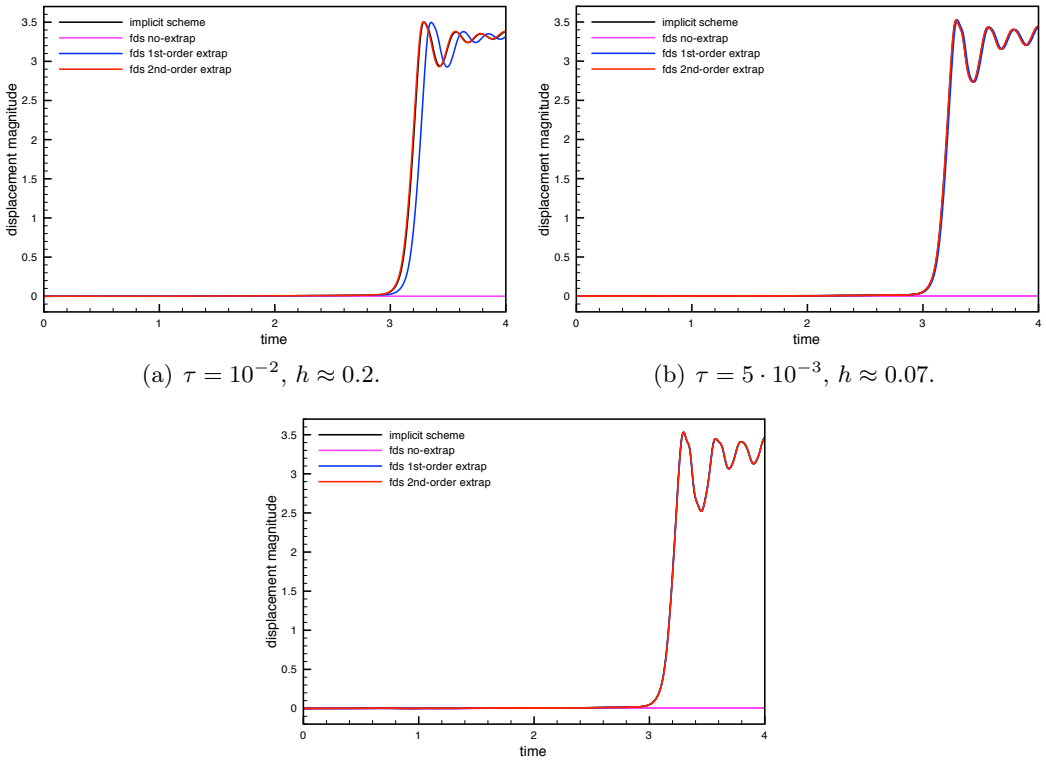

(a) $\tau = 10^{-2}$, $h \approx 0.2$.

(b) $\tau = 5 \cdot 10^{-3}$, $h \approx 0.07$.

(c) $\tau = 2.5 \cdot 10^{-3}$, $h \approx 0.04$.

Figure 2.11: Comparison of the bottom interface mid-point displacement *vs.* time for different levels of space-time refinement. Algorithm 2.2 with $s = 0$ and the implicit coupling scheme.

pressure.

For comparison purposes, we have reported in Figure 2.11 the interface mid-point displacement magnitude of the lower structure obtained with Algorithm 2.2 ($s = 0$, $r = 0, 1, 2$) and a first-order implicitly coupled scheme (including a monolithic time-stepping in the fluid), for the following values of τ and h: $\tau = 10^{-2}$, $h \approx 0.2$; $\tau = 5 \cdot 10^{-3}$, $h \approx 0.07$ and $\tau = 2.5 \cdot 10^{-3}$, $h \approx 0.04$. The lack of accuracy for the scheme with $r = 0$ is striking. Even after two space-time refinements, the unphysical excess of mass-loss across the interface impedes the buckling of the bottom structure. Conversely, the fully decoupled schemes with $r = 1$ and $r = 2$ are able to retrieve the accuracy of the implicit scheme.

	Algorithm 2.2	Implicit scheme
$\tau = 10^{-2}$, $h \approx 0.2$	1	12.5
$\tau = 5 \cdot 10^{-3}$, $h \approx 0.07$	13.5	162
$\tau = 2.5 \cdot 10^{-3}$, $h \approx 0.04$	92.5	1200

Table 2.2: Elapsed CPU-time (dimensionless)

In order to illustrate the efficiency of the proposed methods, the elapsed CPU-times, for the above degrees of space and time refinement, are provided in Table 2.2. We compare Algorithm 2.2 ($s = 0$, $r = 1$) and the implicit scheme solved, as in the previous example, with a partitioned Robin-Neumann procedure. For a similar level of accuracy (see Figure 2.11(b)), the speed-up provided by the fully decoupled scheme is around 12 times faster than the implicit solver.

2.4.4 Blood flow in an abdominal aortic aneurysm

In this example we simulate the blood flow within an in-vitro abdominal aortic aneurysm geometry (see, e.g., [SSCL06, ACF09, FMV13]). The physical system is

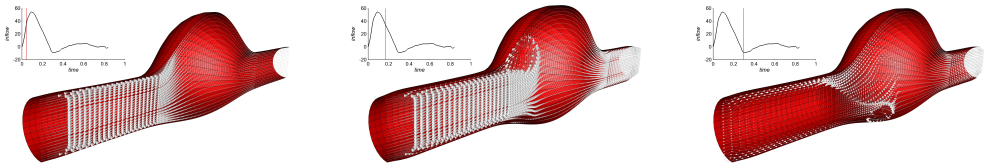

Figure 2.12: Snapshots of the fluid velocity field at the time instants $t = 0.042, 0.168, 0.294$ (from left to right). Algorithm 2.2 with $s = 0$, $r = 1$, $\tau = 4.2 \cdot 10^{-4}$ and $h \approx 0.2$.

here described by the coupled problem (2.27)-(2.28), with a Saint Venant-Kirchhoff constitutive relation for the aneurysm wall. The fluid-solid interface has a length of 22.95 and a uniform thickness of $\epsilon = 0.17$. All units are expressed in the CGS system. We take $\rho^{\mathrm{f}} = 1.0$ and $\mu = 0.035$ in the fluid and $\rho^{\mathrm{s}} = 1.2$, $E = 3{\cdot}10^6$, $\nu = 0.5$, $\alpha_0 = 1$ and $\alpha_1 = 10^{-3}$ in the solid. The fluid and structure are initially at rest. On the inlet boundary, we impose a physiological flow rate waveform (see Figure 2.12) measured at the level of the infrarenal aorta (see [OPR+97]). A resistance boundary condition is enforced on the outlet boundary. The value of the resistance is set to $R_{\mathrm{out}} = 600$.

We consider Algorithm 2.2 with the same spatial discretization as in the previous example. The simulations are performed over a full cardiac cycle (0.84 seconds). For illustration purposes, the velocity field and the solid deformation at $t = 0.042, 0.168, 0.294$, obtained from Algorithm 2.2 with $s = 0$, $r = 1$, $\tau = 4.2{\cdot}10^{-4}$ and $h \approx 0.2$ are displayed in Figure 2.12 (half the geometry), showing a stable numerical approximation.

In Figure 2.13, the interface mid-point displacements are compared with those obtained with a first-order implicit coupling scheme, for different values of τ and h, namely: $\tau = 4.2 \cdot 10^{-4}$, $h \approx 0.2$; $\tau = 3 \cdot 10^{-4}$, $h \approx 0.15$ and $\tau = 2.1 \cdot 10^{-4}$, $h \approx 0.1$. The low accuracy of the fully decoupled scheme with $r = 0$ is, once more, striking: the numerical solution has an extremely poor accuracy, even with the finest discretization, which makes the scheme useless in practice. On the contrary, the convergent behavior of the variant with $r = 1$ is clearly visible and delivers much more reasonable results (see Figure 2.13(b)). The fully decoupled scheme with $r = 2$ gives practically the same accuracy than the implicit scheme.

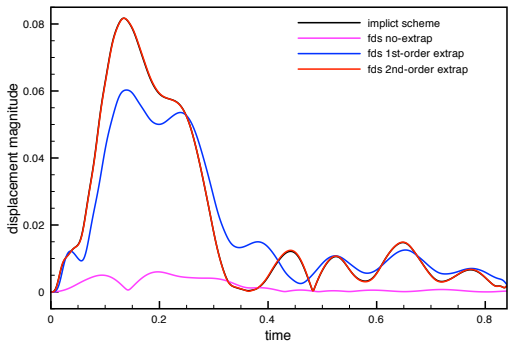

(a) $\tau = 4.2 \cdot 10^{-4}$, $h \approx 0.2$.

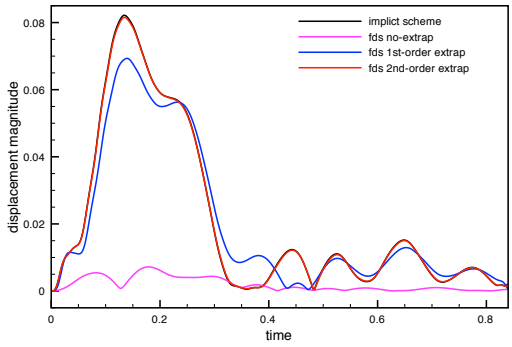

(b) $\tau = 3 \cdot 10^{-4}$, $h \approx 0.15$.

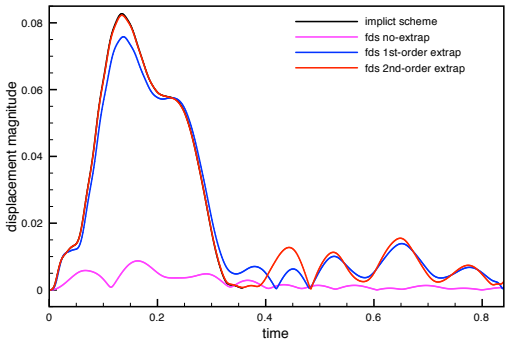

(c) $\tau = 2.1 \cdot 10^{-4}$, $h \approx 0.1$.

Figure 2.13: Comparison of the solid displacements at $t = 0.015$ for different levels of space-time refinement. Algorithm 2.2 with $s = 0$ and the implicit coupling scheme.

At last, in Table 2.3, we compare the performance of the proposed fully decoupled scheme ($s = 0$, $r = 1$) and the implicit scheme. Instead of the Robin-Neumann iterative procedure considered in the previous examples, here the implicit scheme is solved via a (parameter-free) *Dirichlet-Neumann GMRES partitioned Newton method* (see, e.g., [FM05]). The reason is that, in this case, the convergence speed of the Robin-Neumann iterations appeared to be highly sensitive to the value of the Robin coefficient and, hence, required careful tuning. As shown in Table 2.3, the savings in terms of computational effort are striking. For the finest discretizations, for which we obtain comparable levels of accuracy, the fully decoupled scheme is around 60 times faster than the implicit method.

	Algorithm 2.2	Implicit scheme
$\tau = 4.2 \cdot 10^{-4}$, $h \approx 0.2$	1	41.8
$\tau = 3 \cdot 10^{-4}$, $h \approx 0.15$	3.4	192
$\tau = 2.1 \cdot 10^{-4}$, $h \approx 0.1$	10	671.7

Table 2.3: Elapsed CPU time (dimensionless).

2.4.5 Blood flow in a patient-specific aorta

The last numerical example is devoted to the numerical simulation of blood flow within a patient-specific thoracic aorta (with a mild coarctation) under physiological rest conditions. The computational 3D geometry (see Figure 2.14) and the inlet fluid flow rate are obtained from the data provided by the 2nd CFD Challenge organized within the STACOM 2013 conference (see [STA]). In this example, the CGS system is adopted for all the physical units.

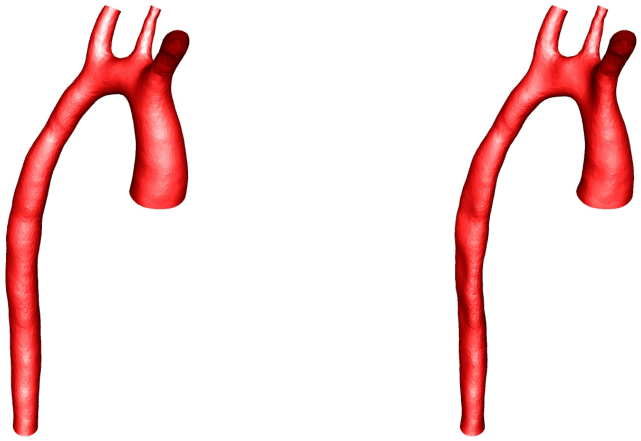

(a) Given stressed configuration. (b) Inferred stress-free configuration.

Figure 2.14: Reference configurations for the ALE map (a) and solid (b).

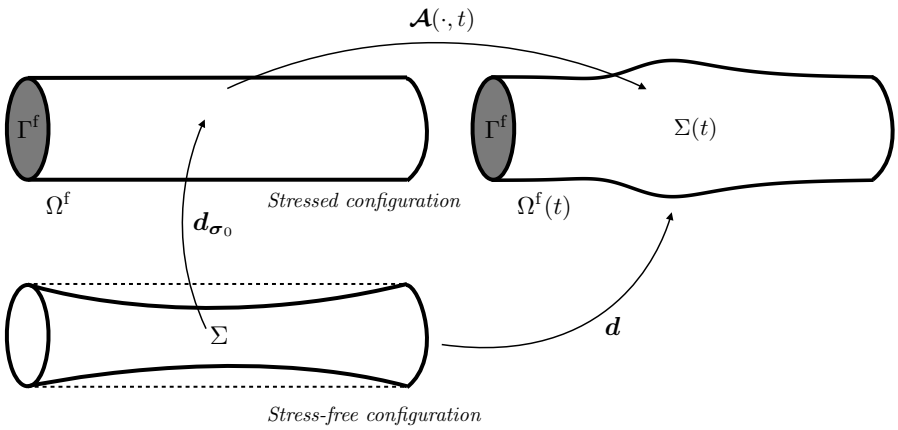

Figure 2.15: Geometrical configuration and mappings.

The mechanical interaction between blood and the aortic wall is modeled by the coupled system (2.27)-(2.28). Note that (2.28) involves a Saint Venant-Kirchhoff model as constitutive relation for the aortic wall. Furthermore, it assumes a stress-free solid reference configuration Σ. The reconstructed aorta geometry, see Figure 2.14(a), corresponds to a deformed in vivo stress condition (obtained from magnetic resonance angiography). The ambient pressure for the rest state is 67000. In

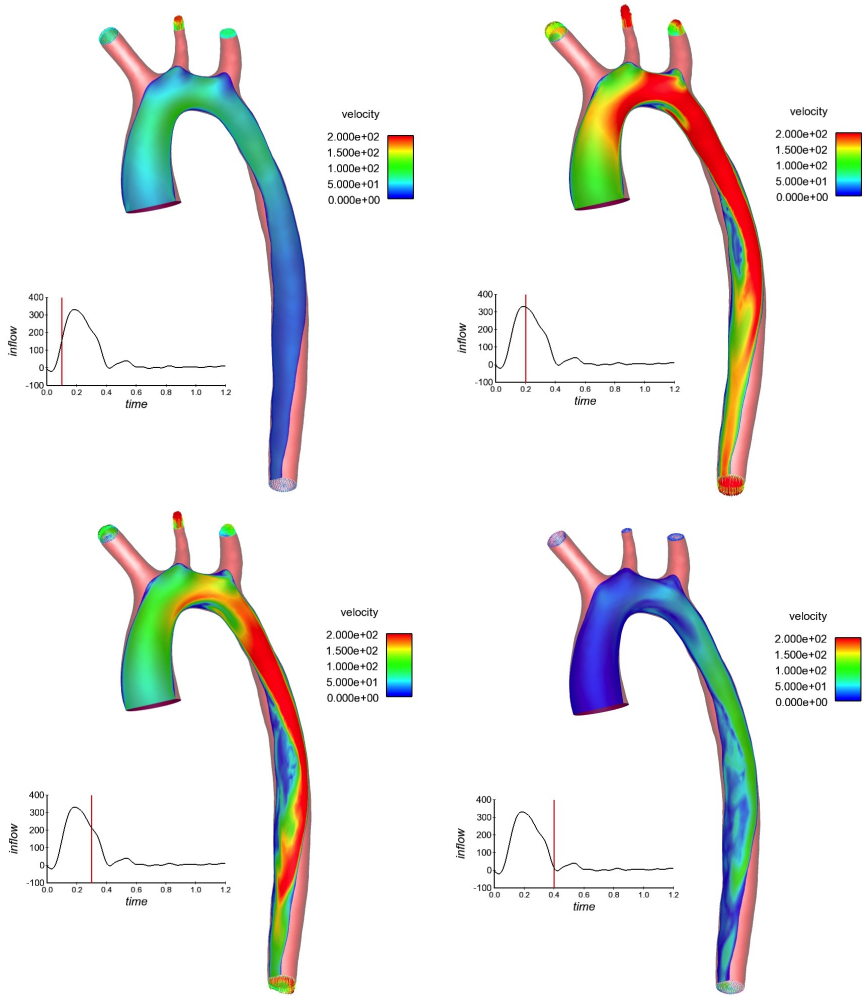

Figure 2.16: Snapshots of the fluid velocity at the time instants $t = 0.1$, 0.2, 0.3, 0.4 (from left to right and top to bottom). Algorithm 2.2 with $s = 0$ and $r = 1$.

order to perform the simulation with physiological pressure levels, a stress-free solid reference configuration Σ is inferred from the provided configuration (Figure 2.14(a)) by solving an inverse solid problem (see, e.g., [GFW10, MXA+12]), in such a way that the in vivo stressed configuration is retrieved when the rest ambient pressure conditions are prescribed on the unknown stress-free reference configuration (see Figure 2.14(b)). We refer to this reference displacement as $\boldsymbol{d}_{\boldsymbol{\sigma}_0}$. A graphical illustration of the situation is given in Figure 2.15. Note that, in this case, the set $\partial\Omega^{\mathrm{f}}\backslash\Gamma^{\mathrm{f}}$ in the ALE reference configuration, and the reference configuration Σ of the solid problem, does not coincide. In practice, the ALE mapping is obtained by extending the increment of the displacement on $\partial\Omega^{\mathrm{f}}\backslash\Gamma^{\mathrm{f}}$ defined as

$$\delta\boldsymbol{d}(x) = \boldsymbol{d} \circ \boldsymbol{d}_{\boldsymbol{\sigma}_0}^{-1}(x) - x \quad \text{on} \quad \partial\Omega^{\mathrm{f}}\backslash\Gamma^{\mathrm{f}},$$

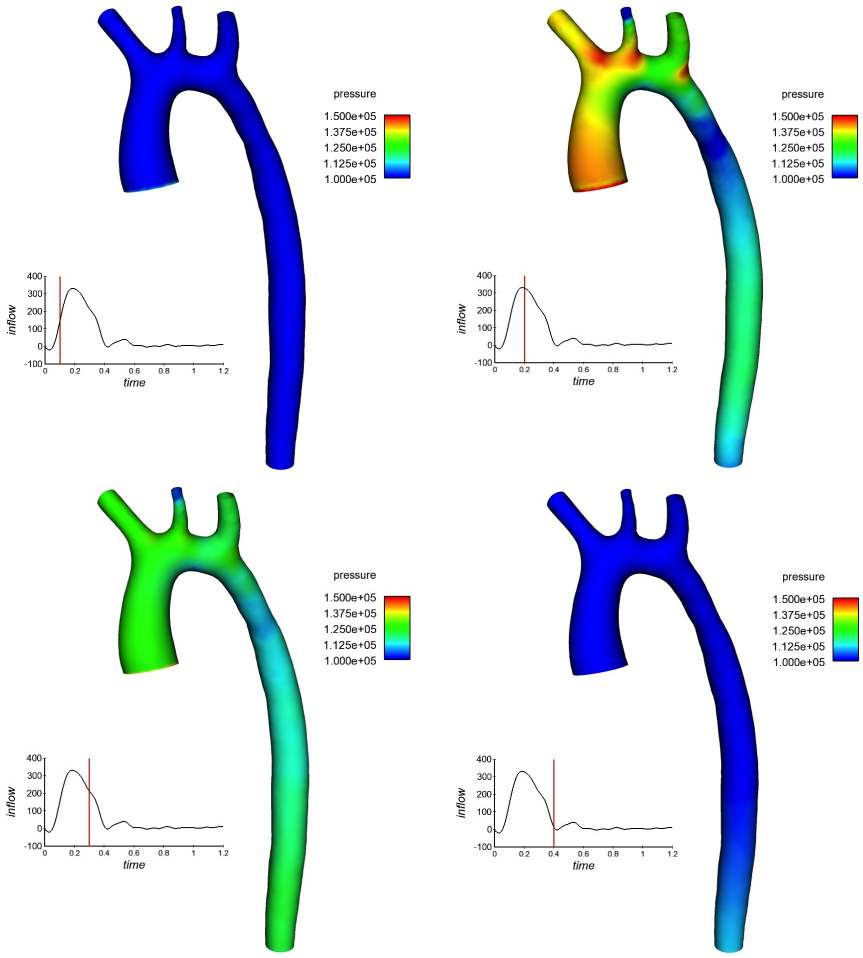

Figure 2.17: Snapshots of the fluid pressure at the time instants $t = 0.1, 0.2, 0.3, 0.4$ (from left to right and top to bottom). Algorithm 2.2 with $s = 0$ and $r = 1$.

over the reference fluid domain Ω^{f}.

The aortic wall is assumed to have uniform thickness and density of $\epsilon = 0.2$ and $\rho^{\mathrm{s}} = 1.2$, respectively, with the mechanical parameters set to $E = 3 \cdot 10^6$, $\nu = 0.5$, $\alpha_0 = 1$ and $\alpha_1 = 10^{-3}$. The blood dynamic viscosity and density are $\mu = 0.04$ and $\rho^{\mathrm{f}} = 1$. On the inlet boundary (ascending aorta), we prescribe the physiological fluid flow rate provided in [STA] for the rest condition. On the remaining outlet boundaries (innominate, left carotid, left subclavian and descending aorta), explicit *RCR Windkessel 0D-models* are used to take into account the effect of the surrounding vascular network. The Windkessel parameters are those reported in [PFGVC14]. The initial displacement of the structure equation (2.28) is set to $\boldsymbol{d}(0) = \boldsymbol{d}_{\boldsymbol{\sigma}_0}$. The remaining fluid-structure system unknowns are initialized to zero.

All the fluid steps of Algorithm 2.2 are discretized in space using affine finite elements. Triangular MITC3 elements are used for the shell problem (see [CB11, Section 8.2.1]). The adapted fluid mesh (from [PFGVC14]) is made of 375149 tetra-

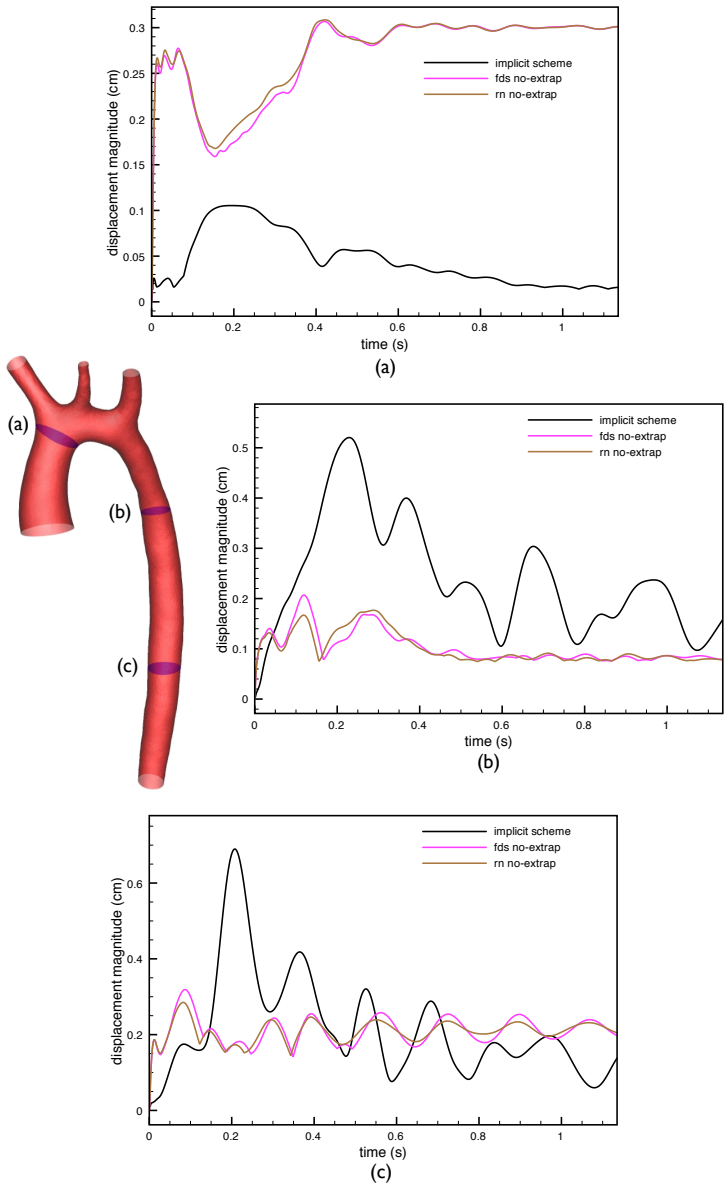

Figure 2.18: Maximum displacement magnitude at sections (a), (b) and (c) of the structure *vs.* time. Comparison of the implicit scheme, Robin-Neumann scheme (from [FMV13, Algorithm 4]) with $r = 0$, and Algorithm 2.2 with $s = r = 0$.

hedra. The resulting matching solid mesh is made of 21752 triangles. We have simulated $1.2 \cdot 10^4$ time-steps of size $\tau = 10^{-4}$, which corresponds to a full cardiac cycle. Figures 2.16 and 2.17 present, respectively, some snapshots of the fluid velocity and pressure fields obtained from Algorithm 2.2 $s = 0$ and $r = 1$ at four different time instants of a cardiac cycle. A stable numerical solution is obtained which shows physiological values in both the velocity and pressure fields. To the best of our knowledge, this is the first time that such a blood flow simulation is

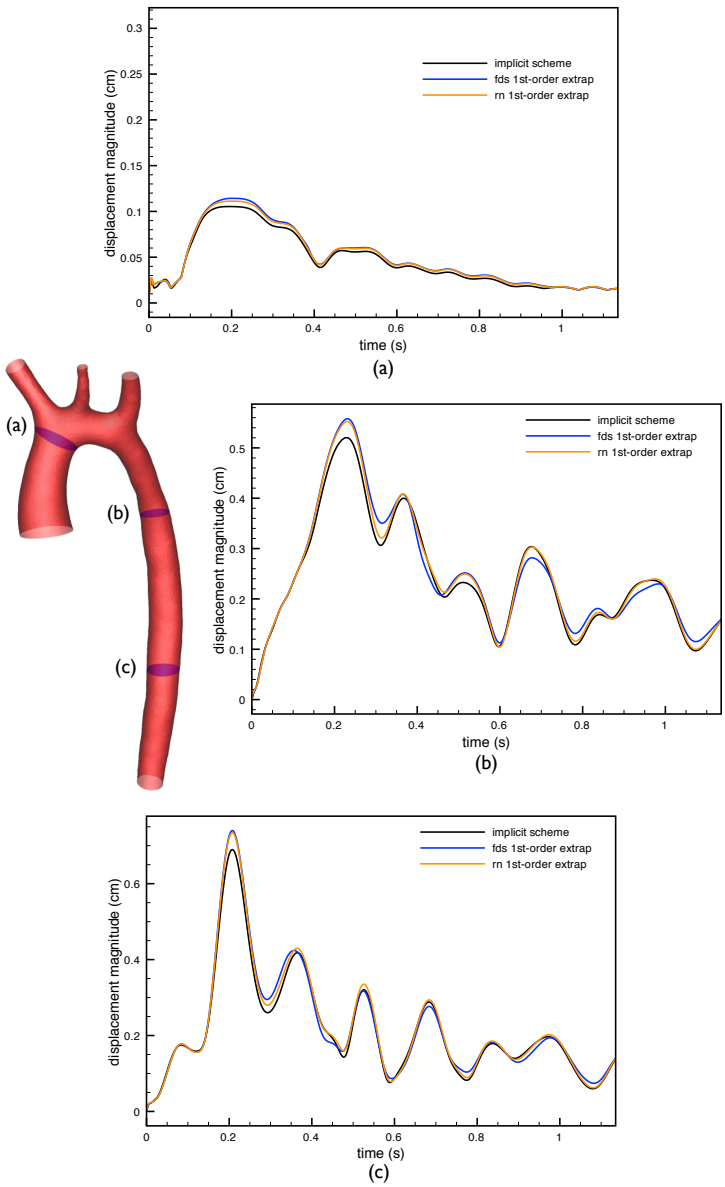

Figure 2.19: Maximum displacement magnitude at sections (a), (b) and (c) of the structure *vs.* time. Comparison of the implicit scheme, Robin-Neumann scheme (from [FMV13, Algorithm 4]) with $r = 1$, and Algorithm 2.2 with $s = 0$ and $r = 1$.

performed with an explicit coupling scheme.

Implicit scheme	Explicit Robin-Neumann schemes ([FMV13])	Algorithm 2.2
10	1.2	1

Table 2.4: Elapsed CPU time (dimensionless).

To illustrate the accuracy of the results, in Figures 2.18-2.20 we compare the

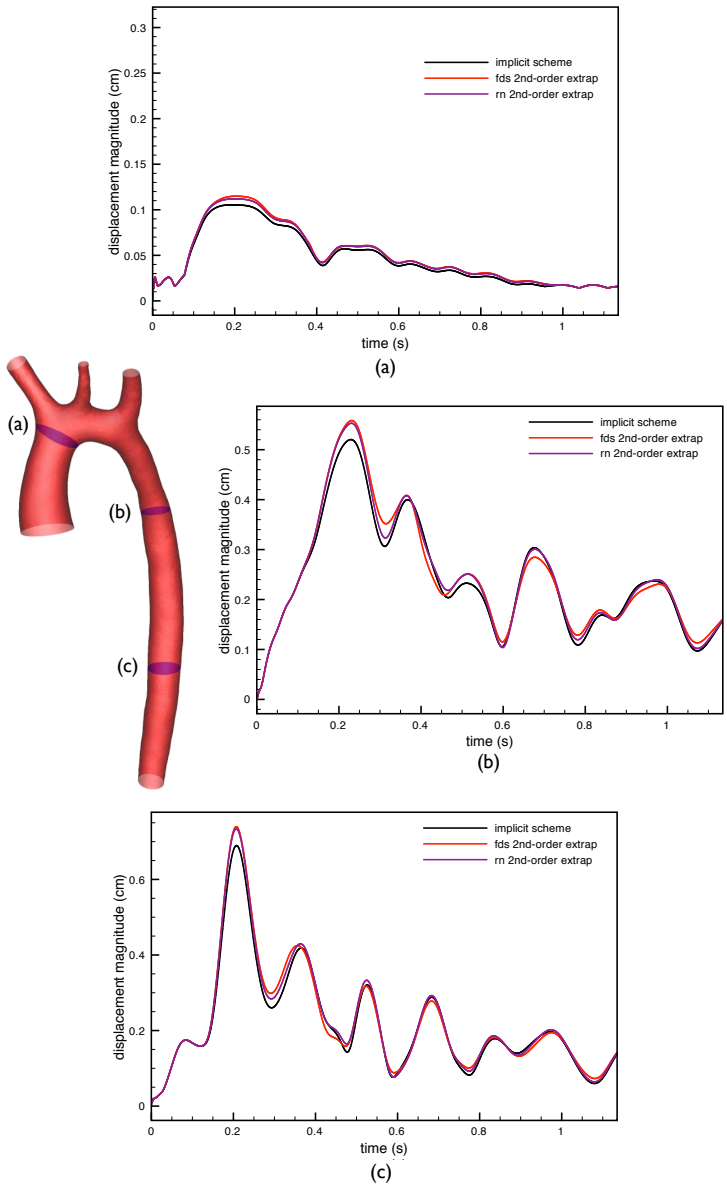

Figure 2.20: Maximum displacement magnitude at sections (a), (b) and (c) of the structure *vs.* time. Comparison of the implicit scheme, Robin-Neumann scheme (from [FMV13, Algorithm 4]) with $r = 2$, and Algorithm 2.2 with $s = 0$ and $r = 2$.

maximum magnitude of the displacement, at three different sections of the aorta, obtained with the implicit scheme, the original Robin-Neumann schemes (from [FMV13, Algorithm 4]) and Algorithm 2.2 with $s = 0$ and $r = 0, 1, 2$, respectively. For comparison purposes, the results of the implicit scheme are reported in the three figures. We retrieve basically the same accuracy behavior than in the previous examples. Figure 2.18 shows that the Robin-Neumann schemes and Algorithm 2.2 with $s = r = 0$ are unable to retrieve the overall dynamics of the implicit solution

and yield approximations with extremely poor accuracy. The variants with interface extrapolations $r = 1$ and $r = 2$, whose results are shown in Figures 2.19 and 2.20, give practically the same accuracy as the implicit scheme. The small differences between the explicit Robin-Neumann schemes and Algorithm 2.2 are due to the different time-seppting of (2.3) in the fluid: monolithic and projection method ($s = 0$), respectively. Once again, this confirms that the fully decoupled schemes reported in Algorithm 2.2 preserve the accuracy properties of the original Robin-Neumann schemes introduced in [FMV13].

The comparison of the elapsed-CPU times reported in Table 2.4, and the results of Figures 2.19 and 2.20, plead in favor of the schemes proposed in the present paper with $r = 1$ or $r = 2$.

2.5 Conclusion

In this chapter we have introduced a new class of numerical methods for fluid-structure interaction problems involving an incompressible fluid and a general thin-walled viscoelastic structure. The methods proposed allow a fully decoupled time-marching of the complete fluid-solid state: fluid velocity, fluid pressure and solid displacement. The basic ingredients of this new fluid-solid splitting paradigm are:

- projection method in the fluid;
- appropriate fractional-step time-marching of the interface Robin consistency (2.3), which yields explicit interface Robin conditions for the fluid velocity and pressure substeps. The implicit treatment of the solid inertia is enough to guarantee stability;
- fluid stresses are transferred to the thin-walled structure in a standard fashion.

Unconditional stability has been proved for some of the variants ($s = 0$ and $r = 0, 1$; $s = 1$ and $r = 0$) in a representative liner setting involving a general linear viscoelastic shell model (Theorem 2.1). Though not covered by the stability analysis, numerical evidence has shown that the remaining schemes are stable for a reasonable range of the physical and discretization parameters. The numerical study indicates also that the non-incremental ($s = 0$) or incremental ($s = 1$) nature of the projection scheme in the fluid has a limited impact on the overall accuracy of the methods, which is mainly driven by the consistency of the fluid-solid splitting (determined by the extrapolation order $r = 0, 1, 2$). The best accuracy and robustness are obtained with $r = 1, 2$, which retrieve the (optimal) first-order accuracy of the implicit scheme. In particular, the results of Section 2.4.5 demonstrate, for the first time, that physiological blood flow simulations can be effectively performed with an explicit coupling paradigm.

Chapter 3

Second-order time-accurate coupling schemes for incompressible fluid/thin-walled structure interaction

In this chapter we investigate how the explicit Robin-Neumann coupling paradigm of Section 1.4.3.5 can be extended to deliver second-order time-accuracy. In particular, we show that this coupling procedure tolerates, in terms of stability, second-order time-stepping in both the fluid and solid subproblems (viz., via Crank-Nicholson time-stepping). The rationale of these fundamental stability properties is provided within a simplified setting. Numerical experiments in a benchmark confirm those results and show that, for some of the variants considered, the optimal second-order time-accuracy is retrieved.

Some of the results of this chapter have been reported in:

- M. A. Fernández, M. Landajuela, J. Mullaert, M. Vidrascu, **Robin-Neumann schemes for incompressible fluid-structure interaction**. *In Domain Decomposition Methods in Science and Engineering XXII, Lecture Notes in Computer Science (LNCS), Lugano, Switzerland, 2015,* https://hal.inria.fr/hal-01113088.

Contents

3.1 Introduction

Second-order time-accuracy in incompressible fluid-structure interaction can be achieved via strongly coupled schemes (see, e.g., [NPV13]). However, the development of explicit coupling schemes delivering such high-order accuracy appears

to be an open problem. A fundamental difficulty that has to be faced is related to the fact that the combination of second-order time-marching in each subsystem with an enhanced consistency at the interface can spoil the stability properties of the original first-order coupling scheme (see, e.g., [BF14a]). For purely elastic thin-walled structures, some attempts have been presented in [LMRHZ13] by combining a *Strang operator splitting* approach with the ideas reported in [GGCC09]. Though the accuracy of the splitting is improved, second-order time-accuracy is still not achieved.

In this chapter we focus on the coupling with a general viscoelastic thin-walled structure. We combine the explicit Robin-Neumann coupling paradigm reported in Section 1.4.3.5 with second-order time-stepping in the fluid and in the solid. Theoretical results in a simplified setting suggest that the stability properties of the original Robin-Neumann schemes (Theorem 1.5) are not compromised. Two potentially second-order time-accurate approaches are then considered: (i) second-order extrapolation and (ii) first-order extrapolation with one defect-correction. The resulting schemes are investigated through a series of numerical studies in a benchmark.

This chapter is organized as follows. Section 3.2 is devoted to the derivation of the methods. The stability properties of some of the proposed schemes are analyzed within a representative simplified setting in Section 3.3. Section 3.4 is devoted to the numerical experiments. We conclude in Section 3.5 with a summary of the conclusions.

The model problem We consider the coupling of the Stokes equations (1.34) with the linear Kirchhoff-Love shell model (1.18). The problem, which has been already considered in Section 1.4.3.5, is repeated it here for the sake of convenience. It reads: find the fluid velocity $\boldsymbol{u} : \Omega^{\mathrm{f}} \times \mathbb{R}^+ \to \mathbb{R}^d$, the fluid pressure $p : \Omega^{\mathrm{f}} \times \mathbb{R}^+ \to \mathbb{R}$, the solid displacement $\boldsymbol{d} : \Sigma \times \mathbb{R}^+ \to \mathbb{R}^d$ and the solid velocity $\dot{\boldsymbol{d}} : \Sigma \times \mathbb{R}^+ \to \mathbb{R}^d$ such that

$$\begin{cases} \rho^{\mathrm{f}} \partial_t \boldsymbol{u} - \mathbf{div}\boldsymbol{\sigma}(\boldsymbol{u}, p) = \mathbf{0} & \text{in} \quad \Omega^{\mathrm{f}}, \\ \mathrm{div}\boldsymbol{u} = 0 & \text{in} \quad \Omega^{\mathrm{f}}, \\ \boldsymbol{\sigma}(\boldsymbol{u}, p)\boldsymbol{n} = -p_\Gamma \boldsymbol{n} & \text{on} \quad \Gamma^{\mathrm{f}}, \end{cases} \tag{3.1}$$

$$\begin{cases} \boldsymbol{u} = \dot{\boldsymbol{d}} & \text{on} \quad \Sigma, \\ \dot{\boldsymbol{d}} = \partial_t \boldsymbol{d} & \text{on} \quad \Sigma, \\ \rho^{\mathrm{s}} \epsilon \partial_t \dot{\boldsymbol{d}} + \boldsymbol{L}^{\mathrm{e}} \boldsymbol{d} + \boldsymbol{L}^{\mathrm{v}} \dot{\boldsymbol{d}} = -\boldsymbol{\sigma}(\boldsymbol{u}, p)\boldsymbol{n} & \text{on} \quad \Sigma, \\ \boldsymbol{d} = \mathbf{0} & \text{on} \quad \partial\Sigma, \end{cases} \tag{3.2}$$

complemented with the initial conditions $\boldsymbol{u}(0) = \boldsymbol{u}_0$, $\boldsymbol{d}(0) = \boldsymbol{d}_0$ and $\dot{\boldsymbol{d}}(0) = \dot{\boldsymbol{d}}_0$. Here, p_Γ denotes a given inlet/outlet pressure on Γ^{f}. The linear solid operators $\boldsymbol{L}^{\mathrm{e}}$ and $\boldsymbol{L}^{\mathrm{v}}$ describe, respectively, the elastic and viscous behavior of the structure model (we may consider, for instance, (1.21) and (1.22), respectively).

3.2 Second-order time-stepping

In this section we address the time semi-discretization of the coupled problem (3.1)-(3.2). The aim is to achieve second-order accuracy in time, hence time-stepping of (at least) second-order is mandatory for both the fluid and solid subproblems. In this chapter we will consider the *Crank-Nicholson scheme*. Alternatively, we may also consider a *second-order backward differentiation formula* (or BDF2) for the approximation of time derivatives in (3.1)-(3.2) (see Remark 3.3).

In the sequel, $\tau > 0$ denotes the time-step size, $t_n \overset{\text{def}}{=} n\tau$ the current time-instant, $\partial_\tau x^n \overset{\text{def}}{=} \big(x^n - x^{n-1}\big)/\tau$ the first-order backward difference in time and $x^{n-\frac{1}{2}} \overset{\text{def}}{=} \big(x^n + x^{n-1}\big)/2$ the midpoint. We will also make extensive use of the superscript $^{n-\frac{1}{2},\star}$ to indicate zeroth- (i.e., without), first-order or second-order extrapolation from the previous time-steps to the midpoint $x^{n-\frac{1}{2}}$, i.e.,

$$x^{n-\frac{1}{2},\star} = \begin{cases} 0 & \text{if} \quad r = 0, \\ x^{n-1} & \text{if} \quad r = 1, \\ \frac{3}{2}x^{n-1} - \frac{1}{2}x^{n-2} & \text{if} \quad r = 2, \end{cases}$$

where r denotes the extrapolation order.

To achieve the full fluid-solid splitting while avoiding the infamous instabilities related to the added mass effect, we follow the strategy of Section 1.4.3.5. The starting point is the interface Robin consistency (1.79), which is repeated here for the sake of completeness,

$$\boldsymbol{\sigma}(\boldsymbol{u}, p)\boldsymbol{n} + \rho^{\mathrm{s}}\epsilon\partial_t\boldsymbol{u} = -\boldsymbol{L}^{\mathrm{e}}\boldsymbol{d} - \boldsymbol{L}^{\mathrm{v}}\dot{\boldsymbol{d}} \quad \text{on} \quad \Sigma. \tag{3.3}$$

The idea is to discretize in time (3.3) combining an explicit treatment of the solid viscoelastic contributions (via extrapolations) and a strong fluid-solid hydrodynamic coupling (viz., fluid stresses and solid inertia contributions are treated implicitly). The former enables the fluid-solid splitting while the latter guarantees stability. If Crank-Nicholson solvers are considered for problems (3.1) and (3.2), we propose to discretize (3.3) as follows

$$\boldsymbol{\sigma}(\boldsymbol{u}^{n-\frac{1}{2}}, p^{n-\frac{1}{2}})\boldsymbol{n} + \frac{\rho^{\mathrm{s}}\epsilon}{\tau}\boldsymbol{u}^n = \frac{\rho^{\mathrm{s}}\epsilon}{\tau}\dot{\boldsymbol{d}}^{n-1} - \boldsymbol{L}^{\mathrm{e}}\boldsymbol{d}^{n-\frac{1}{2},\star} - \boldsymbol{L}^{\mathrm{v}}\dot{\boldsymbol{d}}^{n-\frac{1}{2},\star} \quad \text{on} \quad \Sigma. \tag{3.4}$$

The resulting schemes are displayed in Algorithm 3.1.

REMARK 3.1 *Note that (3.5) uniquely determines $\boldsymbol{u}^n$, since $\boldsymbol{u}^0$ is given. For the pressure, however, neither p^n nor p^{n-1} is used in (3.5). Therefore, by working with $p^{n-1/2}$ as the pressure variable, we do not need to provide an initial condition for the pressure. An approximation of p^n may be obtained by extrapolation.*

REMARK 3.2 *If we consider a pure elastic solid problem, we take $r = 0$ and*

Algorithm 3.1 Crank-Nicholson Robin-Neumann explicit schemes.

For $n > 0$ if $r = 0, 1$ *or* for $n > 1$ if $r = 2$:

1. Fluid step: Find $\boldsymbol{u}^n : \Omega^{\mathrm{f}} \times \mathbb{R}^+ \to \mathbb{R}^d$ and $p^{n-\frac{1}{2}} : \Omega^{\mathrm{f}} \times \mathbb{R}^+ \to \mathbb{R}$ such that

$$\begin{cases} \rho^{\mathrm{f}} \partial_\tau \boldsymbol{u}^n - \mathbf{div}\boldsymbol{\sigma}(\boldsymbol{u}^{n-\frac{1}{2}}, p^{n-\frac{1}{2}}) = \mathbf{0} & \text{in} \quad \Omega^{\mathrm{f}}, \\ \mathrm{div}\boldsymbol{u}^{n-\frac{1}{2}} = 0 & \text{in} \quad \Omega^{\mathrm{f}}, \\ \boldsymbol{\sigma}(\boldsymbol{u}^{n-\frac{1}{2}}, p^{n-\frac{1}{2}})\boldsymbol{n} = -p_\Gamma{}^{n-\frac{1}{2}}\boldsymbol{n} & \text{on} \quad \Gamma^{\mathrm{f}}, \\ \boldsymbol{\sigma}(\boldsymbol{u}^{n-\frac{1}{2}}, p^{n-\frac{1}{2}})\boldsymbol{n} + \dfrac{\rho^{\mathrm{s}}\epsilon}{\tau}\boldsymbol{u}^n = \dfrac{\rho^{\mathrm{s}}\epsilon}{\tau}\dot{\boldsymbol{d}}^{n-1} - \boldsymbol{L}^{\mathrm{e}}\boldsymbol{d}^{n-\frac{1}{2},\star} - \boldsymbol{L}^{\mathrm{v}}\dot{\boldsymbol{d}}^{n-\frac{1}{2},\star} & \text{on} \quad \Sigma. \end{cases} \tag{3.5}$$

2. Solid step: Find $\boldsymbol{d}^n : \Sigma \times \mathbb{R}^+ \to \mathbb{R}^d$ and $\dot{\boldsymbol{d}}^n : \Sigma \times \mathbb{R}^+ \to \mathbb{R}^d$ such that

$$\begin{cases} \dot{\boldsymbol{d}}^{n-\frac{1}{2}} = \partial_\tau \boldsymbol{d}^n & \text{on} \quad \Sigma, \\ \rho^{\mathrm{s}}\epsilon\partial_\tau\dot{\boldsymbol{d}}^n + \boldsymbol{L}^{\mathrm{e}}\boldsymbol{d}^{n-\frac{1}{2}} + \boldsymbol{L}^{\mathrm{v}}\dot{\boldsymbol{d}}^{n-\frac{1}{2}} = -\boldsymbol{\sigma}(\boldsymbol{u}^{n-\frac{1}{2}}, p^{n-\frac{1}{2}})\boldsymbol{n} & \text{on} \quad \Sigma, \\ \boldsymbol{d}^n = 0 & \text{on} \quad \partial\Sigma. \end{cases} \tag{3.6}$$

substitute $(3.6)_1$ *by*

$$\frac{\dot{\boldsymbol{d}}^n + \boldsymbol{u}^n}{2} = \partial_\tau \boldsymbol{d}^n \quad \text{on} \quad \Sigma,$$

then Algorithm 3.1 yields the kinematic splitting algorithm presented in [LMRHZ13], here with a Crank-Nicholson discretization of the fluid step. If viscous effects are considered in the structure model, that work advocates for an implicit treatment of the viscous terms in (3.3). Thus, instead of $(3.5)_4$*, the following Robin condition is considered in [LMRHZ13],*

$$\boldsymbol{\sigma}(\boldsymbol{u}^{n-\frac{1}{2}}, p^{n-\frac{1}{2}})\boldsymbol{n} + \frac{\rho^{\mathrm{s}}\epsilon}{\tau}\boldsymbol{u}^n + \boldsymbol{L}^{\mathrm{v}}\boldsymbol{u}^{n-\frac{1}{2}} = \frac{\rho^{\mathrm{s}}\epsilon}{\tau}\dot{\boldsymbol{d}}^{n-1} \quad \text{on} \quad \Sigma.$$

As pointed out in [FMV13], this transmission condition leads to a coupling scheme which is not explicit: it is semi-implicit. Moreover, the resulting solution procedure is not partitioned either, since the solid viscous contribution $\boldsymbol{L}^{\mathrm{v}}$ *has to be embedded within the fluid solver.*

Remark 3.3 *Recall that the BDF2 formula reads as* $\partial_\tau^{BDF2} x^n \overset{\text{def}}{=} \left(3x^n - 4x^{n-1} + x^{n-2}\right)/2\tau$*. If we consider a BDF2 scheme for the numerical integration of problems (3.1) and (3.2), the interface Robin condition (3.3) must be accordingly discretized as follows*

$$\boldsymbol{\sigma}(\boldsymbol{u}^n, p^n)\boldsymbol{n} + \frac{3\rho^{\mathrm{s}}\epsilon}{2\tau}\boldsymbol{u}^n = \frac{2\rho^{\mathrm{s}}\epsilon}{\tau}\dot{\boldsymbol{d}}^{n-1} - \frac{\rho^{\mathrm{s}}\epsilon}{2\tau}\dot{\boldsymbol{d}}^{n-2} - \boldsymbol{L}^{\mathrm{e}}\boldsymbol{d}^{n,\star} - \boldsymbol{L}^{\mathrm{v}}\dot{\boldsymbol{d}}^{n,\star} \quad \text{on} \quad \Sigma,$$

where the superscript ^{n,*} *indicates zeroth- (i.e., without), first-order or second-order*

extrapolation from the previous time-steps to x^n *, i.e,*

$$x^{n,\star} = \begin{cases} 0 & \text{if} \quad r = 0, \\ x^{n-1} & \text{if} \quad r = 1, \\ 2x^{n-1} - x^{n-2} & \text{if} \quad r = 2, \end{cases} \tag{3.7}$$

with r *denoting the extrapolation order.*

REMARK 3.4 *The discretization* (3.6) *of the solid problem can be regarded as a particular realization of the Newmark method [New59], the so called trapezoidal Newmark scheme, which is widely used in engineering for the time integration of elastodynamic problems. For a review of time integration techniques for second-order hyperbolic problems we refer to [BG10].*

3.2.1 Defect-correction iterations

Similarly to (1.87) for Algorithm 1.5, Algorithm 3.1 can be regarded as an interface kinematic perturbation of an underlying second-order implicit scheme, the corresponding perturbation being

$$\boldsymbol{u}^n = \dot{\boldsymbol{d}}^n + \frac{\tau}{\rho^{\mathrm{s}}\epsilon}\left[\boldsymbol{L}^{\mathrm{e}}\big(\boldsymbol{d}^{n-\frac{1}{2}} - \boldsymbol{d}^{n-\frac{1}{2},\star}\big) + \boldsymbol{L}^{\mathrm{v}}\big(\dot{\boldsymbol{d}}^{n-\frac{1}{2}} - \dot{\boldsymbol{d}}^{n-\frac{1}{2},\star}\big)\right] \quad \text{on} \quad \Sigma. \tag{3.8}$$

In view of the error analysis performed in [Fer13, FMV13] (see Theorem 1.6), the consistency errors induced by (3.8) scale as $\mathcal{O}(\tau^{2^{r-1}})$. Thus, despite both the fluid and structure solvers feature a quadratic-convergence rate when considering separately, second-order accuracy in the splitting error is restricted to the case $r = 2$.

In order to enhance the overall accuracy when lower order extrapolations are used, we follow the *defect-correction approach* (see [Ste78]). Basically, the idea is to reduce the error between the solution obtained with Algorithm 3.1 and the one of the underlying implicit scheme, by iteratively improving the perturbation (or defect) induced by the former (i.e., the last term of (3.8)). In this way, for $r = 1$, taking $K > 0$ defect-corrections, the perturbation of the kinematic constraint scales as $\mathcal{O}(\tau^{K+1})$. Hence, one defect-correction iteration is required to achieve the second-order accuracy of the global discretization error.

The resulting schemes are displayed in Algorithm 3.2, where $K \geq 0$ denotes the number of defect-correction iterations and $x^{n-\frac{1}{2},k} \overset{\text{def}}{=} \big(x^{n,k} + x^{n-1}\big)/2$ stands for the midpoint between the previous value x^{n-1} and the k-step approximation $x^{n,k+1}$ to x^n. The superscript ^{n,*} notation must be interpreted as in (3.7). Note that taking $K = 0$ and $r = 1, 2$ in Algorithm 3.2, we recover the corresponding extrapolated variants in Algorithm 3.1. According to the above discussion, in order to achieve overall second-order time-accuracy, two approaches are investigated:

- *Genuine explicit scheme:* Algorithm 3.1 with $r = 2$, or equivalently, Algorithm 3.2 with $r = 2$ and $K = 0$.

Algorithm 3.2 Crank-Nicholson Robin-Neumann schemes with $K \geq 0$ corrections.

For $n > 0$ if $r = 0, 1$ *or* for $n > 1$ if $r = 2$:

1. Extrapolation: $\boldsymbol{d}^{n,0} = \boldsymbol{d}^{n,\star}$, $\dot{\boldsymbol{d}}^{n,0} = \dot{\boldsymbol{d}}^{n,\star}$.

2. For $0 < k \leq K$:

   (a) Fluid step: Find $\boldsymbol{u}^{n,k} : \Omega^{\mathrm{f}} \times \mathbb{R}^+ \to \mathbb{R}^d$ and $p^{n-\frac{1}{2},k} : \Omega^{\mathrm{f}} \times \mathbb{R}^+ \to \mathbb{R}$ such that

$$\begin{cases} \dfrac{\rho^{\mathrm{f}}}{\tau}\big(\boldsymbol{u}^{n,k} - \boldsymbol{u}^{n-1}\big) - \mathbf{div}\boldsymbol{\sigma}(\boldsymbol{u}^{n-\frac{1}{2},k}, p^{n-\frac{1}{2},k}) = \mathbf{0} & \text{in} \quad \Omega^{\mathrm{f}}, \\ \mathrm{div}\boldsymbol{u}^{n-\frac{1}{2},k} = 0 & \text{in} \quad \Omega^{\mathrm{f}}, \\ \boldsymbol{\sigma}(\boldsymbol{u}^{n-\frac{1}{2},k}, p^{n-\frac{1}{2},k})\boldsymbol{n} = -{p_\Gamma}^{n-\frac{1}{2}}\boldsymbol{n} & \text{on} \quad \Gamma^{\mathrm{f}}, \\ \boldsymbol{\sigma}(\boldsymbol{u}^{n-\frac{1}{2},k}, p^{n-\frac{1}{2},k})\boldsymbol{n} + \dfrac{\rho^{\mathrm{s}}\epsilon}{\tau}\boldsymbol{u}^{n,k} = \dfrac{\rho^{\mathrm{s}}\epsilon}{\tau}\dot{\boldsymbol{d}}^{n-1} & \\ \quad + \boldsymbol{L}^{\mathrm{e}}\boldsymbol{d}^{n-\frac{1}{2},k-1} + \boldsymbol{L}^{\mathrm{v}}\dot{\boldsymbol{d}}^{n-\frac{1}{2},k-1} & \text{on} \quad \Sigma. \end{cases}$$

   (b) Solid step: Find $\boldsymbol{d}^{n,k} : \Sigma \times \mathbb{R}^+ \to \mathbb{R}^d$ and $\dot{\boldsymbol{d}}^{n,k} : \Sigma \times \mathbb{R}^+ \to \mathbb{R}^d$ such that

$$\begin{cases} \dot{\boldsymbol{d}}^{n-\frac{1}{2},k} = \dfrac{1}{\tau}\big(\boldsymbol{d}^{n,k} - \boldsymbol{d}^{n-1}\big) & \text{on} \quad \Sigma, \\ \dfrac{\rho^{\mathrm{s}}\epsilon}{\tau}\big(\dot{\boldsymbol{d}}^{n,k} - \dot{\boldsymbol{d}}^{n-1}\big) + \boldsymbol{L}^{\mathrm{e}}\boldsymbol{d}^{n-\frac{1}{2},k} + \boldsymbol{L}^{\mathrm{v}}\dot{\boldsymbol{d}}^{n-\frac{1}{2},k} = & \\ \quad -\boldsymbol{\sigma}(\boldsymbol{u}^{n-\frac{1}{2},k}, p^{n-\frac{1}{2},k})\boldsymbol{n} & \text{on} \quad \Sigma, \\ \boldsymbol{d}^{n,k} = \mathbf{0} & \text{on} \quad \partial\Sigma. \end{cases}$$

3. Solution update:

$$\boldsymbol{u}^n = \boldsymbol{u}^{n,K}, \ p^{n-\frac{1}{2}} = p^{n-\frac{1}{2},K}, \ \boldsymbol{d}^n = \boldsymbol{d}^{n,K}, \ \dot{\boldsymbol{d}}^n = \dot{\boldsymbol{d}}^{n,K}.$$

- *Predictor-corrector scheme:* Algorithm 3.2 with $r = 1$ and $K = 1$.

3.3 Stability analysis in a simplified setting

The aim of this section is to provide some insight into the stability properties of Algorithm 3.1. We perform the type of analysis proposed in [CGN05] (see also [BNV08]), where a simplified fluid-structure interaction model is considered. The model is simple enough to enable a mathematical stability analysis but, at the same time, complex enough to mimic more realistic situations. In particular, it reproduces propagation phenomena and accounts for the added-mass effect.

The model problem concerns the coupling of an incompressible inviscid 2D fluid

with the 1D generalized string model introduced in (1.23). The fluid computational domain is the rectangle $\Omega^{\mathrm{f}} = [0, L] \times [0, R]$ with left, right, lower and upper edge given, respectively, by Γ^1, Γ^2, Γ^3 and Σ (see Figure 3.1). The fluid-structure interface is located on Σ. A symmetry condition is imposed on the lower edge Γ^3. The coupled problem reads as follows: find the fluid velocity $\boldsymbol{u} : \Omega^{\mathrm{f}} \times \mathbb{R}^+ \to \mathbb{R}^d$, the fluid pressure $p : \Omega^{\mathrm{f}} \times \mathbb{R}^+ \to \mathbb{R}$, the solid displacement $\eta : \Sigma \times \mathbb{R}^+ \to \mathbb{R}$ and the solid velocity $\dot{\eta} : \Sigma \times \mathbb{R}^+ \to \mathbb{R}$ such that

$$\begin{cases} \rho^{\mathrm{f}} \partial_t \boldsymbol{u} + \boldsymbol{\nabla} p = \boldsymbol{0} & \text{in} \quad \Omega^{\mathrm{f}}, \\ \mathrm{div} \boldsymbol{u} = 0 & \text{in} \quad \Omega^{\mathrm{f}}, \\ p = 0 & \text{on} \quad \Gamma^1 \cup \Gamma^2, \\ \boldsymbol{u} \cdot \boldsymbol{n} = 0 & \text{on} \quad \Gamma^3, \\ \boldsymbol{u} \cdot \boldsymbol{n} = \dot{\eta} & \text{on} \quad \Sigma, \end{cases} \tag{3.9}$$

$$\begin{cases} \dot{\eta} = \partial_t \eta & \text{on} \quad \Sigma, \\ \rho^{\mathrm{s}} \epsilon \partial_t \dot{\eta} + L^{\mathrm{e}} \eta + L^{\mathrm{v}} \dot{\eta} = p & \text{in} \quad \Sigma, \\ \eta = 0 & \text{on} \quad \partial\Sigma, \end{cases} \tag{3.10}$$

satisfying the initial conditions $\boldsymbol{u}(0) = \boldsymbol{u}_0$, $\eta(0) = \eta_0$ and $\dot{\eta}(0) = \dot{\eta}_0$. For the sake of completeness, we recall that the string differential operators, defined in (1.23), read as $L^{\mathrm{e}}\eta = -c_1 \partial_{xx} \eta + c_0 \eta$ and $L^{\mathrm{v}} \dot{\eta} = -\beta c_1 \partial_{xx} \dot{\eta} + \alpha \rho^{\mathrm{s}} \epsilon \dot{\eta}$, with $c_1 = \frac{E\epsilon}{2(1+\nu)}$, $c_0 = \frac{E\epsilon}{R^2(1-\nu^2)}$ and $\beta, \alpha > 0$.

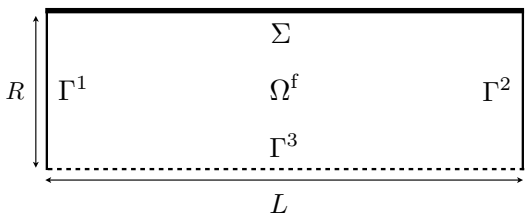

Figure 3.1: Geometrical configuration.

3.3.1 Preliminaries

For conciseness, we omit in the sequel the temporal superscript $^{n-\frac{1}{2}}$ in the extrapolated quantities, i.e, the superscript * must be interpreted as $^{n-\frac{1}{2},\star}$. Application of Algorithm 3.1 to problem (3.9)-(3.10) leads to the following explicit scheme:

1. Fluid step: Find $\boldsymbol{u}^n : \Omega^{\mathrm{f}} \times \mathbb{R}^+ \to \mathbb{R}^d$ and $p^{n-\frac{1}{2}} : \Omega^{\mathrm{f}} \times \mathbb{R}^+ \to \mathbb{R}$ such that

$$\begin{cases} \rho^{\mathrm{f}} \partial_\tau \boldsymbol{u}^n + \boldsymbol{\nabla} p^{n-\frac{1}{2}} = \boldsymbol{0} & \text{in} \quad \Omega^{\mathrm{f}}, \\ \mathrm{div} \boldsymbol{u}^{n-\frac{1}{2}} = 0 & \text{in} \quad \Omega^{\mathrm{f}}, \\ p^{n-\frac{1}{2}} = 0 & \text{on} \quad \Gamma^1 \cup \Gamma^2, \\ \boldsymbol{u}^n \cdot \boldsymbol{n} = 0 & \text{on} \quad \Gamma^3, \\ -p^{n-\frac{1}{2}} + \dfrac{\rho^{\mathrm{s}} \epsilon}{\tau} \boldsymbol{u}^n \cdot \boldsymbol{n} = \dfrac{\rho^{\mathrm{s}} \epsilon}{\tau} \dot{\eta}^{n-1} - L^{\mathrm{e}} \eta^\star - L^{\mathrm{v}} \dot{\eta}^\star & \text{on} \quad \Sigma. \end{cases} \tag{3.11}$$

2. Solid step: Find $\eta^n : \Sigma \times \mathbb{R}^+ \to \mathbb{R}$ and $\dot{\eta}^n : \Sigma \times \mathbb{R}^+ \to \mathbb{R}$ such that

$$\begin{cases} \dot{\eta}^{n-\frac{1}{2}} = \partial_\tau \eta^n & \text{on} \quad \Sigma, \\ \rho^{\mathrm{s}} \epsilon \partial_\tau \dot{\eta}^n + L^{\mathrm{e}} \eta^{n-\frac{1}{2}} + L^{\mathrm{v}} \dot{\eta}^{n-\frac{1}{2}} = p^{n-\frac{1}{2}} & \text{in} \quad \Sigma, \\ \eta^n = 0 & \text{on} \quad \partial\Sigma, \end{cases} \tag{3.12}$$

for $n > 0$ if $r = 0, 1$ or for $n > 1$ if $r = 2$.

Assuming that the solution is regular enough, the fluid step (3.11) can be conveniently reformulated as the following pressure Poisson problem:

$$\begin{cases} -\Delta p^{n-\frac{1}{2}} = 0 & \text{in} \quad \Omega^{\mathrm{f}}, \\ p^{n-\frac{1}{2}} = 0 & \text{on} \quad \Gamma^1 \cup \Gamma^2, \\ \dfrac{\partial p^{n-\frac{1}{2}}}{\partial \boldsymbol{n}} = 0 & \text{on} \quad \Gamma^3, \\ \dfrac{\partial p^{n-\frac{1}{2}}}{\partial \boldsymbol{n}} = -\rho^{\mathrm{f}} \partial_\tau \boldsymbol{u}^n \cdot \boldsymbol{n} & \text{on} \quad \Sigma. \end{cases} \tag{3.13}$$

We denote by $\mathcal{M}_{\mathcal{A}} : H^{-\frac{1}{2}}(\Sigma) \to H^{\frac{1}{2}}(\Sigma)$ the added-mass operator (*Neumann-to-Dirichlet map*) defined, for $w \in H^{-\frac{1}{2}}(\Sigma)$, as $\mathcal{M}_{\mathcal{A}} w = \mathcal{R} w|_\Sigma$ with $\mathcal{R} w \in H^1_{\Gamma^1 \cup \Gamma^2}(\Omega^{\mathrm{f}})$ solution of

$$\begin{cases} -\Delta \mathcal{R} w = 0 & \text{in} \quad \Omega^{\mathrm{f}}, \\ \mathcal{R} w = 0 & \text{on} \quad \Gamma^1 \cup \Gamma^2, \\ \dfrac{\partial \mathcal{R} w}{\partial \boldsymbol{n}} = 0 & \text{on} \quad \Gamma^3, \\ \dfrac{\partial \mathcal{R} w}{\partial \boldsymbol{n}} = w & \text{on} \quad \Sigma. \end{cases}$$

Thus, the solution $p^{n-\frac{1}{2}}$ of (3.13) on the fluid-structure interface is given by

$$p^{n-\frac{1}{2}} = -\rho^{\mathrm{f}} \mathcal{M}_{\mathcal{A}} \big(\partial_\tau \boldsymbol{u}^n \cdot \boldsymbol{n} \big) \quad \text{on } \Sigma. \tag{3.14}$$

It can be shown that the operator $\mathcal{M}_{\mathcal{A}}$ is compact, self-adjoint and positive in $L^2(\Sigma)$ (see [CGN05]). For the geometry at hand (Figure 3.1), the eigenvalues of

$\mathcal{M}_{\mathcal{A}}$ are given by

$$\left\{\mu_i = \frac{L}{i\pi \tanh\left(\frac{i\pi R}{L}\right)}\right\}_{i=1}^{\infty},$$

with associated orthonormal eigenfunctions

$$\left\{g_i = \sqrt{\frac{2}{L}} \sin\left(\frac{i\pi x}{L}\right)\right\}_{i=1}^{\infty}. \tag{3.15}$$

The largest eigenvalue is given by $\mu_{\max} = \frac{L}{\pi \tanh\left(\frac{\pi R}{L}\right)}$, which corresponds to $i = 1$.

3.3.2 Modal stability analysis

For the sake of simplicity, we assume that the $\alpha = \beta = 0$ in (3.10), i.e., no damping effect is considered in the solid problem. The results obtained can be generalized to the case $\alpha \neq 0$ or $\beta \neq 0$ (See Remark 3.5 below). The kinematic perturbation (3.8) induced by the scheme (3.11)-(3.12) reads as

$$\boldsymbol{u}^n \cdot \boldsymbol{n} = \dot{\eta}^n + \frac{\tau}{\rho^{\mathrm{s}}\epsilon} L^{\mathrm{e}}\left(\eta^{n-\frac{1}{2}} - \eta^{\star}\right) \quad \text{on } \Sigma. \tag{3.16}$$

According to (3.16) and (3.14), the solid problem (3.12) can be reformulated, for $n > 0$ if $r = 0, 1$ or for $n > 1$ if $r = 2$, as

$$\begin{cases} \dot{\eta}^{n-\frac{1}{2}} = \partial_\tau \eta^n & \text{on} \quad \Sigma, \\ \left(\rho^{\mathrm{s}}\epsilon + \rho^{\mathrm{f}}\mathcal{M}_{\mathcal{A}}\right)\partial_\tau \dot{\eta}^n + L^{\mathrm{e}}\eta^{n-\frac{1}{2}} + \dfrac{\rho^{\mathrm{f}}\tau}{\rho^{\mathrm{s}}\epsilon}\mathcal{M}_{\mathcal{A}} L^{\mathrm{e}}\left(\partial_\tau(\eta^{n-\frac{1}{2}} - \eta^{\star})\right) = 0 & \text{in} \quad \Sigma, \\ \eta^n = 0 & \text{on} \quad \partial\Sigma. \end{cases}$$

To investigate the stability of Algorithm (3.11)-(3.12), we consider expansions of the solid solutions in the $L^2(\Sigma)$ orthonormal basis given by (3.15), i.e, $\eta^n = \sum_i \eta_i^n g_i$ and $\dot{\eta}^n = \sum_i \dot{\eta}_i^n g_i$. Note that functions in (3.15) are also eigenfunctions of the *Laplace operator* $-\partial_{xx}$ on Σ, with corresponding eigenvalues

$$\left\{\lambda_i = \frac{i^2\pi^2}{L^2}\right\}_{i=1}^{\infty}.$$

The Fourier coefficients η_i^n and $\dot{\eta}_i^n$ satisfy, for all $i \in \{1, \ldots, \infty\}$, the following recurrence relation

$$\begin{cases} \dfrac{\dot{\eta}_i^n + \dot{\eta}_i^{n-1}}{2} = \dfrac{\eta_i^n - \eta_i^{n-1}}{\tau}, \\ \left(\rho^{\mathrm{s}}\epsilon + \rho^{\mathrm{f}}\mu_i\right)\dfrac{\dot{\eta}_i^n - \dot{\eta}_i^{n-1}}{\tau} + \left(c_0 + c_1\lambda_i\right)\dfrac{\eta_i^n + \eta_i^{n-1}}{2} + \dfrac{\rho^{\mathrm{f}}}{\rho^{\mathrm{s}}\epsilon}\mu_i\left(c_0 + c_1\lambda_i\right) X_{i,r}^n = 0, \end{cases} \tag{3.17}$$

for $n > 1$ if $r = 0, 1$ or for $n > 2$ if $r = 2$, and where

$$X_{i,r}^n = \begin{cases} \dfrac{\eta_i^n - \eta_i^{n-2}}{2} & \text{if} \quad r = 0, \\ \dfrac{\eta_i^n + 2\eta_i^{n-1} - \eta_i^{n-2}}{2} & \text{if} \quad r = 1, \\ \dfrac{\eta_i^n - 3\eta_i^{n-1} + 3\eta_i^{n-2} - \eta_i^{n-3}}{2} & \text{if} \quad r = 2. \end{cases}$$

For $r = 0$ or $r = 1$, the following proposition establishes that the recurrence relation (3.17) is stable, meaning that its solution converges to a fixed value, irrespectively of the physical and discretization parameters.

Proposition 3.1 *Let $\{\eta_i^n\}_{n=0}^{\infty}$ denote the sequence given by (3.17) for a fixed $i \in \{1, \ldots, \infty\}$. Then, if $r = 0$ or $r = 1$,*

$$|\eta_i^n| \underset{n \to +\infty}{\longrightarrow} 0, \quad \forall i \in \{1, \ldots, \infty\},$$

irrespectively of the physical and discretization parameters.

Proof. For $r = 0$ or $r = 1$, the recurrence relation (3.17) can be conveniently reformulated, for all $i \in \{1, \ldots, \infty\}$, as

$$2(\rho^{\mathrm{s}}\epsilon + \rho^{\mathrm{f}}\mu_i)\frac{\eta_i^n - 2\eta_i^{n-1} + \eta_i^{n-2}}{\tau^2} + (c_0 + c_1\lambda_i)\,\frac{\eta_i^n + 2\eta_i^{n-1} + \eta_i^{n-2}}{2} + \frac{\rho^{\mathrm{f}}}{\rho^{\mathrm{s}}\epsilon}\mu_i\,(c_0 + c_1\lambda_i)\,Y_{i,r}^n = 0, \quad (3.18)$$

for $n > 2$, with suitable initialization conditions and with

$$Y_{i,r}^n \overset{\text{def}}{=} \begin{cases} \dfrac{\eta_i^n + \eta_i^{n-1} - \eta_i^{n-2} - \eta_i^{n-3}}{2} & \text{if} \quad r = 0, \\ \dfrac{\eta_i^n - \eta_i^{n-1} - \eta_i^{n-2} + \eta_i^{n-3}}{2} & \text{if} \quad r = 1. \end{cases}$$

We now proceed by treating each case of extrapolation separately.
Case $r = 0$. The characteristic polynomial $\chi_{i,0}(x) \in \mathbb{P}^3$ of the difference equation (3.18) reads as

$$\begin{aligned} \chi_{i,0}(x) = &\left(\frac{1}{2}\,(c_0 + c_1\lambda_i) + \frac{(c_0 + c_1\lambda_i)\,\mu_i\rho^{\mathrm{f}}}{2\epsilon\rho^{s}} + \frac{2\mu_i\rho^{\mathrm{f}}}{\tau^2} + \frac{2\epsilon\rho^{\mathrm{s}}}{\tau^2}\right)x^3 \\ &+ \left((c_0 + c_1\lambda_i) + \frac{(c_0 + c_1\lambda_i)\,\mu_i\rho^{\mathrm{f}}}{2\epsilon\rho^{\mathrm{s}}} - \frac{4\mu_i\rho^{\mathrm{f}}}{\tau^2} - \frac{4\epsilon\rho^{\mathrm{s}}}{\tau^2}\right)x^2 \\ &+ \left(\frac{1}{2}\,(c_0 + c_1\lambda_i) - \frac{(c_0 + c_1\lambda_i)\,\mu_i\rho^{\mathrm{f}}}{2\epsilon\rho^{\mathrm{s}}} + \frac{2\mu_i\rho^{\mathrm{f}}}{\tau^2} + \frac{2\epsilon\rho^{\mathrm{s}}}{\tau^2}\right)x - \frac{(c_0 + c_1\lambda_i)\,\mu_i\rho^{\mathrm{f}}}{2\epsilon\rho^{\mathrm{s}}}. \end{aligned}$$

The recurrence relation (3.18) is stable if the roots of $\chi_{i,0}(x)$ lie in the complex unit

circle $\{z \in \mathbb{C} \,/\, \|z\| < 1\}$. To demonstrate that this is indeed the case, we apply to $\chi_{i,0}(x)$ the one-to-one transformation $x = \frac{z+1}{z-1}$, which maps the complex left half plane $\{z \in \mathbb{C} \,/\, \mathrm{Re}(z) < 0\}$ into the unit circle, and multiply the resulting equation by $(z-1)^3$, obtaining the polynomial

$$\hat{\chi}_{i,0}(z) = 2\,(c_0 + c_1\lambda_i)\,z^3 + \left(2\,(c_0 + c_1\lambda_i) + \frac{4\,(c_0 + c_1\lambda_i)\,\mu_i\rho^{\mathrm{f}}}{\epsilon\rho^{\mathrm{s}}}\right) z^2 + \frac{8\left(\mu_i\rho^{\mathrm{f}} + \epsilon\rho^{\mathrm{s}}\right)}{\tau^2} z + \frac{8\left(\mu_i\rho^{\mathrm{f}} + \epsilon\rho^{\mathrm{s}}\right)}{\tau^2}.$$

Hence, the question about the stability of (3.18) comes down to discern whether or not the roots of $\hat{\chi}_{i,0}(z)$ lie in the complex left half plane. To tackle this problem we use the *Routh-Hurwitz criterion* (see [Rou77, Hur95]), which gives necessary and sufficient conditions for all the roots of a polynomial (with real coefficients) to lie in the complex left half plane. For a third-order polynomial $P(s) = a_3 s^3 + a_2 s^2 + a_1 s + a_0 = 0$, these conditions are

$$a_3 > 0, \quad a_2 a_1 > a_3 a_0.$$

This is obviously the case for polynomial $\hat{\chi}_{i,0}(z)$ for all $i \in \{1, \ldots, \infty\}$.

$\underline{r = 1.}$ We proceed as in the previous case. The corresponding polynomial $\hat{\chi}_{i,1}(z)$ reads

$$\hat{\chi}_{i,1}(z) = 2\,(c_0 + c_1\lambda_i)\,z^3 + 2\,(c_0 + c_1\lambda_i)\,z^2 + \left(\frac{8\left(\mu_i\rho^{\mathrm{f}} + \epsilon\rho^{\mathrm{s}}\right)}{\tau^2} + \frac{4\,(c_0 + c_1\lambda_i)\,\mu_i\rho^{\mathrm{f}}}{\epsilon\rho^{\mathrm{s}}}\right) z + \frac{8\left(\mu_i\rho^{\mathrm{f}} + \epsilon\rho^{\mathrm{s}}\right)}{\tau^2}.$$

We conclude using the Routh-Hurwitz criterion. ∎

Proposition 3.1 establishes that whenever the Fourier series expansion of η^n is truncated (i.e., whenever the spatial discretization is fixed) the solution of Algorithm 3.1, under the above assumptions, is stable with zeroth- and first-order extrapolations. Thus, the stability of the original Robin-Neumann schemes, with zeroth- and first-order extrapolations, is somehow preserved. For the second-order extrapolated variant, a CFL-like condition is expected to guarantee stability (see Theorem 1.5). The previous modal analysis is not able to capture this condition since the effect of the spatial discretization is not taken into account.

REMARK 3.5 *If we consider damping effects ($\alpha \neq 0$ or $\beta \neq 0$) on the structure equation (3.10), then a viscous extrapolated contribution has to be added to (3.16). It can be proven, under the same assumptions and in the same fashion as above, that the corresponding solution sequence $\{\eta_i^n\}_{n=0}^{\infty}$ for $r = 0$ or $r = 1$, is such that*

$$|\eta_i^n| \underset{n \to +\infty}{\longrightarrow} 0, \quad \forall i \in \{1, \ldots, \infty\},$$

irrespectively of the physical and discretization parameters. A parabolic-CFL condition (see Remark 1.18) is expected for stability in the case $r = 2$.

3.4 Numerical experiments

In order to illustrate the accuracy of the proposed schemes, we consider the problem of the pressure-wave propagation within an elastic tube described in Section 2.4.1, which involves the generalized string model (3.10). Stabilized piece-wise affine continuous finite elements are used for the discretization in space. The computations have been performed with FreeFem++ [Hec12].

To provide evidence on the $\mathcal{O}(\tau^2)$ convergence behavior of the proposed schemes, Figure 3.2 reports the time-convergence history, with $h = 25 \cdot 10^{-3}$ fixed, of the solid displacement at time $t = 0.015$, in the relative elastic energy-norm, obtained with Algorithms 3.1 and 3.2 and a fully implicit second-order scheme. We have refined in time according to $\tau = 5 \cdot 10^{-4}/2^i$ with $i = 0, \ldots, 4$. The reference solution has been generated using the implicit scheme with $\tau = 10^{-6}$ and the same h. The corresponding displacements for the first four τ-refinement levels are provided in Figure 3.3. In Figure 3.2, we can clearly see that the two variants proposed, Algorithm 3.1 (Alg. 1 in the figure) with $r = 2$ and Algorithm 3.2 (Alg. 2 in the figure) with $r = 1$ and $K = 1$, retrieve the second-order convergence in time of the implicit scheme.

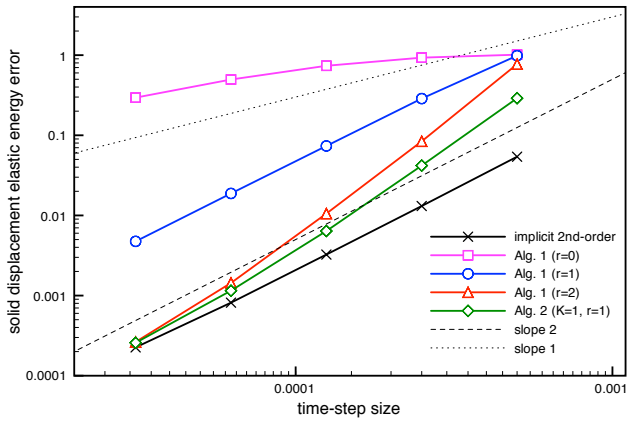

Figure 3.2: Time-convergence history of the displacement at $t = 0.015$ with $h = 25 \cdot 10^{-3}$ fixed.

On the other hand, the results of Figures 3.2-3.3 corresponding to the zeroth- and first-order extrapolated variants of Algorithm 3.1 are in agreement with the stability analysis performed in Section 3.3.2. Regarding the case with second-order extrapolation, the unstable approximation obtained in Figure 3.3 (a) for the larger τ (the case $i = 0$) points towards the expected underlying parabolic-CFL condition (see Remark 3.5).

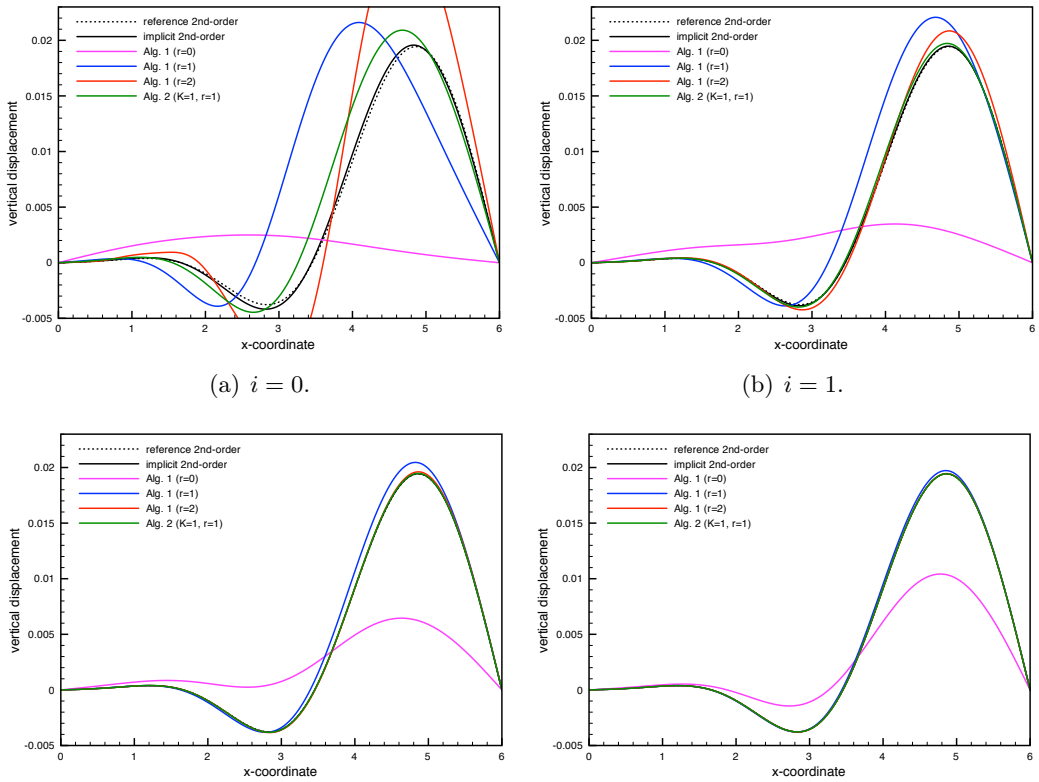

(a) $i = 0$. (b) $i = 1$.

(c) $i = 2$. (d) $i = 3$.

Figure 3.3: Comparison of the solid displacements at $t = 0.015$ for different levels of τ-refinement, given by $\tau = 5 \cdot 10^{-4}/2^i$.

The h-uniformity for the zeroth- and first-order extrapolated variants is guaranteed by Figure 3.4, where we have refined both in time and space according to $h = \mathcal{O}(\tau^2)$. Specifically, we consider $\tau = 5 \cdot 10^{-4}/2^i$, $h = 0.1/4^i$ for $i = 0, 1, 2$. The reference solution has been now obtained with $\tau = 10^{-6}$ and $h = 3 \cdot 10^{-3}$. We do not consider in this case the alternative given by Algorithm 3.1 with $r = 2$ since the discretization parameters do no satisfy the aforementioned condition for stability.

In summary, Algorithm 3.1 with $r = 2$ provides a quadratic-convergence rate in time (see Figure 3.2) whenever a parabolic-CFL condition is satisfied (see Figure 3.3 (a)). The alternative given by Algorithm 3.2 with $K = 1$ and $r = 1$ provides second-order convergence (see Figure 3.2) irrespectively of the discretization parameters. Furthermore, the h-uniformity of this latter alternative is confirmed by Figure 3.4.

3.5 Conclusion

We have introduced a class of time-accurate coupling schemes for fluid-structure interaction problems involving an incompressible fluid and a general thin-walled

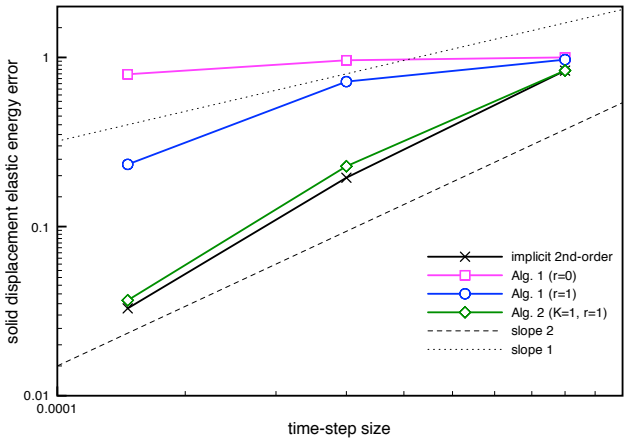

Figure 3.4: Time-convergence history of the displacement at $t = 0.015$, with $h = \mathcal{O}(\tau^2)$.

viscoelastic structure. The key ingredients in the derivation of these methods are:

- second-order time-stepping in both the fluid and solid subproblems;
- enhanced consistency in the explicit discretization (3.4) of (3.3) through second-order extrapolation (Algorithm 3.2 with $r = 2$ and $K = 0$) or first-order extrapolation with one defect-correction iteration (Algorithm 3.2 with $r = 1$ and $K = 1$).

A stability analysis in a simplified setting (Proposition 3.1) has provided some insight into the stability properties of these strategies. Numerical experiments in a benchmark have shown second-order convergence in time for both alternatives. The best balance between accuracy and robustness is obtained with the predictor-corrector scheme given by Algorithm 3.2 with $r = 1$ and $K = 1$.

Chapter 4

Coupling schemes for the FSI forward prediction challenge: comparative study and validation

In this chapter we present a numerical study in which several partitioned solution procedures, belonging to the three main families of coupling schemes discussed in Section 1.3.2, are compared and validated against the results of an experimental FSI benchmark. We consider, in particular, the splitting paradigm of Chapter 2. Very good agreement is observed between the numerical and experimental results.

The results presented in this chapter have been reported in:

- M. Landajuela, M. Vidrascu, D. Chapelle, M. A. Fernández, **Coupling schemes for the FSI forward prediction challenge: comparative study and validation**. Submitted to *International Journal for Numerical Methods in Biomedical Engineering*. https://hal.inria.fr/hal-01239931.

Contents

4.1 Introduction

Numerical methods for fluid-structure interaction are generally validated and compared between them using reference synthetic data, that is, generated via numerical experiments (see, e.g., [KGF+09, THR+10, Fer11a, Deg13]). Comparisons between numerical and experimental results are rare in the FSI literature, and often limited to a single numerical method (see [PGYLS11, MXA+12, MBX+13, BBG+14]).

The main objective of this chapter is to compare and validate some of the state-of-the-art coupling schemes for fluid-structure interaction (see Section 1.3.2), including the fully decoupled schemes introduced in Chapter 2, within the framework of the FSI experimental benchmark presented in [Nor15]. All the solution procedures discussed are partitioned and, from the coupling algorithm standpoint, parameter free.

The chapter is organized as follows. Section 4.2 presents the mathematical models and formulations considered in this work. The numerical algorithms used to simulate the benchmark experiments are described in Section 4.3. In Section 4.4, the numerical results are discussed and compared with the experimental data. Finally, a summary of the conclusions is presented in Section 4.5.

4.2 Problem setting

This section presents the different mathematical models considered in this work. Full details on the experimental setup are given in [Nor15]. The fluid, an aqueous glycerol solution, is modeled by the ALE Navier-Stokes equations (1.4). The solid filament, made of silicone, is described by a non-linear viscoelastic (3D or shell) model.

4.2.1 Geometry

As reference configuration for the coupled system, we consider the domain $\Omega^{\mathrm{f}} \cup \Omega^{\mathrm{s}}$ depicted in Figure 4.1(left). For all $t \in \mathbb{R}^+$, the current configuration of the solid is denoted by $\Omega^{\mathrm{s}}(t)$, whereas the fluid is supposed to fill the moving control volume $\Omega^{\mathrm{f}}(t)$. We denote by $\Sigma(t) \overset{\text{def}}{=} \partial\Omega^{\mathrm{f}}(t) \cap \partial\Omega^{\mathrm{s}}(t)$ the current configuration of the fluid-structure interface. Correspondingly, $\Sigma \overset{\text{def}}{=} \partial\Omega^{\mathrm{f}} \cap \partial\Omega^{\mathrm{s}}$ stands for the reference fluid-structure interface. The remaining parts of the fluid and solid boundaries $\partial\Omega^{\mathrm{f}} \backslash \Sigma$ and $\partial\Omega^{\mathrm{s}} \backslash \Sigma$ are assumed to be independent of time and partitioned as

$$\partial\Omega^{\mathrm{f}} = \Gamma_{\mathrm{top}} \cup \Gamma_{\mathrm{bot}} \cup \Gamma_{\mathrm{out}} \cup \Gamma_{\mathrm{wall}} \cup \Sigma, \quad \partial\Omega^{\mathrm{s}} = \Gamma^{\mathrm{s}}_{\mathrm{wall}} \cup \Sigma,$$

respectively. In the succeeding text, $\boldsymbol{n}$ and $\boldsymbol{n}^{\mathrm{s}}$ refer to the outward normal vectors, on either the current or reference configuration, of the fluid and solid boundaries respectively. Furthermore, for a given vector field $\boldsymbol{v}$ defined on the surface Σ, the

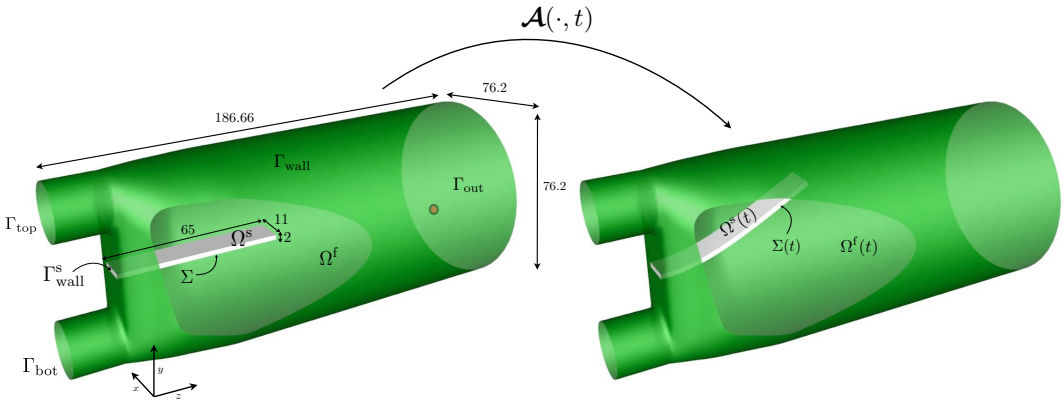

Figure 4.1: Reference and current geometrical configurations. Lengths are given in millimetres.

symbols $\boldsymbol{v}_\perp \overset{\text{def}}{=} (\boldsymbol{v}\cdot\boldsymbol{n})\boldsymbol{n}$ and $\boldsymbol{v}_\parallel \overset{\text{def}}{=} \boldsymbol{v} - \boldsymbol{v}_\perp$ denote, respectively, the normal and tangential components of $\boldsymbol{v}$.

The moving fluid domain $\Omega^{\text{f}}(t)$ is parametrized as $\Omega^{\text{f}}(t) = \boldsymbol{\mathcal{A}}(\Omega^{\text{f}}, t)$ where $\boldsymbol{\mathcal{A}} : \Omega^{\text{f}} \times \mathbb{R}^+ \to \mathbb{R}^3$ stands for the ALE map (see Figure 4.1), given by the relation $\boldsymbol{\mathcal{A}} = \boldsymbol{I}_{\Omega^{\text{f}}} + \boldsymbol{d}^{\text{f}}$ in terms of the fluid domain displacement $\boldsymbol{d}^{\text{f}} : \Omega \times \mathbb{R}^+ \to \mathbb{R}^3$. The symbol $\dot{\boldsymbol{d}}^{\text{f}} \overset{\text{def}}{=} \partial_t \boldsymbol{\mathcal{A}} = \partial_t \boldsymbol{d}^{\text{f}}$ denotes the fluid domain velocity, $\boldsymbol{F} \overset{\text{def}}{=} \boldsymbol{\nabla}\boldsymbol{\mathcal{A}}$ the gradient of deformation and $J \overset{\text{def}}{=} \det \boldsymbol{F}$ the Jacobian (see Section 1.2.1.2).

REMARK 4.1 *In order to ease the presentation, the change of variables* (1.3) *will not be specified in the following equations.*

4.2.2 The coupled fluid-structure problem

We will consider both cases in which the solid filament is modeled as a thick-walled (3D) solid or as a thin-walled (shell) solid.

4.2.2.1 Coupling with 3D solid model

We consider the ALE-Lagrangian coupled problem presented in Section 1.2.3.1. The coupled problem reads as follows: find the fluid domain displacement $\boldsymbol{d}^{\text{f}} : \Omega^{\text{f}} \times \mathbb{R}^+ \to \mathbb{R}^d$, the fluid velocity $\widehat{\boldsymbol{u}} : \Omega^{\text{f}} \times \mathbb{R}^+ \to \mathbb{R}^d$, the fluid pressure $\widehat{p} : \Omega^{\text{f}} \times \mathbb{R}^+ \to \mathbb{R}$, the structure displacement $\boldsymbol{d} : \Omega^{\text{s}} \times \mathbb{R}^+ \to \mathbb{R}^d$ and the structure velocity

$\dot{\boldsymbol{d}} : \Omega^{\mathrm{s}} \times \mathbb{R}^+ \to \mathbb{R}^d$, such that

$$\begin{cases} \rho^{\mathrm{f}} \partial_t \boldsymbol{u}|_{\boldsymbol{\mathcal{A}}} + \rho^{\mathrm{f}} (\boldsymbol{u} - \dot{\boldsymbol{d}}^{\mathrm{f}}) \cdot \boldsymbol{\nabla} \boldsymbol{u} - \mathbf{div} \boldsymbol{\sigma}(\boldsymbol{u}, p) = \rho^{\mathrm{f}} \boldsymbol{g} & \text{in} \quad \Omega^{\mathrm{f}}(t), \\ \mathrm{div} \boldsymbol{u} = 0 & \text{in} \quad \Omega^{\mathrm{f}}(t), \\ \boldsymbol{u} = \boldsymbol{0} & \text{on} \quad \Gamma_{\mathrm{wall}}, \\ \boldsymbol{u} = \boldsymbol{u}_{\mathrm{top}} & \text{on} \quad \Gamma_{\mathrm{top}}, \\ \boldsymbol{u} = \boldsymbol{u}_{\mathrm{bot}} & \text{on} \quad \Gamma_{\mathrm{bot}}, \\ \boldsymbol{\sigma}(\boldsymbol{u}, p) \boldsymbol{n} = -p_{\mathrm{out}} \boldsymbol{n} & \text{on} \quad \Gamma_{\mathrm{out}}, \end{cases} \tag{4.1}$$

$$\begin{cases} \rho^{\mathrm{s}} \partial_t \dot{\boldsymbol{d}} - \mathbf{div} \boldsymbol{\Pi}(\boldsymbol{d}, \dot{\boldsymbol{d}}) = \rho^{\mathrm{s}} \boldsymbol{g} & \text{in} \quad \Omega^{\mathrm{s}}, \\ \dot{\boldsymbol{d}} = \partial_t \boldsymbol{d} & \text{in} \quad \Omega^{\mathrm{s}}, \\ \boldsymbol{d} = \boldsymbol{0} & \text{on} \quad \Gamma^{\mathrm{s}}_{\mathrm{wall}}, \end{cases} \tag{4.2}$$

$$\begin{cases} \boldsymbol{d}^{\mathrm{f}} = \mathrm{Ext}\left(\boldsymbol{d}|_{\Sigma}\right), \quad \dot{\boldsymbol{d}}^{\mathrm{f}} = \partial_t \boldsymbol{d}^{\mathrm{f}}, \quad \boldsymbol{\mathcal{A}} = \boldsymbol{I}_{\Omega^{\mathrm{f}}} + \boldsymbol{d}^{\mathrm{f}}, \quad \Omega^{\mathrm{f}}(t) = \boldsymbol{\mathcal{A}}(\Omega^{\mathrm{f}}, t), \\ \boldsymbol{u} = \dot{\boldsymbol{d}} \quad \text{on} \quad \Sigma, \\ \boldsymbol{\Pi}(\boldsymbol{d}, \dot{\boldsymbol{d}}) \boldsymbol{n}^{\mathrm{s}} = -J \boldsymbol{\sigma}(\boldsymbol{u}, p) \boldsymbol{F}^{-\mathrm{T}} \boldsymbol{n} \quad \text{on} \quad \Sigma. \end{cases} \tag{4.3}$$

The velocity profiles, $\boldsymbol{u}_{\mathrm{top}}$ and $\boldsymbol{u}_{\mathrm{bot}}$, and the pressure field, p_{out}, are assumed to be given data on Γ_{top}, Γ_{bot} and Γ_{out}, respectively. Here, we use the expression (1.6) of the first Piola-Kirchhoff stress tensor, that we recall here for convenience,

$$\boldsymbol{\Pi}(\boldsymbol{d}, \dot{\boldsymbol{d}}) \overset{\mathrm{def}}{=} \boldsymbol{\Lambda}(\boldsymbol{d}) + \beta \boldsymbol{\partial}_{\boldsymbol{d}} \boldsymbol{\Lambda}(\boldsymbol{0}) \dot{\boldsymbol{d}},$$

with $\beta > 0$ the damping coefficient. The coupled system (4.1)-(4.3) is complemented with the following initial conditions

$$\boldsymbol{u}(0) = \boldsymbol{0}, \quad \boldsymbol{d}(0) = \boldsymbol{d}_0, \quad \dot{\boldsymbol{d}}(0) = \boldsymbol{0}, \tag{4.4}$$

where $\boldsymbol{d}_0$ denotes the displacement undergone by the solid in its hydrostatic equilibrium, viz., solution of (4.1)-(4.3) with $\boldsymbol{u}_{\mathrm{in}}^{\mathrm{top}} = \boldsymbol{u}_{\mathrm{in}}^{\mathrm{bot}} = \boldsymbol{0}$ (no flow conditions).

4.2.2.2 Coupling with thin-walled solid model

We consider the non-linear Reissner-Mindlin shell model of Section 2.3 with reference configuration given by the mid-surface of Ω^{s} (see Figure 4.2). As described in Section 1.2.3, we identify this mid-surface with the fluid-structure interface Σ and neglect shell thickness effects in the interface coupling.

We denote by $\Gamma^{\Sigma}_{\mathrm{wall}}$ the part of the boundary $\partial\Sigma$ that lies in $\Gamma^{\mathrm{s}}_{\mathrm{wall}}$. The interface Σ is assumed to be oriented by a unit surface normal vector field (pointing upwards) denoted by $\boldsymbol{n}^{\mathrm{s}}$. This defines a positive and a negative side in the fluid domain Ω^{f}, with respective unit normals $\boldsymbol{n}^+ \overset{\mathrm{def}}{=} \boldsymbol{n}^{\mathrm{s}}$ and $\boldsymbol{n}^- \overset{\mathrm{def}}{=} -\boldsymbol{n}^{\mathrm{s}}$ on Σ. For a given continuous scalar or tensorial field f defined in Ω^{f} (possibly discontinuous across Σ), we define its sided-restrictions to Σ, denoted by f^+ and f^-, as $f^+(\boldsymbol{x}) \overset{\mathrm{def}}{=} \lim_{\xi \to 0^+} f(\boldsymbol{x} + \xi \boldsymbol{n}^+)$ and $f^-(\boldsymbol{x}) \overset{\mathrm{def}}{=} \lim_{\xi \to 0^+} f(\boldsymbol{x} + \xi \boldsymbol{n}^-)$ for all $\boldsymbol{x} \in \Sigma$. We also define the following jumps

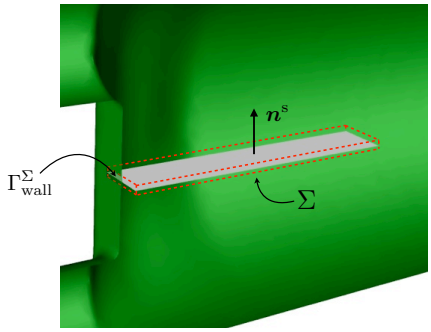

Figure 4.2: Shell mid-surface and virtual volume of displaced fluid.

across the interface Σ:

$$[\![f]\!] \overset{\text{def}}{=} f^+ - f^-, \quad [\![f\boldsymbol{n}]\!] \overset{\text{def}}{=} f^+\boldsymbol{n}^+ + f^-\boldsymbol{n}^-.$$

In this framework, the resulting coupled fluid-structure problem reads as follows: find the fluid domain displacement $\boldsymbol{d}^{\text{f}} : \Omega^{\text{f}} \times \mathbb{R}^+ \to \mathbb{R}^d$, the fluid velocity $\boldsymbol{u} : \Omega^{\text{f}} \times \mathbb{R}^+ \to \mathbb{R}^d$, the fluid pressure $p : \Omega^{\text{f}} \times \mathbb{R}^+ \to \mathbb{R}$, the solid mid-surface displacement $\boldsymbol{d} : \Sigma \times \mathbb{R}^+ \to \mathbb{R}^3$ and the director vector $\boldsymbol{a} : \Sigma \times \mathbb{R}^+ \to \mathbb{R}^3$ of unit length $|\boldsymbol{a}| = 1$, such that (4.1) and

$$\begin{cases} \rho^{\text{s}}\epsilon\partial_t\dot{\boldsymbol{d}} + \boldsymbol{L}^{\text{e}}_{\boldsymbol{d}}(\boldsymbol{d},\boldsymbol{a}) + \boldsymbol{L}^{\text{v}}\dot{\boldsymbol{d}} = \boldsymbol{f}^{\text{f}} + (\rho^{\text{s}} - \rho^{\text{f}})\epsilon\boldsymbol{g} & \text{on} \quad \Sigma, \\ \boldsymbol{L}^{\text{e}}_{\boldsymbol{a}}(\boldsymbol{d},\boldsymbol{a}) = \boldsymbol{0} & \text{on} \quad \Sigma, \\ \dot{\boldsymbol{d}} = \partial_t\boldsymbol{d}, & \text{on} \quad \Sigma, \\ \boldsymbol{d} = \boldsymbol{0}, \quad \boldsymbol{a} = \boldsymbol{n}^{\text{s}} & \text{on} \quad \Gamma^\Sigma_{\text{wall}}, \end{cases} \tag{4.5}$$

$$\begin{cases} \boldsymbol{d}^{\text{f}} = \text{Ext}\left(\boldsymbol{d}|_\Sigma\right), \quad \dot{\boldsymbol{d}}^{\text{f}} = \partial_t\boldsymbol{d}^{\text{f}}, \quad \boldsymbol{\mathcal{A}} = \boldsymbol{I}_{\Omega^{\text{f}}} + \boldsymbol{d}^{\text{f}}, \quad \Omega^{\text{f}}(t) = \boldsymbol{\mathcal{A}}(\Omega^{\text{f}}, t), \\ \boldsymbol{u} = \dot{\boldsymbol{d}} \quad \text{on} \quad \Sigma, \\ \boldsymbol{f}^{\text{f}} = -[\![J\boldsymbol{\sigma}(\boldsymbol{u},p)(\boldsymbol{F})^{-\text{T}}\boldsymbol{n}]\!] \quad \text{on} \quad \Sigma, \end{cases} \tag{4.6}$$

hold for all $t > 0$. Physical damping is modeled through (2.31) with $\alpha = 0$, viz.,

$$\boldsymbol{L}^{\text{v}}\dot{\boldsymbol{d}} \overset{\text{def}}{=} \beta\boldsymbol{\partial}_{\boldsymbol{d}}\boldsymbol{L}^{\text{e}}(\boldsymbol{0},\boldsymbol{0})\dot{\boldsymbol{d}},$$

with $\beta > 0$. Rotational inertia is neglected, and gravitational effects are taken into account through the surface force $\rho^{\text{s}}\epsilon\boldsymbol{g}$. Note that, since the solid is geometrically assimilated to a surface, it does not displace any fluid and, hence, no buoyant force is undergone by the structure. This is corrected by including the buoyant force in an approximate static manner, namely, by adding the Archimedes surface force term $-\rho^{\text{f}}\epsilon\boldsymbol{g}$.

As pointed out in Section 1.2.3.2, the jump of the hydrodynamic stress through the immersed solid results in pressure and velocity solutions that are, respectively, strongly and weakly discontinuous along the moving fluid-structure interface. This

requires a specific treatment at the discrete level (see Section 4.3.2).

4.2.3 Fluid

Two different experimental phases, corresponding to a stationary or a pulsatile flow regime, are considered (see [Nor15]). In (4.1) we take $\boldsymbol{g} = -g\mathbf{e}_y$ with $g \stackrel{\text{def}}{=} 9.80665 \cdot 10^3\ mm\ s^{-2}$. An hydrostatic pressure profile of the form

$$p_{\text{out}}(y) = p_0 - \rho^{\text{f}} g\,(y - y_0)\,,$$

is prescribed on the outlet boundary Γ_{out}, where $p_0 = 1782.7\ Pa$ is a given pressure value measured at point $(30.00, -26.38, 160.20)$ (the red point in Figure 4.1).

4.2.3.1 Phase I experiment

During this phase, the fluid is pumped in the domain with a constant flow rate. The z-components of the inlet velocity profiles $\boldsymbol{u}_{\text{top}}$ and $\boldsymbol{u}_{\text{bot}}$ are parabolic with a peak velocity of 630 $mm\ s^{-1}$ and 615 $mm\ s^{-1}$, respectively. The other components are set to zero. The density and dynamic viscosity of the fluid are given in Table 4.1. These values were measured with the glycerol at a temperature of $T = 23.6$ °C (see [Nor15]).

ρ^{f}	μ
$1.1633 \cdot 10^{-3}\ g\ mm^{-3}$	$12.5 \cdot 10^{-3}\ g\ mm^{-1}\ s^{-1}$

Table 4.1: Fluid physical parameters (Phase I experiment).

4.2.3.2 Phase II experiment

In the second phase of the experiment, the fluid is pumped with a pulsatile flow rate of frequency $f = 1/6\ s^{-1}$. The profiles of the $x-$, $y-$ and $z-$ components of $\boldsymbol{u}_{\text{top}}$ are parabolic with peak values over time given in Figure 4.3. The $z-$ and $x-$ components of the bottom inlet velocity $\boldsymbol{u}_{\text{bot}}$ are the same as in $\boldsymbol{u}_{\text{top}}$, but its $y-$component is set to zero. The density and dynamic viscosity of the fluid are given in Table 4.2. In this case, the measurements were obtained for the glycerol at $T = 22$ °C (see [Nor15]).

ρ^{f}	μ
$1.164 \cdot 10^{-3}\ g\ mm^{-3}$	$13.37 \cdot 10^{-3}\ g\ mm^{-1}\ s^{-1}$

Table 4.2: Fluid physical parameters (Phase II experiment).

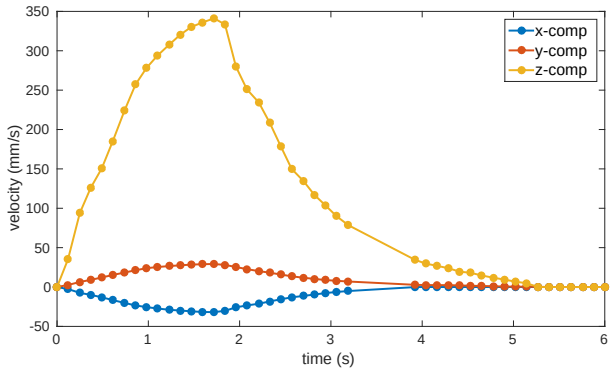

Figure 4.3: Measured peak values in the $x-$, $y-$ and $z-$ components of the inlet velocity $\boldsymbol{u}_{\text{top}}$.

4.2.4 Solid

The silicone filament is assumed to be homogeneous. Its elastic properties are described with the Saint Venant-Kirchhoff model (1.8). The density and damping coefficient for the solid are given in Table 4.3.

ρ^{s}	β
$1.063 \cdot 10^{-3}\ g\ mm^{-3}$	$2.5 \cdot 10^{-4}\ s^{-1}$

Table 4.3: Solid physical parameters (Phase I and II experiments).

4.2.4.1 Solid parameters estimation

Young's modulus E and the Poisson ratio ν for the silicone were determined from the data obtained in the *uniaxial traction test* (see [Nor15]). For each loading step we computed the component of the second Piola-Kirchhoff stress tensor in the traction direction, i.e., along the z-axis, the corresponding component of the Green-Lagrange strain tensor (1.7), and the transverse component of this same strain tensor. Retaining only the first 20 loading steps, linear regression was performed to estimate Young's modulus and the Poisson ratio, yielding the values given in Table 4.4. Figure 4.4 compares the regressions with the experimental points of the complete dataset. We can see that the linear regression is quite accurate for extension rates of up to 25%, which justifies the use of a linear stress-strain law - namely, the Saint Venant-Kirchhoff constitutive equation - for representing the behavior of this material in the stress-strain ranges of practical interest in our study.

4.3 Numerical methods

This section presents the numerical methods considered in this chapter for the approximation of the coupled problems (4.1)-(4.3) and (4.1), (4.5)-(4.6). Sec-

E	ν
$2.1626 \cdot 10^5\ Pa$	0.3151

Table 4.4: Estimated constitutive parameters (Young's modulus E and Poisson ratio ν) based on uniaxial traction data from [Nor15].

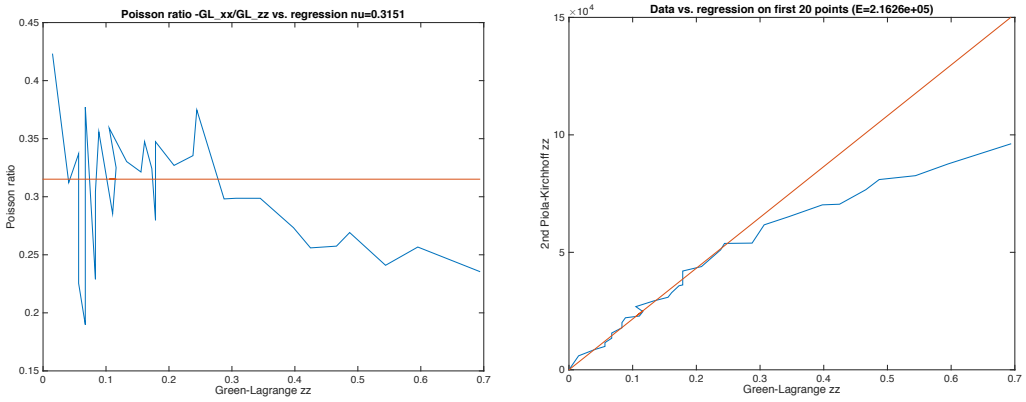

(a) ν (b) E

Figure 4.4: Poisson ration and Young's modulus regressions.

tion 4.3.1 is devoted to the discretization in time and to the fluid-solid splitting schemes. Some ingredients of the spatial discretization are given in Section 4.3.2. Finally, Section 4.3.3 presents the mesh update technique in the fluid, namely, the discrete counterpart of the extension operator $\mathrm{Ext}(\cdot)$.

4.3.1 Time discretization: coupling schemes

In what follows, the symbol $\tau > 0$ denotes the time-step length, $t_n \overset{\text{def}}{=} n\tau$, for $n \in \mathbb{N}$ and $\partial_\tau x^n \overset{\text{def}}{=} \left(x^n - x^{n-1}\right)/\tau$ the first-order backward difference in time. For the time discretization of the fluid subsystem (4.1) we will consider either the following monolithic backward Euler scheme:

$$\begin{cases} \rho^{\mathrm{f}} \partial_\tau|_{\boldsymbol{\mathcal{A}}} \boldsymbol{u}^n + \rho^{\mathrm{f}}(\boldsymbol{u}^{n-1} - \dot{\boldsymbol{d}}^{\mathrm{f},n}) \cdot \boldsymbol{\nabla} \boldsymbol{u}^n - \mathbf{div}\boldsymbol{\sigma}(\boldsymbol{u}^n, p^n) = \rho^{\mathrm{f}} \boldsymbol{g}, & \text{in} \quad \Omega^{\mathrm{f},n}, \\ \mathrm{div}\boldsymbol{u}^n = 0 & \text{in} \quad \Omega^{\mathrm{f},n}, \\ \boldsymbol{u}^n = \boldsymbol{0} & \text{on} \quad \Gamma_{\mathrm{wall}}, \\ \boldsymbol{u}^n = \boldsymbol{u}^n_{\mathrm{top}} & \text{on} \quad \Gamma_{\mathrm{top}}, \\ \boldsymbol{u}^n = \boldsymbol{u}^n_{\mathrm{bot}} & \text{on} \quad \Gamma_{\mathrm{bot}}, \\ \boldsymbol{\sigma}(\boldsymbol{u}^n, p^n)\boldsymbol{n} = -p^n_{\mathrm{out}} \boldsymbol{n} & \text{on} \quad \Gamma_{\mathrm{out}}; \end{cases} \tag{4.7}$$

or the following incremental pressure-correction scheme:

1. Fluid convective-viscous substep:

$$\begin{cases} \rho^{\mathrm{f}} \dfrac{\tilde{\boldsymbol{u}}^n - \boldsymbol{u}^{n-1}}{\tau}\Big|_{\boldsymbol{\mathcal{A}}} + \rho^{\mathrm{f}}\big(\tilde{\boldsymbol{u}}^{n-1} - \dot{\boldsymbol{d}}^{\mathrm{f},n}\big)\cdot\boldsymbol{\nabla}\tilde{\boldsymbol{u}}^n - \mathbf{div}\boldsymbol{\sigma}(\tilde{\boldsymbol{u}}^n, p^{n-1}) = \mathbf{0} & \text{in} \quad \Omega^{\mathrm{f},n}, \\ \tilde{\boldsymbol{u}}^n = \mathbf{0} & \text{on} \quad \Gamma_{\mathrm{wall}}, \\ \tilde{\boldsymbol{u}}^n = \boldsymbol{u}^n_{\mathrm{top}} & \text{on} \quad \Gamma_{\mathrm{top}}, \\ \tilde{\boldsymbol{u}}^n = \boldsymbol{u}^n_{\mathrm{bot}} & \text{on} \quad \Gamma_{\mathrm{bot}}, \\ \boldsymbol{\sigma}(\tilde{\boldsymbol{u}}^n, p^{n-1})\boldsymbol{n} = -p^{n-1}_{\mathrm{out}}\boldsymbol{n} & \text{on} \quad \Gamma_{\mathrm{out}}, \end{cases} \tag{4.8}$$

2. Fluid projection substep:

$$\begin{cases} -\dfrac{\tau}{\rho^{\mathrm{f}}}\Delta\phi^n = -\mathrm{div}\tilde{\boldsymbol{u}}^n & \text{in} \quad \Omega^{\mathrm{f},n}, \\ \dfrac{\tau}{\rho^{\mathrm{f}}}\dfrac{\partial\phi^n}{\partial\boldsymbol{n}} = 0 & \text{on} \quad \Gamma_{\mathrm{top}}\cup\Gamma_{\mathrm{bot}}, \\ \phi^n = p^n_{\mathrm{out}} - p^{n-1} & \text{on} \quad \Gamma_{\mathrm{out}}, \end{cases} \tag{4.9}$$

and thereafter we set $p^n = \phi^n + p^{n-1}$, $\boldsymbol{u}^n = \tilde{\boldsymbol{u}}^n - \dfrac{\tau}{\rho^{\mathrm{f}}}\boldsymbol{\nabla}\phi^n$ in Ω^{f}.

Note that a standard semi-implicit treatment of the convective term is employed in (4.7) and in (4.8). For the solid, we consider a backward Euler time-stepping of the 3D solid subsystem (4.2),

$$\begin{cases} \rho^{\mathrm{s}}\partial_\tau\dot{\boldsymbol{d}}^n - \mathbf{div}\boldsymbol{\Pi}^n = \rho^{\mathrm{s}}\boldsymbol{g} & \text{in} \quad \Omega^{\mathrm{s}}, \\ \dot{\boldsymbol{d}}^n = \partial_\tau\boldsymbol{d}^n & \text{in} \quad \Omega^{\mathrm{s}}, \\ \boldsymbol{d}^n = \mathbf{0} & \text{on} \quad \Gamma^{\mathrm{s}}_{\mathrm{wall}}, \end{cases} \tag{4.10}$$

with the notation $\boldsymbol{\Pi}^n \overset{\mathrm{def}}{=} \boldsymbol{\Lambda}(\boldsymbol{d}^n) + \beta\boldsymbol{\partial_d}\boldsymbol{\Lambda}(\mathbf{0})\dot{\boldsymbol{d}}^n$. The shell subsystem (4.5) is also discretized as

$$\begin{cases} \rho^{\mathrm{s}}\epsilon\partial_\tau\dot{\boldsymbol{d}}^n + \boldsymbol{L}^{\mathrm{e}}_{\boldsymbol{d}}(\boldsymbol{d}^n, \boldsymbol{a}^n) + \boldsymbol{L}^{\mathrm{v}}\dot{\boldsymbol{d}}^n = \boldsymbol{f}^{\mathrm{f},n} + (\rho^{\mathrm{s}} - \rho^{\mathrm{f}})\epsilon\boldsymbol{g} & \text{on} \quad \Sigma, \\ \boldsymbol{L}^{\mathrm{e}}_{\boldsymbol{a}}(\boldsymbol{d}^n, \boldsymbol{a}^n) = \mathbf{0} & \text{on} \quad \Sigma, \\ \dot{\boldsymbol{d}}^n = \partial_\tau\boldsymbol{d}^n & \text{on} \quad \Sigma, \\ \boldsymbol{d}^n = \mathbf{0}, \quad \boldsymbol{a}^n = \boldsymbol{n}^{\mathrm{s}} & \text{on} \quad \Gamma^{\Sigma}_{\mathrm{wall}}. \end{cases} \tag{4.11}$$

REMARK 4.2 *Second-order time-stepping may be considered in the solid. Preliminary results (not reported here) showed, however, no significant differences with respect to the first-order time-stepping adopted in* (4.10) *and* (4.11).

In all the forthcoming solution procedures, we adopt an explicit treatment of the geometric compatibility condition $(4.3)_1$, namely,

$$\boldsymbol{d}^{\mathrm{f},n} = \mathrm{Ext}(\boldsymbol{d}^{n-1}|_\Sigma), \quad \dot{\boldsymbol{d}}^{\mathrm{f},n} = \partial_\tau\boldsymbol{d}^{\mathrm{f},n}, \quad \boldsymbol{\mathcal{A}}^n \overset{\mathrm{def}}{=} \boldsymbol{I}_{\Omega^{\mathrm{f}}} + \boldsymbol{d}^{\mathrm{f},n}, \quad \Omega^{\mathrm{f},n} \overset{\mathrm{def}}{=} \boldsymbol{\mathcal{A}}^n\big(\Omega^{\mathrm{f}}\big) \tag{4.12}$$

and thereafter we set $\boldsymbol{F}^n \overset{\text{def}}{=} \boldsymbol{\nabla}\boldsymbol{\mathcal{A}}^n$ and $J^n \overset{\text{def}}{=} \det \boldsymbol{F}^n$ (see Remark 2.11). The numerical methods presented in the next paragraphs mainly differ on the time-stepping of the interface conditions $(4.3)_{2,3}$.

4.3.1.1 Strongly coupled schemes

The first class of numerical methods considered in this paper performs a fully implicit treatment of the kinematic and dynamic coupling conditions $(4.3)_{2,3}$ and $(4.6)_{2,3}$. This yields the time-marching schemes reported in Algorithms 4.1 and 4.2. We recall that schemes for which (4.13) or (4.14) hold are often referred to in the literature as strongly coupled (See Section 1.3.2.1). Basically, their main advantage lies in the fact that they induce a correct discrete energy balance across the interface and, hence, guarantee energy stability (see, e.g., [SS06, BNV08, SM08, NPV13]).

Algorithm 4.1 Strongly coupled scheme (coupling with 3D solid).

For $n \geq 1$:

1. Update fluid domain via (4.12);
2. Find $\boldsymbol{u}^n : \Omega^{\mathrm{f}} \to \mathbb{R}^3$, $p^n : \Omega^{\mathrm{f}} \to \mathbb{R}$, $\boldsymbol{d}^n : \Omega^{\mathrm{s}} \to \mathbb{R}^3$ and $\dot{\boldsymbol{d}}^n : \Omega^{\mathrm{s}} \to \mathbb{R}^3$ satisfying (4.7), (4.10) and

$$\begin{cases} \boldsymbol{u}^n = \dot{\boldsymbol{d}}^n & \text{on} \quad \Sigma, \\ \boldsymbol{\Pi}^n \boldsymbol{n}^{\mathrm{s}} = -J^n \boldsymbol{\sigma}(\boldsymbol{u}^n, p^n)(\boldsymbol{F}^n)^{-\mathrm{T}} \boldsymbol{n} & \text{on} \quad \Sigma. \end{cases} \tag{4.13}$$

The price to pay for this superior stability is the resolution of a highly-coupled nonlinear system at each time-step (Step 2 of Algorithms 4.1 and 4.2), which can be computationally demanding in practice. In this work, we consider the partitioned solution strategy proposed in [FM05], which involves interface Dirichlet-Neumann GMRES iterations.

Algorithm 4.2 Strongly coupled scheme (coupling with thin-walled solid).

For $n \geq 1$:

1. Update fluid domain via (4.12);
2. Find $\boldsymbol{u}^n : \Omega^{\mathrm{f}} \to \mathbb{R}^3$, $p^n : \Omega^{\mathrm{f}} \to \mathbb{R}$, $\boldsymbol{d}^n : \Sigma \to \mathbb{R}^3$, $\dot{\boldsymbol{d}}^n : \Sigma \to \mathbb{R}^3$ and $\boldsymbol{a}^n : \Sigma \to \mathbb{R}^3$ with $|\boldsymbol{a}^n| = 1$, satisfying (4.7), (4.11) and

$$\begin{cases} \boldsymbol{u}^n = \dot{\boldsymbol{d}}^n & \text{on} \quad \Sigma, \\ \boldsymbol{f}^{\mathrm{f},n} = -[\![J^n \boldsymbol{\sigma}(\boldsymbol{u}^n, p^n)(\boldsymbol{F}^n)^{-\mathrm{T}} \boldsymbol{n}]\!] & \text{on} \quad \Sigma. \end{cases} \tag{4.14}$$

4.3.1.2 Projection-based semi-implicit coupling schemes

In this section we consider a suitable non-linear formulation of the incremental projection-based semi-implicit scheme reported in Section 1.4.3.2. The resulting scheme avoids strong coupling without compromising stability and accuracy. The fundamental idea consists in combining the fractional-step time-marching in the fluid (4.8)-(4.9) with a specific explicit-implicit treatment of the kinematic and dynamic coupling conditions $(4.3)_{2,3}$ and $(4.6)_{2,3}$. The solution procedures are detailed in Algorithms 4.3 and 4.4.

ALGORITHM 4.3 Semi-implicit coupling scheme (coupling with 3D solid).

For $n \geq 2$:

1. Update the fluid domain via (4.12);
2. Explicit step: find $\tilde{\boldsymbol{u}}^n : \Omega^{\mathrm{f}} \to \mathbb{R}^3$ satisfying (4.8) and
$$\tilde{\boldsymbol{u}}^n = \dot{\boldsymbol{d}}^{n-1} \quad \text{on} \quad \Sigma.$$
3. Implicit step: find $\phi^n : \Omega^{\mathrm{f}} \to \mathbb{R}$, $\boldsymbol{d}^n : \Omega^{\mathrm{s}} \to \mathbb{R}^3$ and $\dot{\boldsymbol{d}}^n : \Omega^{\mathrm{s}} \to \mathbb{R}^3$, satisfying (4.9), (4.10) and
$$\begin{cases} \dfrac{\tau}{\rho^{\mathrm{f}}} \dfrac{\partial \phi^n}{\partial \boldsymbol{n}} = \left(\tilde{\boldsymbol{u}}^n - \dot{\boldsymbol{d}}^n\right) \cdot \boldsymbol{n} & \text{on} \quad \Sigma, \\ \boldsymbol{\Pi}^n \boldsymbol{n}^{\mathrm{s}} = -J^n \boldsymbol{\sigma}(\tilde{\boldsymbol{u}}^n, p^n)(\boldsymbol{F}^n)^{-\mathrm{T}} \boldsymbol{n} & \text{on} \quad \Sigma. \end{cases}$$

ALGORITHM 4.4 Semi-implicit coupling scheme (coupling with thin-walled solid).

For $n \geq 2$:

1. Update the fluid domain via (4.12);
2. Explicit step: find $\tilde{\boldsymbol{u}}^n : \Omega^{\mathrm{f}} \to \mathbb{R}^3$ satisfying (4.8) and
$$\tilde{\boldsymbol{u}}^n = \dot{\boldsymbol{d}}^{n-1} \quad \text{on} \quad \Sigma.$$
3. Implicit step: find $\phi^n : \Omega^{\mathrm{f}} \to \mathbb{R}$, $\boldsymbol{d}^n : \Sigma \to \mathbb{R}^3$ and $\boldsymbol{a}^n : \Sigma \to \mathbb{R}^3$ with $|\boldsymbol{a}^n| = 1$, satisfying (4.9), (4.11) and
$$\begin{cases} \dfrac{\tau}{\rho^{\mathrm{f}}} \dfrac{\partial \phi^n}{\partial \boldsymbol{n}} = \left(\tilde{\boldsymbol{u}}^n - \dot{\boldsymbol{d}}^n\right) \cdot \boldsymbol{n} & \text{on} \quad \Sigma, \\ \boldsymbol{f}^{\mathrm{f},n} = -[\![J^n \boldsymbol{\sigma}(\tilde{\boldsymbol{u}}^n, p^n)(\boldsymbol{F}^n)^{-\mathrm{T}} \boldsymbol{n}]\!] & \text{on} \quad \Sigma. \end{cases}$$

The fluid convective-viscous step (4.8) is explicitly coupled with the solid, this reduces computational complexity without compromising stability. On the other

hand, the fluid projection step (4.9) is implicitly coupled to the solid to avoid added-mass stability issues (see Section 1.4.3.2). Note that this implicit part of the coupling (i.e., Step 3 of Algorithms 4.3 and 4.4) is less computationally onerous than Step 2 of Algorithms 4.1 and 4.2. In this work, the resulting pressure-solid systems are solved via interface Neumann-Neumann GMRES iterations.

4.3.1.3 Explicit coupling chemes

In this section, we focus on the case of the coupling with a thin-walled solid model, namely, the coupled problem (4.1), (4.5)-(4.6). We consider suitable non-linear formulations of the Robin-Neumann explicit coupling scheme (with $r = 1$) reported in Section 1.4.3.5 and of the fully decoupled scheme (with $s = 1$, $r = 1$) introduced in Chapter 2. The resulting methods perform a complete splitting of the fluid and solid time-steppings. The fundamental ingredient in the derivation of these methods (see Sections 1.4.3.5 and 2.2) is the notion of interface Robin consistency. For the problem at hand, it reads

$$[\![J\boldsymbol{\sigma}(\boldsymbol{u},p)\boldsymbol{F}^{-\mathrm{T}}\boldsymbol{n}]\!] + \rho^{\mathrm{s}}\epsilon\partial_t\boldsymbol{u} = -\boldsymbol{L}^{\mathrm{e}}_{\boldsymbol{d}}(\boldsymbol{d},\boldsymbol{a}) - \boldsymbol{L}^{\mathrm{v}}\dot{\boldsymbol{d}} + (\rho^{\mathrm{s}}-\rho^{\mathrm{f}})\epsilon\boldsymbol{g} \quad \text{on} \quad \Sigma, \tag{4.15}$$

owing to $(4.5)_1$ and $(4.6)_{2,3}$. The key idea is hence to perform the fluid-solid splitting by discretizing in time (4.15) instead of $(4.6)_2$. Then, owing to the dynamic coupling condition $(4.6)_3$, the resulting interface fluid stresses are transferred to the thin-walled solid through the "Neumann"-like relation

$$\boldsymbol{f}^{\mathrm{f},n} = -[\![J^n\boldsymbol{\sigma}(\boldsymbol{u}^n,p^n)(\boldsymbol{F}^n)^{-\mathrm{T}}\boldsymbol{n}]\!] \quad \text{on} \quad \Sigma. \tag{4.16}$$

Robin-Neumann explicit coupling scheme. Following Section 1.4.3.5, the consistent interface relation (4.15) is discretized in time as

$$\begin{aligned}[\![J^n\boldsymbol{\sigma}(\boldsymbol{u}^n,p^n)(\boldsymbol{F}^n)^{-\mathrm{T}}\boldsymbol{n}]\!] + \frac{\rho^{\mathrm{s}}\epsilon}{\tau}\boldsymbol{u}^n = \frac{\rho^{\mathrm{s}}\epsilon}{\tau}\dot{\boldsymbol{d}}^{n-1} \\ - \boldsymbol{L}^{\mathrm{e}}_{\boldsymbol{d}}(\boldsymbol{d}^{n-1},\boldsymbol{a}^{n-1}) - \boldsymbol{L}^{\mathrm{v}}\dot{\boldsymbol{d}}^{n-1} + (\rho^{\mathrm{s}}-\rho^{\mathrm{f}})\epsilon\boldsymbol{g} \quad \text{on} \quad \Sigma,\end{aligned} \tag{4.17}$$

which provides an explicit Robin condition for the fluid sub-system (4.7). Note that the solid inertia is implicitly coupled to the fluid, via the Robin term in the left-hand side of (4.17), while the solid viscoelastic terms are treated explicitly in (4.17). The first guarantees (added-mass free) stability whereas the second enables the splitting between the fluid and solid time-steppings.

Owing to (4.11) and (4.16), for $n \geq 2$ the Robin condition (4.17) can be reformulated in a more convenient fashion as follows

$$\begin{aligned}[\![J^n\boldsymbol{\sigma}(\boldsymbol{u}^n,p^n)(\boldsymbol{F}^n)^{-\mathrm{T}}\boldsymbol{n}]\!] + \frac{\rho^{\mathrm{s}}\epsilon}{\tau}\boldsymbol{u}^n \\ = \frac{\rho^{\mathrm{s}}\epsilon}{\tau}\big(\dot{\boldsymbol{d}}^{n-1} + \tau\partial_\tau\dot{\boldsymbol{d}}^{n-1}\big) + [\![J^{n-1}\boldsymbol{\sigma}(\boldsymbol{u}^{n-1},p^{n-1})(\boldsymbol{F}^{n-1})^{-\mathrm{T}}\boldsymbol{n}]\!] \quad \text{on} \quad \Sigma.\end{aligned}$$

ALGORITHM 4.5 Robin-Neumann explicit coupled scheme.

For $n \geq 2$:

1. Update the fluid domain via (4.12);
2. Fluid step: find $\boldsymbol{u}^n : \Omega^{\mathrm{f}} \to \mathbb{R}^3$ and $p^n : \Omega^{\mathrm{f}} \to \mathbb{R}$ satisfying (4.7) and

$$\begin{aligned}\llbracket J^n \boldsymbol{\sigma}(\boldsymbol{u}^n, p^n)(\boldsymbol{F}^n)^{-\mathrm{T}} \boldsymbol{n} \rrbracket + \frac{\rho^{\mathrm{s}} \epsilon}{\tau} \boldsymbol{u}^n = \frac{\rho^{\mathrm{s}} \epsilon}{\tau} \big(\dot{\boldsymbol{d}}^{n-1} + \tau \partial_\tau \dot{\boldsymbol{d}}^{n-1} \big) \\ + \llbracket J^{n-1} \boldsymbol{\sigma}(\boldsymbol{u}^{n-1}, p^{n-1})(\boldsymbol{F}^{n-1})^{-\mathrm{T}} \boldsymbol{n} \rrbracket \quad \text{on} \quad \Sigma.\end{aligned}$$

3. Solid step: $\boldsymbol{d}^n : \Sigma \to \mathbb{R}^3$, $\dot{\boldsymbol{d}}^n : \Sigma \to \mathbb{R}^3$ and $\boldsymbol{a}^n : \Sigma \to \mathbb{R}^3$ with $|\boldsymbol{a}^n| = 1$, satisfying (4.11) and

$$\boldsymbol{f}^{\mathrm{f},n} = -\llbracket J^n \boldsymbol{\sigma}(\boldsymbol{u}^n, p^n)(\boldsymbol{F}^n)^{-\mathrm{T}} \boldsymbol{n} \rrbracket \quad \text{on} \quad \Sigma.$$

ALGORITHM 4.6 Fully decoupled scheme (based on Chapter 2).

For $n \geq 2$:

1. Update the fluid domain via (4.12);
2. Fluid viscous substep: find $\tilde{\boldsymbol{u}}^n : \Omega^{\mathrm{f}} \to \mathbb{R}^3$ satisfying (4.8) and

$$\begin{aligned}\llbracket J^n \boldsymbol{\sigma}(\tilde{\boldsymbol{u}}^n, p^{n-1})(\boldsymbol{F}^n)^{-\mathrm{T}} \boldsymbol{n} \rrbracket + \frac{\rho^{\mathrm{s}} \epsilon}{\tau} \tilde{\boldsymbol{u}}^n = \frac{\rho^{\mathrm{s}} \epsilon}{\tau} \big(\dot{\boldsymbol{d}}^{n-1} + \tau \partial_\tau \dot{\boldsymbol{d}}_{\parallel}^{n-1} \big) \\ + 2\mu \big(J \boldsymbol{\varepsilon}(\tilde{\boldsymbol{u}}) \boldsymbol{F}^{-\mathrm{T}} \boldsymbol{n} \big)_{\parallel}^{n-1} \quad \text{on} \quad \Sigma.\end{aligned}$$

3. Fluid projection substep: find $\phi^n : \Omega^{\mathrm{f}} \to \mathbb{R}$ satisfying (4.9) and

$$\frac{\tau}{\rho^{\mathrm{f}}} \frac{\partial \phi^n}{\partial \boldsymbol{n}} + \frac{\tau}{\rho^{\mathrm{s}} \epsilon} \llbracket \phi^n \rrbracket = \frac{\tau}{\rho^{\mathrm{s}} \epsilon} \llbracket \phi^{n-1} \rrbracket + \big(\tilde{\boldsymbol{u}}^{n-1} - \dot{\boldsymbol{d}}^{n-1} \big) \cdot \boldsymbol{n} \quad \text{on} \quad \Sigma.$$

4. Solid step: find $\boldsymbol{d}^n : \Sigma \to \mathbb{R}^3$, $\dot{\boldsymbol{d}}^n : \Sigma \to \mathbb{R}^3$ and $\boldsymbol{a}^n : \Sigma \to \mathbb{R}^3$ with $|\boldsymbol{a}^n| = 1$, satisfying (4.11) and

$$\boldsymbol{f}^{\mathrm{f},n} = -\llbracket J^n \boldsymbol{\sigma}(\tilde{\boldsymbol{u}}^n, p^n)(\boldsymbol{F}^n)^{-\mathrm{T}} \boldsymbol{n} \rrbracket \quad \text{on} \quad \Sigma.$$

The complete explicit coupling scheme is reported in Algorithm 4.5.

Fully decoupled scheme. Using the arguments reported in Chapter 2, the above explicit Robin-Neumann paradigm can also be effectively combined with the fractional-step fluid time-stepping (4.8)-(4.9). The resulting method is presented in Algorithm 4.6. A salient feature of this solution procedure is that it enables a fully

decoupled sequential computation of the whole fluid-solid state: $\boldsymbol{u}^n$, p^n and $(\boldsymbol{d}^n, \boldsymbol{a}^n)$.

4.3.2 Space discretization

In Phase I, we take advantage of the symmetry of the problem along the $z-$axis to reduce the computational domain to half of the physical domain (see Figures 4.5(a) and 4.6(a)). A symmetry boundary condition is enforced on the symmetry plane $\Gamma_{\text{sym}} \overset{\text{def}}{=} \{x = 0\}$:

$$\boldsymbol{u} \cdot \boldsymbol{n} = 0, \quad (\boldsymbol{\sigma}(\boldsymbol{u}, p)\boldsymbol{n})_{\|} = \boldsymbol{0} \quad \text{on} \quad \Gamma_{\text{sym}}.$$

The entire physical domain is considered as computational domain in Phase II. The fluid domain is discretized with a tetrahedral mesh $\mathcal{T}_h$ (see Figures 4.5 and 4.6), whereas a hexahedral $\mathcal{H}_h$ or quadrilateral mesh $\mathcal{Q}_h$ is considered for the solid domain, depending on wether it is a volume (see Figure 4.5) or a surface (see Figure 4.6). The meshes are built in such a way that the nodes lying on the interface are matching (see [GVF05]). The current fluid mesh $\mathcal{T}_h^n$ of $\Omega^{\text{f},n}$ is obtained by displacing the nodes of $\mathcal{T}_h$ by $\boldsymbol{d}_h^{\text{f},n}$ (see Section 4.3.3).

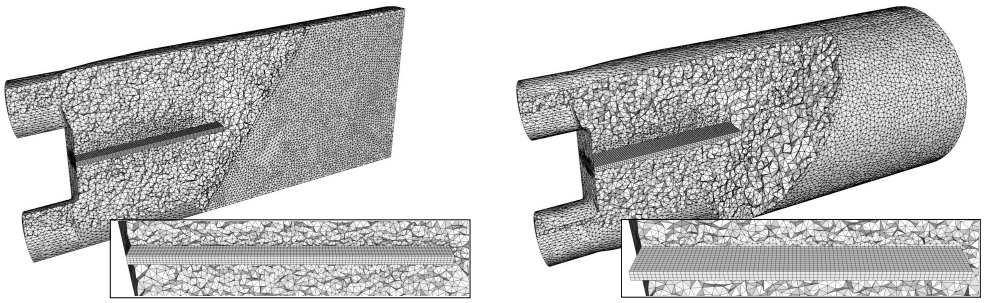

(a) $\mathcal{T}_h$: 485331 tetrahedra, $\mathcal{H}_h$: 4000 hexahedra.

(b) $\mathcal{T}_h$: 624440 tetrahedra, $\mathcal{H}_h$: 3840 hexahedra.

Figure 4.5: Meshes for 3D solid model.

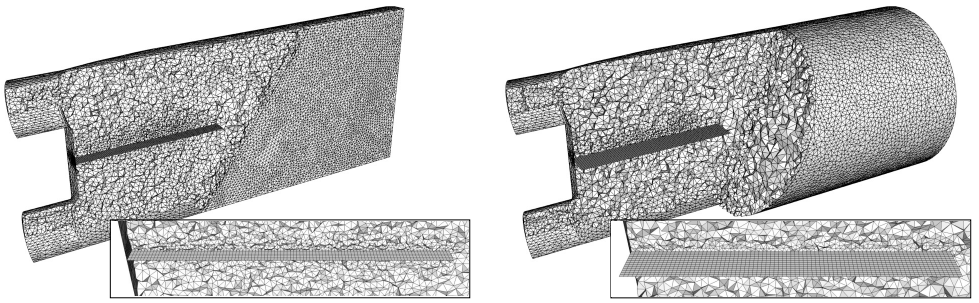

(a) $\mathcal{T}_h$: 476810 tetrahedra, $\mathcal{Q}_h$: 1000 quadrilaterals.

(b) $\mathcal{T}_h$: 609752 tetrahedra, $\mathcal{Q}_h$: 1280 quadrilaterals.

Figure 4.6: Meshes for shell solid model.

The fluid equations are discretized in space using $\mathbb{P}_1$ finite elements. As usual, we use the subscript h to denote the discrete approximations. For Algorithms 4.1, 4.2 and 4.5, we resort to the SUPG/PSPG method to stabilize the velocity/pressure pair and the convective effects (see, e.g., [Tez92]). Furthermore, a *backflow stabilization method* is used in the outlet boundary (see, e.g., [MBH+11, BGH+09]). In summary, we add the following stabilization terms to the fully discrete fluid problem:

$$\sum_{K\in\mathcal{T}_h^n}\int_K \tau_K\left(\rho^{\mathrm{f}}\left(\boldsymbol{u}_h^{n-1}\cdot\nabla\right)\boldsymbol{v}_h+\nabla q_h\right)\cdot\left(\rho^{\mathrm{f}}\left(\boldsymbol{u}_h^{n-1}\cdot\nabla\right)\boldsymbol{u}_h^n+\nabla p_h^n-\rho^{\mathrm{f}}\boldsymbol{g}\right) + \frac{\rho^{\mathrm{f}}}{2}\int_{\Gamma_{\mathrm{out}}}\left(\boldsymbol{u}_h^n\cdot\boldsymbol{n}\right)_-\boldsymbol{u}_h^n\cdot\boldsymbol{v}_h, \tag{4.18}$$

where $\boldsymbol{v}_h$ and q_h are the velocity and pressure test functions, the symbol $(\boldsymbol{u}^n\cdot\boldsymbol{n})_-$ denotes the negative part of $\boldsymbol{u}^n\cdot\boldsymbol{n}$ and τ_K is the SUPG/PSPG stabilization parameter. For Algorithms 4.3, 4.4 and 4.6, we split the stabilization (4.18) in its velocity and pressure parts, adding the following SUPG contribution to the convective-viscous substep (4.8):

$$\sum_{K\in\mathcal{T}_h^n}\int_K \left(\tau_K\rho^{\mathrm{f}}\left(\tilde{\boldsymbol{u}}_h^{n-1}\cdot\nabla\right)\boldsymbol{v}_h\right)\cdot\left(\rho^{\mathrm{f}}\left(\tilde{\boldsymbol{u}}_h^{n-1}\cdot\nabla\right)\tilde{\boldsymbol{u}}_h^n+\nabla p_h^{n-1}-\rho^{\mathrm{f}}\boldsymbol{g}\right) + \frac{\rho^{\mathrm{f}}}{2}\int_{\Gamma_{\mathrm{out}}}\left(\tilde{\boldsymbol{u}}_h^n\cdot\boldsymbol{n}\right)_-\tilde{\boldsymbol{u}}_h^n\cdot\boldsymbol{v}_h,$$

and the following PSPG contribution to the projection step (4.9):

$$\sum_{K\in\mathcal{T}_h^n}\int_K \tau_K\nabla q_h\cdot\left(\rho^{\mathrm{f}}\left(\tilde{\boldsymbol{u}}_h^{n-1}\cdot\nabla\right)\tilde{\boldsymbol{u}}_h^n+\nabla p_h^n-\rho^{\mathrm{f}}\boldsymbol{g}\right).$$

In Algorithms 4.2, 4.4-4.6, which involve the thin-walled solid model (4.5), discontinuous approximations of the pressure are allowed by duplicating the pressure degrees of freedom matching at the interface, creating an internal discontinuous boundary around the interface.

The space-discretization of the solid elastodynamics equations in Algorithm 4.1 is performed with $\mathbb{Q}_1$ finite elements. The shell equation in Algorithms 4.2 and 4.4-4.6, is discretized in space by quadrilateral MITC4 elements (see [CB11, Section 8.2.1]).

4.3.3 Mesh update technique

We adopt a *mesh moving technique* in which the displacement of the nodes is based on the equations of linear elasticity. The Lamé parameters are chosen element-wise in order to stiffen the smallest elements (see [STB03]), whose deformation can potentially make the mesh invalid. In order to take into account the actual deformation of the mesh, the lifted displacement is computed on the current configuration

of mesh by computing the incremental displacement. Given $\boldsymbol{d}_h^{n-1}|_\Sigma$, we compute

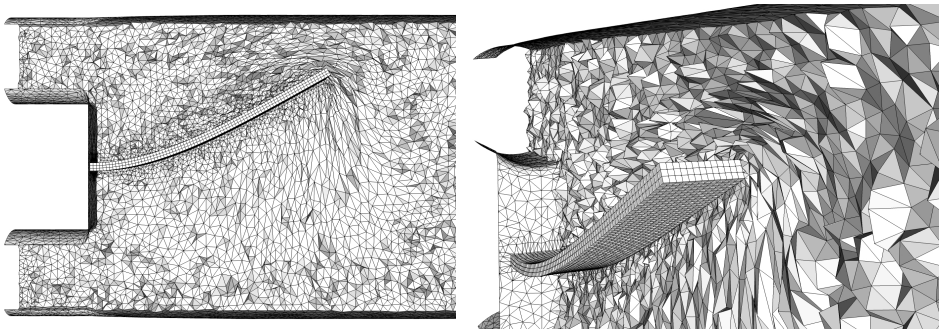

(a) Horizontal perspective. (b) Detail of the deformed mesh.

Figure 4.7: Initial condition for the meshes. Application of the operator $\mathrm{Ext}\,(\cdot)$.

the lifted displacement $\boldsymbol{d}_h^{\mathrm{f},n} = \mathrm{Ext}\big(\boldsymbol{d}_h^{n-1}|_\Sigma\big)$ by the following procedure:

1. Compute the solid displacement increment at the reference interface:

$$\delta\boldsymbol{d}_h^{n-1} = \boldsymbol{d}_h^{n-1}|_\Sigma - \boldsymbol{d}_h^{n-2}|_\Sigma.$$

2. Compute the extension $\delta\boldsymbol{d}_h^{\mathrm{f},n}$ of the increment $\delta\boldsymbol{d}_h^{n-1}$ solving the following linear elasticity problem in the previous configuration $\Omega^{\mathrm{f},n-1}$:

$$\begin{cases} \delta\boldsymbol{d}_h^{\mathrm{f},n}|_{\Sigma^{n-1}} = \delta\boldsymbol{d}_h^{n-1} \circ (\boldsymbol{\mathcal{A}}_h^{n-1})^{-1}, \quad \delta\boldsymbol{d}_h^{\mathrm{f},n}|_{\Omega^{\mathrm{f},n-1}/\Sigma^{n-1}} = \boldsymbol{0}, \\ \displaystyle\sum_{K\in\mathcal{T}_h^{n-1}} \int_K \big(L_{1,K}\ \mathrm{div}\big(\delta\boldsymbol{d}_h^{\mathrm{f},n}\big)\ \mathrm{div}\boldsymbol{w}_h + 2L_{2,K}\ \boldsymbol{\varepsilon}(\delta\boldsymbol{d}_h^{\mathrm{f},n}) : \boldsymbol{\varepsilon}(\boldsymbol{w}_h)\big) = 0 \quad \forall \boldsymbol{w}_h, \end{cases}$$

where the Lamé parameters $L_{1,K}$, $L_{2,K}$ are defined element-wise as

$$L_{1,K} = \frac{\widetilde{L}_1}{V_K}, \quad L_{2,K} = \frac{\widetilde{L}_2}{V_K},$$

with $\widetilde{L}_1, \widetilde{L}_2 > 0$ given constants and V_K the volume of the element $K \in \mathcal{T}_h^{n-1}$.

3. Update the fluid displacement in the reference configuration:

$$\boldsymbol{d}_h^{\mathrm{f},n} = \boldsymbol{d}_h^{\mathrm{f},n-1} + \delta\boldsymbol{d}_h^{\mathrm{f},n} \circ \boldsymbol{\mathcal{A}}^{n-1}$$

An example of deformed mesh (involving large interface defections) obtained with this procedure ($\widetilde{L}_1 = 1$, $\widetilde{L}_2 = 15$) is displayed in Figure 4.7.

4.4 Comparison with experimental data

Experimental data of the solid displacement and fluid velocity was provided by the challenge organizers (see [Nor15]). They used a combination of synchronized

geometrical and flow scans with temporal resolution to carry out the measurements. For Phase I experiment, the velocity was recorded at the cutting planes $z = 10$ and $z = 30$ (see Figure 4.8(a)). For Phase II, experimental measurements of the fluid velocity components at different time-steps were obtained at the cutting planes $z = 3.5$, $z = 13.5$, $z = 23.5$ and $z = 33.5$. (see Figure 4.8(b)).

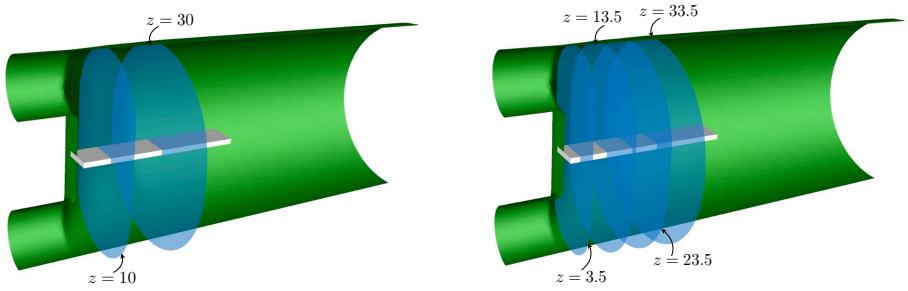

(a) Phase I (b) Phase II

Figure 4.8: Scanning planes for Phase I and Phase II.

The numerical results presented below were generated with a partitioned master/slave implementation of Algorithms 4.1-4.6. Data exchanges across the fluid-solid interface are managed by a master code (based on PVM [GBD+94]), with the slaves being the fluid and solid solvers (see, e.g., [GV03, LCY+06]). Different parallel methods are used for the solid and the fluid. The parallel structural solver uses Newton iterations at each time-step. The resulting tangent systems are solved with a balancing domain decomposition method (see, e.g., [Man93, LTV96, LT94a]). The fluid solver FELiScE (see [Fel]) is based on PETSc (see [BAA+14a, BAA+14b, BGMS97]) and uses an additive Schwarz algorithm (see, e.g., [SBG96]) with local ILU preconditioning.

4.4.1 Initial configuration

According to (4.4), the Phases I and II experiments are initialized with the solid configuration in its hydrostatic equilibrium $\boldsymbol{d}_0$. An approximation of this configuration is used to initialize $\boldsymbol{d}^0$ in Algorithms 4.1-4.6. This approximation can be obtained as the steady state solution provided by Algorithms 4.1-4.6 with $\boldsymbol{d}^0 = \mathbf{0}$, $\boldsymbol{u}^n_{\text{top}} = \boldsymbol{u}^n_{\text{bot}} = \mathbf{0}$. Figure 4.9 reports the solid hydrostatic equilibrium obtained with the implicit schemes (Algorithms 4.1-4.2). Similar results are also obtained with the rest of the methods. Note that these results underestimate the deflections measured in the experiment for Phases I and II, which are 29.5 mm and 25.65 mm, respectively. In particular, we do not observe such a difference between the results for Phases I and II, despite the modifications introduced in the fluid physical parameters (see Sections 4.2.3.1-4.2.3.2). Figure 4.9 also shows that the thin-walled shell model provides slightly larger deflections.

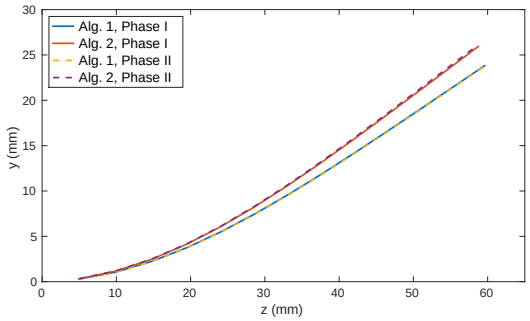

Figure 4.9: Initial conditions $\boldsymbol{d}^0$ for Phase I and Phase II obtained with Algorithms 4.1-4.2.

4.4.2 Phase I experiment

The solid filament is initially at the hydrostatic equilibrium computed in Section 4.4.1. The constant flow rate described in Section 4.2.3.1 is imposed on the top and bottom inlet boundaries. We have simulated 6000 time-steps of constant length $\tau = 2.5 \cdot 10^{-3}$ s with Algorithms 4.1-4.6. After a brief transition phase, the system reaches a steady state equilibrium with the filament deflected and holding a stable position. Figure 4.10 shows the steady state velocity field magnitude and the deformed solid configuration provided by Algorithm 4.1 (3D solid model) and Algorithm 4.2 (shell solid model). Similar results are obtained with the rest of methods, that are omitted here for the sake of conciseness.

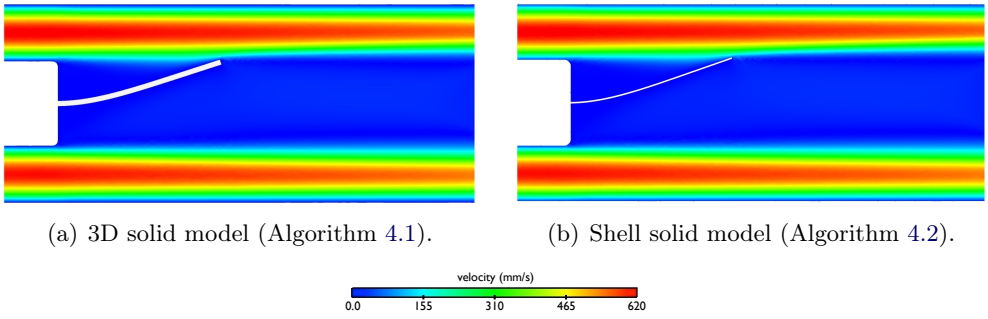

(a) 3D solid model (Algorithm 4.1). (b) Shell solid model (Algorithm 4.2).

Figure 4.10: Steady state velocity magnitude and deformed solid configuration in Phase I.

In Figure 4.11, we compare the measured final filament configuration and the approximations provided by Algorithms 4.1-4.6. In order to better highlight the differences, the y-range has been rescaled with respect to Figure 4.9. We can clearly see that all the methods considered provide numerical solutions that are very close to the experimental data. Moreover, the results obtained with Algorithms 4.1 and 4.3 (3D solid model) are practically the same. Similar behaviour is observed for Algorithms 4.2 and 4.4-4.6 (shell solid model). This is clear indication that, in this case, the choice of the coupling scheme has a limited impact on the quality of

the approximation, which is mainly driven by the solid modelling assumptions. In general, the 3D solid model gives slightly better results than the shell model, which tends to overestimate the deflection of the filament.

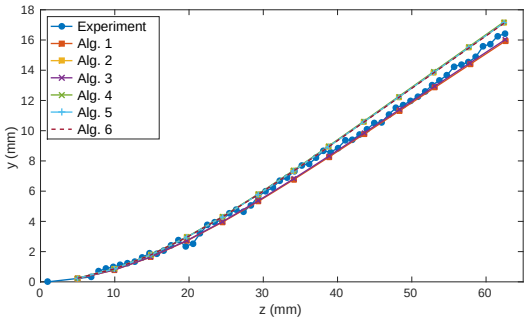

Figure 4.11: Deflection of the silicone filament at steady state in Phase I. Comparison of the experimental data with the predictions obtained with Algorithms 4.1-4.6.

In Figure 4.12, we compare the experimental results for the fluid velocity components with the numerical approximations obtained with Algorithm 4.1 (monolithic fluid solver and 3D solid model) and Algorithm 4.6 (incremental pressure-correction fluid solver and shell solid model). Very similar results were obtained with the rest of algorithms. These results display a good agreement between the simulations and the experimental data (irrespectively of the fluid-solver/solid-model used).

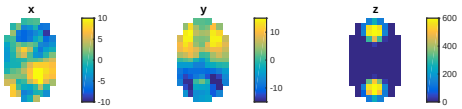

(a) Experiment at $z = 10$.

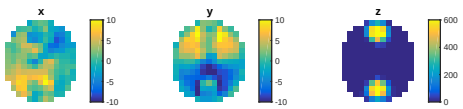

(b) Experiment at $z = 30$.

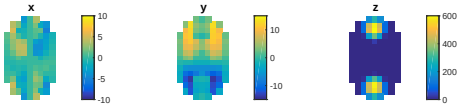

(c) Algorithm 4.1 at $z = 10$.

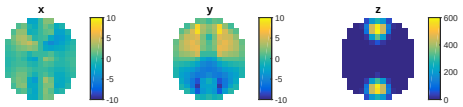

(d) Algorithm 4.1 at $z = 30$.

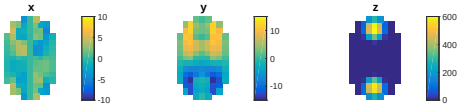

(e) Algorithm 4.6 at $z = 10$.

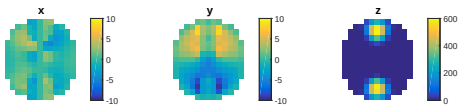

(f) Algorithm 4.6 at $z = 30$.

Figure 4.12: Fluid velocity components at steady state in Phase I. Comparison of the experimental data with the predictions obtained with Algorithms 4.1 and 4.6. Units are in $mm\ s^{-1}$.

In order to provide some insight on the computational performance of the different numerical methods, we have reported in Table 4.5 a comparison of the elapsed CPU-times (dimensionless) obtained with Algorithms 4.1-4.6 during the first 10

time-steps. The experiments were run in the same machine, with 16 and 8 processors allocated for the fluid and the solid solvers, respectively. We can observe that, when using a 3D solid model and for practically the same level of accuracy, Algorithm 4.3 is about 6 times faster than Algorithm 4.1. An even higher speed-up is observed when a shell solid model is used and we compare Algorithm 4.6 with Algorithm 4.2. In that case, the former is 18 times faster than the latter.

Alg. 4.6	Alg. 4.5	Alg. 4.4	Alg. 4.3	Alg. 4.2	Alg. 4.1
1	2	2	3	17	18

Table 4.5: Elapsed CPU-time (dimensionless) for Algorithms 4.1-4.6 in Phase I.

4.4.3 Phase II experiment

The solid filament is initially in its hydrostatic equilibrium simulated in Section 4.4.1. On the inlet boundaries, we impose the pulsatile flow profile described in Section 4.2.3.2. We have simulated 6000 time-steps of constant length $\tau = 10^{-3}\ s$ with Algorithms 4.1-4.6, which corresponds to a full cycle ($6\,s$) of the pulsatile flow.

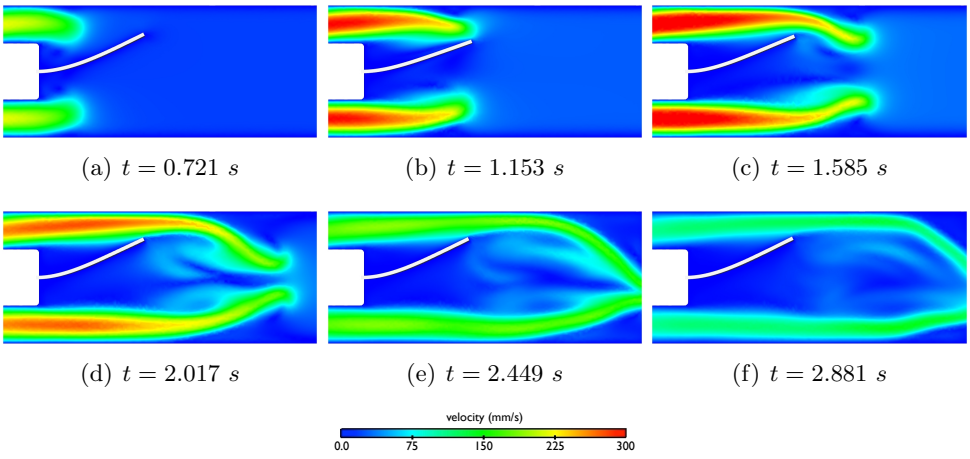

(a) $t = 0.721\ s$ (b) $t = 1.153\ s$ (c) $t = 1.585\ s$

(d) $t = 2.017\ s$ (e) $t = 2.449\ s$ (f) $t = 2.881\ s$

Figure 4.13: Snapshots of the fluid velocity magnitude and deformed solid configuration in Phase II with Algorithm 4.1.

Figures 4.13 and 4.15 present some snapshots of the fluid velocity magnitude at different time instants obtained with Algorithm 4.1 (3D solid model) and Algorithm 4.2 (shell solid model), respectively. The fluid front hits the filament, and makes it to deflect. As soon as the fluid flow diminishes, the filament returns to its original position. For illustration purposes, Figures 4.14 and 4.16, report some vortical structures obtained as iso-surfaces of the *Q-criterion* (see [HWM88]). The rest of the algorithms deliver very similar results. We can clearly see in these figures the initial deflection of the structure due to the impact of the fluid jet. Further numerical results are displayed in Figure A.1 of Appendix A.

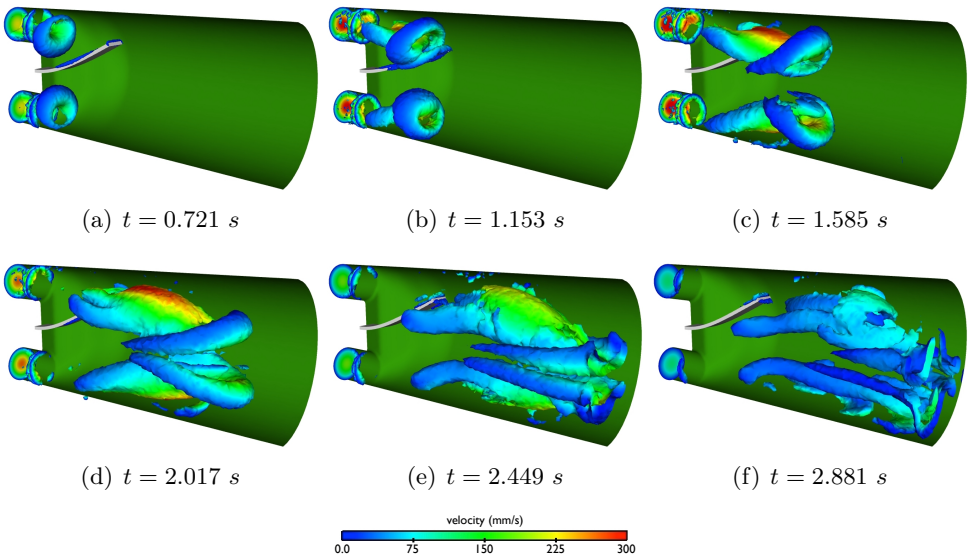

(a) $t = 0.721\ s$ (b) $t = 1.153\ s$ (c) $t = 1.585\ s$

(d) $t = 2.017\ s$ (e) $t = 2.449\ s$ (f) $t = 2.881\ s$

Figure 4.14: Isosurface $Q = 12$ of the Q-criterion colored by the velocity magnitude in Phase II with Algorithm 4.1.

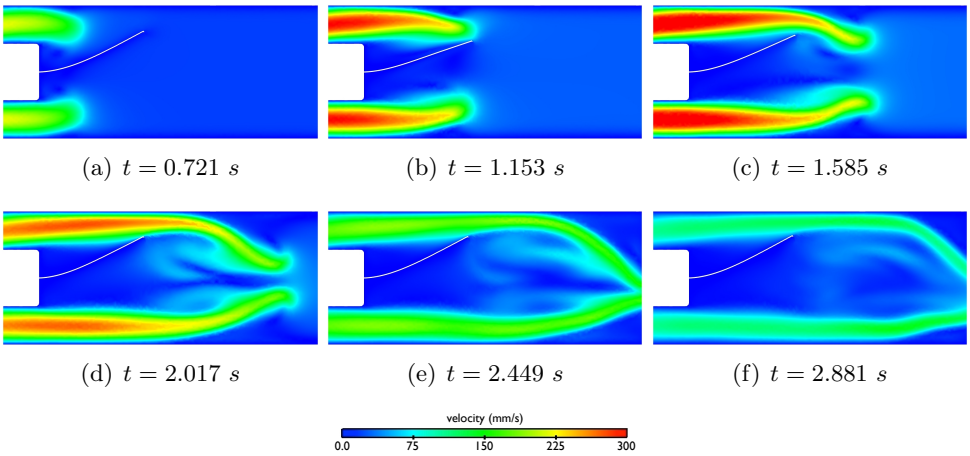

(a) $t = 0.721\ s$ (b) $t = 1.153\ s$ (c) $t = 1.585\ s$

(d) $t = 2.017\ s$ (e) $t = 2.449\ s$ (f) $t = 2.881\ s$

Figure 4.15: Snapshots of the fluid velocity magnitude and deformed solid configuration in Phase II with Algorithm 4.2.

Figure 4.17 presents a comparison of the measured deflections and the results obtained with Algorithms 4.1-4.6 at different time-steps in $[0, 3]$ (where the main transient phenomena occur). Additional results over the whole cycle $[0, 6]$ are displayed in Figure A.2 of Appendix A. Note that the experimentally measured deflection is truncated over $x \in [0, 53.193]$, whereas the whole results are displayed for the simulations. We can observe that all the numerical methods are able to capture the main dynamics of the system. In order to provide further insight in this comparison, Figure 4.18 displays the y-component of the point in the structure

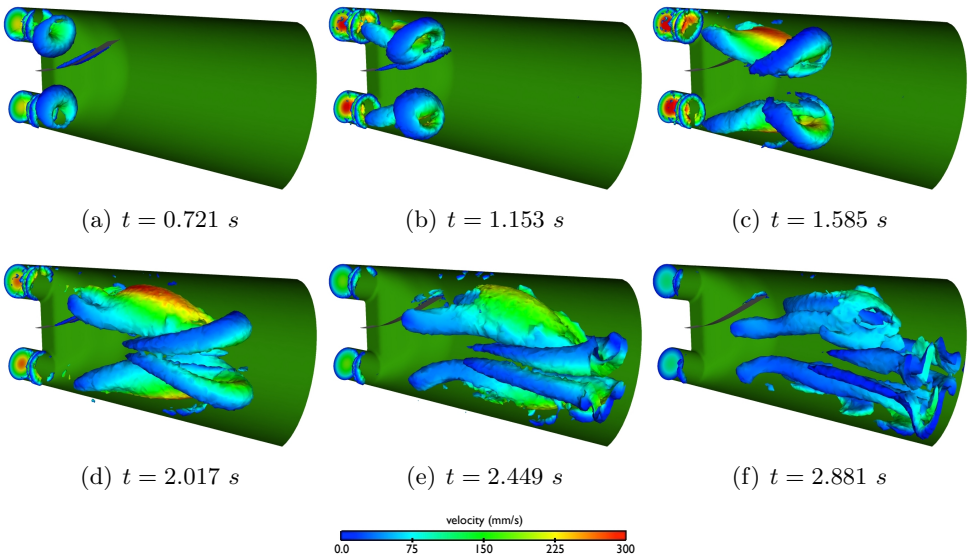

(a) $t = 0.721\ s$ (b) $t = 1.153\ s$ (c) $t = 1.585\ s$

(d) $t = 2.017\ s$ (e) $t = 2.449\ s$ (f) $t = 2.881\ s$

Figure 4.16: Isosurface $Q = 12$ of the Q-criterion colored by the velocity magnitude in Phase II with Algorithm 4.2.

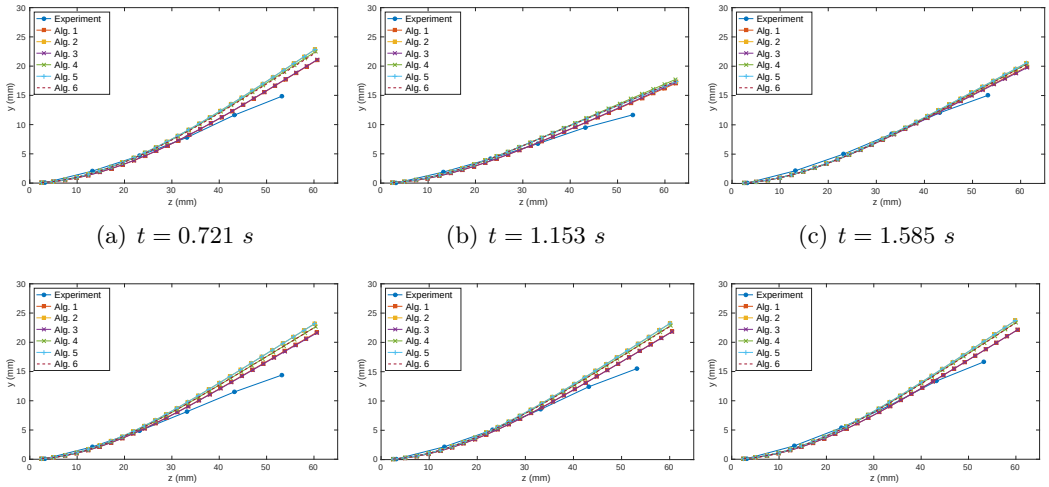

(a) $t = 0.721\ s$ (b) $t = 1.153\ s$ (c) $t = 1.585\ s$

(d) $t = 2.017\ s$ (e) $t = 2.449\ s$ (f) $t = 2.881\ s$

Figure 4.17: Deflection of the silicone filament in Phase II at different time instants during the window $[0, 3]\ s$. Comparison of the experimental data with the predictions obtained with Algorithms 4.1-4.6.

with coordinate $x = 53.193$ for all $t \in [0, 6]$. We can see that the first impact of the fluid into the solid causes the main deflection of the filament at $t = 1.153\ s$. The instant in which the filament reaches this maximum deflection is perfectly predicted by all the methods (see also Figure 4.17(b)). Afterwards, the solid starts to go up due to the buoyant force and hits again the fluid jet at $t = 1.585\ s$. Then, a second, much more mitigated, bounce starts which is, however, captured with a delay in all

the simulations. Figure 4.18 shows also the general tendency of the shell model to overestimate the deflection of the filament, especially during the second half of the cycle.

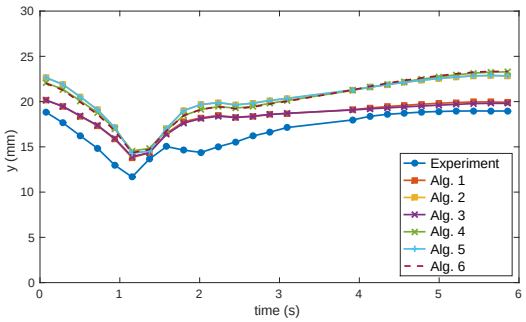

Figure 4.18: Track of y-component of the point in the structure with coordinate $x = 53.193$ for all $t \in [0, 6]$ in Phase II.

Figure 4.19 shows the experimental results for the fluid velocity components and the numerical approximations obtained, at two different time-steps, with Algorithm 4.1 (monolithic fluid solver and 3D solid model) and Algorithm 4.6 (incremental pressure-correction fluid solver and shell solid model) at $z = 33.5$ (the furthest from the inlet boundary, which corresponds to the most difficult scenario). Additional results over the four cutting planes of Figure 4.8(b) can be found in Figures A.3, A.4, A.5 and A.6 of Appendix A. Although slightly diffusive, the simulations are in good agreement with the experimental data (irrespectively of the fluid-solver/solid-model used). In particular, the main patterns of the flow are clearly captured. Similar results, not reported here for the sake of conciseness, were obtained with the rest of methods.

Finally, in Table 4.6, we compare the performance of Algorithms 4.1-4.6 in terms of the elapsed CPU-time during the first 10 time-steps. This is carried out in the same machine, with 16 and 8 processors allocated for the fluid and the solid solvers, respectively. As in the simulations of Phase I, superior performance is obtained with the loosely coupled and semi-implicit methods.

Alg. 4.6	Alg. 4.5	Alg. 4.4	Alg. 4.3	Alg. 4.2	Alg. 4.1
1	2	2.5	2.5	18	17.5

Table 4.6: Elapsed CPU-time (dimensionless) for Algorithms 4.1-4.6 in Phase II.

4.5 Conclusion

Different partitioned solution procedures have been compared and validated using the experimental results of the FSI benchmark presented in [Nor15]. All the

(a) Experiment at $t = 1.153$.

(b) Experiment at $t = 2.449$.

(c) Algorithm 4.1 at $t = 1.153$.

(d) Algorithm 4.1 at $t = 2.449$.

(e) Algorithm 4.6 at $t = 1.153$.

(f) Algorithm 4.6 at $t = 2.449$.

Figure 4.19: Fluid velocity components in Phase II. Comparison of the experimental data with the predictions obtained with Algorithms 4.1 and 4.6. Plane $z = 33.5$. Units are $mm\ s^{-1}$.

methods discussed are algorithmically parameter free and represent an important sample of the state-of-the-art in coupling schemes for FSI.

The comparisons in Section 4.4 showed, in general, a very good agreement between the numerical and the experimental results, particularly, in Phase I where the matching is excellent. A slight deviation is observed in the case of the coupling with the shell model, which can be related to the approximation of the Archimedes force.

With regard to the computational efficiency, the comparisons indicate that the best performance is obtained with the splitting schemes of Algorithms 4.3 and 4.6, respectively, in the case of the coupling with a 3D and a shell solid model. It should be noted also that these results confirm that strong coupling (Algorithms 4.1-4.2) can be avoided via semi-implicit or explicit coupling (Algorithms 4.3-4.6) without compromising both stability and accuracy, and at significantly reduced computational cost (see, e.g., Table 4.6).

Part II

Unfitted mesh methods

Chapter 5

Splitting schemes for incompressible fluid/thin-walled structure interaction using unfitted meshes

In this chapter we investigate how the explicit Robin-Neumann coupling paradigm of Section 1.4.3.5 can be generalized to the unfitted mesh framework of Section 1.4.2.3. As a result, two new classes of splitting methods (semi-implicit and explicit) are obtained. Their semi-implicit or explicit nature is dictated by the order in which the spatial and time discretizations are performed. Stability and optimal accuracy are achieved without restrictive CFL conditions or correction iterations.

The results presented in this chapter have been reported in:

- M. A. Fernández, M. Landajuela, **Splitting schemes for incompressible fluid/thin-walled structure interaction with unfitted meshes**. *Comptes Rendus Mathématique, 353(7):647-652, 2015*

- M. A. Fernández, M. Landajuela, **Unfitted formulations and splitting schemes for incompressible fluid/thin-walled structure interaction**. Submitted to *ESAIM: Mathematical Modelling and Numerical Analysis*.

Contents

5.1 Introduction

Over the last years, significant progress has been achieved in the development and analysis of stable and accurate explicit coupling schemes for the approximation of the coupled problem (1.34),(1.37) (see Section 1.4.3). Most of these studies (see, e.g., [BF09, GGCC09, Fer13, FMV13, BF14a, BCG+13, LMRHZ13]) consider fitted meshes (see Section 1.4.2.2). For much applications, it is well known however that this assumption rapidly becomes cumbersome (see Section 1.3.1.1).

Within the unfitted mesh framework of Section 1.4.2.3, splitting schemes of explicit nature are reported and analyzed in [BCG11] using the finite element immersed boundary method, and in [BF14b] using an unfitted Nitsche's method (see Algorithm 1.4). A major drawback of these approaches is that either stability or accuracy demands severe time-step restrictions (e.g., parabolic-CFL) or correction iterations.

In this chapter, we present two new numerical methods (semi-implicit and explicit) which bypass these stability and accuracy issues. Their semi-implicit or explicit nature depends on the order in which the spatial and time discretizations are performed. These methods generalize (for the first time) the Robin-Neumann splitting paradigm of Section 1.4.3.5 to the unfitted mesh framework. A complete energy-based stability and a priori error analysis is presented for the semi-implicit class of schemes. In particular, unconditional stability and optimal accuracy is obtained with one of the variants. This type of analysis is only partially conducted for the explicit class of schemes, showing unconditional stability and convergence for one of the variants considered.

This chapter is organized as follows. Section 5.2 is devoted to the case in which the space discretization is performed in the first place. The resulting semi-implicit schemes are presented in Section 5.2.1, and their stability and convergence analysis is addressed in Section 5.2.2. The alternative of performing the time discretization in the first place is considered is Section 5.3. The resulting explicit schemes are presented in Section 5.3.1. One of the explicit variants is analyzed in Section 5.3.2. A thorough numerical study in a benchmark is presented in Section 5.4. The conclusions are summarized in Section 5.5.

The model problem We consider the coupled problem introduced in Section 1.4.1, involving the Stokes system (1.34) and the thin-walled solid problem (1.37). The problem, which we repeat here for the sake of convenience, reads: find the fluid velocity $\boldsymbol{u} : \Omega^{\mathrm{f}} \times \mathbb{R}^+ \to \mathbb{R}^d$, the fluid pressure $p : \Omega^{\mathrm{f}} \times \mathbb{R}^+ \to \mathbb{R}$, the structure displacement $\boldsymbol{d} : \Sigma \times \mathbb{R}^+ \to \mathbb{R}^d$ and the structure velocity $\dot{\boldsymbol{d}} : \Sigma \times \mathbb{R}^+ \to \mathbb{R}^d$, such that

$$\begin{cases} \rho^{\mathrm{f}} \partial_t \boldsymbol{u} - \mathbf{div}\boldsymbol{\sigma}(\boldsymbol{u}, p) = \mathbf{0} & \text{in} \quad \Omega^{\mathrm{f}}, \\ \mathrm{div}\boldsymbol{u} = 0 & \text{in} \quad \Omega^{\mathrm{f}}, \\ \boldsymbol{u} = \mathbf{0} & \text{on} \quad \Gamma^{\mathrm{f}}, \end{cases} \tag{5.1}$$

$$\begin{cases} \boldsymbol{u} = \dot{\boldsymbol{d}} & \text{on} \quad \Sigma, \\ \rho^{\mathrm{s}}\epsilon\partial_t\dot{\boldsymbol{d}} + \boldsymbol{L}^{\mathrm{e}}\boldsymbol{d} = -\boldsymbol{\sigma}(\boldsymbol{u},p)\boldsymbol{n} & \text{on} \quad \Sigma, \\ \dot{\boldsymbol{d}} = \partial_t\boldsymbol{d} & \text{on} \quad \Sigma, \\ \boldsymbol{d} = \boldsymbol{0} & \text{on} \quad \partial\Sigma, \end{cases} \tag{5.2}$$

complemented with the initial conditions $\boldsymbol{u}(0) = \boldsymbol{u}_0$, $\boldsymbol{d}(0) = \boldsymbol{d}_0$ and $\dot{\boldsymbol{d}}(0) = \dot{\boldsymbol{d}}_0$. The abstract surface operator $\boldsymbol{L}^{\mathrm{e}} : \boldsymbol{D}(\boldsymbol{L}^{\mathrm{e}}) \subset [L^2(\Sigma)]^d \to [L^2(\Sigma)]^d$ describes the solid elastic effects.

Recall that the L^2-scalar product on ω is denoted by $(\cdot,\cdot)_\omega$ and its associated norm by $\|\cdot\|_{0,\omega}$. For the weak formulation of the problem we consider the fluid and solid spaces introduced in Section 1.4.2.1 for the case of coupling with a thin-walled solid, viz.,

$$\boldsymbol{V} = [H^1_{\Gamma^{\mathrm{f}}}(\Omega^{\mathrm{f}})]^d, \quad Q = L^2(\Omega^{\mathrm{f}}), \quad \boldsymbol{W} \subset [H^1_{\partial\Sigma}(\Sigma)]^d.$$

The weak formulation of (5.1)-(5.2) obtained in Section 1.4.2.1 reads: for $t > 0$, find

$$(\boldsymbol{u}(t), p(t), \boldsymbol{d}(t), \dot{\boldsymbol{d}}(t)) \in \boldsymbol{V} \times Q \times \boldsymbol{W} \times \boldsymbol{W}$$

such that

$$\begin{cases} \boldsymbol{u}|_\Sigma = \dot{\boldsymbol{d}}, \quad \dot{\boldsymbol{d}} = \partial_t\boldsymbol{d}, \\ \rho^{\mathrm{f}}\big(\partial_t\boldsymbol{u},\boldsymbol{v}\big)_{\Omega^{\mathrm{f}}} + a^{\mathrm{f}}\big((\boldsymbol{u},p),(\boldsymbol{v},q)\big) + \rho^{\mathrm{s}}\epsilon\big(\partial_t\dot{\boldsymbol{d}},\boldsymbol{w}\big)_\Sigma + a^{\mathrm{s}}(\boldsymbol{d},\boldsymbol{w}) = 0, \end{cases} \tag{5.3}$$

for all $(\boldsymbol{v},q,\boldsymbol{w}) \in \boldsymbol{V} \times Q \times \boldsymbol{W}$ with $\boldsymbol{v}|_\Sigma = \boldsymbol{w}$. Recall that a^{f} is given by $a^{\mathrm{f}}\big((\boldsymbol{u},p),(\boldsymbol{v},q)\big) \overset{\mathrm{def}}{=} a(\boldsymbol{u},\boldsymbol{v}) + b(p,\boldsymbol{v}) - b(q,\boldsymbol{u})$, with $a : \boldsymbol{V}\times\boldsymbol{V} \to \mathbb{R}$ and $b : Q\times\boldsymbol{V} \to \mathbb{R}$ the standard Stokes bilinear forms given in (1.40). The elastic bilinear form a^{s} is given by (1.38). In particular, the continuity estimate (1.39), which we repeat here for the sake of completeness, is assumed:

$$\|\boldsymbol{w}\|^2_{\mathrm{s}} \le \beta^{\mathrm{s}}\|\boldsymbol{w}\|^2_{1,\Sigma}, \quad \forall \boldsymbol{w} \in \boldsymbol{W}, \tag{5.4}$$

with $\beta^{\mathrm{s}} > 0$ and $\|\cdot\|_{\mathrm{s}} = a^{\mathrm{s}}(\cdot,\cdot)^{\frac{1}{2}}$.

5.2 First discretize in space and then in time

The first class of methods arises as the the result of performing the fractional-step time-marching (1.84) to the unfitted mesh spatial approximation (1.57). In this section, we present the method and address its stability and convergence analysis. In particular, unconditional stability and optimal first-order accuracy is derived for one of the variants considered. A salient feature of our analysis is that it also covers the fully discretized implicit scheme presented in [BF14b, Algorithm 1].

Unfitted mesh spatial semi-discretization For the sake of simplicity, we assume that Ω^{f} and Σ are polyhedral. We consider the unfitted mesh spatial semi-discretization of problem (5.3) described in Section 1.4.2.3. Families of solid triangulations $\{\mathcal{T}_h^{\mathrm{f}}\}_{0<h\leq 1}$, satisfying (1.42), and fluid triangulations $\{\mathcal{T}_h^{\mathrm{s}}\}_{0<h\leq 1}$, satisfying (A1)-(A3) in Section 1.4.2.3, are considered. See Figure 1.15(b) for a possible configuration. We assume that the elements of $\mathcal{T}_h^{\mathrm{s}}$ can be grouped in disjoint $(d-1)$-dimensional macropatches P_i, with $\mathrm{meas}(P_i) = \mathcal{O}(h^{d-1})$. Each macropatch is assumed to contain at least one interior node and the union of the P_i is assumed to cover Σ, that is, $\cup_i P_i = \Sigma$.

Recall that we denote by Ω_h the domain covered by $\mathcal{T}_h^{\mathrm{f}}$ (computational domain, see (1.50)). The approximation spaces for the solid, $\boldsymbol{W}_h$, and the fluid, $\boldsymbol{V}_h$ and Q_h, are defined in (1.43) and (1.51), respectively. We consider the space semi-discretization (1.57), namely: for $t > 0$, find

$$\big(\boldsymbol{u}_h(t), p_h(t), \dot{\boldsymbol{d}}_h(t), \boldsymbol{d}_h(t)\big) \in \boldsymbol{V}_h \times Q_h \times \boldsymbol{W}_h \times \boldsymbol{W}_h,$$

such that $\dot{\boldsymbol{d}}_h = \partial_t \boldsymbol{d}_h$ and

$$\begin{cases} \rho^{\mathrm{f}}\big(\partial_t \boldsymbol{u}_h, \boldsymbol{v}_h\big)_{\Omega^{\mathrm{f}}} + a^{\mathrm{f}}\big((\boldsymbol{u}_h, p_h), (\boldsymbol{v}_h, q_h)\big) + S_h\big((\boldsymbol{u}_h, p_h), (\boldsymbol{v}_h, q_h)\big) \\ + \rho^{\mathrm{s}}\big(\partial_t \dot{\boldsymbol{d}}_h, \boldsymbol{w}_h\big)_{\Sigma} + a^{\mathrm{s}}(\boldsymbol{d}_h, \boldsymbol{w}_h) - \big(\boldsymbol{\sigma}(\boldsymbol{u}_h, p_h)\boldsymbol{n}, \boldsymbol{v}_h - \boldsymbol{w}_h\big)_{\Sigma} \\ - \big(\boldsymbol{u}_h - \dot{\boldsymbol{d}}_h, \boldsymbol{\sigma}(\boldsymbol{v}_h, -q_h)\boldsymbol{n}\big)_{\Sigma} + \dfrac{\gamma\mu}{h}\big(\boldsymbol{u}_h - \dot{\boldsymbol{d}}_h, \boldsymbol{v}_h - \boldsymbol{w}_h\big)_{\Sigma} = 0 \end{cases} \tag{5.5}$$

for all $(\boldsymbol{v}_h, q_h, \boldsymbol{w}_h) \in \boldsymbol{V}_h \times Q_h \times \boldsymbol{W}_h$. Here, $\gamma > 0$ denotes the Nitsche's penalty parameter and

$$S_h\big((\boldsymbol{u}_h, p_h), (\boldsymbol{v}_h, q_h)\big) \stackrel{\mathrm{def}}{=} s_h(p_h, q_h) + g_h(\boldsymbol{u}_h, \boldsymbol{v}_h). \tag{5.6}$$

In (5.6), the term $s_h(p_h, q_h)$ stands for the pressure stabilization bilinear form (e.g., (1.53)) and $g_h(\boldsymbol{u}_h, \boldsymbol{v}_h)$ for the ghost penalty interface stabilization (e.g., (1.55)). These operators are supposed to enter the framework described in Section 1.4.2.3. In particular, we assume that

$$c_1 \mu^{-1} h^2 |q_h|^2_{1,\Omega_h} \leq s_p(q_h, q_h) \leq c_2 \mu^{-1} h^2 |q_h|^2_{1,\Omega_h}, \tag{5.7}$$

or all $q_h \in Q_h$ and with $c_1, c_2 > 0$, and that

$$\tilde{c}_{\mathrm{g}} \left(\mu \|\boldsymbol{\varepsilon}(\boldsymbol{v}_h)\|^2_{0,\Omega_h} + g_h(\boldsymbol{v}_h, \boldsymbol{v}_h)\right) \leq \mu \|\boldsymbol{\varepsilon}(\boldsymbol{v}_h)\|^2_{0,\Omega^{\mathrm{f}}} + g_h(\boldsymbol{v}_h, \boldsymbol{v}_h), \tag{5.8}$$

with $\tilde{c}_{\mathrm{g}} > 0$. Associated to the overall stabilization operator S_h, we define the semi-norm

$$|(u_h, p_h)|_S \stackrel{\mathrm{def}}{=} S_h\big((\boldsymbol{u}_h, p_h), (\boldsymbol{v}_h, q_h)\big)^{\frac{1}{2}}.$$

5.2.1 Fully discrete formulation: semi-implicit coupling scheme with unfitted meshes

As usual in this work, $\tau > 0$ denotes the time-step length, $t_n \overset{\text{def}}{=} n\tau$ for $n \in \mathbb{N}$, and $\partial_\tau x^n \overset{\text{def}}{=} \frac{1}{\tau}\big(x^n - x^{n-1}\big)$ stands for the first-order backward difference. The superscript ^{n,*} denotes the r-th order explicit extrapolations to x^n, namely,

$$x^{n,\star} \overset{\text{def}}{=} \begin{cases} 0 & \text{if} \quad r = 0, \\ x^{n-1} & \text{if} \quad r = 1, \\ 2x^{n-1} - x^{n-2} & \text{if} \quad r = 2. \end{cases} \tag{5.9}$$

In Section 1.4.3.4, we have considered an explicit discretization of (5.5) based on the partitioned formulation (1.59)-(1.58). The stability of the resulting splitting scheme (Algorithm 1.4) was stablished in Theorem 1.4. Unfortunately, as discussed there, the accuracy of Algorithm 1.4 is non-uniform in h, requiring restrictive CFL-like conditions or correction iterations.

A possible remedy is to consider the fully implicit time discretization of (5.5) proposed in [BF14b, Algorithm 1] and reported here in Algorithm 5.1. As a matter of fact, Algorithm 5.1 is stable and delivers optimal first-order accuracy in the energy norm (see Remark 5.3 and Corollary 5.2 below). However, this is achieved at the price of solving system (5.10) at each time-step, which can be computationally demanding. Besides, general thin-walled solid models are known to yield ill-conditioned stiffness matrices, requiring specific solvers.

Algorithm 5.1 Implicit coupling scheme.

For $n \geq 1$, find $\big(\boldsymbol{u}_h^n, p_h^n, \dot{\boldsymbol{d}}_h^n, \boldsymbol{d}_h^n\big) \in \boldsymbol{V}_h \times Q_h \times \boldsymbol{W}_h \times \boldsymbol{W}_h$, such that $\dot{\boldsymbol{d}}_h = \partial_\tau \boldsymbol{d}_h^n$ and

$$\begin{cases} \rho^{\mathrm{f}}\big(\partial_\tau \boldsymbol{u}_h^n, \boldsymbol{v}_h\big)_{\Omega^{\mathrm{f}}} + a^{\mathrm{f}}\big((\boldsymbol{u}_h^n, p_h^n), (\boldsymbol{v}_h, q_h)\big) + S_h\big((\boldsymbol{u}_h^n, p_h^n), (\boldsymbol{v}_h, q_h)\big) \\ + \rho^{\mathrm{s}}\epsilon\big(\partial_\tau \dot{\boldsymbol{d}}_h^n, \boldsymbol{w}_h\big)_\Sigma + a^{\mathrm{s}}(\boldsymbol{d}_h^n, \boldsymbol{w}_h) - \big(\boldsymbol{\sigma}(\boldsymbol{u}_h^n, p_h^n)\boldsymbol{n}, \boldsymbol{v}_h - \boldsymbol{w}_h\big)_\Sigma \\ - \big(\boldsymbol{u}_h^n - \dot{\boldsymbol{d}}_h^n, \boldsymbol{\sigma}(\boldsymbol{v}_h, -q_h)\boldsymbol{n}\big)_\Sigma + \dfrac{\gamma\mu}{h}\big(\boldsymbol{u}_h^n - \dot{\boldsymbol{d}}_h^n, \boldsymbol{v}_h - \boldsymbol{w}_h\big)_\Sigma = 0 \end{cases} \tag{5.10}$$

for all $(\boldsymbol{v}_h, q_h, \boldsymbol{w}_h) \in \boldsymbol{V}_h \times Q_h \times \boldsymbol{W}_h$.

In the fitted mesh framework of Section 1.4.2.2, an efficient alternative to avoid implicit coupling without comprising stability an optimal accuracy, is given by the Robin-Neumann coupling schemes introduced in Section 1.4.3.5. Recall that the former schemes are based on the fractional-step time-marching (1.84) of the solid subproblem. In this section, we consider the same fractional-step treatment for the solid subproblem and discretize (5.5) with the following *incremental displacement-correction* scheme, for $n > 0$ if $r = 0, 1$ or for $n > 1$ if $r = 2$:

1. Fluid with solid inertia substep: find $\big(\boldsymbol{u}_h^n, p_h^n, \dot{\boldsymbol{d}}_h^{n-\frac{1}{2}}\big) \in \boldsymbol{V}_h \times Q_h \times \boldsymbol{W}_h$ such

that

$$\begin{cases} \rho^{\mathrm{f}}\big(\partial_\tau \boldsymbol{u}_h^n, \boldsymbol{v}_h\big)_{\Omega^{\mathrm{f}}} + a^{\mathrm{f}}\big((\boldsymbol{u}_h^n, p_h^n), (\boldsymbol{v}_h, q_h)\big) + S_h\big((\boldsymbol{u}_h^n, p_h^n), (\boldsymbol{v}_h, q_h)\big) \\ + \dfrac{\rho^{\mathrm{s}}\epsilon}{\tau}\big(\dot{\boldsymbol{d}}_h^{n-\frac{1}{2}} - \dot{\boldsymbol{d}}_h^{n-1}, \boldsymbol{w}_h\big)_\Sigma + a^{\mathrm{s}}(\boldsymbol{d}_h^{n,\star}, \boldsymbol{w}_h) - \big(\boldsymbol{\sigma}(\boldsymbol{u}_h^n, p_h^n)\boldsymbol{n}, \boldsymbol{v}_h - \boldsymbol{w}_h\big)_\Sigma \\ - \big(\boldsymbol{u}_h^n - \dot{\boldsymbol{d}}_h^{n-\frac{1}{2}}, \boldsymbol{\sigma}(\boldsymbol{v}_h, -q_h)\boldsymbol{n}\big)_\Sigma + \dfrac{\gamma\mu}{h}\big(\boldsymbol{u}_h^n - \dot{\boldsymbol{d}}_h^{n-\frac{1}{2}}, \boldsymbol{v}_h - \boldsymbol{w}_h\big)_\Sigma = 0 \end{cases} \tag{5.11}$$

for all $(\boldsymbol{v}_h, q_h, \boldsymbol{w}_h) \in \boldsymbol{V}_h \times Q_h \times \boldsymbol{W}_h$.

2. Solid substep: find $\big(\dot{\boldsymbol{d}}_h^n, \boldsymbol{d}_h^n\big) \in \boldsymbol{W}_h \times \boldsymbol{W}_h$ such that $\dot{\boldsymbol{d}}_h^n = \partial_\tau \boldsymbol{d}_h^n$ and

$$\frac{\rho^{\mathrm{s}}\epsilon}{\tau}\big(\dot{\boldsymbol{d}}_h^n - \dot{\boldsymbol{d}}_h^{n-\frac{1}{2}}, \boldsymbol{w}_h\big)_\Sigma + a^{\mathrm{s}}(\boldsymbol{d}_h^n - \boldsymbol{d}_h^{n,\star}, \boldsymbol{w}_h) = 0 \tag{5.12}$$

for all $\boldsymbol{w}_h \in \boldsymbol{W}_h$.

Steps (5.11)-(5.12) give a partially segregated solution of problem (5.5). Note that in (5.11), the intermediate solid velocity $\dot{\boldsymbol{d}}_h^{n-\frac{1}{2}}$ is implicitly coupled to the fluid through the solid inertial term. The remaining solid elastic contributions are treated explicitly (or ignored) in (5.11) via extrapolation. This level of fluid-solid coupling in enough to guarantee (added-mass free) stability (see Section 5.2.2.1 below), while allowing a significant degree of fluid-solid splitting. The end-of-step solid velocity $\dot{\boldsymbol{d}}_h^n$ is obtained by solving the solid correction step (5.12).

Remark 5.1 *It should be noted that the intermediate solid-velocity $\dot{\boldsymbol{d}}_h^{n-\frac{1}{2}}$ cannot be eliminated in (5.11) and, hence, the coupling scheme is not explicit. This is a major difference with respect to the case of fitted meshes and conformal discretizations considered in Section 1.4.3.5. In that case, we can take $\dot{\boldsymbol{d}}_h^{n-\frac{1}{2}} = \boldsymbol{u}_h^n|_\Sigma$ and $\boldsymbol{w}_h = \boldsymbol{v}_h|_\Sigma$ in (5.11), which yields a standard fluid problem with an explicit Robin condition on the interface Σ (see Remark 1.17).*

In the spirit of Section 1.4.3.5, it is convenient to reformulate the solid correction step (5.12) as a traction problem, by eliminating the quantities $\dot{\boldsymbol{d}}_h^{n-\frac{1}{2}}$ and $\boldsymbol{d}_h^{n,\star}$ in (5.12). To this purpose, we observe that testing (5.11) with $\boldsymbol{v}_h = \boldsymbol{0}$ and $q_h = 0$ yields

$$\frac{\rho^{\mathrm{s}}\epsilon}{\tau}\big(\dot{\boldsymbol{d}}_h^{n-\frac{1}{2}} - \dot{\boldsymbol{d}}_h^{n-1}, \boldsymbol{w}_h\big)_\Sigma + a^{\mathrm{s}}(\boldsymbol{d}_h^{n,\star}, \boldsymbol{w}_h) = -\big(\boldsymbol{\sigma}(\boldsymbol{u}_h^n, p_h^n)\boldsymbol{n}, \boldsymbol{w}_h\big)_\Sigma + \frac{\gamma\mu}{h}\big(\boldsymbol{u}_h^n - \dot{\boldsymbol{d}}_h^{n-\frac{1}{2}}, \boldsymbol{w}_h\big)_\Sigma$$

for all $\boldsymbol{w}_h \in \boldsymbol{W}_h$. Hence, by adding this expression to (5.12) we get

$$\rho^{\mathrm{s}}\epsilon\big(\partial_\tau \dot{\boldsymbol{d}}_h^n, \boldsymbol{w}_h\big)_\Sigma + a^{\mathrm{s}}(\boldsymbol{d}_h^n, \boldsymbol{w}_h) = -\big(\boldsymbol{\sigma}(\boldsymbol{u}_h^n, p_h^n)\boldsymbol{n}, \boldsymbol{w}_h\big)_\Sigma + \frac{\gamma\mu}{h}\big(\boldsymbol{u}_h^n - \dot{\boldsymbol{d}}_h^{n-\frac{1}{2}}, \boldsymbol{w}_h\big)_\Sigma$$

for all $\boldsymbol{w}_h \in \boldsymbol{W}_h$. In addition, for $n > r$, it follows that

$$a^{\mathrm{s}}(\boldsymbol{d}_h^{n,\star}, \boldsymbol{w}_h) = -\rho^{\mathrm{s}}\epsilon\big(\partial_\tau \dot{\boldsymbol{d}}_h^{n,\star}, \boldsymbol{w}_h\big)_\Sigma - \big(\boldsymbol{\sigma}(\boldsymbol{u}_h^{n,\star}, p_h^{n,\star})\boldsymbol{n}, \boldsymbol{w}_h\big)_\Sigma + \frac{\gamma\mu}{h}\big(\boldsymbol{u}_h^{n,\star} - \dot{\boldsymbol{d}}_h^{n-\frac{1}{2},\star}, \boldsymbol{w}_h\big)_\Sigma$$

for all $\boldsymbol{w}_h \in \boldsymbol{W}_h$. This relation gives an (intrinsic) expression of the elastic extrapolations in (5.11), exclusively in terms of interface fluid quantities and solid velocities. Owing to these observations, the considered fully discrete solution procedure is displayed in Algorithm 5.2.

Algorithm 5.2 Semi-implicit coupling schemes.

For $n > r$:

1. Fluid with solid inertia substep: find $\big(\boldsymbol{u}_h^n, p_h^n, \dot{\boldsymbol{d}}_h^{n-\frac{1}{2}}\big) \in \boldsymbol{V}_h \times Q_h \times \boldsymbol{W}_h$ such that

$$\begin{cases} \rho^{\mathrm{f}}\big(\partial_\tau \boldsymbol{u}_h^n, \boldsymbol{v}_h\big)_{\Omega^{\mathrm{f}}} + a^{\mathrm{f}}\big((\boldsymbol{u}_h^n, p_h^n), (\boldsymbol{v}_h, q_h)\big) + S_h\big((\boldsymbol{u}_h^n, p_h^n), (\boldsymbol{v}_h, q_h)\big) \\ + \dfrac{\rho^{\mathrm{s}}\epsilon}{\tau}\big(\dot{\boldsymbol{d}}_h^{n-\frac{1}{2}} - (\dot{\boldsymbol{d}}_h^{n-1} + \tau\partial_\tau \dot{\boldsymbol{d}}_h^{n,\star}), \boldsymbol{w}_h\big)_\Sigma - \big(\boldsymbol{\sigma}(\boldsymbol{u}_h^n, p_h^n)\boldsymbol{n}, \boldsymbol{v}_h - \boldsymbol{w}_h\big)_\Sigma \\ - \big(\boldsymbol{u}_h^n - \dot{\boldsymbol{d}}_h^{n-\frac{1}{2}}, \boldsymbol{\sigma}(\boldsymbol{v}_h, -q_h)\boldsymbol{n}\big)_\Sigma + \dfrac{\gamma\mu}{h}\big(\boldsymbol{u}_h^n - \dot{\boldsymbol{d}}_h^{n-\frac{1}{2}}, \boldsymbol{v}_h - \boldsymbol{w}_h\big)_\Sigma \\ - \big(\boldsymbol{\sigma}(\boldsymbol{u}_h^{n,\star}, p_h^{n,\star})\boldsymbol{n}, \boldsymbol{w}_h\big)_\Sigma + \dfrac{\gamma\mu}{h}\big(\boldsymbol{u}_h^{n,\star} - \dot{\boldsymbol{d}}_h^{n-\frac{1}{2},\star}, \boldsymbol{w}_h\big)_\Sigma = 0 \end{cases} \tag{5.13}$$

   for all $(\boldsymbol{v}_h, q_h, \boldsymbol{w}_h) \in \boldsymbol{V}_h \times Q_h \times \boldsymbol{W}_h$.

2. Solid substep: find $\big(\dot{\boldsymbol{d}}_h^n, \boldsymbol{d}_h^n\big) \in \boldsymbol{W}_h \times \boldsymbol{W}_h$ such that $\dot{\boldsymbol{d}}_h^n = \partial_\tau \boldsymbol{d}_h^n$ and

$$\frac{\rho^{\mathrm{s}}\epsilon}{\tau}\big(\partial_\tau \dot{\boldsymbol{d}}_h^n, \boldsymbol{w}_h\big)_\Sigma + a^{\mathrm{s}}(\boldsymbol{d}_h^n, \boldsymbol{w}_h) = -\big(\boldsymbol{\sigma}(\boldsymbol{u}_h^n, p_h^n)\boldsymbol{n}, \boldsymbol{w}_h\big)_\Sigma + \frac{\gamma\mu}{h}\big(\boldsymbol{u}_h^n - \dot{\boldsymbol{d}}_h^{n-\frac{1}{2}}, \boldsymbol{w}_h\big)_\Sigma$$

   for all $\boldsymbol{w}_h \in \boldsymbol{W}_h$.

Remark 5.2 *It should be noted that for $r = 1, 2$ additional data is needed to start the time-marching in Algorithm 5.2. In practice, this data can be obtained by performing one step of the scheme with $r = 0$, this yields $(\boldsymbol{u}_h^1, p_h^1, \dot{\boldsymbol{d}}_h^1)$, and then one step of the scheme with $r = 1$, which gives $(\boldsymbol{u}_h^2, p_h^2, \dot{\boldsymbol{d}}_h^2)$.*

It is worth noting that the semi-implicit coupling scheme provided by Algorithm 5.2 has a reduced computational complexity with respect to Algorithm 5.1. Indeed, the solid contribution to (5.13) reduces to a simple interface mass-matrix, which does not degrade the conditioning of the system matrix. This reduction in the coupling complexity is particularly important when considering general shell models (see, e.g., [CB11]), whose elastic contributions incorporate additional unknowns (e.g., rotations).

In the following sections, we show that Algorithm 5.2 preserves the stability and accuracy properties of the explicit coupling schemes introduced in Section 1.4.3.5 with fitted meshes. Moreover, it overcomes the severe stability restrictions observed in [BCG11] for the traditional time-marching schemes of the immersed boundary method. It is worth noting that these stability conditions have been recently overcome in [BCG15] by resorting to a full implicit treatment of the kinematic-dynamic

coupling (in the spirit of Algorithm 5.1), which yields a solution procedure much more computationally demanding than Algorithm 5.2.

Algorithm 5.2 with $r = 1$ delivers unconditional optimal overall first-order accuracy. This is also significant progress with respect to Algorithm 1.4, whose accuracy, as already mentioned, is non-uniform in h.

Kinematic perturbation of implicit coupling. We conclude this section by pointing out a fundamental property of Algorithm 5.2. To this purpose, we will make use of the discrete reconstruction $\boldsymbol{L}_h^{\mathrm{e}} : \boldsymbol{W} \to \boldsymbol{W}_h$ of the elastic solid operator introduced in (1.88). Owing to (1.88) and (5.12), we infer that

$$\dot{\boldsymbol{d}}_h^{n-\frac{1}{2}} = \dot{\boldsymbol{d}}_h^n + \frac{\tau}{\rho^{\mathrm{s}}\epsilon}\boldsymbol{L}_h^{\mathrm{e}}(\boldsymbol{d}_h^n - \boldsymbol{d}_h^{n,\star}) \tag{5.14}$$

for $n > r$. On the other hand, adding (5.11) and (5.12) yields

$$\left\{\begin{array}{l} \rho^{\mathrm{f}}\big(\partial_\tau \boldsymbol{u}_h^n, \boldsymbol{v}_h\big)_{\Omega^{\mathrm{f}}} + a^{\mathrm{f}}\big((\boldsymbol{u}_h^n, p_h^n), (\boldsymbol{v}_h, q_h)\big) + S_h\big((\boldsymbol{u}_h^n, p_h^n), (\boldsymbol{v}_h, q_h)\big) \\ + \rho^{\mathrm{s}}\epsilon\big(\partial_\tau \dot{\boldsymbol{d}}_h^n, \boldsymbol{w}_h\big)_\Sigma + a^{\mathrm{s}}(\boldsymbol{d}_h^n, \boldsymbol{w}_h) - \big(\boldsymbol{\sigma}(\boldsymbol{u}_h^n, p_h^n)\boldsymbol{n}, \boldsymbol{v}_h - \boldsymbol{w}_h\big)_\Sigma \\ - \big(\boldsymbol{u}_h^n - \dot{\boldsymbol{d}}_h^{n-\frac{1}{2}}, \boldsymbol{\sigma}(\boldsymbol{v}_h, -q_h)\boldsymbol{n}\big)_\Sigma + \dfrac{\gamma\mu}{h}\big(\boldsymbol{u}_h^n - \dot{\boldsymbol{d}}_h^{n-\frac{1}{2}}, \boldsymbol{v}_h - \boldsymbol{w}_h\big)_\Sigma = 0 \end{array}\right. \tag{5.15}$$

for all $(\boldsymbol{v}_h, q_h, \boldsymbol{w}_h) \in \boldsymbol{V}_h \times Q_h \times \boldsymbol{W}_h$ and $n > r$. Thus, Algorithm 5.2 can be regarded as a kinematic perturbation of the fully implicit time discretization given by Algorithm 5.1. As a matter of fact, Algorithm 5.1 formally enforces (through Nitsche's method) the interface condition

$$\boldsymbol{u}_h^n \simeq \dot{\boldsymbol{d}}_h^n,$$

whereas (5.14)-(5.15) imposes

$$\boldsymbol{u}_h^n \simeq \dot{\boldsymbol{d}}_h^n + \frac{\tau}{\rho^{\mathrm{s}}\epsilon}\boldsymbol{L}_h^{\mathrm{e}}(\boldsymbol{d}_h^n - \boldsymbol{d}_h^{n,\star}).$$

Note that the size of the perturbation depends on the extrapolation order r. The basic idea in the forthcoming analysis is to investigate how the kinematic perturbation (5.14) affects the stability and convergence of the underlying implicit coupling scheme (Algorithm 5.1). Thus, this approach unifies, in the same framework, the analysis of Algorithm 5.1 and Algorithm 5.2.

5.2.2 Stability and convergence analysis

We consider the following mesh-dependent semi-norms for function values f on the interface Σ,

$$\|f\|^2_{\frac{1}{2},h,\Sigma} = \sum_{K\in\mathcal{G}_h} h_K^{-1}\|f\|^2_{0,\Sigma_K}, \quad \|f\|^2_{-\frac{1}{2},h,\Sigma} = \sum_{K\in\mathcal{G}_h} h_K\|f\|^2_{0,\Sigma_K}.$$

For the rest of the section, we assume that γ and c_{g} are taken so that Lemma 1.2 holds. The following estimates involving the solid elastic operator will be used,

$$\|\boldsymbol{L}_h^{\mathrm{e}}\boldsymbol{d}\|_{0,\Sigma} \leq \|\boldsymbol{L}^{\mathrm{e}}\boldsymbol{d}\|_{0,\Sigma}, \tag{5.16}$$

$$\|\boldsymbol{w}_h\|_{\mathrm{s}}^2 \leq \frac{\beta^{\mathrm{s}} C_{\mathrm{I}}^2}{h^2}\|\boldsymbol{w}_h\|_{0,\Sigma}^2, \tag{5.17}$$

$$\|\boldsymbol{L}_h^{\mathrm{e}}\boldsymbol{w}_h\|_{\mathrm{s}} \leq \frac{\beta^{\mathrm{s}} C_{\mathrm{I}}^2}{h^2}\|\boldsymbol{w}_h\|_{\mathrm{s}}, \tag{5.18}$$

$$\|\boldsymbol{L}_h^{\mathrm{e}}\boldsymbol{w}_h\|_{0,\Sigma} \leq \frac{(\beta^{\mathrm{s}})^{\frac{1}{2}} C_{\mathrm{I}}}{h}\|\boldsymbol{w}_h\|_{\mathrm{s}}, \tag{5.19}$$

for all $\boldsymbol{d} \in \boldsymbol{D}$ and $\boldsymbol{w}_h \in \boldsymbol{W}_h$ and with $C_{\mathrm{I}} > 0$ the constant of a discrete inverse inequality. Estimates (5.16)-(5.19) follow readily from application of the Cauchy-Schwarz inequality, the definition (1.88) and the continuity estimate (5.4) (see [Fer13, Appendix A] for the details). Finally, the *discrete Gronwall lemma* (see, e.g., [HR90]), which we collect here without a proof, will also be used.

Lemma 5.1 *Let τ, B and a_m, b_m, c_m, η_m (for integers $m \geq 1$) be nonnegative numbers such that*

$$a_n + \tau \sum_{m=1}^{n} b_m \leq \tau \sum_{m=1}^{n} \eta_m a_m + \tau \sum_{m=1}^{n} c_m + B$$

for $n \geq 1$. Suppose that $\tau\eta_m < 1$ for all $m \geq 1$. Then, there holds

$$a_n + \tau \sum_{m=1}^{n} b_m \leq \exp\left(\tau \sum_{m=1}^{n} \frac{\eta_m}{1-\tau\eta_m}\right)\left(\tau \sum_{m=1}^{n} c_m + B\right)$$

for $n \geq 1$.

5.2.2.1 Stability analysis

At time-step t_n, we define the total discrete energy by

$$E_h^n \stackrel{\mathrm{def}}{=} \rho^{\mathrm{f}}\|\boldsymbol{u}_h^n\|_{0,\Omega^{\mathrm{f}}}^2 + \rho^{\mathrm{s}}\epsilon\|\dot{\boldsymbol{d}}_h^n\|_{0,\Sigma}^2 + \|\boldsymbol{d}_h^n\|_{\mathrm{s}}^2, \tag{5.20}$$

and the dissipation as

$$\begin{aligned} D_h^n \stackrel{\mathrm{def}}{=} &\frac{\rho^{\mathrm{f}}}{\tau}\|\boldsymbol{u}_h^n - \boldsymbol{u}_h^{n-1}\|_{0,\Omega^{\mathrm{f}}}^2 + \frac{\rho^{\mathrm{s}}\epsilon}{\tau}\|\dot{\boldsymbol{d}}_h^n - \dot{\boldsymbol{d}}_h^{n-1}\|_{0,\Sigma}^2 + \frac{1}{\tau}\|\boldsymbol{d}_h^n - \boldsymbol{d}_h^{n-1}\|_{\mathrm{s}}^2 \\ &+ c_{\mathrm{g}}\left(\mu\|\boldsymbol{\nabla}\boldsymbol{u}_h^n\|_{0,\Omega_h}^2 + \gamma\mu\|\boldsymbol{u}_h^n - \dot{\boldsymbol{d}}_h^{n-\frac{1}{2}}\|_{\frac{1}{2},h,\Sigma}^2 + |(\boldsymbol{u}_h^n, p_h^n)|_S^2\right). \end{aligned}$$

The following result states the energy stability of the semi-implicit schemes reported in Algorithm 5.2. In the succeeding text, the symbol $\lesssim$ indicates an inequality up to a multiplicative constant (independent of the physical and discretization parameters and of the fluid-interface intersection).

Theorem 5.1 *Let* $\{(\boldsymbol{u}_h^n, p_h^n, \dot{\boldsymbol{d}}_h^{n-\frac{1}{2}}, \boldsymbol{d}_h^n, \dot{\boldsymbol{d}}_h^n)\}_{n>r}$ *be the sequence given by Algorithm 5.2, with the initialization procedure of Remark 5.2 for* $r = 1, 2$. *Assume that* $\gamma > 0$ *is given by Lemma 1.2. Then, we have the following a priori energy estimates:*

- *For* $r = 0, 1$ *and* $n > r$, *there holds*

$$E_h^n + \tau \sum_{m=r+1}^{n} D_h^m \lesssim E_h^0, \tag{5.21}$$

  irrespectively of the discretization parameters.

- *For* $r = 2$ *and* $n > 2$, *there holds*

$$E_h^n + \tau \sum_{m=3}^{n} D_h^m \lesssim \exp\left(\frac{t_n \zeta}{1 - \tau\zeta}\right) E_h^0, \tag{5.22}$$

  provided the following conditions hold

$$\tau(\omega^{\mathrm{s}})^{\frac{6}{5}} \leq \zeta h^{\frac{6}{5}}, \quad \tau\zeta < 1, \quad \zeta > 0, \tag{5.23}$$

  with $\omega^{\mathrm{s}} \overset{\text{def}}{=} C_{\mathrm{I}} \sqrt{\beta^{\mathrm{s}}/(\rho^{\mathrm{s}}\epsilon)}$.

Proof. The proof follows by combining arguments from [BF14b] and [Fer13]. We first test (5.15) with

$$(\boldsymbol{v}_h, q_h, \boldsymbol{w}_h) = \tau(\boldsymbol{u}_h^n, p_h^n, \dot{\boldsymbol{d}}_h^{n-\frac{1}{2}})$$

for $n > r$. This yields the following discrete energy equation,

$$\begin{aligned}
\frac{\rho^{\mathrm{f}}}{2}\Big(\tau\partial_\tau\|\boldsymbol{u}_h^n\|_{0,\Omega^{\mathrm{f}}}^2 + \|\boldsymbol{u}_h^n - \boldsymbol{u}_h^{n-1}\|_{0,\Omega^{\mathrm{f}}}^2\Big) + 2\mu\tau\|\boldsymbol{\varepsilon}(\boldsymbol{u}_h^n)\|_{0,\Omega^{\mathrm{f}}}^2 + \tau|(\boldsymbol{u}_h^n, p_h^n)|_S^2 \\
+ \rho^{\mathrm{s}}\epsilon\tau\big(\partial_\tau\dot{\boldsymbol{d}}_h^n, \dot{\boldsymbol{d}}_h^{n-\frac{1}{2}}\big)_\Sigma + \tau a^{\mathrm{s}}(\boldsymbol{d}_h^n, \dot{\boldsymbol{d}}_h^{n-\frac{1}{2}}) + 2\tau\big(\boldsymbol{\sigma}(\boldsymbol{u}_h^n, 0)\boldsymbol{n}, \boldsymbol{u}_h^n - \dot{\boldsymbol{d}}_h^{n-\frac{1}{2}}\big)_\Sigma \\
+ \gamma\mu\tau\|\boldsymbol{u}_h^n - \dot{\boldsymbol{d}}_h^{n-\frac{1}{2}}\|_{\frac{1}{2},h,\Sigma}^2 = 0
\end{aligned}$$

for $n > r$. Hence, from Lemma 1.2, we have that

$$\begin{aligned}
\frac{\rho^{\mathrm{f}}}{2}\Big(\tau\partial_\tau\|\boldsymbol{u}_h^n\|_{0,\Omega^{\mathrm{f}}}^2 + \|\boldsymbol{u}_h^n - \boldsymbol{u}_h^{n-1}\|_{0,\Omega^{\mathrm{f}}}^2\Big) \\
+ c_{\mathrm{g}}\tau\left(\mu\|\boldsymbol{\nabla}\boldsymbol{u}_h^n\|_{0,\Omega_h}^2 + \gamma\mu\|\boldsymbol{u}_h^n - \dot{\boldsymbol{d}}_h^{n-\frac{1}{2}}\|_{\frac{1}{2},h,\Sigma}^2 + |(\boldsymbol{u}_h^n, p_h^n)|_S^2\right) \\
+ \rho^{\mathrm{s}}\epsilon\tau\big(\partial_\tau\dot{\boldsymbol{d}}_h^n, \dot{\boldsymbol{d}}_h^{n-\frac{1}{2}}\big)_\Sigma + \tau a^{\mathrm{s}}(\boldsymbol{d}_h^n, \dot{\boldsymbol{d}}_h^{n-\frac{1}{2}}) \leq 0
\end{aligned}$$

and, owing to (5.14), we finally get the following fundamental energy inequality

$$\begin{aligned}
&\frac{\rho^{\mathrm{f}}}{2}\left(\tau\partial_\tau\|\boldsymbol{u}_h^n\|_{0,\Omega^{\mathrm{f}}}^2+\|\boldsymbol{u}_h^n-\boldsymbol{u}_h^{n-1}\|_{0,\Omega^{\mathrm{f}}}^2\right)\\
&\qquad+c_{\mathrm{g}}\tau\left(\mu\|\boldsymbol{\nabla}\boldsymbol{u}_h^n\|_{0,\Omega_h}^2+\gamma\mu\|\boldsymbol{u}_h^n-\dot{\boldsymbol{d}}_h^{n-\frac{1}{2}}\|_{\frac{1}{2},h,\Sigma}^2+|(\boldsymbol{u}_h^n,p_h^n)|_S^2\right)\\
&+\frac{\rho^{\mathrm{s}}\epsilon}{2}\left(\tau\partial_\tau\|\dot{\boldsymbol{d}}_h^n\|_{0,\Sigma}^2+\|\dot{\boldsymbol{d}}_h^n-\dot{\boldsymbol{d}}_h^{n-1}\|_{0,\Sigma}^2\right)+\frac{1}{2}\left(\tau\partial_\tau\|\boldsymbol{d}_h^n\|_{\mathrm{s}}^2+\|\boldsymbol{d}_h^n-\boldsymbol{d}_h^{n-1}\|_{\mathrm{s}}^2\right)\\
&\qquad+\underbrace{\tau^2\left(\partial_\tau\dot{\boldsymbol{d}}_h^n,\boldsymbol{L}_h^{\mathrm{e}}(\boldsymbol{d}_h^n-\boldsymbol{d}_h^{n,\star})\right)_\Sigma}_{T_1}+\underbrace{\frac{\tau^2}{\rho^{\mathrm{s}}\epsilon}\left(\boldsymbol{L}_h^{\mathrm{e}}\boldsymbol{d}_h^n,\boldsymbol{L}_h^{\mathrm{e}}(\boldsymbol{d}_h^n-\boldsymbol{d}_h^{n,\star})\right)_\Sigma}_{T_2}\lesssim 0 \qquad (5.24)
\end{aligned}$$

for $n>r$. The terms T_1 and T_2, introduced by the perturbed kinematic condition (5.14), can be controlled as in [Fer13, Theorem 1] for each extrapolation order $r=0,1,2$. For the sake of completeness, the different estimates are briefly recalled below.

Algorithm 5.2 with $r=0$. In this case, using Young's inequality, we have

$$T_1+T_2\geq-\frac{\rho^{\mathrm{s}}\epsilon}{3}\|\dot{\boldsymbol{d}}_h^n-\dot{\boldsymbol{d}}_h^{n-1}\|_{0,\Sigma}^2+\frac{\tau^2}{4\rho^{\mathrm{s}}\epsilon}\|\boldsymbol{L}_h^{\mathrm{e}}\boldsymbol{d}_h^n\|_{0,\Sigma}^2 \qquad (5.25)$$

for $n>0$. Hence, the estimate (5.21) follows by inserting this expression into (5.24) and summing over $m=1,\dots,n$.

Algorithm 5.2 with $r=1$. In this case we have

$$T_1=\frac{\tau^2}{2}\left(\tau\partial_\tau\|\dot{\boldsymbol{d}}_h^n\|_{\mathrm{s}}^2+\|\dot{\boldsymbol{d}}_h^n-\dot{\boldsymbol{d}}_h^{n-1}\|_{\mathrm{s}}^2\right) \qquad (5.26)$$

and

$$T_2=\frac{\tau^2}{2\rho^{\mathrm{s}}\epsilon}\left(\tau\partial_\tau\|\boldsymbol{L}_h^{\mathrm{e}}\boldsymbol{d}_h^n\|_{0,\Sigma}^2+\|\boldsymbol{L}_h^{\mathrm{e}}(\boldsymbol{d}_h^n-\boldsymbol{d}_h^{n-1})\|_{0,\Sigma}^2\right) \qquad (5.27)$$

for $n>1$. Hence, by inserting this expression into (5.24) and summing over $m=2,\dots,n$ we get the estimate

$$E_h^n+\tau\sum_{m=2}^{n}D_h^m\lesssim E_h^1+\frac{\tau^2}{2}\|\dot{\boldsymbol{d}}_h^1\|_{\mathrm{s}}^2+\frac{\tau^2}{2\rho^{\mathrm{s}}\epsilon}\|\boldsymbol{L}_h^{\mathrm{e}}\boldsymbol{d}_h^1\|_{0,\Sigma}^2.$$

The last two terms, related to the initialization of the scheme (see Remark 5.2), can be bounded using (5.21) with $r=0$, $n=1$ and the additional control given by (5.25). This yields the estimate (5.21) in the case $r=1$.

Algorithm 5.2 with $r=2$. In this case, the term T_1 in (5.24) reduces simply to

$$T_1=\tau\left(\dot{\boldsymbol{d}}_h^n-\dot{\boldsymbol{d}}_h^{n-1},\boldsymbol{L}^{\mathrm{e}}(\boldsymbol{d}_h^n-2\boldsymbol{d}_h^{n-1}+\boldsymbol{d}_h^{n-2})\right)_\Sigma=\tau^2\|\dot{\boldsymbol{d}}_h^n-\dot{\boldsymbol{d}}_h^{n-1}\|_{\mathrm{s}}^2. \qquad (5.28)$$

The term T_2, which reads as

$$T_2 = \frac{\tau^3}{\rho^{\mathrm{s}}\epsilon}\left(\boldsymbol{L}_h^{\mathrm{e}}\boldsymbol{d}_h^n, \boldsymbol{L}_h^{\mathrm{e}}(\dot{\boldsymbol{d}}_h^n - \dot{\boldsymbol{d}}_h^{n-1})\right)_\Sigma, \tag{5.29}$$

is treated as in [Fer13, Page 38] using (5.17) and (5.18), which yields

$$T_2 \geq -\tau^6\frac{(\omega^{\mathrm{s}})^6}{h^6}\|\boldsymbol{d}_h^n\|_{\mathrm{s}}^2 - \frac{\rho^{\mathrm{s}}\epsilon}{4}\|\dot{\boldsymbol{d}}_h^n - \dot{\boldsymbol{d}}_h^{n-1}\|_{0,\Sigma}^2. \tag{5.30}$$

We now proceed by inserting (5.28) and (5.30) into (5.24) and summing over $m = 3, \ldots, n$. The last term of (5.30) is controlled by the numerical dissipation provided by (5.24), while the first is handled via Lemma 5.1 under condition (5.23). This yields the bound

$$E_h^n + \sum_{m=3}^{n} D_h^m \lesssim \exp\left(\frac{t_n\zeta}{1-\tau\zeta}\right)E_h^2.$$

The estimate (5.22) for $r = 2$ then follows by using the energy estimate (5.21) with $r = 1$ and $n = 2$, the additional control provided by (5.26) and (5.27), and the stability condition (5.23).

■

Remark 5.3 *Note that testing* (5.10) *with* $(\boldsymbol{v}_h, q_h, \boldsymbol{w}_h) = \tau(\boldsymbol{u}_h^n, p_h^n, \dot{\boldsymbol{d}}_h^n)$ *for* $n > 0$, *equation* (5.24) *holds with* $\dot{\boldsymbol{d}}_h^{n-\frac{1}{2}} = \dot{\boldsymbol{d}}_h^n$ *and* $T_1 = T_2 = 0$. *Thus, for Algorithm 5.1, the following energy estimate holds,*

$$E_h^n + \tau\sum_{m=1}^{n} D_h^m \lesssim E_h^0$$

for $n > 0$ *and* $\gamma > 0$ *given by Lemma 1.2, irrespectively of the discretization parameters.*

5.2.2.2 Convergence analysis

In the following, we use the notation $f^n \overset{\text{def}}{=} f(n\tau)$ for a given time dependent function f. We may consider then $\partial_\tau f^n$ and $f^{n,\star}$, involving the quantities f^n, f^{n-1} and f^{n-2}. Furthermore, for the sake of the notation, we will use $\partial_t f^n$ to denote $(\partial_t f)^n$.

Interpolation operators. In this section we assume that the interface Σ is flat. Basically, the discrete interpolation operators are those used in [BF14b, Section 3.3] for the error analysis of the space semi-discrete formulation (5.5). For the solid displacement, we consider the *elastic Ritz-projection operator* $\boldsymbol{\pi}_h^{\mathrm{s}} : \boldsymbol{W} \to \boldsymbol{W}_h$ defined by the relation

$$a^{\mathrm{s}}(\boldsymbol{w} - \boldsymbol{\pi}_h^{\mathrm{s}}\boldsymbol{w}, \boldsymbol{w}_h) = 0$$

for all $\boldsymbol{w}_h \in \boldsymbol{W}_h$, and for which there holds

$$\|\boldsymbol{w} - \boldsymbol{\pi}_h^{\mathrm{s}} \boldsymbol{w}\|_{0,\Sigma} \lesssim h^2 |\boldsymbol{w}|_{2,\Sigma}$$

for all $\boldsymbol{w} \in [H^2(\Sigma)]^d \cap \boldsymbol{W}$. Thus, from standard approximation theory, it holds

$$\|\boldsymbol{w} - \boldsymbol{\pi}_h^{\mathrm{s}} \boldsymbol{w}\|_{0,\Sigma} + h\|\boldsymbol{\nabla}(\boldsymbol{w} - \boldsymbol{\pi}_h^{\mathrm{s}} \boldsymbol{w})\|_{0,\Sigma} \lesssim h^2 |\boldsymbol{w}|_{2,\Sigma} \tag{5.31}$$

for all $\boldsymbol{w} \in [H^2(\Sigma)]^d \cap \boldsymbol{W}$. Note also that owing to definition (1.88), we have

$$(\boldsymbol{L}_h^{\mathrm{e}} \boldsymbol{\pi}_h^{\mathrm{s}} \boldsymbol{w}, \boldsymbol{w}_h)_\Sigma = a^{\mathrm{s}}(\boldsymbol{\pi}_h^{\mathrm{s}} \boldsymbol{w}, \boldsymbol{w}_h) = a^{\mathrm{s}}(\boldsymbol{w}, \boldsymbol{w}_h) = (\boldsymbol{L}_h^{\mathrm{e}} \boldsymbol{w}, \boldsymbol{w}_h)_\Sigma,$$

and thus

$$\boldsymbol{L}_h^{\mathrm{e}} \boldsymbol{\pi}_h^{\mathrm{s}} = \boldsymbol{L}_h^{\mathrm{e}}. \tag{5.32}$$

For the solid velocity, we consider the operator $\boldsymbol{\mathcal{I}}_h : \boldsymbol{W} \to \boldsymbol{W}_h$ defined by the relation

$$\boldsymbol{\mathcal{I}}_h \boldsymbol{w} \overset{\text{def}}{=} \boldsymbol{\pi}_h^{\mathrm{s}} \boldsymbol{w} + \sum_i \alpha_i \boldsymbol{\varphi}_i,$$

with $\alpha_i \in \mathbb{R}$. The $\boldsymbol{\varphi}_i$ are functions with support in the macropatches P_i, such that

$$0 \le \boldsymbol{\varphi}_i \le 1, \quad \|\boldsymbol{\varphi}_i\|_{0,P_i} \lesssim h^{\frac{d-1}{2}}$$

and take the value 1, component-wise, in the interior nodes of the associated patch P_i. The scalars α_i are chosen so that the following orthogonality condition holds

$$\int_{P_i} (\boldsymbol{w} - \boldsymbol{\mathcal{I}}_h \boldsymbol{w}) \cdot \boldsymbol{n} = 0. \tag{5.33}$$

We refer to [BF14b, BBH09] for the detailed construction of such an operator. It can be shown (see [BF14b, Lemma 3.3]) that

$$\|\boldsymbol{w} - \boldsymbol{\mathcal{I}}_h \boldsymbol{w}\|_{0,\Sigma} + h\|\boldsymbol{\nabla}(\boldsymbol{w} - \boldsymbol{\mathcal{I}}_h \boldsymbol{w})\|_{0,\Sigma} \lesssim h^2 |\boldsymbol{w}|_{2,\Sigma} \tag{5.34}$$

for all $\boldsymbol{w} \in [H^2(\Sigma)]^d \cap \boldsymbol{W}$.

Since the fluid physical solution is defined in Ω^{f} and the discrete one in Ω_h, with $\Omega^{\mathrm{f}} \subset \Omega_h$, we consider two *linear continuous lifting operators* $E_2 : H^2(\Omega^{\mathrm{f}}) \to H^2(\mathbb{R}^d)$ and $E_1 : H^1(\Omega^{\mathrm{f}}) \to H^1(\mathbb{R}^d)$, satisfying the bounds $\|E_1 v\|_{H^1(\mathbb{R}^d)} \lesssim \|v\|_{H^1(\Omega^{\mathrm{f}})}$ and $\|E_2 v\|_{H^2(\mathbb{R}^d)} \lesssim \|v\|_{H^2(\Omega^{\mathrm{f}})}$ (see, e.g, [Eva10]). To interpolate the resulting extended fluid solution we consider the *Scott-Zhang operator* i_{sz} (see, e.g., [EG04]). Then it holds (see [BF14b, Lemma 3.3]),

$$\begin{aligned}
&\|\boldsymbol{v} - i_{\mathrm{sz}} E_2 \boldsymbol{v}\|_{0,\Omega^{\mathrm{f}}} + h\|\boldsymbol{\nabla}(\boldsymbol{v} - i_{\mathrm{sz}} E_2 \boldsymbol{v})\|_{0,\Omega^{\mathrm{f}}} \lesssim h^2 |\boldsymbol{v}|_{2,\Omega^{\mathrm{f}}}, \\
&\|q - i_{\mathrm{sz}} E_1 q\|_{0,\Omega^{\mathrm{f}}} + h\|\boldsymbol{\nabla}(q - i_{\mathrm{sz}} E_1 q)\|_{0,\Omega^{\mathrm{f}}} \lesssim h |q|_{1,\Omega^{\mathrm{f}}}, \\
&\|\boldsymbol{\sigma}(\boldsymbol{v} - i_{\mathrm{sz}} E_2 \boldsymbol{v}, q - i_{\mathrm{sz}} E_1 q)\boldsymbol{n}\|_{-\frac{1}{2},h,\Sigma} \lesssim h \left(\|\boldsymbol{v}\|_{2,\Omega^{\mathrm{f}}} + \|q\|_{1,\Omega^{\mathrm{f}}} \right)
\end{aligned} \tag{5.35}$$

for all $\boldsymbol{v} \in [H^2(\Omega^{\mathrm{f}})]^d$ and $q \in H^1(\Omega^{\mathrm{f}})$.

On the other hand, we assume that the stabilization operator (5.6) satisfies

$$\left|\left(i_{\mathrm{sz}}E_2\boldsymbol{v}, i_{\mathrm{sz}}E_1 q\right)\right|_S \lesssim h\left(\mu^{\frac{1}{2}}|\boldsymbol{v}|_{2,\Omega^{\mathrm{f}}} + \mu^{-\frac{1}{2}}|q|_{1,\Omega^{\mathrm{f}}}\right) \tag{5.36}$$

for all $\boldsymbol{v} \in [H^2(\Omega^{\mathrm{f}})]^d$ and $q \in H^1(\Omega^{\mathrm{f}})$. The pressure estimate follows readily from (5.7), the H^1-stability of the Scott-Zhang interpolant and the stability of the extension operator (see [BF14b]). For the estimate regarding the ghost penalty operator (1.55) we refer to [BH12].

Finally, owing to (1.60),(5.35)$_1$ and (5.34), the following result involving both the fluid and solid velocity projections holds

$$\begin{aligned} \|\boldsymbol{v} - i_{\mathrm{sz}}E_2\boldsymbol{v}\|_{\frac{1}{2},h,\Sigma} &\lesssim h\|\boldsymbol{v}\|_{2,\Omega^{\mathrm{f}}}, \\ \|\boldsymbol{w} - \boldsymbol{\mathcal{I}}_h\boldsymbol{w}\|_{\frac{1}{2},h,\Sigma} &\lesssim h^{\frac{3}{2}}\|\boldsymbol{w}\|_{2,\Sigma}, \end{aligned} \tag{5.37}$$

for all $\boldsymbol{v} \in [H^2(\Omega^{\mathrm{f}})]^d$ and $\boldsymbol{w} \in [H^2(\Sigma)]^d \cap \boldsymbol{W}$ (see [BF14b, Lemma 3.3]).

A priori error estimates. We assume that the exact solution of problem (5.1)-(5.2) has the following regularity, for a given final time $T \geq \tau$:

$$\begin{aligned} \boldsymbol{u} &\in \left[H^1\big(0,T;H^2(\Omega^{\mathrm{f}})\big)\right]^d, \quad \boldsymbol{u}|_\Sigma \in \left[H^1\big(0,T;H^2(\Sigma)\big)\right]^d, \\ \partial_{tt}\boldsymbol{u} &\in \left[L^2\big(0,T;L^2(\Omega^{\mathrm{f}})\big)\right]^d, \quad \partial_{tt}\boldsymbol{u}|_\Sigma \in \left[L^2\big(0,T;L^2(\Sigma)\big)\right]^d, \\ p &\in C^0\big([0,T];H^1(\Omega^{\mathrm{f}})\big) \end{aligned} \tag{5.38}$$

and

$$\boldsymbol{L}^{\mathrm{e}}\boldsymbol{d} \in \begin{cases} \left[C^0\big([0,T];L^2(\Sigma)\big)\right]^d & \text{if} \quad r = 0, \\ \left[H^r\big(0,T;L^2(\Sigma)\big)\right]^d & \text{if} \quad r = 1,2. \end{cases} \tag{5.39}$$

For the derivation of the error estimate, let us write the approximation errors for the fluid as,

$$\begin{aligned} E_2\boldsymbol{u}^n - \boldsymbol{u}_h^n &= \underbrace{E_2\boldsymbol{u}^n - i_{\mathrm{sz}}E_2\boldsymbol{u}^n}_{\stackrel{\mathrm{def}}{=}\boldsymbol{\theta}_\pi^n} + \underbrace{i_{\mathrm{sz}}E_2\boldsymbol{u}^n - \boldsymbol{u}_h^n}_{\stackrel{\mathrm{def}}{=}\boldsymbol{\theta}_h^n} \quad \text{in} \quad \Omega_h, \\ E_1 p^n - p_h^n &= \underbrace{E_1 p^n - i_{\mathrm{sz}}E_1 p^n}_{\stackrel{\mathrm{def}}{=} y_\pi^n} + \underbrace{i_{\mathrm{sz}}E_1 p^n - p_h^n}_{\stackrel{\mathrm{def}}{=} y_h^n} \quad \text{in} \quad \Omega_h. \end{aligned} \tag{5.40}$$

Similarly, for the solid we have

$$\begin{aligned} \boldsymbol{d}^n - \boldsymbol{d}_h^n &= \underbrace{\boldsymbol{d}^n - \boldsymbol{\pi}_h^{\mathrm{s}}\boldsymbol{d}^n}_{\stackrel{\mathrm{def}}{=}\boldsymbol{\xi}_\pi^n} + \underbrace{\boldsymbol{\pi}_h^{\mathrm{s}}\boldsymbol{d}^n - \boldsymbol{d}_h^n}_{\stackrel{\mathrm{def}}{=}\boldsymbol{\xi}_h^n} \quad \text{in} \quad \Sigma, \\ \dot{\boldsymbol{d}}^n - \dot{\boldsymbol{d}}_h^n &= \underbrace{\dot{\boldsymbol{d}}^n - \boldsymbol{\mathcal{I}}_h\dot{\boldsymbol{d}}^n}_{\stackrel{\mathrm{def}}{=}\dot{\boldsymbol{\xi}}_\pi^n} + \underbrace{\boldsymbol{\mathcal{I}}_h\dot{\boldsymbol{d}}^n - \dot{\boldsymbol{d}}_h^n}_{\stackrel{\mathrm{def}}{=}\dot{\boldsymbol{\xi}}_h^n} \quad \text{in} \quad \Sigma. \end{aligned} \tag{5.41}$$

Finally, the error in the intermediate solid velocity is split as

$$\dot{\boldsymbol{d}}^n - \dot{\boldsymbol{d}}_h^{n-\frac{1}{2}} = \underbrace{\dot{\boldsymbol{d}}^n - \boldsymbol{\mathcal{I}}_h\dot{\boldsymbol{d}}^n}_{\stackrel{\text{def}}{=}\dot{\boldsymbol{\xi}}_\pi^n} + \underbrace{\boldsymbol{\mathcal{I}}_h\dot{\boldsymbol{d}}^n - \dot{\boldsymbol{d}}_h^{n-\frac{1}{2}}}_{\stackrel{\text{def}}{=}\boldsymbol{\chi}_h^n} \quad \text{in} \quad \Sigma. \tag{5.42}$$

In the sequel, the following equation, relating $\dot{\boldsymbol{\xi}}_h^n$ and $\partial_\tau\boldsymbol{\xi}_h^n$, will be used

$$\dot{\boldsymbol{\xi}}_h^n = \partial_\tau\boldsymbol{\xi}_h^n + \underbrace{\boldsymbol{\mathcal{I}}_h\dot{\boldsymbol{d}}^n - \boldsymbol{\pi}_h^{\mathrm{s}}\partial_\tau\boldsymbol{d}^n}_{\stackrel{\text{def}}{=}\boldsymbol{z}_h^n}. \tag{5.43}$$

Similarly, the discrete error counterpart of (5.14) reads as

$$\begin{aligned}\boldsymbol{\chi}_h^n &= \boldsymbol{\mathcal{I}}_h\dot{\boldsymbol{d}}^n - \dot{\boldsymbol{d}}_h^{n-\frac{1}{2}}\\ &= \boldsymbol{\mathcal{I}}_h\dot{\boldsymbol{d}}^n - \dot{\boldsymbol{d}}_h^n - \frac{\tau}{\rho^{\mathrm{s}}\epsilon}\boldsymbol{L}_h^{\mathrm{e}}(\boldsymbol{d}_h^n - \boldsymbol{d}_h^\star)\\ &= \dot{\boldsymbol{\xi}}_h^n + \frac{\tau}{\rho^{\mathrm{s}}\epsilon}\boldsymbol{L}_h^{\mathrm{e}}(\boldsymbol{\xi}_h^n - \boldsymbol{\xi}_h^{n,\star}) - \frac{\tau}{\rho^{\mathrm{s}}\epsilon}\boldsymbol{L}_h^{\mathrm{e}}(\boldsymbol{d}^n - \boldsymbol{d}^{n,\star})\end{aligned} \tag{5.44}$$

for $n > r$, where we have used (5.32).

We first provide an a priori estimate for the discrete errors $(\boldsymbol{\theta}_h^n, y_h^n, \boldsymbol{\xi}_h^n, \dot{\boldsymbol{\xi}}_h^n, \boldsymbol{\chi}_h^n)$. We define the energy-norm of the discrete error at time step t_n, as

$$\begin{aligned}\mathcal{E}_h^n \stackrel{\text{def}}{=} &(\rho^{\mathrm{f}})^{\frac{1}{2}}\|\boldsymbol{\theta}_h^n\|_{0,\Omega^{\mathrm{f}}} + (\rho^{\mathrm{s}}\epsilon)^{\frac{1}{2}}\|\dot{\boldsymbol{\xi}}_h^n\|_{0,\Sigma} + \|\boldsymbol{\xi}_h^n\|_{\mathrm{s}} + \left(\sum_{m=r+1}^{n} c_{\mathrm{g}}\tau\mu\|\boldsymbol{\nabla}\boldsymbol{\theta}_h^n\|_{0,\Omega^{\mathrm{f}}}^2\right)^{\frac{1}{2}}\\ &+ \left(\sum_{m=r+1}^{n} c_{\mathrm{g}}\tau|(\boldsymbol{\theta}_h^n, y_h^n)|_S^2\right)^{\frac{1}{2}} + \left(\sum_{m=r+1}^{n} c_{\mathrm{g}}\tau\gamma\mu\|\boldsymbol{\theta}_h^n - \boldsymbol{\chi}_h^n\|_{\frac{1}{2},h,\Sigma}^2\right)^{\frac{1}{2}}\end{aligned}$$

for $n > r$.

THEOREM 5.2 *Let $(\boldsymbol{u}, p, \boldsymbol{d}, \dot{\boldsymbol{d}})$ be the solution of the coupled problem (5.1)-(5.2) and $\{(\boldsymbol{u}_h^n, p_h^n, \dot{\boldsymbol{d}}_h^{n-\frac{1}{2}}, \boldsymbol{d}_h^n, \dot{\boldsymbol{d}}_h^n)\}_{n>r}$ be the approximation given by Algorithm 5.2 with initial data $\left(\boldsymbol{u}_h^0, \boldsymbol{d}_h^0, \dot{\boldsymbol{d}}_h^0\right) = \left(i_{\mathrm{sz}}E_2\boldsymbol{u}^0, \boldsymbol{\pi}_h^{\mathrm{s}}\boldsymbol{d}^0, \mathcal{I}_h\dot{\boldsymbol{d}}^0\right)$. The initialization procedure of Remark 5.2 is considered for the schemes with $r = 1, 2$. Suppose that the exact solution has the regularity (5.38)-(5.39). Assume that $\gamma > 0$ is given by Lemma 1.2. For the scheme with $r = 2$ we assume, in addition, that the stability condition (5.23) holds. Then, we have the following error estimates, for $n > r$ and $n\tau < T$:*

$$\mathcal{E}_h^n \lesssim c_1 h + c_2\tau + c_3\tau^{2^{r-1}}. \tag{5.45}$$

Here, the symbols $\{c_i\}_{i=1}^3$ denote positive constants independent of h and τ, but which depend on the physical parameters and on the regularity of $(\boldsymbol{u}, p, \boldsymbol{d}, \dot{\boldsymbol{d}})$.

Proof. The proof combines some of the arguments reported in [BF14b] and [Fer13], with following additional difficulties:

- Only the spatial semi-discrete case is considered in [BF14b];

- The intermediate solid velocity $\dot{\boldsymbol{d}}_h^{n-\frac{1}{2}}$ cannot be eliminated in terms of $\boldsymbol{u}_h^n$, as in [Fer13], which requires the control of an extrapolation dependent term $T_{2,r}$.

The spatial semi-discrete formulation (5.5) is weakly consistent with the coupled problem (5.1)-(5.2). In fact, if we multiply $(5.1)_1$ by $\boldsymbol{v}_h \in \boldsymbol{V}_h$, $(5.1)_2$ by $q_h \in Q_h$ and $(5.2)_1$ by $\boldsymbol{w}_h \in \boldsymbol{W}_h$, integrate by parts and add the resulting equations, we get

$$\begin{aligned}
&\rho^{\mathrm{f}}\big(\partial_t \boldsymbol{u}, \boldsymbol{v}_h\big)_{\Omega^{\mathrm{f}}} + a^{\mathrm{f}}\big((\boldsymbol{u}, p), (\boldsymbol{v}_h, q_h)\big) + \rho^{\mathrm{s}}\epsilon\big(\partial_t \dot{\boldsymbol{d}}, \boldsymbol{w}_h\big)_{\Sigma} + a^{\mathrm{s}}(\boldsymbol{d}, \boldsymbol{w}_h) \\
&- \big(\boldsymbol{\sigma}(\boldsymbol{u}, p)\boldsymbol{n}, \boldsymbol{v}_h - \boldsymbol{w}_h\big)_{\Sigma} - \big(\boldsymbol{u} - \dot{\boldsymbol{d}}, \boldsymbol{\sigma}(\boldsymbol{v}_h, -q_h)\boldsymbol{n}\big)_{\Sigma} + \frac{\gamma\mu}{h}\big(\boldsymbol{u} - \dot{\boldsymbol{d}}, \boldsymbol{v}_h - \boldsymbol{w}_h\big)_{\Sigma} = 0
\end{aligned} \tag{5.46}$$

for all $\boldsymbol{v}_h, q_h, \boldsymbol{w}_h \in \boldsymbol{V}_h \times Q_h \times \boldsymbol{W}_h$. Taking the difference between the continuous problem (5.46) at time $t = t_n$ and the expression (5.15), we obtain, after adding and subtracting $\partial_\tau \boldsymbol{u}^n$ and $\partial_\tau \dot{\boldsymbol{d}}^n$, the following modified Galerkin orthogonality:

$$\begin{aligned}
&\rho^{\mathrm{f}}\,(\partial_\tau(\boldsymbol{u}^n - \boldsymbol{u}_h^n), \boldsymbol{v}_h)_{\Omega^{\mathrm{f}}} + a^{\mathrm{f}}\big((\boldsymbol{u}^n - \boldsymbol{u}_h^n, p^n - p_h^n), (\boldsymbol{v}_h, q_h)\big) \\
&+ \rho^{\mathrm{s}}\epsilon\big(\partial_\tau(\dot{\boldsymbol{d}}^n - \dot{\boldsymbol{d}}_h^n), \boldsymbol{w}_h\big)_{\Sigma} + a^{\mathrm{s}}\big(\boldsymbol{d}^n - \boldsymbol{d}_h^n, \boldsymbol{w}_h\big) - \big(\boldsymbol{\sigma}(\boldsymbol{u}^n - \boldsymbol{u}_h^n, p^n - p_h^n)\boldsymbol{n}, \boldsymbol{v}_h - \boldsymbol{w}_h\big)_{\Sigma} \\
&- \big((\boldsymbol{u}^n - \boldsymbol{u}_h^n) - (\dot{\boldsymbol{d}}^n - \dot{\boldsymbol{d}}_h^{n-\frac{1}{2}}), \boldsymbol{\sigma}(\boldsymbol{v}_h, -q_h)\boldsymbol{n}\big)_{\Sigma} + \frac{\gamma\mu}{h}\big((\boldsymbol{u}^n - \boldsymbol{u}_h^n) - (\dot{\boldsymbol{d}}^n - \dot{\boldsymbol{d}}_h^{n-\frac{1}{2}}), \boldsymbol{v}_h - \boldsymbol{w}_h\big)_{\Sigma} \\
&= -\rho^{\mathrm{f}}\big((\partial_t - \partial_\tau)\boldsymbol{u}^n, \boldsymbol{v}_h\big)_{\Omega^{\mathrm{f}}} - \rho^{\mathrm{s}}\epsilon\big((\partial_t - \partial_\tau)\dot{\boldsymbol{d}}^n, \boldsymbol{w}_h\big)_{\Sigma} + S_h\big((\boldsymbol{u}_h^n, p_h^n), (\boldsymbol{v}_h, q_h)\big)
\end{aligned} \tag{5.47}$$

for all $(\boldsymbol{v}_h, q_h, \boldsymbol{w}_h) \in \boldsymbol{V}_h \times Q_h \times \boldsymbol{W}_h$. Hence, from (5.40)-(5.42), we infer the following equation for the discrete errors $\boldsymbol{\theta}_h^n$, y_h^n, $\boldsymbol{\xi}_h^n$, $\dot{\boldsymbol{\xi}}_h^n$ and $\boldsymbol{\chi}_h^n$:

$$\begin{aligned}
&\rho^{\mathrm{f}}\big(\partial_\tau \boldsymbol{\theta}_h^n, \boldsymbol{v}_h\big)_{\Omega^{\mathrm{f}}} + a^{\mathrm{f}}\big((\boldsymbol{\theta}_h^n, y_h^n), (\boldsymbol{v}_h, q_h)\big) + S_h\big((\boldsymbol{\theta}_h^n, y_h^n), (\boldsymbol{v}_h, q_h)\big) + \rho^{\mathrm{s}}\epsilon\big(\partial_\tau \dot{\boldsymbol{\xi}}_h^n, \boldsymbol{w}_h\big)_{\Sigma} \\
&\quad + a^{\mathrm{s}}\big(\boldsymbol{\xi}_h^n, \boldsymbol{w}_h\big) - \big(\boldsymbol{\sigma}(\boldsymbol{\theta}_h^n, y_h^n)\boldsymbol{n}, \boldsymbol{v}_h - \boldsymbol{w}_h\big)_{\Sigma} - \big(\boldsymbol{\theta}_h^n - \boldsymbol{\chi}_h^n, \boldsymbol{\sigma}(\boldsymbol{v}_h, -q_h)\boldsymbol{n}\big)_{\Sigma} \\
&\quad + \frac{\gamma\mu}{h}\big(\boldsymbol{\theta}_h^n - \boldsymbol{\chi}_h^n, \boldsymbol{v}_h - \boldsymbol{w}_h\big)_{\Sigma} = -\rho^{\mathrm{f}}\big((\partial_t - \partial_\tau)\boldsymbol{u}^n, \boldsymbol{v}_h\big)_{\Omega^{\mathrm{f}}} - \rho^{\mathrm{f}}\,(\partial_\tau \boldsymbol{\theta}_\pi^n, \boldsymbol{v}_h)_{\Omega^{\mathrm{f}}} \\
&\qquad - \rho^{\mathrm{s}}\epsilon\big((\partial_t - \partial_\tau)\dot{\boldsymbol{d}}^n, \boldsymbol{w}_h\big)_{\Sigma} - \rho^{\mathrm{s}}\epsilon\big(\partial_\tau \dot{\boldsymbol{\xi}}_\pi^n, \boldsymbol{w}_h\big)_{\Sigma} - a^{\mathrm{s}}\big(\boldsymbol{\xi}_\pi^n, \boldsymbol{w}_h\big) \\
&\qquad + S_h\big((i_{\mathrm{sz}} E_2 \boldsymbol{u}^n, i_{\mathrm{sz}} E_1 p^n), (\boldsymbol{v}_h, q_h)\big) - \frac{\gamma\mu}{h}\big(\boldsymbol{\theta}_\pi^n - \dot{\boldsymbol{\xi}}_\pi^n, \boldsymbol{v}_h - \boldsymbol{w}_h\big)_{\Sigma} \\
&\quad - a^{\mathrm{f}}\big((\boldsymbol{\theta}_\pi^n, y_\pi^n), (\boldsymbol{v}_h, q_h)\big) + \big(\boldsymbol{\sigma}(\boldsymbol{\theta}_\pi^n, y_\pi^n)\boldsymbol{n}, \boldsymbol{v}_h - \boldsymbol{w}_h\big)_{\Sigma} + \big(\boldsymbol{\theta}_\pi^n - \dot{\boldsymbol{\xi}}_\pi^n, \boldsymbol{\sigma}(\boldsymbol{v}_h, -q_h)\boldsymbol{n}\big)_{\Sigma}
\end{aligned} \tag{5.48}$$

for all $(\boldsymbol{v}_h, q_h, \boldsymbol{w}_h) \in \boldsymbol{V}_h \times Q_h \times \boldsymbol{W}_h$ and $n > r$. Note that $a^{\mathrm{s}}\big(\boldsymbol{\xi}_\pi^n, \boldsymbol{w}_h\big) = 0$ due to the definition of the solid projection operator $\boldsymbol{\pi}_h^{\mathrm{s}}$. Taking $(\boldsymbol{v}_h, q_h, \boldsymbol{w}_h) = \tau(\boldsymbol{\theta}_h^n, y_h^n, \boldsymbol{\chi}_h^n)$ in (5.48), using Lemma 1.2, (5.43) and (5.44), yields the following energy inequality

for the discrete errors:

$$\begin{aligned}
&\frac{\rho^{\mathrm{f}}}{2}\left(\tau\partial_\tau\|\boldsymbol{\theta}_h^n\|_{0,\Omega^{\mathrm{f}}}^2+\tau^2\|\partial_\tau\boldsymbol{\theta}_h^n\|_{0,\Omega^{\mathrm{f}}}^2\right)+\frac{\rho^{\mathrm{s}}\epsilon}{2}\left(\tau\partial_\tau\|\dot{\boldsymbol{\xi}}_h^n\|_{0,\Sigma}^2+\tau^2\|\partial_\tau\dot{\boldsymbol{\xi}}_h^n\|_{0,\Sigma}^2\right)\\
&\qquad+c_{\mathrm{g}}\tau\left(\mu\|\boldsymbol{\nabla}\boldsymbol{\theta}_h^n\|_{0,\Omega_h^{\mathrm{f}}}^2+\gamma\mu\|\boldsymbol{\theta}_h^n-\boldsymbol{\chi}_h^n\|_{\frac{1}{2},h,\Sigma}^2+|(\boldsymbol{\theta}_h^n,y_h^n)|_S^2\right)\\
&+\frac{1}{2}\left(\tau\partial_\tau\|\boldsymbol{\xi}_h^n\|_{\mathrm{s}}^2+\tau^2\|\partial_\tau\boldsymbol{\xi}_h^n\|_{\mathrm{s}}^2\right)\lesssim\underbrace{-\rho^{\mathrm{f}}\tau\big((\partial_t-\partial_\tau)\boldsymbol{u}^n,\boldsymbol{\theta}_h^n\big)_{\Omega^{\mathrm{f}}}-\rho^{\mathrm{f}}\tau\left(\partial_\tau\boldsymbol{\theta}_\pi^n,\boldsymbol{\theta}_h^n\right)_{\Omega^{\mathrm{f}}}}_{T_1}\\
&\qquad\underbrace{-\rho^{\mathrm{s}}\epsilon\tau\big((\partial_t-\partial_\tau)\dot{\boldsymbol{d}}^n,\boldsymbol{\chi}_h^n\big)_\Sigma-\rho^{\mathrm{s}}\epsilon\tau\big(\partial_\tau\dot{\boldsymbol{\xi}}_\pi^n,\boldsymbol{\chi}_h^n\big)_\Sigma}_{T_2}\underbrace{-\tau a^{\mathrm{s}}(\boldsymbol{\xi}_h^n,\boldsymbol{z}_h^n)}_{T_3}\\
&\qquad\underbrace{+\tau S_h\big((i_{\mathrm{sz}}E_2\boldsymbol{u}^n,i_{\mathrm{sz}}E_1p^n),(\boldsymbol{\theta}_h^n,y_h^n)\big)}_{T_4}\underbrace{-\tau\frac{\gamma\mu}{h}\big(\boldsymbol{\theta}_\pi^n-\dot{\boldsymbol{\xi}}_\pi^n,\boldsymbol{\theta}_h^n-\boldsymbol{\chi}_h^n\big)_\Sigma}_{T_5}\\
&\underbrace{+\tau\big(\boldsymbol{\sigma}(\boldsymbol{\theta}_\pi^n,y_\pi^n)\boldsymbol{n},\boldsymbol{\theta}_h^n-\boldsymbol{\chi}_h^n\big)_\Sigma}_{T_6}\underbrace{-\tau a^{\mathrm{f}}\big((\boldsymbol{\theta}_\pi^n,y_\pi^n),(\boldsymbol{\theta}_h^n,y_h^n)\big)+\tau\big(\boldsymbol{\theta}_\pi^n-\dot{\boldsymbol{\xi}}_\pi^n,\boldsymbol{\sigma}(\boldsymbol{\theta}_h^n,-y_h^n)\boldsymbol{n}\big)_\Sigma}_{T_7}\\
&\qquad\underbrace{-\tau^2\left(\partial_\tau\dot{\boldsymbol{\xi}}_h^n,\boldsymbol{L}_h^{\mathrm{e}}(\boldsymbol{\xi}_h^n-\boldsymbol{\xi}_h^{n,\star})\right)_\Sigma-\frac{\tau^2}{\rho^{\mathrm{s}}\epsilon}\left(\boldsymbol{L}_h^{\mathrm{e}}\boldsymbol{\xi}_h^n,\boldsymbol{L}_h^{\mathrm{e}}(\boldsymbol{\xi}_h^n-\boldsymbol{\xi}_h^{n,\star})\right)_\Sigma}_{T_8}\\
&\qquad\underbrace{+\tau^2\left(\partial_\tau\dot{\boldsymbol{\xi}}_h^n,\boldsymbol{L}_h^{\mathrm{e}}(\boldsymbol{d}^n-\boldsymbol{d}^{n,\star})\right)_\Sigma}_{T_9}\underbrace{+\frac{\tau^2}{\rho^{\mathrm{s}}\epsilon}\left(\boldsymbol{L}_h^{\mathrm{e}}\boldsymbol{\xi}_h^n,\boldsymbol{L}_h^{\mathrm{e}}(\boldsymbol{d}^n-\boldsymbol{d}^{n,\star})\right)_\Sigma}_{T_{10}}
\end{aligned}\tag{5.49}$$

for $n>r$. The terms T_1-T_4 stem from the time-stepping and stabilization methods. The terms T_5-T_7 come from Nitsche's method. Finally, terms T_8-T_{10} are due to the kinematic perturbation and depend on the extrapolation order. We proceed by treating each term separately.

Term T_1 can be bounded using a Taylor expansion, (5.35) and the Poincaré inequality with constant C_{P}. This yields

$$\begin{aligned}
T_1&\leq\rho^{\mathrm{f}}\tau\left(\|\partial_t\boldsymbol{u}^n-\partial_\tau\boldsymbol{u}^n\|_{0,\Omega^{\mathrm{f}}}+\|\partial_\tau\boldsymbol{\theta}_\pi^n\|_{0,\Omega^{\mathrm{f}}}\right)\|\boldsymbol{\theta}_h^n\|_{0,\Omega^{\mathrm{f}}}\\
&\leq\rho^{\mathrm{f}}\tau\left(\tau^{\frac{1}{2}}\|\partial_{tt}\boldsymbol{u}\|_{L^2(t_{n-1},t_n;L^2(\Omega^{\mathrm{f}}))}+\tau^{-\frac{1}{2}}\|\partial_t\boldsymbol{\theta}_\pi\|_{L^2(t_{n-1},t_n;L^2(\Omega^{\mathrm{f}}))}\right)\|\boldsymbol{\theta}_h^n\|_{0,\Omega^{\mathrm{f}}}\\
&\leq\frac{(\rho^{\mathrm{f}}C_{\mathrm{P}})^2}{2\varepsilon_1\mu}\left(\tau^2\|\partial_{tt}\boldsymbol{u}\|_{L^2(t_{n-1},t_n;L^2(\Omega^{\mathrm{f}}))}^2+\|\partial_t\boldsymbol{\theta}_\pi\|_{L^2(t_{n-1},t_n;L^2(\Omega^{\mathrm{f}}))}^2\right)+\varepsilon_1\tau\mu\|\boldsymbol{\nabla}\boldsymbol{\theta}_h^n\|_{0,\Omega_h}^2\\
&\lesssim\frac{(\rho^{\mathrm{f}}C_{\mathrm{P}})^2}{2\varepsilon_1\mu}\tau^2\|\partial_{tt}\boldsymbol{u}\|_{L^2(t_{n-1},t_n;L^2(\Omega^{\mathrm{f}}))}^2+\frac{(\rho^{\mathrm{f}}C_{\mathrm{P}})^2}{2\varepsilon_1\mu}h^2\|\partial_t\boldsymbol{u}\|_{L^2(t_{n-1},t_n;H^2(\Omega^{\mathrm{f}}))}^2\\
&\quad+\varepsilon_1\tau\mu\|\boldsymbol{\nabla}\boldsymbol{\theta}_h^n\|_{0,\Omega_h}^2,
\end{aligned}\tag{5.50}$$

with $\varepsilon_1>0$. Note that, by choosing ε_1 small enough, the last term of (5.50) can be absorbed by the left-hand side of (5.49).

For term T_2, using again a Taylor expansion we have

$$\begin{aligned} T_2 &\leq \rho^{\mathrm{s}}\epsilon\tau\big(\|(\partial_t-\partial_\tau)\dot{\boldsymbol{d}}^n\|_{0,\Sigma}+\|\partial_\tau\dot{\boldsymbol{\xi}}_\pi^n\|_{0,\Sigma}\big)\|\boldsymbol{\chi}_h^n\|_{0,\Sigma}\\ &\leq \rho^{\mathrm{s}}\epsilon\tau\left(\tau^{1/2}\|\partial_{tt}\boldsymbol{u}\|_{L^2(t_{n-1},t_n;L^2(\Sigma))}+\tau^{-1/2}\|\partial_t\dot{\boldsymbol{\xi}}_\pi\|_{L^2(t_{n-1},t_n;L^2(\Sigma))}\right)\|\boldsymbol{\chi}_h^n\|_{0,\Sigma}\\ &\lesssim \frac{\rho^{\mathrm{s}}\epsilon T}{2\varepsilon_2}\left(\tau^2\|\partial_{tt}\boldsymbol{u}\|^2_{L^2(t_{n-1},t_n;L^2(\Sigma))}+h^2\|\partial_t\boldsymbol{u}\|^2_{L^2(t_{n-1},t_n;H^2(\Sigma))}\right)+\underbrace{\varepsilon_2\tau\frac{\rho^{\mathrm{s}}\epsilon}{T}\|\boldsymbol{\chi}_h^n\|^2_{0,\Sigma}}_{T_{2,r}}. \end{aligned} \tag{5.51}$$

For the last term, using (5.44) and a triangular inequality, and since $\tau\leq T$, we have

$$\begin{aligned} T_{2,r} &\leq \varepsilon_2\tau\frac{\rho^{\mathrm{s}}\epsilon}{T}\|\dot{\boldsymbol{\xi}}_h^n\|^2_{0,\Sigma}+\varepsilon_2\frac{\tau^3}{\rho^{\mathrm{s}}\epsilon T}\|\boldsymbol{L}_h^{\mathrm{e}}(\boldsymbol{\xi}_h^n-\boldsymbol{\xi}_h^{n,\star})\|^2_{0,\Sigma}+\varepsilon_2\frac{\tau^3}{\rho^{\mathrm{s}}\epsilon T}\|\boldsymbol{L}_h^{\mathrm{e}}(\boldsymbol{d}^n-\boldsymbol{d}^{n,\star})\|^2_{0,\Sigma}\\ &\leq \varepsilon_2\tau\frac{\rho^{\mathrm{s}}\epsilon}{T}\|\dot{\boldsymbol{\xi}}_h^n\|^2_{0,\Sigma}+\varepsilon_2\frac{\tau^2}{\rho^{\mathrm{s}}\epsilon}\|\boldsymbol{L}_h^{\mathrm{e}}(\boldsymbol{\xi}_h^n-\boldsymbol{\xi}_h^{n,\star})\|^2_{0,\Sigma}+\varepsilon_2\frac{\tau^2}{\rho^{\mathrm{s}}\epsilon}\|\boldsymbol{L}_h^{\mathrm{e}}(\boldsymbol{d}^n-\boldsymbol{d}^{n,\star})\|^2_{0,\Sigma}. \end{aligned} \tag{5.52}$$

The first term will be treated via Lemma 5.1 in (5.49). The remaining two terms will, respectively, be controlled bellow via the numerical dissipation provided by the fluid-solid splitting and a Taylor expansion. Since the bound depends on the extrapolation order, we postpone the analysis of $T_{2,r}$ to treat it together with the extrapolation-dependent terms T_8-T_{10}.

For term T_3 using (5.32), (5.4), a triangular inequality, a Taylor expansion and approximation, we have

$$\begin{aligned} T_3 =& -\tau a^{\mathrm{s}}\big(\boldsymbol{\xi}_h^n,\boldsymbol{\mathcal{I}}_h\dot{\boldsymbol{d}}^n-\partial_\tau\boldsymbol{d}^n\big)\leq\tau\|\boldsymbol{\xi}_h^n\|_{\mathrm{s}}\|\boldsymbol{\mathcal{I}}_h\dot{\boldsymbol{d}}^n-\partial_\tau\boldsymbol{d}^n\|_{\mathrm{s}}\\ \leq&\tau T\left(\|\boldsymbol{\mathcal{I}}_h\dot{\boldsymbol{d}}^n-\dot{\boldsymbol{d}}^n\|^2_{\mathrm{s}}+\|\dot{\boldsymbol{d}}^n-\partial_\tau\boldsymbol{d}^n\|^2_{\mathrm{s}}\right)+\frac{\tau}{2T}\|\boldsymbol{\xi}_h^n\|^2_{\mathrm{s}}\\ \lesssim&\tau h^2\beta^{\mathrm{s}}T\|\boldsymbol{u}^n\|^2_{2,\Sigma}+\tau^2\beta^{\mathrm{s}}T\|\partial_t\boldsymbol{u}\|^2_{L^2(t_{n-1},t_n;H^1(\Sigma))}+\frac{\tau}{2T}\|\boldsymbol{\xi}_h^n\|^2_{\mathrm{s}}, \end{aligned} \tag{5.53}$$

where the last term can be controlled via Lemma 5.1 in (5.49).

For term T_4, using the weak consistency of the stabilization operator (5.36), we observe that

$$\begin{aligned} T_4 \leq&\tau\frac{1}{2\varepsilon_4}|(i_{\mathrm{sz}}E_2\boldsymbol{u}^n,i_{\mathrm{sz}}E_1p^n)|^2_S+\tau\frac{\varepsilon_4}{2}|(\boldsymbol{\theta}_h^n,y_h^n)|^2_S\\ \lesssim&\tau h^2\frac{1}{\varepsilon_4\mu}\big(\mu\|\boldsymbol{u}^n\|^2_{2,\Omega^{\mathrm{f}}}+\mu^{-1}\|p^n\|^2_{1,\Omega^{\mathrm{f}}}\big)+\tau\frac{\varepsilon_4}{2}|(\boldsymbol{\theta}_h^n,y_h^n)|^2_S \end{aligned} \tag{5.54}$$

where the third term in the right hand side is absorbed in the left-hand side of (5.49), for $\varepsilon_4>0$ sufficiently small.

The boundary penalty term T_5 is handled using Cauchy-Schwarz inequality fol-

lowed by (5.37),

$$\begin{aligned} T_5 &\leq \tau\frac{1}{2\varepsilon_5}\gamma\mu\|\boldsymbol{\theta}_\pi^n - \dot{\boldsymbol{\xi}}_\pi^n\|^2_{\frac{1}{2},h,\Sigma} + \tau\frac{\varepsilon_5}{2}\gamma\mu\|\boldsymbol{\theta}_h^n - \boldsymbol{\chi}_h^n\|^2_{\frac{1}{2},h,\Sigma} \\ &\lesssim \tau h^2\frac{\gamma\mu}{\varepsilon_5}(\|\boldsymbol{u}^n\|^2_{2,\Omega^{\mathrm{f}}} + h\|\dot{\boldsymbol{d}}^n\|^2_{2,\Sigma}) + \tau\frac{\varepsilon_5}{2}\gamma\mu\|\boldsymbol{\theta}_h^n - \boldsymbol{\chi}_h^n\|^2_{\frac{1}{2},h,\Sigma}. \end{aligned} \tag{5.55}$$

Note that the second term can be absorbed in the left-hand side of (5.49), for $\varepsilon_5 > 0$ small enough.

Similarly, for the consistency term T_6, using $(5.35)_3$, we have

$$\begin{aligned} T_6 \leq& \tau\frac{1}{2\varepsilon_6\gamma\mu}\|\boldsymbol{\sigma}(\boldsymbol{\theta}_\pi^n, y_\pi^n)\boldsymbol{n}\|^2_{-\frac{1}{2},h,\Sigma} + \tau\frac{\varepsilon_6}{2}\gamma\mu\|\boldsymbol{\theta}_h^n - \boldsymbol{\chi}_h^n\|^2_{\frac{1}{2},h,\Sigma} \\ \lesssim& \tau h^2\frac{1}{\varepsilon_6\gamma\mu}\left(\|\boldsymbol{u}^n\|^2_{2,\Omega^{\mathrm{f}}} + \|p^n\|^2_{1,\Omega^{\mathrm{f}}}\right) + \tau\frac{\varepsilon_6}{2}\gamma\mu\|\boldsymbol{\theta}_h^n - \boldsymbol{\chi}_h^n\|^2_{\frac{1}{2},h,\Sigma}. \end{aligned} \tag{5.56}$$

Note that the first term has the right convergence order and the second term can be absorbed in the left hand side of (5.49), for $\varepsilon_6 > 0$ small enough.

To estimate T_7, we split it into two parts as in [BF14b]. The velocity-velocity coupling part can be easily handled by using approximation and the robust trace inequality (1.61), as follows:

$$\begin{aligned} &-\tau a(\boldsymbol{\theta}_\pi^n, \boldsymbol{\theta}_h^n) + \tau\big(\boldsymbol{\sigma}(\boldsymbol{\theta}_h^n, 0)\boldsymbol{n}, \boldsymbol{\theta}_\pi^n - \dot{\boldsymbol{\xi}}_\pi^n\big)_\Sigma \\ &\quad\leq -\tau a(\boldsymbol{\theta}_\pi^n, \boldsymbol{\theta}_h^n) + \tau\mu\varepsilon_7\|\boldsymbol{\varepsilon}(\boldsymbol{\theta}_h^n)\boldsymbol{n}\|^2_{-\frac{1}{2},h,\Sigma} + \tau\mu\frac{1}{\varepsilon_7}\|\boldsymbol{\theta}_\pi^n - \dot{\boldsymbol{\xi}}_\pi^n\|^2_{\frac{1}{2},h,\Sigma} \\ &\quad\lesssim \tau h^2\frac{\mu}{\varepsilon_7 C_{\mathrm{TI}}}\|\boldsymbol{u}^n\|^2_{2,\Omega^{\mathrm{f}}} + \tau\mu\frac{2}{\varepsilon_7}h^2\left(\|\boldsymbol{u}^n\|^2_{2,\Omega^{\mathrm{f}}} + \|\dot{\boldsymbol{d}}^n\|^2_{2,\Sigma}\right) + 2\tau\varepsilon_7\mu C_{\mathrm{TI}}\|\boldsymbol{\nabla}\boldsymbol{\theta}_h^n\|^2_{0,\Omega_h}. \end{aligned} \tag{5.57}$$

The last term can be, once again, absorbed in the left hand side of (5.49), for $\varepsilon_7 > 0$ sufficiently small. For the velocity-pressure coupling part we write, using integration by parts in the continuity equation,

$$\begin{aligned} &-\tau b(y_\pi^n, \boldsymbol{\theta}_h^n) + \tau b(y_h^n, \boldsymbol{\theta}_\pi^n) + \tau\big(\boldsymbol{\sigma}(0, -y_h^n)\boldsymbol{n}, \boldsymbol{\theta}_\pi^n - \dot{\boldsymbol{\xi}}_\pi^n\big)_\Sigma \\ &\qquad= \tau(y_\pi^n, \mathrm{div}\boldsymbol{\theta}_h^n)_{\Omega^{\mathrm{f}}} - \tau(y_h^n, \mathrm{div}\boldsymbol{\theta}_\pi^n)_{\Omega^{\mathrm{f}}} + \tau\big(\boldsymbol{\sigma}(0, -y_h^n)\boldsymbol{n}, \boldsymbol{\theta}_\pi^n - \dot{\boldsymbol{\xi}}_\pi^n\big)_\Sigma \\ &\qquad\qquad= \underbrace{\tau(y_\pi^n, \mathrm{div}\boldsymbol{\theta}_h^n)_{\Omega^{\mathrm{f}}}}_{T_{7,1}} \underbrace{+\tau(\boldsymbol{\nabla} y_h^n, \boldsymbol{\theta}_\pi^n)_{\Omega^{\mathrm{f}}}}_{T_{7,2}} \underbrace{-\tau\big(y_h^n\boldsymbol{n}, \dot{\boldsymbol{\xi}}_\pi^n\big)_\Sigma}_{T_{7,3}}. \end{aligned}$$

For the terms $T_{7,1}$ and $T_{7,2}$, using the Cauchy-Schwarz inequality, (5.35) and (5.36), we have

$$\begin{aligned} T_{7,1} \lesssim& \tau h^2\frac{1}{2\varepsilon_{7,1}\mu}\|p^n\|^2_{1,\Omega^{\mathrm{f}}} + \tau\frac{\varepsilon_{7,1}}{2}\mu\|\boldsymbol{\nabla}\boldsymbol{\theta}_h^n\|^2_{0,\Omega^{\mathrm{f}}}, \\ T_{7,2} \lesssim& \tau h^2\frac{\mu}{2\varepsilon_{7,2}}\|\boldsymbol{u}^n\|^2_{2,\Omega^{\mathrm{f}}} + \tau\frac{\varepsilon_{7,2}}{2}|(0, y_h^n)|^2_S, \end{aligned} \tag{5.58}$$

where the last terms of these inequalities can be absorbed in (5.49), for $\varepsilon_{7,1}, \varepsilon_{7,2} > 0$ small enough. For the third term $T_{7,3}$, denoting by $y_i^n \in \mathbb{R}$ the average of y_h^n over the

interface patch P_i , using the property (5.33) of the operator $\boldsymbol{\mathcal{I}}_h$ and the standard orthogonal projection inequality

$$\|y_h^n - y_i^n\|_{0,P_i} \lesssim h\|\boldsymbol{\nabla} y_h^n\|_{0,P_i},$$

together with the trace inequality (1.60) and (5.7), we get

$$\begin{aligned} T_{7,3} = -\tau \sum_i \left(y_h^n - y_i^n, \dot{\boldsymbol{\xi}}_\pi^n \cdot \boldsymbol{n}\right)_{P_i} \lesssim & \tau \sum_i h\|\boldsymbol{\nabla} y_h^n\|_{0,P_i} h^2 \|\dot{\boldsymbol{\xi}}_\pi^n\|_{2,P_i} \\ \lesssim & \tau h^3 \frac{\mu}{2\varepsilon_{7,3}} \|\dot{\boldsymbol{d}}^n\|_{2,\Sigma}^2 + \tau h^2 \frac{\varepsilon_{7,3}}{2\mu} \|\boldsymbol{\nabla} y_h^n\|_{0,\Omega_h}^2, \quad (5.59) \\ \lesssim & \tau h^3 \frac{\mu}{2\varepsilon_{7,3}} \|\dot{\boldsymbol{d}}^n\|_{2,\Sigma}^2 + \tau \frac{\varepsilon_{7,3}}{2} |(0, y_h^n)|_S^2 \end{aligned}$$

the last terms of these inequality can be absorbed in (5.49), for $\varepsilon_{7,3} > 0$ small enough. The above estimations of $T_{7,1}$, $T_{7,2}$ and $T_{7,3}$ provide bounds which involve either terms with the right convergence order or contributions that can be absorbed by the left-hand side of (5.49).

We now proceed with the extrapolation-dependent terms $T_8 - T_{10}$ and the term $T_{2,r}$ from (5.51). We consider each case of extrapolation separately. Basically, the terms $T_8 - T_{10}$ are controlled as in [Fer13, Theorem 2]. We include these estimates here for the sake of completeness.

Algorithm 5.2 with $r = 0$. We have the bound

$$T_8 \leq -\frac{\tau^2}{\rho^s \epsilon}\left(1 - \frac{1}{2\varepsilon_8}\right) \|\boldsymbol{L}_h^e \boldsymbol{\xi}_h^n\|_{0,\Sigma}^2 + \varepsilon_8 \frac{\rho^s \epsilon}{2} \|\dot{\boldsymbol{\xi}}_h^n - \dot{\boldsymbol{\xi}}_h^{n-1}\|_{0,\Sigma}^2,$$

with $\varepsilon_8 > 0$. On the other hand, we have

$$\begin{aligned} T_9 = & \tau\left(\dot{\boldsymbol{\xi}}_h^n - \dot{\boldsymbol{\xi}}_h^{n-1}, \boldsymbol{L}_h^e \boldsymbol{d}^n\right)_\Sigma \leq \tau \|\dot{\boldsymbol{\xi}}_h^n - \dot{\boldsymbol{\xi}}_h^{n-1}\|_{0,\Sigma} \|\boldsymbol{L}_h^e \boldsymbol{d}^n\|_{0,\Sigma} \\ \leq & \frac{\varepsilon_9 \rho^s \epsilon}{2} \|\dot{\boldsymbol{\xi}}_h^n - \dot{\boldsymbol{\xi}}_h^{n-1}\|_{0,\Sigma}^2 + \frac{\tau^2}{2\varepsilon_9 \rho^s \epsilon} \|\boldsymbol{L}^e \boldsymbol{d}^n\|_{0,\Sigma}^2, \end{aligned}$$

with $\varepsilon_9 > 0$, where we have used the h-uniform bound (5.16). For the last term, we have

$$T_{10} = \frac{\tau^2}{\rho^s \epsilon}\left(\boldsymbol{L}_h^e \boldsymbol{\xi}_h^n, \boldsymbol{L}_h^e \boldsymbol{d}^n\right)_\Sigma \leq \frac{\varepsilon_{10} \tau^2}{2\rho^s \epsilon} \|\boldsymbol{L}_h^e \boldsymbol{\xi}_h^n\|_{0,\Sigma}^2 + \frac{\tau^2}{2\varepsilon_{10} \rho^s \epsilon} \|\boldsymbol{L}^e \boldsymbol{d}^n\|_{0,\Sigma}^2,$$

with $\varepsilon_{10} > 0$. On the other hand, owing to (5.52), we have that for $r = 0$ it holds

$$T_{2,0} \leq \varepsilon_2 \tau \frac{\rho^s \epsilon}{T} \|\dot{\boldsymbol{\xi}}_h^n\|_{0,\Sigma}^2 + \varepsilon_2 \frac{\tau^2}{\rho^s \epsilon} \|\boldsymbol{L}_h^e \boldsymbol{\xi}_h^n\|_{0,\Sigma}^2 + \varepsilon_2 \frac{\tau^2}{\rho^s \epsilon} \|\boldsymbol{L}^e \boldsymbol{d}^n\|_{0,\Sigma}^2.$$

Thus, we get

$$T_8+T_9+T_{10}+T_{2,0}\le \varepsilon_2\tau\frac{\rho^{\mathrm{s}}\epsilon}{T}\|\dot{\boldsymbol{\xi}}_h^n\|_{0,\Sigma}^2-\frac{\tau^2}{\rho^{\mathrm{s}}\epsilon}\left(1-\frac{1}{2\varepsilon_8}-\frac{\varepsilon_{10}}{2}-\varepsilon_2\right)\|\boldsymbol{L}_h^{\mathrm{e}}\boldsymbol{\xi}_h^n\|_{0,\Sigma}^2 + \frac{\tau^2}{2\rho^{\mathrm{s}}\epsilon}\left(\frac{1}{\varepsilon_9}+\frac{1}{\varepsilon_{10}}+\varepsilon_2\right)\|\boldsymbol{L}^{\mathrm{e}}\boldsymbol{d}^n\|_{0,\Sigma}^2+\frac{\rho^{\mathrm{s}}\epsilon}{2}(\varepsilon_8+\varepsilon_9)\|\dot{\boldsymbol{\xi}}_h^n-\dot{\boldsymbol{\xi}}_h^{n-1}\|_{0,\Sigma}^2. \quad (5.60)$$

Taking $\varepsilon_8=\frac{3}{4}$, $\varepsilon_{10}=\frac{1}{3}$ and $\varepsilon_2<\frac{1}{6}$, we have

$$1-\frac{1}{2\varepsilon_8}-\frac{\varepsilon_{10}}{2}-\varepsilon_2>0$$

and the second term on the right-hand side of (5.60) is negative. The last term of (5.60) can be absorbed into the left-hand side of (5.49), for $\varepsilon_9>0$ small enough. In summary, the estimate (5.45) follows by inserting the above estimates into (5.49), summing over $m=1,\dots,n$, and applying Lemma 5.1 with

$$a_m=\frac{\rho^{\mathrm{f}}}{2}\|\boldsymbol{\theta}_h^m\|_{0,\Omega^{\mathrm{f}}}^2+\frac{\rho^{\mathrm{s}}\epsilon}{2}\|\dot{\boldsymbol{\xi}}_h^m\|_{0,\Sigma}^2+\frac{1}{2}\|\boldsymbol{\xi}_h^m\|_{\mathrm{s}}^2,\quad \eta_m=\frac{1}{T}.$$

Note that, owing to the selection of the initial data, we have

$$\boldsymbol{\theta}_h^0=\mathbf{0},\quad \dot{\boldsymbol{\xi}}_h^0=\boldsymbol{\xi}_h^0=\mathbf{0}. \quad (5.61)$$

Algorithm 5.2 with $r=1$. For the term T_8, using (5.32), we have

$$T_8=-\frac{\tau^2}{2}\left(\|\dot{\boldsymbol{\xi}}_h^n\|_{\mathrm{s}}^2-\|\dot{\boldsymbol{\xi}}_h^{n-1}\|_{\mathrm{s}}^2+\|\dot{\boldsymbol{\xi}}_h^n-\dot{\boldsymbol{\xi}}_h^{n-1}\|_{\mathrm{s}}^2\right)\underbrace{+\tau^2\big(\dot{\boldsymbol{\xi}}_h^n-\dot{\boldsymbol{\xi}}_h^{n-1},\boldsymbol{L}_h^{\mathrm{e}}(\boldsymbol{\mathcal{I}}_h\dot{\boldsymbol{d}}^n-\partial_\tau\boldsymbol{d}^n)\big)_\Sigma}_{T_{8,1}} - \frac{\tau^2}{2\rho^{\mathrm{s}}\epsilon}\left(\|\boldsymbol{L}_h^{\mathrm{e}}\boldsymbol{\xi}_h^n\|_{0,\Sigma}^2-\|\boldsymbol{L}_h^{\mathrm{e}}\boldsymbol{\xi}_h^{n-1}\|_{0,\Sigma}^2+\|\boldsymbol{L}_h^{\mathrm{e}}(\boldsymbol{\xi}_h^n-\boldsymbol{\xi}_h^{n-1})\|_{0,\Sigma}^2\right).$$

Similarly to (5.53), we get

$$\begin{aligned}T_{8,1}=&\tau^2a^{\mathrm{s}}\big(\dot{\boldsymbol{\xi}}_h^n-\dot{\boldsymbol{\xi}}_h^{n-1},\boldsymbol{\mathcal{I}}_h\dot{\boldsymbol{d}}^n-\partial_\tau\boldsymbol{d}^n\big)\\ \lesssim&\frac{\tau^2}{4}\|\dot{\boldsymbol{\xi}}_h^n-\dot{\boldsymbol{\xi}}_h^{n-1}\|_{\mathrm{s}}^2+h^2\beta^{\mathrm{s}}\tau^2\|\boldsymbol{u}^n\|_{2,\Sigma}^2+\tau^3\beta^{\mathrm{s}}\|\partial_t\boldsymbol{u}\|_{L^2(t_{n-1},t_n;H^1(\Sigma))}^2,\end{aligned}$$

and, thus,

$$\begin{aligned}T_8\lesssim&-\frac{\tau^2}{2}\left(\|\dot{\boldsymbol{\xi}}_h^n\|_{\mathrm{s}}^2-\|\dot{\boldsymbol{\xi}}_h^{n-1}\|_{\mathrm{s}}^2\right)-\frac{\tau^2}{4}\|\dot{\boldsymbol{\xi}}_h^n-\dot{\boldsymbol{\xi}}_h^{n-1}\|_{\mathrm{s}}^2\\ &-\frac{\tau^2}{2\rho^{\mathrm{s}}\epsilon}\left(\|\boldsymbol{L}_h^{\mathrm{e}}\boldsymbol{\xi}_h^n\|_{0,\Sigma}^2-\|\boldsymbol{L}_h^{\mathrm{e}}\boldsymbol{\xi}_h^{n-1}\|_{0,\Sigma}^2+\|\boldsymbol{L}_h^{\mathrm{e}}(\boldsymbol{\xi}_h^n-\boldsymbol{\xi}_h^{n-1})\|_{0,\Sigma}^2\right)\\ &+h^2\beta^{\mathrm{s}}\tau^2\|\boldsymbol{u}^n\|_{2,\Sigma}^2+\tau^3\beta^{\mathrm{s}}\|\partial_t\boldsymbol{u}\|_{L^2(t_{n-1},t_n;H^1(\Sigma))}^2.\end{aligned} \quad (5.62)$$

For T_9, using (5.16) and a Taylor expansion, we get

$$\begin{aligned} T_9 =&\tau\big(\dot{\boldsymbol{\xi}}_h^n - \dot{\boldsymbol{\xi}}_h^{n-1}, \boldsymbol{L}_h^{\mathrm{e}}(\boldsymbol{d}^n - \boldsymbol{d}^{n-1})\big)_\Sigma \le \tau\|\dot{\boldsymbol{\xi}}_h^n - \dot{\boldsymbol{\xi}}_h^{n-1}\|_{0,\Sigma}\|\boldsymbol{L}_h^{\mathrm{e}}(\boldsymbol{d}^n - \boldsymbol{d}^{n-1})\|_{0,\Sigma} \\ \le&\tau\frac{\rho^{\mathrm{s}}\epsilon}{4T}\left(\|\dot{\boldsymbol{\xi}}_h^n\|_{0,\Sigma}^2 + \|\dot{\boldsymbol{\xi}}_h^{n-1}\|_{0,\Sigma}^2\right) + \frac{\tau T}{\rho^{\mathrm{s}}\epsilon}\|\boldsymbol{L}^{\mathrm{e}}(\boldsymbol{d}^n - \boldsymbol{d}^{n-1})\|_{0,\Sigma}^2 \\ \le&\tau\frac{\rho^{\mathrm{s}}\epsilon}{4T}\left(\|\dot{\boldsymbol{\xi}}_h^n\|_{0,\Sigma}^2 + \|\dot{\boldsymbol{\xi}}_h^{n-1}\|_{0,\Sigma}^2\right) + \frac{\tau^2 T}{\rho^{\mathrm{s}}\epsilon}\|\boldsymbol{L}^{\mathrm{e}}\partial_t\boldsymbol{d}\|_{L^2(t_{n-1},t_n;L^2(\Sigma))}^2. \end{aligned} \tag{5.63}$$

The first term of (5.63) is controlled by (5.49) via Lemma 5.1. Similarly, for term T_{10}, we obtain

$$\begin{aligned} T_{10} =&\frac{\tau^2}{\rho^{\mathrm{s}}\epsilon}\big(\boldsymbol{L}_h^{\mathrm{e}}\boldsymbol{\xi}_h^n, \boldsymbol{L}_h^{\mathrm{e}}(\boldsymbol{d}^n - \boldsymbol{d}^{n-1})\big)_\Sigma \\ \le&\frac{\tau^3}{2T\rho^{\mathrm{s}}\epsilon}\|\boldsymbol{L}_h^{\mathrm{e}}\boldsymbol{\xi}_h^n\|_{0,\Sigma}^2 + \frac{\tau T}{2\rho^{\mathrm{s}}\epsilon}\|\boldsymbol{L}(\boldsymbol{d}^n - \boldsymbol{d}^{n-1})\|_{0,\Sigma}^2 \\ \le&\frac{\tau^3}{2T\rho^{\mathrm{s}}\epsilon}\|\boldsymbol{L}_h^{\mathrm{e}}\boldsymbol{\xi}_h^n\|_{0,\Sigma}^2 + \frac{\tau^2 T}{2\rho^{\mathrm{s}}\epsilon}\|\boldsymbol{L}^{\mathrm{e}}\partial_t\boldsymbol{d}\|_{L^2(t_{n-1},t_n;L^2(\Sigma))}^2. \end{aligned} \tag{5.64}$$

The first term in the right-hand side of (5.64) is controlled by (5.62) and Lemma 5.1. On the other hand, from (5.52), we have

$$\begin{aligned} T_{2,1} \le&\ \varepsilon_2\tau\frac{\rho^{\mathrm{s}}\epsilon}{T}\|\dot{\boldsymbol{\xi}}_h^n\|_{0,\Sigma}^2 + \varepsilon_2\frac{\tau^2}{\rho^{\mathrm{s}}\epsilon}\|\boldsymbol{L}_h^{\mathrm{e}}(\boldsymbol{\xi}_h^n - \boldsymbol{\xi}_h^{n-1})\|_{0,\Sigma}^2 + \varepsilon_2\frac{\tau^2}{\rho^{\mathrm{s}}\epsilon}\|\boldsymbol{L}^{\mathrm{e}}(\boldsymbol{d}^n - \boldsymbol{d}^{n-1})\|_{0,\Sigma}^2 \\ \le&\ \varepsilon_2\tau\frac{\rho^{\mathrm{s}}\epsilon}{T}\|\dot{\boldsymbol{\xi}}_h^n\|_{0,\Sigma}^2 + \varepsilon_2\frac{\tau^2}{\rho^{\mathrm{s}}\epsilon}\|\boldsymbol{L}_h^{\mathrm{e}}(\boldsymbol{\xi}_h^n - \boldsymbol{\xi}_h^{n-1})\|_{0,\Sigma}^2 + \varepsilon_2\frac{\tau^3}{\rho^{\mathrm{s}}\epsilon}\|\boldsymbol{L}^{\mathrm{e}}\partial_t\boldsymbol{d}\|_{L^2(t_{n-1},t_n;L^2(\Sigma))}^2. \end{aligned}$$

In summary, the estimate (5.45) follows by inserting the above estimates into (5.49), summing over $m = 2, \ldots, n$, and applying Lemma 5.1 with

$$a_m = \frac{\rho^{\mathrm{f}}}{2}\|\boldsymbol{\theta}_h^m\|_{0,\Omega^{\mathrm{f}}}^2 + \frac{\rho^{\mathrm{s}}\epsilon}{2}\|\dot{\boldsymbol{\xi}}_h^m\|_{0,\Sigma}^2 + \frac{1}{2}\|\boldsymbol{\xi}_h^m\|_{\mathrm{s}}^2 + \frac{\tau^2}{2\rho^{\mathrm{s}}\epsilon}\|\boldsymbol{L}_h^{\mathrm{e}}\boldsymbol{\xi}_h^m\|_{0,\Sigma}^2, \quad \eta_m = \frac{1}{T}.$$

The right-hand side contributions obtained at time t_1, can be controlled (due to the initialization procedure) by using (5.45) with $r = 0$, $T = \tau$ and $n = 1$.

Algorithm 5.2 with $r = 2$. Let us first consider the term T_9. Using (5.16) followed by a Taylor expansion, we have

$$\begin{aligned} T_9 =&\tau^2\big(\dot{\boldsymbol{\xi}}_h^n - \dot{\boldsymbol{\xi}}_h^{n-1}, \boldsymbol{L}_h^{\mathrm{e}}(\partial_\tau\boldsymbol{d}^n - \dot{\boldsymbol{d}}^{n-1})\big)_\Sigma \\ \le&\tau\frac{\rho^{\mathrm{s}}\epsilon}{4T}\left(\|\dot{\boldsymbol{\xi}}_h^n\|_{0,\Sigma}^2 + \|\dot{\boldsymbol{\xi}}_h^{n-1}\|_{0,\Sigma}^2\right) + \frac{\tau^3 T}{\rho^{\mathrm{s}}\epsilon}\|\boldsymbol{L}^{\mathrm{e}}(\partial_\tau\boldsymbol{d}^n - \dot{\boldsymbol{d}}^{n-1})\|_{0,\Sigma}^2 \\ \le&\tau\frac{\rho^{\mathrm{s}}\epsilon}{4T}\left(\|\dot{\boldsymbol{\xi}}_h^n\|_{0,\Sigma}^2 + \|\dot{\boldsymbol{\xi}}_h^{n-1}\|_{0,\Sigma}^2\right) + \frac{\tau^4 T}{\rho^{\mathrm{s}}\epsilon}\|\boldsymbol{L}^{\mathrm{e}}\partial_{tt}\boldsymbol{d}\|_{L^2(t_{n-1},t_n;L^2(\Sigma))}^2. \end{aligned} \tag{5.65}$$

The first term in the bound (5.65) is controlled via Lemma 5.1 and (5.49). For the

term T_{10}, using the inverse estimate (5.19) and the $\frac{6}{5}$-CFL condition (5.23), we have

$$\begin{aligned} T_{10} =& \frac{\tau^3}{\rho^{\mathrm{s}}\epsilon}\big(\boldsymbol{L}_h^{\mathrm{e}}\boldsymbol{\xi}_h^n, \boldsymbol{L}_h^{\mathrm{e}}(\partial_\tau \boldsymbol{d}^n - \dot{\boldsymbol{d}}^{n-1})\big)_\Sigma \\ \leq& \frac{\tau^3}{2T\rho^{\mathrm{s}}\epsilon}\|\boldsymbol{L}_h^{\mathrm{e}}\boldsymbol{\xi}_h^n\|_{0,\Sigma}^2 + \frac{\tau^3 T}{2\rho^{\mathrm{s}}\epsilon}\|\boldsymbol{L}(\partial_\tau \boldsymbol{d}^n - \dot{\boldsymbol{d}}^{n-1})\|_{0,\Sigma}^2 \\ \leq& \frac{\tau^3}{2T\rho^{\mathrm{s}}\epsilon}\|\boldsymbol{L}_h^{\mathrm{e}}\boldsymbol{\xi}_h^n\|_{0,\Sigma}^2 + \frac{\tau^4 T}{2\rho^{\mathrm{s}}\epsilon}\|\partial_{tt}\boldsymbol{L}^{\mathrm{e}}\boldsymbol{d}\|_{L^2(t_{n-1},t_n;L^2(\Sigma))}^2 \\ \leq& \frac{\tau^3(\omega^{\mathrm{s}}C_{\mathrm{I}})^2}{2Th^2}\|\boldsymbol{\xi}_h^n\|_{\mathrm{s}}^2 + \frac{\tau^4 T}{2\rho^{\mathrm{s}}\epsilon}\|\partial_{tt}\boldsymbol{L}^{\mathrm{e}}\boldsymbol{d}\|_{L^2(t_{n-1},t_n;L^2(\Sigma))}^2 \\ \leq& \frac{\tau\alpha^{\frac{5}{3}}\tau^{\frac{1}{3}}}{2T}\|\boldsymbol{\xi}_h^n\|_{\mathrm{s}}^2 + \frac{\tau^4 T}{2\rho^{\mathrm{s}}\epsilon}\|\partial_{tt}\boldsymbol{L}^{\mathrm{e}}\boldsymbol{d}\|_{L^2(t_{n-1},t_n;L^2(\Sigma))}^2. \end{aligned} \tag{5.66}$$

The first term in the bound (5.66) is controlled via Lemma 5.1 and (5.49). Note that

$$\boldsymbol{\xi}_h^{n,\star} = \boldsymbol{\xi}_h^{n-1} + \tau\dot{\boldsymbol{\xi}}_h^{n-1} + \tau(\boldsymbol{\pi}_h^{\mathrm{s}}\dot{\boldsymbol{d}}^{n-1} - \boldsymbol{\mathcal{I}}_h\dot{\boldsymbol{d}}^{n-1}).$$

Hence, for the term T_8, we get

$$\begin{aligned} T_8 =& -\tau^2\big(\dot{\boldsymbol{\xi}}_h^n - \dot{\boldsymbol{\xi}}_h^{n-1}, \boldsymbol{L}_h^{\mathrm{e}}(\dot{\boldsymbol{\xi}}_h^n - \dot{\boldsymbol{\xi}}_h^{n-1})\big)_\Sigma - \frac{\tau^3}{\rho^{\mathrm{s}}\epsilon}\big(\boldsymbol{L}_h^{\mathrm{e}}\boldsymbol{\xi}_h^n, \boldsymbol{L}_h^{\mathrm{e}}(\dot{\boldsymbol{\xi}}_h^n - \dot{\boldsymbol{\xi}}_h^{n-1})\big)_\Sigma \\ &\underbrace{+\tau^2\Big(\dot{\boldsymbol{\xi}}_h^n - \dot{\boldsymbol{\xi}}_h^{n-1}, \boldsymbol{L}_h^{\mathrm{e}}\big(\boldsymbol{\mathcal{I}}_h(\dot{\boldsymbol{d}}^n - \dot{\boldsymbol{d}}^{n-1}) - \partial_\tau \boldsymbol{d}^n + \dot{\boldsymbol{d}}^{n-1}\big)\Big)_\Sigma}_{T_{8,1}} \\ &\underbrace{+\frac{\tau^3}{\rho^{\mathrm{s}}\epsilon}\Big(\boldsymbol{L}_h^{\mathrm{e}}\boldsymbol{\xi}_h^n, \boldsymbol{L}_h^{\mathrm{e}}\big(\boldsymbol{\mathcal{I}}_h(\dot{\boldsymbol{d}}^n - \dot{\boldsymbol{d}}^{n-1}) - \partial_\tau \boldsymbol{d}^n + \dot{\boldsymbol{d}}^{n-1}\big)\Big)_\Sigma}_{T_{8,2}}. \end{aligned}$$

Under the $\frac{6}{5}$-CFL condition (5.23), we proceed similarly to (5.28) and (5.30), and we have

$$T_8 \leq -\tau^2\|\dot{\boldsymbol{\xi}}_h^n - \dot{\boldsymbol{\xi}}_h^{n-1}\|_{\mathrm{s}}^2 + \frac{\rho^{\mathrm{s}}}{4}\|\dot{\boldsymbol{\xi}}_h^n - \dot{\boldsymbol{\xi}}_h^{n-1}\|_{0,\Sigma}^2 + \tau\alpha^5\|\boldsymbol{\xi}_h^n\|_{\mathrm{s}}^2 + T_{8,1} + T_{8,2}. \tag{5.67}$$

We consider the terms $T_{8,1}$ and $T_{8,2}$ separetely. Adding and subtracting $\dot{\boldsymbol{d}}^n$ in $T_{8,1}$ yields

$$\begin{aligned} T_{8,1} =& \tau^2 a^{\mathrm{s}}\big(\dot{\boldsymbol{\xi}}_h^n - \dot{\boldsymbol{\xi}}_h^{n-1}, \boldsymbol{\mathcal{I}}_h(\dot{\boldsymbol{d}}^n - \dot{\boldsymbol{d}}^{n-1}) - (\dot{\boldsymbol{d}}^n - \dot{\boldsymbol{d}}^{n-1})\big) \\ &+ \tau^2\big(\dot{\boldsymbol{\xi}}_h^n - \dot{\boldsymbol{\xi}}_h^{n-1}, \boldsymbol{L}_h^{\mathrm{e}}(\dot{\boldsymbol{d}}^n - \partial_\tau \boldsymbol{d}^n)\big)_\Sigma. \end{aligned}$$

Owing to (5.4) and the approximation properties, we have

$$\begin{aligned} T_{8,1} \lesssim& \frac{\tau^2}{2}\|\dot{\boldsymbol{\xi}}_h^n - \dot{\boldsymbol{\xi}}_h^{n-1}\|_{\mathrm{s}}^2 + h^2\beta^{\mathrm{s}}\tau^2\|\boldsymbol{u}^n - \boldsymbol{u}^{n-1}\|_{2,\Sigma}^2 \\ &+ \tau\frac{\rho^{\mathrm{s}}\epsilon}{4T}\Big(\|\dot{\boldsymbol{\xi}}_h^n\|_{0,\Sigma}^2 + \|\dot{\boldsymbol{\xi}}_h^{n-1}\|_{0,\Sigma}^2\Big) + \frac{\tau^4 T}{\rho^{\mathrm{s}}\epsilon}\|\boldsymbol{L}^{\mathrm{e}}\partial_{tt}\boldsymbol{d}\|_{L^2(t_{n-1},t_n;L^2(\Sigma))}^2. \end{aligned} \tag{5.68}$$

For the term $T_{8,2}$ we have

$$\begin{aligned} T_{8,2} =& \frac{\tau^3}{\rho^{\mathrm{s}}\epsilon} a^{\mathrm{s}}\big(\boldsymbol{L}_h^{\mathrm{e}}\boldsymbol{\xi}_h^n, \boldsymbol{\mathcal{I}}_h(\dot{\boldsymbol{d}}^n - \dot{\boldsymbol{d}}^{n-1}) - (\dot{\boldsymbol{d}}^n - \dot{\boldsymbol{d}}^{n-1})\big) \\ &+ \frac{\tau^3}{\rho^{\mathrm{s}}\epsilon}\big(\boldsymbol{L}_h^{\mathrm{e}}\boldsymbol{\xi}_h^n, \boldsymbol{L}_h^{\mathrm{e}}(\dot{\boldsymbol{d}}^n - \partial_\tau \boldsymbol{d}^n)\big)_\Sigma. \end{aligned} \tag{5.69}$$

The second term in the right-hand side of (5.69) is treated similarly to (5.66). The estimate for the first term follow by the inverse estimates (5.18), (5.19) and the $\frac{6}{5}$-CFL condition (5.23). We have

$$\begin{aligned} T_{8,2} \leq& \frac{\tau^5}{2T(\rho^{\mathrm{s}}\epsilon)^2}\|\boldsymbol{L}_h^{\mathrm{e}}\boldsymbol{\xi}_h^n\|_{\mathrm{s}}^2 + \frac{\tau T}{2}\|\boldsymbol{\mathcal{I}}_h(\dot{\boldsymbol{d}}^n - \dot{\boldsymbol{d}}^{n-1}) - (\dot{\boldsymbol{d}}^n - \dot{\boldsymbol{d}}^{n-1})\|_{\mathrm{s}}^2 \\ &+ \frac{\tau\alpha^{\frac{5}{3}}\tau^{\frac{1}{3}}}{2T}\|\boldsymbol{\xi}_h^n\|_{\mathrm{s}}^2 + \frac{\tau^4 T}{2\rho^{\mathrm{s}}\epsilon}\|\partial_{tt}\boldsymbol{L}^{\mathrm{e}}\boldsymbol{d}\|^2_{L^2(t_{n-1},t_n;L^2(\Sigma))} \\ \lesssim& \left(\frac{\tau\alpha^{\frac{10}{3}}\tau^{\frac{2}{3}}}{2T} + \frac{\tau\alpha^{\frac{5}{3}}\tau^{\frac{1}{3}}}{2T}\right)\|\boldsymbol{\xi}_h^n\|_{\mathrm{s}}^2 + h^2\beta^{\mathrm{s}}\tau T\|\boldsymbol{u}^n - \boldsymbol{u}^{n-1}\|_{2,\Sigma}^2 \\ &+ \frac{\tau^4 T}{2\rho^{\mathrm{s}}\epsilon}\|\partial_{tt}\boldsymbol{L}^{\mathrm{e}}\boldsymbol{d}\|^2_{L^2(t_{n-1},t_n;L^2(\Sigma))}. \end{aligned} \tag{5.70}$$

Substitution of (5.68) and (5.70) into (5.67), yields

$$\begin{aligned} T_8 \lesssim& -\frac{\tau^2}{2}\|\dot{\boldsymbol{\xi}}_h^n - \dot{\boldsymbol{\xi}}_h^{n-1}\|_{\mathrm{s}}^2 + \frac{\rho^{\mathrm{s}}}{4}\|\dot{\boldsymbol{\xi}}_h^n - \dot{\boldsymbol{\xi}}_h^{n-1}\|_{0,\Sigma}^2 + \tau\frac{\rho^{\mathrm{s}}\epsilon}{4T}\left(\|\dot{\boldsymbol{\xi}}_h^n\|_{0,\Sigma}^2 + \|\dot{\boldsymbol{\xi}}_h^{n-1}\|_{0,\Sigma}^2\right) \\ &+ \tau\left(\alpha^5 + \frac{\alpha^{\frac{10}{3}}\tau^{\frac{2}{3}}}{2T} + \frac{\alpha^{\frac{5}{3}}\tau^{\frac{1}{3}}}{2T}\right)\|\boldsymbol{\xi}_h^n\|_{\mathrm{s}}^2 + \frac{\tau^4 T}{\rho^{\mathrm{s}}\epsilon}\|\boldsymbol{L}^{\mathrm{e}}\partial_{tt}\boldsymbol{d}\|^2_{L^2(t_{n-1},t_n;L^2(\Sigma))} \\ &+ h^2\beta^{\mathrm{s}}(T+\tau)\tau\|\boldsymbol{u}^n - \boldsymbol{u}^{n-1}\|_{2,\Sigma}^2. \end{aligned} \tag{5.71}$$

The first term on the right hand side is absorbed into the left-hand side of (5.49) and, the following two are treated via Lemma 5.1.

On the other hand, regarding the term $T_{2,2}$ from (5.52), we get

$$\begin{aligned} T_{2,2} &\leq \varepsilon_2\tau\frac{\rho^{\mathrm{s}}\epsilon}{T}\|\dot{\boldsymbol{\xi}}_h^n\|_{0,\Sigma}^2 + \varepsilon_2\frac{\tau^2}{\rho^{\mathrm{s}}\epsilon}\|\boldsymbol{L}_h^{\mathrm{e}}(\boldsymbol{\xi}_h^n - \boldsymbol{\xi}_h^{n,\star})\|_{0,\Sigma}^2 + \varepsilon_2\frac{\tau^4}{\rho^{\mathrm{s}}\epsilon}\|\boldsymbol{L}^{\mathrm{e}}(\partial_\tau\boldsymbol{d}^n - \dot{\boldsymbol{d}}^{n-1})\|_{0,\Sigma}^2 \\ &\leq \varepsilon_2\tau\frac{\rho^{\mathrm{s}}\epsilon}{T}\|\dot{\boldsymbol{\xi}}_h^n\|_{0,\Sigma}^2 \underbrace{+\varepsilon_2\frac{\tau^2}{\rho^{\mathrm{s}}\epsilon}\|\boldsymbol{L}_h^{\mathrm{e}}(\boldsymbol{\xi}_h^n - \boldsymbol{\xi}_h^{n,\star})\|_{0,\Sigma}^2}_{T_{2,2,1}} + \varepsilon_2\frac{\tau^5}{\rho^{\mathrm{s}}\epsilon}\|\boldsymbol{L}^{\mathrm{e}}\partial_{tt}\boldsymbol{d}\|^2_{L^2(t_{n-1},t_n;L^2(\Sigma))}. \end{aligned}$$

Moreover, we have

$$\begin{aligned}T_{2,2,1} \leq & \varepsilon_2 \frac{\tau^4}{\rho^{\mathrm{s}}\epsilon}\|\boldsymbol{L}_h^{\mathrm{e}}(\dot{\boldsymbol{\xi}}_h^n - \dot{\boldsymbol{\xi}}_h^{n-1}) + \boldsymbol{L}_h^{\mathrm{e}}(\boldsymbol{z}_h^n - \boldsymbol{z}_h^{n-1})\|_{0,\Sigma}^2 \\ \leq & 2\varepsilon_2 \frac{\tau^4 \beta^{\mathrm{s}}}{h^2 \rho^{\mathrm{s}}\epsilon}\big(\|\dot{\boldsymbol{\xi}}_h^n - \dot{\boldsymbol{\xi}}_h^{n-1}\|_{\mathrm{s}}^2 + \|\boldsymbol{z}_h^n - \boldsymbol{z}_h^{n-1}\|_{\mathrm{s}}^2\big) \\ \leq & 2\varepsilon_2 (\gamma\tau)^{\frac{1}{3}} \tau^2 \big(\|\dot{\boldsymbol{\xi}}_h^n - \dot{\boldsymbol{\xi}}_h^{n-1}\|_{\mathrm{s}}^2 + \|\boldsymbol{z}_h^n - \boldsymbol{z}_h^{n-1}\|_{\mathrm{s}}^2\big).\end{aligned}$$

The first term can be controlled with the numerical dissipation of (5.71) and the second term can be estimated as in the previous estimations. The estimate (5.45) then follows by inserting the above estimates into (5.49), summing over $m = 3, \ldots, n$, using (5.61) and applying Lemma 5.1 with

$$a_m = \frac{\rho^{\mathrm{f}}}{2}\|\boldsymbol{\theta}_h^m\|_{0,\Omega^{\mathrm{f}}}^2 + \frac{\rho^{\mathrm{s}}\epsilon}{2}\|\dot{\boldsymbol{\xi}}_h^m\|_{0,\Sigma}^2 + \frac{1}{2}\|\boldsymbol{\xi}_h^m\|_{\mathrm{s}}^2, \quad \gamma_m = \max\left\{\frac{1}{T}, 2\alpha^5, \frac{\alpha^{\frac{10}{3}}\tau^{\frac{2}{3}} + \alpha^{\frac{5}{3}}\tau^{\frac{1}{3}}}{T}\right\}.$$

The right-hand side contributions obtained at time t_2, can be controlled (due to the initialization procedure) by using (5.45) with $r = 1$, $T = 2\tau$ and $n = 2$. Hence, the proof is complete. ∎

We define the energy-norm of the error at time step t_n, as

$$\begin{aligned}\mathcal{Z}_h^n \stackrel{\mathrm{def}}{=} & (\rho^{\mathrm{f}})^{\frac{1}{2}}\|\boldsymbol{u}^n - \boldsymbol{u}_h^n\|_{0,\Omega^{\mathrm{f}}} + (\rho^{\mathrm{s}}\epsilon)^{\frac{1}{2}}\|\dot{\boldsymbol{d}}^n - \dot{\boldsymbol{d}}_h^n\|_{0,\Sigma} + \|\boldsymbol{d}^n - \boldsymbol{d}_h^n\|_{\mathrm{s}} \\ & + \left(\sum_{m=r+1}^{n} c_{\mathrm{g}}\tau\mu\|\boldsymbol{\nabla}(\boldsymbol{u}^m - \boldsymbol{u}_h^m)\|_{0,\Omega^{\mathrm{f}}}^2\right)^{\frac{1}{2}} + \left(\sum_{m=r+1}^{n} c_{\mathrm{g}}\tau\gamma\mu\|\boldsymbol{u}_h^m - \dot{\boldsymbol{d}}_h^{m-\frac{1}{2}}\|_{\frac{1}{2},h,\Sigma}^2\right)^{\frac{1}{2}} \\ & + \left(\sum_{m=r+1}^{n} c_{\mathrm{g}}\tau|(\boldsymbol{u}_h^m, p_h^m)|_S^2\right)^{\frac{1}{2}}\end{aligned}$$

for $n > r$. As a corollary of Theorem 5.2, we have the following a priori estimate.

Corollary 5.1 *Under the assumptions of Theorem 5.2, we have the following error estimate, for $n > r$ and $n\tau < T$:*

$$\mathcal{Z}_h^n \lesssim c_1 h + c_2\tau + c_3\tau^{2^{r-1}}.$$

Here, the symbols $\{c_i\}_{i=1}^3$ denote positive constants independent of h and τ, but which depend on the physical parameters and on the regularity of $(\boldsymbol{u}, p, \boldsymbol{d}, \dot{\boldsymbol{d}})$.

Proof. The proof follows directly as a consequence of a triangle inequality, Theorem 5.2 and the optimal approximation properties of the interpolation operators. ∎

Thus, the scheme retrieves optimal accuracy for the extrapolated variants ($r = 1, 2$) while a suboptimal convergence rate is expected without extrapolation ($r = 0$). We then retrieve the same convergence rate than in the fitted case for the Robin-

Neumann schemes of Section 1.4.3.5 (see Theorem 1.6).

From the proofs of Theorem 5.2 and Corollary 5.1, we can readily obtain the following optimal error estimate for Algorithm 5.1.

Corollary 5.2 *Let $(\boldsymbol{u}, p, \boldsymbol{d}, \dot{\boldsymbol{d}})$ be the solution of the coupled problem (5.1)-(5.2) and $\{(\boldsymbol{u}_h^n, p_h^n, \boldsymbol{d}_h^n, \dot{\boldsymbol{d}}_h^n)\}_{n>r}$ be the approximation given by Algorithm 5.1 with initial data $\big(\boldsymbol{u}_h^0, \boldsymbol{d}_h^0, \dot{\boldsymbol{d}}_h^0\big) = \big(i_{\mathrm{sz}} E_2 \boldsymbol{u}^0, \boldsymbol{\pi}_h^{\mathrm{s}} \boldsymbol{d}^0, \mathcal{I}_h \dot{\boldsymbol{d}}^0\big)$. Suppose that the exact solution has the regularity (5.38)-(5.39). Then, we have the following error estimates, for $n > 0$ and $n\tau < T$:*

$$\mathcal{Z}_h^n \lesssim c_1 h + c_2 \tau$$

with c_1 and c_2 positive constants independent of h and τ, but depending on the physical parameters and on the regularity of $(\boldsymbol{u}, p, \boldsymbol{d}, \dot{\boldsymbol{d}})$.

Proof. Taking $(\boldsymbol{v}_h, q_h, \boldsymbol{w}_h) = \tau(\boldsymbol{\theta}_h^n, y_h^n, \dot{\boldsymbol{\xi}}_h^n)$ in (5.48), the energy inequality (5.49) holds with $\boldsymbol{\chi}_h^n = \dot{\boldsymbol{\xi}}_h^n$ and $T_8 = T_9 = T_{10} = 0$.

The terms T_5 and T_6 are treated similarly to (5.55) and (5.56). Note that the Nitsche's dissipation on the interface is given in this case by

$$c_{\mathrm{g}} \tau \gamma \mu \|\boldsymbol{\theta}_h^n - \dot{\boldsymbol{\xi}}_h^n\|^2_{\frac{1}{2},h,\Sigma}.$$

Similarly to (5.51), for the term T_2, we have

$$T_2 \lesssim \frac{\rho^{\mathrm{s}} \epsilon T}{2\varepsilon_2} \big(\tau^2 \|\partial_{tt} \boldsymbol{u}\|^2_{L^2(t_{n-1},t_n;L^2(\Sigma))} + h^2 \|\partial_t \boldsymbol{u}\|^2_{L^2(t_{n-1},t_n;H^2(\Sigma))}\big) + \varepsilon_2 \tau \frac{\rho^{\mathrm{s}} \epsilon}{T} \|\dot{\boldsymbol{\xi}}_h^n\|^2_{0,\Sigma}.$$

The last term may be controlled by Lemma 5.1. The remaining terms T_1, T_3, T_4 and T_7 are treated exactly as above. We obtain thus an optimal a priori estimate for the discrete errors. We conclude as in Corollary 5.1. ∎

5.3 First discretize in time and then in space

Step (5.13) of Algorithm 5.2 has a computational complexity larger than a single fluid problem, due to the additional unknown $\dot{\boldsymbol{d}}_h^{n-\frac{1}{2}}$. In this section, we introduce a new explicit coupling scheme which overcomes this issue without compromising stability and accuracy. The fundamental idea consists in performing the space and time discretization reversely.

Robin-Neumann explicit coupling schemes. The starting point of the methods is the explicit coupling schemes introduced in Section 1.4.3.5. Note that these schemes may be derived by applying first the fractional-step splitting of Section 5.2.1 to the continuous problem (5.1)-(5.2) and then eliminating, contrarily to Algorithm 5.2, the intermediate solid velocity $\dot{\boldsymbol{d}}^{n-\frac{1}{2}}$ (see Remark 1.17). Applied to the continuous problem (5.1)-(5.2), these schemes read: for $n > r$

1. Fluid substep: find $\boldsymbol{u}^n : \Omega^{\mathrm{f}} \times \mathbb{R}^+ \to \mathbb{R}^d$ and $p^n : \Omega^{\mathrm{f}} \times \mathbb{R}^+ \to \mathbb{R}$ such that

$$\begin{cases} \rho^{\mathrm{f}} \partial_\tau \boldsymbol{u}^n - \mathbf{div}\boldsymbol{\sigma}(\boldsymbol{u}^n, p^n) = \mathbf{0} & \text{in} \quad \Omega^{\mathrm{f}}, \\ \mathrm{div}\boldsymbol{u}^n = 0 & \text{in} \quad \Omega^{\mathrm{f}}, \\ \boldsymbol{u}^n = \mathbf{0} & \text{on} \quad \Gamma^{\mathrm{f}}, \\ \boldsymbol{\sigma}(\boldsymbol{u}^n, p^n)\boldsymbol{n} + \kappa \boldsymbol{u}^n = \kappa \dot{\boldsymbol{d}}^{n-1} + \boldsymbol{g}^{n,\star} & \text{on} \quad \Sigma, \end{cases} \tag{5.72}$$

with

$$\kappa \stackrel{\text{def}}{=} \frac{\rho^{\mathrm{s}} \epsilon}{\tau}, \quad \boldsymbol{g}^{n,\star} \stackrel{\text{def}}{=} \rho^{\mathrm{s}} \epsilon \partial_\tau \boldsymbol{d}^{n,\star} + \boldsymbol{\sigma}(\boldsymbol{u}^{n,\star}, p^{n,\star})\boldsymbol{n}.$$

2. Solid substep: find $\boldsymbol{d}^n : \Sigma \times \mathbb{R}^+ \to \mathbb{R}^d$ and $\dot{\boldsymbol{d}}^n : \Sigma \times \mathbb{R}^+ \to \mathbb{R}^d$ such that $\dot{\boldsymbol{d}}^n = \partial_\tau \boldsymbol{d}^n$ and

$$\begin{cases} \rho^{\mathrm{s}} \epsilon \partial_\tau \dot{\boldsymbol{d}}^n + \boldsymbol{L}^{\mathrm{e}} \boldsymbol{d}^n = -\boldsymbol{\sigma}(\boldsymbol{u}^n, p^n)\boldsymbol{n} & \text{on} \quad \Sigma, \\ \boldsymbol{d}^n = \mathbf{0} & \text{on} \quad \partial\Sigma. \end{cases} \tag{5.73}$$

5.3.1 Fully discrete formulation: explicit coupling scheme with unfitted meshes

The fundamental idea consists in performing directly an unfitted interface treatment (à la Nitsche) of the time splitting $(5.72)_4$-$(5.73)_1$. This is achieved by extending the arguments introduced in [BF14b, CFGM11] (see also [JS09]) to the present Robin-Neumann framework, in such a way that robustness with respect to the Robin coefficient κ is guaranteed. The proposed numerical methods build on the following consistency result.

PROPOSITION 5.1 (Consistency) *Let* $\{(\boldsymbol{u}^n, p^n, \dot{\boldsymbol{d}}^n, \boldsymbol{d}^n)\}_{n>r}$ *be given by* (5.72)-(5.73). *Then, there holds*

$$\begin{cases} \rho^{\mathrm{f}} \big(\partial_\tau \boldsymbol{u}^n, \boldsymbol{v}_h\big)_{\Omega^{\mathrm{f}}} + a^{\mathrm{f}}\big((\boldsymbol{u}^n, p^n), (\boldsymbol{v}_h, q_h)\big) + \rho^{\mathrm{s}} \epsilon \big(\partial_\tau \dot{\boldsymbol{d}}^n, \boldsymbol{w}_h\big)_\Sigma + a^{\mathrm{s}}(\boldsymbol{d}^n, \boldsymbol{w}_h) \\ + \dfrac{\gamma\kappa\mu}{\gamma\mu + \kappa h} \big(\boldsymbol{u}^n - \dot{\boldsymbol{d}}^{n-1}, \boldsymbol{v}_h - \boldsymbol{w}_h\big)_\Sigma - \dfrac{\gamma\mu}{\gamma\mu + \kappa h} \big(\boldsymbol{g}^{n,\star}, \boldsymbol{v}_h - \boldsymbol{w}_h\big)_\Sigma \\ - \dfrac{\kappa h}{\gamma\mu + \kappa h} \Big[\big(\boldsymbol{\sigma}(\boldsymbol{u}^n, p^n)\boldsymbol{n}, \boldsymbol{v}_h - \boldsymbol{w}_h\big)_\Sigma + \big(\boldsymbol{u}^n - \dot{\boldsymbol{d}}^{n-1}, \boldsymbol{\sigma}(\boldsymbol{v}_h, -q_h)\boldsymbol{n}\big)_\Sigma \Big] \\ - \dfrac{h}{\gamma\mu + \kappa h} \big(\boldsymbol{\sigma}(\boldsymbol{u}^n, p^n)\boldsymbol{n}, \boldsymbol{\sigma}(\boldsymbol{v}_h, -q_h)\boldsymbol{n}\big)_\Sigma + \dfrac{h}{\gamma\mu + \kappa h} \big(\boldsymbol{g}^{n,\star}, \boldsymbol{\sigma}(\boldsymbol{v}_h, -q_h)\boldsymbol{n}\big)_\Sigma = 0 \end{cases} \tag{5.74}$$

for all $(\boldsymbol{v}_h, q_h, \boldsymbol{w}_h) \in \boldsymbol{V}_h \times Q_h \times \boldsymbol{W}_h$.

Proof. Multiplying $(5.72)_1$ and $(5.72)_2$ by $\boldsymbol{v}_h$ and q_h respectively, integrating by parts over Ω^{f} and adding both equations we get

$$\rho^{\mathrm{f}} \big(\partial_\tau \boldsymbol{u}^n, \boldsymbol{v}_h\big)_{\Omega^{\mathrm{f}}} + a^{\mathrm{f}}\big((\boldsymbol{u}^n, p^n), (\boldsymbol{v}_h, q_h)\big) - \big(\boldsymbol{\sigma}(\boldsymbol{u}^n, p^n)\boldsymbol{n}, \boldsymbol{v}_h\big)_\Sigma = 0. \tag{5.75}$$

On the other hand, multiplying $(5.73)_1$ by $\boldsymbol{w}_h$ and integrating over Σ we get

$$\rho^{\mathrm{s}}\epsilon\big(\partial_\tau \dot{\boldsymbol{d}}^n, \boldsymbol{w}_h\big)_\Sigma + a^{\mathrm{s}}(\boldsymbol{d}^n, \boldsymbol{w}_h) + \big(\boldsymbol{\sigma}(\boldsymbol{u}^n, p^n)\boldsymbol{n}, \boldsymbol{w}_h\big)_\Sigma = 0. \tag{5.76}$$

Adding (5.75) and (5.76), we obtain

$$\begin{aligned}\rho^{\mathrm{f}}\big(\partial_\tau \boldsymbol{u}^n, \boldsymbol{v}_h\big)_{\Omega^{\mathrm{f}}} + a^{\mathrm{f}}\big((\boldsymbol{u}^n, p^n), (\boldsymbol{v}_h, q_h)\big) + \rho^{\mathrm{s}}\epsilon\big(\partial_\tau \dot{\boldsymbol{d}}^n, \boldsymbol{w}_h\big)_\Sigma + a^{\mathrm{s}}(\boldsymbol{d}^n, \boldsymbol{w}_h) \\ - \big(\boldsymbol{\sigma}(\boldsymbol{u}^n, p^n)\boldsymbol{n}, \boldsymbol{v}_h - \boldsymbol{w}_h\big)_\Sigma = 0.\end{aligned} \tag{5.77}$$

Multiplying the interface condition $(5.72)_4$ by $\dfrac{\gamma\mu}{\gamma\mu + \kappa h}\big(\boldsymbol{v}_h - \boldsymbol{w}_h\big)$ and integrating over Σ, we get

$$\begin{aligned}\frac{\gamma\kappa\mu}{\gamma\mu + \kappa h}\big(\boldsymbol{u}^n - \dot{\boldsymbol{d}}^{n-1}, \boldsymbol{v}_h - \boldsymbol{w}_h\big)_\Sigma + \frac{\gamma\mu}{\gamma\mu + \kappa h}\big(\boldsymbol{\sigma}(\boldsymbol{u}^n, p^n)\boldsymbol{n}, \boldsymbol{v}_h - \boldsymbol{w}_h\big)_\Sigma \\ - \frac{\gamma\mu}{\gamma\mu + \kappa h}\big(\boldsymbol{g}^{n,\star}, \boldsymbol{v}_h - \boldsymbol{w}_h\big)_\Sigma = 0.\end{aligned} \tag{5.78}$$

Multiplying the interface condition $(5.72)_4$ by $-\dfrac{h}{\gamma\mu + \kappa h}\boldsymbol{\sigma}(\boldsymbol{v}_h, -q_h)\boldsymbol{n}$ and integrating over Σ, we get

$$\begin{aligned}-\frac{\kappa h}{\gamma\mu + \kappa h}\big(\boldsymbol{u}^n - \dot{\boldsymbol{d}}^{n-1}, \boldsymbol{\sigma}(\boldsymbol{v}_h, -q_h)\boldsymbol{n}\big)_\Sigma - \frac{h}{\gamma\mu + \kappa h}\big(\boldsymbol{\sigma}(\boldsymbol{u}^n, p^n)\boldsymbol{n}, \boldsymbol{\sigma}(\boldsymbol{v}_h, -q_h)\boldsymbol{n}\big)_\Sigma \\ + \frac{h}{\gamma\mu + \kappa h}\big(\boldsymbol{g}^{n,\star}, \boldsymbol{\sigma}(\boldsymbol{v}_h, -q_h)\boldsymbol{n}\big)_\Sigma = 0.\end{aligned} \tag{5.79}$$

Finally, by adding (5.77)-(5.79) we recover (5.74), which completes the proof. ∎

The key feature of (5.74) is the fact that for $\kappa \to \infty$ (i.e., whenever $\tau \to 0$) we formally retrieve the unfitted formulation (5.5). Alternatively, if $h \to 0$ we formally retrieve the the weak formulation of the Robin-Neumann splitting (5.72)-(5.73). Taking successively $\boldsymbol{w}_h = \boldsymbol{0}$ and $(\boldsymbol{v}_h, q_h) = (\boldsymbol{0}, 0)$ in (5.74) we obtain the following partitioned formulation of (5.74):

- Fluid:

$$\begin{cases}\rho^{\mathrm{f}}\big(\partial_\tau \boldsymbol{u}^n, \boldsymbol{v}_h\big)_{\Omega^{\mathrm{f}}} + a^{\mathrm{f}}\big((\boldsymbol{u}^n, p^n), (\boldsymbol{v}_h, q_h)\big) + \dfrac{\gamma\kappa\mu}{\gamma\mu + \kappa h}\big(\boldsymbol{u}^n - \dot{\boldsymbol{d}}^{n-1}, \boldsymbol{v}_h\big)_\Sigma \\ - \dfrac{\gamma\mu}{\gamma\mu + \kappa h}\big(\boldsymbol{g}^{n,\star}, \boldsymbol{v}_h\big)_\Sigma - \dfrac{h}{\gamma\mu + \kappa h}\big(\boldsymbol{\sigma}(\boldsymbol{u}^n, p^n)\boldsymbol{n}, \boldsymbol{\sigma}(\boldsymbol{v}_h, -q_h)\boldsymbol{n}\big)_\Sigma \\ - \dfrac{\kappa h}{\gamma\mu + \kappa h}\Big[\big(\boldsymbol{\sigma}(\boldsymbol{u}^n, p^n)\boldsymbol{n}, \boldsymbol{v}_h\big)_\Sigma + \big(\boldsymbol{u}^n - \dot{\boldsymbol{d}}^{n-1}, \boldsymbol{\sigma}(\boldsymbol{v}_h, -q_h)\boldsymbol{n}\big)_\Sigma\Big] \\ + \dfrac{h}{\gamma\mu + \kappa h}\big(\boldsymbol{g}^{n,\star}, \boldsymbol{\sigma}(\boldsymbol{v}_h, -q_h)\boldsymbol{n}\big)_\Sigma = 0\end{cases}$$

  for all $(\boldsymbol{v}_h, q_h) \in \boldsymbol{V}_h \times Q_h$.

- Solid:

$$\begin{cases} \rho^{\mathrm{s}}\epsilon\big(\partial_\tau \dot{\boldsymbol{d}}^n, \boldsymbol{w}_h\big)_\Sigma + a^{\mathrm{s}}(\boldsymbol{d}^n, \boldsymbol{w}_h) = -\dfrac{\kappa h}{\gamma\mu + \kappa h}\big(\boldsymbol{\sigma}(\boldsymbol{u}^n, p^n)\boldsymbol{n}, \boldsymbol{w}_h\big)_\Sigma \\ \qquad\qquad + \dfrac{\gamma\kappa\mu}{\gamma\mu + \kappa h}\big(\boldsymbol{u}^n - \dot{\boldsymbol{d}}^{n-1}, \boldsymbol{w}_h\big)_\Sigma - \dfrac{\gamma\mu}{\gamma\mu + \kappa h}\big(\boldsymbol{g}^{n,\star}, \boldsymbol{w}_h\big)_\Sigma \end{cases}$$

for all $\boldsymbol{w}_h \in \boldsymbol{W}_h$.

This motivates the fully discrete method reported in Algorithm 5.3. Note that the resulting coupling scheme is explicit.

Algorithm 5.3 Explicit coupling schemes.

For $n > r$:

1. Fluid substep: find $\big(\boldsymbol{u}_h^n, p_h^n\big) \in \boldsymbol{V}_h \times Q_h$ such that

$$\begin{cases} r\rho^{\mathrm{f}}\big(\partial_\tau \boldsymbol{u}_h^n, \boldsymbol{v}_h\big)_{\Omega^{\mathrm{f}}} + a_h^{\mathrm{f}}\big((\boldsymbol{u}_h^n, p_h^n), (\boldsymbol{v}_h, q_h)\big) + \dfrac{\gamma\kappa\mu}{\gamma\mu + \kappa h}\big(\boldsymbol{u}_h^n - \dot{\boldsymbol{d}}_h^{n-1}, \boldsymbol{v}_h\big)_\Sigma \\ - \dfrac{\gamma\mu}{\gamma\mu + \kappa h}\big(\boldsymbol{g}_h^{n,\star}, \boldsymbol{v}_h\big)_\Sigma - \dfrac{h}{\gamma\mu + \kappa h}\big(\boldsymbol{\sigma}(\boldsymbol{u}_h^n, p_h^n)\boldsymbol{n}, \boldsymbol{\sigma}(\boldsymbol{v}_h, -q_h)\boldsymbol{n}\big)_\Sigma \\ - \dfrac{\kappa h}{\gamma\mu + \kappa h}\Big[\big(\boldsymbol{\sigma}(\boldsymbol{u}_h^n, p_h^n)\boldsymbol{n}, \boldsymbol{v}_h\big)_\Sigma + \big(\boldsymbol{u}_h^n - \dot{\boldsymbol{d}}_h^{n-1}, \boldsymbol{\sigma}(\boldsymbol{v}_h, -q_h)\boldsymbol{n}\big)_\Sigma\Big] \\ + \dfrac{h}{\gamma\mu + \kappa h}\big(\boldsymbol{g}_h^{n,\star}, \boldsymbol{\sigma}(\boldsymbol{v}_h, -q_h)\boldsymbol{n}\big)_\Sigma = 0 \end{cases} \tag{5.80}$$

for all $(\boldsymbol{v}_h, q_h) \in \boldsymbol{V}_h \times Q_h$.

2. Solid substep: find $\big(\dot{\boldsymbol{d}}_h^n, \boldsymbol{d}_h^n\big) \in \boldsymbol{W}_h \times \boldsymbol{W}_h$ such that $\dot{\boldsymbol{d}}_h^n = \partial_\tau \boldsymbol{d}_h^n$ and

$$\begin{cases} \rho^{\mathrm{s}}\epsilon\big(\partial_\tau \dot{\boldsymbol{d}}_h^n, \boldsymbol{w}_h\big)_\Sigma + a^{\mathrm{s}}(\boldsymbol{d}_h^n, \boldsymbol{w}_h) = -\dfrac{\kappa h}{\gamma\mu + \kappa h}\big(\boldsymbol{\sigma}(\boldsymbol{u}_h^n, p_h^n)\boldsymbol{n}, \boldsymbol{w}_h\big)_\Sigma \\ \qquad + \dfrac{\gamma\kappa\mu}{\gamma\mu + \kappa h}\big(\boldsymbol{u}_h^n - \dot{\boldsymbol{d}}_h^{n-1}, \boldsymbol{w}_h\big)_\Sigma - \dfrac{\gamma\mu}{\gamma\mu + \kappa h}\big(\boldsymbol{g}_h^{n,\star}, \boldsymbol{w}_h\big)_\Sigma \end{cases} \tag{5.81}$$

for all $\boldsymbol{w}_h \in \boldsymbol{W}_h$.

5.3.2 Stability and convergence analysis for $r = 0$

We present in this section an energy-based stability and a priori error analysis for Algorithm 5.3 with $r = 0$. The stability and convergence properties of Algorithm 5.3 with $r = 1, 2$ are investigated in Section 5.4 via numerical experiments.

5.3.2.1 Stability analysis

We consider the discrete energy E_h^n given by (5.20) at time-step t_n. The dissipation is given in this case by

$$\widetilde{D}_h^n \stackrel{\text{def}}{=} \frac{\rho^{\mathrm{f}}}{\tau}\|\boldsymbol{u}_h^n - \boldsymbol{u}_h^{n-1}\|_{0,\Omega^{\mathrm{f}}}^2 + c_{\mathrm{g}}\mu\|\boldsymbol{\nabla}\boldsymbol{u}_h^n\|_{0,\Omega_h}^2 + \frac{\gamma\kappa\mu}{\gamma\mu+\kappa h}\|\boldsymbol{u}_h^n - \dot{\boldsymbol{d}}_h^n\|_{0,\Sigma}^2 + |(\boldsymbol{u}_h^n, p_h^n)|_S^2$$
$$+ \frac{\rho^{\mathrm{s}}\epsilon}{\tau}\frac{\kappa h}{\gamma\mu+\kappa h}\|\dot{\boldsymbol{d}}_h^n - \dot{\boldsymbol{d}}_h^{n-1}\|_{0,\Sigma}^2 + \frac{1}{\tau}\|\boldsymbol{d}_h^n - \boldsymbol{d}_h^{n-1}\|_{\mathrm{s}}^2 + \frac{h}{\gamma\mu+\kappa h}\|p_h^n\|_{0,\Sigma}^2.$$

The following result establishes the unconditional energy stability of Algorithm 5.3 with $r = 0$.

Theorem 5.3 *Let $\{(\boldsymbol{u}_h^n, p_h^n, \dot{\boldsymbol{d}}_h^n, \boldsymbol{d}_h^n)\}_{n\geq 1}$ be given by Algorithm 5.3 with $r = 0$. For*

$$\gamma > \frac{12C_{\mathrm{TI}}}{\tilde{c}_{\mathrm{g}}},$$

we have

$$E_h^n + \tau\sum_{m=1}^{n}\widetilde{D}_h^m \lesssim E_h^0. \tag{5.82}$$

Proof. We first note that in the case $r = 0$ we have $\boldsymbol{g}_h^{n,\star} = \boldsymbol{0}$. Thus, by taking $(\boldsymbol{v}_h, q_h) = \tau(\boldsymbol{u}_h^n, p_h^n)$ in (5.80) and $\boldsymbol{w}_h = \tau\dot{\boldsymbol{d}}_h^n$ in (5.81), adding the resulting equations and applying (5.8), we get the following discrete energy inequality

$$\frac{\rho^{\mathrm{f}}}{2}\left(\tau\partial_\tau\|\boldsymbol{u}_h^n\|_{0,\Omega^{\mathrm{f}}}^2 + \|\boldsymbol{u}_h^n - \boldsymbol{u}_h^{n-1}\|_{0,\Omega^{\mathrm{f}}}^2\right) + \tilde{c}_{\mathrm{g}}\tau\left(\mu\|\boldsymbol{\varepsilon}(\boldsymbol{u}_h^n)\|_{0,\Omega_h}^2 + g_h(\boldsymbol{u}_h^n, \boldsymbol{u}_h^n)\right)$$
$$+ \tau s_h(p_h^n, p_h^n) + \frac{1}{2}\left(\tau\partial_\tau\|\boldsymbol{d}_h^n\|_{\mathrm{s}}^2 + \|\boldsymbol{d}_h^n - \boldsymbol{d}_h^{n-1}\|_{\mathrm{s}}^2\right)$$
$$\underbrace{-\frac{\kappa h}{\gamma\mu+\kappa h}\tau\left[\left(\boldsymbol{\sigma}(\boldsymbol{u}_h^n, p_h^n)\boldsymbol{n}, \boldsymbol{u}_h^n - \dot{\boldsymbol{d}}_h^n\right)_\Sigma + \left(\boldsymbol{u}_h^n - \dot{\boldsymbol{d}}_h^{n-1}, \boldsymbol{\sigma}(\boldsymbol{u}_h^n, -p_h^n)\boldsymbol{n}\right)_\Sigma\right]}_{T_1}$$
$$\underbrace{+\tau\kappa\left(\dot{\boldsymbol{d}}_h^n - \dot{\boldsymbol{d}}_h^{n-1}, \dot{\boldsymbol{d}}_h^n\right)_\Sigma + \frac{\gamma\kappa\mu}{\gamma\mu+\kappa h}\tau\left(\boldsymbol{u}_h^n - \dot{\boldsymbol{d}}_h^{n-1}, \boldsymbol{u}_h^n - \dot{\boldsymbol{d}}_h^n\right)_\Sigma}_{T_2}$$
$$\underbrace{-\frac{h}{\gamma\mu+\kappa h}\tau\left(\boldsymbol{\sigma}(\boldsymbol{u}_h^n, p_h^n)\boldsymbol{n}, \boldsymbol{\sigma}(\boldsymbol{u}_h^n, -p_h^n)\boldsymbol{n}\right)_\Sigma}_{T_3} \leq 0. \tag{5.83}$$

Note that the solid inertia term is included in term T_2. We now proceed by esti-

mating separately the terms T_1, T_2 and T_3. For the first, we have

$$T_1 = \underbrace{-\frac{\kappa h}{\gamma\mu+\kappa h}2\tau\big(\boldsymbol{\sigma}(\boldsymbol{u}_h^n,0)\boldsymbol{n},\boldsymbol{u}_h^n-\dot{\boldsymbol{d}}_h^n\big)_\Sigma}_{T_{1,1}}\underbrace{-\frac{\kappa h}{\gamma\mu+\kappa h}\tau\big(\boldsymbol{\sigma}(\boldsymbol{u}_h^n,0)\boldsymbol{n},\dot{\boldsymbol{d}}_h^n-\dot{\boldsymbol{d}}_h^{n-1}\big)_\Sigma}_{T_{1,2}}$$
$$\underbrace{+\frac{\kappa h}{\gamma\mu+\kappa h}\tau\big(\boldsymbol{\sigma}(\boldsymbol{0},p_h^n)\boldsymbol{n},\dot{\boldsymbol{d}}_h^n-\dot{\boldsymbol{d}}_h^{n-1}\big)_\Sigma}_{T_{1,3}}.$$

By combining the Cauchy-Schwarz and Young inequalities with the robust trace inequality (1.61), we obtain the following estimates:

$$\begin{aligned}
T_{1,1} &\geq -\frac{\kappa h}{\gamma(\gamma\mu+\kappa h)}4\mu\tau\|\boldsymbol{\varepsilon}(\boldsymbol{u}_h^n)\|_{0,\Sigma}\|\boldsymbol{u}_h^n-\dot{\boldsymbol{d}}_h^n\|_{0,\Sigma}\\
&\geq -\frac{1}{2\varepsilon_1}\frac{\kappa h}{\gamma(\gamma\mu+\kappa h)}16\mu C_{\mathrm{TI}}\tau\|\boldsymbol{\varepsilon}(\boldsymbol{u}_h^n)\|_{0,\Omega_h}^2-\frac{\varepsilon_1}{2}\frac{\gamma\kappa\mu\tau}{\gamma\mu+\kappa h}\|\boldsymbol{u}_h^n-\dot{\boldsymbol{d}}_h^n\|_{0,\Sigma}^2,\\
T_{1,2} &\geq -\frac{\kappa h}{\gamma\mu+\kappa h}2\mu\tau\|\boldsymbol{\varepsilon}(\boldsymbol{u}_h^n)\|_{0,\Sigma}\|\dot{\boldsymbol{d}}_h^n-\dot{\boldsymbol{d}}_h^{n-1}\|_{0,\Sigma}\\
&\geq -\frac{1}{2\varepsilon_2}\frac{\mu}{\gamma\mu+\kappa h}4\mu C_{\mathrm{TI}}\tau\|\boldsymbol{\varepsilon}(\boldsymbol{u}_h^n)\|_{0,\Omega_h}^2-\frac{\varepsilon_2}{2}\frac{\kappa^2h\tau}{\gamma\mu+\kappa h}\|\dot{\boldsymbol{d}}_h^n-\dot{\boldsymbol{d}}_h^{n-1}\|_{0,\Sigma}^2,\\
T_{1,3} &\geq -\frac{\kappa h}{\gamma\mu+\kappa h}\tau\|p_h^n\|_{0,\Sigma}\|\dot{\boldsymbol{d}}_h^n-\dot{\boldsymbol{d}}_h^{n-1}\|_{0,\Sigma}\\
&\geq -\frac{1}{2\varepsilon_3}\frac{h}{\gamma\mu+\kappa h}\tau\|p_h^n\|_{0,\Sigma}^2-\frac{\varepsilon_3}{2}\frac{\kappa^2h\tau}{\gamma\mu+\kappa h}\|\dot{\boldsymbol{d}}_h^n-\dot{\boldsymbol{d}}_h^{n-1}\|_{0,\Sigma}^2.
\end{aligned}$$

On the other hand, by adding and subtracting suitable terms, for the second term we have

$$\begin{aligned}
T_2 =&\tau\kappa\big(\dot{\boldsymbol{d}}_h^n-\dot{\boldsymbol{d}}_h^{n-1},\dot{\boldsymbol{d}}_h^n\big)_\Sigma+\frac{\gamma\kappa\mu\tau}{\gamma\mu+\kappa h}\big(\boldsymbol{u}_h^n-\dot{\boldsymbol{d}}_h^{n-1},\boldsymbol{u}_h^n-\dot{\boldsymbol{d}}_h^n\big)_\Sigma\\
=&\tau\kappa\big(\dot{\boldsymbol{d}}_h^n-\dot{\boldsymbol{d}}_h^{n-1},\dot{\boldsymbol{d}}_h^n\big)_\Sigma+\frac{\gamma\kappa\mu\tau}{\gamma\mu+\kappa h}\big(\boldsymbol{u}_h^n-\dot{\boldsymbol{d}}_h^n+\dot{\boldsymbol{d}}_h^n-\dot{\boldsymbol{d}}_h^{n-1},\boldsymbol{u}_h^n-\dot{\boldsymbol{d}}_h^n\big)_\Sigma\\
=&\tau\kappa\big(\dot{\boldsymbol{d}}_h^n-\dot{\boldsymbol{d}}_h^{n-1},\dot{\boldsymbol{d}}_h^n\big)_\Sigma+\frac{\gamma\kappa\mu\tau}{\gamma\mu+\kappa h}\big(\dot{\boldsymbol{d}}_h^n-\dot{\boldsymbol{d}}_h^{n-1},\boldsymbol{u}_h^n-\dot{\boldsymbol{d}}_h^n\big)_\Sigma+\frac{\gamma\kappa\mu\tau}{\gamma\mu+\kappa h}\big\|\boldsymbol{u}_h^n-\dot{\boldsymbol{d}}_h^n\big\|_{0,\Sigma}^2.
\end{aligned}$$

Hence, using the Cauchy-Schwarz inequality, we infer the following fundamental lower bound

$$T_2 \geq \frac{\rho^{\mathrm{s}}\epsilon}{2}\tau\partial_\tau\|\dot{\boldsymbol{d}}_h^n\|_{0,\Sigma}^2+\frac{1}{2}\frac{\kappa^2h\tau}{\gamma\mu+\kappa h}\|\dot{\boldsymbol{d}}_h^n-\dot{\boldsymbol{d}}_h^{n-1}\|_{0,\Sigma}^2+\frac{1}{2}\frac{\gamma\kappa\mu\tau}{\gamma\mu+\kappa h}\|\boldsymbol{u}_h^n-\dot{\boldsymbol{d}}_h^n\|_{0,\Sigma}^2.$$

Finally, for the last term, using once more the Cauchy-Schwarz and Young inequalities, we get

$$T_3 \geq -\frac{\mu}{\gamma\mu+\kappa h}4\mu C_{\mathrm{TI}}\tau\|\boldsymbol{\varepsilon}(\boldsymbol{u}_h^n)\|_{0,\Omega_h}^2+\frac{h\tau}{\gamma\mu+\kappa h}\|p_h^n\|_{0,\Sigma}^2.$$

By collecting the above bounds for T_1, T_2 and T_3 and inserting them into (5.83), we obtain

$$\begin{aligned}
&\frac{\rho^{\mathrm{f}}}{2}\left(\tau\partial_\tau\|\boldsymbol{u}_h^n\|_{0,\Omega^{\mathrm{f}}}^2+\|\boldsymbol{u}_h^n-\boldsymbol{u}_h^{n-1}\|_{0,\Omega^{\mathrm{f}}}^2\right)+\tilde{c}_{\mathrm{g}}\tau g_h(\boldsymbol{u}_h^n,\boldsymbol{u}_h^n)+\tau s_h(p_h^n,p_h^n)\\
&\qquad+\frac{\rho^{\mathrm{s}}\epsilon}{2}\tau\partial_\tau\|\dot{\boldsymbol{d}}_h^n\|_{0,\Sigma}^2+\frac{1}{2}\left(\tau\partial_\tau\|\boldsymbol{d}_h^n\|_{\mathrm{s}}^2+\|\boldsymbol{d}_h^n-\boldsymbol{d}_h^{n-1}\|_{\mathrm{s}}^2\right)\\
&\qquad+\tau\mu\left[\tilde{c}_{\mathrm{g}}-\frac{4C_{\mathrm{TI}}}{\gamma}\frac{\left(1+\frac{1}{2\varepsilon_2}\right)\gamma\mu+\frac{2}{\varepsilon_1}\kappa h}{\gamma\mu+\kappa h}\right]\|\boldsymbol{\varepsilon}(\boldsymbol{u}_h^n)\|_{0,\Omega_h}^2\\
&+\frac{1}{2}\frac{\gamma\kappa\mu}{\gamma\mu+\kappa h}\tau\left(1-\varepsilon_1\right)\|\boldsymbol{u}_h^n-\dot{\boldsymbol{d}}_h^n\|_{0,\Sigma}^2+\frac{1}{2}\kappa\frac{\kappa h}{\gamma\mu+\kappa h}\tau\left(1-(\varepsilon_2+\varepsilon_3)\right)\|\dot{\boldsymbol{d}}_h^n-\dot{\boldsymbol{d}}_h^{n-1}\|_{0,\Sigma}^2\\
&\qquad+\frac{h}{\gamma\mu+\kappa h}\tau\left(1-\frac{1}{2\varepsilon_3}\right)\|p_h^n\|_{0,\Sigma}^2\leq 0.
\end{aligned}$$

The estimate (5.82) then follows by choosing

$$\varepsilon_1=\frac{2}{3},\quad \varepsilon_2=\frac{1}{4},\quad \varepsilon_3=\frac{5}{8},\quad \gamma>\frac{12C_{\mathrm{TI}}}{\tilde{c}_{\mathrm{g}}},$$

using Korn's inequality and summing over $m=1,\ldots,n$. This completes the proof. ■

5.3.2.2 Convergence analysis

In the sequel we assume that the interface Σ is flat and that the exact solution of problem (5.1)-(5.2) has the regularity given by (5.38) and (5.39) for a given final time $T\geq\tau$. For the derivation of the error estimate, we also build on the decomposition of the error given by (5.40)-(5.41). Let us first estimate the discrete errors $(\boldsymbol{\theta}_h^n,y_h^n,\boldsymbol{\xi}_h^n,\dot{\boldsymbol{\xi}}_h^n)$. An a priori bound is stated in Theorem 5.4 below, with the energy-norm of the discrete error being defined, at time step t_n, as

$$\begin{aligned}
\widetilde{\mathcal{E}}_h^n\overset{\mathrm{def}}{=}&(\rho^{\mathrm{f}})^{\frac{1}{2}}\|\boldsymbol{\theta}_h^n\|_{0,\Omega^{\mathrm{f}}}+(\rho^{\mathrm{s}}\epsilon)^{\frac{1}{2}}\|\dot{\boldsymbol{\xi}}_h^n\|_{0,\Sigma}+\|\boldsymbol{\xi}_h^n\|_{\mathrm{s}}+\left(\sum_{m=1}^n c_{\mathrm{g}}\tau\mu\|\boldsymbol{\nabla}\boldsymbol{\theta}_h^n\|_{0,\Omega^{\mathrm{f}}}^2\right)^{\frac{1}{2}}\\
&+\left(\sum_{m=1}^n c_{\mathrm{g}}\tau|(\boldsymbol{\theta}_h^n,y_h^n)|_S^2\right)^{\frac{1}{2}}+\left(\sum_{m=1}^n\frac{\gamma\kappa\mu}{\gamma\mu+\kappa h}\tau\|\boldsymbol{\theta}_h^n-\dot{\boldsymbol{\xi}}_h^n\|_{0,\Sigma}^2\right)^{\frac{1}{2}}\\
&+\left(\sum_{m=1}^n\frac{h}{\gamma\mu+\kappa h}\tau\|y_h^n\|_{0,\Sigma}^2\right)^{\frac{1}{2}}
\end{aligned}$$

for $n>0$.

Theorem 5.4 *Let $(\boldsymbol{u},p,\boldsymbol{d},\dot{\boldsymbol{d}})$ be the solution of the coupled problem (5.1)-(5.2) and $\{(\boldsymbol{u}_h^n,p_h^n,\boldsymbol{d}_h^n,\dot{\boldsymbol{d}}_h^n)\}_{n>r}$ be the approximation given by Algorithm 5.3 with initial*

data $\left(\boldsymbol{u}_h^0, \boldsymbol{d}_h^0, \dot{\boldsymbol{d}}_h^0\right) = \left(i_{\mathrm{sz}} E_2 \boldsymbol{u}^0, \boldsymbol{\pi}_h^{\mathrm{s}} \boldsymbol{d}^0, \mathcal{I}_h \dot{\boldsymbol{d}}^0\right)$ *and* $r = 0$. *We assume that the exact solution has the regularity* (5.38)-(5.39). *Assume that* $\gamma > 0$ *is given by Theorem* 5.3. *Then, we have the following error estimates, for* $n > r$ *and* $n\tau < T$:

$$\widetilde{\mathcal{E}}_h^n \lesssim c_1 h + c_2 \tau + c_3 \tau^{\frac{1}{2}}. \tag{5.84}$$

Here, the symbols $\{c_i\}_{i=1}^3$ *denote positive constants independent of* h *and* τ, *but which depend on the physical parameters and on the regularity of* $(\boldsymbol{u}, p, \boldsymbol{d}, \dot{\boldsymbol{d}})$.

Proof. At time t^n, the exact solution $(\boldsymbol{u}, p, \boldsymbol{d}, \dot{\boldsymbol{d}})$ of the coupled problem (5.1)-(5.2) satisfies

$$\begin{cases} \rho^{\mathrm{f}} \partial_t \boldsymbol{u}^n - \mathbf{div} \boldsymbol{\sigma}(\boldsymbol{u}^n, p^n) = \mathbf{0} & \text{in} \quad \Omega^{\mathrm{f}}, \\ \mathrm{div} \boldsymbol{u}^n = 0 & \text{in} \quad \Omega^{\mathrm{f}}, \\ \boldsymbol{u}^n = \mathbf{0} & \text{on} \quad \Gamma^{\mathrm{f}}, \\ \boldsymbol{\sigma}(\boldsymbol{u}^n, p^n)\boldsymbol{n} + \kappa \boldsymbol{u}^n = \kappa \dot{\boldsymbol{d}}^{n-1} - \boldsymbol{L}^{\mathrm{e}} \boldsymbol{d}^n - \rho^{\mathrm{s}} \epsilon (\partial_t - \partial_\tau) \dot{\boldsymbol{d}}^n & \text{on} \quad \Sigma, \end{cases}$$

$$\begin{cases} \boldsymbol{u}^n = \dot{\boldsymbol{d}}^n & \text{on} \quad \Sigma, \\ \rho^{\mathrm{s}} \epsilon \partial_t \dot{\boldsymbol{d}}^n + \boldsymbol{L}^{\mathrm{e}} \boldsymbol{d}^n = -\boldsymbol{\sigma}(\boldsymbol{u}^n, p^n)\boldsymbol{n} & \text{on} \quad \Sigma, \\ \dot{\boldsymbol{d}}^n = \partial_t \boldsymbol{d}^n & \text{on} \quad \Sigma, \\ \boldsymbol{d}^n = \mathbf{0} & \text{on} \quad \partial\Sigma. \end{cases}$$

Recall that, for a given time dependent function f, we use the notation f^n to denote $f(n\tau)$ and $\partial_t f^n$ to denote $(\partial_t f)^n$. Then, similarly to Proposition 5.1, we can show that the exact solution, at time t^n, of the coupled problem (5.1)-(5.2) satisfies

$$\begin{aligned} &\rho^{\mathrm{f}} \left(\partial_t \boldsymbol{u}^n, \boldsymbol{v}_h\right)_{\Omega^{\mathrm{f}}} + a^{\mathrm{f}}\left((\boldsymbol{u}^n, p^n), (\boldsymbol{v}_h, q_h)\right) + \rho^{\mathrm{s}} \epsilon \left(\partial_t \dot{\boldsymbol{d}}^n, \boldsymbol{w}_h\right)_\Sigma + a^{\mathrm{s}}(\boldsymbol{d}^n, \boldsymbol{w}_h) \\ &+ \frac{\gamma\kappa\mu}{\gamma\mu + \kappa h} \left(\boldsymbol{u}^n - \dot{\boldsymbol{d}}^{n-1}, \boldsymbol{v}_h - \boldsymbol{w}_h\right)_\Sigma + \frac{\gamma\mu}{\gamma\mu + \kappa h} \left(\boldsymbol{L}^{\mathrm{e}} \boldsymbol{d}^n + \rho^{\mathrm{s}} \epsilon (\partial_t - \partial_\tau) \dot{\boldsymbol{d}}^n, \boldsymbol{v}_h - \boldsymbol{w}_h\right)_\Sigma \\ &\quad - \frac{\kappa h}{\gamma\mu + \kappa h} \left[\left(\boldsymbol{\sigma}(\boldsymbol{u}^n, p^n)\boldsymbol{n}, \boldsymbol{v}_h - \boldsymbol{w}_h\right)_\Sigma + \left(\boldsymbol{u}^n - \dot{\boldsymbol{d}}^{n-1}, \boldsymbol{\sigma}(\boldsymbol{v}_h, -q_h)\boldsymbol{n}\right)_\Sigma \right] \\ &\quad\quad - \frac{h}{\gamma\mu + \kappa h} \left(\boldsymbol{L}^{\mathrm{e}} \boldsymbol{d}^n + \rho^{\mathrm{s}} \epsilon (\partial_t - \partial_\tau) \dot{\boldsymbol{d}}^n, \boldsymbol{\sigma}(\boldsymbol{v}_h, -q_h)\boldsymbol{n}\right)_\Sigma \\ &\quad\quad\quad - \frac{h}{\gamma\mu + \kappa h} \left(\boldsymbol{\sigma}(\boldsymbol{u}^n, p^n)\boldsymbol{n}, \boldsymbol{\sigma}(\boldsymbol{v}_h, -q_h)\boldsymbol{n}\right)_\Sigma = 0 \end{aligned} \tag{5.85}$$

for all $\boldsymbol{v}_h, q_h, \boldsymbol{w}_h \in \boldsymbol{V}_h \times Q_h \times \boldsymbol{W}_h$. Subtracting (5.80) and (5.81) to the continuous problem (5.85) we obtain, after adding and subtracting $\partial_\tau \boldsymbol{u}^n$ and $\partial_\tau \dot{\boldsymbol{d}}^n$, the following

modified Galerkin orthogonality:

$$
\begin{aligned}
&\rho^{\mathrm{f}}\left(\partial_\tau(\boldsymbol{u}^n-\boldsymbol{u}_h^n),\boldsymbol{v}_h\right)_{\Omega^{\mathrm{f}}}+a^{\mathrm{f}}\big((\boldsymbol{u}^n-\boldsymbol{u}_h^n,p^n-p_h^n),(\boldsymbol{v}_h,q_h)\big)\\
&\qquad\qquad+\rho^{\mathrm{s}}\epsilon\big(\partial_\tau(\dot{\boldsymbol{d}}^n-\dot{\boldsymbol{d}}_h^n),\boldsymbol{w}_h\big)_\Sigma+a^{\mathrm{s}}\big(\boldsymbol{d}^n-\boldsymbol{d}_h^n,\boldsymbol{w}_h\big)\\
&-\frac{\kappa h}{\gamma\mu+\kappa h}\Big[\big(\boldsymbol{\sigma}(\boldsymbol{u}^n-\boldsymbol{u}_h^n,p^n-p_h^n)\boldsymbol{n},\boldsymbol{v}_h-\boldsymbol{w}_h\big)_\Sigma+\big((\boldsymbol{u}^n-\boldsymbol{u}_h^n)-(\dot{\boldsymbol{d}}^{n-1}-\dot{\boldsymbol{d}}_h^{n-1}),\boldsymbol{\sigma}(\boldsymbol{v}_h,-q_h)\boldsymbol{n}\big)_\Sigma\Big]\\
&\qquad+\frac{\gamma\kappa\mu}{\gamma\mu+\kappa h}\big((\boldsymbol{u}^n-\boldsymbol{u}_h^n)-(\dot{\boldsymbol{d}}^{n-1}-\dot{\boldsymbol{d}}_h^{n-1}),\boldsymbol{v}_h-\boldsymbol{w}_h\big)_\Sigma\\
&\qquad-\frac{h}{\gamma\mu+\kappa h}\big(\boldsymbol{\sigma}(\boldsymbol{u}^n-\boldsymbol{u}_h^n,p^n-p_h^n)\boldsymbol{n},\boldsymbol{\sigma}(\boldsymbol{v}_h,-q_h)\boldsymbol{n}\big)_\Sigma\\
&=-\rho^{\mathrm{f}}\big((\partial_t-\partial_\tau)\boldsymbol{u}^n,\boldsymbol{v}_h\big)_{\Omega^{\mathrm{f}}}-\rho^{\mathrm{s}}\epsilon\big((\partial_t-\partial_\tau)\dot{\boldsymbol{d}}^n,\boldsymbol{w}_h\big)_\Sigma+S_h\big((\boldsymbol{u}_h^n,p_h^n),(\boldsymbol{v}_h,q_h)\big)\\
&\qquad-\frac{\gamma\mu}{\gamma\mu+\kappa h}\big(\boldsymbol{L}^{\mathrm{e}}\boldsymbol{d}^n+\rho^{\mathrm{s}}\epsilon(\partial_t-\partial_\tau)\dot{\boldsymbol{d}}^n,\boldsymbol{v}_h-\boldsymbol{w}_h\big)_\Sigma\\
&\qquad+\frac{h}{\gamma\mu+\kappa h}\big(\boldsymbol{L}^{\mathrm{e}}\boldsymbol{d}^n+\rho^{\mathrm{s}}\epsilon(\partial_t-\partial_\tau)\dot{\boldsymbol{d}}^n,\boldsymbol{\sigma}(\boldsymbol{v}_h,-q_h)\boldsymbol{n}\big)_\Sigma
\end{aligned}
\tag{5.86}
$$

for all $(\boldsymbol{v}_h,q_h,\boldsymbol{w}_h)\in\boldsymbol{V}_h\times Q_h\times\boldsymbol{W}_h$. Hence, from (5.40)-(5.41), we infer the following equation for the discrete errors $\boldsymbol{\theta}_h^n$, y_h^n, $\boldsymbol{\xi}_h^n$ and $\dot{\boldsymbol{\xi}}_h^n$:

$$
\begin{aligned}
&\rho^{\mathrm{f}}\big(\partial_\tau\boldsymbol{\theta}_h^n,\boldsymbol{v}_h\big)_{\Omega^{\mathrm{f}}}+a^{\mathrm{f}}\big((\boldsymbol{\theta}_h^n,y_h^n),(\boldsymbol{v}_h,q_h)\big)+S_h\big((\boldsymbol{\theta}_h^n,y_h^n),(\boldsymbol{v}_h,q_h)\big)\\
&\qquad\qquad+\rho^{\mathrm{s}}\epsilon\big(\partial_\tau\dot{\boldsymbol{\xi}}_h^n,\boldsymbol{w}_h\big)_\Sigma+a^{\mathrm{s}}\big(\boldsymbol{\xi}_h^n,\boldsymbol{w}_h\big)\\
&\qquad-\frac{\kappa h}{\gamma\mu+\kappa h}\Big[\big(\boldsymbol{\sigma}(\boldsymbol{\theta}_h^n,y_h^n)\boldsymbol{n},\boldsymbol{v}_h-\boldsymbol{w}_h\big)_\Sigma+\big(\boldsymbol{\theta}_h^n-\dot{\boldsymbol{\xi}}_h^{n-1},\boldsymbol{\sigma}(\boldsymbol{v}_h,-q_h)\boldsymbol{n}\big)_\Sigma\Big]\\
&\quad+\frac{\gamma\kappa\mu}{\gamma\mu+\kappa h}\big(\boldsymbol{\theta}_h^n-\dot{\boldsymbol{\xi}}_h^{n-1},\boldsymbol{v}_h-\boldsymbol{w}_h\big)_\Sigma-\frac{h}{\gamma\mu+\kappa h}\big(\boldsymbol{\sigma}(\boldsymbol{\theta}_h^n,y_h^n)\boldsymbol{n},\boldsymbol{\sigma}(\boldsymbol{v}_h,-q_h)\boldsymbol{n}\big)_\Sigma\\
=\;&-\rho^{\mathrm{f}}\big((\partial_t-\partial_\tau)\boldsymbol{u}^n,\boldsymbol{v}_h\big)_{\Omega^{\mathrm{f}}}-\rho^{\mathrm{f}}\left(\partial_\tau\boldsymbol{\theta}_\pi^n,\boldsymbol{v}_h\right)_{\Omega^{\mathrm{f}}}-\rho^{\mathrm{s}}\epsilon\big((\partial_t-\partial_\tau)\dot{\boldsymbol{d}}^n,\boldsymbol{w}_h\big)_\Sigma-\rho^{\mathrm{s}}\epsilon\big(\partial_\tau\dot{\boldsymbol{\xi}}_\pi^n,\boldsymbol{w}_h\big)_\Sigma\\
&\quad-a^{\mathrm{s}}\big(\boldsymbol{\xi}_\pi^n,\boldsymbol{w}_h\big)+S_h\big((i_{\mathrm{sz}}E_2\boldsymbol{u}^n,i_{\mathrm{sz}}E_1p^n),(\boldsymbol{v}_h,q_h)\big)-a^{\mathrm{f}}\big((\boldsymbol{\theta}_\pi^n,y_\pi^n),(\boldsymbol{v}_h,q_h)\big)\\
&\qquad+\frac{\kappa h}{\gamma\mu+\kappa h}\Big[\big(\boldsymbol{\sigma}(\boldsymbol{\theta}_\pi^n,y_\pi^n)\boldsymbol{n},\boldsymbol{v}_h-\boldsymbol{w}_h\big)_\Sigma+\big(\boldsymbol{\theta}_\pi^n-\dot{\boldsymbol{\xi}}_\pi^{n-1},\boldsymbol{\sigma}(\boldsymbol{v}_h,-q_h)\boldsymbol{n}\big)_\Sigma\Big]\\
&\quad-\frac{\gamma\kappa\mu}{\gamma\mu+\kappa h}\big(\boldsymbol{\theta}_\pi^n-\dot{\boldsymbol{\xi}}_\pi^{n-1},\boldsymbol{v}_h-\boldsymbol{w}_h\big)_\Sigma+\frac{h}{\gamma\mu+\kappa h}\big(\boldsymbol{\sigma}(\boldsymbol{\theta}_\pi^n,y_\pi^n)\boldsymbol{n},\boldsymbol{\sigma}(\boldsymbol{v}_h,-q_h)\boldsymbol{n}\big)_\Sigma\\
&\qquad-\frac{\gamma\mu}{\gamma\mu+\kappa h}\big(\boldsymbol{L}^{\mathrm{e}}\boldsymbol{d}^n+\rho^{\mathrm{s}}\epsilon(\partial_t-\partial_\tau)\dot{\boldsymbol{d}}^n,\boldsymbol{v}_h-\boldsymbol{w}_h\big)_\Sigma\\
&\qquad+\frac{h}{\gamma\mu+\kappa h}\big(\boldsymbol{L}^{\mathrm{e}}\boldsymbol{d}^n+\rho^{\mathrm{s}}\epsilon(\partial_t-\partial_\tau)\dot{\boldsymbol{d}}^n,\boldsymbol{\sigma}(\boldsymbol{v}_h,-q_h)\boldsymbol{n}\big)_\Sigma
\end{aligned}
\tag{5.87}
$$

for all $(\boldsymbol{v}_h,q_h,\boldsymbol{w}_h)\in\boldsymbol{V}_h\times Q_h\times\boldsymbol{W}_h$ and $n>r$. Note that $a^{\mathrm{s}}\big(\boldsymbol{\xi}_\pi^n,\boldsymbol{w}_h\big)=0$ due to the definition of the solid projection operator $\boldsymbol{\pi}_h^{\mathrm{s}}$. Taking $(\boldsymbol{v}_h,q_h,\boldsymbol{w}_h)=\tau(\boldsymbol{\theta}_h^n,y_h^n,\dot{\boldsymbol{\xi}}_h^n)$ in (5.87), using the stability estimate reported in Theorem 5.3 and (5.43), yields the following energy inequality for the discrete errors:

$$
\begin{aligned}
&\frac{\rho^{\mathrm{f}}}{2}\left(\tau\partial_\tau\|\boldsymbol{\theta}_h^n\|_{0,\Omega^{\mathrm{f}}}^2+\tau^2\|\partial_\tau\boldsymbol{\theta}_h^n\|_{0,\Omega^{\mathrm{f}}}^2\right)+\tilde{\tilde{c}}_{\mathrm{g}}\tau\left(\mu\|\boldsymbol{\nabla}\boldsymbol{\theta}_h^n\|_{0,\Omega_h^{\mathrm{f}}}^2+|(\boldsymbol{\theta}_h^n,y_h^n)|_S^2\right)\\
&+\frac{1}{2}\left(\tau\partial_\tau\|\boldsymbol{\xi}_h^n\|_{\mathrm{s}}^2+\tau^2\|\partial_\tau\boldsymbol{\xi}_h^n\|_{\mathrm{s}}^2\right)+\frac{1}{6}\frac{\gamma\kappa\mu}{\gamma\mu+\kappa h}\tau\|\boldsymbol{\theta}_h^n-\dot{\boldsymbol{\xi}}_h^n\|_{0,\Sigma}^2\\
&+\frac{1}{5}\frac{h}{\gamma\mu+\kappa h}\tau\|y_h^n\|_{0,\Sigma}^2+\frac{\rho^{\mathrm{s}}\epsilon}{2}\left(\tau\partial_\tau\|\dot{\boldsymbol{\xi}}_h^n\|_{0,\Sigma}^2+\frac{1}{8}\frac{\kappa h}{\gamma\mu+\kappa h}\tau^2\|\partial_\tau\dot{\boldsymbol{\xi}}_h^n\|_{0,\Sigma}^2\right)\\
&\leq\underbrace{-\rho^{\mathrm{f}}\tau\big((\partial_t-\partial_\tau)\boldsymbol{u}^n,\boldsymbol{\theta}_h^n\big)_{\Omega^{\mathrm{f}}}-\rho^{\mathrm{f}}\tau\left(\partial_\tau\boldsymbol{\theta}_\pi^n,\boldsymbol{\theta}_h^n\right)_{\Omega^{\mathrm{f}}}}_{T_1}\\
&\underbrace{-\rho^{\mathrm{s}}\epsilon\tau\big((\partial_t-\partial_\tau)\dot{\boldsymbol{d}}^n,\dot{\boldsymbol{\xi}}_h^n\big)_\Sigma-\rho^{\mathrm{s}}\epsilon\tau\big(\partial_\tau\dot{\boldsymbol{\xi}}_\pi^n,\dot{\boldsymbol{\xi}}_h^n\big)_\Sigma}_{T_2}\underbrace{-\tau a^{\mathrm{s}}(\boldsymbol{\xi}_h^n,\boldsymbol{z}_h^n)}_{T_3}\\
&\underbrace{+\tau S_h\big((i_{\mathrm{sz}}E_2\boldsymbol{u}(t),i_{\mathrm{sz}}E_1p(t)),(\boldsymbol{\theta}_h^n,y_h^n)\big)}_{T_4}\underbrace{-\tau\frac{\gamma\kappa\mu}{\gamma\mu+\kappa h}\big(\boldsymbol{\theta}_\pi^n-\dot{\boldsymbol{\xi}}_\pi^n,\boldsymbol{\theta}_h^n-\dot{\boldsymbol{\xi}}_h^n\big)_\Sigma}_{T_5}\\
&\underbrace{+\tau\frac{\kappa h}{\gamma\mu+\kappa h}\big(\boldsymbol{\sigma}(\boldsymbol{\theta}_\pi^n,y_\pi^n)\boldsymbol{n},\boldsymbol{\theta}_h^n-\dot{\boldsymbol{\xi}}_h^n\big)_\Sigma}_{T_6}\\
&\underbrace{-\tau a^{\mathrm{f}}\big((\boldsymbol{\theta}_\pi^n,y_\pi^n),(\boldsymbol{\theta}_h^n,y_h^n)\big)+\tau\frac{\kappa h}{\gamma\mu+\kappa h}\big(\boldsymbol{\theta}_\pi^n-\dot{\boldsymbol{\xi}}_\pi^n,\boldsymbol{\sigma}(\boldsymbol{\theta}_h^n,-y_h^n)\boldsymbol{n}\big)_\Sigma}_{T_7}\\
&\underbrace{+\tau\frac{h}{\gamma\mu+\kappa h}\big(\boldsymbol{\sigma}(\boldsymbol{\theta}_\pi^n,y_\pi^n)\boldsymbol{n},\boldsymbol{\sigma}(\boldsymbol{\theta}_h^n,-y_h^n)\boldsymbol{n}\big)_\Sigma}_{T_8}\underbrace{-\tau\frac{\gamma\kappa\mu}{\gamma\mu+\kappa h}\big(\dot{\boldsymbol{\xi}}_\pi^n-\dot{\boldsymbol{\xi}}_\pi^{n-1},\boldsymbol{\theta}_h^n-\dot{\boldsymbol{\xi}}_h^n\big)_\Sigma}_{T_9}\\
&\underbrace{+\tau\frac{\kappa h}{\gamma\mu+\kappa h}\big(\dot{\boldsymbol{\xi}}_\pi^n-\dot{\boldsymbol{\xi}}_\pi^{n-1},\boldsymbol{\sigma}(\boldsymbol{\theta}_h^n,-y_h^n)\boldsymbol{n}\big)_\Sigma}_{T_{10}}\\
&\underbrace{-\frac{\gamma\mu}{\gamma\mu+\kappa h}\big(\boldsymbol{L}^{\mathrm{e}}\boldsymbol{d}^n+\rho^{\mathrm{s}}\epsilon(\partial_t-\partial_\tau)\dot{\boldsymbol{d}}^n,\boldsymbol{\theta}_h^n-\dot{\boldsymbol{\xi}}_h^n\big)_\Sigma}_{T_{11}}\\
&\underbrace{+\frac{h}{\gamma\mu+\kappa h}\big(\boldsymbol{L}^{\mathrm{e}}\boldsymbol{d}^n+\rho^{\mathrm{s}}\epsilon(\partial_t-\partial_\tau)\dot{\boldsymbol{d}}^n,\boldsymbol{\sigma}(\boldsymbol{\theta}_h^n,-y_h^n)\boldsymbol{n}\big)_\Sigma}_{T_{12}}
\end{aligned}
\tag{5.88}
$$

with $\tilde{\tilde{c}}_{\mathrm{g}}>0$. The terms T_1-T_4 stem from the time-stepping and the stabilization methods. The terms T_5-T_8 come from the generalized Nitsche's method. Finally, terms T_9-T_{12} are due to the kinematic perturbation and, hence, are inherent to the fluid-solid time-splitting scheme.

Note that terms T_1, T_3 and T_4 can be bounded exactly as in (5.50), (5.53) and

(5.54). For term T_2 we can proceed in a similar manner to (5.51) to get

$$T_2 \lesssim \frac{\rho^{\mathrm{s}}\epsilon T}{2\varepsilon_2}\big(\tau^2\|\partial_{tt}\boldsymbol{u}\|^2_{L^2(t_{n-1},t_n;L^2(\Sigma))} + h^2\|\partial_t\dot{\boldsymbol{d}}\|^2_{L^2(t_{n-1},t_n;H^2(\Sigma))}\big) + \varepsilon_2\tau\frac{\rho^{\mathrm{s}}\epsilon}{T}\|\dot{\boldsymbol{\xi}}_h^n\|^2_{0,\Sigma}. \tag{5.89}$$

The last term will be treated using Lemma 5.1.

The boundary penalty term T_5 can be handled in a similar manner to (5.55) yielding

$$T_5 \lesssim \tau h^2\frac{\gamma\mu}{\varepsilon_5}(\|\boldsymbol{u}^n\|^2_{2,\Omega^{\mathrm{f}}} + h\|\dot{\boldsymbol{d}}^n\|^2_{2,\Sigma}) + \tau\frac{\varepsilon_5}{2}\frac{\gamma\kappa\mu}{\gamma\mu+\kappa h}\|\boldsymbol{\theta}_h^n - \dot{\boldsymbol{\xi}}_\pi^n\|^2_{0,\Sigma},$$

where we have used that

$$0 < \frac{\kappa h}{\gamma\mu+\kappa h} < 1.$$

Note that the second term can be absorbed in the left-hand side of (5.88), for $\varepsilon_5 > 0$ small enough.

Similarly, for the consistency term T_6, we have, using (5.35)

$$T_6 \lesssim \tau h^2\frac{1}{\varepsilon_6\gamma\mu}\left(\|\boldsymbol{u}^n\|^2_{2,\Omega^{\mathrm{f}}} + \|p^n\|^2_{1,\Omega^{\mathrm{f}}}\right) + \tau\frac{\varepsilon_6}{2}\frac{\gamma\kappa\mu}{\gamma\mu+\kappa h}\|\boldsymbol{\theta}_h^n - \dot{\boldsymbol{\xi}}_\pi^n\|^2_{0,\Sigma}.$$

Note that the first term has the right convergence order and the second term can be absorbed in the left hand side of (5.88), for $\varepsilon_6 > 0$ sufficiently small.

As in the proof of Theorem 5.2, we split T_7 into two parts. The velocity-velocity coupling contribution can be easily handled as in (5.57), viz.,

$$\begin{aligned}
&-\tau a(\boldsymbol{\theta}_\pi^n, \boldsymbol{\theta}_h^n) + \tau\frac{\kappa h}{\gamma\mu+\kappa h}\big(\boldsymbol{\sigma}(\boldsymbol{\theta}_h^n, 0)\boldsymbol{n}, \boldsymbol{\theta}_\pi^n - \dot{\boldsymbol{\xi}}_\pi^n\big)_\Sigma \\
&\quad\lesssim \tau h^2\frac{\mu}{\varepsilon_7 C_{\mathrm{TI}}}\|\boldsymbol{u}^n\|^2_{2,\Omega^{\mathrm{f}}} + \tau\mu\frac{2}{\varepsilon_7}h^2\left(\|\boldsymbol{u}^n\|^2_{2,\Omega^{\mathrm{f}}} + \|\dot{\boldsymbol{d}}^n\|^2_{2,\Sigma}\right) + 2\tau\varepsilon_7\mu C_{\mathrm{TI}}\|\boldsymbol{\nabla}\boldsymbol{\theta}_h^n\|^2_{0,\Omega_h}.
\end{aligned}$$

The last term can be, once again, absorbed in the left hand side of (5.88), for $\varepsilon_7 > 0$ sufficiently small. For the velocity-pressure coupling part we write, using integration by parts in the continuity equation,

$$\begin{aligned}
&-\tau b(y_\pi^n, \boldsymbol{\theta}_h^n) + \tau b(y_h^n, \boldsymbol{\theta}_\pi^n) + \tau\frac{\kappa h}{\gamma\mu+\kappa h}\big(\boldsymbol{\sigma}(\mathbf{0}, -y_h^n)\boldsymbol{n}, \boldsymbol{\theta}_\pi^n - \dot{\boldsymbol{\xi}}_\pi^n\big)_\Sigma \\
&\quad= \underbrace{\tau(y_\pi^n, \mathrm{div}\boldsymbol{\theta}_h^n)_{\Omega^{\mathrm{f}}}}_{T_{7,1}} \underbrace{+\tau(\boldsymbol{\nabla} y_h^n, \boldsymbol{\theta}_\pi^n)_{\Omega^{\mathrm{f}}}}_{T_{7,2}} \underbrace{-\tau\frac{\kappa h}{\gamma\mu+\kappa h}\big(y_h^n\boldsymbol{n}, \dot{\boldsymbol{\xi}}_\pi^n\big)_\Sigma}_{T_{7,3}} \underbrace{-\tau\frac{\gamma\mu}{\gamma\mu+\kappa h}\big(y_h^n\boldsymbol{n}, \boldsymbol{\theta}_\pi^n\big)_\Sigma}_{T_{7,4}}.
\end{aligned}$$

Terms $T_{7,1}$ and $T_{7,2}$ can be bounded as in (5.58). The control for $T_{7,3}$ follows as in

(5.59). For $T_{7,4}$, using (5.37), we have

$$\begin{aligned} T_{7,4} &\leq \tau \frac{1}{2\varepsilon_{7,4}} \gamma\mu \|\boldsymbol{\theta}_\pi^n\|^2_{\frac{1}{2},h,\Sigma} + \tau \frac{\varepsilon_{7,4}}{2} \frac{h}{\gamma\mu+\kappa h} \|y_h^n\|^2_{0,\Sigma} \\ &\lesssim \tau h^2 \frac{\gamma\mu}{\varepsilon_{7,4}} \|\boldsymbol{u}^n\|^2_{2,\Omega^{\mathrm{f}}} + \tau \frac{\varepsilon_{7,4}}{2} \frac{h}{\gamma\mu+\kappa h} \|y_h^n\|^2_{0,\Sigma}, \end{aligned}$$

the last term can be absorbed in the left hand side of (5.88), for $\varepsilon_{7,4} > 0$ small enough. The above estimations of $T_{7,1}$, $T_{7,2}$, $T_{7,3}$ and $T_{7,4}$ provide bounds which involve either terms with the right convergence order or contributions that can be absorbed by the left-hand side of (5.88).

For the term T_8 we have

$$\begin{aligned} T_8 &= \tau \frac{h}{\gamma\mu+\kappa h} \big(\boldsymbol{\sigma}(\boldsymbol{\theta}_\pi^n, y_\pi^n)\boldsymbol{n}, \boldsymbol{\sigma}(\boldsymbol{\theta}_h^n, 0)\boldsymbol{n}\big)_\Sigma + \tau \frac{h}{\gamma\mu+\kappa h} \big(\boldsymbol{\sigma}(\boldsymbol{\theta}_\pi^n, y_\pi^n)\boldsymbol{n}, y_h^n \boldsymbol{n}\big)_\Sigma \\ &\leq \tau \frac{1}{\varepsilon_8} \frac{1}{\gamma\mu+\kappa h} \|\boldsymbol{\sigma}(\boldsymbol{\theta}_\pi^n, y_\pi^n)\boldsymbol{n}\|^2_{-\frac{1}{2},h,\Sigma} + 2\tau\varepsilon_8 \frac{\mu}{\gamma\mu+\kappa h} \mu \|\boldsymbol{\varepsilon}(\boldsymbol{\theta}_h^n)\boldsymbol{n}\|^2_{-\frac{1}{2},h,\Sigma} \\ &\quad + \tau \frac{\varepsilon_8}{2} \frac{h}{\gamma\mu+\kappa h} \|y_h^n\|^2_{0,\Sigma}, \\ &\lesssim \tau h^2 \frac{1}{\varepsilon_8 \gamma\mu} \left(\|\boldsymbol{u}^n\|^2_{2,\Omega^{\mathrm{f}}} + \|p^n\|^2_{1,\Omega^{\mathrm{f}}} \right) + 2\tau\varepsilon_8 \frac{1}{\gamma} \mu C_{\mathrm{TI}} \|\boldsymbol{\nabla}\boldsymbol{\theta}_h^n\|^2_{0,\Omega_h} \\ &\quad + \tau \frac{\varepsilon_8}{2} \frac{h}{\gamma\mu+\kappa h} \|y_h^n\|^2_{0,\Sigma}, \end{aligned}$$

and the last two terms can be absorbed by the left-hand side of (5.88), for $\varepsilon_8 > 0$ small enough.

The boundary penalty term T_9 can be controlled using a Taylor expansion

$$\begin{aligned} T_9 &\leq \tau \frac{1}{2\varepsilon_9} \frac{\gamma\kappa\mu}{\gamma\mu+\kappa h} \|\tau \partial_\tau \dot{\boldsymbol{\xi}}_\pi^n\|^2_{0,\Sigma} + \tau \frac{\varepsilon_9}{2} \frac{\gamma\kappa\mu}{\gamma\mu+\kappa h} \|\boldsymbol{\theta}_h^n - \dot{\boldsymbol{\xi}}_h^n\|^2_{0,\Sigma} \\ &\lesssim \tau^2 \frac{1}{2\varepsilon_9} \frac{\gamma\kappa\mu}{\gamma\mu+\kappa h} \|\partial_t \dot{\boldsymbol{\xi}}_\pi\|^2_{L^2(t_{n-1},t_n;L^2(\Sigma))} + \tau \frac{\varepsilon_9}{2} \frac{\gamma\kappa\mu}{\gamma\mu+\kappa h} \|\boldsymbol{\theta}_h^n - \dot{\boldsymbol{\xi}}_h^n\|^2_{0,\Sigma} \\ &\lesssim \tau \frac{1}{2\varepsilon_9} h^2 \rho^{\mathrm{s}} \epsilon \|\partial_t \boldsymbol{u}\|^2_{L^2(t_{n-1},t_n;H^2(\Sigma))} + \tau \frac{\varepsilon_9}{2} \frac{\gamma\kappa\mu}{\gamma\mu+\kappa h} \|\boldsymbol{\theta}_h^n - \dot{\boldsymbol{\xi}}_h^n\|^2_{0,\Sigma}. \end{aligned}$$

Note that the second term can be absorbed in the left-hand side of (5.88), for $\varepsilon_9 > 0$ small enough.

Similarly, the boundary penalty term T_{10} is bounded by

$$\begin{aligned} T_{10} &= \tau \frac{\kappa h}{\gamma\mu+\kappa h} \big(\dot{\boldsymbol{\xi}}_\pi^n - \dot{\boldsymbol{\xi}}_\pi^{n-1}, \boldsymbol{\sigma}(\boldsymbol{\theta}_h^n, 0)\boldsymbol{n}\big)_\Sigma + \tau \frac{\kappa h}{\gamma\mu+\kappa h} \big(\dot{\boldsymbol{\xi}}_\pi^n - \dot{\boldsymbol{\xi}}_\pi^{n-1}, y_h^n \boldsymbol{n}\big)_\Sigma \\ &\lesssim \tau \frac{1}{2\varepsilon_{10}} h^2 \rho^{\mathrm{s}} \epsilon \|\partial_t \dot{\boldsymbol{d}}\|^2_{L^2(t_{n-1},t_n;H^2(\Sigma))} + 2\tau\varepsilon_{10} \mu C_{\mathrm{TI}} \|\boldsymbol{\nabla}\boldsymbol{\theta}_h^n\|^2_{0,\Omega_h} \\ &\quad + \tau \frac{\varepsilon_{10}}{2} \frac{h}{\gamma\mu+\kappa h} \|y_h^n\|^2_{0,\Sigma}, \end{aligned}$$

Note that the second term can be absorbed in the left-hand side of (5.88), for $\varepsilon_{10} > 0$

small enough.

Similarly, the boundary penalty term T_{11} is bounded by

$$T_{11} \lesssim \tau \frac{1}{2\varepsilon_{11}} \rho^{\mathrm{s}} \epsilon \tau^2 \|\partial_{tt} \boldsymbol{u}\|^2_{L^2(t_{n-1},t_n;L^2(\Sigma))} + \tau \frac{1}{2\varepsilon_{11}} \frac{\tau}{\rho^{\mathrm{s}}\epsilon} \|\boldsymbol{L}^{\mathrm{e}} \boldsymbol{d}^n\|^2_{0,\Sigma} + \tau \frac{\varepsilon_{11}}{2} \frac{\gamma\kappa\mu}{\gamma\mu + \kappa h} \|\boldsymbol{\theta}_h^n - \dot{\boldsymbol{\xi}}_h^n\|^2_{0,\Sigma}.$$

The last term can be absorbed in the left-hand side of (5.88), for $\varepsilon_{11} > 0$ sufficiently small.

Similarly, the boundary penalty term T_{12} is bounded by

$$T_{12} \lesssim \tau \frac{1}{\varepsilon_{12}} \rho^{\mathrm{s}} \epsilon \tau^2 \|\partial_{tt} \boldsymbol{u}\|^2_{L^2(t_{n-1},t_n;L^2(\Sigma))} + \tau \frac{1}{\varepsilon_{12}} \frac{\tau}{\rho^{\mathrm{s}}\epsilon} \|\boldsymbol{L}^{\mathrm{e}} \boldsymbol{d}^n\|^2_{0,\Sigma} + \tau\varepsilon_{12} C_{\mathrm{TI}} \mu \|\boldsymbol{\nabla} \boldsymbol{\theta}_h^n\|^2_{0,\Omega_h} + \tau\varepsilon_{12} \frac{h}{\gamma\mu + \kappa h} \|y_h^n\|^2_{0,\Sigma},$$

The last term can be absorbed in the left-hand side of (5.88), for $\varepsilon_{12} > 0$ small enough.

The estimate (5.84) follows by inserting the above estimates into (5.88), summing over $m = 1, \ldots, n$, and applying Lemma 5.1 with

$$a_m = \frac{\rho^{\mathrm{f}}}{2} \|\boldsymbol{\theta}_h^m\|^2_{0,\Omega^{\mathrm{f}}} + \frac{\rho^{\mathrm{s}}\epsilon}{2} \|\dot{\boldsymbol{\xi}}_h^m\|^2_{0,\Sigma} + \frac{1}{2} \|\boldsymbol{\xi}_h^m\|^2_{\mathrm{s}}, \quad \eta_m = \frac{1}{T}.$$

Note in particular that, owing to the selection of the initial data, we have

$$\boldsymbol{\theta}_h^0 = \boldsymbol{0}, \quad \dot{\boldsymbol{\xi}}_h^0 = \boldsymbol{\xi}_h^0 = \boldsymbol{0}.$$

■

We define the energy-norm of the error and dissipation error, at time step t_n, as

$$\widetilde{\mathcal{Z}}_h^n \stackrel{\mathrm{def}}{=} (\rho^{\mathrm{f}})^{\frac{1}{2}} \|\boldsymbol{u}^n - \boldsymbol{u}_h^n\|_{0,\Omega^{\mathrm{f}}} + (\rho^{\mathrm{s}}\epsilon)^{\frac{1}{2}} \|\dot{\boldsymbol{d}}^n - \dot{\boldsymbol{d}}_h^n\|_{0,\Sigma} + \|\boldsymbol{d}^n - \boldsymbol{d}_h^n\|_{\mathrm{s}}, \left(\sum_{m=1}^n c_{\mathrm{g}} \tau \mu \|\boldsymbol{\nabla}(\boldsymbol{u}^m - \boldsymbol{u}_h^m)\|_{0,\Omega^{\mathrm{f}}} \right)^{\frac{1}{2}} + \left(\sum_{m=1}^n c_{\mathrm{g}} \tau |(\boldsymbol{u}_h^m, p_h^m)|^2_S \right)^{\frac{1}{2}} + \left(\sum_{m=1}^n c_{\mathrm{g}} \tau \frac{\gamma\kappa\mu}{\gamma\mu + \kappa h} \|\boldsymbol{u}_h^m - \dot{\boldsymbol{d}}_h^m\|^2_{0,\Sigma} \right)^{\frac{1}{2}}$$

for $n > 0$. We have the following a priori estimate as a corollary of Theorem 5.4.

Corollary 5.3 *Under the assumptions of Theorem 5.4, we have the following error estimates, for $n > r$ and $n\tau < T$:*

$$\widetilde{\mathcal{Z}}_h^n \lesssim c_1 h + c_2 \tau + c_3 \tau^{\frac{1}{2}}. \tag{5.90}$$

Here, the symbols $\{c_i\}_{i=1}^3$ *denote positive constants independent of* h *and* τ*, but which depend on the physical parameters and on the regularity of* $(\boldsymbol{u}, p, \boldsymbol{d}, \dot{\boldsymbol{d}})$.

Proof. The proof follows directly as a consequence of a triangle inequality, Theorem 5.4 and the optimal approximation properties of the interpolation operators. ■

5.4 Numerical experiments

In order to highlight the stability and accuracy of the proposed schemes, we consider the problem of the pressure-wave propagation within an elastic tube described in Section 2.4.1 with no damping effects in the solid (viz., $\alpha = \beta = 0$ in (1.23)). We compare the results obtained with the unfitted-mesh Algorithms 5.1-5.3 and the first-order fully implicit scheme using fitted meshes reported in Algorithm 1.1. An example of the fitted and unfitted mesh configurations considered in this study is given in Figure 5.1. In Algorithms 5.1-5.3, the Nitsche's parameter is set to $\gamma = 10^3$ and the pressure and ghost penalty stabilization terms in (5.6) are given by (1.53) and (1.55), respectively, with $\gamma_{\mathrm{p}} = 10^{-3}$ and $\gamma_{\mathrm{g}} = 1$. The computations have been performed with FreeFem++ [Hec12].

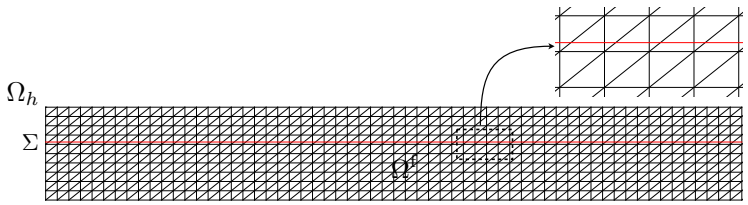

(a) Unfitted configuration

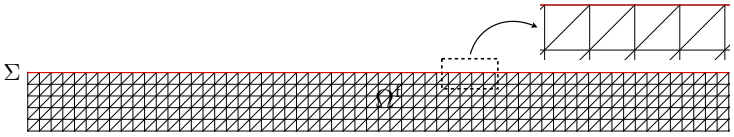

(b) Fitted configuration

Figure 5.1: Example of unfitted fictitious domain (Figure 5.1(a)) and fitted (Figure 5.1(b)) configurations

Figure 5.2 presents the snapshots of the pressure field and the solid displacement (amplified by a factor 5) at the time instants $t = 0.005$, 0.01 and 0.015, obtained with $\tau = 2 \cdot 10^{-4}$ and $h = 0.01$ using Algorithm 1.1 (Figure 5.2(a)), Algorithm 5.1 (Figure 5.2(b)), Algorithm 5.2 with $r = 1$ (Figure 5.2(c)) and Algorithm 5.3 with $r = 1$ (Figure 5.2(d)). The schemes reproduce a stable pressure-wave propagation. Note that this stable behavior was predicted for Algorithms 5.2 and 5.1 by Theorem 5.1 and Remark 5.3, respectively.

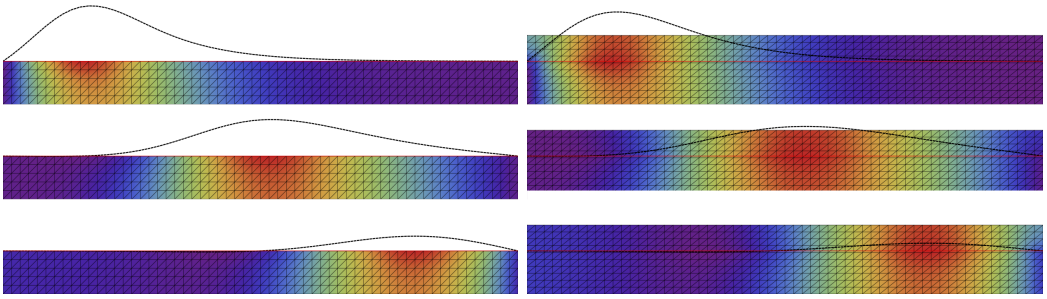

(a) Implicit fitted (Algorithm 1.1) (b) Implicit unfitted (Algorithm 5.1)

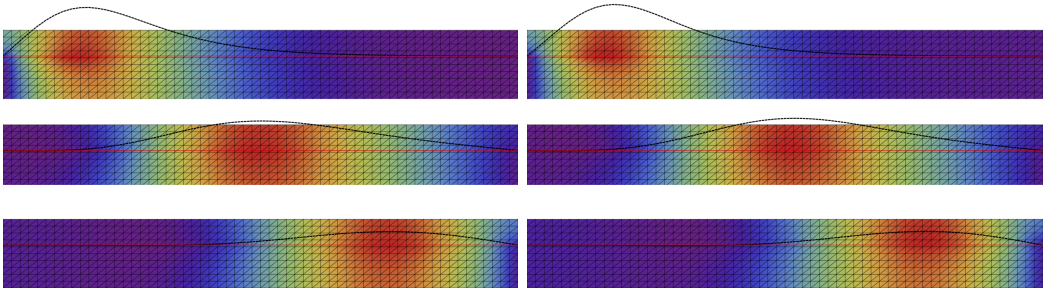

(c) Algorithm 5.2 with $r = 1$ (d) Algorithm 5.3 with $r = 1$

Figure 5.2: Snapshots of the fluid pressure and (exaggerated) solid displacement at time instants $t = 0.005, 0.01, 0.015$. The discretization parameters are given by $\tau = 2 \cdot 10^{-4}$ and $h = 0.01$

In order to assess the overall convergence rate of Algorithms 5.1-5.3, we have uniformly refined in time and in space according to

$$(\tau, h) = \{2 \cdot 10^{-4}/2^i, 10^{-1}/2^i\}_{i=0}^{4}. \tag{5.91}$$

Note that $\tau = \mathcal{O}(h)$. Figure (5.3) reports the relative elastic energy-norm error of the solid displacement, at time $t = 0.015$, obtained with all the different variants of Algorithm 5.2 (Alg. 2 in Figure 5.3(a)) and Algorithm 5.3 (Alg. 3 in Figure 5.3(b)). For comparison purposes, the results obtained with both the fitted-mesh and unfitted-mesh implicit schemes, Algorithm 1.1 and Algorithm 5.1 (Alg. 1 in Figures 5.3(a) and 5.3(b)), are also reported in Figures 5.3(a) and 5.3(b). The reference solution has been computed with Algorithm 1.1 with a high space-time resolution: $h = 3.125 \cdot 10^{-3}$ and $\tau = 10^{-6}$.

The results of Figure 5.3(a) show an overall $\mathcal{O}(\tau)$ optimal accuracy for Algorithm 5.2 with $r = 1, 2$, while a sub-optimal $\mathcal{O}(\tau^{\frac{1}{2}})$ is obtained with $r = 0$. This is in agreement with the error estimates provided in Corollary 5.1. Very similar results are observed for Algorithm 5.3 in Figure 5.3(b): an optimal $\mathcal{O}(\tau)$ convergence is obtained with $r = 1, 2$ and a sub-optimal $\mathcal{O}(\tau^{\frac{1}{2}})$ convergence is retrieved with $r = 0$. We recall that the sub-optimality in Algorithm 5.3 for the non-extrapolated case was predicted by Corollary 5.3. Finally, the first-order convergence rate $\mathcal{O}(\tau)$

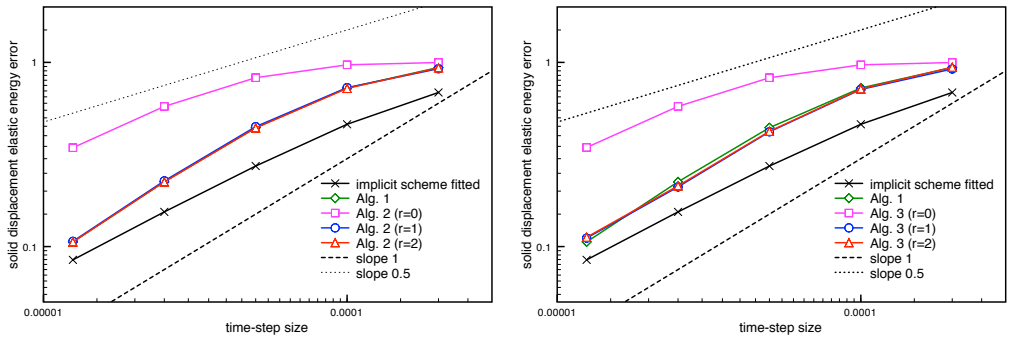

(a) Algorithm 5.2 (b) Algorithm 5.3

Figure 5.3: Time convergence history of the solid displacement in the relative elastic energy norm using Algorithm 5.2 (left) and Algorithm 5.3 (right) with $\tau = \mathcal{O}(h)$.

predicted by Corollary 5.2 is observed for Algorithm 5.1.

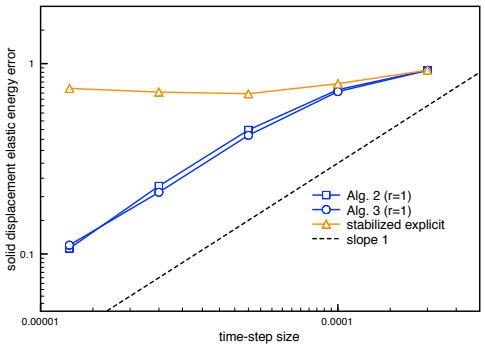

Figure 5.4: Time convergence history of the solid displacement in the relative elastic energy norm using Algorithm 5.2 ($r = 1$), Algorithm 5.3 ($r = 1$) and Algorithm 1.4 with $\tau = \mathcal{O}(h)$.

For comparison purposes, we show in Figure 5.4 the results obtained with the first-order extrapolated variants of Algorithms 5.2 and 5.3 and with the stabilized explicit scheme reported in Algorithm 1.4. The results in Figure 5.4 demonstrate the significant progress achieved by the schemes proposed in this chapter: the extrapolated variants of Algorithms 5.2 and 5.3 solve the non-uniformity in h behavior of Algorithm 1.4 (which clearly prevents the scheme from converging).

We provide further numerical evidence of the above observations in Figures 5.5 and 5.6, where we have displayed the displacements at $t = 0.015$ obtained with Algorithms 5.2 and 5.3, respectively, for different levels of space-time refinement. For illustration purposes, the displacements obtained with the implicit schemes, Algorithm 1.1 and Algorithm 5.1, are also reported in both Figures 5.3(a) and 5.3(b).

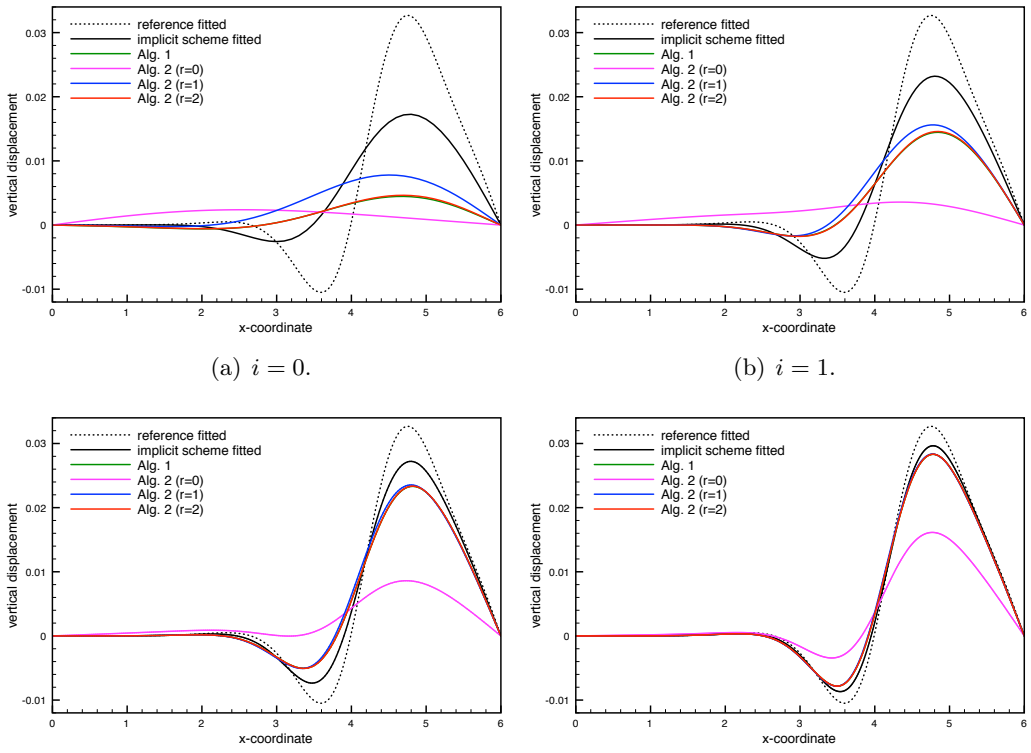

(a) $i = 0$. (b) $i = 1$.

(c) $i = 2$. (d) $i = 3$.

Figure 5.5: Algorithm 5.2. Comparison of the solid displacements at $t = 0.015$ for different levels of (τ, h)-refinement (5.91).

5.5 Conclusion

In this chapter we have introduced two new classes of splitting methods (semi-implicit and explicit) for fluid/thin-walled structure interaction using unfitted meshes. The methods proposed allow different degrees of fluid-solid splitting which overcome the stability and accuracy issues of the explicit methods reported in [BCG11, BF14b]. The semi-implicit or explicit nature of the methods proposed in this chapter is dictated by the order in which the space and time discretizations were performed:

- discretizing first in space using the unfitted formulation (1.57) and then in time via (1.84) led to the semi-implicit schemes reported in Algorithm 5.2;
- discretizing first in time using (1.81) and then in space using a variant of Nitsche's method for general boundary conditions led to the explicit schemes reported in Algorithm 5.3.

For the semi-implicit class of schemes, a complete energy-based stability (Theorem 5.1) and a priori error analysis (Theorem 5.2) have been presented. In particular, unconditional stability and optimal accuracy have been shown for the variant

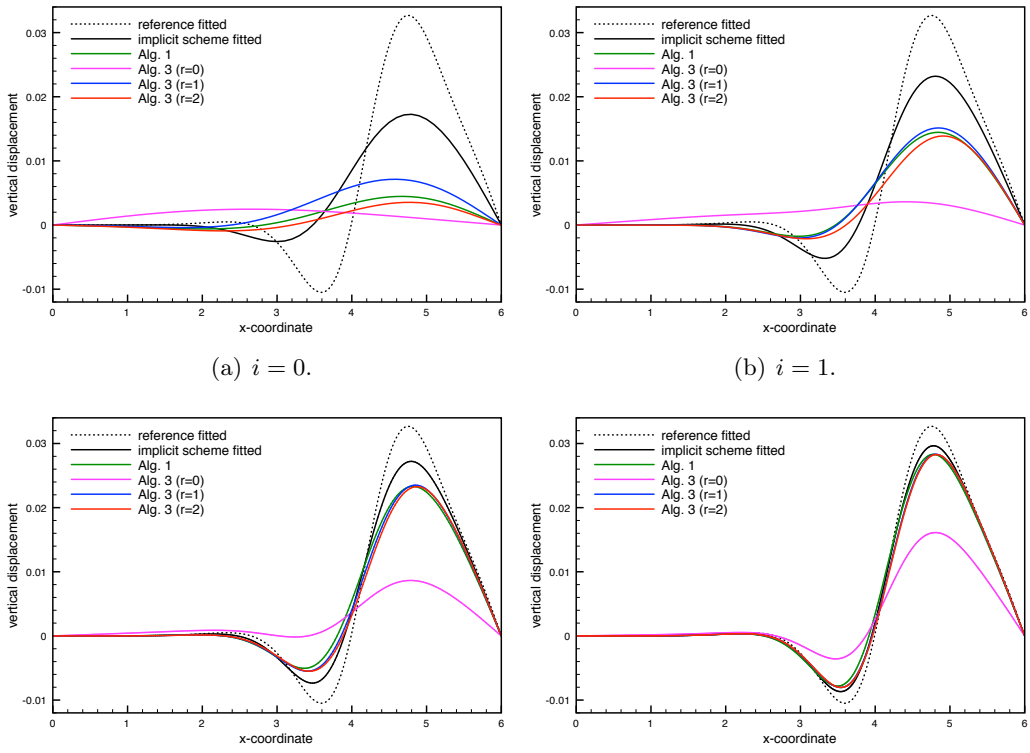

(a) $i = 0$. (b) $i = 1$.

(c) $i = 2$. (d) $i = 3$.

Figure 5.6: Algorithm 5.3. Comparison of the solid displacements at $t = 0.015$ for different levels of (τ, h)-refinement (5.91).

$r = 1$. For the explicit scheme with $r = 0$, stability (Theorem 5.3) and a priori error estimates (Theorem 5.4) have been reported. In the numerical experiments carried out in Section 5.4, Algorithms 5.2 and 5.3 have delivered, in spite of their different semi-implicit and explicit nature, practically the same behavior: stability was obtained with all the variants, optimal first-order convergence was obtained with the extrapolated ones ($r = 1, 2$) and a sub-optimal convergence rate was exhibited when non-extrapolation was performed ($r = 0$).

Chapter 6

Nitsche-XFEM for the coupling of an incompressible fluid with immersed thin-walled structures

In this chapter we extend the unfitted Nitsche space semi-discretization presented in Section 1.4.2.3 to the case of coupling with immersed thin-walled structures using the extended finite element method. For the temporal discretization, several splitting schemes are investigated. The resulting methods are also formulated in a non-linear setting involving dynamic interfaces. A series of numerical test in 2D, involving static and moving interfaces, illustrates the performance of the different methods proposed.

The results presented in this chapter have been reported in:

- F. Alauzet, B. Fabrèges, M. A. Fernández, M. Landajuela, **Nitsche-XFEM for the coupling of an incompressible fluid with immersed thin-walled structures**. *Computer Methods in Applied Mechanics and Engineering,* To appear*, 2015,* https://hal.inria.fr/hal-01149225 .

Contents

6.1 Introduction

In this chapter we consider the mechanical interaction of an incompressible viscous fluid with an immersed thin-walled flexible structure. As pointed out in Section 1.2.3.2, the thin-walled nature of the immersed solid introduces jumps on the fluid stresses which, respectively, results in weak and strong discontinuities of the velocity and pressure fields (see Figure 1.4). Standard finite element approximations, not allowing for such discontinuities, are known to deliver suboptimal convergence behavior and spurious numerical oscillations in the vicinity of the immersed solid (see, e.g., [DSGB08, KHS+15, BCG15]).

The discontinuous features of the fluid solution can be readily incorporated within a standard finite element approximation by considering fitted fluid-solid meshes (see Section 1.3.1.1). This approach was adopted in Chapter 4 whenever the solid was modeled as a thin-walled (shell) solid (see Section 4.3.2). It is well known, however, that maintaining fitted meshes may be cumbersome or unfeasible in the presence of large interface deflections and topological changes (see Section 1.3.1.1). Though a number of advanced mesh update techniques have been reported in the literature (see, e.g., [STB04, YSH08, Wic11, Ala14, TTBA14]), the favoured alternative is to consider an unfitted mesh formulation, in which the fluid-structure interface moves independently of a background fluid mesh. Among these approaches, we can mention the Immersed Boundary/Fictitious Domain methods (e.g., [Pes02, GPHJ99b, Baa01, ZGWL04, AGPT09, BCG11, KHS+15, BCG15]) and the methodologies based on a fully Eulerian description of the problem (see Section 1.3.1.2). In general, these methods are known to be inaccurate in space due to the continuous nature of the fluid approximations across the interface or to the discrete treatment of the interface conditions. As already mentioned in Section 1.3.1.2, the current trend to overcome these consistency issues is to combine a local XFEM enrichment with a cut-FEM methodology and a Lagrange multiplier treatment of the interface coupling (see, e.g., [LCB06, ZL08, GW08, ST11]). The price to pay, with respect to the original IB and FD methods, is the need of a specific tracking of the interface intersections (see, e.g., [MGW09, WGMF12, MLL13]) and a loss of robustness with respect to how the interface intersects the background fluid mesh (see, e.g., [FB10, BCH+15]).

A well-known alternative to the discrete treatment of the interface conditions via Lagrange multipliers is Nitsche's method (see, e.g., [Nit71, Ste95, Han05]). Because of its flexibility and mathematical soundness, the Nitsche mortaring has been applied to the design of numerical methods for a number of interface problems, including XFEM for elasticity [HH02, HH04, BBH09], XFEM for two-phase transport problems [LR12, LR13], XFEM for incompressible flow [SW14] and robust and accurate FD methods for elliptic and mixed problems [BH12, MLLR14, BH14]. Nitsche's method was first applied to fluid-structure interaction problems with fitted meshes in [HHS04] and used to design stable explicit coupling (or loosely coupled) schemes in [BF09, BF14a]. It has recently been extended to fluid-structure interaction problems with unfitted meshes in [BF14b], yielding robust and optimal a

priori error estimates (fixed interface). The case of the coupling with thin-walled solids in [BF14b] is restricted to structures surrounding the fluid domain (i.e., not immersed).

The first contribution of this chapter consists in the introduction of a robust and accurate Nitsche-XFEM method for fluid-structure interaction problems involving a thin-walled elastic structure immersed in an incompressible viscous fluid. We consider an Eulerian description for the fluid and a Lagrangian formulation for the solid (see Section 1.3.1.2). The fluid domain is discretized with an unstructured mesh not fitted to the solid mid-surface deformed mesh. In this unfitted mesh framework, the (strong) consistency of the proposed fluid-solid coupling builds on the following two ingredients:

- across the interface, locally enriched piecewise affine fluid velocity and pressure approximations respectively allow for weak and strong discontinuities (using the XFEM approach of [HH04, BBH09]);
- the kinematic/dynamic fluid-solid coupling is enforced through a fluid-sided Nitsche's mortaring (based on the unfitted mesh formulation reported in Section 1.4.2.3).

Besides, consistent symmetric stabilization operators are added to guarantee robustness with respect to arbitrary interface/element intersections (see Section 1.4.2.3) and to circumvent the classical inf-sup and convective related instabilities (see, e.g., [BP84, BFH06, BF07, SW14]). In this regard, it is worth noting that for robustness these operators act on the fictitious region of the computational domain, without compromising the overall optimal accuracy of the method (in the energy norm).

The second contribution of this chapter has to do with the time-discretization. Several coupling schemes with different levels of fluid-solid splitting are proposed: implicit, explicit and semi-implicit. These schemes are the generalization to the coupling with immersed thin-walled structures of Algorithms 5.1, 1.4 and 5.2, respectively. The stability and convergence properties of the resulting fully discrete methods are analyzed within a representative linear setting (static interfaces), by naturally extending the arguments presented for the aforementioned schemes. The salient features of the semi-implicit schemes presented in this chapter are twofold: (i) they deliver superior stability and accuracy with respect to alternative methods of explicit nature (see, e.g., [BCG11]); (ii) they avoid the strong coupling of alternative coupling methods (see, e.g., [NFGK07, BCG15]).

Finally, the theoretical findings are substantiated by a series of numerical examples in 2D, involving static and moving interfaces, which illustrate the performance of the methods proposed by comparing with analytic solutions and fitted mesh approaches.

This chapter is organized as follows. Section 6.2 is devoted to the derivation and the analysis of the methods within a linear setting (fixed interface). The space semi-discrete Nitsche-XFEM formulation is introduced in Section 6.2.1. Section 6.2.3 presents the time discretization and the different coupling schemes. In Section 6.3,

the numerical methods are formulated within a non-linear setting involving moving interfaces. Numerical evidence illustrating the performance of the methods proposed is reported and discussed in Section 6.4. Finally, a summary of the conclusions is given in Section 6.5.

6.2 A linear model problem: static interface

We consider a linear coupled problem similar to the one introduced in Section 1.4.1, involving the Stokes system (1.34) and the thin-walled solid problem (1.37), but in which the structure is immersed within the fluid. The fluid domain is denoted by $\Omega^{\mathrm{f}} \subset \mathbb{R}^d$ ($d = 2, 3$) and the mid-surface of the structure is represented by the oriented manifold $\Sigma \subset \Omega^{\mathrm{f}}$ of codimension 1 and unitary normal vector $\boldsymbol{n}$. For the time being, we assume that Σ divides Ω^{f} into two open domains Ω_1 and Ω_2 (see Figure 6.1). In Section 6.2.1.3 we address the general case in which Ω^{f} is partially intersected by Σ. We denote the outward unit normal to Ω_i on Σ by $\boldsymbol{n}_i$, $i = 1, 2$. Note that we choose Ω_1 and Ω_2 so that $\boldsymbol{n}_1 = \boldsymbol{n}$ and $\boldsymbol{n}_2 = -\boldsymbol{n}$. We set $\Gamma_i = \partial\Omega_i \backslash \Sigma$, $i = 1, 2$.

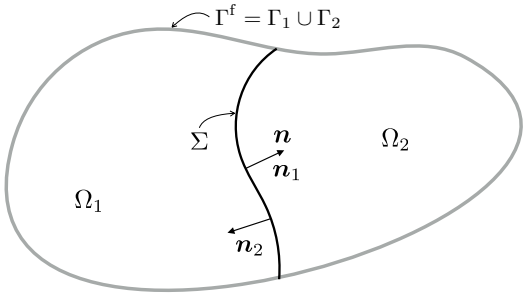

Figure 6.1: Geometric description.

In the following, for a given continuous scalar or tensorial field f defined in Ω^{f} (possibly discontinuous across Σ) we define its sided-restrictions to Σ, noted by f_1 and f_2, as

$$f_1(\boldsymbol{x}) \stackrel{\text{def}}{=} \lim_{\xi \to 0^+} f(\boldsymbol{x} + \xi \boldsymbol{n}_1), \quad f_2(\boldsymbol{x}) \stackrel{\text{def}}{=} \lim_{\xi \to 0^+} f(\boldsymbol{x} + \xi \boldsymbol{n}_2) \quad \forall \boldsymbol{x} \in \Sigma.$$

We also define the following jumps and average across the interface Σ:

$$[\![f]\!] \stackrel{\text{def}}{=} f_1 - f_2, \quad [\![f\boldsymbol{n}]\!] \stackrel{\text{def}}{=} f_1 \boldsymbol{n}_1 + f_2 \boldsymbol{n}_2, \quad \{\!\{f\}\!\} \stackrel{\text{def}}{=} \frac{1}{2}(f_1 + f_2).$$

The coupled problem reads as follows: find the fluid velocity and pressure $\boldsymbol{u} : \Omega^{\mathrm{f}} \times \mathbb{R}^+ \to \mathbb{R}^d$, $p : \Omega^{\mathrm{f}} \times \mathbb{R}^+ \to \mathbb{R}$, the solid displacement and velocity $\boldsymbol{d} : \Sigma \times \mathbb{R}^+ \to \mathbb{R}^d$, $\dot{\boldsymbol{d}} : \Sigma \times \mathbb{R}^+ \to \mathbb{R}^d$ such that

$$\begin{cases} \rho^{\mathrm{f}}\partial_t \boldsymbol{u} - \mathbf{div}\boldsymbol{\sigma}(\boldsymbol{u},p) = \mathbf{0} & \text{in} \quad \Omega_i \times \mathbb{R}^+, \quad i=1,2 \\ \mathrm{div}\boldsymbol{u} = 0 & \text{in} \quad \Omega_i \times \mathbb{R}^+, \quad i=1,2 \\ \boldsymbol{u} = \mathbf{0} & \text{on} \quad \Gamma_i \times \mathbb{R}^+, \quad i=1,2 \end{cases} \tag{6.1}$$

$$\begin{cases} \boldsymbol{u}_1 = \boldsymbol{u}_2 = \dot{\boldsymbol{d}} & \text{on} \quad \Sigma \times \mathbb{R}^+, \\ \rho^{\mathrm{s}}\epsilon\partial_t\dot{\boldsymbol{d}} + \boldsymbol{L}^{\mathrm{e}}\boldsymbol{d} = -[\![\boldsymbol{\sigma}(\boldsymbol{u},p)\boldsymbol{n}]\!] & \text{in} \quad \Sigma \times \mathbb{R}^+, \\ \dot{\boldsymbol{d}} = \partial_t \boldsymbol{d} & \text{in} \quad \Sigma \times \mathbb{R}^+, \\ \boldsymbol{d} = \mathbf{0} & \text{on} \quad \partial\Sigma \times \mathbb{R}^+, \end{cases} \tag{6.2}$$

complemented with standard initial conditions $\boldsymbol{u}(0) = \boldsymbol{u}_0$, $\boldsymbol{d}(0) = \boldsymbol{d}_0$ and $\dot{\boldsymbol{d}}(0) = \dot{\boldsymbol{d}}_0$.

The rest of this section is devoted to the derivation of a weak formulation of the coupled problem (6.1)-(6.2). We recall that $H^m(\omega)$ $(m \geq 0)$ denotes the standard Sobolev spaces, with norm $\|\cdot\|_{m,\omega}$. Here, the closed subspaces $H^1_{\Gamma^{\mathrm{f}}}(\omega)$, of functions in $H^1(\omega)$ with zero trace on Γ^{f}, and $L^2_0(\omega)$, of functions in $L^2(\omega)$ with zero mean in ω, will also be used. Recall that the scalar product in $L^2(\omega)$ is denoted by $(\cdot,\cdot)_\omega$ and its norm by $\|\cdot\|_{0,\omega}$. Similarly to Section 1.4.2.1, we consider $\boldsymbol{V} \overset{\text{def}}{=} [H^1_{\Gamma^{\mathrm{f}}}(\Omega^{\mathrm{f}})]^d$ and $Q \overset{\text{def}}{=} L^2_0(\Omega^{\mathrm{f}})$ as the fluid velocity and pressure functional spaces, respectively. The space $\boldsymbol{W} \subset [H^1_0(\Sigma)]^d$ denotes the space of solid admissible displacements.

The standard Stokes bilinear forms (1.40) are collected here in

$$a^{\mathrm{f}}_{\Omega^{\mathrm{f}}}\big((\boldsymbol{u},p),(\boldsymbol{v},q)\big) \overset{\text{def}}{=} 2\mu\big(\boldsymbol{\varepsilon}(\boldsymbol{u}),\boldsymbol{\varepsilon}(\boldsymbol{v})\big)_{\Omega^{\mathrm{f}}} - (p,\mathrm{div}\boldsymbol{v})_{\Omega^{\mathrm{f}}} + (q,\mathrm{div}\boldsymbol{u})_{\Omega^{\mathrm{f}}}.$$

As in Section 1.4.2.1, the elastic bilinear form $a^{\mathrm{s}} : \boldsymbol{W} \times \boldsymbol{W} \to \mathbb{R}$ will represent the weak form of the (unbounded linear) surface differential operator $\boldsymbol{L}^{\mathrm{e}} : \boldsymbol{D}(\boldsymbol{L}^{\mathrm{e}}) \subset [L^2(\Sigma)]^d \to [L^2(\Sigma)]^d$, namely,

$$a^{\mathrm{s}}(\boldsymbol{d},\boldsymbol{w}) = (\boldsymbol{L}^{\mathrm{e}}\boldsymbol{d},\boldsymbol{w})_\Sigma$$

for all $\boldsymbol{d} \in \boldsymbol{D}(\boldsymbol{L}^{\mathrm{e}})$ and $\boldsymbol{w} \in \boldsymbol{W}$. We assume a^{s} to be symmetric, coercive and continuous on $\boldsymbol{W}$ with associated norm $\|\boldsymbol{w}\|_{\mathrm{s}} \overset{\text{def}}{=} (a^{\mathrm{s}}(\boldsymbol{w},\boldsymbol{w}))^{\frac{1}{2}}$. The weak form of the linear coupled problem (6.1)–(6.2) reads as follows: for $t > 0$, find $(\boldsymbol{u}(t),p(t),\boldsymbol{d}(t),\dot{\boldsymbol{d}}(t)) \in \boldsymbol{V} \times Q \times \boldsymbol{W} \times \boldsymbol{W}$ such that

$$\begin{cases} \boldsymbol{u}_1|_\Sigma = \boldsymbol{u}_2|_\Sigma = \dot{\boldsymbol{d}}, \quad \dot{\boldsymbol{d}} = \partial_t \boldsymbol{d}, \\ \rho^{\mathrm{f}}\big(\partial_t\boldsymbol{u},\boldsymbol{v}\big)_{\Omega^{\mathrm{f}}} + a^{\mathrm{f}}_{\Omega^{\mathrm{f}}}\big((\boldsymbol{u},p),(\boldsymbol{v},q)\big) + \rho^{\mathrm{s}}\epsilon\big(\partial_t\dot{\boldsymbol{d}},\boldsymbol{w}\big)_\Sigma + a^{\mathrm{s}}(\boldsymbol{d},\boldsymbol{w}) = 0, \end{cases} \tag{6.3}$$

for all $(\boldsymbol{v},q,\boldsymbol{w}) \in \boldsymbol{V} \times Q \times \boldsymbol{W}$ with $\boldsymbol{v}|_\Sigma = \boldsymbol{w}$. Taking $(\boldsymbol{v},q,\boldsymbol{w}) = (\boldsymbol{u}(t),p(t),\dot{\boldsymbol{d}}(t))$ in

(6.3) we get, for $t > 0$, the following standard energy identity

$$\frac{\rho^{\mathrm{f}}}{2}\|\boldsymbol{u}(t)\|^2_{0,\Omega^{\mathrm{f}}} + \frac{\rho^{\mathrm{s}}\epsilon}{2}\|\dot{\boldsymbol{d}}(t)\|^2_{0,\Sigma} + \frac{1}{2}\|\boldsymbol{d}(t)\|^2_{\mathrm{s}} + 2\mu\int_0^t \|\boldsymbol{\varepsilon}(\boldsymbol{u}(s))\|^2_{0,\Omega^{\mathrm{f}}}\,\mathrm{d}s = \frac{\rho^{\mathrm{f}}}{2}\|\boldsymbol{u}_0\|^2_{0,\Omega^{\mathrm{f}}} + \frac{\rho^{\mathrm{s}}}{2}\|\dot{\boldsymbol{d}}_0\|^2_{0,\Sigma} + \frac{1}{2}\|\boldsymbol{d}_0\|^2_{\mathrm{s}}. \quad (6.4)$$

6.2.1 Space semi-discretization

The dynamic relation $(6.2)_2$ introduces jumps in the fluid pressure and in the velocity gradient across the interface Σ. We propose to approximate the fluid velocity and pressure on triangulations of Ω^{f} which are independent of the interface Σ (see Figure 6.2(a)). In order to guarantee the optimality of the approximations, we allow the discrete fluid solution to be discontinuous inside the elements which are intersected by the interface. In this unfitted framework, the interface coupling conditions $(6.2)_{1,2}$ will be enforced through a generalization of the Nitsche's type mortaring reported in Section 1.4.2.3.

6.2.1.1 Nitsche-XFEM semi-discrete formulation

For the sake of simplicity, we assume that Ω^{f} and Σ are polyhedral. For the construction of the discrete approximation spaces in the fluid, we follow the unfitted approach reported in [HH02, HH04, BBH09]. To this purpose, we consider two family of meshes $\{\mathcal{T}^{\mathrm{f}}_{i,h}\}_{0<h<1}$, $i = 1, 2$, where each $\mathcal{T}^{\mathrm{f}}_{i,h}$ covers the fluid region Ω_i. Each mesh $\mathcal{T}^{\mathrm{f}}_{i,h}$ is fitted to the exterior boundary Γ_i but, in general, not to Σ (see Figure 6.2(b)). Moreover, we assume that for every element $K \in \mathcal{T}^{\mathrm{f}}_{1,h} \cap \mathcal{T}^{\mathrm{f}}_{2,h}$ we have $K \cap \Sigma \neq \emptyset$. Note that $\mathcal{T}^{\mathrm{f}}_{1,h} \cup \mathcal{T}^{\mathrm{f}}_{2,h}$ gives a conforming triangulation of the whole fluid domain Ω^{f}. We denote by $\Omega_{i,h}$ the domain covered by $\mathcal{T}^{\mathrm{f}}_{i,h}$, viz.,

$$\Omega_{i,h} \stackrel{\mathrm{def}}{=} \mathrm{int}\left(\cup_{K\in\mathcal{T}^{\mathrm{f}}_{i,h}} K\right).$$

Finally, for the solid, we consider a family of triangulations $\{\mathcal{T}^{\mathrm{s}}_h\}_{0<h<1}$ of Σ. For the sake of simplicity, we assume that the three families of triangulations are quasi-uniform.

We introduce the following standard spaces of continuous piecewise affine functions:

$$\begin{aligned} X^{\mathrm{f}}_{i,h} &\stackrel{\mathrm{def}}{=} \left\{ v_h \in C^0(\overline{\Omega_{i,h}}) \,/\, v_{h|K} \in \mathbb{P}_1(K) \quad \forall K \in \mathcal{T}^{\mathrm{f}}_{i,h} \right\}, \\ X^{\mathrm{s}}_{h} &\stackrel{\mathrm{def}}{=} \left\{ v_h \in C^0(\overline{\Sigma}) \,/\, v_{h|K} \in \mathbb{P}_1(K) \quad \forall K \in \mathcal{T}^{\mathrm{s}}_{h} \right\}. \end{aligned} \quad (6.5)$$

Associated with $X^{\mathrm{f}}_{i,h}$, we define the spaces

$$\boldsymbol{V}_{i,h} \stackrel{\mathrm{def}}{=} \left\{ \boldsymbol{v}_{i,h} \in [X^{\mathrm{f}}_{i,h}]^d \,/\, \boldsymbol{v}_{i,h}|_{\Gamma_i} = 0 \right\}, \quad Q_{i,h} \stackrel{\mathrm{def}}{=} X^{\mathrm{f}}_{i,h}, \quad i = 1, 2. \quad (6.6)$$

For the approximation of the fluid velocity and pressure we will consider the product

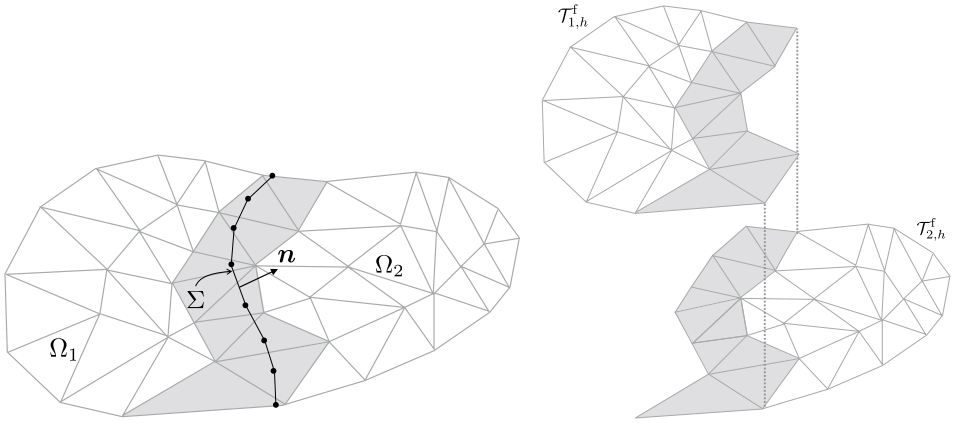

(a) (b)

Figure 6.2: Unfitted fluid-solid meshes. In grey the elements intersected by Σ (a). The triangulations $\mathcal{T}^{\mathrm{f}}_{1,h}$ and $\mathcal{T}^{\mathrm{f}}_{2,h}$, with the overlapping region in grey (b).

spaces $\boldsymbol{V}_h \overset{\text{def}}{=} \boldsymbol{V}_{1,h} \times \boldsymbol{V}_{2,h}$ and $Q_h \overset{\text{def}}{=} Q_{1,h} \times Q_{2,h}$, respectively. The solid displacement and velocity are approximated in $\boldsymbol{W}_h \overset{\text{def}}{=} [X^{\mathrm{s}}_h]^d \cap \boldsymbol{W}$.

Remark 6.1 *Note that the discrete velocity and pressure are two-valued in the overlap interfacial region. Hence, for $f_h = (f_{1,h}, f_{2,h}) \in X^{\mathrm{f}}_{1,h} \times X^{\mathrm{f}}_{2,h}$, the associated function*

$$f_{\Omega^{\mathrm{f}},h} \overset{\text{def}}{=} \begin{cases} f_{1,h}|_{\Omega_1} & \text{in} \quad \Omega_1, \\ f_{2,h}|_{\Omega_2} & \text{in} \quad \Omega_2, \end{cases}$$

may develop discontinuities across the interface Σ. This feature is illustrated in Figures 6.3 and 6.5. This is one of the fundamental ingredients of the present XFEM approach to approximate the solution of (6.1)-(6.2).

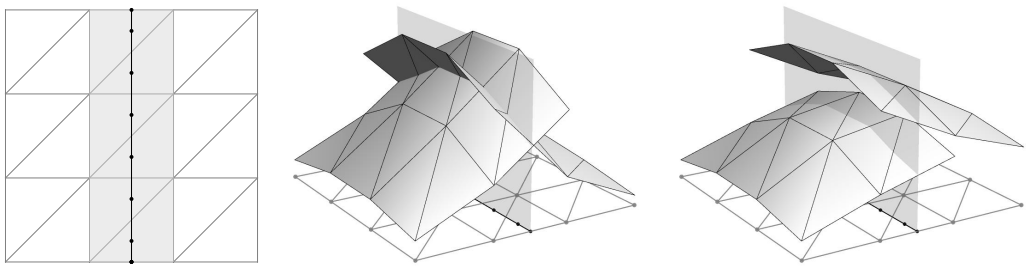

(a) Unfitted meshes (b) Weak discontinuity (c) Strong discontinuity

Figure 6.3: Idealized fully intersected configuration. Example of functions $f_h \in X^{\mathrm{f}}_{1,h} \times X^{\mathrm{f}}_{2,h}$.

Since velocity/pressure discrete spaces $\boldsymbol{V}_h/Q_h$ fail to satisfy the inf-sup condition, we consider a symmetric pressure stabilization operator $s_h : Q_h \times Q_h \to \mathbb{R}$. For

instance, the classical Brezzi-Pitkäranta method is used in the following fashion

$$s_h(p_h, q_h) \stackrel{\text{def}}{=} \gamma_{\text{p}} \frac{h^2}{\mu} \sum_{i=1,2} \big(\boldsymbol{\nabla} p_{i,h}, \boldsymbol{\nabla} q_{i,h}\big)_{\Omega_{i,h}},$$

with $\gamma_p > 0$ a user-defined parameter. Note that the stabilization acts on the whole computational domain $\Omega_{1,h} \times \Omega_{2,h}$.

In order to guarantee robustness of the method with respect to the way the fluid mesh $\mathcal{T}^{\text{f}}_{1,h} \cup \mathcal{T}^{\text{f}}_{2,h}$ is intersected by the solid mesh $\mathcal{T}^{\text{s}}_h$ (see Section 1.4.2.3), we consider the ghost-penalty stabilization operator $g_h : \boldsymbol{V}_h \times \boldsymbol{V}_h \to \mathbb{R}$ defined by

$$g_h(\boldsymbol{u}_h, \boldsymbol{v}_h) = \gamma_{\text{g}} \mu h \sum_{i=1}^{2} \sum_{F \in \mathcal{F}^{\Sigma}_{i,h}} \big(\llbracket \boldsymbol{\nabla} \boldsymbol{u}_{i,h} \rrbracket_F, \llbracket \boldsymbol{\nabla} \boldsymbol{v}_{i,h} \rrbracket_F\big)_F,$$

where $\gamma_{\text{g}} > 0$ is a user-defined parameter and the symbol $\llbracket \, \rrbracket_F$ denotes the jump across the edge or face F belonging to $\mathcal{F}^{\Sigma}_{i,h}$, the set of interior edges or faces of the elements of $\mathcal{T}^{\text{f}}_{i,h}$ intersected by Σ, i.e., $F \in \mathcal{F}^{\Sigma}_{i,h}$ if F is a $(d-1)$-manifold and there exist $K_1, K_2 \in \mathcal{T}^{\text{f}}_{i,h}$, with $K_1 \cap \Sigma \neq \varnothing$ or $K_2 \cap \Sigma \neq \varnothing$, such that $F = K_1 \cap K_2$. From (1.54), it follows that this operator extends the natural H^1-coercivity in the physical domain to the whole $\Omega_{1,h} \times \Omega_{2,h}$, viz.,

$$\tilde{c}_{\text{g}} \left(\sum_{i=1}^{2} \mu \|\boldsymbol{\varepsilon}(\boldsymbol{v}_{i,h})\|^2_{0,\Omega_{i,h}} + g_h(\boldsymbol{v}_h, \boldsymbol{v}_h) \right) \leq \mu \sum_{i=1}^{2} \|\boldsymbol{\varepsilon}(\boldsymbol{v}_{i,h})\|^2_{0,\Omega_i} + g_h(\boldsymbol{v}_h, \boldsymbol{v}_h), \tag{6.7}$$

for all $\boldsymbol{v}_h \in \boldsymbol{V}_h$, with $\tilde{c}_{\text{g}} > 0$ depending on γ_{g}. The total stabilization operator is hence given by

$$S_h\big((\boldsymbol{u}_h, p_h), (\boldsymbol{v}_h, q_h)\big) \stackrel{\text{def}}{=} s_h(q_h, q_h) + g_h(\boldsymbol{u}_h, \boldsymbol{v}_h),$$

with the associated semi-norm $|(\boldsymbol{v}_h, q_h)|_S \stackrel{\text{def}}{=} \sqrt{S_h\big((\boldsymbol{v}_h, p_h), (\boldsymbol{v}_h, q_h)\big)}$. We also introduce the fluid discrete bilinear form

$$a^{\text{f}}_h\big((\boldsymbol{u}_h, p_h), (\boldsymbol{v}_h, q_h)\big) \stackrel{\text{def}}{=} a^{\text{f}}_{\Omega_1 \cup \Omega_2}\big((\boldsymbol{u}_h, p_h), (\boldsymbol{v}_h, q_h)\big) + S_h\big((\boldsymbol{u}_h, p_h), (\boldsymbol{v}_h, q_h)\big). \tag{6.8}$$

The proposed space semi-discrete approximation of (6.1)-(6.2) reads as follows: for $t > 0$, find

$$\big(\boldsymbol{u}_h(t), p_h(t), \dot{\boldsymbol{d}}_h(t), \boldsymbol{d}_h(t)\big) \in \boldsymbol{V}_h \times Q_h \times \boldsymbol{W}_h \times \boldsymbol{W}_h,$$

such that $\dot{\boldsymbol{d}}_h(t) = \partial_t \boldsymbol{d}_h(t)$ and

$$\begin{cases} \rho^{\mathrm{f}}\big(\partial_t \boldsymbol{u}_h, \boldsymbol{v}_h\big)_{\Omega^{\mathrm{f}}} + a_h^{\mathrm{f}}\big((\boldsymbol{u}_h, p_h), (\boldsymbol{v}_h, q_h)\big) + \rho^{\mathrm{s}}\epsilon\big(\partial_t \dot{\boldsymbol{d}}_h, \boldsymbol{w}_h\big)_{\Sigma} + a^{\mathrm{s}}(\boldsymbol{d}_h, \boldsymbol{w}_h) \\ \quad - \sum_{i=1}^{2} \big(\boldsymbol{\sigma}(\boldsymbol{u}_{i,h}, p_{i,h})\boldsymbol{n}_i, \boldsymbol{v}_{i,h} - \boldsymbol{w}_h\big)_{\Sigma} - \sum_{i=1}^{2} \big(\boldsymbol{u}_{i,h} - \dot{\boldsymbol{d}}_h, \boldsymbol{\sigma}(\boldsymbol{v}_{i,h}, -q_{i,h})\boldsymbol{n}_i\big)_{\Sigma} \\ \quad + \dfrac{\gamma\mu}{h} \sum_{i=1}^{2} \big(\boldsymbol{u}_{i,h} - \dot{\boldsymbol{d}}_h, \boldsymbol{v}_{i,h} - \boldsymbol{w}_h\big)_{\Sigma} = 0 \end{cases} \tag{6.9}$$

for all $(\boldsymbol{v}_h, q_h, \boldsymbol{w}_h) \in \boldsymbol{V}_h \times Q_h \times \boldsymbol{W}_h$. Here, $\gamma > 0$ is a positive parameter given by Lemma 6.1 below (see also Remark 1.11).

Remark 6.2 *It should be noted that, unlike [KHS+15, Section 4.1], the interface fluid tractions from opposite sides do not cancel in (6.9). This is a direct consequence of the XFEM nature of the velocity/pressure space $\boldsymbol{V}_h \times Q_h$, which guarantees the strong consistency of (6.9) with (6.1)-(6.2).*

Remark 6.3 *In the case of a non-polyhedral interface (see Figure 6.1), Σ and $a^{\mathrm{s}}(\cdot,\cdot)$ in (6.9) have to be replaced by their corresponding h-dependent approximations Σ_h and $a_h^{\mathrm{s}}(\cdot,\cdot)$, respectively.*

The above space semi-discretized formulation can be viewed as an extension of the unfitted mesh method formulation (1.57) to the case of coupling with an immersed thin-walled structure. In the next section, we will build on this relation to briefly discuss the stability and convergence properties of (6.9).

6.2.1.2 Stability and convergence

The next lemma, which generalizes Lemma 1.2 to the case of coupling with an immersed thin-walled structure, exploits property (6.7) to guarantee the coercivity of the Stokes-Nitsche operator in (6.9).

Lemma 6.1 *For*

$$\gamma > \frac{8C_{\mathrm{TI}}}{\tilde{c}_{\mathrm{g}}},$$

there exists a constant $c_{\mathrm{g}} > 0$ such that

$$\begin{aligned} & c_{\mathrm{g}} \left(\mu \sum_{i=1}^{2} \|\boldsymbol{\nabla} \boldsymbol{v}_{i,h}\|^2_{0,\Omega_{i,h}} + \frac{\gamma\mu}{h} \sum_{i=1}^{2} \|\boldsymbol{v}_{i,h} - \boldsymbol{w}_h\|^2_{0,\Sigma} + |(\boldsymbol{v}_h, q_h)|_S^2 \right) \\ & \leq a_h^{\mathrm{f}}\big((\boldsymbol{v}_h, q_h), (\boldsymbol{v}_h, q_h)\big) - \sum_{i=1}^{2} \big(\boldsymbol{\sigma}(\boldsymbol{v}_{i,h}, q_{i,h})\boldsymbol{n}_i, \boldsymbol{v}_{i,h} - \boldsymbol{w}_h\big)_{\Sigma} \\ & \quad - \sum_{i=1}^{2} \big(\boldsymbol{v}_{i,h} - \boldsymbol{w}_h, \boldsymbol{\sigma}(\boldsymbol{v}_{i,h}, -q_{i,h})\boldsymbol{n}_i\big)_{\Sigma} + \frac{\gamma\mu}{h} \sum_{i=1}^{2} \|\boldsymbol{v}_{i,h} - \boldsymbol{w}_h\|^2_{0,\Sigma} + |(\boldsymbol{v}_h, q_h)|_S^2 \end{aligned}$$

for all $(\boldsymbol{v}_h, q_h, \boldsymbol{w}_h) \in \boldsymbol{V}_h \times Q_h \times \boldsymbol{W}_h$.

Proof. The proof follows from direct adaptation of the arguments reported in the proof of Lemma 1.2. First, we have

$$
\begin{aligned}
&a_h^{\mathrm{f}}\big((\boldsymbol{v}_h,q_h),(\boldsymbol{v}_h,q_h)\big)-\sum_{i=1}^{2}\big(\boldsymbol{\sigma}(\boldsymbol{v}_{i,h},q_{i,h})\boldsymbol{n}_i,\boldsymbol{v}_{i,h}-\boldsymbol{w}_h\big)_\Sigma\\
&\quad-\sum_{i=1}^{2}\big(\boldsymbol{v}_{i,h}-\boldsymbol{w}_h,\boldsymbol{\sigma}(\boldsymbol{v}_{i,h},-q_{i,h})\boldsymbol{n}_i\big)_\Sigma+\frac{\gamma\mu}{h}\sum_{i=1}^{2}\|\boldsymbol{v}_{i,h}-\boldsymbol{w}_h\|_{0,\Sigma}^2+|(\boldsymbol{v}_h,q_h)|_S^2\\
&=2\mu\sum_{i=1}^{2}\|\boldsymbol{\varepsilon}(\boldsymbol{v}_{i,h})\|_{0,\Omega_i}^2-2\sum_{i=1}^{2}\big(\boldsymbol{\sigma}(\boldsymbol{v}_{i,h},0)\boldsymbol{n},\boldsymbol{v}_{i,h}-\boldsymbol{w}_h\big)_\Sigma\\
&\quad+\sum_{i=1}^{2}\frac{\gamma\mu}{h}\|\boldsymbol{v}_{i,h}-\boldsymbol{w}_h\|_{0,\Sigma}^2+|(\boldsymbol{v}_h,q_h)|_S^2.
\end{aligned}
$$

Combining the Cauchy-Schwarz inequality with the (robust) trace inequality (1.61), we have

$$
\sum_{i=1}^{2}\big(2\boldsymbol{\sigma}(\boldsymbol{v}_{i,h},0)\boldsymbol{n},\boldsymbol{v}_{i,h}-\boldsymbol{w}_h\big)_\Sigma\le\frac{8C_{\mathrm{TI}}}{\gamma}\mu\sum_{i=1}^{2}\|\boldsymbol{\varepsilon}(\boldsymbol{v}_{i,h})\|_{0,\Omega_{i,h}}^2+\frac{1}{2}\sum_{i=1}^{2}\frac{\gamma\mu}{h}\|\boldsymbol{v}_{i,h}-\boldsymbol{w}_h\|_{0,\Sigma}^2.
$$

We conclude by using the strengthened stability (6.7) provided by the ghost-penalty operator , taking

$$
\gamma>\frac{8C_{\mathrm{TI}}}{\tilde{c}_{\mathrm{g}}}
$$

and using Korn's inequality. ∎

If we take $\boldsymbol{v}_h=\boldsymbol{u}_h(t)$, $q_h=p_h(t)$ and $\boldsymbol{w}_h=\dot{\boldsymbol{d}}_h(t)$ in (6.9) and apply the result of Lemma 6.1 we get the following discrete counterpart of (6.4):

$$
\begin{aligned}
&\frac{\rho^{\mathrm{f}}}{2}\|\boldsymbol{u}_h(t)\|_{0,\Omega^{\mathrm{f}}}^2+\frac{\rho^{\mathrm{s}}}{2}\|\dot{\boldsymbol{d}}_h(t)\|_{0,\Sigma}^2+\frac{1}{2}\|\boldsymbol{d}_h(t)\|_{\mathrm{s}}^2\\
&+c_{\mathrm{g}}\int_0^t\left(\sum_{i=1}^{2}\mu\|\boldsymbol{\nabla}\boldsymbol{u}_{i,h}(s)\|_{0,\Omega_{i,h}}^2+\sum_{i=1}^{2}\frac{\gamma\mu}{h}\|\boldsymbol{u}_{i,h}(s)-\dot{\boldsymbol{d}}_h(s)\|_{0,\Sigma}^2+\big|\big(\boldsymbol{u}_h(s),p_h(s)\big)\big|_S^2\right)\mathrm{d}s\\
&\qquad\le\frac{\rho^{\mathrm{f}}}{2}\|\boldsymbol{u}_h(0)\|_{0,\Omega^{\mathrm{f}}}^2+\frac{\rho^{\mathrm{s}}}{2}\|\dot{\boldsymbol{d}}_h(0)\|_{0,\Sigma}^2+\frac{1}{2}\|\boldsymbol{d}_h(0)\|_{\mathrm{s}}^2,\quad(6.10)
\end{aligned}
$$

which guarantees the energy stability of (6.9).

The following result states the optimal accuracy of (6.9) in the energy norm, under regularity assumptions on the solution of (6.1)-(6.2). It is a generalization of Theorem 1.2. The symbol $\lesssim$ denotes inequality up to a multiplicative constant independent of h.

Theorem 6.1 *Let* $(\boldsymbol{u},p,\dot{\boldsymbol{d}},\boldsymbol{d})$ *be the solution of* (6.1)-(6.2) *and* $(\boldsymbol{u}_h,p_h,\dot{\boldsymbol{d}}_h,\boldsymbol{d}_h)$

be given by (6.9). We assume that the interface Σ is flat and that

$$\boldsymbol{u} \in [H^1(\mathbb{R}^+; H^2(\Omega_1 \cup \Omega_2))]^d,\ p \in C^0(\mathbb{R}^+; H^1(\Omega_1 \cup \Omega_2)),\ \boldsymbol{d}, \dot{\boldsymbol{d}} \in [H^1(\mathbb{R}^+; H^2(\Sigma))]^d.$$

For $t > 0$, there holds:

$$\frac{\rho^{\mathrm{f}}}{2}\|(\boldsymbol{u}_h - \boldsymbol{u})(t)\|^2_{0,\Omega^{\mathrm{f}}} + \frac{\rho^{\mathrm{s}}}{2}\|(\dot{\boldsymbol{d}}_h - \dot{\boldsymbol{d}})(t)\|^2_{0,\Sigma} + \frac{1}{2}\|(\boldsymbol{d}_h - \boldsymbol{d})(t)\|^2_{\mathrm{s}} + c_{\mathrm{g}} \int_0^t \sum_{i=1}^{2} \left(\mu \|\boldsymbol{\nabla}(\boldsymbol{u}_{i,h} - \boldsymbol{u})(s)\|^2_{0,\Omega_i} + \frac{\gamma\mu}{h}\|(\boldsymbol{u}_{i,h} - \dot{\boldsymbol{d}}_{i,h})(s)\|^2_{0,\Sigma} \right) \mathrm{d}s \lesssim h^2,$$

where $\gamma > 0$ is given by Lemma 6.1.

Proof. The result follows by applying the arguments of the proof of Theorem 1.2 (see [BF14b, Theorem 3.1]) to each $\Omega_{i,h}$, $i = 1, 2$. ∎

6.2.1.3 Partially intersected fluid domain

In this section we discuss how the space semi-discrete formulation (6.9) can be generalized to the case in which the interface Σ only partially intersects the domain Ω^{f} (see Figure 6.4(a)). In order to set up the new discrete spaces $\boldsymbol{V}_h$ and Q_h for the fluid, we consider a fictitious prolongation of Σ, denoted by Σ_h^{tip}, so that $\Sigma \cup \Sigma_h^{\mathrm{tip}}$ divides Ω^{f} into two open domains (see Figure 6.4(a)). The *fluid-fluid fictitious interface* is defined in terms of the partition $\Sigma_h^{\mathrm{tip}} = \widetilde{\Sigma}_h \cup \widehat{\Sigma}_h$ where:

- The part $\widetilde{\Sigma}_h$ is included in the set of elements containing the tip of Σ. Moreover, within each of these elements, it is defined as the prolongation of the interface up to the point which is opposite to the edge or face intersected by Σ.
- The part $\widehat{\Sigma}_h$ is aligned with the edges or faces of the mesh.

We now proceed, as in Section 6.2.1.1, by introducing two overlapping triangulations $\mathcal{T}^{\mathrm{f}}_{i,h}$, $i = 1, 2$ (see Figure 6.4(b)). Note that the overlap region reduces to the set of elements intersected by Σ. The associated discrete spaces $X^{\mathrm{f}}_{i,h}$, $i = 1, 2$, are then defined as in (6.5). At last, the fluid velocity and pressure spaces are derived from (6.6) by strongly enforcing the continuity of the velocity and pressure across $\widehat{\Sigma}_h$ (see Figure 6.5), viz.:

$$\begin{aligned} \boldsymbol{V}_h &\stackrel{\mathrm{def}}{=} \left\{ \boldsymbol{v}_h = (\boldsymbol{v}_{1,h}, \boldsymbol{v}_{2,h}) \in \boldsymbol{V}_{1,h} \times \boldsymbol{V}_{2,h} \,/\, \boldsymbol{v}_{1,h} = \boldsymbol{v}_{2,h} \text{ on } \widehat{\Sigma}_h \right\}, \\ Q_h &\stackrel{\mathrm{def}}{=} \left\{ q_h = (q_{1,h}, q_{2,h}) \in Q_{1,h} \times Q_{2,h} \,/\, q_{1,h} = q_{2,h} \text{ on } \widehat{\Sigma}_h \right\}. \end{aligned} \tag{6.11}$$

The functions of these spaces are continuous in the domain

$$\Omega_h \stackrel{\mathrm{def}}{=} \Omega^{\mathrm{f}} \backslash (\Sigma \cup \widetilde{\Sigma}_h),$$

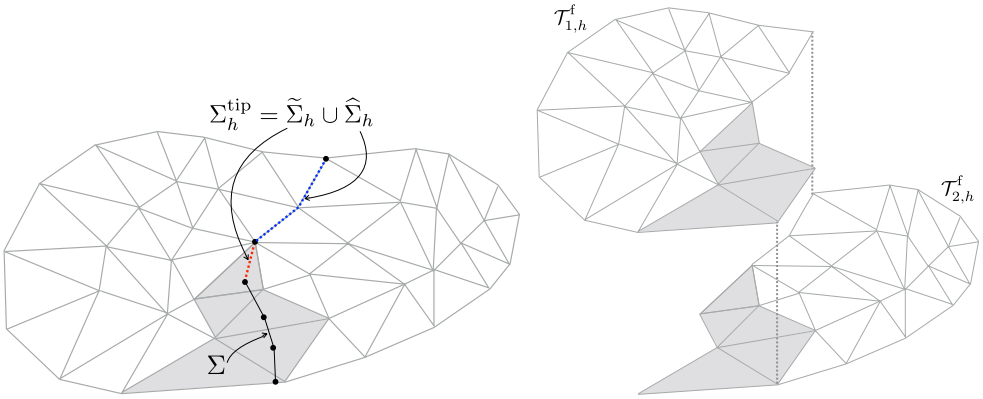

(a) (b)

Figure 6.4: The fluid-solid interface Σ and the fluid-fluid fictitious interface $\widetilde{\Sigma}_h$ in red (a). The two new triangulations with the overlapping region in grey (b).

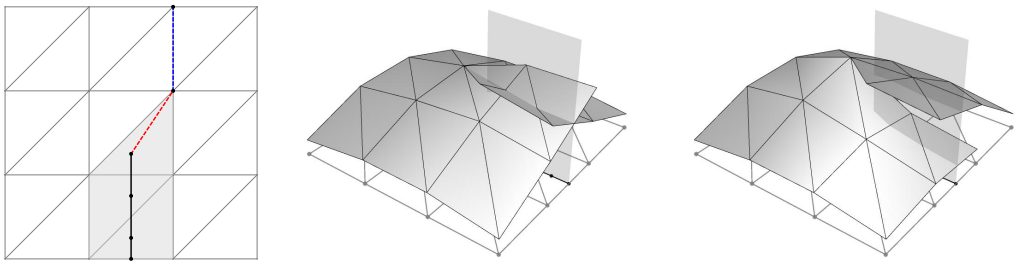

(a) Unfitted meshes (b) Weak discontinuity (c) Strong discontinuity

Figure 6.5: Idealized partially intersected configuration (the red dotted line represents the fictitious fluid-fluid interface). Example of functions $f_h \in X_{1,h}^{\mathrm{f}} \times X_{2,h}^{\mathrm{f}}$.

but discontinuous across the interface $\Sigma \cup \widetilde{\Sigma}_h$. The fluid discrete bilinear form (6.8) is hence redefined as

$$a_h^{\mathrm{f}}\big((\boldsymbol{u}_h, p_h), (\boldsymbol{v}_h, q_h)\big) \overset{\mathrm{def}}{=} a_{\Omega_h}^{\mathrm{f}}\big((\boldsymbol{u}_h, p_h), (\boldsymbol{v}_h, q_h)\big) + S_h\big((\boldsymbol{u}_h, p_h), (\boldsymbol{v}_h, q_h)\big).$$

The continuity of velocity and stress across the fictitious fluid-fluid interface $\widetilde{\Sigma}_h$ will be enforced in a consistent weak fashion, using Nitsche's method (see, e.g., [DPE12, Section 6.1.2]). In summary, the resulting semi-discrete approximation of (6.1)-(6.2) reads as follows: for $t > 0$, find

$$\big(\boldsymbol{u}_h(t), p_h(t), \dot{\boldsymbol{d}}_h(t), \boldsymbol{d}_h(t)\big) \in \boldsymbol{V}_h \times Q_h \times \boldsymbol{W}_h \times \boldsymbol{W}_h,$$

such that $\dot{\boldsymbol{d}}_h(t) = \partial_t \boldsymbol{d}_h(t)$ and

$$\begin{cases} \rho^{\mathrm{f}}\big(\partial_t \boldsymbol{u}_h, \boldsymbol{v}_h\big)_{\Omega^{\mathrm{f}}} + a_h^{\mathrm{f}}\big((\boldsymbol{u}_h, p_h), (\boldsymbol{v}_h, q_h)\big) + \rho^{\mathrm{s}}\epsilon\big(\partial_t \dot{\boldsymbol{d}}_h, \boldsymbol{w}_h\big)_{\Sigma} + a^{\mathrm{s}}(\boldsymbol{d}_h, \boldsymbol{w}_h) \\ - \displaystyle\sum_{i=1}^{2} \big(\boldsymbol{\sigma}(\boldsymbol{u}_{i,h}, p_{i,h})\boldsymbol{n}_i, \boldsymbol{v}_{i,h} - \boldsymbol{w}_h\big)_{\Sigma} - \sum_{i=1}^{2} \big(\boldsymbol{u}_{i,h} - \dot{\boldsymbol{d}}_h, \boldsymbol{\sigma}(\boldsymbol{v}_{i,h}, -q_{i,h})\boldsymbol{n}_i\big)_{\Sigma} \\ + \dfrac{\gamma\mu}{h} \displaystyle\sum_{i=1}^{2} \big(\boldsymbol{u}_{i,h} - \dot{\boldsymbol{d}}_h, \boldsymbol{v}_{i,h} - \boldsymbol{w}_h\big)_{\Sigma} - \big(\{\!\{\boldsymbol{\sigma}(\boldsymbol{u}_h, p_h)\}\!\}\boldsymbol{n}, [\![\boldsymbol{v}_h]\!]\big)_{\widetilde{\Sigma}_h} \\ - \big(\{\!\{\boldsymbol{\sigma}(\boldsymbol{v}_h, -q_h)\}\!\}\boldsymbol{n}, [\![\boldsymbol{u}_h]\!]\big)_{\widetilde{\Sigma}_h} + \dfrac{\gamma\mu}{h}\big([\![\boldsymbol{u}_h]\!], [\![\boldsymbol{v}_h]\!]\big)_{\widetilde{\Sigma}_h} = 0 \end{cases} \tag{6.12}$$

for all $(\boldsymbol{v}_h, q_h, \boldsymbol{w}_h) \in \boldsymbol{V}_h \times Q_h \times \boldsymbol{W}_h$.

Remark 6.4 *It should be noted that the sole differences between (6.9) and (6.12) are the definition of the discrete fluid space $\boldsymbol{V}_h \times Q_h$ and the three additional terms acting on the fictitious fluid-fluid interface $\widetilde{\Sigma}_h$.*

Standard arguments show that the energy stability (6.10) also holds for (6.12). The extension of Theorem 6.1 is more delicate due to the lack of regularity in the vicinity of the interface tip (see, e.g. [Dim04]).

6.2.2 Implementation aspects

The bilinear forms of the space semi-discrete formulations (6.9) and (6.12) require the evaluation of integrals over cut elements. This is a consequence of the fact that, for consistency, the fluid equations are integrated only in the physical zone of $\Omega_{i,h}$, $i = 1, 2$. This is a non-standard implementation problem which requires a specific track of the interface intersections (see, e.g., [MLL13]), namely:

- evaluation of the intersections between the unfitted fluid and solid meshes, i.e., the detection and computation of the cut elements;
- evaluation of the integrals over the cut elements.

This can be challenging in practice, particularly if (as in the present framework) the unfitted fluid and solid meshes are unstructured. Regarding the first point, a few algorithms have been recently reported in the literature (see, e.g., [MGW09, WGMF12, MLL13]). The second is usually faced by sub-dividing the cut elements into subelements for the purpose of the numerical integration (see, e.g., [FB10, MGW09]). Such subdivision can however be involved in 3D (particularly for general unstructured meshes). An alternative is the use of the divergence theorem to obtain a boundary representation of the integrals (see, e.g., [MLL13, SMdAW14]).

Furthermore, the construction of the overlapping meshes $\mathcal{T}_{1,h}^{\mathrm{f}}$ and $\mathcal{T}_{2,h}^{\mathrm{f}}$ requires, in practice, the duplication of the elements that are intersected by the interface.

6.2.2.1 Mesh intersection and subtriangulation

In the numerical examples of Section 6.4, a customized 2D algorithm, that simultaneously yields the mesh intersections and the cut elements subdivisions (see Figure 6.6), has been used. Its main steps are the following:

1. We first localize all the solid mesh vertices inside the fluid mesh. This is carried out using a *barycentric coordinates based algorithm*, which efficiently identifies the element of the fluid mesh containing a given point (see, e.g., [FG08, Section 2.10] or [AM10, Section 3] for details). Once localized, the solid vertices are inserted into the fluid mesh. For efficiency, simple insertion patterns are used, instead of complex vertex insertion operators (such as the *Delaunay kernel* [FG08]). In this regard, it is worth recalling that the quality of the intersected mesh is definitely not a concern here, whose sole purpose is numerical quadrature in cut elements (not interpolation). Therefore, simple mesh validity suffices. When a point is inserted into a 2D mesh composed of triangles, three cases may arise (two of them being degenerated):

   - the point falls inside a triangle, then the triangle is split into three triangles;
   - the point is on a mesh edge, then the edge is split into two and the two triangles sharing this edge are split into two triangles;
   - the point coincides with an existing mesh vertex, then nothing is done.

   This step is illustrated in Figures 6.6(a)–6.6(b).

2. We consider a *partitioning algorithm* (see, e.g., [GBS03]) to insert the structure mesh edges into the mesh resulting from step 1. Each edge is treated one at a time. Its endpoints are vertices of the current (intersected) mesh thanks to step 1. Let AB be an edge of the solid mesh. Starting from one of its endpoints, say A, we seek for the first current mesh edge intersected by AB. The intersection point P_1 is computed (see [AM10, Section 5] for details) and inserted into the current mesh. The two triangles sharing the intersected edge containing P_1 are split into two triangles. At this stage, part of edge AB (i.e., the segment AP_1) has been added to the current mesh. Then, the process is pursued by seeking for the intersection between subedge P_1B and the current mesh edges, which will give a new intersection point P_2 and so on. If after n intersection steps the subedge P_nB belongs to the current mesh, the whole solid edge AB has been inserted into this mesh. It should be noted that, for efficiency, this algorithm works only locally and progresses only through neighboring elements. This step is illustrated in Figures 6.6(b)-6.6(c).

Once the mesh intersection has been resolved via the above two steps, the data structures needed for the *element duplication* and *integration over cut elements* in formulations (6.9) and (6.12) are updated accordingly.

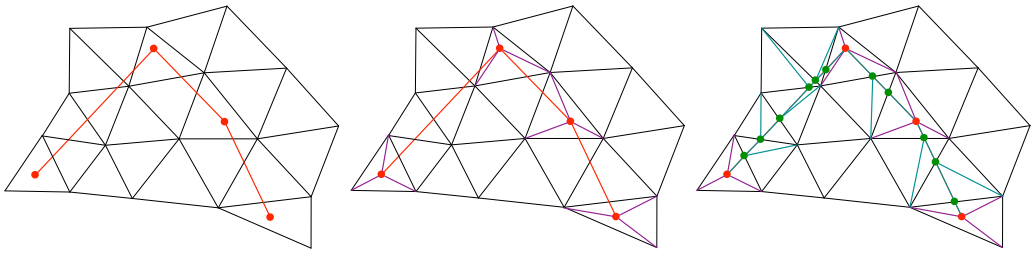

(a) (b) (c)

Figure 6.6: Main steps of the mesh intersection algorithm: (a) initial state where the solid mesh (in red) and the fluid mesh are not fitted; (b) end of step 1 where the solid mesh vertices have been inserted inside the fluid mesh; (c) end of step 2 where the solid mesh edges have been enforced inside the fluid mesh by a partitioning method. The resulting mesh is the intersected mesh where both meshes are fitted.

6.2.2.2 Element duplication

In practice, we construct the overlapping meshes $\mathcal{T}_{1,h}^{\mathrm{f}}$ and $\mathcal{T}_{2,h}^{\mathrm{f}}$ starting from a conforming triangulation $\mathcal{T}_h^{\mathrm{f}}$ of the whole fluid domain Ω^{f} and duplicating the elements that are intersected by the interface. The procedure goes as follows. Let

$$\mathcal{G}_h \overset{\text{def}}{=} \left\{ K \in \mathcal{T}_h^{\mathrm{f}} \,/\, K \cap \Sigma \neq \varnothing \right\}$$

be the subset of elements intersected by Σ, given by the procedure of the previous section. For each element $K \in \mathcal{G}_h$, with nodes $\{i, j, k\}$, we consider a duplication $\{i', j', k'\}$ of its nodes. If a node l has been already duplicated, we assume that l' refers to the preexisting duplication. Suppose that the node i is in Ω_1 whereas j, k are in Ω_2 (see Figure 6.7). We consider two identical copies K' and K'' of K defined by the set of elements $\{i, j', k'\}$ and $\{i', j, k\}$, respectively (see Figure 6.7). At the end of this process, we have, de facto, two independent meshes $\mathcal{T}_{1,h}^{\mathrm{f}}$ and $\mathcal{T}_{2,h}^{\mathrm{f}}$ covering Ω_1 and Ω_2, respectively. Note that the correct connectivity of the meshes is guaranteed by keeping the original nodes on each side of the interface and checking for preexisting node duplications.

6.2.2.3 Integration over cut elements

Consider the situation depicted in the top-left picture of Figure 6.8, in which an element $K \in \mathcal{G}_h$ is completely intersected by an edge of the solid mesh. In that case, the procedure described in Section 6.2.2.1 gives a subtriangulation $\{K_1, K_2, K_3\}$ of K and determines the subsegment S of the solid mesh edge that is intersected by K.

Let ϕ be a function defined in K. This section is devoted to the approximation of integrals of the form $\int_{K_i} \phi(x)\, \mathrm{d}x$, for $i \in \{1, 2, 3\}$, and $\int_S \phi(x)\, \mathrm{d}S$. These computations are needed, respectively, for the evaluation of the fluid's bulk and Nitsche's interfacial terms in the space semi-discrete formulations (6.9) and (6.12). In the

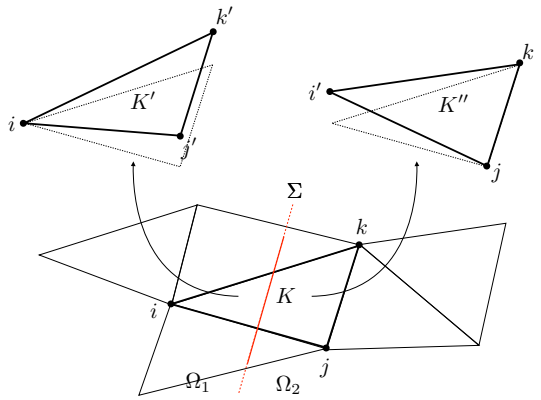

Figure 6.7: Duplication of an intersected element.

following, the reference 2D triangle is given by $\widehat{K}$ with nodes $\{(0,0),(1,0),(0,1)\}$ and the 1D reference segment is given by $\widehat{S} \stackrel{\text{def}}{=} [-1,1]$. We denote by $\boldsymbol{T}_{\widehat{K}\to K}$ and $\boldsymbol{T}_{\widehat{S}\to S}$, the standard mappings from $\widehat{K}$ to K and from $\widehat{S}$ to S, respectively. As usual, we will make use of quadrature formulas over the reference elements to approximate the above integrals. In the following formulae, we assume that we can evaluate the function $\widehat{\phi} = \phi \circ \boldsymbol{T}_{\widehat{K}\to K}$ over $\widehat{K}$.

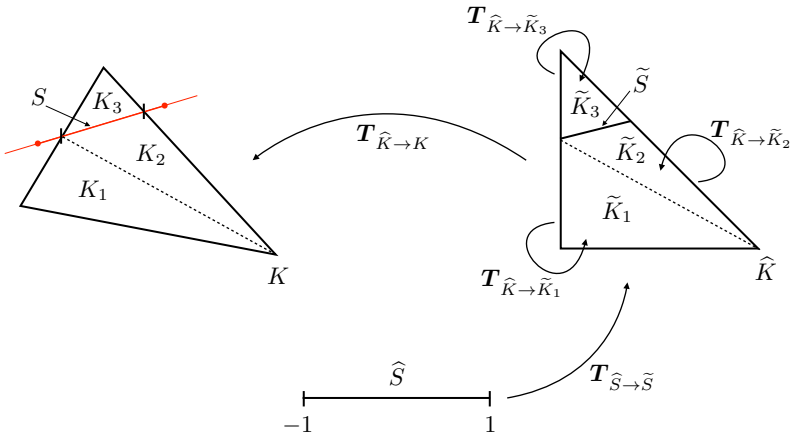

Figure 6.8: Subintegration maps.

Let us consider first, the integration over the volume subelements. The gradient and Jacobian of the transformation $\boldsymbol{T}_{\widehat{K}\to K}$ are given by

$$\boldsymbol{F}_{\widehat{K}\to K} \stackrel{\text{def}}{=} \boldsymbol{\nabla}\boldsymbol{T}_{\widehat{K}\to K}, \quad J_{\widehat{K}\to K} \stackrel{\text{def}}{=} \det \boldsymbol{F}_{\widehat{K}\to K}.$$

The image of $K_i \subset K$ under the transformation $(\boldsymbol{T}_{\widehat{K}\to K})^{-1}$ is denoted by $\widetilde{K}_i \subset \widehat{K}$, for $i \in \{1,2,3\}$. We consider also the mappings $\boldsymbol{T}_{\widehat{K}\to\widetilde{K}_i}$ from $\widehat{K}$ to $\widetilde{K}_i$, with corresponding tensors $\boldsymbol{F}_{\widehat{K}\to\widetilde{K}_i}$ and $J_{\widehat{K}\to\widetilde{K}_i}$, for $i \in \{1,2,3\}$. Using successively the

change of variables $x = \boldsymbol{T}_{\widehat{K}\to K}(\tilde{x})$ and $\tilde{x} = \boldsymbol{T}_{\widehat{K}\to\widetilde{K}_i}(\widehat{\xi}_l)$, we may write

$$\begin{aligned}\int_{K_i} \phi(x)\,\mathrm{d}x &= \int_{\widetilde{K}_i} \phi(\boldsymbol{T}_{\widehat{K}\to K}(\tilde{x}))J_{\widehat{K}\to K}(\tilde{x})\,\mathrm{d}\tilde{x}\\ &= \int_{\widetilde{K}_i} \widehat{\phi}(\tilde{x})J_{\widehat{K}\to K}(\tilde{x})\,\mathrm{d}\tilde{x}\\ &= \int_{\widehat{K}} \widehat{\phi}(\boldsymbol{T}_{\widehat{K}\to\widetilde{K}_i}(\widehat{x}))J_{\widehat{K}\to K}(\boldsymbol{T}_{\widehat{K}\to\widetilde{K}_i}(\widehat{x}))J_{\widehat{K}\to\widetilde{K}_i}(\widehat{x})\,\mathrm{d}\widehat{x}\\ &\approx \sum_{l=1}^{l_\mathrm{q}} \widehat{\phi}(\boldsymbol{T}_{\widehat{K}\to\widetilde{K}_i}(\widehat{\xi}_l))J_{\widehat{K}\to K}(\boldsymbol{T}_{\widehat{K}\to\widetilde{K}_i}(\widehat{\xi}_l))J_{\widehat{K}\to\widetilde{K}_i}(\widehat{\xi}_l)\widehat{\omega}_l\end{aligned}$$

where $\{\widehat{\xi}_l\}_{l=1}^{l_\mathrm{q}}$ are the quadrature points on $\widehat{K}$ with $\{\widehat{\omega}_l\}_{l=1}^{l_\mathrm{q}}$ the corresponding quadrature weights. When using the isoparametric approach with $\mathbb{P}_1$ finite elements, the Jacobians are constant and the approximation of the integral writes,

$$\int_{K_i} \phi(x)\,\mathrm{d}x \approx \sum_{l=1}^{l_\mathrm{q}} \widehat{\phi}(\boldsymbol{T}_{\widehat{K}\to\widetilde{K}_i}(\widehat{\xi}_l))J_{\widehat{K}\to K}J_{\widehat{K}\to\widetilde{K}_i}\widehat{\omega}_l. \tag{6.13}$$

Formula (6.13) requires the computation of the points $\boldsymbol{T}_{\widehat{K}\to\widetilde{K}_i}(\widehat{\xi}_l) \in \widetilde{K}_i$.

Let us consider now the integration over the interface subsegment. The gradient and metric tensor associated to $\boldsymbol{T}_{\widehat{S}\to S}$ are given by

$$\boldsymbol{F}_{\widehat{S}\to S} \overset{\text{def}}{=} \boldsymbol{\nabla}\boldsymbol{T}_{\widehat{S}\to S}, \quad \boldsymbol{a}_{\widehat{S}\to S} \overset{\text{def}}{=} (\boldsymbol{F}_{\widehat{S}\to S})^{\mathrm{T}}\boldsymbol{F}_{\widehat{S}\to S}.$$

The image of S under the transformation $(\boldsymbol{T}_{\widehat{K}\to K})^{-1}$ is denoted by $\widetilde{S}$. In the same fashion as above, we consider the mapping $\boldsymbol{T}_{\widehat{S}\to\widetilde{S}}$ with the associated tensors $\boldsymbol{F}_{\widehat{S}\to\widetilde{S}}$ and $\boldsymbol{a}_{\widehat{S}\to\widetilde{S}}$. Owing to the properties of the Piola transform (see [Cia88, Theorem 1.7-1]), we may write

$$\begin{aligned}&\int_S \phi(x)\,\mathrm{d}S = \int_{\widetilde{S}} \phi(\boldsymbol{T}_{\widehat{K}\to K}(\tilde{x}))J_{\widehat{K}\to K}(\tilde{x})\|(\boldsymbol{F}_{\widehat{K}\to K})^{-\mathrm{T}}(\tilde{x})\widetilde{\boldsymbol{n}}\|\,\mathrm{d}\widetilde{S}\\ &= \int_{\widehat{S}} \widehat{\phi}(\boldsymbol{T}_{\widehat{S}\to\widetilde{S}}(\widehat{x}))J_{\widehat{K}\to K}(\boldsymbol{T}_{\widehat{S}\to\widetilde{S}}(\widehat{x}))\|(\boldsymbol{F}_{\widehat{K}\to K})^{-\mathrm{T}}(\boldsymbol{T}_{\widehat{S}\to\widetilde{S}}(\widehat{x}))\widetilde{\boldsymbol{n}}\|\sqrt{\det\,\boldsymbol{a}_{\widehat{S}\to\widetilde{S}}(\widehat{x})}\,\mathrm{d}\widehat{S}\\ &\approx \sum_{l=1}^{l_\mathrm{q}^\partial} \widehat{\phi}(\boldsymbol{T}_{\widehat{S}\to\widetilde{S}}(\widehat{\xi}_l^\partial))J_{\widehat{K}\to K}(\boldsymbol{T}_{\widehat{S}\to\widetilde{S}}(\widehat{\xi}_l^\partial))\|(\boldsymbol{F}_{\widehat{K}\to K})^{-\mathrm{T}}(\boldsymbol{T}_{\widehat{S}\to\widetilde{S}}(\widehat{\xi}_l^\partial))\widetilde{\boldsymbol{n}}\|\sqrt{\det\,\boldsymbol{a}_{\widehat{S}\to\widetilde{S}}(\widehat{\xi}_l^\partial)}\widehat{\omega}_l^\partial,\end{aligned}$$

where $\widetilde{\boldsymbol{n}}$ is the normal to $\widetilde{S}$, and we have considered a quadrature on $\widehat{S}$ with l_q^∂ points. Under a $\mathbb{P}_1$ isoparametric approach, the above formula reduces to

$$\int_S \phi(x)\,\mathrm{d}S \approx \sum_{l=1}^{l_\mathrm{q}^\partial} \widehat{\phi}(\boldsymbol{T}_{\widehat{S}\to\widetilde{S}}(\widehat{\xi}_l^\partial))J_{\widehat{K}\to K}\|(\boldsymbol{F}_{\widehat{K}\to K})^{-\mathrm{T}}\widetilde{\boldsymbol{n}}\|\sqrt{\det\,\boldsymbol{a}_{\widehat{S}\to\widetilde{S}}}\,\widehat{\omega}_l^\partial. \tag{6.14}$$

Formula (6.14) requires the computation of the points $\boldsymbol{T}_{\widehat{S}\to\widetilde{S}}(\widehat{\xi}_l^{\partial}) \in \widetilde{S}$.

6.2.3 Time discretization: fully discrete schemes

This section is devoted to the time discretization of the unfitted spatial semi-discrete formulations (6.9) and (6.12). In order to simplify the presentation, we mainly consider the case of (6.9). The extension to (6.12) simply follows by adding suitable fluid terms (see Remark 6.4). Several coupling strategies will be discussed, which differ in their degree of fluid-solid splitting: implicit, explicit and semi-implicit nature (Algorithms 6.1-6.3 below). These schemes generalize Algorithms 5.1, 1.4 and 5.2, respectively, to the case of coupling with an immersed thin-walled structure. The theoretical discussion on the stability and accuracy of the methods introduced will be substantiated by numerical experiments in Section 6.4.1.

As usual in this manuscript, $\tau > 0$ denotes the time-step length, $t_n \overset{\text{def}}{=} n\tau$ for $n \in \mathbb{N}$, and $\partial_\tau x^n \overset{\text{def}}{=} \frac{1}{\tau}\big(x^n - x^{n-1}\big)$ stands for the first-order backward difference. The superscript ^{n,*} will denote explicit extrapolations of order $r \in \{0,1,2\}$ to x^n, namely,

$$x^{n,\star} \overset{\text{def}}{=} \begin{cases} 0 & \text{if} \quad r = 0, \\ x^{n-1} & \text{if} \quad r = 1, \\ 2x^{n-1} - x^{n-2} & \text{if} \quad r = 2. \end{cases}$$

6.2.3.1 Implicit coupling scheme

An overall backward Euler time-stepping of (6.9) yields the implicit coupling scheme reported in Algorithm 6.1. This guarantees unconditional stability and optimal accuracy. In particular, by denoting

$$E^n \overset{\text{def}}{=} \frac{\rho^{\mathrm{f}}}{2}\|\boldsymbol{u}_h^n\|_{0,\Omega^{\mathrm{f}}}^2 + \frac{\rho^{\mathrm{s}}}{2}\|\dot{\boldsymbol{d}}_h^n\|_{0,\Sigma}^2 + \frac{1}{2}\|\boldsymbol{d}_h^n\|_{\mathrm{s}}^2,$$

the total energy of the discrete system at time t_n, and by

$$\mathcal{E}^n \overset{\text{def}}{=} \left(\frac{\rho^{\mathrm{f}}}{2}\|\boldsymbol{u}_h^n - \boldsymbol{u}(t_n)\|_{0,\Omega^{\mathrm{f}}}^2 + \frac{\rho^{\mathrm{s}}\epsilon}{2}\|\dot{\boldsymbol{d}}_h^n - \dot{\boldsymbol{d}}(t_n)\|_{0,\Sigma}^2 + \frac{1}{2}\|\boldsymbol{d}_h^n - \boldsymbol{d}(t_n)\|_{\mathrm{s}}^2\right)^{\frac{1}{2}},$$

the energy norm of the approximation error, the following theorem holds. We recall that $\lesssim$, $\gtrsim$ denote inequalities up to multiplicative constants independent of h and τ.

Theorem 6.2 *Let $\{(\boldsymbol{u}_h^n, p_h^n, \dot{\boldsymbol{d}}_h^n, \boldsymbol{d}_h^n)\}_{n\geq 1}$ be the sequence given by Algorithm 6.1. Then, for $\gamma > 0$ given by Lemma 6.1 and $n \geq 1$, there holds*

$$E^n \leq E^0.$$

Moreover, under for smooth enough solutions, the following a priori error estimate

holds

$$\mathcal{E}^n \lesssim h + \tau.$$

Proof. The first result is a straightforward consequence of Lemma 6.1, after taking $(\boldsymbol{v}_h, q_h, \boldsymbol{w}_h) = (\boldsymbol{u}_h^n, p_h^n, \dot{\boldsymbol{d}}_h^n)$ in (6.15). This generalizes the result presented in Remark 5.3. The a priori error estimate readily follows from the arguments reported in Corollary 5.2. ∎

ALGORITHM 6.1 Implicit coupling scheme.

For $n \geq 1$, find $\left(\boldsymbol{u}_h^n, p_h^n, \dot{\boldsymbol{d}}_h^n, \boldsymbol{d}_h^n\right) \in \boldsymbol{V}_h \times Q_h \times \boldsymbol{W}_h \times \boldsymbol{W}_h$, such that $\dot{\boldsymbol{d}}_h = \partial_\tau \boldsymbol{d}_h^n$ and

$$\begin{cases} \rho^{\mathrm{f}}\left(\partial_\tau \boldsymbol{u}_h^n, \boldsymbol{v}_h\right)_{\Omega^{\mathrm{f}}} + a_h^{\mathrm{f}}\left((\boldsymbol{u}_h^n, p_h^n), (\boldsymbol{v}_h, q_h)\right) + \rho^{\mathrm{s}}\epsilon\left(\partial_\tau \dot{\boldsymbol{d}}_h^n, \boldsymbol{w}_h\right)_\Sigma + a^{\mathrm{s}}(\boldsymbol{d}_h^n, \boldsymbol{w}_h) \\ - \sum_{i=1}^{2} \left(\boldsymbol{\sigma}(\boldsymbol{u}_{i,h}^n, p_{i,h}^n)\boldsymbol{n}_i, \boldsymbol{v}_{i,h} - \boldsymbol{w}_h\right)_\Sigma - \sum_{i=1}^{2} \left(\boldsymbol{u}_{i,h}^n - \dot{\boldsymbol{d}}_{i,h}^n, \boldsymbol{\sigma}(\boldsymbol{v}_{i,h}, -q_{i,h})\boldsymbol{n}\right)_\Sigma \\ + \dfrac{\gamma\mu}{h} \sum_{i=1}^{2} \left(\boldsymbol{u}_{i,h}^n - \dot{\boldsymbol{d}}_h^n, \boldsymbol{v}_{i,h} - \boldsymbol{w}_h\right)_\Sigma = 0 \end{cases} \tag{6.15}$$

for all $(\boldsymbol{v}_h, q_h, \boldsymbol{w}_h) \in \boldsymbol{V}_h \times Q_h \times \boldsymbol{W}_h$.

Therefore, due to Theorem 6.2, Algorithm 6.1 exhibits optimal first-order accuracy (in the energy norm) both in time and space. The price to pay for the above unconditional stability and accuracy properties of Algorithm 6.1, is that, at each time level, the fluid $(\boldsymbol{u}_h^n, p_h^n)$ and solid $(\dot{\boldsymbol{d}}_h^n, \boldsymbol{d}_h^n)$ states are fully coupled, which can be computationally demanding in practice. Indeed, besides the hybrid nature of the coupled problem, general thin-walled solid models discretized by finite elements are known to yield very ill-conditioned stiffness matrices requiring specific solvers (see, e.g., [GRW05]). In the next two sections, we introduce two alternative time discretizations of (6.9) with a certain degree of splitting between the time-stepping of the fluid and of the solid.

6.2.3.2 Stabilized explicit schemes

We consider the stabilized explicit coupling paradigm reported in Section 1.4.3.4. We apply here those ideas to the Nitsche-XFEM spatial semi-discrete formulation (6.9). To this purpose, we first formulate (6.9) in terms of two coupled subproblems by successively taking $(\boldsymbol{v}_h, q_h) = (\boldsymbol{0}, 0)$ and $\boldsymbol{w}_h = \boldsymbol{0}$ in (6.9). This yields:

- Solid subproblem:

$$\begin{cases} \rho^{\mathrm{s}}\epsilon\left(\partial_t \dot{\boldsymbol{d}}_h, \boldsymbol{w}_h\right)_\Sigma + a^{\mathrm{s}}(\boldsymbol{d}_h, \boldsymbol{w}_h) + \left(\llbracket \boldsymbol{\sigma}(\boldsymbol{u}_h, p_h)\boldsymbol{n} \rrbracket, \boldsymbol{w}_h\right)_\Sigma \\ + \dfrac{2\gamma\mu}{h}\left(\dot{\boldsymbol{d}}_h - \{\!\{\boldsymbol{u}_h\}\!\}, \boldsymbol{w}_h\right)_\Sigma = 0 \end{cases} \tag{6.16}$$

  for all $\boldsymbol{w}_h \in \boldsymbol{W}_h$.

- Fluid subproblem:

$$\begin{cases} \rho^{\mathrm{f}}\big(\partial_t \boldsymbol{u}_h, \boldsymbol{v}_h\big)_{\Omega^{\mathrm{f}}} + a_h^{\mathrm{f}}\big((\boldsymbol{u}_h, p_h), (\boldsymbol{v}_h, q_h)\big) - \displaystyle\sum_{i=1}^{2} \big(\boldsymbol{\sigma}(\boldsymbol{u}_{i,h}, p_{i,h})\boldsymbol{n}_i, \boldsymbol{v}_{i,h}\big)_{\Sigma} \\ \quad - \displaystyle\sum_{i=1}^{2} \big(\boldsymbol{u}_{i,h} - \dot{\boldsymbol{d}}_h, \boldsymbol{\sigma}(\boldsymbol{v}_{i,h}, -q_{i,h})\boldsymbol{n}_i\big)_{\Sigma} + \frac{\gamma\mu}{h} \displaystyle\sum_{i=1}^{2} \big(\boldsymbol{u}_{i,h} - \dot{\boldsymbol{d}}_h, \boldsymbol{v}_{i,h}\big)_{\Sigma} = 0 \end{cases} \tag{6.17}$$

  for all $(\boldsymbol{v}_h, q_h) \in \boldsymbol{V}_h \times Q_h$.

We combine a backward Euler time-stepping of the fluid and solid bulk terms in (6.16)-(6.17) with an explicit treatment of the interface coupling terms. More precisely, for $n \geq 1$, we have:

1. Solid substep: find $\big(\dot{\boldsymbol{d}}_h^n, \boldsymbol{d}_h^n\big) \in \boldsymbol{W}_h \times \boldsymbol{W}_h$ with $\dot{\boldsymbol{d}}_h^n = \partial_\tau \boldsymbol{d}_h^n$ and such that

$$\begin{cases} \rho^{\mathrm{s}}\epsilon\big(\partial_\tau \dot{\boldsymbol{d}}_h^n, \boldsymbol{w}_h\big)_{\Sigma} + a^{\mathrm{s}}(\boldsymbol{d}_h^n, \boldsymbol{w}_h) + \dfrac{2\gamma\mu}{h}\big(\dot{\boldsymbol{d}}_h^n, \boldsymbol{w}_h\big)_{\Sigma} \\ \quad = \dfrac{2\gamma\mu}{h}\big(\{\!\{\boldsymbol{u}_h^{n-1}\}\!\}, \boldsymbol{w}_h\big)_{\Sigma} - \big([\![\boldsymbol{\sigma}(\boldsymbol{u}_h^{n-1}, p_h^{n-1})\boldsymbol{n}]\!], \boldsymbol{w}_h\big)_{\Sigma} \end{cases} \tag{6.18}$$

   for all $\boldsymbol{w}_h \in \boldsymbol{W}_h$.

2. Fluid substep: find $(\boldsymbol{u}_h^n, p_h^n) \in \boldsymbol{V}_h \times Q_h$ such that

$$\begin{cases} \rho^{\mathrm{f}}\big(\partial_\tau \boldsymbol{u}_h^n, \boldsymbol{v}_h\big)_{\Omega^{\mathrm{f}}} + a_h^{\mathrm{f}}\big((\boldsymbol{u}_h^n, p_h^n), (\boldsymbol{v}_h, q_h)\big) + \dfrac{\gamma\mu}{h} \displaystyle\sum_{i=1}^{2} \big(\boldsymbol{u}_{i,h}^n, \boldsymbol{v}_{i,h}\big)_{\Sigma} \\ \quad - \displaystyle\sum_{i=1}^{2} \big(\boldsymbol{u}_{i,h}^n - \dot{\boldsymbol{d}}_h^n, \boldsymbol{\sigma}(\boldsymbol{v}_{i,h}, -q_{i,h})\boldsymbol{n}_i\big)_{\Sigma} + \dfrac{\gamma_0 h}{\gamma\mu} \displaystyle\sum_{i=1}^{2} \big(p_{i,h}^n - p_{i,h}^{n-1}, q_{i,h}\big)_{\Sigma} \\ \quad = \dfrac{\gamma\mu}{h} \displaystyle\sum_{i=1}^{2} \big(\dot{\boldsymbol{d}}_h^n, \boldsymbol{v}_{i,h}\big)_{\Sigma} + \displaystyle\sum_{i=1}^{2} \big(\boldsymbol{\sigma}(\boldsymbol{u}_{i,h}^{n-1}, p_{i,h}^{n-1})\boldsymbol{n}_i, \boldsymbol{v}_{i,h}\big)_{\Sigma} \end{cases} \tag{6.19}$$

   for all $(\boldsymbol{v}_h, q_h) \in \boldsymbol{V}_h \times Q_h$.

A salient feature of this approach is that the explicit treatment of the interface coupling in (6.18) uncouples the computation of $(\dot{\boldsymbol{d}}_h^n, \boldsymbol{d}_h^n)$ and $(\boldsymbol{u}_h^n, p_h^n)$. The fundamental ingredient for the stabitity of the scheme is the weakly consistent term

$$\frac{\gamma_0 h}{\gamma\mu} \sum_{i=1}^{2} \big(p_{i,h}^n - p_{i,h}^{n-1}, q_{i,h}\big)_{\Sigma}, \quad \gamma_0 > 0,$$

which controls the temporal interface pressure fluctuations induced by the fluid-solid splitting in time and, hence, avoids added-mass stability issues. It corresponds to the two-sided extension of the term (1.76).

The next result establishes the conditional stability of the fully discrete method (6.18)-(6.19).

THEOREM 6.3 *Let $\{(\boldsymbol{u}_h^n, p_h^n, \dot{\boldsymbol{d}}_h^n, \boldsymbol{d}_h^n)\}_{n\geq 1}$ be the sequence given by (6.18)-(6.19). Then, under conditions $\gamma \gtrsim C_{\mathrm{TI}}/\tilde{c}_{\mathrm{g}}$, $\gamma\tau \lesssim h$ and $\gamma_0 \gtrsim 1$, there holds*

$$E^n \lesssim E^0 + \sum_{i=1}^{2} \left(\mu \|\boldsymbol{u}_{i,h}^0\|_{0,\Sigma}^2 + \mu \|\boldsymbol{\varepsilon}(\boldsymbol{u}_{i,h}^0)\|_{0,\Omega_{i,h}}^2 + \frac{\gamma_0 h}{\gamma\mu} \tau \|p_{i,h}^0\|_{0,\Sigma}^2 \right)$$

for $n \geq 1$.

Proof. Similarly to Theorem 1.4, the result follows by combining Lemma 6.1 with the arguments reported in [BF09, Section 5.1]. ∎

Like Algorithm 1.4, the main drawback of the scheme (6.18)-(6.19) is that it delivers poor accuracy in practice. More precisely, the explicit treatment of the penalty term in the solid substep (6.18), i.e,

$$2\frac{\gamma\mu}{h}\left(\dot{\boldsymbol{d}}_h^n - \{\!\{\boldsymbol{u}_h^{n-1}\}\!\}, \boldsymbol{w}_h\right)_\Sigma, \tag{6.20}$$

induces an splitting error $\mathcal{O}(\tau/h)$ which is not uniform in h. In the spirit of [BF14a, BF14b], we propose to circumvent this issue by combining (6.18)-(6.19) with a predictor-corrector strategy (with $K \geq 0$ corrections). The resulting solution procedure is detailed in Algorithm 6.2, where we have used the notation

$$\partial_\tau x^{n,k} \overset{\text{def}}{=} \frac{1}{\tau}(x^{n,k} - x^{n-1}).$$

The key idea is that if, instead of the first-order extrapolation (6.20), we consider a second-order extrapolation of the fluid velocity ($r = 2$), after K correction iterations, the error induced by the explicit treatment of the penalty term becomes

$$\mathcal{O}\left(\left(\tau^2/h\right)^{K+1}\right) \tag{6.23}$$

As a result, the contribution of the penalty term becomes $\mathcal{O}(\tau^2/h)$ with $K = 0$ and, hence, $\tau = \mathcal{O}(h)$ suffices to achieve overall first-order accuracy. Nevertheless, numerical evidence indicates that $K \geq 1$ is mandatory for stability (see, e.g., the discussion of Section 6.4.2.2).

REMARK 6.5 *The original stabilized explicit coupling scheme (6.18)-(6.19) can be retrieved from Algorithm 6.2 by taking $K = 0$ (no correction) and with first-order extrapolation for the initial guess of the fluid velocity ($r = 1$). On the other hand, if we let $K \to \infty$ the splitting error (6.23) tends to zero and we retrieve the implicit coupling solution provided by Algorithm 6.1. In other words, Algorithm 6.2 with enough correction iterations (i.e., until convergence) provides a partitioned iterative solution procedure for Algorithm 6.1.*

Algorithm 6.2 Stabilized explicit coupling scheme with $K \geq 0$ corrections.

For $n \geq 1$:

1. Set initial guess for predictor:

$$\boldsymbol{u}_h^{n,0} = \boldsymbol{u}_h^{n,\star}, \quad p_h^{n,0} = p_h^{n-1}, \quad \boldsymbol{d}_h^{n,0} = \boldsymbol{d}_h^{n-1}, \quad \dot{\boldsymbol{d}}_h^{n,0} = \dot{\boldsymbol{d}}_h^{n-1}.$$

2. Correction iterations. For $k = 1, \ldots, K+1$:

   (a) Find $\left(\dot{\boldsymbol{d}}_h^{n,k}, \boldsymbol{d}_h^{n,k}\right) \in \boldsymbol{W}_h \times \boldsymbol{W}_h$ with $\dot{\boldsymbol{d}}_h^{n,k} = \partial_\tau \boldsymbol{d}_h^{n,k}$ and such that

$$\begin{cases} \rho^{\mathrm{s}} \epsilon \left(\partial_\tau \dot{\boldsymbol{d}}_h^{n,k}, \boldsymbol{w}_h\right)_\Sigma + a^{\mathrm{s}}(\boldsymbol{d}_h^{n,k}, \boldsymbol{w}_h) + \dfrac{2\gamma\mu}{h} \left(\dot{\boldsymbol{d}}_h^{n,k}, \boldsymbol{w}_h\right)_\Sigma \\ = \dfrac{2\gamma\mu}{h} \left(\{\!\{ \boldsymbol{u}_h^{n,k-1} \}\!\}, \boldsymbol{w}_h\right)_\Sigma - \left([\![\boldsymbol{\sigma}(\boldsymbol{u}_h^{n,k-1}, p_h^{n,k-1}) \boldsymbol{n}]\!], \boldsymbol{w}_h\right)_\Sigma \end{cases} \tag{6.21}$$

   for all $\boldsymbol{w}_h \in \boldsymbol{W}_h$.

   (b) Find $(\boldsymbol{u}_h^{n,k}, p_h^{n,k}) \in \boldsymbol{V}_h \times Q_h$ such that

$$\begin{cases} \rho^{\mathrm{f}} \left(\partial_\tau \boldsymbol{u}_h^{n,k}, \boldsymbol{v}_h\right)_{\Omega^{\mathrm{f}}} + a_h^{\mathrm{f}}\left((\boldsymbol{u}_h^{n,k}, p_h^{n,k}), (\boldsymbol{v}_h, q_h)\right) + \dfrac{\gamma\mu}{h} \displaystyle\sum_{i=1}^{2} \left(\boldsymbol{u}_{i,h}^{n,k}, \boldsymbol{v}_{i,h}\right)_\Sigma \\ - \displaystyle\sum_{i=1}^{2} \left(\boldsymbol{u}_{i,h}^{n,k} - \dot{\boldsymbol{d}}_h^{n,k}, \boldsymbol{\sigma}(\boldsymbol{v}_{i,h}, -q_{i,h}) \boldsymbol{n}_i\right)_\Sigma + \dfrac{\gamma_0 h}{\gamma\mu} \displaystyle\sum_{i=1}^{2} \left(p_{i,h}^{n,k} - p_{i,h}^{n,k-1}, q_{i,h}\right)_\Sigma \\ = \dfrac{\gamma\mu}{h} \displaystyle\sum_{i=1}^{2} \left(\dot{\boldsymbol{d}}_h^{n,k}, \boldsymbol{v}_{i,h}\right)_\Sigma + \displaystyle\sum_{i=1}^{2} \left(\boldsymbol{\sigma}(\boldsymbol{u}_{i,h}^{n,k-1}, p_{i,h}^{n,k-1}) \boldsymbol{n}_i, \boldsymbol{v}_{i,h}\right)_\Sigma \end{cases} \tag{6.22}$$

   for all $(\boldsymbol{v}_h, q_h) \in \boldsymbol{V}_h \times Q_h$.

3. Set

$$\boldsymbol{u}_h^n = \boldsymbol{u}_h^{n,K+1}, \quad p_h^n = p_h^{n,K+1}, \quad \boldsymbol{d}_h^n = \boldsymbol{d}_h^{n,K+1}, \quad \dot{\boldsymbol{d}}_h^n = \dot{\boldsymbol{d}}_h^{n,K+1}.$$

6.2.3.3 Semi-implicit schemes

The main drawback of the explicit coupling schemes introduced in the previous section is that the splitting error is not uniform in h. Enough correction iterations with suitable predictions (Algorithm 6.2) are hence needed to enhance accuracy. In this section, we propose to overcome these issues by extending the operator splitting approach reported in Section 5.2.1 to the Nitsche-XFEM spatial semi-discrete formulation (6.9). The resulting schemes deliver stability and overall first-order accuracy (uniform in h) while keeping a certain degree of fluid-solid splitting (semi-implicit coupling schemes).

To this purpose, we consider the following fractional-step time-marching of (6.9): for $n > 1$,

1. Find $\big(\boldsymbol{u}_h^n, p_h^n, \dot{\boldsymbol{d}}_h^{n-\frac{1}{2}}\big) \in \boldsymbol{V}_h \times Q_h \times \boldsymbol{W}_h$ such that

$$\left\{\begin{aligned} &\rho^{\mathrm{f}}\big(\partial_\tau \boldsymbol{u}_h^n, \boldsymbol{v}_h\big)_{\Omega^{\mathrm{f}}} + a_h^{\mathrm{f}}\big((\boldsymbol{u}_h^n, p_h^n), (\boldsymbol{v}_h, q_h)\big) + \frac{\rho^{\mathrm{s}}\epsilon}{\tau}\big(\dot{\boldsymbol{d}}_h^{n-\frac{1}{2}} - \dot{\boldsymbol{d}}_h^{n-1}, \boldsymbol{w}_h\big)_\Sigma \\ &- \sum_{i=1}^{2}\big(\boldsymbol{\sigma}(\boldsymbol{u}_{i,h}^n, p_{i,h}^n)\boldsymbol{n}_i, \boldsymbol{v}_{i,h} - \boldsymbol{w}_h\big)_\Sigma - \sum_{i=1}^{2}\big(\boldsymbol{u}_{i,h}^n - \dot{\boldsymbol{d}}_h^{n-\frac{1}{2}}, \boldsymbol{\sigma}(\boldsymbol{v}_{i,h}, -q_{i,h})\boldsymbol{n}_i\big)_\Sigma \\ &+ \sum_{i=1}^{2}\frac{\gamma\mu}{h}\big(\boldsymbol{u}_{i,h}^n - \dot{\boldsymbol{d}}_h^{n-\frac{1}{2}}, \boldsymbol{v}_{i,h} - \boldsymbol{w}_h\big)_\Sigma = -a^{\mathrm{s}}\big(\boldsymbol{d}_h^{n,\star}, \boldsymbol{w}_h\big). \end{aligned}\right. \tag{6.24}$$

   for all $(\boldsymbol{v}_h, q_h, \boldsymbol{w}_h) \in \boldsymbol{V}_h \times Q_h \times \boldsymbol{W}_h$.

2. Find $\big(\dot{\boldsymbol{d}}_h^n, \boldsymbol{d}_h^n\big) \in \boldsymbol{W}_h \times \boldsymbol{W}_h$ with $\dot{\boldsymbol{d}}_h^n = \partial_\tau \boldsymbol{d}_h^n$ and such that

$$\frac{\rho^{\mathrm{s}}\epsilon}{\tau}\big(\dot{\boldsymbol{d}}_h^n - \dot{\boldsymbol{d}}_h^{n-\frac{1}{2}}, \boldsymbol{w}_h\big)_\Sigma + a^{\mathrm{s}}\big(\boldsymbol{d}_h^n, \boldsymbol{w}_h\big) = a^{\mathrm{s}}\big(\boldsymbol{d}_h^{n,\star}, \boldsymbol{w}_h\big) \tag{6.25}$$

   for all $\boldsymbol{w}_h \in \boldsymbol{W}_h$.

The introduction in step (6.24) of the intermediate solid-velocity $\dot{\boldsymbol{d}}_h^{n-\frac{1}{2}}$ enables the implicit treatment of the solid inertia within the fluid. This is enough to guarantee added-mass free stability. The remaining solid elastic contributions are treated explicitly (or ignored) via extrapolation. The end-of-step velocity $\dot{\boldsymbol{d}}_h^n \in \boldsymbol{W}_h$ is recovered by solving the solid problem (6.25). Note that unlike, Algorithm 6.2, the scheme (6.24)-(6.25) does not involve any correction iteration.

Remark 6.6 *The relation (6.24) has somme similarities with the explicit time-splitting procedures commonly used in the immersed boundary (IB) method (see, e.g., [Pes02, NFGK07, BCG11]). Indeed, substep (6.24) simultaneously includes the fluid and solid inertia whereas the solid elastic contributions are treated explicitly. The key difference concerns the solid substep (6.25), which in the IB method consists of a simple displacement-velocity relation (i.e., the structure solver is never called), which in practice enforces restrictive CFL conditions for stability. Theorem 6.4 below shows that (6.24)-(6.25) circumvents this issue.*

It is worth noting that the semi-implicit coupling scheme provided by (6.24)-(6.25) has a reduced computational complexity with respect to Algorithm 6.1. Indeed, the solid contribution to (6.24) reduces to a simple interface mass-matrix, which does not degrade the conditioning of the system matrix. This reduction in the coupling complexity is particularly important when considering general shell models (see, e.g., [CB11]), whose elastic contributions incorporate additional unknowns (e.g., rotations). Moreover, unlike Algorithm 6.2, the scheme (6.24)–(6.25) does not involve any correction iteration.

As in Section 5.2.1, the solid step (6.25) can be reformulated as a standard solid problem. Indeed, by taking $\boldsymbol{v}_h = \boldsymbol{0}$ and $q_h = 0$ in (6.24) and adding the resulting

expression to (6.25), we get

$$\rho^{\mathrm{s}}\epsilon\big(\partial_\tau \dot{\boldsymbol{d}}_h^n, \boldsymbol{w}_h\big)_\Sigma + a^{\mathrm{s}}(\boldsymbol{d}_h^n, \boldsymbol{w}_h) = -\big(\llbracket \boldsymbol{\sigma}(\boldsymbol{u}_h^n, p_h^n)\boldsymbol{n}\rrbracket, \boldsymbol{w}_h\big)_\Sigma + \frac{2\gamma\mu}{h}\big(\{\!\{\boldsymbol{u}_h^n\}\!\} - \dot{\boldsymbol{d}}_h^{n-\frac{1}{2}}, \boldsymbol{w}_h\big)_\Sigma \tag{6.26}$$

for all $\boldsymbol{w}_h \in \boldsymbol{W}_h$. We can also avoid the extrapolations of the solid elastic term in (6.24) (which can be cumbersome in practice), by reformulating step (6.24) in a more intrinsic fashion. To this purpose, we note that from (6.26), we have

$$\begin{aligned} a^{\mathrm{s}}(\boldsymbol{d}_h^{n,\star}, \boldsymbol{w}_h) = &-\rho^{\mathrm{s}}\epsilon\big(\partial_\tau \dot{\boldsymbol{d}}_h^{n,\star}, \boldsymbol{w}_h\big)_\Sigma - \big(\llbracket \boldsymbol{\sigma}(\boldsymbol{u}_h^{n,\star}, p_h^{n,\star})\boldsymbol{n}\rrbracket, \boldsymbol{w}_h\big)_\Sigma \\ &+ \frac{2\gamma\mu}{h}\big(\{\!\{\boldsymbol{u}_h^{n,\star}\}\!\} - \dot{\boldsymbol{d}}_h^{n-\frac{1}{2},\star}, \boldsymbol{w}_h\big)_\Sigma \end{aligned} \tag{6.27}$$

for all $\boldsymbol{w}_h \in \boldsymbol{W}_h$ and $n > r$. Owing to (6.26) and (6.27), the semi-implicit scheme (6.24)-(6.25) can be reformulated as shown in Algorithm 6.3.

Algorithm 6.3 Semi-implicit coupling scheme.

For $n > r$:

1. Fluid-with-solid-inertia substep: find $\big(\boldsymbol{u}_h^n, p_h^n, \dot{\boldsymbol{d}}_h^{n-\frac{1}{2}}\big) \in \boldsymbol{V}_h \times Q_h \times \boldsymbol{W}_h$ such that

$$\begin{cases} \rho^{\mathrm{f}}\big(\partial_\tau \boldsymbol{u}_h^n, \boldsymbol{v}_h\big)_{\Omega^{\mathrm{f}}} + a_h^{\mathrm{f}}\big((\boldsymbol{u}_h^n, p_h^n), (\boldsymbol{v}_h, q_h)\big) + \dfrac{\rho^{\mathrm{s}}\epsilon}{\tau}\big(\dot{\boldsymbol{d}}_h^{n-\frac{1}{2}}, \boldsymbol{w}_h\big)_\Sigma \\ -\displaystyle\sum_{i=1}^{2}\big(\boldsymbol{\sigma}(\boldsymbol{u}_{i,h}^n, p_{i,h}^n)\boldsymbol{n}_i, \boldsymbol{v}_{i,h} - \boldsymbol{w}_h\big)_\Sigma - \sum_{i=1}^{2}\big(\boldsymbol{u}_{i,h}^n - \dot{\boldsymbol{d}}_h^{n-\frac{1}{2}}, \boldsymbol{\sigma}(\boldsymbol{v}_{i,h}, -q_{i,h})\boldsymbol{n}_i\big)_\Sigma \\ +\displaystyle\sum_{i=1}^{2}\frac{\gamma\mu}{h}\big(\boldsymbol{u}_{i,h}^n - \dot{\boldsymbol{d}}_h^{n-\frac{1}{2}}, \boldsymbol{v}_{i,h} - \boldsymbol{w}_h\big)_\Sigma = \frac{\rho^{\mathrm{s}}\epsilon}{\tau}\big(\dot{\boldsymbol{d}}_h^{n-1} + \tau\partial_\tau \dot{\boldsymbol{d}}_h^{n,\star}, \boldsymbol{w}_h\big)_\Sigma \\ +\big(\llbracket \boldsymbol{\sigma}(\boldsymbol{u}_h^{n,\star}, p_h^{n,\star})\boldsymbol{n}\rrbracket, \boldsymbol{w}_h\big)_\Sigma - \dfrac{2\gamma\mu}{h}\big(\{\!\{\boldsymbol{u}_h^{n,\star}\}\!\} - \dot{\boldsymbol{d}}_h^{n-\frac{1}{2},\star}, \boldsymbol{w}_h\big)_\Sigma \end{cases} \tag{6.28}$$

   for all $(\boldsymbol{v}_h, q_h, \boldsymbol{w}_h) \in \boldsymbol{V}_h \times Q_h \times \boldsymbol{W}_h$.

2. Solid substep: find $\big(\dot{\boldsymbol{d}}_h^n, \boldsymbol{d}_h^n\big) \in \boldsymbol{W}_h \times \boldsymbol{W}_h$ with $\dot{\boldsymbol{d}}_h^n = \partial_\tau \boldsymbol{d}_h^n$ and such that

$$\begin{cases} \rho^{\mathrm{s}}\epsilon\big(\partial_\tau \dot{\boldsymbol{d}}_h^n, \boldsymbol{w}_h\big)_\Sigma + a^{\mathrm{s}}(\boldsymbol{d}_h^n, \boldsymbol{w}_h) = -\big(\llbracket \boldsymbol{\sigma}(\boldsymbol{u}_h^n, p_h^n)\boldsymbol{n}\rrbracket, \boldsymbol{w}_h\big)_\Sigma \\ \qquad\qquad + \dfrac{2\gamma\mu}{h}\big(\{\!\{\boldsymbol{u}_h^n\}\!\} - \dot{\boldsymbol{d}}_h^{n-\frac{1}{2}}, \boldsymbol{w}_h\big)_\Sigma \end{cases}$$

   for all $\boldsymbol{w}_h \in \boldsymbol{W}_h$.

Remark 6.7 *Algorithm 6.3 with $r = 1, 2$ is a multi-step method on the interface. Thus, additional data is needed to start the time-marching. In practice, this data can be obtained by performing one step of the scheme with $r = 0$ and then one step of the scheme with $r = 1$.*

The following result states the stability and convergence properties of the semi-implicit schemes reported in Algorithm 6.3.

THEOREM 6.4 *Let* $\{(\boldsymbol{u}_h^n, p_h^n, \dot{\boldsymbol{d}}_h^{n-\frac{1}{2}}, \boldsymbol{d}_h^n, \dot{\boldsymbol{d}}_h^n)\}_{n>r}$ *be the sequence given by Algorithm 6.3, initialized as indicated in Remark 6.7 for* $r \geq 1$. *Let* $\gamma > 0$ *be given by Lemma 6.1. There holds*

$$E^n \leq E^0$$

for all $n > r$, *unconditionally for* $r \in \{0, 1\}$ *and under the CFL-like condition* $\tau \lesssim \alpha h^{\frac{6}{5}}$, $\tau\alpha < 1$ *and* $\alpha > 0$, *for* $r = 2$. *In addition, for smooth enough solutions, there holds*

$$\mathcal{E}^n \lesssim h + \tau + \tau^{2^{r-1}}.$$

Proof. The result follows from a straightforward adaptation of the arguments used in Theorem 5.1 and Corollary 5.1 ∎

The contribution of the splitting error in the a priori energy estimate of Theorem 6.4 is given by the $\mathcal{O}(\tau^{2^{r-1}})$ term. Note that this guarantees the h-uniformity of the error, which is a major advantage with respect to Algorithm 6.2. Moreover, Algorithm 6.3 with $r = 1$ simultaneously yields unconditional stability and overall first-order accuracy, without resorting to any correction iteration.

REMARK 6.8 *Algorithms 6.1-6.3 can be adapted to the time discretisation of (6.12) with minor modifications. Indeed, it suffices to add the corresponding fictitious fluid-fluid interface terms*

$$-\big(\{\!\{\boldsymbol{\sigma}(\boldsymbol{u}_h^n, p_h^n)\}\!\}\boldsymbol{n}, [\![\boldsymbol{v}_h]\!]\big)_{\widetilde{\Sigma}_h} - \big(\{\!\{\boldsymbol{\sigma}(\boldsymbol{v}_h, -q_h)\}\!\}\boldsymbol{n}, [\![\boldsymbol{u}_h^n]\!]\big)_{\widetilde{\Sigma}_h} + \frac{\gamma\mu}{h}\big([\![\boldsymbol{u}_h^n]\!], [\![\boldsymbol{v}_h]\!]\big)_{\widetilde{\Sigma}_h}$$

to the discrete problems (6.15), (6.22) and (6.28), respectively.

6.3 The non-linear case: dynamic interfaces

In this section we extend the numerical methods of Section 6.2.3 to the case of a non-linear fluid-structure interaction problem, involving an incompressible viscous fluid and an immersed thin-walled structure. The fluid is described by the incompressible Navier-Stokes equations in Eulerian form (1.1) and the structure by a (possibly) non-linear membrane or shell model.

6.3.1 Problem setting

Let $\Sigma \subset \mathbb{R}^d$ be the reference configuration of the solid mid-surface. The current position of the interface, denoted by $\Sigma(t)$, is parametrized by the one-to-one deformation map $\boldsymbol{\phi} : \Sigma \times \mathbb{R}^+ \longrightarrow \mathbb{R}^d$ as $\Sigma(t) = \boldsymbol{\phi}(\Sigma, t)$, with $\boldsymbol{\phi} \overset{\text{def}}{=} \boldsymbol{I}_{\Sigma\times\mathbb{R}^+} + \boldsymbol{d}$ and where $\boldsymbol{d}$ denotes the displacement of the solid. In order to ease the presentation, we introduce the notation $\boldsymbol{\phi}_t \overset{\text{def}}{=} \boldsymbol{\phi}(\cdot, t)$, so that we also have $\Sigma(t) = \boldsymbol{\phi}_t(\Sigma)$. The

structure is supposed to move within a domain $\Omega^{\mathrm{f}} \subset \mathbb{R}^d$ with boundary $\Gamma^{\mathrm{f}} \stackrel{\mathrm{def}}{=} \partial\Omega^{\mathrm{f}}$ (see Figure 6.9). For simplicity and without loss of generality, Ω^{f} is assumed to be fixed. The fluid is described in the time-dependent control volume

$$\Omega^{\mathrm{f}}(t) \stackrel{\mathrm{def}}{=} \Omega^{\mathrm{f}} \backslash \Sigma(t) \subset \mathbb{R}^d,$$

with its boundary partitioned as $\partial\Omega^{\mathrm{f}}(t) = \Sigma(t) \cup \Gamma^{\mathrm{f}}$.

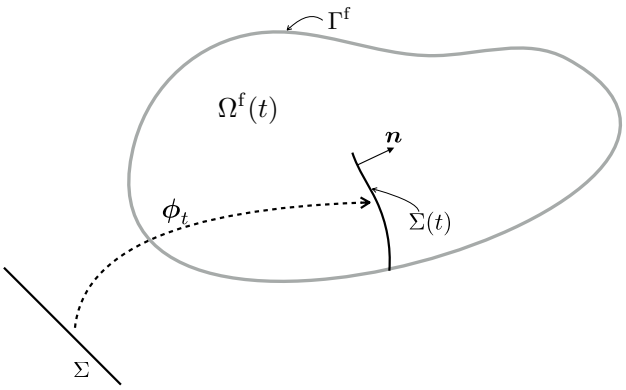

Figure 6.9: Geometric description.

The considered non-linear coupled problem reads as follow: find the fluid velocity and pressure $\boldsymbol{u} : \Omega^{\mathrm{f}} \times \mathbb{R}^+ \to \mathbb{R}^d$, $p : \Omega^{\mathrm{f}} \times \mathbb{R}^+ \to \mathbb{R}$ and the solid displacement and velocity $\boldsymbol{d} : \Sigma \times \mathbb{R}^+ \to \mathbb{R}^d$, $\dot{\boldsymbol{d}} : \Sigma \times \mathbb{R}^+ \to \mathbb{R}^d$ such that

$$\begin{cases} \Omega^{\mathrm{f}}(t) \stackrel{\mathrm{def}}{=} \Omega^{\mathrm{f}} \backslash \Sigma(t), \quad \Sigma(t) = \boldsymbol{\phi}_t(\Sigma), \quad \boldsymbol{\phi}_t \stackrel{\mathrm{def}}{=} \boldsymbol{I}_\Sigma + \boldsymbol{d}(t), \\ \qquad \rho^{\mathrm{f}}\big(\partial_t \boldsymbol{u} + (\boldsymbol{u} \cdot \nabla)\boldsymbol{u}\big) - \mathbf{div}\boldsymbol{\sigma}(\boldsymbol{u}, p) = \boldsymbol{0} \quad \text{in} \quad \Omega^{\mathrm{f}}(t), \\ \qquad\qquad\qquad\qquad \mathrm{div}\boldsymbol{u} = 0 \quad \text{in} \quad \Omega^{\mathrm{f}}(t), \\ \qquad\qquad\qquad\qquad \boldsymbol{u} = \boldsymbol{0} \quad \text{on} \quad \Gamma^{\mathrm{f}}, \end{cases} \tag{6.29}$$

$$\begin{cases} \boldsymbol{u}_1 = \boldsymbol{u}_2 = \dot{\boldsymbol{d}} \circ \boldsymbol{\phi}_t^{-1} \quad \text{on} \quad \Sigma(t), \\ \boldsymbol{d}(t) \in \boldsymbol{W}, \quad \dot{\boldsymbol{d}} = \partial_t \boldsymbol{d}, \\ \rho^{\mathrm{s}} \epsilon\big(\partial_t \dot{\boldsymbol{d}}, \boldsymbol{w}\big)_\Sigma + a^{\mathrm{s}}\big(\boldsymbol{d}, \boldsymbol{w}\big) = -\displaystyle\int_{\Sigma(t)} [\![\boldsymbol{\sigma}(\boldsymbol{u}, p)\boldsymbol{n}]\!] \cdot \boldsymbol{w} \circ \boldsymbol{\phi}_t^{-1} \quad \forall \boldsymbol{w} \in \boldsymbol{W}, \end{cases} \tag{6.30}$$

complemented with standard initial conditions $\boldsymbol{u}(0) = \boldsymbol{u}_0$, $\boldsymbol{d}(0) = \boldsymbol{d}_0$ and $\dot{\boldsymbol{d}}(0) = \dot{\boldsymbol{d}}_0$. We recall that $\boldsymbol{W} \subset [H^1(\Sigma)]^d$ denotes the space of solid admissible displacements and $a^{\mathrm{s}} : \boldsymbol{W} \times \boldsymbol{W} \to \mathbb{R}$ describes the (possibly non-linear) elastic behavior of the structure.

For the fluid, we consider the same velocity and pressure functional spaces as in Section 6.2 and we introduce the convective trilinear form

$$c_{\Omega^{\mathrm{f}}}(\boldsymbol{z}, \boldsymbol{u}, \boldsymbol{v}) \stackrel{\mathrm{def}}{=} \rho^{\mathrm{f}}\big(\boldsymbol{z} \cdot \boldsymbol{\nabla}\boldsymbol{u}, \boldsymbol{v}\big)_{\Omega^{\mathrm{f}}}. \tag{6.31}$$

We recall that, if $\boldsymbol{z} \in \{\boldsymbol{v} \in \boldsymbol{V} \,/\, \mathrm{div}\boldsymbol{v} = 0 \text{ in } \Omega^{\mathrm{f}}\}$, using integration by parts we have

$$c_{\Omega^{\mathrm{f}}}(\boldsymbol{z}, \boldsymbol{v}, \boldsymbol{v}) = 0 \quad \forall \boldsymbol{v} \in \boldsymbol{V}. \tag{6.32}$$

The weak form of the linear coupled problem (6.29)-(6.30) reads as follows: for $t > 0$, find

$$(\boldsymbol{u}(t), p(t), \boldsymbol{d}(t), \dot{\boldsymbol{d}}(t)) \in \boldsymbol{V} \times Q \times \boldsymbol{W} \times \boldsymbol{W}$$

such that

$$\begin{cases} \boldsymbol{\phi}_t = \boldsymbol{I}_\Sigma + \boldsymbol{d}(t), \quad \Sigma(t) = \boldsymbol{\phi}_t(\Sigma), \\ \boldsymbol{u}_1 = \boldsymbol{u}_2 = \dot{\boldsymbol{d}} \circ \boldsymbol{\phi}_t^{-1} \quad \text{on} \quad \Sigma(t), \quad \dot{\boldsymbol{d}} = \partial_t \boldsymbol{d}, \\ \rho^{\mathrm{f}}(\partial_t \boldsymbol{u}, \boldsymbol{v})_\Omega + c_{\Omega^{\mathrm{f}}}(\boldsymbol{u}, \boldsymbol{u}, \boldsymbol{v}) + a^{\mathrm{f}}_{\Omega^{\mathrm{f}}}\big((\boldsymbol{u}, p), (\boldsymbol{v}, q)\big) \\ \quad + \rho^{\mathrm{s}} \epsilon \big(\partial_t \dot{\boldsymbol{d}}, \boldsymbol{w}\big)_\Sigma + a^{\mathrm{s}}(\boldsymbol{d}, \boldsymbol{w}) = 0 \end{cases} \tag{6.33}$$

for all $(\boldsymbol{v}, q, \boldsymbol{w}) \in \boldsymbol{V} \times Q \times \boldsymbol{W}$ with $\boldsymbol{v}|_{\Sigma(t)} = \boldsymbol{w} \circ \boldsymbol{\phi}_t^{-1}$.

Assuming that $a^{\mathrm{s}}(\boldsymbol{d}, \partial_t \boldsymbol{d}) = \frac{1}{2}\partial_t a^{\mathrm{s}}(\boldsymbol{d}, \boldsymbol{d})$, taking $(\boldsymbol{v}, q, \boldsymbol{w}) = (\boldsymbol{u}(t), p(t), \dot{\boldsymbol{d}}(t))$ in (6.33) and using (6.32) we retrieve an energy equality similar to (6.4).

6.3.2 Numerical methods

The next section presents the formulation of the numerical methods introduced in Section 6.2.3 within the framework of the non-linear coupled problem (6.29)-(6.30). The basic idea consists in combining the different coupling paradigms with an explicit treatment of the geometrical compatibility $(6.29)_1$. Finally, in Section 6.3.2.2, we briefly comment on how to handle the integration of quantities associated with different time levels.

6.3.2.1 Nitsche-XFEM formulation and coupling schemes

For simplicity, we assume that Ω^{f} and Σ are polyhedral. We consider the general case in which the interface partially intersects the fluid domain (see Figure 6.9). The approximation space for the solid, $\boldsymbol{W}_h$, is the same as in Section 6.2.1. For a given discrete displacement $\boldsymbol{d}_h^{n-1} \in \boldsymbol{W}_h$ at time level $n-1$, we introduce its corresponding deformation map $\boldsymbol{\phi}_h^{n-1} \overset{\mathrm{def}}{=} \boldsymbol{I}_\Sigma + \boldsymbol{d}_h^{n-1}$. The current configuration (i.e., at time level n) of the discrete interface is defined as

$$\Sigma_h^n \overset{\mathrm{def}}{=} \boldsymbol{\phi}_h^{n-1}(\Sigma). \tag{6.34}$$

In other words, the geometric compatibility $(6.29)_1$ is treated in an explicit fashion.

For the construction of the fluid discrete spaces, we proceed as in Section 6.2.1.3 with the sole difference that, in the present framework, the fluid-solid interface Σ_h^n depends on the discrete displacement $\boldsymbol{d}_h^{n-1}$. As a result, the fictitious fluid-fluid interface $\widetilde{\Sigma}_h^n \cup \widehat{\Sigma}_h^n$ and the fluid spaces, $\boldsymbol{V}_h^n$ and Q_h^n given by (6.11), depend both on the mesh step h and on the time level n. We recall that the functions of these

spaces are continuous in the fluid domain

$$\Omega_h^n \overset{\text{def}}{=} \Omega^{\text{f}} \backslash \big(\Sigma_h^n \cup \widetilde{\Sigma}_h^n\big),$$

but discontinuous across the moving interface $\Sigma_h^n \cup \widetilde{\Sigma}_h^n$.

It should be noted that the discrete fluid velocities do not satisfy the assumptions of (6.32), namely, they are not divergence free and $\boldsymbol{V}_h^n \not\subset \boldsymbol{V}$. Therefore, we need to modify the trilinear form (6.31) in order to retrieve a suitable discrete counterpart of (6.32). This is a well-known issue when dealing with *discontinuous Galerkin approximations* of the Navier-Stokes equations (see, e.g., [DPE12, Section 6.2.2]). The key idea consists in combining the so-called *Temam's trick* with the fact that, owing to $(6.30)_1$, the velocity field $\boldsymbol{u}$ is continuous across $\Sigma_h^n \cup \widetilde{\Sigma}_h^n$. To this purpose, we introduce the discrete trilinear form

$$\begin{aligned} c_h^n(\boldsymbol{z}_h, \boldsymbol{u}_h, \boldsymbol{v}_h) \overset{\text{def}}{=} c_{\Omega_h^n}(\boldsymbol{z}_h, \boldsymbol{u}_h, \boldsymbol{v}_h) + \frac{\rho^{\text{f}}}{2}\big((\text{div}\boldsymbol{z}_h)\boldsymbol{u}_h, \boldsymbol{v}_h\big)_{\Omega_h^n} \\ - \rho^{\text{f}}\big(\{\!\{\boldsymbol{z}_h\}\!\} \cdot \boldsymbol{n}[\![\boldsymbol{u}_h]\!], \{\!\{\boldsymbol{v}_h\}\!\}\big)_{\Sigma_h^n \cup \widetilde{\Sigma}_h^n} - \frac{\rho^{\text{f}}}{2}\big([\![\boldsymbol{z}_h \cdot \boldsymbol{n}]\!], \{\!\{\boldsymbol{u}_h \cdot \boldsymbol{v}_h\}\!\}\big)_{\Sigma_h^n \cup \widetilde{\Sigma}_h^n}. \end{aligned}$$

Note that the last three terms are strongly consistent. Moreover, using integration by parts in Ω_h^n we can infer that, if $\boldsymbol{z}_h \in \boldsymbol{V}_h^n$, there holds

$$c_h^n(\boldsymbol{z}_h, \boldsymbol{v}_h, \boldsymbol{v}_h) = 0 \quad \forall \boldsymbol{v}_h \in \boldsymbol{V}_h^n. \tag{6.35}$$

To cope with the numerical instabilities related to the inf-sup incompatibility of the discrete spaces and to large local Reynolds numbers, we need to resort to a stabilisation method (see, e.g., [BH82, HFB86, Tez92, Cod02, BFH06, BBJL07, BF07, GT10, APV15] and the references therein). The objective of such a procedure is basically twofold: guarantee the well-posedness of the discrete problem and improve the convergence of the approximations while limiting the propagation of spurious oscillations. A successful approach is the so-called SUPG/PSPG method (see, e.g., [BH82, HFB86, Tez92]), which offers an unified treatment of the velocity and pressure stabilization by adding to the Galerkin formulation an element-wise weighted residual of the equation. The residual based nature of the stabilization operator guarantees the consistency of the method.

Within the present unfitted framework this last property is more delicate. Indeed, as discussed in Section 6.2.1.1 (see also [BH14, BF14b]), the theoretical analysis indicates that the stabilization operator must act on the whole computational domain, that is, including the fictitious zone of the overlapping region. However, in this zone, we cannot guarantee that the residual of a smooth extension of the solution vanishes. An alternative to circumvent this issue (see also [SW14]) is to use symmetric stabilization methods whose consistency does not rely on the residual (see, e.g., [Cod02, BFH06, BF07, GT10, APV15]). As an example, we consider here the *continuous interior penalty* (CIP) stabilization method of [BFH06, BF07]. To this purpose, we first introduce the set $\mathcal{F}_{i,h}^n$ of interior edges or faces of $\mathcal{T}_{i,h}^{n,\text{f}}$. The

ALGORITHM 6.4 Non-linear version of Algorithm 6.1.

For $n \geq 1$,

1. Interface update: $\boldsymbol{\phi}_h^{n-1} = \boldsymbol{I}_\Sigma + \boldsymbol{d}_h^{n-1}$, $\Sigma_h^n = \boldsymbol{\phi}_h^{n-1}(\Sigma)$, $\Omega_h^n = \Omega^{\mathrm{f}} \backslash \big(\Sigma_h^n \cup \widetilde{\Sigma}_h^n\big)$.
2. Find $\big(\boldsymbol{u}_h^n, p_h^n, \dot{\boldsymbol{d}}_h^n, \boldsymbol{d}_h^n\big) \in \boldsymbol{V}_h^n \times Q_h^n \times \boldsymbol{W}_h \times \boldsymbol{W}_h$, such that $\dot{\boldsymbol{d}}_h = \partial_\tau \boldsymbol{d}_h^n$ and

$$\begin{cases} \rho^{\mathrm{f}}\big(\partial_\tau \boldsymbol{u}_h^n, \boldsymbol{v}_h\big)_{\Omega^{\mathrm{f}}} + a_h^{\mathrm{f},n}\big(\boldsymbol{u}_h^n; (\boldsymbol{u}_h^n, p_h^n), (\boldsymbol{v}_h, q_h)\big) + \rho^{\mathrm{s}}\epsilon\big(\partial_\tau \dot{\boldsymbol{d}}_h^n, \boldsymbol{w}_h\big)_\Sigma + a^{\mathrm{s}}(\boldsymbol{d}_h^n, \boldsymbol{w}_h) \\ - \displaystyle\sum_{i=1}^{2} \big(\boldsymbol{\sigma}(\boldsymbol{u}_{i,h}^n, p_{i,h}^n)\boldsymbol{n}_i, \boldsymbol{v}_{i,h} - \boldsymbol{w}_h\big)_{\Sigma_h^n} - \sum_{i=1}^{2} \big(\boldsymbol{u}_{i,h}^n - \dot{\boldsymbol{d}}_h^n, \boldsymbol{\sigma}(\boldsymbol{v}_{i,h}, -q_{i,h})\boldsymbol{n}_i\big)_{\Sigma_h^n} \\ - \big(\{\!\{\boldsymbol{\sigma}(\boldsymbol{u}_h^n, p_h^n)\}\!\}\boldsymbol{n}, [\![\boldsymbol{v}_h]\!]\big)_{\widetilde{\Sigma}_h^n} - \big(\{\!\{\boldsymbol{\sigma}(\boldsymbol{v}_h, -q_h)\}\!\}\boldsymbol{n}, [\![\boldsymbol{u}_h^n]\!]\big)_{\widetilde{\Sigma}_h^n} \\ + \dfrac{\gamma\mu}{h} \displaystyle\sum_{i=1}^{2} \big(\boldsymbol{u}_{i,h}^n - \dot{\boldsymbol{d}}_h^n, \boldsymbol{v}_{i,h} - \boldsymbol{w}_h\big)_{\Sigma_h^n} + \dfrac{\gamma\mu}{h}\big([\![\boldsymbol{u}_h^n]\!], [\![\boldsymbol{v}_h]\!]\big)_{\widetilde{\Sigma}_h^n} = 0 \end{cases}$$

for all $(\boldsymbol{v}_h, q_h, \boldsymbol{w}_h) \in \boldsymbol{V}_h^n \times Q_h^n \times \boldsymbol{W}_h$.

corresponding velocity and pressure stabilization operators are, respectively, given by the relations

$$\begin{aligned} s_{\mathrm{v},h}^n(\boldsymbol{z}_h; \boldsymbol{u}_h, \boldsymbol{v}_h) &\overset{\mathrm{def}}{=} \gamma_{\mathrm{v},1} h^2 \sum_{i=1}^{2} \sum_{F \in \mathcal{F}_{i,h}^n} \xi\big(\mathrm{Re}_F(\boldsymbol{z}_h)\big) \|\boldsymbol{z}_h \cdot \boldsymbol{n}\|_{L^\infty(F)} \big([\![\boldsymbol{\nabla}\boldsymbol{u}_h]\!]_F, [\![\boldsymbol{\nabla}\boldsymbol{v}_h]\!]_F\big)_F \\ &\quad + \gamma_{\mathrm{v},2} h^2 \sum_{i=1}^{2} \sum_{F \in \mathcal{F}_{i,h}^n} \|\boldsymbol{z}_h\|_{L^\infty(F)} \big([\![\mathrm{div}\boldsymbol{u}_h]\!]_F, [\![\mathrm{div}\boldsymbol{v}_h]\!]_F\big)_F, \\ s_{\mathrm{p},h}^n(\boldsymbol{z}_h; p_h, q_h) &\overset{\mathrm{def}}{=} \gamma_{\mathrm{p}} h^2 \sum_{i=1}^{2} \sum_{F \in \mathcal{F}_{i,h}^n} \frac{\xi\big(\mathrm{Re}_F(\boldsymbol{z}_h)\big)}{\|\boldsymbol{z}_h\|_{L^\infty(F)}} \big([\![\boldsymbol{\nabla} p_h]\!]_F, [\![\boldsymbol{\nabla} q_h]\!]_F\big)_F, \end{aligned} \tag{6.36}$$

where $\mathrm{Re}_F(\boldsymbol{z}_h) \overset{\mathrm{def}}{=} \rho^{\mathrm{f}} \|\boldsymbol{z}_h\|_{L^\infty(F)} h \mu^{-1}$ denotes the local Reynolds number, $\xi(x) \overset{\mathrm{def}}{=} \min\{1, x\}$ is a cut-off function and $\gamma_{\mathrm{p}}, \gamma_{\mathrm{v},i} > 0$, $i = 1, 2$, are user-defined parameters. At last, we collect all the above fluid contributions in a single term

$$\begin{aligned} a_h^{\mathrm{f},n}\big(\boldsymbol{z}_h; (\boldsymbol{u}_h, p_h), (\boldsymbol{v}_h, q_h)\big) &\overset{\mathrm{def}}{=} c_h^n(\boldsymbol{z}_h, \boldsymbol{u}_h, \boldsymbol{v}_h) + a_{\Omega_h^n}^{\mathrm{f}}\big((\boldsymbol{u}_h, p_h), (\boldsymbol{v}_h, q_h)\big) \\ &\quad + s_{\mathrm{v},h}^n(\boldsymbol{z}_h; \boldsymbol{u}_h, \boldsymbol{v}_h) + s_{\mathrm{p},h}^n(\boldsymbol{z}_h; p_h, q_h) + g_h^n(\boldsymbol{u}_h, \boldsymbol{v}_h), \end{aligned} \tag{6.37}$$

with the time-dependent ghost-penalty operator now given by

$$g_h^n(\boldsymbol{u}_h, \boldsymbol{v}_h) \overset{\mathrm{def}}{=} \gamma_{\mathrm{g}} \mu h \sum_{i=1}^{2} \sum_{F \in \mathcal{F}_{i,h}^{n,\Sigma}} \big([\![\boldsymbol{\nabla}\boldsymbol{u}_{i,h}]\!]_F, [\![\boldsymbol{\nabla}\boldsymbol{v}_{i,h}]\!]_F\big)_F \tag{6.38}$$

Algorithm 6.5 Non-linear version of Algorithm 6.2.

For $n \geq 1$:

1. Interface update: $\boldsymbol{\phi}_h^{n-1} = \boldsymbol{I}_\Sigma + \boldsymbol{d}_h^{n-1}$, $\Sigma_h^n = \boldsymbol{\phi}_h^{n-1}(\Sigma)$, $\Omega_h^n = \Omega^{\mathrm{f}} \backslash \big(\Sigma_h^n \cup \widetilde{\Sigma}_h^n\big)$.

2. Set initial guess for predictor:

$$\boldsymbol{u}_h^{n,0} = \boldsymbol{u}_h^{n,\star}, \quad p_h^{n,0} = p_h^{n-1}, \quad \boldsymbol{d}_h^{n,0} = \boldsymbol{d}_h^{n-1}, \quad \dot{\boldsymbol{d}}_h^{n,0} = \dot{\boldsymbol{d}}_h^{n-1}.$$

3. Correction iterations. For $k = 1, \ldots, K+1$:

   (a) Find $\big(\dot{\boldsymbol{d}}_h^{n,k}, \boldsymbol{d}_h^{n,k}\big) \in \boldsymbol{W}_h \times \boldsymbol{W}_h$ with $\dot{\boldsymbol{d}}_h^{n,k} = \partial_\tau \boldsymbol{d}_h^{n,k}$ and such that

$$\begin{cases} \rho^{\mathrm{s}} \epsilon \big(\partial_\tau \dot{\boldsymbol{d}}_h^{n,k}, \boldsymbol{w}_h\big)_\Sigma + a^{\mathrm{s}}(\boldsymbol{d}_h^{n,k}, \boldsymbol{w}_h) + \dfrac{2\gamma\mu}{h} \big(\dot{\boldsymbol{d}}_h^{n,k}, \boldsymbol{w}_h\big)_{\Sigma_h^n} \\ \quad = \dfrac{2\gamma\mu}{h} \big(\{\!\{ \boldsymbol{u}_h^{n,k-1} \}\!\}, \boldsymbol{w}_h\big)_{\Sigma_h^n} - \big([\![\boldsymbol{\sigma}(\boldsymbol{u}_h^{n,k-1}, p_h^{n,k-1}) \boldsymbol{n}]\!], \boldsymbol{w}_h\big)_{\Sigma_h^n} \end{cases}$$

   for all $\boldsymbol{w}_h \in \boldsymbol{W}_h$.

   (b) Find $(\boldsymbol{u}_h^{n,k}, p_h^{n,k}) \in \boldsymbol{V}_h^n \times Q_h^n$ such that

$$\begin{cases} \rho^{\mathrm{f}} \big(\partial_\tau \boldsymbol{u}_h^{n,k}, \boldsymbol{v}_h\big)_{\Omega^{\mathrm{f}}} + a_h^{\mathrm{f},n}\big(\boldsymbol{u}_h^{n,k}; (\boldsymbol{u}_h^{n,k}, p_h^{n,k}), (\boldsymbol{v}_h, q_h)\big) + \dfrac{\gamma\mu}{h} \displaystyle\sum_{i=1}^{2} \big(\boldsymbol{u}_{i,h}^{n,k}, \boldsymbol{v}_{i,h}\big)_{\Sigma_h^n} \\ - \displaystyle\sum_{i=1}^{2} \big(\boldsymbol{u}_{i,h}^{n,k} - \dot{\boldsymbol{d}}_h^{n,k}, \boldsymbol{\sigma}(\boldsymbol{v}_{i,h}, -q_{i,h}) \boldsymbol{n}_i\big)_{\Sigma_h^n} + \dfrac{\gamma_0 h}{\gamma\mu} \displaystyle\sum_{i=1}^{2} \big(p_{i,h}^{n,k} - p_{i,h}^{n,k-1}, q_{i,h}\big)_{\Sigma_h^n} \\ - \big(\{\!\{ \boldsymbol{\sigma}(\boldsymbol{u}_h^{n,k}, p_h^{n,k}) \}\!\} \boldsymbol{n}, [\![\boldsymbol{v}_h]\!]\big)_{\widetilde{\Sigma}_h^n} - \big(\{\!\{ \boldsymbol{\sigma}(\boldsymbol{v}_h, -q_h) \}\!\} \boldsymbol{n}, [\![\boldsymbol{u}_h^{n,k}]\!]\big)_{\widetilde{\Sigma}_h^n} \\ + \dfrac{\gamma\mu}{h} \big([\![\boldsymbol{u}_h^{n,k}]\!], [\![\boldsymbol{v}_h]\!]\big)_{\widetilde{\Sigma}_h^n} = \dfrac{\gamma\mu}{h} \displaystyle\sum_{i=1}^{2} \big(\dot{\boldsymbol{d}}_h^{n,k}, \boldsymbol{v}_{i,h}\big)_{\Sigma_h^n} \\ + \displaystyle\sum_{i=1}^{2} \big(\boldsymbol{\sigma}(\boldsymbol{u}_{i,h}^{n,k-1}, p_{i,h}^{n,k-1}) \boldsymbol{n}_i, \boldsymbol{v}_{i,h}\big)_{\Sigma_h^n} \end{cases}$$

   for all $(\boldsymbol{v}_h, q_h) \in \boldsymbol{V}_h^n \times Q_h^n$.

4. Set $\boldsymbol{u}_h^n = \boldsymbol{u}_h^{n,K+1}$, $p_h^n = p_h^{n,K+1}$, $\boldsymbol{d}_h^n = \boldsymbol{d}_h^{n,K+1}$, $\dot{\boldsymbol{d}}_h^n = \dot{\boldsymbol{d}}_h^{n,K+1}$.

and where $\mathcal{F}_{i,h}^{n,\Sigma}$ denotes the set of interior edges or faces of the elements intersected by Σ_h^n.

We now have all the ingredients to extend the numerical methods of Section 6.2.3 to the approximation of the non-linear coupled problem (6.29)-(6.30). By combining the explicit treatment of the geometric compatibility (6.34) with the implicit coupling paradigm of Section 6.2.3.1 we get the solution procedure given in Algorithm 6.4.

ALGORITHM 6.6 Non-linear version of Algorithm 6.3.

For $n > r$:

1. Interface update: $\boldsymbol{\phi}_h^{n-1} = \boldsymbol{I}_\Sigma + \boldsymbol{d}_h^{n-1}$, $\Sigma_h^n = \boldsymbol{\phi}_h^{n-1}(\Sigma)$, $\Omega_h^n = \Omega^{\mathrm{f}} \backslash \big(\Sigma_h^n \cup \widetilde{\Sigma}_h^n\big)$.

2. Find $\big(\boldsymbol{u}_h^n, p_h^n, \dot{\boldsymbol{d}}_h^{n-\frac{1}{2}}\big) \in \boldsymbol{V}_h \times Q_h \times \boldsymbol{W}_h$ such that

$$\begin{cases} \rho^{\mathrm{f}}\big(\partial_\tau \boldsymbol{u}_h^n, \boldsymbol{v}_h\big)_{\Omega^{\mathrm{f}}} + a_h^{\mathrm{f},n}\big(\boldsymbol{u}_h^n; (\boldsymbol{u}_h^n, p_h^n), (\boldsymbol{v}_h, q_h)\big) + \dfrac{\rho^{\mathrm{s}}\epsilon}{\tau}\big(\dot{\boldsymbol{d}}_h^{n-\frac{1}{2}}, \boldsymbol{w}_h\big)_\Sigma \\ - \displaystyle\sum_{i=1}^{2} \big(\boldsymbol{\sigma}(\boldsymbol{u}_{i,h}^n, p_{i,h}^n)\boldsymbol{n}_i, \boldsymbol{v}_{i,h} - \boldsymbol{w}_h\big)_{\Sigma_h^n} - \displaystyle\sum_{i=1}^{2} \big(\boldsymbol{u}_{i,h}^n - \dot{\boldsymbol{d}}_h^{n-\frac{1}{2}}, \boldsymbol{\sigma}(\boldsymbol{v}_{i,h}, -q_{i,h})\boldsymbol{n}_i\big)_{\Sigma_h^n} \\ + \displaystyle\sum_{i=1}^{2} \frac{\gamma\mu}{h}\big(\boldsymbol{u}_{i,h}^n - \dot{\boldsymbol{d}}_h^{n-\frac{1}{2}}, \boldsymbol{v}_{i,h} - \boldsymbol{w}_h\big)_{\Sigma_h^n} - \big(\{\!\{\boldsymbol{\sigma}(\boldsymbol{u}_h^n, p_h^n)\}\!\}\boldsymbol{n}, [\![\boldsymbol{v}_h]\!]\big)_{\widetilde{\Sigma}_h^n} \\ - \big(\{\!\{\boldsymbol{\sigma}(\boldsymbol{v}_h, -q_h)\}\!\}\boldsymbol{n}, [\![\boldsymbol{u}_h^n]\!]\big)_{\widetilde{\Sigma}_h^n} + \dfrac{\gamma\mu}{h}\big([\![\boldsymbol{u}_h^n]\!], [\![\boldsymbol{v}_h]\!]\big)_{\widetilde{\Sigma}_h^n} = \dfrac{\rho^{\mathrm{s}}\epsilon}{\tau}\big(\dot{\boldsymbol{d}}_h^{n-1} + \tau\partial_\tau \dot{\boldsymbol{d}}_h^{n,\star}, \boldsymbol{w}_h\big)_\Sigma \\ + \big([\![\boldsymbol{\sigma}(\boldsymbol{u}_h^{n,\star}, p_h^{n,\star})\boldsymbol{n}]\!], \boldsymbol{w}_h\big)_{\Sigma_h^n} - \dfrac{2\gamma\mu}{h}\big(\{\!\{\boldsymbol{u}_h^{n,\star}\}\!\} - \dot{\boldsymbol{d}}_h^{n-\frac{1}{2},\star}, \boldsymbol{w}_h\big)_{\Sigma_h^n} \end{cases}$$

   for all $(\boldsymbol{v}_h, q_h, \boldsymbol{w}_h) \in \boldsymbol{V}_h^n \times Q_h^n \times \boldsymbol{W}_h$.

3. Find $\big(\dot{\boldsymbol{d}}_h^n, \boldsymbol{d}_h^n\big) \in \boldsymbol{W}_h \times \boldsymbol{W}_h$ with $\dot{\boldsymbol{d}}_h^n = \partial_\tau \boldsymbol{d}_h^n$ and such that

$$\begin{cases} \rho^{\mathrm{s}}\epsilon\big(\partial_\tau \dot{\boldsymbol{d}}_h^n, \boldsymbol{w}_h\big)_\Sigma + a^{\mathrm{s}}(\boldsymbol{d}_h^n, \boldsymbol{w}_h) = -\big([\![\boldsymbol{\sigma}(\boldsymbol{u}_h^n, p_h^n)\boldsymbol{n}]\!], \boldsymbol{w}_h\big)_{\Sigma_h^n} \\ + \dfrac{2\gamma\mu}{h}\big(\{\!\{\boldsymbol{u}_h^n\}\!\} - \dot{\boldsymbol{d}}_h^{n-\frac{1}{2}}, \boldsymbol{w}_h\big)_{\Sigma_h^n} \end{cases}$$

   for all $\boldsymbol{w}_h \in \boldsymbol{W}_h$.

REMARK 6.9 *In Algorithms 6.4, all the appearances of $\dot{\boldsymbol{d}}_h^n$ and $\boldsymbol{w}_h$ in the interface terms of Σ_h^n must be understood as $\dot{\boldsymbol{d}}_h^n \circ (\boldsymbol{\phi}_h^n)^{-1}$ and $\boldsymbol{w}_h \circ (\boldsymbol{\phi}_h^n)^{-1}$, respectively. The purpose of this little abuse of notation is simply to ease the presentation.*

In Algorithm 6.5 we have reported the non-linear counterpart of the stabilized explicit coupling paradigm of Section 6.2.3.2. It should be noted that the $K \geq 0$ corrections are performed with the same configuration of the interface Σ_h^n. At last, Algorithm 6.6 presents the extension of the semi-implicit scheme introduced in Section 6.2.3.3 to the present non-linear framework.

The stability results of Theorems 6.2-6.4 remain valid for Algorithm 6.4, Algorithm 6.5 with $K = 0$ and $r = 1$, and Algorithm 6.6, respectively. The proofs follow by combining the identity (6.35) with the result of Lemma 6.1 and the arguments used in the proofs of the static case (Section 6.2.3). This shows that the explicit treatment of the interface location in the fluid, (6.34), does not compromise the energy stability of the methods. Similar conclusions are known for strongly coupled time discretizations of the immersed boundary method (see, e.g.,

[NFGK07, BCG15]).

It should be noted, however, that the semi-implicit schemes of Algorithm 6.6 have a reduced computational complexity with respect to alternative schemes used in the immersed boundary method (see, e.g., [NFGK07, BCG15]), which treat the fluid-solid kinematic-dynamic coupling in a fully implicit fashion (strong coupling), as Algorithm 6.4.

6.3.2.2 Integrals with discontinuous functions at different time levels

At each time level, the first step of Algorithms 6.4-6.6 involves the computation of the new interface intersections and the new sub-divisions of the cut elements. In other words, we perform the intersection algorithm of Section 6.2.2.1 at each time-step. Some of the fluid integrals in Algorithms 6.4-6.6, however, involve fluid discrete functions associated with different time levels, namely, the bulk term related to the time-stepping scheme in the fluid,

$$\frac{\rho^{\mathrm{f}}}{\tau}(\boldsymbol{u}_h^{n-1}, \boldsymbol{v}_h)_{\Omega^{\mathrm{f}}},$$

and the interface terms

$$\big(\boldsymbol{\sigma}(\boldsymbol{u}_{i,h}^{n-1}, p_{i,h}^{n-1})\boldsymbol{n}_i, \boldsymbol{v}_{i,h}\big)_{\Sigma_h^n}, \quad \frac{\gamma_0 h}{\gamma\mu}\big(p_{i,h}^{n-1}, q_{i,h}\big)_{\Sigma_h^n},$$

associated with the fluid-solid splitting of Algorithm 6.5. A practical difficulty arises

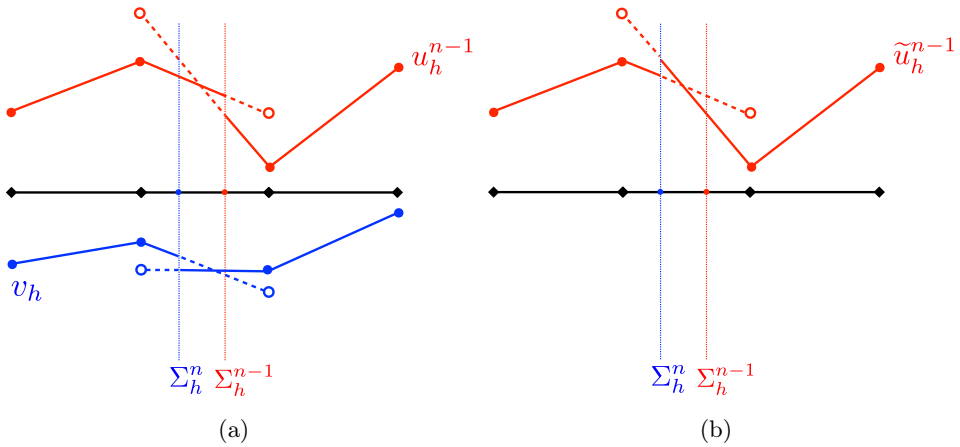

Figure 6.10: The previous solution $u_h^{n-1} \in V_h^{n-1}$ and the test function $v_h \in V_h^n$ are discontinuous at different locations, Σ_h^{n-1} and Σ_h^n respectively, within the same element. The dotted lines represent the value of the functions in the fictitious zone of the overlapping region and the circles the ghost values (a). Approximation of the function u_h^{n-1} with the discontinuity at Σ_h^n (b).

whenever $(\boldsymbol{u}_h^{n-1}, p_h^{n-1}) \in \boldsymbol{V}_h^{n-1} \times Q_h^{n-1}$ and $(\boldsymbol{v}_h, q_h) \in \boldsymbol{V}_h^n \times Q_h^n$ are discontinuous at different locations within the same element. This issue is illustrated in 1D in

Figure 6.10(a), which shows that the evaluation of the bulk terms is much more involved than in the static framework of Section 6.2, since the interface locations at t_{n-1} and t_n have to be considered in the evaluation of the intersections and subdivisions of the same element. Instead, we propose to approximate the quantities defined at t_{n-1} by shifting the discontinuity to the location of the interface at t_n (see Figure 6.10(b)). Basically, this amounts to evaluate part of the functions defined at t_{n-1} in the fictitious zone of the overlapping region. In this sense, it can be viewed as a class of *ghost fluid method* (see, e.g., [Fed02]). A similar approach is discussed in [FZ09] (therein called Alternative 2) in the framework of time-stepping schemes for XFEM methods with dynamic interfaces.

6.4 Numerical experiments

The purpose of this section is to illustrate, via a series of 2D numerical examples, the stability and accuracy of the methods introduced in Sections 6.2.3 and 6.3.2. We consider a simple string model for the solid, so that in (6.2) and (6.30) we have

$$\boldsymbol{d} = \eta \boldsymbol{n}, \quad \boldsymbol{L}^{\mathrm{e}}\boldsymbol{d} = \big(-\lambda_1 \partial_s^2 \eta + \lambda_0 \eta \big) \boldsymbol{n},$$

where $\eta : \Sigma \times \mathbb{R}^+ \to \mathbb{R}$ denotes the normal displacement and $\lambda_1, \lambda_0 > 0$ are given coefficients.

6.4.1 Static interface

We first consider the case of the linear model problem of Section 6.2 (static interface). The next two paragraphs illustrate numerically the accuracy properties of Algorithms 6.1-6.3 in two different configurations. We retrieve, in particular, the convergence rates reported in Section 6.2.3. Along this section, the user-defined parameters of Algorithms 6.1-6.3 are fixed to $\gamma_{\mathrm{p}} = 10^{-3}$, $\gamma_{\mathrm{g}} = 1$, $\gamma = 10^3$ and (in Algorithm 6.2) $\gamma_0 = 1$.

6.4.1.1 Idealized closed valve

The purpose of this first example is to mimic the behavior of a closed valve under a given pressure drop. We consider a rectangular fluid domain with the thin-walled solid immersed along its middle cross section (see Figure 6.11). We take $\Omega = (0, 4) \times (0, 1)$ and $\Sigma = \{2\} \times (0, 1)$ in (6.1)-(6.2). All the units are given in the CGS system. The fluid physical parameters are $\rho^{\mathrm{f}} = 1$ and $\mu = 0.035$. For the solid we have $\rho^{\mathrm{s}} = 1.1$, $\epsilon = 0.1$, $\lambda_1 = E\epsilon/(2(1+\nu))$ and $\lambda_0 = 0$, with Young's modulus $E = 0.75 \cdot 10^6$ and Poisson's ratio $\nu = 0.5$. The external boundary conditions for the fluid problem are shown in Figure 6.11. A steady pressure drop of magnitude $P_0 = 20000$ is enforced between the fluid inlet and outlet boundaries. The structure is fixed on its extremities.

After a brief transition phase, the system reaches a steady state with a pressure jump across the interface. For this simple configuration, the exact solution can be

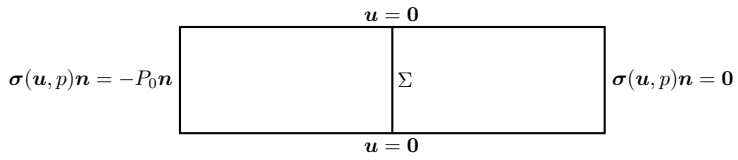

Figure 6.11: Geometric configuration and external boundary conditions.

computed analytically. The fluid and solid velocities vanish and the pressure is a piecewise constant function taking the value P_0 on the left side and zero on the right one. Hence, the solid equation reduces to the single 1D boundary value problem

$$-\lambda_1 \partial_y^2 \eta = [\![p]\!] = P_0 \quad \text{in} \quad (0,1), \quad \eta(0) = \eta(1) = 0, \tag{6.39}$$

whose solution is given by

$$\eta(y) = \frac{P_0}{2\lambda_1} y(1-y). \tag{6.40}$$

This analytic solution is used to evaluate the spatial accuracy of the methods.

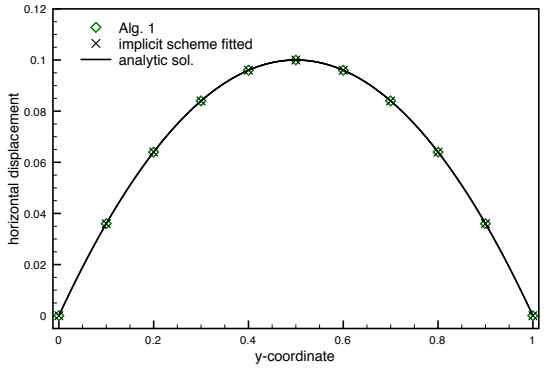

Figure 6.12: Steady state displacement.

Because of the time independent nature of the problem, we limit the discussion to the implicit scheme given by Algorithm 6.1. We consider four pairs of unfitted fluid-solid meshes with increasing degree of refinement, namely,

$$h \in \left\{0.1/2^i\right\}_{i=0}^{3}.$$

For illustration purposes, we have displayed in Figure 6.12 the steady state displacement provided by Algorithm 6.1 for $h = 0.1$, together with the analytical solution (6.40) and the approximation obtained with an implicit fitted method. Note that both the fitted and the unfitted approximations perfectly match the analytical solution. The corresponding pressure fields are reported in Figure 6.13. The unfitted method is able to perfectly capture the pressure drop without spurious oscillations. The overlap of the approximation at the interfacial zone is also clearly visible.

Finally, Figure 6.14 presents the convergence history of the displacement approx-

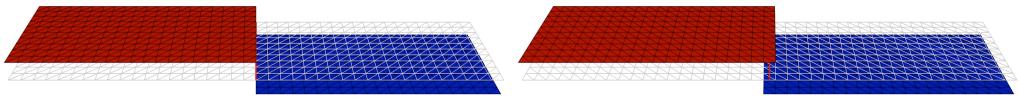

(a) Fitted method (b) Algorithm 6.1

Figure 6.13: Steady state pressure approximations.

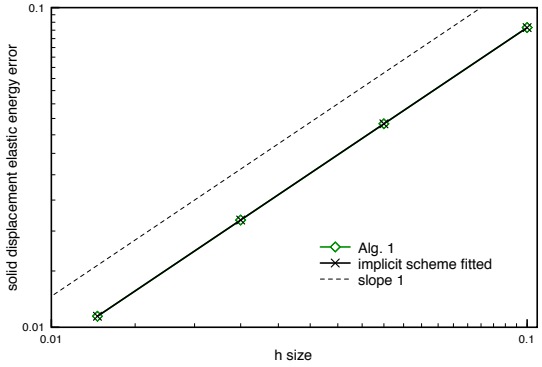

Figure 6.14: Convergence history in space.

imations in the energy norm, for the fitted and the unfitted methods. As expected, we retrieve the optimal first-order convergence rate predicted by Theorem 6.2 for Algorithm 6.1.

6.4.1.2 Pressure-waves

This example is a variant of the problem of the pressure-wave propagation within an elastic tube described in Section 2.4.1 The fluid domain is given by the rectangle $\Omega = (0, 6) \times (0, 0.8)$ and the interface by the segment $\Sigma = (0, 6) \times \{0.54\}$ (see Figure 6.15). As in the previous example, all the units are given in the CGS system. The fluid physical parameters are $\rho^{\mathrm{f}} = 1.0$, $\mu = 0.035$. For the solid we have $\rho^{\mathrm{s}} = 1.1$, $\epsilon = 0.1$, $\lambda_1 = E\epsilon/(2(1+\nu))$ and $\lambda_0 = E\epsilon/(0.25(1-\nu^2))$, with Young's modulus $E = 0.75 \cdot 10^6$ and Poisson's ratio $\nu = 0.5$. The boundary conditions for the fluid are reported in Figure 6.15. On the inlet boundary $\{0\} \times [0, 0.54]$ we impose a sinusoidal pressure $p_{\mathrm{in}}(t)$, of maximal amplitude $2 \cdot 10^4$, during $5 \cdot 10^{-3}$ seconds (half a period). The solid is clamped on its extremities.

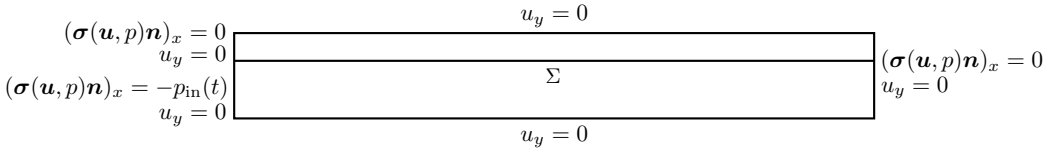

Figure 6.15: Geometric configuration and external boundary conditions.

Figure 6.16 shows some snapshots of the elevated pressure field at three different

time instants obtained with an implicit fitted method and Algorithm 6.1. The zooms included in Figures 6.16(a) and 6.16(b) illustrate the fitted and unfitted nature of the meshes. Algorithm 6.1 gives practically the same accuracy as the fitted method, predicting the propagation of a pressure jump along the tube.

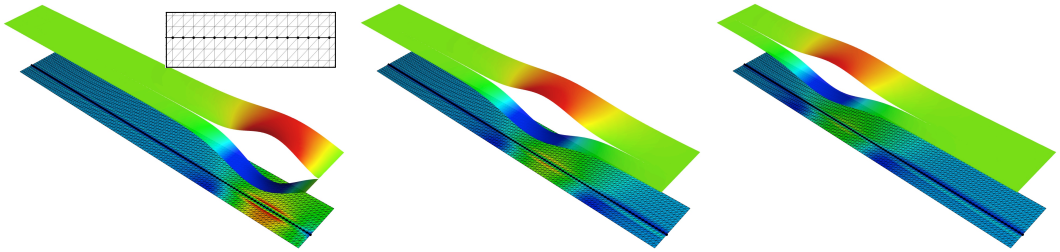

(a) Fitted method

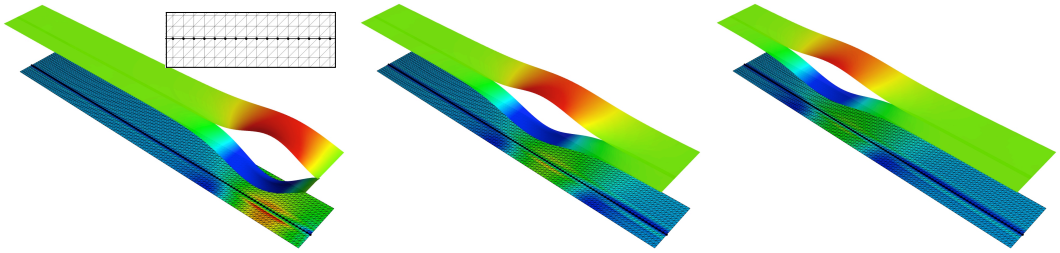

(b) Algorithm 6.1

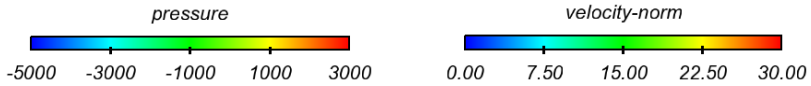

Figure 6.16: Snapshots of the fluid velocity magnitude and elevated pressure at time $t = 0.005$, 0.01, 0.015 (from left to right) obtained with $h = 0.05$ and $\tau = 10^{-4}$.

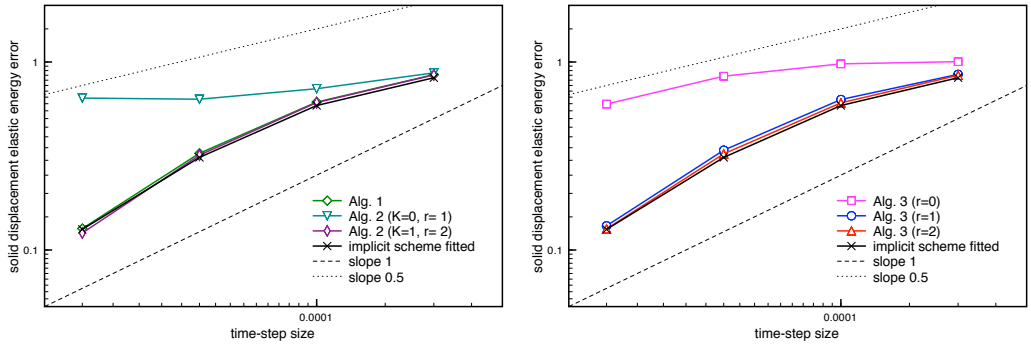

(a) Algorithms 6.1 and 6.2

(b) Algorithm 6.3

Figure 6.17: Time-convergence history of the displacement at $t = 0.015$ obtained with $h = \mathcal{O}(\tau)$.

In order to provide numerical evidence on the convergence rates of Algorithms 6.1–6.3, we have uniformly refined both in time and in space according to the pa-

rameters

$$(\tau, h) \in \left\{(2 \cdot 10^{-4}/2^i, 0.1/2^i)\right\}_{i=0}^{3}. \tag{6.41}$$

Note that $\tau = \mathcal{O}(h)$. A reference solution has been generated with the fitted implicit method using $\tau = 6.25 \cdot 10^{-6}$ and $h = 3.125 \cdot 10^{-3}$ (i.e., $i = 5$ in (6.41)). Figure 6.17 reports the convergence histories of the displacement error in the elastic energy norm at $t = 0.015$ obtained with Algorithms 6.1-6.3. For comparison purposes, the convergence history of the fitted implicit approximations is also displayed. The corresponding displacements, for each level of space-time refinement, are reported in Figures 6.18 and 6.19.

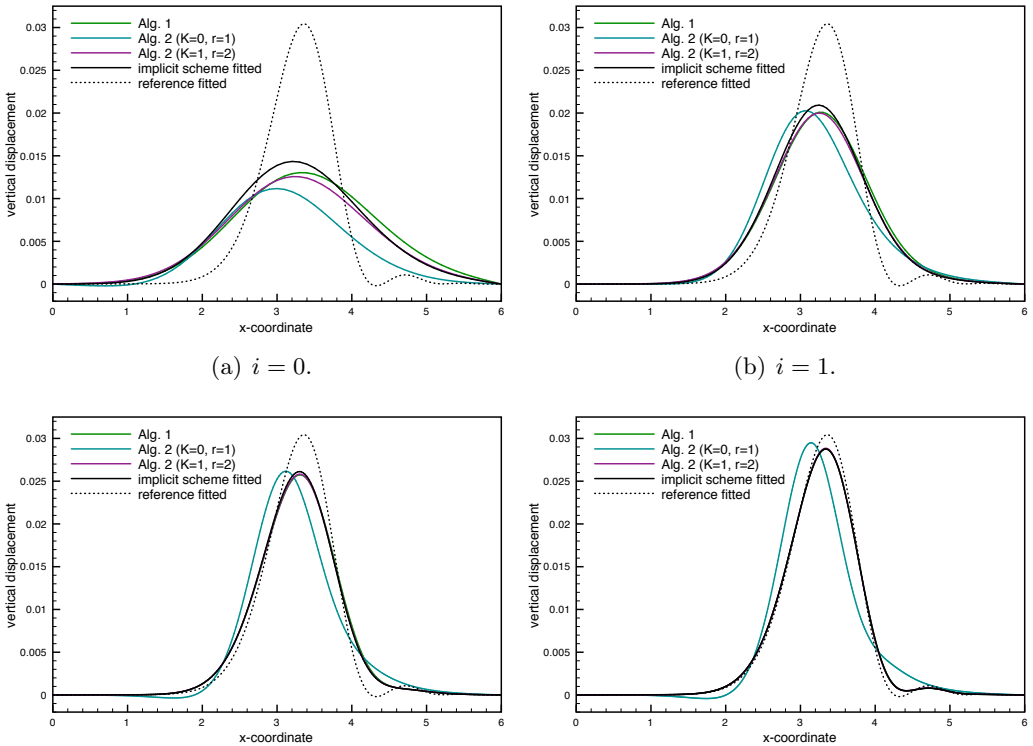

(a) $i = 0$. (b) $i = 1$.

(c) $i = 2$. (d) $i = 3$.

Figure 6.18: Algorithms 6.1 and 6.2. Comparison of the solid displacements at $t = 0.015$ for different levels of (τ, h)-refinement (6.41).

Figure 6.17(a) retrieves the first-order optimal convergence rate predicted by Theorem 6.2 for Algorithm 6.1. This convergent behavior is also clearly visible in Figure 6.18, which points out the good agreement with the approximations provided by the implicit fitted method. As regards Algorithm 6.2, Figure 6.17(a) indicates that the variant without extrapolation ($K = 0, r = 1$) fails to converge under $\tau = \mathcal{O}(h)$. On the contrary, stable and first-order accurate approximations are obtained with a second-order prediction and one correction iteration ($K = 1, r = 2$). This behavior is also clearly visible in Figure 6.18, hence confirming the theoretical discussion on the accuracy of the methods of Section 6.2.3.2.

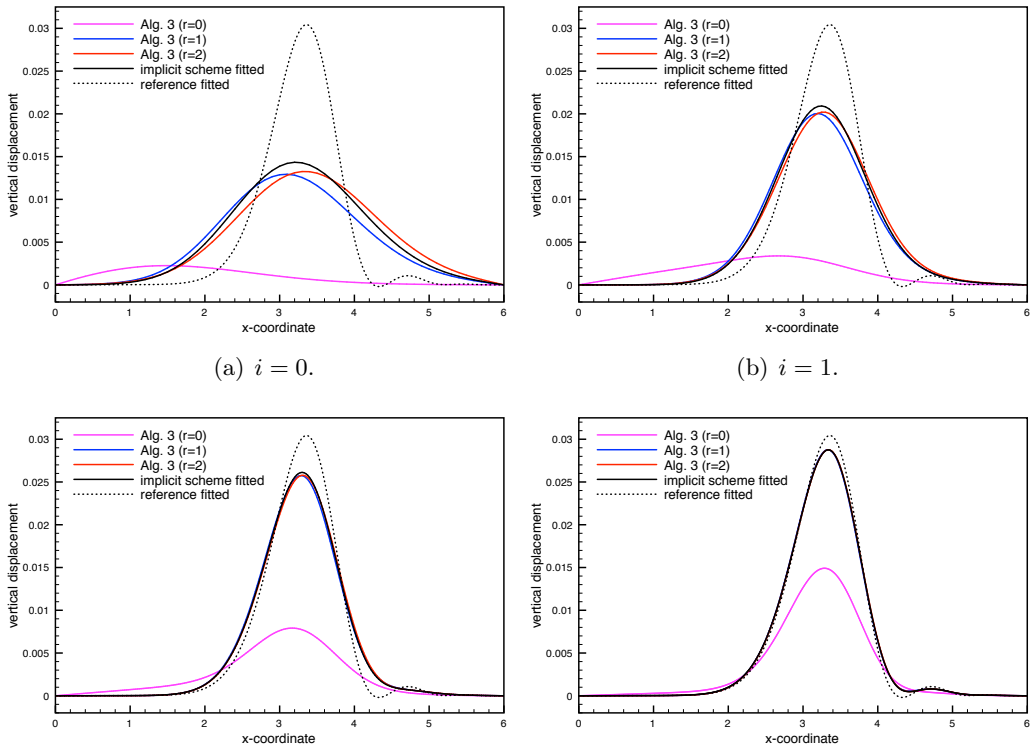

(a) $i = 0$. (b) $i = 1$.

(c) $i = 2$. (d) $i = 3$.

Figure 6.19: Algorithm 6.3. Comparison of the solid displacements at $t = 0.015$ for different levels of (τ, h)-refinement (6.41).

Finally, we comment on the results obtained with Algorithm 6.3. Figure 6.17(b) shows convergence for the three variants. Note, however, that sub-optimal accuracy is obtained with the variant without extrapolation ($r = 0$). This behavior is also striking in Figure 6.19, which points out the extremely poor accuracy of the displacement approximations for all the space-time refinement levels. On the contrary, the variants with $r = 1$ and $r = 2$ retrieve the optimal first-order accuracy of the fitted implicit scheme, hence confirming the convergence rates reported in Theorem 6.4.

6.4.2 Dynamic interface

In this section we provide numerical evidence on the stability and the accuracy properties of Algorithms 6.4-6.6 in different examples. For comparison purposes, we consider as reference solution an implicit fitted-ALE approximation of problem (6.33), where the discrete ALE mapping is built from a simple harmonic lifting of the solid displacement (no advanced mesh update strategy is hence used). Along this section, the user-defined parameters in Algorithms 6.4-6.6 are always chosen to be $\gamma_{\mathrm{p}} = 10^{-2}$, $\gamma_{\mathrm{v},1} = 10^{-2}$, $\gamma_{\mathrm{v},2} = 0$, $\gamma_{\mathrm{g}} = 1$, $\gamma = 10^{2}$ and (in Algorithm 6.5) $\gamma_0 = 1$. Furthermore, for simplicity, a standard semi-implicit treatment of the fluid convective term, $a_h^{\mathrm{f},n}\big(\boldsymbol{u}_h^{n-1}; (\boldsymbol{u}_h^n, p_h^n), (\boldsymbol{v}_h, q_h)\big)$, is adopted in Algorithms 6.4-6.6.

6.4.2.1 Idealized closed valve

We consider the idealized closed valve test of Section 6.4.1.1 within the nonlinear framework of Section 6.3. The geometrical configuration, physical parameters and boundary conditions are those of Section 6.4.1.1. A remarkable feature of this setting is that both the static and the dynamic interface cases share the same steady state displacement solution. Indeed, using the parameterization of the interface configuration $\Sigma(t)$, in terms of the steady state displacement, given by $\boldsymbol{r}(y) = \big(\eta(y), y\big),\ y \in [0,1]$, we have

$$
\begin{aligned}
-\int_{\Sigma(t)} [\![\boldsymbol{\sigma}(\boldsymbol{u},p)\boldsymbol{n}]\!] \cdot \boldsymbol{w} \circ \boldsymbol{\phi}_t^{-1} &= \int_0^1 P_0\ \boldsymbol{n}\big(\boldsymbol{r}(y)\big) \cdot \boldsymbol{w}\big(\boldsymbol{\phi}_t^{-1}\left(\boldsymbol{r}(y)\right)\big)\ |\boldsymbol{r}'(y)|\mathrm{d}y \\
&= \int_0^1 P_0\ |\boldsymbol{r}'(y)|^{-1}(1,-\eta'(y)) \cdot (w(y),0)\ |\boldsymbol{r}'(y)|\mathrm{d}y = \int_0^1 P_0 w(y)\mathrm{d}y
\end{aligned}
$$

for all $\boldsymbol{w} \in \boldsymbol{W}$. We hence recover (6.39), as the strong form of (6.30), and the analytical expression for the displacement given by (6.40).

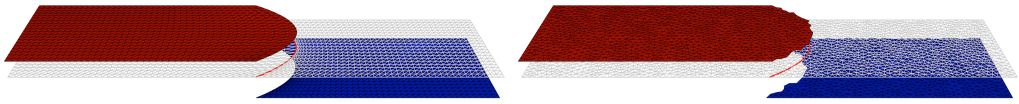

(a) Fitted method (b) Algorithm 6.4

Figure 6.20: Steady state pressure approximation and deformed solid configuration.

Due to the stationary nature of the problem, we limit the discussion to the implicit scheme given by Algorithm 6.4, and compare its accuracy with the implicit ALE-fitted method. Prototypical approximations obtained with both approaches are displayed in Figure 6.20. The mesh size for the fitted (structured) and the unfitted (unstructured) meshes is approximately $h \approx 0.05$. Note the distortion of the fluid mesh in Figure 6.20(a), prescribed by the ALE fitted approach, in order to fit the solid mesh. In Figure 6.20(b), on the contrary, the structure mesh moves independently of the fluid background mesh. This is more visible in Figure 6.21, which presents the mesh intersection and the cut elements subdivisions resulting from the algorithm described in Section 6.2.2.1.

In order to show the capabilities of the proposed unfitted methods to handle situations with large interface displacements, we consider a series of increasing inlet pressures $P_0 \in \{10^4 + 12{\cdot}10^3{\cdot}i\}_{i=0}^{7}$. In Figure 6.22, we have reported the displacement approximations obtained with the fitted and the unfitted methods. The analytical solutions given by (6.40) are also displayed. We observe that both approaches are in excellent agreement with the analytical solution until $i = 5$. From this point on, the considered ALE mesh update fails. On the contrary, the unfitted approach is able to continue for $i \geq 6$ while keeping a perfect match with the analytic solution.

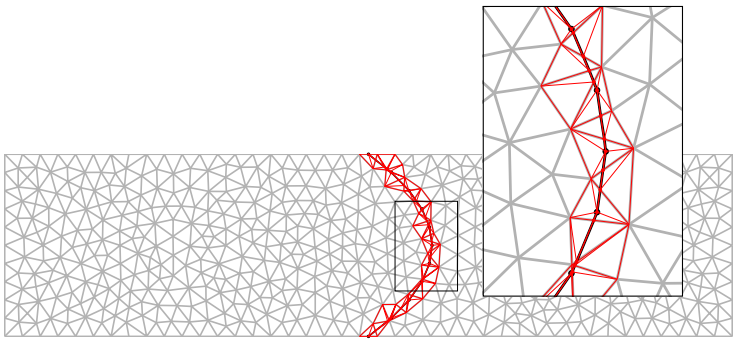

Figure 6.21: Mesh intersection and the cut elements subdivisions.

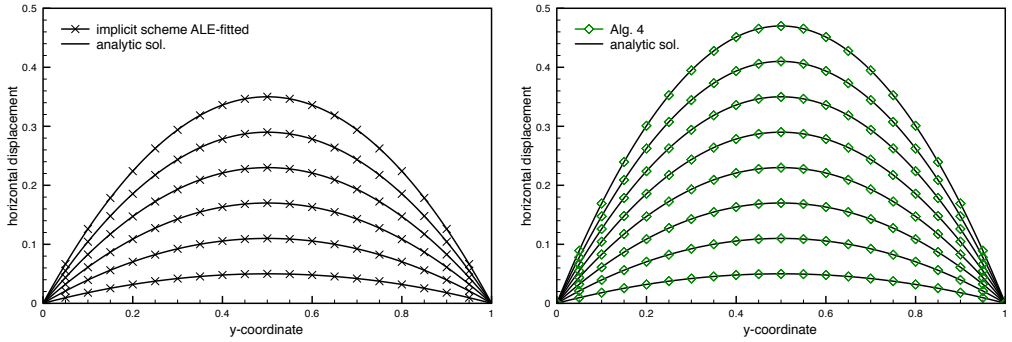

(a) Fitted method (b) Algorithm 6.4

Figure 6.22: Steady state displacements for increasing inlet pressures.

6.4.2.2 Double cavity

We consider a variant of the classical lid-driven cavity problem in which a second cavity is attached below the lower flexible wall. The fluid domain is given by the rectangle $\Omega = (-0.5, 0.5) \times (-0.5, 1.5)$ and the interface by the segment $\Sigma = (-0.5, 0.5) \times \{0.5\}$ (see Figure 6.23). All units are given in the SI system. The

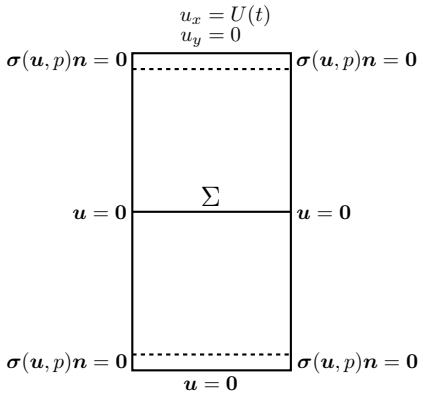

Figure 6.23: Geometric configuration and external boundary conditions.

fluid physical parameters are given by $\rho^{\mathrm{f}} = 1.0$ and $\mu = 0.2$. For the solid we have $\rho^{\mathrm{s}} = 250$, $\epsilon = 0.01$, $\lambda_1 = E\epsilon/(2(1+\nu))$ and $\lambda_0 = 0$, with $\nu = 0$ and we consider three different values for the Young modulus, $E = \{125000/2^i\}_{i=0}^{2}$. The fluid external boundary conditions are given in Figure 6.23, with $U(t) \stackrel{\text{def}}{=} 100[1 - \cos(0.4\pi t)]$. The solid is clamped on its extremities.

Figure 6.24 presents some snapshots of the fluid velocity magnitude and of the elevated fluid pressure obtained with the ALE-fitted method and Algorithm 6.4 for a value of the Young modulus, $E = 62500$, which gives relatively large interface displacements. The time-step length is $\tau = 0.005$ and the mesh step is approximately $h \approx 0.025$ in both simulations. The good agreement between the fitted and unfitted approaches is noticeable.

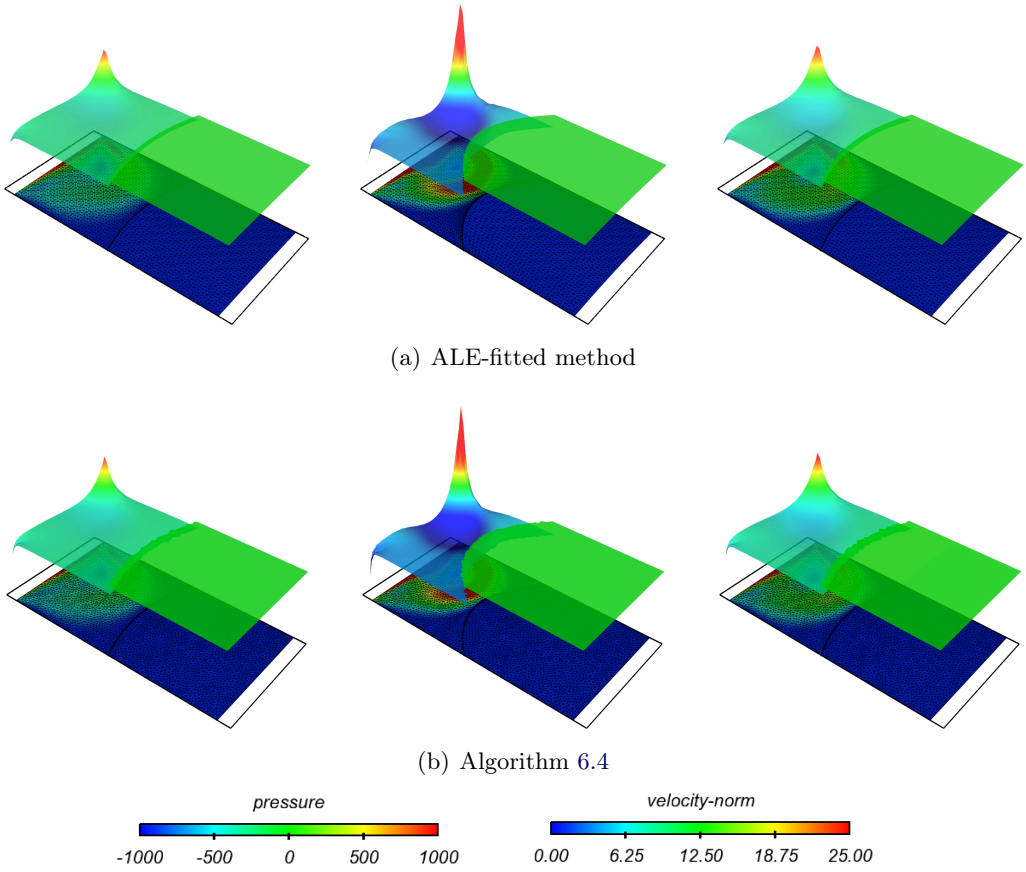

(a) ALE-fitted method

(b) Algorithm 6.4

Figure 6.24: Snapshots of the fluid velocity magnitude and elevated pressure at time $t = 6.25$, 7.5 and 8.75 (from left to right) obtained with $E = 62500$, $\tau = 5 \cdot 10^{-3}$ and $h \approx 0.025$.

Figures 6.25 and 6.26 present a closer view of the discrete solutions at time $t = 7.5$, showing the elevated pressure and velocity components. The comparison of these figures demonstrates the capability of the present unfitted approach to accurately capture the weak and strong discontinuities of the velocity and pressure

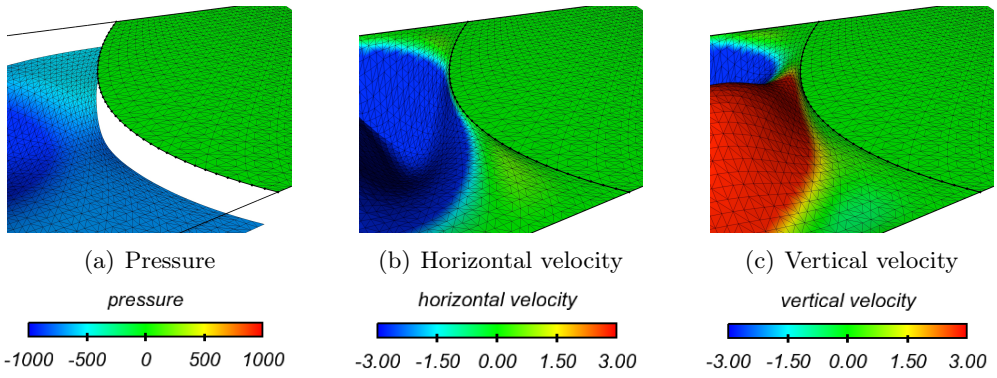

(a) Pressure (b) Horizontal velocity (c) Vertical velocity

Figure 6.25: ALE-fitted method. Strong (pressure) and weak (velocity) discontinuities of the approximated solution at time $t = 7.5$ with $E = 62500$, $\tau = 5 \cdot 10^{-3}$ and $h \approx 0.025$.

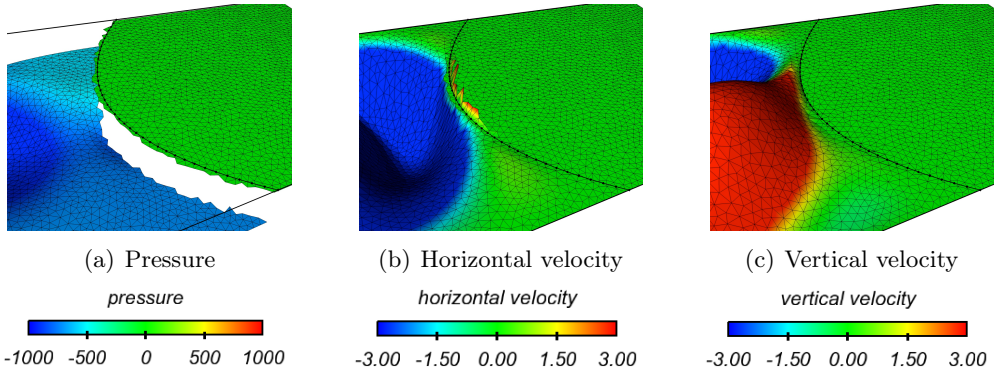

(a) Pressure (b) Horizontal velocity (c) Vertical velocity

Figure 6.26: Algorithm 6.4. Strong (pressure) and weak (velocity) discontinuities of the approximated solution at time $t = 7.5$ with $E = 62500$, $\tau = 5 \cdot 10^{-3}$ and $h \approx 0.025$.

fields across the interface. No spurious oscillations appear. Note that the unfitted approximation is two-valued in the set of elements intersected by the interface, only its value in the physical zone of the overlapping region must be compared with the results of Figures 6.25.

In order to investigate the accuracy of the different coupling schemes, we have reported in Figures 6.27 and 6.28 the time history of the solid displacement at point $(-0.2, 0.5)$ obtained with Algorithms 6.4-6.5 and Algorithm 6.6, respectively, for the three different values of the Young modulus. For comparison purposes, the corresponding results for the ALE-fitted method are also plotted.

Figure 6.27 shows that Algorithm 6.4 gives similar results as the ALE-fitted method in all the regimes. As expected, the higher the Young modulus, the lower the displacement amplitude. Note that for $E = 31250$, the considered ALE-fitted method fails at a certain level of interface deformation (due to the breakdown of the mesh update technique), while Algorithm 6.4 does not show any lack of robustness.

The situation is more delicate for the explicit coupling schemes given by Algorithm 6.5. The two explicit variants do deliver stable approximations, but some spurious time oscillations appear in the case of the largest interface deflections. This issue is related to the non-uniformity in space of the splitting error discussed in Section 6.2.3.2. Indeed, as shown in Figure 6.29, reducing the time-step length τ (while keeping h fixed) improves the quality of the approximations. The enhanced accuracy of the variant with second-order prediction and one correction iteration ($K = 1, r = 2$) is also noticeable. Numerical evidence, not reported here, shows however that this variant may lack stability if $\gamma\tau/h$ is not sufficiently small. As an example, with $\gamma = 1000$, as in Section 6.4.1, stability requires more than one correction iteration ($K > 1$).

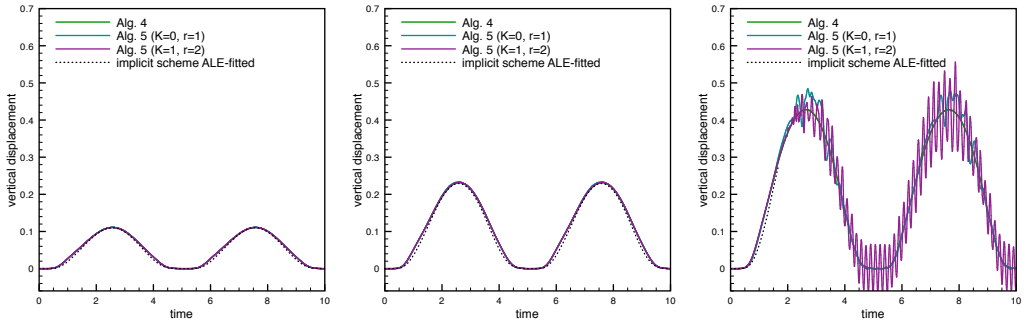

(a) $E = 125000$ (b) $E = 62500$ (c) $E = 31250$

Figure 6.27: Time history of the solid displacement at point $(-0.2, 0.5)$ obtained with Algorithms 6.4 and 6.5, $\tau = 5 \cdot 10^{-3}$.

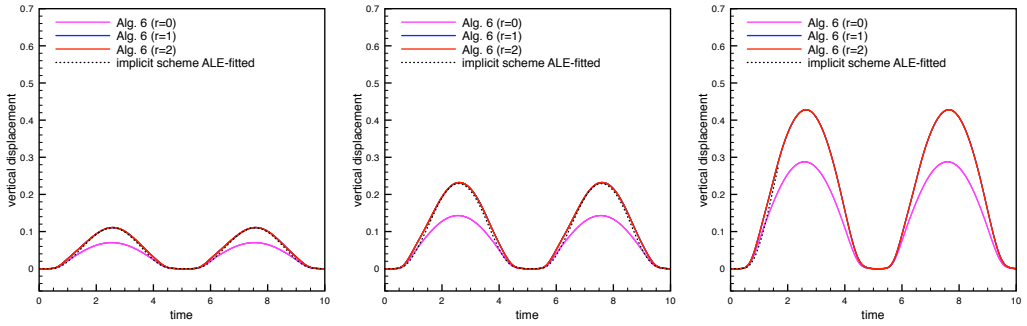

(a) $E = 125000$ (b) $E = 62500$ (c) $E = 31250$

Figure 6.28: Time history of the solid displacement at point $(-0.2, 0.5)$ obtained with Algorithm 6.6, $\tau = 5 \cdot 10^{-3}$.

The results reported in Figure 6.28 indicate that the semi-implicit schemes given by Algorithm 6.6 with $r = 1$ and $r = 2$ do not suffer from the above issues. These variants deliver comparable accuracy to the implicit ALE-fitted method. On the contrary, the variant with $r = 0$ provides poor approximations in all the regimes.

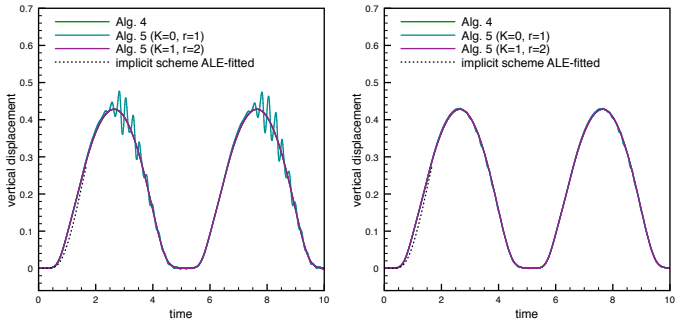

(a) $\tau = 2.5 \cdot 10^{-3}$ (b) $\tau = 1.25 \cdot 10^{-3}$

Figure 6.29: Time history of the solid displacement at point $(-0.2, 0.5)$ obtained with Algorithms 6.4 and 6.5, $E = 31250$.

We thus retrieve, also in the dynamic interface framework, the essential ingredients of the accuracy result given by Theorem 6.4.

6.4.2.3 Idealized open valve

This example is intended to mimic the behavior of an open valve (without contact). The fluid domain corresponds to the rectangle $\Omega = (0, 4) \times (0, 1)$ and the solid domain is made of two segments $\Sigma = \{1.9\} \times (0, 0.6) \cup \{2.1\} \times (0.4, 1)$, as shown in Figure 6.30. All the units are given in the CGS system. The physical parameters

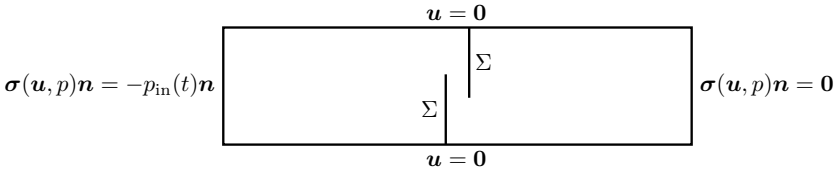

Figure 6.30: Geometric configuration and external boundary conditions.

for the fluid are $\rho^{\text{f}} = 1$ and $\mu = 0.03$. For the structure we have $\rho^{\text{s}} = 1.2$, $\epsilon = 0.065$, $\lambda_1 = E\epsilon/(2(1 + \nu))$ and $\lambda_0 = 0$, with Young's modulus $E = 10000$ and Poisson's ratio $\nu = 0.5$. The external boundary conditions for the fluid are detailed in Figure 6.30, with the inlet pressure given by $p_{\text{in}}(t) \overset{\text{def}}{=} P_{\max} \sin(2\pi t)$ with $P_{\max} = 150$. The solid is clamped at its bottom and top extremities, i.e., at $(1.9, 0.6)$ and $(2.1, 1)$.

Figure 6.31 presents some snapshots of the fluid velocity magnitude and of the elevated fluid pressure obtained with the ALE-fitted method and Algorithm 6.4. The time step is $\tau = 0.0025$ and the step parameter of the fluid and solid meshes is approximately $h \approx 0.05$. The unfitted method is able to capture the dynamics of the pressure jump across the interface delivered by the fitted approximation without any spurious oscillation. This feature is even more striking in Figures 6.32 and 6.33, where we present a closer view of the elevated pressure and velocity components at time $t = 0.25$. We can also remark how the unfitted approximation is able

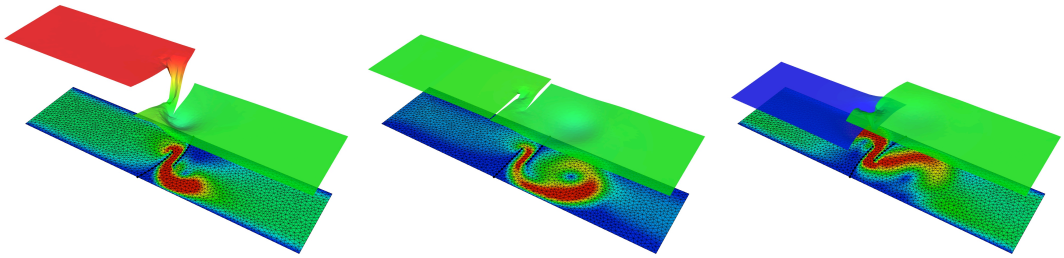

(a) ALE-fitted method

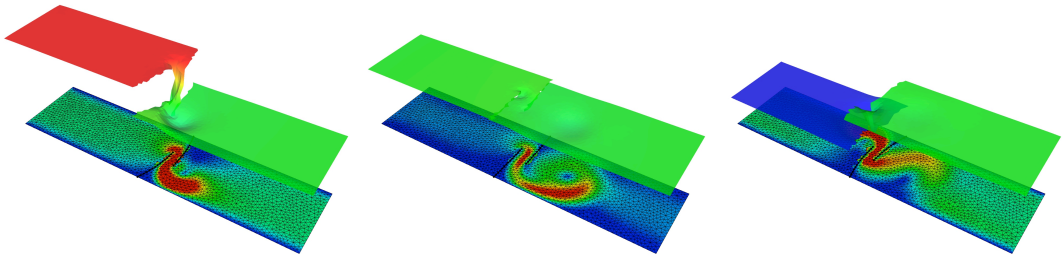

(b) Algorithm 6.4

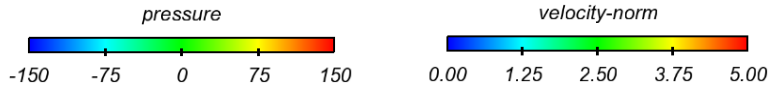

Figure 6.31: Snapshots of the fluid velocity magnitude and elevated pressure at time $t = 0.25$, 0.5 and 0.75 (from left to right) obtained with $P_{\max} = 150$, $\tau = 2.5 \cdot 10^{-3}$ and $h \approx 0.05$.

to reproduce accurately strong and weak discontinuities in the case of partially intersected fluid domains (see Section 6.2.1.3).

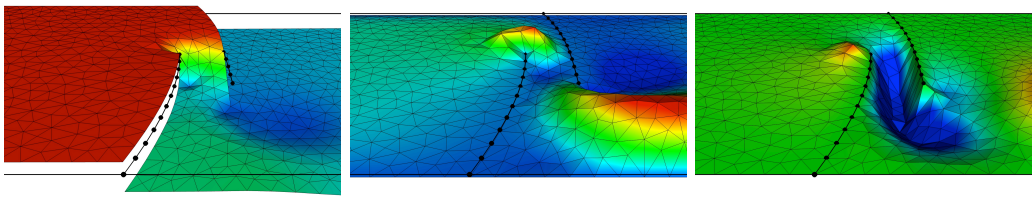

(a) Pressure (b) Horizontal velocity (c) Vertical velocity

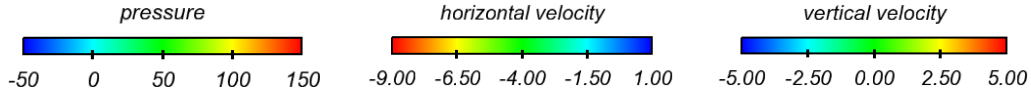

Figure 6.32: ALE-fitted method. Strong (pressure) and weak (velocity) discontinuities of the approximated solution at time $t = 0.25$ obtained with $P_{\max} = 150$, $\tau = 2.5 \cdot 10^{-3}$ and $h \approx 0.05$.

We now turn our attention to the accuracy of the different coupling schemes proposed in Section 6.3.2. To this purpose, we have reported in Figure 6.34 the time history of the solid displacement at point $(1.9, 0)$ (tip of the left leaflet) obtained with

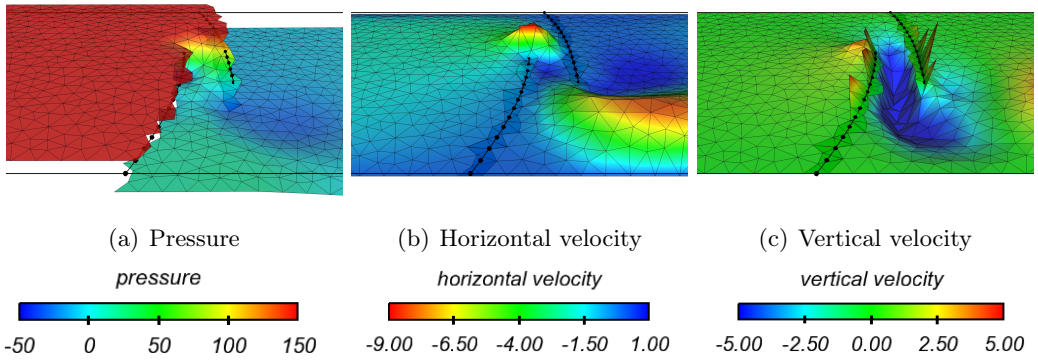

(a) Pressure (b) Horizontal velocity (c) Vertical velocity

Figure 6.33: Algorithm 6.4. Strong (pressure) and weak (velocity) discontinuities of the approximated solution fields at time $t = 0.25$ obtained with $P_{\max} = 150$, $\tau = 2.5 \cdot 10^{-3}$ and $h \approx 0.05$.

Algorithms 6.4–6.6 and the implicit ALE-fitted method. Figure 6.34(a) confirms the results of the above qualitative discussion on the accuracy of Algorithm 6.4 with respect to the reference ALE-fitted method. As regards the time splitting schemes given by Algorithms 6.5 and Algorithm 6.6, Figure 6.34 indicates that the best performance is obtained with the variants $(K = 1, r = 2)$ and $r = 1$, 2, respectively. Once again, this numerical evidence is consistent with the theoretical discussion of Section 6.2.3.

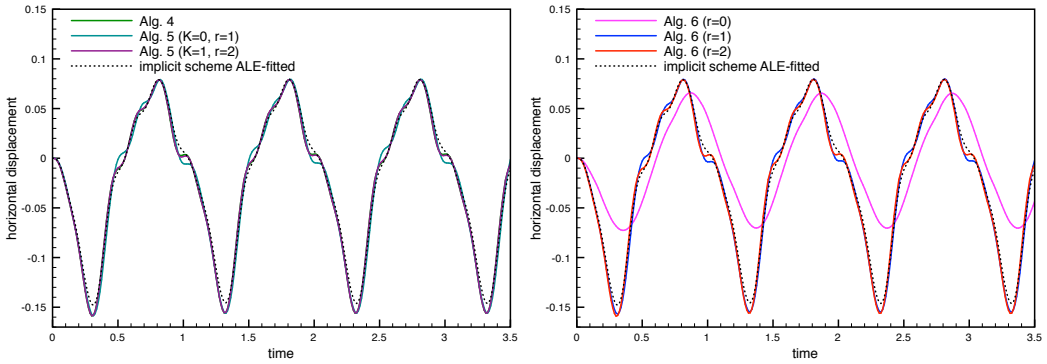

(a) Algorithms 6.4 and 6.5 (b) Algorithm 6.6

Figure 6.34: Time history of the solid displacement at point $(1.9, 0.6)$ obtained with $P_{\max} = 150$, $\tau = 2.5 \cdot 10^{-3}$ and $h \approx 0.05$.

Finally, in order to illustrate the capability of the proposed unfitted approach to handle very large interface deflections we have performed the simulation with an increased maximum pressure drop of $P_{\max} = 400$. Since the present computer implementation is not able to handle contact, the top leaflet has been removed. Some snapshots of the discrete solution obtained with Algorithm 6.4 are displayed in Figure 6.35. Figure 6.36 shows the time history of the tip displacement provided

by Algorithm 6.4 and the ALE-fitted algorithm. Both approaches give similar results up to a certain degree of interface deformation, above which the ALE-fitted method fails while the unfitted method still delivers a stable numerical approximation.

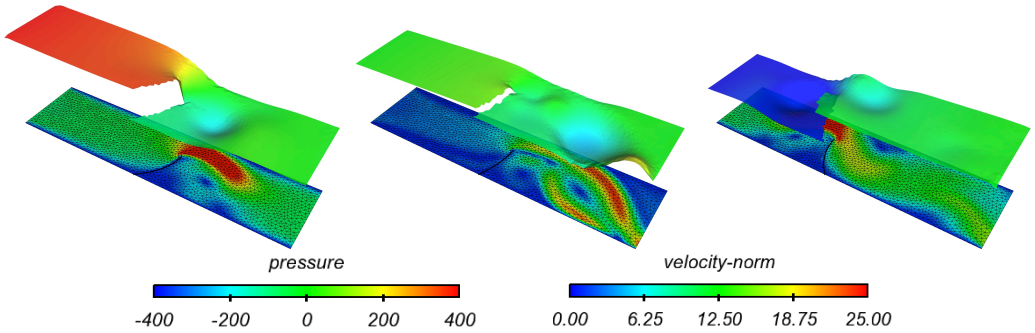

Figure 6.35: Snapshots of the fluid velocity magnitude and elevated pressure at time $t = 0.25$, 0.5 and 0.75 (from left to right) obtained with Algorithm 6.4, $P_{\max} = 400$, $\tau = 2.5 \cdot 10^{-3}$ and $h \approx 0.05$.

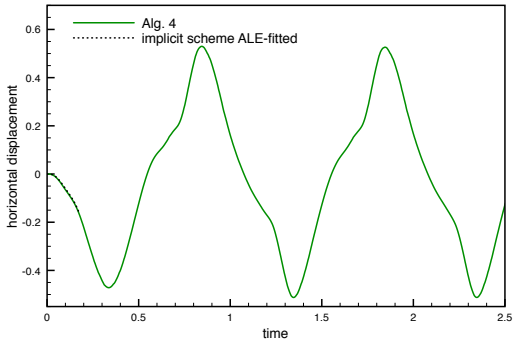

Figure 6.36: Time history of the solid displacement at point $(1.9, 0.6)$ obtained with $P_{\max} = 400$, $\tau = 2.5 \cdot 10^{-3}$ and $h \approx 0.05$.

6.5 Conclusion

We have introduced a Nitsche-XFEM method for incompressible fluid-structure interaction problems involving immersed thin-walled structures. Eulerian and Lagrangian formalisms are, respectively, considered for the fluid and the solid. The key features of the spatial discretization proposed are:

- unfitted (unstructured) fluid and solid meshes;
- affine finite element approximations including weak and strong discontinuities for the velocity and the pressure, respectively (based on the XFEM method of [HH04, BBH09]);
- integration of the fluid equations only in the physical domain (cut elements);

- consistent treatment of the kinematic/dynamic fluid-solid coupling via Nitsche's method;
- symmetric velocity/pressure and ghost-penalty stabilization to guarantee robustness without compromising accuracy.

In the case of static interfaces, a priori error estimates (Theorem 6.1) guaranteeing optimal convergence (in the energy norm) towards non-singular solutions have been derived using the arguments reported in [BF14b].

Several splitting schemes (implicit, explicit, semi-implicit) have been proposed, including their formulation with moving interfaces. The fundamental ingredients for the stability and accuracy of the resulting fully discrete methods have been discussed. These theoretical stability and convergence results have then been confirmed via numerical evidence in a series of 2D examples involving static and moving interfaces. The comparison of the different methods indicates that the best performance (in terms of accuracy and computational complexity) is obtained with Algorithms 6.3 and 6.6. A salient feature of this semi-implicit method is that it simultaneously yields unconditional stability and optimal convergence in the energy norm, while avoiding the strong coupling of [NFGK07, BCG15].

General conclusion and perspectives

In this thesis, we have considered the interaction of a viscous incompressible fluid with a general thin-walled viscoelastic structure with fitted and unfitted fluid and solid meshes. Within these two frameworks, the Robin-Neumann splitting paradigm of [Fer13, FMV13] has been shown to be successful in avoiding strong coupling without compromising stability and accuracy. In the unfitted case, this has been achieved through specific unfitted spatial discretizations that build on the ideas reported in [HH04, BF14b].

The results of Chapter 2 have shown that this explicit coupling paradigm can be effectively combined with a fractional-step time-marching in the fluid, which is one of the most widely used techniques for the large scale simulation of incompressible flow. From the analysis point of view, this introduces additional difficulties and, hence, only some of the variants have been analyzed. Interestingly, this splitting yields a solution procedure that enables a fully decoupled evaluation of the fluid-solid state. The computational performance of this approach has also been highlighted in Chapter 4 where, for the first time, an archetypical sample of partitioned solution procedures for incompressible fluid-structure interaction are compared and validated against the results of an experimental benchmark. With regard to second-order accuracy in time, the numerical investigations of Chapter 3 indicate that this can be achieved by combining the Robin-Neumann splitting with a predictor-corrector strategy. The analysis of these methods is, however, much more delicate than in the first-order case. Some insight on their stability has been provided in a simplified setting.

The results of Part II have shown that the Robin-Neumann coupling combined with the robust Nitsche and Nitsche-XFEM unfitted mesh frameworks yields solution strategies with many interesting features. First, as shown theoretically and numerically, they preserve the stability and accuracy of the original methods in the fitted framework. Second, the resulting semi-implicit schemes offer an accurate and efficient alternative to the traditional strongly coupled methods used in the immersed boundary method (see, e.g., [NFGK07, BCG15]).

Extensions of this work can explore various research directions. We list and discuss below some of them together with some open problems:

- The families of splitting schemes introduced in Chapters 2 and 3 involve the coupling with a general thin-walled viscoelastic structure. An important problem, not addressed in this work, is the coupling with three-dimensional shell models (see, e.g., [CB11, BR00]). An interesting step in this direction could be to combine the ideas recently reported in [FMV15] to the coupling paradigms described in Chapters 2 and 3. Note that the three-dimensional shell models include higher-order through-the-thickness effects that overcome, in particular, the common modeling assumptions described in Section 1.2.3. Moreover,

in Chapter 4, this would bypass the introduction of the ad hoc Archimedes surface force when considering the coupling with a shell solid model.

- Another interesting approach, not explored in this work, would be the formulation of the splitting schemes of Section 1.4.3.2 and Chapter 2 in the immersed unfitted framework. Note that, in this case, the derivation of a consistent pressure-Poisson problem in the projection step requires a specific care, due to discontinuous nature of the pressure. The Nitsche-XFEM method proposed in Chapter 6 seems to be the natural spatial semi-discrete framework for these approaches.

- From the theoretical point of view, we can consider the analysis in a fully discrete setting and the derivation of a priori error estimates for the schemes introduced in Chapter 2. Some preliminary results indicate its feasibility in the simplest case $s = r = 0$. The cases $s > 0$ and $r > 0$ require further investigations. Further insight on the stability of the high order methods introduced in Chapter 3 could be obtained in a fully discrete setting by using a Von Neumann analysis (e.g., in the spirit of [BHS14]).

- The analysis for $r = 1, 2$ of the explicit coupling schemes proposed in Section 5.3 is an open problem. The formulation of this coupling paradigm in the case of immersed thin-walled solids seems to be also not straightforward. Another interesting point, not addressed in this thesis, is the convergence analysis of the unfitted methods with curved interfaces. The case of dynamic interfaces is also a delicate problem which has received little consideration in the literature (see, e.g., [Zun13] for an analysis in the parabolic case).

- On going investigations are devoted to unfitted Nitsche formulations which are non-symmetric and penalty free. In that case, a priori error estimates may be derived by adapting the ideas recently introduced in [Bur12, BB14] to fluid-structure interaction. Numerical evidence indicates that the stabilized explicit coupling paradigm (used in Algorithms 1.4 and 6.2) delivers first-order accuracy without resorting to any correction iteration (see also [BF14a]).

- Last, but not by means least, on going work related to Chapter 6 is devoted to the incorporation of more complex thin-walled solid models, including contact and fracture mechanics. The extension to 3D presents some technical challenges (see, e.g., the discussion of Section 6.2.2). This extenstions will, in particular, enable the comparison and validation of the unfitted methods with the experimental data of Chapter 4.

Appendix A

Additional results for the FSI benchmark

We present additional numerical results and experimental measurements for Phase II experiment of Chapter 4. Figure A.1 presents some snapshots of the fluid velocity magnitude at different time instants obtained with Algorithm 4.1 at the distant plane $z = 90$. Figure A.2 presents a comparison of the measured deflections and the results obtained with Algorithms 4.1-4.6 at different time-steps over the whole cycle $[0, 6]$. Figures A.3, A.4, A.5 and A.6 show the experimental results and the numerical approximations obtained, at fours different time-steps, with Algorithm 4.1 (monolithic fluid solver and 3D solid model) and Algorithm 4.6 (incremental pressure-correction fluid solver and shell solid model) at the cutting planes $z = 3.5$, $z = 13.5$, $z = 23.5$ and $z = 33.5$ (see Figure 4.8(b)).

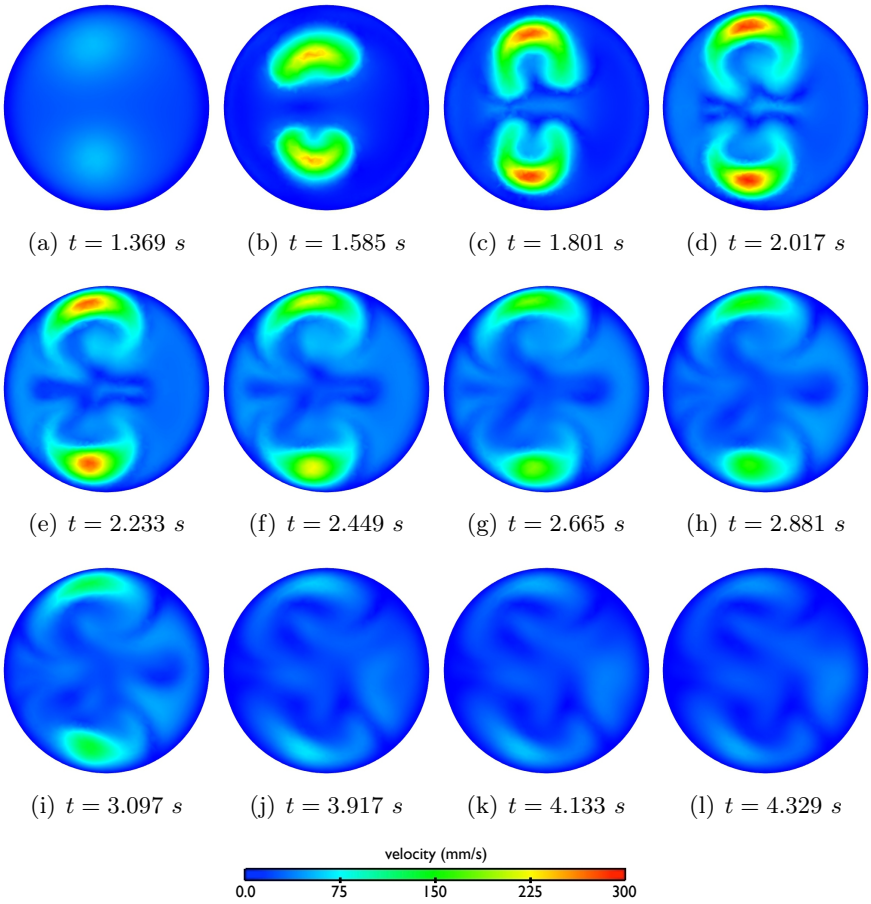

(a) $t = 1.369\ s$ (b) $t = 1.585\ s$ (c) $t = 1.801\ s$ (d) $t = 2.017\ s$

(e) $t = 2.233\ s$ (f) $t = 2.449\ s$ (g) $t = 2.665\ s$ (h) $t = 2.881\ s$

(i) $t = 3.097\ s$ (j) $t = 3.917\ s$ (k) $t = 4.133\ s$ (l) $t = 4.329\ s$

Figure A.1: Snapshots of the fluid velocity magnitude in Phase II with Algorithm 4.1 at the distant plane $z = 90$.

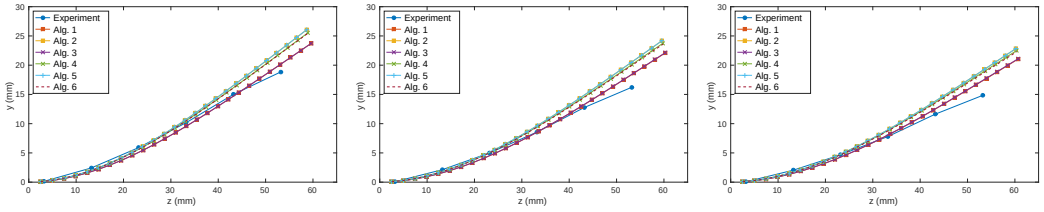

(a) $t = 0.073\ s$ (b) $t = 0.505\ s$ (c) $t = 0.721\ s$

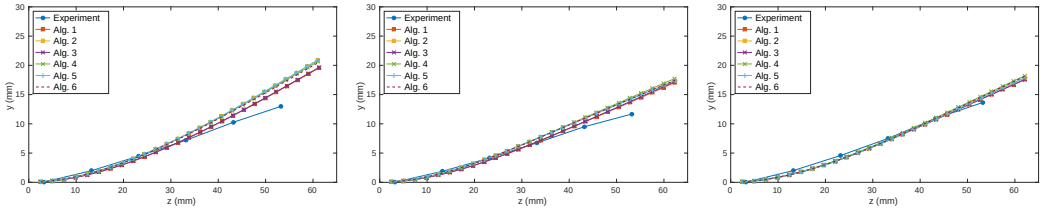

(d) $t = 0.937\ s$ (e) $t = 1.153\ s$ (f) $t = 1.396\ s$

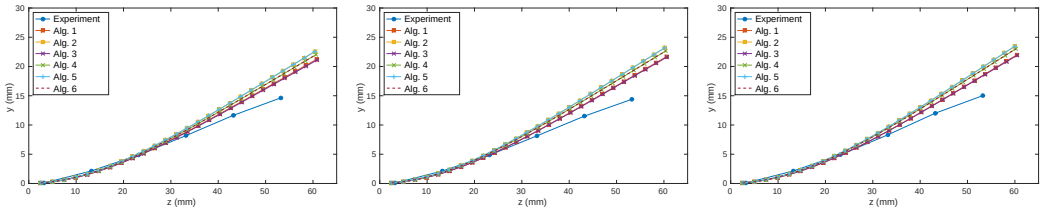

(g) $t = 1.801\ s$ (h) $t = 2.017\ s$ (i) $t = 2.233\ s$

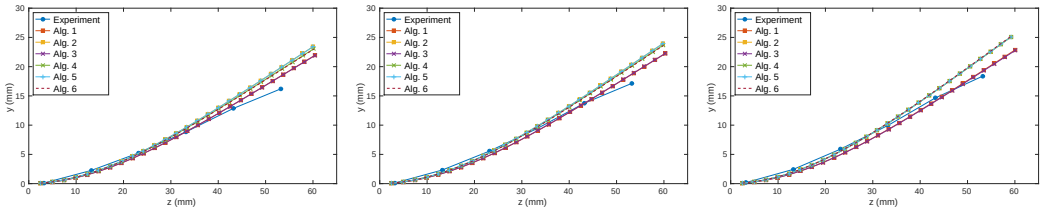

(j) $t = 2.665\ s$ (k) $t = 3.097\ s$ (l) $t = 4.133\ s$

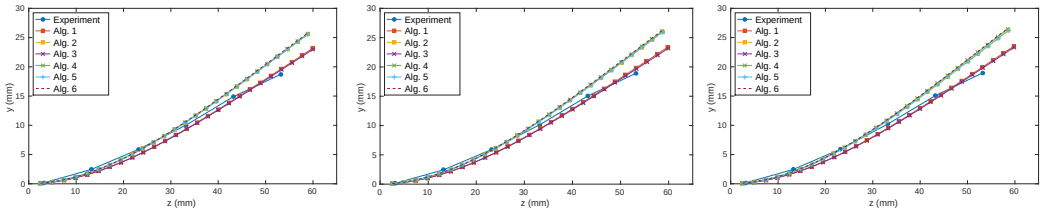

(m) $t = 4.565\ s$ (n) $t = 4.997\ s$ (o) $t = 5.429\ s$

Figure A.2: Deflection of the silicone filament in Phase II at different time instants. Comparison of the experimental data with the predictions obtained with Algorithms 4.1-4.6.

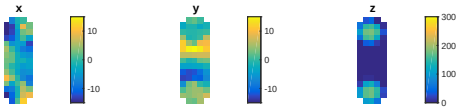

(a) Experiment at $t = 0.721$.

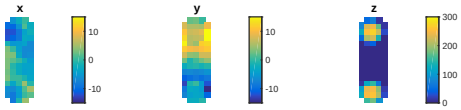

(b) Experiment at $t = 1.153$.

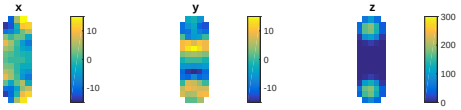

(c) Algorithm 4.1 at $t = 0.721$.

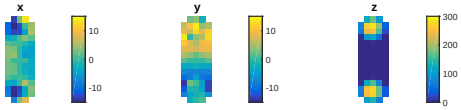

(d) Algorithm 4.1 at $t = 1.153$.

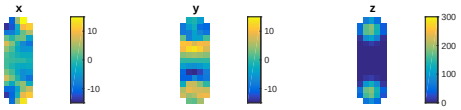

(e) Algorithm 4.6 at $t = 0.721$.

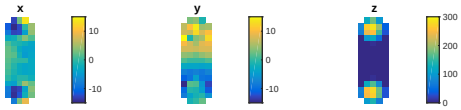

(f) Algorithm 4.6 at $t = 1.153$.

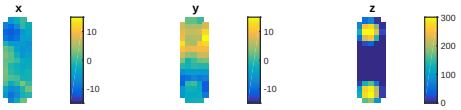

(g) Experiment at $t = 1.585$.

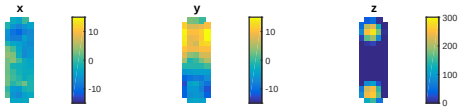

(h) Experiment at $t = 2.017$.

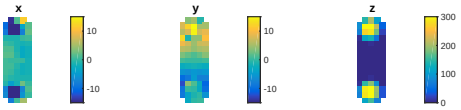

(i) Algorithm 4.1 at $t = 1.585$.

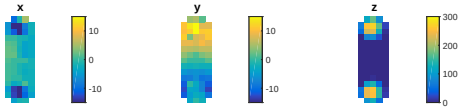

(j) Algorithm 4.1 at $t = 2.017$.

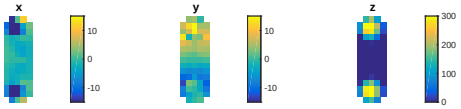

(k) Algorithm 4.6 at $t = 1.585$.

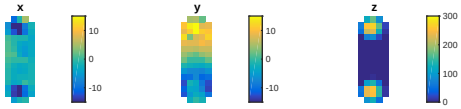

(l) Algorithm 4.6 at $t = 2.017$.

Figure A.3: Fluid velocity components in Phase II. Comparison of the experimental data with the predictions obtained with Algorithms 4.1 and 4.6. Plane $z = 3.5$. Units are $mm\ s^{-1}$.

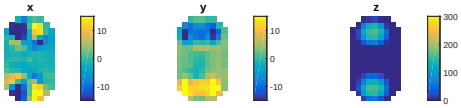

(a) Experiment at $t = 0.721$.

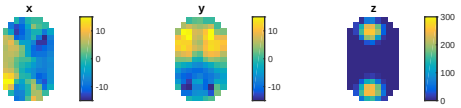

(b) Experiment at $t = 1.153$.

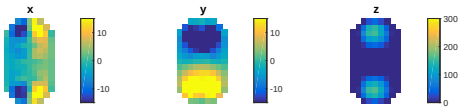

(c) Algorithm 4.1 at $t = 0.721$.

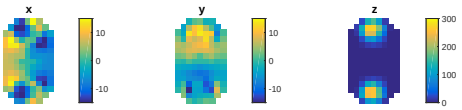

(d) Algorithm 4.1 at $t = 1.153$.

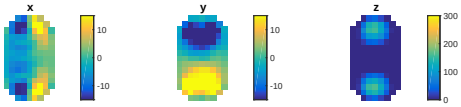

(e) Algorithm 4.6 at $t = 0.721$.

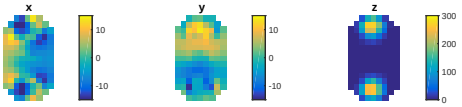

(f) Algorithm 4.6 at $t = 1.153$.

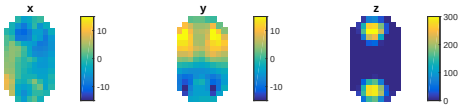

(g) Experiment at $t = 1.585$.

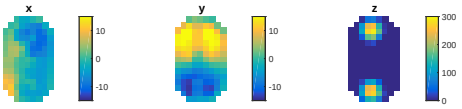

(h) Experiment at $t = 2.017$.

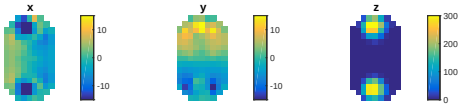

(i) Algorithm 4.1 at $t = 1.585$.

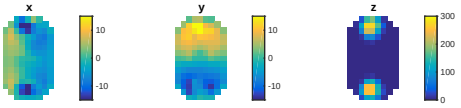

(j) Algorithm 4.1 at $t = 2.017$.

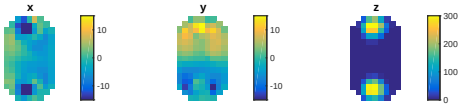

(k) Algorithm 4.6 at $t = 1.585$.

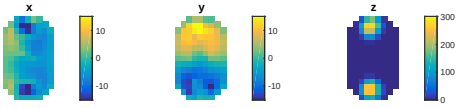

(l) Algorithm 4.6 at $t = 2.017$.

Figure A.4: Fluid velocity components in Phase II. Comparison of the experimental data with the predictions obtained with Algorithms 4.1 and 4.6. Plane $z = 13.5$. Units are $mm\ s^{-1}$.

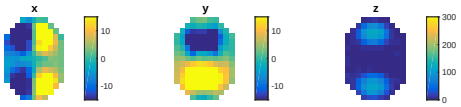

(a) Experiment at $t = 0.721$.

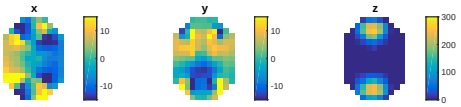

(b) Experiment at $t = 1.153$.

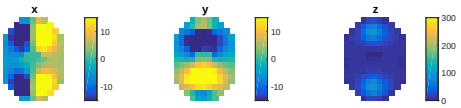

(c) Algorithm 4.1 at $t = 0.721$.

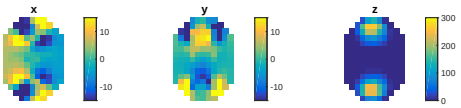

(d) Algorithm 4.1 at $t = 1.153$.

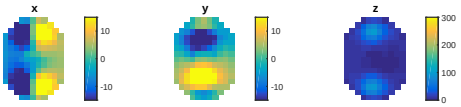

(e) Algorithm 4.6 at $t = 0.721$.

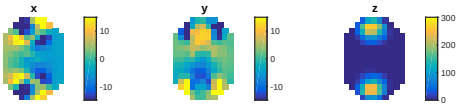

(f) Algorithm 4.6 at $t = 1.153$.

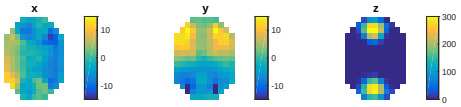

(g) Experiment at $t = 1.585$.

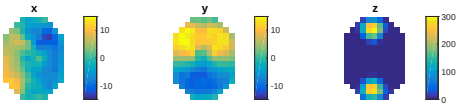

(h) Experiment at $t = 2.017$.

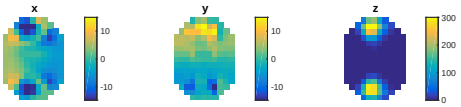

(i) Algorithm 4.1 at $t = 1.585$.

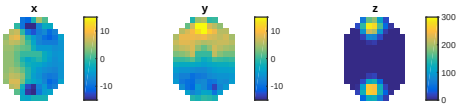

(j) Algorithm 4.1 at $t = 2.017$.

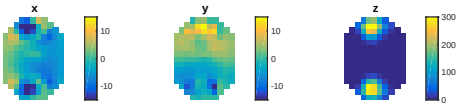

(k) Algorithm 4.6 at $t = 1.585$.

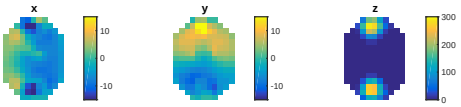

(l) Algorithm 4.6 at $t = 2.017$.

Figure A.5: Fluid velocity components in Phase II. Comparison of the experimental data with the predictions obtained with Algorithms 4.1 and 4.6. Plane $z = 23.5$. Units are $mm\ s^{-1}$.

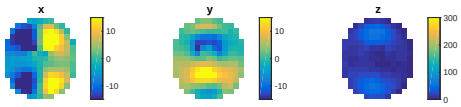

(a) Experiment at $t = 0.721$.

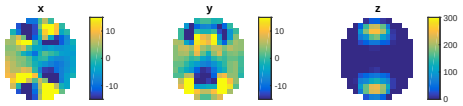

(b) Experiment at $t = 1.153$.

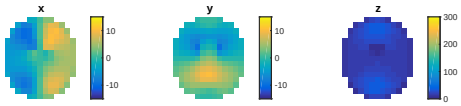

(c) Algorithm 4.1 at $t = 0.721$.

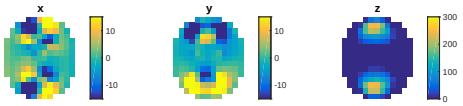

(d) Algorithm 4.1 at $t = 1.153$.

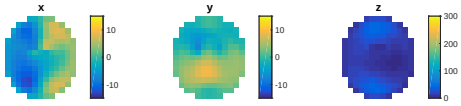

(e) Algorithm 4.6 at $t = 0.721$.

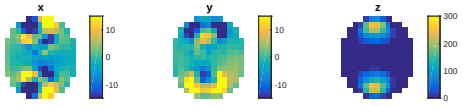

(f) Algorithm 4.6 at $t = 1.153$.

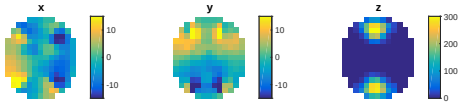

(g) Experiment at $t = 1.585$.

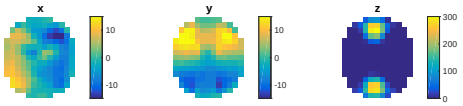

(h) Experiment at $t = 2.017$.

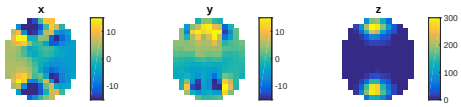

(i) Algorithm 4.1 at $t = 1.585$.

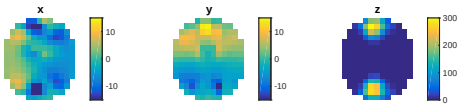

(j) Algorithm 4.1 at $t = 2.017$.

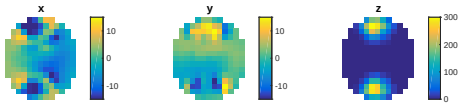

(k) Algorithm 4.6 at $t = 1.585$.

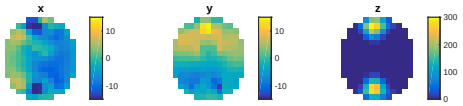

(l) Algorithm 4.6 at $t = 2.017$.

Figure A.6: Fluid velocity components in Phase II. Comparison of the experimental data with the predictions obtained with Algorithms 4.1 and 4.6. Plane $z = 33.5$. Units are $mm\ s^{-1}$.

References

[ACF09] M. Astorino, F. Chouly, and M. A. Fernández. Robin based semi-implicit coupling in fluid-structure interaction: Stability analysis and numerics. *SIAM J. Sci. Comput.*, 31(6):4041–4065, 2009.

[AG10] M. Astorino and C. Grandmont. Convergence analysis of a projection semi-implicit coupling scheme for fluid-structure interaction problems. *Numer. Math.*, 116:721–767, 2010.

[AGPT09] M. Astorino, J.-F. Gerbeau, O. Pantz, and K.-F. Traoré. Fluid-structure interaction and multi-body contact: Application to aortic valves. *Comput. Methods Appl. Mech. Engrg.*, 198(45-46):3603–3612, 2009.

[Ala14] F. Alauzet. A changing-topology moving mesh technique for large displacements. *Eng. Comput.*, 30(2):175–200, 2014.

[AM10] F. Alauzet and M. Mehrenberger. P1-conservative solution interpolation on unstructured triangular meshes. *Internat. J. Numer. Methods Engrg.*, 84(13):1552–1588, 2010.

[APV15] R. Araya, A.H. Poza, and F. Valentin. A low-order local projection method for the incompressible Navier-Stokes equations in two- and three-dimensions. *IMA J. Numer. Anal.*, 2015.

[Ast10] M. Astorino. *Interaction fluide-structure dans le système cardiovasculaire. Analyse numérique et simulation.* PhD thesis, Université Paris VI, France, 2010.

[Baa01] F. Baaijens. A fictitious domain/mortar element method for fluid-structure interaction. *Int. Jour. Num. Meth. Fluids*, 35:743–761, 2001.

[BAA+14a] Satish Balay, Shrirang Abhyankar, Mark F. Adams, Jed Brown, Peter Brune, Kris Buschelman, Victor Eijkhout, William D. Gropp, Dinesh Kaushik, Matthew G. Knepley, Lois Curfman McInnes, Karl Rupp, Barry F. Smith, and Hong Zhang. PETSc Web page, 2014.

[BAA+14b] Satish Balay, Shrirang Abhyankar, Mark F. Adams, Jed Brown, Peter Brune, Kris Buschelman, Victor Eijkhout, William D. Gropp, Dinesh Kaushik, Matthew G. Knepley, Lois Curfman McInnes, Karl Rupp, Barry F. Smith, and Hong Zhang. PETSc users manual. Technical Report ANL-95/11 - Revision 3.5, Argonne National Laboratory, 2014.

[BB14] T. Boiveau and E. Burman. A penalty free nitsche type method for the weak imposition of boundary conditions in compressible and incompressible elasticity. *arXiv preprint arXiv:1407.2229*, 2014.

[BBG+14] C. Bertoglio, D. Barber, N. Gaddum, V. Valverde, M. Rutten, P. Beerbaum, P. Moireau, R. Hose, and J.-F. Gerbeau. Identification of artery wall stiffness: In vitro validation and in vivo results of a data assimilation procedure applied to a 3d fluid–structure interaction model. *J. Biomech.*, 47(5):1027–1034, 2014.

[BBH09] R. Becker, E. Burman, and P. Hansbo. A Nitsche extended finite element method for incompressible elasticity with discontinuous modulus of elasticity. *Comput. Methods Appl. Mech. Engrg.*, 198(41-44):3352–3360, 2009.

[BBJL07] M. Braack, E. Burman, V. John, and G. Lube. Stabilized finite element methods for the generalized Oseen problem. *Comput. Methods Appl. Mech. Engrg.*, 196(4-6):853–866, 2007.

[BBWR04] M. Bischoff, K.-U. Bletzinger, W.A. Wall, and E. Ramm. *Models and Finite Elements for Thin-Walled Structures*, chapter 3. John Wiley & Sons, Ltd, 2004.

[BCG11] D. Boffi, N. Cavallini, and L. Gastaldi. Finite element approach to immersed boundary method with different fluid and solid densities. *Math. Models Methods Appl. Sci.*, 21(12):2523–2550, 2011.

[BCG+13] M. Bukac, C. Canic, R. Glowinski, T. Tambaca, and A. Quaini. Fluid-structure interaction in blood flow capturing non-zero longitudinal structure displacement. *J. Comp. Phys.*, 235(0):515–541, 2013.

[BCG15] D. Boffi, N. Cavallini, and L. Gastaldi. The finite element immersed boundary method with distributed lagrange multiplier. *SIAM J. Numer. Anal.*, 53(6):2584–2604, 2015.

[BCH+15] E. Burman, S. Claus, P. Hansbo, M.-G. Larson, and A. Massing. CutFEM: Discretizing geometry and partial differential equations. *International Journal for Numerical Methods in Engineering*, 104(7):472–501, 2015.

[BCM01] D.L. Brown, R. Cortez, and M.L. Minion. Accurate projection methods for the incompressible Navier-Stokes equations. *J. Comput. Phys.*, 168(2):464–499, 2001.

[BF09] E. Burman and M.A. Fernández. Galerkin finite element methods with symmetric pressure stabilization for the transient Stokes equations: Stability and convergence analysis. *SIAM J. Numer. Anal.*, 47(1):409–439, 2008/09.

[BF07] E. Burman and M.A. Fernández. Continuous interior penalty finite element method for the time-dependent Navier-Stokes equations: Space discretization and convergence. *Numer. Math.*, 107(1):39–77, 2007.

[BF09] E. Burman and M.A. Fernández. Stabilization of explicit coupling in fluid-structure interaction involving fluid incompressibility. *Comput. Methods Appl. Mech. Engrg.*, 198(5-8):766–784, 2009.

[BF14a] E. Burman and M.A. Fernández. Explicit strategies for incompressible fluid-structure interaction problems: Nitsche type mortaring versus Robin–Robin coupling. *Int. J. Num. Meth. Engrg.*, 97(10):739–758, 2014.

[BF14b] E. Burman and M.A. Fernández. An unfitted Nitsche method for incompressible fluid-structure interaction using overlapping meshes. *Comput. Methods Appl. Mech. Engrg.*, 279:497–514, 2014.

[BFH06] E. Burman, M.A. Fernández, and P. Hansbo. Continuous interior penalty finite element method for Oseen's equations. *SIAM J. Numer. Anal.*, 44(3):1248–1274, 2006.

[BG10] W. Bangerth and R. Geiger, M.and Rannacher. Adaptive galerkin finite element methods for the wave equation. *Comput. Methods Appl. Math.*, 10(1):3–48, 2010.

[BGH+09] Y. Bazilevs, J.R. Gohean, T.J.R. Hughes, R.D. Moser, and Y. Zhang. Patient-specific isogeometric fluid–structure interaction analysis of thoracic aortic blood flow due to implantation of the jarvik 2000 left ventricular assist device. *Computer Methods in Applied Mechanics and Engineering*, 198(45):3534–3550, 2009.

[BGMS97] Satish Balay, William D. Gropp, Lois Curfman McInnes, and Barry F. Smith. Efficient management of parallelism in object oriented numerical software libraries. In E. Arge, A. M. Bruaset, and H. P. Langtangen, editors, *Modern Software Tools in Scientific Computing*, pages 163–202. Birkhäuser Press, 1997.

[BH82] A.N. Brooks and T.J.R. Hughes. Streamline upwind/Petrov-Galerkin formulations for convection dominated flows with particular emphasis on the incompressible Navier-Stokes equations. *Comput. Methods Appl. Mech. Engrg.*, 32(1-3):199–259, 1982.

[BH12] E. Burman and P. Hansbo. Fictitious domain finite element methods using cut elements: II. A stabilized nitsche method. *Applied Numerical Mathematics*, 62(4):328–341, 2012.

[BH14] E. Burman and P. Hansbo. Fictitious domain methods using cut elements: III. A stabilized nitsche method for stokes' problem. *ESAIM: Mathematical Modelling and Numerical Analysis*, 48:859–874, 5 2014.

[BHS14] J.W. Banks, W.D. Henshaw, and D.W. Schwendeman. An analysis of a new stable partitioned algorithm for FSI problems. Part II: Incompressible flow and structural shells. *J. Comput. Phys.*, 268:399–416, 2014.

[BK11] H. Baek and G.E. Karniadakis. Sub-iteration leads to accuracy and stability enhancements of semi-implicit schemes for the Navier-Stokes equations. *J. Comput. Phys.*, 230(12):4384–4402, 2011.

[BK12] H. Baek and G.E. Karniadakis. A convergence study of a new partitioned fluid-structure interaction algorithm based on fictitious mass and damping. *J. Comput. Phys.*, 231(2):629–652, 2012.

[BMG12] C. Bertoglio, P. Moireau, and J.-F. Gerbeau. Sequential parameter estimation for fluid–structure problems: Application to hemodynamics. *International Journal for Numerical Methods in Biomedical Engineering*, 28(4):434–455, 2012.

[BNV08] S. Badia, F. Nobile, and C. Vergara. Fluid-structure partitioned procedures based on Robin transmission conditions. *J. Comp. Phys.*, 227:7027–7051, 2008.

[BP84] F. Brezzi and J. Pitkäranta. On the stabilization of finite element approximations of the Stokes equations. In *Efficient solutions of elliptic systems (Kiel, 1984)*, volume 10 of *Notes Numer. Fluid Mech.*, pages 11–19. Vieweg, 1984.

[BQQ08a] S. Badia, A. Quaini, and A. Quarteroni. Modular vs. non-modular preconditioners for fluid-structure systems with large added-mass effect. *Comput. Methods Appl. Mech. Engrg.*, 197(49-50):4216–4232, 2008.

[BQQ08b] S. Badia, A. Quaini, and A. Quarteroni. Splitting methods based on algebraic factorization for fluid-structure interaction. *SIAM J. Sci. Comput.*, 30(4):1778–1805, 2008.

[BR00] M. Bischoff and E. Ramm. On the physical significance of higher order kinematic and static variables in a three-dimensional shell formulation. *Int. J. Solids Structures*, 37:6933–6960, 2000.

[Bur10] E. Burman. Ghost penalty. *Comptes Rendus Mathematique*, 348(21–22):1217 – 1220, 2010.

[Bur12] E. Burman. A penalty-free nonsymmetric nitsche-type method for the weak imposition of boundary conditions. *SIAM Journal on Numerical Analysis*, 50(4):1959–1981, 2012.

[CB11] D. Chapelle and K.J. Bathe. *The Finite Element Analysis of Shells - Fundamentals*. Springer, 2011.

[CDFQ11] P. Crosetto, S. Deparis, G. Fourestey, and A. Quarteroni. Parallel algorithms for fluid-structure interaction problems in haemodynamics. *SIAM J. Sci. Comput.*, 33(4):1598–1622, 2011.

[CF03] D. Chapelle and A. Ferent. Modeling of the inclusion of a reinforcing sheet within a 3D medium. *Math. Models Methods Appl. Sci.*, 13(4):573–595, 2003.

[CFGM11] A. Caiazzo, M.A. Fernández, J.-F. Gerbeau, and V. Martin. Projection schemes for fluid flows through a porous interface. *SIAM J. Sci. Comput.*, 33(2):541–564, 2011.

[CGN05] P. Causin, J.-F. Gerbeau, and F. Nobile. Added-mass effect in the design of partitioned algorithms for fluid-structure problems. *Comput. Methods Appl. Mech. Engrg.*, 194(42–44):4506–4527, 2005.

[Cho68] A.J. Chorin. Numerical solution of the Navier-Stokes equations. *Math. Comp.*, 22:745–762, 1968.

[Cia88] P.G. Ciarlet. *Mathematical elasticity. Vol. I*, volume 20 of *Studies in Mathematics and its Applications*. North-Holland, 1988.

[Cia04] PG Ciarlet. Handbook of numerical analysis, volume xii special volume: Computational models for the human body, guest editor: N. ayache, 2004.

[CMM08] G.-H. Cottet, E. Maitre, and T. Milcent. Eulerian formulation and level set models for incompressible fluid-structure interaction. *M2AN Math. Model. Numer. Anal.*, 42(3):471–492, 2008.

[Cod02] R. Codina. Stabilized finite element approximation of transient incompressible flows using orthogonal subscales. *Comput. Methods Appl. Mech. Engrg.*, 191(39-40):4295–4321, 2002.

[ČTG+06] S. Čanić, J. Tambača, G. Guidoboni, A. Mikelić, C.J. Hartley, and D. Rosenstrauch. Modeling viscoelastic behavior of arterial walls and their interaction with pulsatile blood flow. *SIAM J. Appl. Math.*, 67(1):164–193, 2006.

[DB84] E.N. Dvorkin and K.-J. Bathe. A continuum mechanics based four-node shell element for general non-linear analysis. *Engineering Computations*, 1(1):77–88, 1984.

[Deg13] J. Degroote. Partitioned simulation of fluid-structure interaction. *Arch. Comput. Method E.*, 20(3):185–238, 2013.

[DGH82] J. Donéa, S. Giuliani, and J. P. Halleux. An arbitrary Lagrangian-Eulerian finite element method for transient dynamic fluid-structure interactions. *Comp. Meth. Appl. Mech. Engng.*, pages 689–723, 1982.

[DGHL03] Q. Du, M. D. Gunzburger, L. S. Hou, and J. Lee. Analysis of a linear fluid-structure interaction problem. *Discrete Contin. Dyn. Syst.*, 9(3):633–650, 2003.

[DHV08] P. Degroote, J. Bruggeman, R. Haelterman, and J. Vierendeels. Stability of a coupling technique for partitioned solvers in FSI applications. *Comp. & Struct.*, 86(23-24):2224–2234, 2008.

[Dim04] A. Dimitrov. On singularities in the solution of three-dimensional Stokes flow and incompressible elasticity problems with corners. *Internat. J. Numer. Methods Engrg.*, 60(4):773–801, 2004.

[DPE12] D.A. Di Pietro and A. Ern. *Mathematical aspects of discontinuous Galerkin methods*, volume 69 of *Mathematics & Applications*. Springer, Heidelberg, 2012.

[DR06] T. Dunne and R. Rannacher. Adaptive finite element approximation of fluid-structure interaction based on an eulerian variational formulation. In *Fluid-structure interaction*, pages 110–145. Springer, 2006.

[DSGB08] N. Diniz Dos Santos, J.-F. Gerbeau, and J.-F. Bourgat. A partitioned fluid–structure algorithm for elastic thin valves with contact. *Computer Methods in Applied Mechanics and Engineering*, 197(19):1750–1761, 2008.

[Dun06] T. Dunne. An eulerian approach to fluid–structure interaction and goal-oriented mesh adaptation. *International journal for numerical methods in fluids*, 51(9-10):1017–1039, 2006.

[Dun07] T. Dunne. Adaptive finite element approximation of fluid-structure interaction based on eulerian and arbitrary lagrangian-eulerian variational formulations. 2007.

[EDH10] A. Embar, J. Dolbow, and I. Harari. Imposing Dirichlet boundary conditions with Nitsche's method and spline-based finite elements. *Internat. J. Numer. Methods Engrg.*, 83(7):877–898, 2010.

[EG04] A. Ern and J.-L. Guermond. *Theory and practice of finite elements*. Springer, 2004.

[ESM09] M. Eswaran, U.K. Saha, and D. Maity. Effect of baffles on a partially filled cubic tank: Numerical simulation and experimental validation. *Computers & Structures*, 87(3–4):198–205, 2009.

[Eva10] L.C. Evans. *Partial Differential Equations*. Graduate studies in mathematics. American Mathematical Society, 2010.

[FB10] T.-P. Fries and T. Belytschko. The extended/generalized finite element method: an overview of the method and its applications. *Internat. J. Numer. Methods Engrg.*, 84(3):253–304, 2010.

[Fed02] R.P. Fedkiw. Coupling an Eulerian fluid calculation to a Lagrangian solid calculation with the ghost fluid method. *J. Comput. Phys.*, 175(1):200–224, 2002.

[Fel] Felisce. `http://felisce.gforge.inria.fr`.

[Fer11a] M.A. Fernández. Coupling schemes for incompressible fluid-structure interaction: implicit, semi-implicit and explicit. *SẽMA J.*, 55(1):59–108, 2011.

[Fer11b] M.A. Fernández. Incremental displacement-correction schemes for the explicit coupling of a thin structure with an incompressible fluid. *C. R. Math. Acad. Sci. Paris*, 349(7-8):473–477, 2011.

[Fer13] M.A. Fernández. Incremental displacement-correction schemes for incompressible fluid-structure interaction: stability and convergence analysis. *Numer. Math.*, 123(1):21–65, 2013.

[FFGQ09] M.A. Fernández, L. Formaggia, J.-F. Gerbeau, and A. Quarteroni. The derivation of the equations for fluids and structures. In *Cardiovascular mathematics*, volume 1 of *MS&A. Model. Simul. Appl.*, pages 77–121. Springer, 2009.

[FG08] P.J. Frey and P.L. George. *Mesh generation. Application to finite elements*. ISTE Ltd and John Wiley & Sons, 2nd edition, 2008.

[FG09] M.A. Fernández and J.-F. Gerbeau. Algorithms for fluid-structure interaction problems. In *Cardiovascular mathematics*, volume 1 of *MS&A. Model. Simul. Appl.*, pages 307–346. Springer, 2009.

[FGG07] M.A. Fernández, J.F. Gerbeau, and C. Grandmont. A projection semi-implicit scheme for the coupling of an elastic structure with an incompressible fluid. *Int. J. Num. Meth. Engrg.*, 69(4):794–821, 2007.

[FGNQ02] L. Formaggia, J.-F. Gerbeau, F. Nobile, and A. Quarteroni. Numerical treatment of defective boundary conditions for the navier–stokes

equations. *SIAM Journal on Numerical Analysis*, 40(1):376–401, 2002.

[FL13] M. A. Fernández and M. Landajuela. A fully decoupled scheme for the interaction of a thin-walled structure with an incompressible fluid. *Comptes Rendus Mathématique*, 351(3):161–164, 2013.

[FM05] M.A. Fernández and M. Moubachir. A Newton method using exact Jacobians for solving fluid-structure coupling. *Comp. & Struct.*, 83:127–142, 2005.

[FMV13] M.A. Fernández, J. Mullaert, and M. Vidrascu. Explicit Robin-Neumann schemes for the coupling of incompressible fluids with thin-walled structures. *Comput. Methods Appl. Mech. Engrg.*, 267:566–593, 2013.

[FMV15] M. A. Fernández, J. Mullaert, and M. Vidrascu. Generalized Robin-Neumann explicit coupling schemes for incompressible fluid-structure interaction: stability analysis and numerics. *Internat. J. Numer. Methods Engrg.*, 101(3):199–229, 2015.

[FPQ09] L. Formaggia, K. Perktold, and A. Quarteroni. Basic mathematical models and motivations. In *Cardiovascular mathematics*, volume 1 of *MS&A. Model. Simul. Appl.*, pages 47–75. Springer, 2009.

[FQV09] L. Formaggia, A. Quarteroni, and A. Veneziani, editors. *Cardiovascular Mathematics. Modeling and simulation of the circulatory system*, volume 1 of *Modeling, Simulation and Applications*. Springer, 2009.

[FZ09] T.-P. Fries and A. Zilian. On time integration in the XFEM. *Internat. J. Numer. Methods Engrg.*, 79(1):69–93, 2009.

[GBD+94] A. Geist, A. Beguelin, J. Dongarra, W. Jiang, R. Manchek, and V. Sunderam. *PVM–parallel virtual machine: a users' guide and tutorial for networked parallel computing*. MIT Press, Cambridge, Mass., 1994.

[GBS03] P.L. George, H. Borouchaki, and E. Saltel. 'Ultimate' robustness in meshing an arbitrary polyhedron. *Int. J. Numer. Meth. Engng.*, 58(7):1061–1089, 2003.

[GFW10] M.W. Gee, Ch. Förster, and W.A. Wall. A computational strategy for prestressing patient-specific biomechanical problems under finite deformation. *Int. J. Numer. Meth. Biomed. Engng.*, 26(1):52–72, 2010.

[GGCC09] G. Guidoboni, R. Glowinski, N. Cavallini, and S. Canic. Stable loosely-coupled-type algorithm for fluid-structure interaction in blood flow. *J. Comp. Phys.*, 228(18):6916–6937, 2009.

[GKW11] M.W. Gee, U. Küttler, and W. Wall. Truly monolithic algebraic multigrid for fluid-structure interaction. *Int. J. Numer. Meth. Engng.*, 85(8):987–1016, 2011.

[GMS06] J. L. Guermond, P. Minev, and J. Shen. An overview of projection methods for incompressible flows. *Comput. Methods Appl. Mech. Engrg.*, 195(44-47):6011–6045, 2006.

[GPH+01] R. Glowinski, T.-W. Pan, T.I. Hesla, D.D. Joseph, and J. Periaux. A fictitious domain approach to the direct numerical simulation of incompressible viscous flow past moving rigid bodies: Application to particulate flow. *Journal of Computational Physics*, 169(2):363–426, 2001.

[GPHJ99a] R. Glowinski, T.-W. Pan, T.I. Hesla, and D.D. Joseph. A distributed Lagrange multiplier/fictitious domain method for particulate flows. *Int. J. Multiphase Flow*, 25(5):755–794, 1999.

[GPHJ99b] R. Glowinski, T.-W. Pan, T.I. Hesla, and D.D. Joseph. A distributed Lagrange mutiplier/fictitious domain method for particulate flows. *Int. J. of Multiphase Flow*, 25:755–794, 1999.

[GPP94] R. Glowinski, T.W. Pan, and J. Périaux. A fictitious domain method for Dirichlet problem and applications. *Comput. Methods Appl. Mech. Engrg.*, 111(3-4):283–303, 1994.

[GR86] V. Girault and P.-A. Raviart. *Finite element methods for Navier-Stokes equations*. Springer, 1986.

[GRW05] M. Gee, E. Ramm, and W.-A. Wal. Parallel multilevel solution of nonlinear shell structures. *Comput. Methods Appl. Mech. Engrg.*, 194(21-24):2513–2533, 2005.

[GT10] S.r Ganesan and L. Tobiska. Stabilization by local projection for convection-diffusion and incompressible flow problems. *J. Sci. Comput.*, 43(3):326–342, 2010.

[Gue96] J.-L. Guermond. Some implementation of projection methods for Navier-Stokes equations. *M2AN Math. Model. Numer. Anal.*, 30:637–667, 1996.

[Gur81] M.E. Gurtin. *An introduction to continuum mechanics*, volume 158 of *Mathematics in Science and Engineering*. Academic Press Inc., 1981.

[GV03] J.-F. Gerbeau and M. Vidrascu. A quasi-Newton algorithm based on a reduced model for fluid-structure interactions problems in blood flows. *Math. Model. Num. Anal.*, 37(4):631–648, 2003.

[GVF05] J.-F. Gerbeau, M. Vidrascu, and P. Frey. Fluid-structure interaction in blood flows on geometries based on medical imaging. *Comp. & Struct.*, 83(2–3):155–165, 2005.

[GW08] A. Gerstenberger and W.A. Wall. An extended finite element method/Lagrange multiplier based approach for fluid-structure interaction. *Comput. Methods Appl. Mech. Engrg.*, 197(19-20):1699–1714, 2008.

[Han05] P. Hansbo. Nitsche's method for interface problems in computational mechanics. *GAMM-Mitt.*, 28(2):183–206, 2005.

[Hec12] F. Hecht. New development in FreeFem++. *J. Numer. Math.*, 20(3-4):251–265, 2012.

[HFB86] T.J.R. Hughes, L.P. Franca, and M. Balestra. A new finite element formulation for computational fluid dynamics. V. Circumventing the Babuška-Brezzi condition: a stable Petrov-Galerkin formulation of the Stokes problem accommodating equal-order interpolations. *Comput. Methods Appl. Mech. Engrg.*, 59(1):85–99, 1986.

[HFCC13] E. Hachem, S. Feghali, R. Codina, and T. Coupez. Immersed stress method for fluid-structure interaction using anisotropic mesh adaptation. *Internat. J. Numer. Methods Engrg.*, 94(9):805–825, 2013.

[HH92] I. Harari and T.J.R. Hughes. What are C and h?: Inequalities for the analysis and design of finite element methods. *Comput. Methods Appl. Mech. Engrg.*, 97(2):157–192, 1992.

[HH02] A. Hansbo and P. Hansbo. An unfitted finite element method, based on nitsche's method, for elliptic interface problems. *Computer Methods in Applied Mechanics and Engineering*, 191(47–48):5537 – 5552, 2002.

[HH04] A. Hansbo and P. Hansbo. A finite element method for the simulation of strong and weak discontinuities in solid mechanics. *Comput. Methods Appl. Mech. Engrg.*, 193(33-35):3523–3540, 2004.

[HH11] M. Heil and A.L. Hazel. Fluid-structure interaction in internal physiological flows. In *Annual review of fluid mechanics. Volume 43, 2011*, volume 43 of *Annu. Rev. Fluid Mech.*, pages 141–162. Annual Reviews, 2011.

[HHS04] P. Hansbo, J. Hermansson, and T. Svedberg. Nitsche's method combined with space-time finite elements for ALE fluid-structure interaction problems. *Comput. Methods Appl. Mech. Engrg.*, 193(39-41):4195–4206, 2004.

[HLZ81] T.J.R. Hughes, W. K. Liu, and T. K. Zimmermann. Lagrangian-eulerian finite element formulation for incompressible viscous flows. *Computer methods in applied mechanics and engineering*, 29(3):329–349, 1981.

[Hol00] G.A. Holzapfel. *Nonlinear solid mechanics*. John Wiley & Sons, Ltd., Chichester, 2000.

[HR90] J.G. Heywood and R. Rannacher. Finite-element approximation of the nonstationary Navier-Stokes problem. IV. Error analysis for second-order time discretization. *SIAM J. Numer. Anal.*, 27(2):353–384, 1990.

[Hug87] T.J.R. Hughes. *The finite element method*. Prentice Hall, 1987.

[Hur95] A. Hurwitz. Ueber die bedingungen, unter welchen eine gleichung nur wurzeln mit negativen reellen theilen besitzt. *Mathematische Annalen*, 46(2):273–284, 1895.

[HWL12] G. Hou, J. Wang, and A. Layton. Numerical methods for fluid-structure interaction—a review. *Commun. Comput. Phys.*, 12(2):337–377, 2012.

[HWM88] J.C.R Hunt, A. Wray, and P. Moin. Eddies, stream, and convergence zones in turbulent flows. *Center for turbulence research report CTR-S88*, pages 193–208, 1988.

[JS09] M. Juntunen and R. Stenberg. Nitsche's method for general boundary conditions. *Math. Comp.*, 78(267):1353–1374, 2009.

[KFW06] U. Küttler, C. Förster, and W.A. Wall. A solution for the incompressibility dilemma in partitioned fluid–structure interaction with pure Dirichlet fluid domains. *Comput. Mech.*, 38:417–429, 2006.

[KGF+09] U. Küttler, M.W. Gee, C. Förster, A. Comerford, and W.A. Wall. Coupling strategies for biomedical fluid-structure interaction problems. *Int. J. Numer. Meth. Biomed. Engng.*, 26(3-4):305–321, 2009.

[KHS+15] D. Kamensky, M.-C. Hsu, D. Schillinger, J.A. Evans, A. Aggarwal, Y. Bazilevs, M.S. Sacks, and T.J.R. Hughes. An immersogeometric variational framework for fluid–structure interaction: Application to bioprosthetic heart valves. *Comput. Methods Appl. Mech. Engrg.*, 284:1005–1053, 2015.

[Kir76] G Kirchhoff. Vorlesungen über math. *Phys. Teuber, Leipzig*, 1876.

[KS08] P. Kalita and R. Schaefer. Mechanical models of artery walls. *Arch. Comput. Methods Eng.*, 15(1):1–36, 2008.

[LCB06] A. Legay, J. Chessa, and T. Belytschko. An Eulerian-Lagrangian method for fluid-structure interaction based on level sets. *Computer Methods in Applied Mechanics and Engineering*, 195(17):2070–2087, 2006.

[LCY+06] R. Löhner, J. R. Cebral, C. Yang, J. D. Baum, E. L. Mestreau, and O. Soto. Extending the range and applicability of the loose coupling approach for FSI simulations. In H.-J. Bungartz and M. Schäfer, editors, *Fluid-Structure Interaction*, volume 53 of *Lecture Notes in Computational Science and Engineering*, pages 82–100. Springer Berlin Heidelberg, 2006.

[LJGO+03] J.F. LaDisa Jr, I. Guler, L. E. Olson, D. A. Hettrick, J. R. Kersten, D. C. Warltier, and P. S. Pagel. Three-dimensional computational fluid dynamics modeling of alterations in coronary wall shear stress produced by stent implantation. *Annals of biomedical engineering*, 31(8):972–980, 2003.

[LMRHZ13] M. Lukacova-Medvid'ovaa, G. Rusnakovaa, and A. Hundertmark-Zauskovaa. Kinematic splitting algorithm for fluid-structure interaction in hemodynamics. *Comput. Methods Appl. Mech. Engrg.*, 265(1):83–106, 2013.

[Lov27] AEH Love. *The mathematical theory of elasticity*. 1927.

[LPQR12] M. Lombardi, N. Parolini, A. Quarteroni, and G. Rozza. Numerical simulation of sailing boats: Dynamics, FSI, and shape optimization. In G. Buttazzo and A. Frediani, editors, *Variational Analysis and Aerospace Engineering: Mathematical Challenges for Aerospace Design*, Springer Optimization and Its Applications, pages 339–377. Springer, 2012.

[LR12] C. Lehrenfeld and A. Reusken. Nitsche-XFEM with streamline diffusion stabilization for a two-phase mass transport problem. *SIAM J. Sci. Comput.*, 34(5):A2740–A2759, 2012.

[LR13] C. Lehrenfeld and A. Reusken. Analysis of a Nitsche XFEM-DG discretization for a class of two-phase mass transport problems. *SIAM J. Numer. Anal.*, 51(2):958–983, 2013.

[LS05] A. Libai and J. G. Simmonds. *The nonlinear theory of elastic shells*. Cambridge university press, 2005.

[LT94a] P. Le Tallec. Domain decomposition methods in computational mechanics. In J. Tinsley Oden, editor, *Computational Mechanics Advances*, volume 1 (2), pages 121–220. North-Holland, 1994.

[LT94b] P. Le Tallec. Numerical methods for nonlinear three-dimensional elasticity. In *Handbook of numerical analysis, Vol. III*, pages 465–622. North-Holland, 1994.

[LTM00] P. Le Tallec and S. Mani. Numerical analysis of a linearised fluid-structure interaction problem. *Numer. Math.*, 87(2):317–354, 2000.

[LTV96] P. Le Tallec and M. Vidrascu. *Solving large scale structural problems on parallel computers using domain decomposition techniques*, chapter 3, pages 49–82. J. Wiley, 1996.

[Mal69] L. E Malvern. *Introduction to the Mechanics of a Continuous Medium*. Number Monograph. 1969.

[Man93] J. Mandel. Balancing domain decomposition. *Comm. Numer. Methods Engrg.*, 9(3):233–241, 1993.

[MBH+11] Mahdi Esmaily Moghadam, Yuri Bazilevs, Tain-Yen Hsia, Irene E Vignon-Clementel, Alison L Marsden, et al. A comparison of outlet boundary treatments for prevention of backflow divergence with relevance to blood flow simulations. *Computational Mechanics*, 48(3):277–291, 2011.

[MBX+13] P. Moireau, C. Bertoglio, N. Xiao, C.A. Figueroa, C.A. Taylor, D. Chapelle, and J.-F. Gerbeau. Sequential identification of boundary support parameters in a fluid-structure vascular model using patient image data. *Biomech. Model. Mechanobiol.*, 12(3):475–496, 2013.

[MGW09] U.M. Mayer, A. Gerstenberger, and W.A. Wall. Interface handling for three-dimensional higher-order XFEM-computations in fluid–structure interaction. *Internat. J. Numer. Methods Engrg.*, 79(7):846–869, 2009.

[Min51] R. D Mindlin. Influence of rotary inertia and shear on flexural motions of isotropic elastic plates. 1951.

[MLL13] A. Massing, M. G. Larson, and A. Logg. Efficient implementation of finite element methods on nonmatching and overlapping meshes in three dimensions. *SIAM Journal on Scientific Computing*, 35(1):C23–C47, 2013.

[MLLR14] A. Massing, M.G. Larson, A. Logg, and M.E. Rognes. A stabilized Nitsche fictitious domain method for the Stokes problem. *J. Sci. Comput.*, 61(3):604–628, 2014.

[MMH12] R.L. Muddle, M. Mihajlović, and M. Heil. An efficient preconditioner for monolithically-coupled large-displacement fluid-structure interaction problems with pseudo-solid mesh updates. *J. Comput. Phys.*, 231(21):7315–7334, 2012.

[MXA+12] P. Moireau, N. Xiao, M. Astorino, C. A. Figueroa, D. Chapelle, C. A. Taylor, and J-F. Gerbeau. External tissue support and fluid-structure simulation in blood flows. *Biomech. Model. Mechanobiol.*, 11:1–18, 2012.

[New59] N. M Newmark. A method of computation for structural dynamics. *Journal of the Engineering Mechanics Division*, 85(3):67–94, 1959.

[NFGK07] E.P. Newren, A.L. Fogelson, R.D. Guy, and R.M. Kirby. Unconditionally stable discretizations of the immersed boundary equations. *J. Comput. Phys.*, 222(2):702–719, 2007.

[Nit71] J. Nitsche. Über ein Variationsprinzip zur Lösung von Dirichlet-Problemen bei Verwendung von Teilräumen, die keinen Randbedingungen unterworfen sind. *Abh. Math. Sem. Univ. Hamburg*, 36:9–15, 1971.

[Nob01] F. Nobile. *Numerical approximation of fluid-structure interaction problems with application to haemodynamics.* PhD thesis, EPFL, Switzerland, 2001.

[Nor15] D. Nordsletten. Benchmark experiment for validation of fluid-structure interaction algorithms. In *4th International Conference on Computational & Mathematical Biomedical Engineering (CMBE15)*, Cachan (France), July 2015.

[NPV13] F. Nobile, M. Pozzoli, and C. Vergara. Time accurate partitioned algorithms for the solution of fluid-structure interaction problems in haemodynamics. *Computers & Fluids*, 86(0):470–482, 2013.

[NPV14] F. Nobile, M. Pozzoli, and C. Vergara. Inexact accurate partitioned algorithms for fluid-structure interaction problems with finite elasticity in haemodynamics. *J. Comput. Phys.*, 273:598–617, 2014.

[NV08] F. Nobile and C. Vergara. An effective fluid-structure interaction formulation for vascular dynamics by generalized Robin conditions. *SIAM J. Sci. Comput.*, 30(2):731–763, 2008.

[OPR+97] S. Oyre, E.M. Pedersen, S. Ringgaard, P. Boesiger, and W.P. Paaske. In vivo wall shear stress measured by magnetic resonance velocity mapping in the normal human abdominal aorta. *Eur. J. Vasc. Endovasc. Surg.*, 13:263–271, 1997.

[PB01] S. Piperno and P.E. Bournet. Numerical simulations of wind effects on flexible civil engineering structures. *Rev. Eur. Élém. Finis*, 8(5–6):659–687, 2001.

[Pes02] C.S. Peskin. The immersed boundary method. *Acta Numer.*, 11:479–517, 2002.

[PFGVC14] S. Pant, B. Fabrèges, J.-F. Gerbeau, and I.E. Vignon-Clementel. A methodological paradigm for patient-specific multi-scale CFD simulations: from clinical measurements to parameter estimates for individual analysis. *Int. J. Numer. Meth. Biomed. Engng.*, 30(12):1614–1648, 2014.

[PGYLS11] J. Pereira Gomes, S. Yigit, H. Lienhart, and M. Schäfer. Experimental and numerical study on a laminar fluid-structure interaction reference test case. *J. Fluids Struct.*, 27(1):43–61, 2011.

[Poz10] C. Pozrikidis. *Computational hydrodynamics of capsules and biological cells*. Chapman & Hall/CRC Mathematical and Computational Biology. CRC Press, 2010.

[PPdL11] M.P. Païdoussis, S.J. Price, and E. de Langre. *Fluid-structure interactions: cross-flow-induced instabilities*. Cambridge University Press, 2011.

[Pro97] A. Prohl. *Projection and quasi-compressibility methods for solving the incompressible Navier-Stokes equations*. Advances in Numerical Mathematics. B.G. Teubner, Stuttgart, 1997.

[PVV11] Mauro Perego, Alessandro Veneziani, and Christian Vergara. A variational approach for estimating the compliance of the cardiovascular tissue: An inverse fluid-structure interaction problem. *SIAM journal on scientific computing*, 33(3):1181–1211, 2011.

[QQ07] A. Quaini and A. Quarteroni. A semi-implicit approach for fluid-structure interaction based on an algebraic fractional step method. *Math. Models Methods Appl. Sci.*, 17(6):957–983, 2007.

[Rei45] E. Reissner. The effect of transverse shear deformation on the bending of elastic plates. 1945.

[RF15] P. D. Roshchenko, A.and Minev and W. H. Finlay. A time splitting fictitious domain algorithm for fluid–structure interaction problems (a fictitious domain algorithm for fsi). *J. Fluid Struct.*, 58:109–126, 10 2015.

[Ric13] T. Richter. A fully eulerian formulation for fluid-structure-interaction problems. *J. Comput. Phys.*, 233:227–240, 2013.

[Rou77] E. J. Routh. *A treatise on the stability of a given state of motion: particularly steady motion.* Macmillan and Company, 1877.

[RSÖ14] M. Ruess, D. Schillinger, and A.I. Özcan. Weak coupling for isogeometric analysis of non-matching and trimmed multi-patch geometries. *Comput. Methods Appl. Mech. Engrg.*, 269:46–71, 2014.

[RW10] Th. Richter and Th. Wick. Finite elements for fluid–structure interaction in ALE and fully eulerian coordinates. *Comput. Methods Appl. Mech. Engrg.*, 199(41–44):2633–2642, 2010.

[SBG96] B. Smith, P. Bjorstad, and W. Gropp. *Domain Decomposition: Parallel Multilevel Methods for Elliptic Partial Differential Equations.* Cambridge University Press, 1996.

[SDHBVdV04] J.M.A. Stijnen, J. De Hart, P.H.M. Bovendeerd, and F.N. Van de Vosse. Evaluation of a fictitious domain method for predicting dynamic response of mechanical heart valves. *Journal of Fluids and Structures*, 19(6):835–850, 2004.

[SM08] S. Sy and C.M. Murea. A stable time advancing scheme for solving fluid-structure interaction problem at small structural displacements. *Comput. Methods Appl. Mech. Engrg.*, 198(2):210–222, 2008.

[SMdAW14] Y. Sudhakar, J.P. Moitinho de Almeida, and W.A. Wall. An accurate, robust, and easy-to-implement method for integration over arbitrary polyhedra: Application to embedded interface methods. *J. Comput. Phys.*, 273:393–415, 2014.

[SS04] G. R Stuhne and D. A Steinman. Finite-element modeling of the hemodynamics of stented aneurysms. *Journal of biomechanical engineering*, 126(3):382–387, 2004.

[SS06] E. W. Swim and P. Seshaiyer. A nonconforming finite element method for fluid-structure interaction problems. *Comput. Methods Appl. Mech. Engrg.*, 195(17-18):2088–2099, 2006.

[SSCL06] A.-V. Salsac, S.R. Sparks, J.M. Chomaz, and J.C. Lasheras. Evolution of the wall shear stresses during the progressive enlargement of symmetric abdominal aortic aneurysms. *J. Fluid Mech.*, 550:19–51, 2006.

[ST11] T. Sawada and A. Tezuka. LLM and X-FEM based interface modeling of fluid-thin structure interactions on a non-interface-fitted mesh. *Comput. Mech.*, 48(3):319–332, 2011.

[STA] STACOM2013. 4th International Conference on Statistical Atlases and Computational Models of the Heart.

[STB03] K Stein, T Tezduyar, and R Benney. Mesh moving techniques for fluid-structure interactions with large displacements. *Journal of Applied Mechanics*, 70(1):58–63, 2003.

[STB04] K. Stein, T.E. Tezduyar, and R. Benney. Automatic mesh update with the solid-extension mesh moving technique. *Comput. Methods Appl. Mech. Engrg.*, 193(21–22):2019–2032, 2004.

[Ste78] Hans J Stetter. The defect correction principle and discretization methods. *Numerische Mathematik*, 29(4):425–443, 1978.

[Ste95] R. Stenberg. On some techniques for approximating boundary conditions in the finite element method. *J. Comput. Appl. Math.*, 63(1-3):139–148, 1995.

[SW14] B. Schott and W.A. Wall. A new face-oriented stabilized XFEM approach for 2D and 3D incompressible Navier-Stokes equations. *Comput. Methods Appl. Mech. Engrg.*, 276:233–265, 2014.

[TDK+99] C. A Taylor, M. T Draney, J. P Ku, D. Parker, B. N Steele, K. Wang, and C. K Zarins. Predictive medicine: computational techniques in therapeutic decision-making. *Computer aided surgery*, 4(5):231–247, 1999.

[Tem68] R. Temam. Une méthode d'approximation de la solution des équations de Navier-Stokes. *Bull. Soc. Math. France*, 96:115–152, 1968.

[Tez92] T.E. Tezduyar. Stabilized finite element formulations for incompressible flow computations. In *Advances in applied mechanics, Vol. 28*, volume 28 of *Adv. Appl. Mech.*, pages 1–44. Academic Press, Boston, MA, 1992.

[Thi08] M. Thiriet. *Biology and Mechanics of Blood Flows. Part II: Mechanics and Medical Aspects*. CRM Series in Mathematical Physics. Springer, 2008.

[THR+10] S. Turek, J. Hron, M. Razzaq, H. Wobker, and M. Schäfer. Numerical benchmarking of fluid-structure interaction: A comparison of different discretization and solution approaches. In H.-J. Bungartz, M. Mehl, and M. Schäfer, editors, *Fluid Structure Interaction II*, volume 73 of *Lecture Notes in Computational Science and Engineering*, pages 413–424. Springer Berlin Heidelberg, 2010.

[TT12] K. Takizawa and T.E. Tezduyar. Computational methods for parachute fluid-structure interactions. *Arch. Comput. Methods Eng.*, 19:125–169, 2012.

[TTBA14] K. Takizawa, T.E. Tezduyar, A. Buscher, and S. Asada. Space–time interface-tracking with topology change (ST-TC). *Comput. Mech.*, 54(4):955–971, 2014.

[vB11] E. H. van Brummelen. Partitioned iterative solution methods for fluid-structure interaction. *Int. Jour. Num. Meth. Fluids*, 65(1-3):3–27, 2011.

[VJBH+09] D. Valdez-Jasso, H.T. Banks, M.A. Haider, D. Bia, Y. Zocalo, R.L. Armentano, and M.S. Olufsen. Viscoelastic models for passive arterial wall dynamics. *Adv. Appl. Math. Mech.*, 1(2):151–165, 2009.

[WGMF12] K. Wang, J. Grétarsson, A. Main, and C. Farhat. Computational algorithms for tracking dynamic fluid-structure interfaces in embedded boundary methods. *Internat. J. Numer. Methods Fluids*, 70(4):515–535, 2012.

[Wic11] T. Wick. Fluid-structure interactions using different mesh motion techniques. *Comp. & Struct.*, 89(13–14):1456–1467, 2011.

[Wic13] T. Wick. Fully eulerian fluid–structure interaction for time-dependent problems. *Computer Methods in Applied Mechanics and Engineering*, 255:14–26, 2013.

[YM10] J. Young and S. Mitran. A numerical model of cellular blebbing: A volume-conserving, fluid-structure interaction model of the entire cell. *J. Biomech.*, 43(2):210–220, 2010.

[YSH08] S. Yigit, M. Schäfer, and M. Heck. Grid movement techniques and their influence on laminar fluid–structure interaction computations. *J. Fluids Struct.*, 24(6):819–832, 2008.

[Yu05] Z. Yu. A dlm/fd method for fluid/flexible-body interactions. *Journal of computational physics*, 207(1):1–27, 2005.

[ZGWL04] L. Zhang, A. Gerstenberger, X. Wang, and W.K. Liu. Immersed finite element method. *Comput. Methods Appl. Mech. Engrg.*, 193(21-22):2051–2067, 2004.

[ZL08] A. Zilian and A. Legay. The enriched space-time finite element method (EST) for simultaneous solution of fluid-structure interaction. *Internat. J. Numer. Methods Engrg.*, 75(3):305–334, 2008.

[Zun13] P. Zunino. Analysis of backward Euler/extended finite element discretization of parabolic problems with moving interfaces. *Comput. Methods Appl. Mech. Engrg.*, 258:152–165, 2013.